

## Flavor Physics in the Quark Sector

M. Antonelli<sup>a</sup> D. M. Asner<sup>b</sup> D. Bauer<sup>c</sup> T. Becher<sup>d</sup> M. Beneke<sup>e</sup>  
A. J. Bevan<sup>f</sup> M. Blanke<sup>g,h</sup> C. Bloise<sup>a</sup> M. Bona<sup>i</sup> A. Bondar<sup>j</sup> C. Bozzi<sup>k</sup>  
J. Brod<sup>l</sup> N. Cabibbo<sup>m,n</sup> A. Carbone<sup>o</sup> G. Cavoto<sup>m</sup> V. Cirigliano<sup>p</sup>  
M. Ciuchini<sup>q</sup> J. P. Coleman<sup>r</sup> D. P. Cronin-Hennessy<sup>s</sup> J. P. Dalseno<sup>t</sup>  
C. H. Davies<sup>u</sup> F. Di Lodovico<sup>f</sup> J. Dingfelder<sup>v</sup> Z. Dolezal<sup>w</sup> S. Donati<sup>x</sup>  
W. Dungen<sup>y</sup> U. Egede<sup>c</sup> R. Faccini<sup>m,n</sup> T. Feldmann<sup>g</sup> F. Ferroni<sup>m,n</sup>  
J. M. Flynn<sup>ce</sup> E. Franco<sup>m</sup> M. Fujikawa<sup>z</sup> I. K. Furic<sup>cc</sup> P. Gambino<sup>aa,ab</sup>  
E. Gardi<sup>ac</sup> T. J. Gershon<sup>ad</sup> S. Giagu<sup>m,n</sup> E. Golowich<sup>ae</sup> T. Goto<sup>t</sup>  
C. Greub<sup>be</sup> C. Grojean<sup>af</sup> D. Guadagnoli<sup>g</sup> U. A. Haisch<sup>ag</sup> R. F. Harr<sup>ah</sup>  
A. H. Hoang<sup>h</sup> G. Isidori<sup>a</sup> D. E. Jaffe<sup>ai</sup> A. Jüttner<sup>aj</sup> S. Jäger<sup>g</sup>  
A. Khodjamirian<sup>ak</sup> P. Koppenburg<sup>c</sup> R. V. Kowalewski<sup>al</sup> P. Krokovny<sup>t</sup>  
A. S. Kronfeld<sup>d</sup> J. Laiho<sup>am</sup> G. Lanfranchi<sup>a</sup> T. E. Latham<sup>ad</sup> J. Libby<sup>ao</sup>  
A. Limosani<sup>ap</sup> D. Lopes Pegna<sup>aq</sup> C. D. Lu<sup>ar</sup> V. Lubicz<sup>q,as</sup> E. Lunghi<sup>d</sup>  
V. G. Lüth<sup>r</sup> K. Maltman<sup>au</sup> W. J. Marciano<sup>ai</sup> E. C. Martin<sup>an</sup>  
G. Martinelli<sup>m,n</sup> F. Martinez-Vidal<sup>av</sup> A. Masiero<sup>aw,ay</sup> V. Mateu<sup>h</sup>  
F. Mescia<sup>az</sup> G. Mohanty<sup>ad,ba</sup> M. Moulson<sup>a</sup> M. Neubert<sup>bb</sup> H. Neufeld<sup>bc</sup>  
S. Nishida<sup>t</sup> N. Offen<sup>bd</sup> M. Palutan<sup>a</sup> P. Paradisi<sup>g</sup> Z. Parsa<sup>ai</sup>  
E. Passemar<sup>be</sup> M. Patel<sup>i</sup> B. D. Pecjak<sup>bg</sup> A. A. Petrov<sup>ah</sup> A. Pich<sup>av</sup>  
M. Pierini<sup>i</sup> B. Plaster<sup>bh</sup> A. Powell<sup>br</sup> S. Prell<sup>bi</sup> J. Rademaker<sup>cd</sup>  
M. Rescigno<sup>m</sup> S. Ricciardi<sup>bj</sup> P. Robbe<sup>i,bf</sup> E. Rodrigues<sup>u</sup> M. Rotondo<sup>aw</sup>  
R. Sacco<sup>f</sup> C. J. Schilling<sup>bk</sup> O. Schneider<sup>bℓ</sup> E. E. Scholz<sup>d</sup> B. A. Schumm<sup>cb</sup>  
C. Schwanda<sup>y</sup> A. J. Schwartz<sup>bm</sup> B. Sciascia<sup>a</sup> J. Serrano<sup>bf</sup> J. Shigemitsu<sup>bn</sup>  
I. J. Shipsey<sup>ca</sup> A. Sibidanov<sup>j,a</sup> L. Silvestrini<sup>m</sup> F. Simonetto<sup>ay</sup> S. Simula<sup>q</sup>  
C. Smith<sup>be,bo</sup> A. Soni<sup>ai</sup> L. Sonnenschein<sup>i,bp</sup> V. Sordini<sup>bq</sup> M. Sozzi<sup>x</sup>  
T. Spadaro<sup>a</sup> P. Spradlin<sup>br</sup> A. Stocchi<sup>bf</sup> N. Tantalò<sup>bs</sup> C. Tarantino<sup>q,as</sup>  
A. V. Telnov<sup>aq</sup> D. Tonelli<sup>d</sup> I. S. Towner<sup>bt</sup> K. Trabelsi<sup>t</sup> P. Urquijo<sup>ap</sup>  
R. S. Van de Water<sup>ai</sup> R. J. Van Kooten<sup>bu</sup> J. Virto<sup>m,n</sup> G. Volpi<sup>x</sup>  
R. Wanke<sup>bw</sup> S. Westhoff<sup>bo</sup> G. Wilkinson<sup>br</sup> M. Wingate<sup>bx</sup> Y. Xie<sup>ac</sup>  
J. Zupan<sup>i,by,bz</sup>

- <sup>a</sup>INFN LNF, Via Enrico Fermi 40, 00044 Frascati, Italy
- <sup>b</sup>Carleton University, 1125 Colonel By Drive, Ottawa, ON, Canada K1S 5B6
- <sup>c</sup>Imperial College London, London, SW7 2AZ, United Kingdom
- <sup>d</sup>Fermi National Accelerator Laboratory, P.O. Box 500 Batavia, IL 60510-5011, USA
- <sup>e</sup>Institut fuer Theoretische Physik E, RWTH Aachen University, 52056, Germany
- <sup>f</sup>Queen Mary, University of London, E1 4NS, United Kingdom
- <sup>g</sup>Technische Universität München, Excellence Cluster Universe, Boltzmannstraße 2, 85748 Garching, Germany
- <sup>h</sup>Max-Planck-Institut für Physik, Fohringer Ring 6, 80805 München, Germany
- <sup>i</sup>CERN CH-1211 Geneve 23, Switzerland
- <sup>j</sup>Budker Institute of Nuclear Physics, 11, Prosp. Akademika Lavrentieva Novosibirsk 630090, Russian Federation
- <sup>k</sup>INFN Sez. di Ferrara, Polo Scientifico e Tecnologico. Edificio C. Via Saragat, 1. 44100 Ferrara, Italy
- <sup>l</sup>Universität Karlsruhe, Liefer- und Besuchsanschrift: Kaiserstraße 12 - 76131 Karlsruhe Germany
- <sup>m</sup>INFN Sez. di Roma, Piazzale Aldo Moro, 2 00185 Roma, Italy
- <sup>n</sup>Università di Roma 'Sapienza', Dipartimento di Fisica, Piazzale Aldo Moro, 5 00185, Roma, Italy
- <sup>o</sup>INFN Sez. di Bologna, Via Irnerio 46, I-40126 Bologna, Italy
- <sup>p</sup>Los Alamos National Laboratory, Los Alamos, NM 87545, USA
- <sup>q</sup>INFN Sez. di Roma Tre, Via della Vasca Navale, 84 00146 Rome, Italy
- <sup>r</sup>SLAC National Accelerator Laboratory, 2575 Sand Hill Road, Menlo Park, CA 94025
- <sup>s</sup>University of Minnesota, Minneapolis, Minnesota 55455, USA
- <sup>t</sup>High Energy Accelerator Research Organization (KEK), 1-1 Oho, Tsukuba, Ibaraki 305-0801 Japan
- <sup>u</sup>University of Glasgow, Glasgow G12 8QQ, UK
- <sup>v</sup>Physikalisches Institut Freiburg, Hermann-Herder-Str.3, 79104 Freiburg, Germany
- <sup>w</sup>IPNP, Charles University in Prague, Faculty of Mathematics and Physics, V Holesovickach 2, 180 00 Prague 8, Czech Republic
- <sup>x</sup>Dipartimento di Fisica, Università di Pisa, Largo Pontecorvo 3, 56126 Pisa, Italy
- <sup>y</sup>Institute of High Energy Physics, A-1050 Vienna
- <sup>z</sup>Nara Women's University, Nara, Japan
- <sup>aa</sup>INFN Sez. di Torino, Via Pietro Giuria 1, 10125 Torino, Italy
- <sup>ab</sup>Dip. di Fisica Teorica, Univ. di Torino, Via Pietro Giuria 1, 10125 Torino, Italy
- <sup>ac</sup>University of Edinburgh, Edinburgh EH9 3JZ, United Kingdom
- <sup>ad</sup>Department of Physics, University of Warwick, Coventry CV4 7AL, United Kingdom
- <sup>ae</sup>University of Massachusetts, Amherst, Massachusetts 01003, USA
- <sup>af</sup>CERN PH-TH, CH-1211, Geneve 23, Switzerland
- <sup>ag</sup>Johannes Gutenberg-Universität, 55099 Mainz, Germany
- <sup>ah</sup>Wayne State University, Detroit, MI 48202, USA
- <sup>ai</sup>Brookhaven National Laboratory, Upton, P.O. Box 5000 Upton, NY 11973-5000 (631)344-8000, USA
- <sup>aj</sup>Institut fuer Theoretische Kernphysik, Johannes-Gutenberg Universitaet Mainz, Johann-Joachim-Becher Weg 45, 55099 Mainz, Germany
- <sup>ak</sup>Universität Siegen, Walter Flex Str.3, Emmy Noether Campus, D-57068 Siegen, Germany
- <sup>al</sup>University of Victoria, Victoria, British Columbia, Canada V8W 3P6
- <sup>am</sup>Washington University, St. Louis, Missouri 63130, USA
- <sup>an</sup>University of California at Irvine, Irvine, California 92697, USA
- <sup>ao</sup>Indian Institute of Technology Madras, IITM Post Office, Chennai, 600032, India
- <sup>ap</sup>The University of Melbourne, The School of Physics, Victoria 3010, Australia
- <sup>aq</sup>Princeton University, Princeton, New Jersey 08544, USA
- <sup>ar</sup>Institute of High Energy Physics, Chinese Academy of Sciences, 19B YuquanLu, Shijingshan District, Beijing, 100049, China
- <sup>as</sup>Università di Roma Tre, Dipartimento di Fisica 'E. Amaldi', Università degli Studi Roma Tre, Via della Vasca Navale 84, 00146 Roma, Italy
- <sup>at</sup>Stanford University, Stanford, CA 94309, USA
- <sup>au</sup>York University, Toronto, ON M3J 1P3, Canada
- <sup>av</sup>IFIC, Universitat de Valencia-CSIC, E-46071 Valencia, Spain

- <sup>aw</sup> *INFN Sez. di Padova, Via F. Marzolo 8, 35131 Padova, Italy*
- <sup>ay</sup> *Universita' di Padova, Dipartimento di Fisica, Via F. Marzolo 8, 35131 Padova, Italy*
- <sup>az</sup> *Universitat de Barcelona, Facultat de Fisica, Departament ECM & ICC, E-08028 Barcelona, Spain*
- <sup>ba</sup> *Tata Institute of Fundamental Research, Homi Bhabha Road, Mumbai 400 005, India*
- <sup>bb</sup> *Institut für Physik, Johannes Gutenberg Universität, Mainz, Staudingerweg 7, 55128, Germany*
- <sup>bc</sup> *Faculty of Physics, University of Vienna, Boltzmanngasse 5, A-1090, Wien, Austria*
- <sup>bd</sup> *Laboratoire de Physique Theorique, CNRS/Univ. Paris-Sud 11 (UMR 8627), F-91405 Orsay, France*
- <sup>be</sup> *Institute for theoretical physics, University of Bern, Sidlerstrasse 5, 3012 Bern, Switzerland*
- <sup>bf</sup> *Laboratoire del Accelérateur Lineaire, Université Paris 11, UMR 8607, Batiment 200 91898 Orsay cedex, France*
- <sup>bg</sup> *THEP, Johannes Gutenberg-Universität, 55099 Mainz, Germany*
- <sup>bh</sup> *University of Kentucky, Lexington, KY 40506, USA*
- <sup>bi</sup> *Iowa State University, Ames, Iowa 50011-3160, USA*
- <sup>bj</sup> *STFC Rutherford Appleton Laboratory, Chilton, Didcot, OX11 0QX, United Kingdom*
- <sup>bj</sup> *University of Texas at Austin, Austin, Texas 78712, USA*
- <sup>bℓ</sup> *Ecole Polytechnique Federale de Lausanne (EPFL), CH 1015 (Centre Est) Lausanne, Switzerland*
- <sup>bm</sup> *University of Cincinnati, P.O. Box 210011, Cincinnati, Ohio 45221, USA*
- <sup>bn</sup> *Ohio State University, Columbus, Ohio 43210, USA*
- <sup>bo</sup> *Universität Karlsruhe, Institut für Theoretische Teilchenphysik, D-76128 Karlsruhe, Germany*
- <sup>bp</sup> *Laboratoire de Physique Nucleaire et de Hautes Energies, LPNHE - Tour 43 Rez-de-chaussée - 4 place Jussieu - 75252 PARIS CEDEX*
- <sup>bq</sup> *ETH Zurich, HG Raemistrasse 101 8092 Zurich Switzerland*
- <sup>br</sup> *University of Oxford, Oxford, United Kingdom*
- <sup>bs</sup> *INFN Sezione di Roma 'Tor Vergata' Via della Ricerca Scientifica, 1 00133 Roma - Italy*
- <sup>bt</sup> *Physics Department, Queen's University, Kingston, Ontario K7L 3N6, Canada*
- <sup>bu</sup> *Indiana University, Bloomington, IN 47405, USA*
- <sup>bw</sup> *Universität Mainz, Institut für Physik, 55099 Mainz, Germany*
- <sup>bx</sup> *University of Cambridge, DAMTP, Wilberforce Road, Cambridge CB3 0WA, UK*
- <sup>by</sup> *Jozef Stefan Institute, Jamova cesta 39, 1000 Ljubljana, Slovenia*
- <sup>bz</sup> *University of Ljubljana, Kongresni trg 12, 1000 Ljubljana, Slovenija*
- <sup>ca</sup> *Purdue University, West Lafayette, IN 47907, USA*
- <sup>cb</sup> *University of California at Santa Cruz, Institute for Particle Physics, Santa Cruz, California 95064, USA*
- <sup>cc</sup> *University of Florida, Gainesville, FL 32611, USA*
- <sup>cd</sup> *University of Bristol, Bristol, BS8 1TL, UK*
- <sup>ce</sup> *School of Physics & Astronomy, University of Southampton, Southampton SO17 1BJ, United Kingdom*

---

## Abstract

In the past decade, one of the major challenges of particle physics has been to gain an in-depth understanding of the role of quark flavor. In this time frame, measurements and the theoretical interpretation of their results have advanced tremendously. A much broader understanding of flavor particles has been achieved, apart from their masses and quantum numbers, there now exist detailed measurements of the characteristics of their interactions allowing stringent tests of Standard Model predictions. Among the most interesting phenomena of flavor physics is the violation of the CP symmetry that has been subtle and difficult to explore. In the past, observations of CP violation were confined to neutral  $K$  mesons, but since the early 1990s, a large number of CP-violating processes have been studied in detail in neutral  $B$  mesons. In parallel, measurements of the couplings of the heavy quarks and the dynamics for their decays

in large samples of  $K$ ,  $D$ , and  $B$  mesons have been greatly improved in accuracy and the results are being used as probes in the search for deviations from the Standard Model.

In the near future, there will be a transition from the current to a new generation of experiments, thus a review of the status of quark flavor physics is timely. This report is the result of the work of the physicists attending the 5<sup>th</sup> CKM workshop, hosted by the University of Rome "La Sapienza", September 9-13, 2008. It summarizes the results of the current generation of experiments that is about to be completed and it confronts these results with the theoretical understanding of the field which has greatly improved in the past decade.

*Key words:*

*PACS:*

## Contents

1	Introduction	7
1.1	CKM matrix and the Unitarity Triangle	7
1.1.1	Standard parametrization	8
1.1.2	Wolfenstein parametrization and its generalization	8
1.1.3	Unitarity Triangle	9
1.2	Plan of the report	11
2	Theory Primers	12
2.1	Effective Weak Hamiltonians	12
2.1.1	$\Delta F = 1$ effective weak Hamiltonians	16
2.1.2	$\Delta F = 2$ effective weak Hamiltonians	19
2.2	Factorization	20
2.3	Lattice QCD	23
2.4	Chiral Perturbation Theory	29
2.5	Beyond the Standard Model	31
2.5.1	Model-independent approaches and the MFV hypothesis	32
2.5.2	The Minimal Supersymmetric extension of the SM (MSSM)	37
2.5.3	Non-supersymmetric extensions of the Standard Model	41
3	Experimental Primers	42
3.1	Overview of experiments	42
3.1.1	Kaon experiments	42
3.1.2	$B$ Factories	45
3.1.3	$\tau$ -charm Factories	47
3.1.4	Hadron Colliders	48
3.2	Common experimental tools	52
3.2.1	Time-dependent measurements	52
3.2.2	$B$ Flavor Tagging	53
3.2.3	Vertexing	58
3.2.4	Charged Particle Identification	61
3.2.5	Background suppression	64
3.2.6	Recoil Tagging Technique	67
3.2.7	Dalitz Plot Analysis	70
4	Determination of $ V_{ud} $ and $ V_{us} $ .	71
4.1	$V_{ud}$ from nuclear decays	72
4.2	$V_{ud}$ from neutron decay	76

4.3	$V_{ud}$ from pionic beta decay	78
4.4	Determination of $ V_{us} $ from $K_{\ell 2}$ and $K_{\ell 3}$	79
4.4.1	$P_{\ell 2}$ ( $P = \pi, K$ ) rates within the SM	79
4.4.2	$K_{\ell 3}$ rates within the SM	80
4.4.3	$K_{\ell 3}$ form factors	82
4.4.4	Lattice determinations of $f_+(0)$ and $f_K/f_\pi$	85
4.4.5	Data Analysis	90
4.5	$ V_{us} $ determination from tau decays	98
4.6	Physics Results	100
4.6.1	Determination of $ V_{us}  \times f_+(0)$ and $ V_{us} / V_{ud}  \times f_K/f_\pi$	100
4.6.2	A test of lattice calculation: the Callan-Treiman relation	101
4.6.3	Test of Cabibbo Universality or CKM unitarity	103
4.6.4	Tests of Lepton Flavor Universality in $K_{\ell 2}$ decays	108
5	Semileptonic $B$ and $D$ decays: $ V_{cx} $ and $ V_{ub} $	109
5.1	Exclusive semileptonic $B$ and $D$ decays to light mesons $\pi$ and $K$	110
5.1.1	Theoretical Background	110
5.1.2	Measurements of $D$ Branching Fractions and $q^2$ Dependence	115
5.1.3	Measurements of $B$ branching fractions and $q^2$ dependence	122
5.1.4	Determination of $ V_{cs} ,  V_{cd} ,  V_{ub} $	126
5.2	$B \rightarrow D^{(*)}\ell\nu$ decays for $ V_{cb} $	128
5.2.1	Theoretical background: HQS and HQET	128
5.2.2	Measurements and Tests	134
5.2.3	Determination of Form Factors and $ V_{cb} $	137
5.3	Inclusive CKM-favored $B$ decays	138
5.3.1	Theoretical Background	138
5.3.2	Measurements of Moments	141
5.3.3	Global Fits for $ V_{cb} $ and $m_b$	142
5.4	Inclusive CKM-suppressed $B$ decays	144
5.4.1	Theoretical Overview	144
5.4.2	Review of $m_b$ determinations	147
5.4.3	Measurements and tests	153
5.4.4	Determination of $ V_{ub} $	156
6	Rare decays and measurements of $ V_{td}/V_{ts} $	159
6.1	Introduction	159
6.2	Inclusive $B \rightarrow X_{s,d}\gamma$	160
6.2.1	Theory of inclusive $B \rightarrow X_{s,d}\gamma$	160
6.2.2	Experimental methods and status of $B \rightarrow X_{s,d}\gamma$	163
6.2.3	Theory of photon energy spectrum and moments	165
6.2.4	Experimental results of photon energy spectrum and moments	167
6.3	Exclusive $B \rightarrow V\gamma$ decays	168
6.3.1	Theory of exclusive $B \rightarrow V\gamma$ decays	168
6.3.2	Experimental results for exclusive $B \rightarrow V\gamma$ decays	170
6.3.3	Determinations of $ V_{td}/V_{ts} $ from $b \rightarrow (s, d)\gamma$	173
6.4	Purely leptonic rare decays	174
6.4.1	Theory of purely leptonic rare decays	174
6.4.2	Experimental results on purely leptonic rare decays	175
6.5	Semileptonic modes	176
6.5.1	$B \rightarrow D\tau\nu$ modes	176
6.6	Semileptonic neutral currents decays	177
6.6.1	Theory of inclusive $B \rightarrow X_s\ell^+\ell^-$	177
6.6.2	Experimental results on inclusive $B \rightarrow X_s\ell^+\ell^-$	179
6.6.3	Theory of exclusive $b \rightarrow s\ell^+\ell^-$ modes	180
6.6.4	Angular observables in $B \rightarrow K^*\ell^+\ell^-$	183
6.6.5	Experimental results on exclusive $b \rightarrow (s, d)\ell^+\ell^-$	185
6.6.6	Rare $K \rightarrow \pi\nu\bar{\nu}, \ell^+\ell^-$ decays in and beyond the SM	189
6.6.7	Experimental status of $K \rightarrow \pi\nu\bar{\nu}$ and $K_L \rightarrow \pi\ell^+\ell^-$	191

6.7	Rare D meson decays	192
6.7.1	Rare leptonic decays	192
6.7.2	$D$ and $D_s$ decay constants from lattice QCD	193
6.7.3	Experimental results on $f_D$	197
7	Measurements of $\Gamma$ , $\Delta\Gamma$ , $\Delta m$ and mixing-phases in $K$ , $B$ , and $D$ meson decays	199
7.1	The $K$ -meson system	203
7.1.1	Theoretical prediction for $\Delta M_K$ , $\varepsilon_K$ , and $\varepsilon'_K/\varepsilon_K$	203
7.1.2	Experimental methods and results	206
7.2	The B-meson system	209
7.2.1	Lifetimes, $\Delta\Gamma_{B_q}$ , $A_{SL}^q$ and $\Delta M_{B_q}$	209
7.2.2	$B$ -mesons mixing	213
7.2.3	Measurements of the angle $\beta$ in tree dominated processes	214
7.2.4	Measurement of the $B_s$ meson mixing phase	216
7.3	The D-meson system	220
7.3.1	Theoretical prediction for $\Delta M_D$ and CP violation within the SM and beyond	220
7.3.2	Experimental results	221
7.4	Future Outlook	225
7.4.1	$B$ meson mixing and lifetimes	225
7.4.2	Measurements of the $B_s$ meson mixing phase	226
7.4.3	$D^0$ mixing and CP violation	228
8	Measurement of the angle $\gamma$ in tree dominated processes	231
8.1	Overview of Theoretically Pristine Approaches to Measure $\gamma$	231
8.2	Experimental results on $\gamma$ from $B \rightarrow DK$ decays	233
8.2.1	GLW analyses	233
8.2.2	ADS analyses	234
8.2.3	Dalitz plot analyses	236
8.2.4	Other techniques	239
8.3	Outlook on the $\gamma$ measurement	241
8.3.1	Model-independent Method	241
8.3.2	Prospects for LHCb	244
9	Measurements of the angles of the unitarity triangle in charmless hadronic $B$ decays	246
9.1	Theory estimates for hadronic amplitudes	246
9.1.1	Angles, physical amplitudes, topological amplitudes	246
9.1.2	Tree amplitudes: results	249
9.1.3	Penguin amplitudes: results	252
9.1.4	Application to angle measurements	253
9.1.5	Prospects	254
9.2	Measurement of $\beta$	255
9.2.1	Theoretical aspects	255
9.2.2	Experimental results	256
9.3	Measurements of $\alpha$	260
9.3.1	Theoretical aspects	260
9.3.2	Experimental measurements	264
9.4	Measurements of $\gamma$ in charmless hadronic $B$ decays	273
9.4.1	Constraints from $B_{(s)} \rightarrow hh$	273
9.4.2	Constraints from $B \rightarrow K\pi\pi$ Dalitz-plot analyses	274
10	Global Fits to the Unitarity Triangle and Constraints on New Physics	278
10.1	Constraints on the Unitarity Triangle Parameters	279
10.1.1	Fitting technique	279
10.1.2	Inputs to the Unitarity Triangle Analysis	281
10.1.3	Results of Global Fits	282
10.1.4	Impact of the Uncertainties on Theoretical Quantities	284
10.1.5	Comparison with the Results of CKMfitter	285
10.2	CKM angles in the presence of New Physics	289
10.2.1	Model independent constraints on New Physics from global fits	289
10.2.2	Impact of flavor physics measurements on grand unified	292

10.2.3 New physics in extra-dimension models	295
11 Acknowledgements	298
References	299

## 1. Introduction

In the past decade, one of the major challenges of particle physics has been to gain an in-depth understanding of the role of quark flavor. In this time frame, measurements and the theoretical interpretation of their results have advanced tremendously. A much broader understanding of flavor particles has been achieved, apart from their masses and quantum numbers, there now exist detailed measurements of the characteristics of their interactions allowing stringent tests of Standard Model predictions.

Among the most interesting phenomena of flavor physics is the violation of the CP symmetry that has been subtle and difficult to explore. In the past, observations of CP violation were confined to neutral  $K$  mesons, but since the early 1990s, a large number of CP-violating processes have been studied in detail in neutral  $B$  mesons. In parallel, measurements of the couplings of the heavy quarks and the dynamics for their decays in large samples of  $K$ ,  $D$ , and  $B$  mesons have been greatly improved in accuracy and the results are being used as probes in the search for deviations from the Standard Model.

In the near future, there will be a transition from the current to a new generation of experiments, thus a review of the status of quark flavor physics is timely. This report is the result of the work of the physicists attending the 5<sup>th</sup> CKM workshop, hosted by the University of Rome "La Sapienza", September 9-13, 2008. It summarizes the results of the current generation of experiments that is about to be completed and it confronts these results with the theoretical understanding of the field which has greatly improved in the past decade.

In this section the basic formalism of the study of the quark couplings will be introduced and the relationship between CKM matrix elements and observables will be discussed. The last paragraph will then detail the plan of the report and the content of the rest of the sections.

### 1.1. CKM matrix and the Unitarity Triangle

The unitary CKM matrix [1, 2] connects the *weak eigenstates* ( $d', s', b'$ ) and the corresponding *mass eigenstates*  $d, s, b$  (in both basis the up-type mass matrix is diagonal and the up-type quarks are unaffected by this transformation):

$$\begin{pmatrix} d' \\ s' \\ b' \end{pmatrix} = \begin{pmatrix} V_{ud} & V_{us} & V_{ub} \\ V_{cd} & V_{cs} & V_{cb} \\ V_{td} & V_{ts} & V_{tb} \end{pmatrix} \begin{pmatrix} d \\ s \\ b \end{pmatrix} \equiv \hat{V}_{\text{CKM}} \begin{pmatrix} d \\ s \\ b \end{pmatrix}. \quad (1)$$

The CKM matrix contains all the flavor-changing and CP-violating couplings of the Standard Model.

Several parameterizations of the CKM matrix have been proposed in the literature. This report will use the standard parametrization [3] recommended by the Particle Data

31 Group [4]. We also introduce the generalization of the Wolfenstein parametrization [5]  
 32 presented in [6] and discuss its connection to the Unitarity Triangle parameters.

33 1.1.1. *Standard parametrization*

With  $c_{ij} = \cos \theta_{ij}$  and  $s_{ij} = \sin \theta_{ij}$  ( $i, j = 1, 2, 3$ ), the standard parametrization is given by:

$$\hat{V}_{\text{CKM}} = \begin{pmatrix} c_{12}c_{13} & s_{12}c_{13} & s_{13}e^{-i\delta} \\ -s_{12}c_{23} - c_{12}s_{23}s_{13}e^{i\delta} & c_{12}c_{23} - s_{12}s_{23}s_{13}e^{i\delta} & s_{23}c_{13} \\ s_{12}s_{23} - c_{12}c_{23}s_{13}e^{i\delta} & -s_{23}c_{12} - s_{12}c_{23}s_{13}e^{i\delta} & c_{23}c_{13} \end{pmatrix}, \quad (2)$$

34 where  $\delta$  is the phase necessary for CP violation.  $c_{ij}$  and  $s_{ij}$  can all be chosen to be positive  
 35 and  $\delta$  may vary in the range  $0 \leq \delta \leq 2\pi$ . However, measurements of CP violation in  
 36  $K$  decays force  $\delta$  to be in the range  $0 < \delta < \pi$ , as the sign of the relevant hadronic  
 37 parameter is fixed.

From phenomenological studies we know that  $s_{13}$  and  $s_{23}$  are small numbers:  $\mathcal{O}(10^{-3})$   
 and  $\mathcal{O}(10^{-2})$ , respectively. Consequently, to a very good accuracy,

$$s_{12} \simeq |V_{us}|, \quad s_{13} \simeq |V_{ub}|, \quad s_{23} \simeq |V_{cb}|. \quad (3)$$

38 Thus these three parameters can be extracted from tree level decays mediated by the  
 39 transitions  $s \rightarrow u$ ,  $b \rightarrow u$  and  $b \rightarrow c$ , respectively. The remaining parameter, the phase  $\delta$ ,  
 40 is responsible for the violation of the CP symmetry. It can clearly be extracted from CP-  
 41 violating transitions but also from CP-conserving ones using three-generation unitarity,  
 42 through the construction of the Unitarity Triangle, as discussed below.

43 1.1.2. *Wolfenstein parametrization and its generalization*

The absolute values of the elements of the CKM matrix show a hierarchical pattern  
 with the diagonal elements being close to unity, the elements  $|V_{us}|$  and  $|V_{cd}|$  being of  
 order 0.2, the elements  $|V_{cb}|$  and  $|V_{ts}|$  of order  $4 \cdot 10^{-2}$  whereas  $|V_{ub}|$  and  $|V_{td}|$  are of order  
 $5 \cdot 10^{-3}$ . The Wolfenstein parametrization [5] exhibits this hierarchy in a transparent  
 manner. It is an approximate parametrization of the CKM matrix in which each element  
 is expanded as a power series in the small parameter  $\lambda \sim |V_{us}| \approx 0.22$ ,

$$\hat{V} = \begin{pmatrix} 1 - \frac{\lambda^2}{2} & \lambda & A\lambda^3(\varrho - i\eta) \\ -\lambda & 1 - \frac{\lambda^2}{2} & A\lambda^2 \\ A\lambda^3(1 - \varrho - i\eta) & -A\lambda^2 & 1 \end{pmatrix} + \mathcal{O}(\lambda^4), \quad (4)$$

and the set (3) is replaced by

$$\lambda, \quad A, \quad \varrho, \quad \text{and} \quad \eta. \quad (5)$$

44 Because of the smallness of  $\lambda$  and the fact that for each element the expansion parameter  
 45 is actually  $\lambda^2$ , this is a rapidly converging expansion.

46 The Wolfenstein parametrization is certainly more transparent than the standard  
 47 parametrization. However, if one requires sufficient level of accuracy, the terms of  $\mathcal{O}(\lambda^4)$   
 48 and  $\mathcal{O}(\lambda^5)$  have to be included in phenomenological applications. This can be done in



49 many ways [6]. The point is that since (4) is only an approximation the *exact* definition  
50 of the parameters in (5) is not unique in terms of the neglected order  $\mathcal{O}(\lambda^4)$ . This situa-  
51 tion is familiar from any perturbative expansion, where different definitions of expansion  
52 parameters (coupling constants) are possible. This is also the reason why in different pa-  
53 pers in the literature different  $\mathcal{O}(\lambda^4)$  terms in (4) can be found. They simply correspond  
54 to different definitions of the parameters in (5). Since the physics does not depend on  
55 a particular definition, it is useful to make a choice for which the transparency of the  
56 original Wolfenstein parametrization is not lost.

In this respect a useful definition adopted by most authors in the literature is to go back  
to the standard parametrization (2) and to *define* the parameters  $(\lambda, A, \varrho, \eta)$  through [6]

$$\lambda \equiv s_{12}, \quad A\lambda^2 \equiv s_{23}, \quad A\lambda^3(\varrho - i\eta) \equiv s_{13}e^{-i\delta} \quad (6)$$

to *all orders* in  $\lambda$ . It follows that

$$\varrho = \frac{s_{13}}{s_{12}s_{23}} \cos \delta, \quad \eta = \frac{s_{13}}{s_{12}s_{23}} \sin \delta. \quad (7)$$

The expressions (6) and (7) represent simply the change of variables from (3) to (5). Mak-  
ing this change of variables in the standard parametrization (2) we find the CKM matrix  
as a function of  $(\lambda, A, \varrho, \eta)$  which satisfies unitarity exactly. Expanding next each element  
in powers of  $\lambda$  we recover the matrix in (4) and in addition find explicit corrections of  
 $\mathcal{O}(\lambda^4)$  and higher order terms. Including  $\mathcal{O}(\lambda^4)$  and  $\mathcal{O}(\lambda^5)$  terms we find

$$\hat{V} = \begin{pmatrix} 1 - \frac{1}{2}\lambda^2 - \frac{1}{8}\lambda^4 & \lambda + \mathcal{O}(\lambda^7) & A\lambda^3(\varrho - i\eta) \\ -\lambda + \frac{1}{2}A^2\lambda^5[1 - 2(\varrho + i\eta)] & 1 - \frac{1}{2}\lambda^2 - \frac{1}{8}\lambda^4(1 + 4A^2) & A\lambda^2 + \mathcal{O}(\lambda^8) \\ A\lambda^3(1 - \bar{\varrho} - i\bar{\eta}) & -A\lambda^2 + \frac{1}{2}A\lambda^4[1 - 2(\varrho + i\eta)] & 1 - \frac{1}{2}A^2\lambda^4 \end{pmatrix} \quad (8)$$

where

$$\bar{\varrho} \simeq \varrho(1 - \frac{\lambda^2}{2}) + \mathcal{O}(\lambda^4), \quad \bar{\eta} = \eta(1 - \frac{\lambda^2}{2}) + \mathcal{O}(\lambda^4). \quad (9)$$

57 An all-order definition of  $\bar{\varrho}$  and  $\bar{\eta}$  will be given in the next section. We emphasize here that  
58 by definition the expression for  $V_{ub}$  remains unchanged relative to the original Wolfenstein  
59 parametrization and the corrections to  $V_{us}$  and  $V_{cb}$  appear only at  $\mathcal{O}(\lambda^7)$  and  $\mathcal{O}(\lambda^8)$ ,  
60 respectively. The advantage of this generalization of the Wolfenstein parametrization is  
61 the absence of relevant corrections to  $V_{us}$ ,  $V_{cd}$ ,  $V_{ub}$  and  $V_{cb}$  and an elegant change in  
62  $V_{td}$  which allows a simple connection to the Unitarity Triangle parameters, as discussed  
63 below.

### 64 1.1.3. Unitarity Triangle

The unitarity of the CKM matrix implies various relations between its elements. In  
particular, we have

$$V_{ud}V_{ub}^* + V_{cd}V_{cb}^* + V_{td}V_{tb}^* = 0. \quad (10)$$

65 Phenomenologically this relation is very interesting as it involves simultaneously the  
66 elements  $V_{ub}$ ,  $V_{cb}$  and  $V_{td}$  which are under extensive discussion at present. Other relevant  
67 unitarity relations will be presented as we proceed.

68 The relation (10) can be represented as a *unitarity triangle* in the complex plane.  
69 The invariance of (10) under any phase-transformations implies that the corresponding

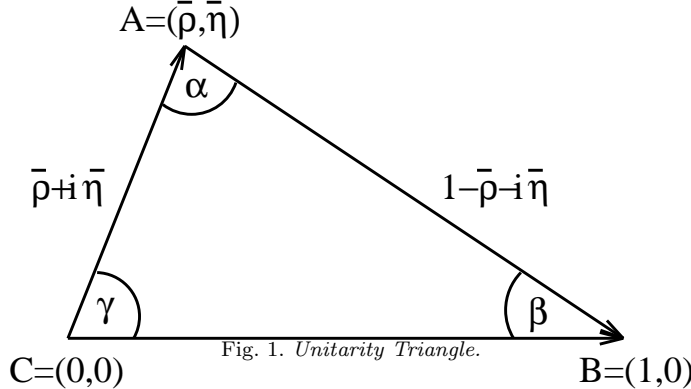
70 triangle is rotated in the plane under such transformations. Since the angles and the  
71 sides (given by the moduli of the elements of the mixing matrix) in this triangle remain  
72 unchanged, they are phase convention independent and are physical observables. Conse-  
73 quently they can be measured directly in suitable experiments. One can construct five  
74 additional unitarity triangles [7, 8] corresponding to other orthogonality relations, like  
75 the one in (10). Some of them should be useful when the data on rare and CP violating  
76 decays improve. The areas ( $A_\Delta$ ) of all unitarity triangles are equal and related to the  
77 measure of CP violation  $J_{CP}$  [9]:  $|J_{CP}| = 2 \cdot A_\Delta$ .

The relation (10) can be represented as the triangle in the complex plane as shown in  
Fig. 1, where

$$\bar{\varrho} + i\bar{\eta} \equiv \vec{CA} = -\text{frac}V_{ub}^*V_{ud}V_{cb}^*V_{cd} \quad (11)$$

78 and

$$\begin{aligned} \vec{AB} &= -\text{frac}V_{tb}^*V_{td}V_{cb}^*V_{cd} = 1 - \bar{\varrho} - i\bar{\eta}, \\ \vec{CB} &= 1. \end{aligned} \quad (12)$$



The parameters  $\bar{\varrho}$  and  $\bar{\eta}$  are the coordinates in the complex plane of the only non-trivial  
apex of the Unitarity Triangle. Using their definition in Eq. (11), the exact relation to  
the parameters  $\varrho$  and  $\eta$  as given in Eq. (6) can be easily found and reads

$$\varrho + i\eta = \sqrt{\frac{1 - A^2\lambda^4}{1 - \lambda^2}} \frac{\bar{\varrho} + i\bar{\eta}}{1 - A^2\lambda^4(\bar{\varrho} + i\bar{\eta})} \simeq \left(1 + \frac{\lambda^2}{2}\right) (\bar{\varrho} + i\bar{\eta}) + \mathcal{O}(\lambda^4). \quad (13)$$

79 Phenomenological analyses of the Unitarity Triangles constrain the values of  $\bar{\varrho}$  and  
80  $\bar{\eta}$ . These can be translated to constraints on  $\varrho$  and  $\eta$  using Eq. (13) and then to the  
81 standard parametrization using Eq. (6). All recent analyses determine the  $\hat{V}_{CKM}$  matrix  
82 elements in this way, without using any expansion.

83 Let us collect useful formulae related to the Unitarity Triangle:

- We can express  $\sin(2\alpha_i)$ ,  $\alpha_i = \alpha, \beta, \gamma$ , in terms of  $(\bar{\varrho}, \bar{\eta})$  using simple trigonometric formulae:

$$\sin(2\alpha) = \frac{2\bar{\eta}(\bar{\eta}^2 + \bar{\varrho}^2 - \bar{\varrho})}{(\bar{\varrho}^2 + \bar{\eta}^2)((1 - \bar{\varrho})^2 + \bar{\eta}^2)}, \quad (14)$$

$$\sin(2\beta) = \frac{2\bar{\eta}(1 - \bar{\varrho})}{(1 - \bar{\varrho})^2 + \bar{\eta}^2}, \quad (15)$$

$$\sin(2\gamma) = \frac{2\overline{\varrho}\overline{\eta}}{\overline{\varrho}^2 + \overline{\eta}^2}. \quad (16)$$

– The lengths of  $AC$  and  $AB$ , denoted by  $R_b$  and  $R_t$  respectively, are given by

$$R_b \equiv \frac{|V_{ub}^* V_{ud}|}{|V_{cb}^* V_{cd}|} = \sqrt{\overline{\varrho}^2 + \overline{\eta}^2} \simeq \left(1 - \frac{\lambda^2}{2}\right) \frac{1}{\lambda} \left| \frac{V_{ub}}{V_{cb}} \right|, \quad (17)$$

$$R_t \equiv \frac{|V_{tb}^* V_{td}|}{|V_{cb}^* V_{cd}|} = \sqrt{(1 - \overline{\varrho})^2 + \overline{\eta}^2} \simeq \frac{1}{\lambda} \left| \frac{V_{td}}{V_{cb}} \right|. \quad (18)$$

– The unitarity relation (10) can be rewritten as

$$R_b e^{i\gamma} + R_t e^{-i\beta} = 1. \quad (19)$$

– The angle  $\alpha$  can be obtained through the relation

$$\alpha + \beta + \gamma = \pi. \quad (20)$$

– In the standard parametrization, the angles  $\beta$  and  $\gamma$  of the unitarity triangle are approximately related to the complex phases of the CKM matrix elements  $V_{td}$  and  $V_{ub}$  respectively. In particular,

$$V_{td} \simeq |V_{td}| e^{-i\beta}, \quad V_{ub} \simeq |V_{ub}| e^{-i\gamma}. \quad (21)$$

## 84 1.2. Plan of the report

85 The goal of the latest generation of flavor experiments has been not only the mea-  
 86 surement of the angles and sides of the unitarity triangles, but the measurement of as  
 87 many redundant observables sensitive to the parameters of the unitarity triangle. On  
 88 one side in fact the consistency of this plethora of measurements is a signal that the CP-  
 89 violation mechanism is fully understood, on the other side possible deviations from the  
 90 Standard Model would spoil such a consistency. Sensitivity to "New Physics" is therefore  
 91 proportional to the accuracy we are able to achieve on the Unitarity Triangle. Finally,  
 92 in case New Physics is observed, the Standard Model Unitarity Triangle will have to be  
 93 measured by means of a subset of observables, those that are not influenced by New  
 94 Physics itself, namely tree dominated processes.

95 In this report, we first describe general theoretical (Sec. 2) and experimental (Sec. 3)  
 96 tools. Next, the single measurements are described and averaged whenever possible. In  
 97 particular Sec. 4 discusses the measurements of the Cabibbo Angle, Sec. 5 the measure-  
 98 ment of  $|V_{cx}|$  and  $|V_{ub}|$  in semileptonic decays. Rare decays and measurements of  $|V_{td}|$   
 99 and  $|V_{ub}|$  are detailed in Sec. 6, while Sec. 7 reports on the mixing and lifetime related  
 100 measurements, including the time-dependent measurements of the phases of the mixing  
 101 diagram, both for  $B_d$  and  $B_s$  mesons. All other measurements of angles of the Unitarity  
 102 Triangle are described in Sec. 8 and 9: the former shows a large number of measurements  
 103 of the  $\gamma$  angle in tree dominated processes, while the latter comprises several techniques  
 104 to measure  $\alpha$ ,  $\beta$ , and  $\gamma$  in charmless  $B$  decays.

105 These measurements are interpreted altogether in Sec. 10. First the results of global  
 106 fits to all observables under the assumption that there is no deviation from the Standard  
 107 Model is presented. This fit returns a very accurate measurement of the position of the  
 108 apex of the unitarity triangle. Next, the redundancy of the measurements is exploited to

109 test the possibility of deviations from the Standard Model both in model independent  
110 frames and under specific New Physics scenarios.

## 111 2. Theory Primers

112 This section contains the description of theoretical tools that are common to different  
113 fields of flavor physics and that will therefore be used as starting point in the subsequent  
114 sections.

### 115 2.1. *Effective Weak Hamiltonians*

116 Flavor-changing hadron transitions are multi-scale processes conveniently studied using  
117 the operator product expansion (OPE) [10,11]. They involve at least two different energy  
118 scales: the electroweak scale, given for instance by the  $W$  boson mass  $M_W$ , relevant for  
119 the flavor-changing weak transition, and the scale of strong interactions  $\Lambda_{\text{QCD}}$ , related to  
120 the hadron formation. Using the OPE, these processes can be described by effective weak  
121 Hamiltonians where the  $W$  boson and all heavier particles are eliminated as dynamical  
122 degrees of freedom from the theory [12–16]. These Hamiltonians are given by the first  
123 term of an expansion in renormalized local operators of increasing dimensions suppressed  
124 by inverse powers of the heavy scale.

125 The OPE realizes the scale separation between short-distance (high-energy) and long-  
126 distance (low-energy) physics. The scale  $\mu$  at which the local operators are renormalized  
127 sets the threshold between the two regimes. The effect of particles heavier than  $M_W$   
128 enters only through the Wilson coefficients, namely the effective couplings multiplying the  
129 operators of the Hamiltonian. Short-distance strong-interaction effects are also contained  
130 in the Wilson coefficients and can be computed using renormalization-group improved  
131 perturbation theory. Indeed, Wilson coefficients obey a renormalization group equation  
132 (RGE) allowing to resum large logs of the form  $\alpha_s(\mu)^{n+m} \log(M_W/\mu)^n$  to all orders  
133 in  $n$ . The leading order (LO) resummation corresponds to  $m = 0$ , the next-to-leading  
134 order (NLO) one to  $m = 1$ , and so on. Since the Wilson coefficients depend on short  
135 distance physics only, they behave as effective couplings in the Hamiltonians. They can  
136 be calculated once and for all, i.e. for any external state used to compute the Hamiltonian  
137 matrix elements. Indeed, the complete definition of an effective weak Hamiltonian requires  
138 the choice of the operators and the computation of the corresponding Wilson coefficients.

139 The dependence on external states, as well as long-distance strong-interaction effects,  
140 is included in the hadronic matrix elements of the local operators and must be evaluated  
141 with a non-perturbative technique (lattice QCD, QCD sum rules, QCDF, SCET, etc.).  
142 As non-perturbative methods can typically compute matrix elements of local operators,  
143 this is a major motivation for using the effective weak Hamiltonians.

144 We now illustrate the procedure to define the effective weak Hamiltonians and to com-  
145 pute the Wilson coefficients discussing the case of  $\Delta F = 1$  transitions, namely processes  
146 where the quark flavor quantum numbers change by one unit.

The starting point is a generic  $S$  matrix element given by the  $T$ -product of two weak  
charged currents computed in the Standard Model (in the following called *full* theory to  
distinguish it from the *effective* theory defined by the effective weak Hamiltonian)

$$\langle F|S|I\rangle = \int d^4x D^{\mu\nu}(x, M_W) \langle F|T(J_\mu^{cc}(x), J_\nu^{cc\dagger}(0))|I\rangle, \quad (22)$$

where  $\langle F|$  and  $|I\rangle$  are the generic final and initial states and

$$J_\mu^{cc}(x) = \frac{g}{\sqrt{2}} \sum_{j=1}^3 \left[ \left( \sum_{i=1}^2 V_{u^i d^j} \bar{u}_L^i(x) \gamma_\mu d_L^j(x) \right) + \bar{e}_L^j(x) \gamma_\mu \nu_L^j(x) \right], \quad (23)$$

147 where  $V$  is the Cabibbo-Kobayashi-Maskawa (CKM) matrix [1, 2],  $u^i = \{u, c\}^1$ ,  $d^i =$   
 148  $\{d, s, b\}$ ,  $e^i = \{e, \mu, \tau\}$ ,  $\nu^i = \{\nu_e, \nu_\mu, \nu_\tau\}$  and the subscript  $L$  denotes the left-handed  
 149 component of the field.

Given that, using for instance the Feynman gauge,

$$D^{\mu\nu}(x, M_W) = \int \frac{d^4q}{(2\pi)^4} e^{-iq \cdot x} \frac{-g^{\mu\nu}}{q^2 - M_W^2 + i\varepsilon} = \delta(x) \frac{g^{\mu\nu}}{M_W^2} + \dots, \quad (24)$$

the two weak currents go at short distances in the large  $M_W$  limit. Thus the  $S$  matrix element can be expanded in terms of local operators and gives

$$\langle F|iS|I\rangle = 4 \frac{G_F}{\sqrt{2}} \sum_i C_i(\mu) \langle F|Q_i(\mu)|I\rangle + \dots, \quad (25)$$

150 where  $G_F$  is the Fermi constant  $G_F/\sqrt{2} = g^2/8M_W^2$ . The dots represent subdominant  
 151 terms suppressed by powers of  $Q^2/M_W^2$  where  $Q$  is the typical energy scale of the process  
 152 under study ( $\Lambda_{\text{QCD}}$  for light hadron decays,  $m_b$  for  $B$  decays, etc.).

The OPE in Eq. (25) is valid for all possible initial and final states. This allows for the definition of the effective weak Hamiltonian, given by the operator relation

$$\mathcal{H}_W^{\Delta F=1} = 4 \frac{G_F}{\sqrt{2}} \sum_i C_i(\mu) Q_i(\mu) = 4 \frac{G_F}{\sqrt{2}} \mathbf{Q}^T(\mu) \cdot \mathbf{C}(\mu). \quad (26)$$

The  $Q_i(\mu)$  are local, dimension-six operators renormalized at the scale  $\mu$  and the  $C_i(\mu)$  are the corresponding Wilson coefficients. The set of operators  $Q_i(\mu)$  forms a complete basis for the OPE. This set contains all the linearly-independent, dimension-six operators with the same quantum numbers of the original weak current product, usually reduced by means of the equations of motion (although off-shell basis can also be considered). In practice, the operators generated by the expansion of the *full* amplitude (in the so-called “matching” procedure described below) must be complemented by the additional operators generated by the renormalization procedure. Notice that, in the absence of QCD (and QED) corrections, the effective Hamiltonian in Eq. (26) reduces to the Fermi theory of weak interactions. For instance, from the leptonic part of the charged currents, one finds

$$\mathcal{H}_{\text{Fermi}} = \frac{G_F}{\sqrt{2}} \bar{e} \gamma^\mu (1 - \gamma_5) \nu_e \bar{\nu}_\mu \gamma_\mu (1 - \gamma_5) \mu, \quad (27)$$

153 i.e. the Fermi Hamiltonian describing the muon decay.

154 For quark transitions, gluonic (and photonic) radiative corrections to amplitudes com-  
 155 puted in terms of local operators produce ultraviolet divergences which are not present  
 156 in the full theory. This implies that the local operators  $Q_i$  need to be renormalized and

---

<sup>1</sup> The top quark is not included as we are building an effective theory valid for energies below  $M_W$ .

157 depend on the renormalization scale  $\mu$ . Therefore  $\mu$ -dependent Wilson coefficients must  
 158 be introduced to cancel this dependence.

159 Provided that one choses a large enough renormalization scale  $\mu \gg \Lambda_{\text{QCD}}$ , short-  
 160 distance QCD (and QED) corrections to the Wilson coefficients can be calculated using  
 161 a renormalization-group-improved perturbation theory, resumming classes of large logs  
 162 potentially dangerous for the perturbative expansion. All non-perturbative effects are  
 163 confined in the matrix elements of the local operators. Their calculation requires a non-  
 164 perturbative technique able to compute matrix elements of operators renormalized at the  
 165 scale  $\mu$ . In the case of leptonic and semi-leptonic hadron decays, the hadronic effects are  
 166 confined to the matrix elements of a single current which can be conveniently written  
 167 using meson decay constants (for matrix elements between one hadron and the vacuum)  
 168 or form factors (for matrix elements between two hadron states) as for example

$$\begin{aligned} \langle 0 | \bar{d}_L \gamma^\mu \gamma_5 u_L | \pi^+(q) \rangle &= i f_\pi q^\mu, \\ \langle \pi^0(p') | \bar{s}_L \gamma^\mu d_L | K^0(p) \rangle &= f_+^0(q^2)(p+p')^\mu + f_-^0(q^2)(p-p')^\mu, \quad q^2 = (p-p')^2. \end{aligned} \quad (28)$$

169 Appearing in different processes, they can be computed using non-perturbative tech-  
 170 niques or measured in one process and used to predict the others. Predictions for non-  
 171 leptonic decays, on the other hand, usually require non-perturbative calculations. Data-  
 172 driven strategies are possible in cases where many measurements related by flavor sym-  
 173 metries are available.

174 The determination of Wilson coefficients at a given order in perturbation theory re-  
 175 quires two steps: (i) the *matching* between the full theory and the effective Hamiltonian  
 176 at a scale  $M \sim O(M_W)$  and (ii) the RGE evolution from the matching scale  $M$  down to  
 177 the renormalization scale  $\mu$ .

Let's discuss the second point first. Since  $\mathcal{H}_W^{\Delta F=1}$  in Eq. (26) is independent of  $\mu$ , i.e.  
 $\mu^2 \frac{d}{d\mu^2} \mathcal{H}_W^{\Delta F=1} = 0$ , the Wilson coefficients  $\mathbf{C}(\mu) = (C_1(\mu), C_2(\mu), \dots)$  must satisfy the  
 RGE

$$\mu^2 \frac{d}{d\mu^2} \mathbf{C}(\mu) = \frac{1}{2} \hat{\gamma}^T \mathbf{C}(\mu), \quad (29)$$

which can be conveniently written as

$$\left( \mu^2 \frac{\partial}{\partial \mu^2} + \beta(\alpha_s) \frac{\partial}{\partial \alpha_s} - \frac{1}{2} \hat{\gamma}^T(\alpha_s) \right) \mathbf{C}(\mu) = 0, \quad (30)$$

where

$$\beta(\alpha_s) = \mu^2 \frac{d\alpha_s}{d\mu^2} \quad (31)$$

is the QCD  $\beta$  function and

$$\hat{\gamma}(\alpha_s) = 2 \hat{Z}^{-1} \mu^2 \frac{d}{d\mu^2} \hat{Z} \quad (32)$$

is the operator anomalous dimension matrix. The matrix  $\hat{Z}$  of the renormalization con-  
 stants is defined by the relation connecting the bare operators  $\mathbf{Q}^B$  to the renormalized  
 ones  $\mathbf{Q}(\mu)$

$$\mathbf{Q}(\mu) = \hat{Z}^{-1}(\mu, \alpha_s) \mathbf{Q}^B. \quad (33)$$

The solution of the system of linear differential equations (30) is found by introducing a suitable evolution matrix  $U(\mu, M_W)$  and by imposing an appropriate set of initial conditions, usually called matching conditions. The coefficients  $\mathbf{C}(\mu)$  are given by<sup>2</sup>

$$\mathbf{C}(\mu) = \hat{U}(\mu, M)\mathbf{C}(M), \quad (34)$$

with

$$\hat{U}(m_1, m_2) = T_{\alpha_s} \exp \left( \int_{\alpha_s(m_1)}^{\alpha_s(m_2)} \frac{d\alpha_s}{\beta(\alpha_s)} \hat{\gamma}^T(\alpha_s) \right). \quad (35)$$

178  $T_{\alpha_s}$  is the ordered product with increasing couplings from right to left.

The matching conditions are found by imposing that, at  $\mu = M \sim O(M_W)$ , the matrix elements of the original  $T$ -product of the currents coincide, up to terms suppressed by inverse powers of  $M_W$ , with the corresponding matrix elements of  $\mathcal{H}_W^{\Delta F=1}$ . To this end, we introduce the vector  $\mathbf{T}$  defined by the relation

$$i\langle\alpha|S|\beta\rangle = 4\frac{G_F}{\sqrt{2}}\langle\alpha|\mathbf{Q}^T|\beta\rangle_0 \cdot \mathbf{T}(M_W, m_t; \alpha_s) + \dots \quad (36)$$

179 where  $\langle\alpha|\mathbf{Q}^T|\beta\rangle_0$  are matrix elements of the operators computed at the tree level and the  
180 dots denote power-suppressed terms. The vector  $\mathbf{T}$  contains the dependence on heavy  
181 masses and has a perturbative expansion in  $\alpha_s$ .<sup>3</sup> On dimensional basis,  $\mathbf{T}$  can only  
182 be a function of  $m_t/M_W$  and of  $\log(p^2/M_W^2)$  where  $p$  generically denotes the external  
183 momenta.

184 We also introduce the matrix  $\hat{M}(\mu)$  such that

$$\begin{aligned} \langle\alpha|\mathcal{H}_W^{\Delta F=1}|\beta\rangle &= 4\frac{G_F}{\sqrt{2}}\langle\alpha|\mathbf{Q}^T(\mu)|\beta\rangle\mathbf{C}(\mu) \\ &= 4\frac{G_F}{\sqrt{2}}\langle\alpha|\mathbf{Q}^T|\beta\rangle_0\hat{M}^T(\mu; \alpha_s)\mathbf{C}(\mu). \end{aligned} \quad (37)$$

In terms of  $\mathbf{T}$  and  $\hat{M}$ , the matching condition

$$i\langle\alpha|S|\beta\rangle = \langle\alpha|\mathcal{H}_W^{\Delta F=1}|\beta\rangle \quad (38)$$

fixes the value of the Wilson coefficients at the scale  $M$  as

$$\mathbf{C}(M) = [\hat{M}^T(M; \alpha_s)]^{-1}\mathbf{T}(M_W, m_t; \alpha_s). \quad (39)$$

185 As the full and the effective theories share the same infrared behavior, the dependence on  
186 the external states on which the matching conditions are imposed drops in Eq. (39), so  
187 that any matrix element can be used, even off-shell ones (with some caution), provided  
188 the *same* external states are used for computing matrix elements in both theories. Notice  
189 that the matching can be imposed at any scale  $M$  such that large logs do not appear in  
190 the calculation of the Wilson coefficients at that scale, i.e.  $\alpha_s \log(M/M_W) \ll 1$ .

Equation (34) is correct if no threshold corresponding to a quark mass between  $\mu$  and  $M_W$  is present. Indeed, as  $\alpha_s$ ,  $\hat{\gamma}$  and  $\beta(\alpha_s)$  depend on the number of “active” flavors, it is necessary to change the evolution matrix  $\hat{U}$  defined in Eq. (35), when passing quark

<sup>2</sup> The problem of the thresholds due to the presence of heavy quarks with a mass  $M_W \gg m_Q \gg \Lambda_{\text{QCD}}$  will be discussed below.

<sup>3</sup> For simplicity, we discuss QCD corrections only. QED corrections can be considered as well and are included in a similar way.

thresholds. The general case then corresponds to a sequence of effective theories with a decreasing number of “active” flavors. By “active” flavor, we mean a dynamical massless ( $\mu \gg m_q$ ) quark field. The theory with  $k$  “active” flavors is matched to the one with  $k + 1$  “active” flavors at the threshold. This procedure changes the solution for the Wilson coefficients. For instance, if one starts with five “active” flavors at the scale  $M_W$  and chooses  $m_c \ll \mu \ll m_b$ , the Wilson coefficients become

$$\mathbf{C}(\mu) = W[\mu, M_W] \mathbf{C}(M_W) = \hat{U}_4(\mu, m_b) \hat{T}_{45} \hat{U}_5(m_b, M_W) \mathbf{C}(M_W). \quad (40)$$

191 The matrix  $\hat{T}_{45}$  matches the four and five flavor theories so that the Wilson coefficients  
 192 are continuous across the threshold. The inclusion of the charm threshold proceeds along  
 193 the same lines.

So far we have presented the formal solution of the matching and the RGE for the Wilson coefficients. In practice, we can calculate the relevant functions ( $\beta$ ,  $\hat{\gamma}$ ,  $\hat{M}$ ,  $\mathbf{T}$ , etc.) in perturbation theory only. At the LO, one has

$$\beta(\alpha_s) = -\frac{\alpha_s^2}{4\pi} \beta_0 + \dots, \quad \hat{\gamma} = \frac{\alpha_s}{4\pi} \hat{\gamma}^{(0)} + \dots, \quad \mathbf{T} = T^{(0)} + \dots, \quad \hat{M} = \hat{1} + \dots, \quad (41)$$

so that the LO Wilson coefficients read

$$\mathbf{C}_{\text{LO}}(\mu) = \left( \frac{\alpha_s(M)}{\alpha_s(\mu)} \right)^{\hat{\gamma}^{(0)T}/2\beta_0} \mathbf{T}^0. \quad (42)$$

194 The explicit solution can be found in the basis where the LO anomalous dimension  
 195 matrix  $\hat{\gamma}^{(0)}$  is diagonal. To go beyond the LO, we have to expand the relevant functions  
 196 to higher order in  $\alpha_s$ . Discussing the details on higher order calculations goes beyond the  
 197 purpose of this primer. They can be found in the original literature cited in the following  
 198 presentation of the actual effective Hamiltonians for  $\Delta F = 1$  and  $\Delta F = 2$  transitions.

### 199 2.1.1. $\Delta F = 1$ effective weak Hamiltonians

200 Even restricting to processes which change each flavor number by no more than one  
 201 unit, namely  $\Delta F = 1$  transitions, several effective Hamiltonians can be introduced. We  
 202 start considering the Hamiltonian relevant for transtions with  $\Delta B = 1$ ,  $\Delta C = 0$ ,  $\Delta S =$   
 203  $-1$ :

$$\begin{aligned} \mathcal{H}_W^{\Delta B=1, \Delta C=0, \Delta S=-1} &= 4 \frac{G_F}{\sqrt{2}} \left( \lambda_c^s (C_1(\mu) Q_1^c(\mu) + C_2(\mu) Q_2^c(\mu)) \right. \\ &\quad \left. + \lambda_u^s (C_1(\mu) Q_1^u(\mu) + C_2(\mu) Q_2^u(\mu)) - \lambda_t^s \sum_{i=3}^{10} C_i(\mu) Q_i(\mu) \right), \end{aligned} \quad (43)$$

where the  $\lambda_q^s = V_{qb}^* V_{qs}$  and the operator basis is given by



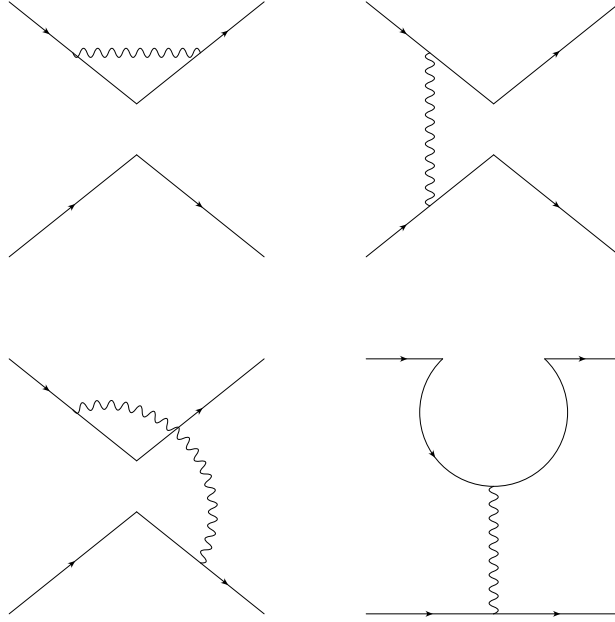


Fig. 2. One-loop correction to the  $\Delta F = 1$  effective weak Hamiltonian.

$$\begin{aligned}
Q_1^q &= \bar{b}_L^\alpha \gamma^\mu q_L^\alpha \bar{q}_L^\beta \gamma_\mu s_L^\beta & Q_2^q &= \bar{b}_L^\alpha \gamma^\mu q_L^\beta \bar{q}_L^\beta \gamma_\mu s_L^\alpha \\
Q_3 &= \bar{b}_L^\alpha \gamma^\mu s_L^\alpha \sum_q \bar{q}_L^\beta \gamma_\mu q_L^\beta & Q_4 &= \bar{b}_L^\alpha \gamma^\mu s_L^\beta \sum_q \bar{q}_L^\beta \gamma_\mu q_L^\alpha \\
Q_5 &= \bar{b}_L^\alpha \gamma^\mu s_L^\alpha \sum_q \bar{q}_R^\beta \gamma_\mu q_R^\beta & Q_6 &= \bar{b}_L^\alpha \gamma^\mu s_L^\beta \sum_q \bar{q}_R^\beta \gamma_\mu q_R^\alpha \\
Q_7 &= \frac{3}{2} \bar{b}_L^\alpha \gamma^\mu s_L^\alpha \sum_q e_q \bar{q}_R^\beta \gamma_\mu q_R^\beta & Q_8 &= \frac{3}{2} \bar{b}_L^\alpha \gamma^\mu s_L^\beta \sum_q e_q \bar{q}_R^\beta \gamma_\mu q_R^\alpha \\
Q_9 &= \frac{3}{2} \bar{b}_L^\alpha \gamma^\mu s_L^\alpha \sum_q e_q \bar{q}_L^\beta \gamma_\mu q_L^\beta & Q_{10} &= \frac{3}{2} \bar{b}_L^\alpha \gamma^\mu s_L^\beta \sum_q e_q \bar{q}_L^\beta \gamma_\mu q_L^\alpha
\end{aligned} \tag{44}$$

204 The sum index  $q$  runs over the “active” flavors,  $\alpha, \beta$  are color indices and  $e_q$  is the electric  
205 charge of the quark  $q$ . Besides  $Q_1$ , which come from the matching, the above operators  
206 are generated by gluon and photon exchanges in the Feynman diagrams of fig. 2. In  
207 particular,  $Q_2^q$  is generated by current–current diagrams while  $Q_3$ – $Q_6$  and  $Q_7$ – $Q_{10}$  are  
208 generated by gluon and photon penguin diagrams respectively. Notice that the choice  
209 of the operator basis is not unique. Different possibilities have been considered in the  
210 literature [17–23].

The operators basis includes the ten independent operators in Eq. (44) in the five-flavor effective theory. Below the bottom threshold, the following relation holds

$$Q_{10} - Q_9 - Q_4 + Q_3 = 0, \tag{45}$$

so that the independent operators become nine. The basis is further reduced in the three-flavor theory, i.e. below the charm threshold, due to the additional relations

$$Q_4 - Q_3 - Q_2 + Q_1 = 0, \quad Q_9 - \frac{3}{2}Q_1 + \frac{1}{2}Q_3 = 0. \tag{46}$$

211 For  $b \rightarrow s$  transitions with a photon or a lepton pair in the final state, additional  
 212 dimension-six operators must be included in the basis, namely

$$\begin{aligned}
 Q_{7\gamma} &= \frac{e}{16\pi^2} m_b \bar{b}_L^\alpha \sigma^{\mu\nu} F_{\mu\nu} s_L^\alpha \\
 Q_{8g} &= \frac{g_s}{16\pi^2} m_b \bar{b}_L^\alpha \sigma^{\mu\nu} G_{\mu\nu}^A T^A s_L^\alpha \\
 Q_{9V} &= \frac{1}{2} \bar{b}_L^\alpha \gamma^\mu s_L^\alpha \bar{l} \gamma_\mu l \\
 Q_{10A} &= \frac{1}{2} \bar{b}_L^\alpha \gamma^\mu s_L^\alpha \bar{l} \gamma_\mu \gamma_5 l
 \end{aligned} \tag{47}$$

213 where  $G_{\mu\nu}^A$  ( $F_{\mu\nu}$ ) is the gluon (photon) field strength tensor and  $T^A$  are the  $SU(3)$   
 214 generators. They contribute an additional term to the Hamiltonian in Eq. (44) so that,  
 215 up to doubly Cabibbo-suppressed terms and neglecting the electroweak penguin operators  
 216  $Q_7$ – $Q_{10}$ , the effective weak Hamiltonian for these processes reads

$$\begin{aligned}
 \mathcal{H}_W &= -4 \frac{G_F}{\sqrt{2}} \lambda_t^s \left( \sum_{i=1}^6 C_i(\mu) Q_i(\mu) + C_{7\gamma}(\mu) Q_{7\gamma}(\mu) + C_{8g}(\mu) Q_{8g}(\mu) \right. \\
 &\quad \left. + C_{9V}(\mu) Q_{9V}(\mu) + C_{10A}(\mu) Q_{10A}(\mu) \right),
 \end{aligned} \tag{48}$$

217 with  $Q_{1,2} = Q_{1,2}^c$  defined in Eq. (44).

218 At present, the  $\Delta F = 1$  effective weak Hamiltonian in Eq. 44, including electroweak  
 219 penguin operators ( $Q_7$ – $Q_{10}$  in Eq. (44)), is known at the NNLO in  $\alpha_s$  [24] and at the  
 220 NLO in  $\alpha_e$  [25,26]. The effective Hamiltonian in Eq. (48) has been fully computed at the  
 221 NNLO in the strong coupling constant [27–30].

222 Effective weak Hamiltonians for other transtions can be obtained by trivial changes  
 223 in the quark fields and in the CKM matrix elements entering eqs. (44) and (44). In  
 224 particular

$$\begin{aligned}
 \Delta B = 1, \Delta C = 0, \Delta S = 0 : s \rightarrow d \\
 \Delta B = 0, \Delta C = 0, \Delta S = 1 : b \rightarrow s, s \rightarrow d \\
 \Delta B = 0, \Delta C = 1, \Delta S = 0 : b \rightarrow c, s \rightarrow u, c \rightarrow s, u \rightarrow d.
 \end{aligned} \tag{49}$$

In other cases, for instance  $\Delta B = 1, \Delta C = -1, \Delta S = 0$  transitions, the Hamiltonian  
 has a simpler structure, namely

$$\mathcal{H}_W^{\Delta B=1, \Delta C=-1, \Delta S=0} = 4 \frac{G_F}{\sqrt{2}} V_{cb}^* V_{ud} \left( C_1(\mu) Q'_1(\mu) + C_2(\mu) Q'_2(\mu) \right) \tag{50}$$

with

$$Q'_1 = \bar{b}_L^\alpha \gamma^\mu c_L^\alpha \bar{u}_L^\beta \gamma_\mu d_L^\beta, \quad Q'_2 = \bar{b}_L^\alpha \gamma^\mu c_L^\beta \bar{u}_L^\beta \gamma_\mu d_L^\alpha. \tag{51}$$

225 Only current–current operators enter this Hamiltonian. Penguin operators are not gener-  
 226 ated as the considered transitions involve four different flavors. Other Hamiltonians share  
 227 this feature and can be obtained from eqs. (50) and (51) with the following replacements

$$\begin{aligned}
& \Delta B = 1, \Delta C = 1, \Delta S = 0 : c \rightarrow u, u \rightarrow c \\
& \Delta B = 1, \Delta C = -1, \Delta S = -1 : d \rightarrow s \\
& \Delta B = 1, \Delta C = 1, \Delta S = -1 : c \rightarrow u, u \rightarrow c, d \rightarrow s \\
& \Delta B = 0, \Delta C = -1, \Delta S = 1 : b \rightarrow s \\
& \Delta B = 0, \Delta C = 1, \Delta S = 1 : b \rightarrow s, c \rightarrow u, u \rightarrow c.
\end{aligned} \tag{52}$$

Clearly the (omitted) Hermitian-conjugate terms in the Hamiltonians mediate transitions with opposite  $\Delta F$ .

Notice that physics beyond the SM could change not only the Wilson coefficients through the matching conditions, but also the operator basis where new spinor and color structures may appear. Indeed the most general  $\Delta F = 1$  basis contains a large number of operators making it hardly useful. On the other hand, a possible definition of the class of new physics models with minimal flavor violation is that these models produce only real corrections to the SM Wilson coefficients without changing the operator basis of the effective weak Hamiltonian [31].

### 2.1.2. $\Delta F = 2$ effective weak Hamiltonians

The  $\Delta F = 2$  effective weak Hamiltonians are simpler than the  $\Delta F = 1$  ones. In the SM, the operator basis includes one operator only. For example, the  $\Delta S = 2$  effective Hamiltonian is commonly written as

$$\mathcal{H}_W^{\Delta S=2} = \frac{G_F^2}{4\pi^2} M_W^2 \left( \lambda_c^2 \eta_1 S_0(x_c) + \lambda_t^2 \eta_2 S_0(x_t) + \lambda_t \lambda_c \eta_3 S_0(x_t, x_c) \right) \hat{Q}_s \tag{53}$$

where  $\lambda_q = V_{qs}^* V_{qd}$ , the functions  $S_0$  of  $x_q = m_q^2/M_W^2$  come from the LO matching conditions, the coefficients  $\eta_i$  account for the RGE running and NLO effects. Starting from the dimension-six operator

$$Q_s = \bar{s}_L \gamma_\mu d_L \bar{s}_L \gamma^\mu d_L. \tag{54}$$

$\hat{Q}_s$  is defined as  $\hat{Q}_s = K(\mu) Q_s(\mu)$ , where  $K(\mu)$  is the appropriate short-distance factor which makes  $\hat{Q}$  independent of  $\mu$  [32]. The matrix element of this operator between  $K^0$  and  $\bar{K}^0$  is parameterised in terms of the RG-invariant bag parameter  $\hat{B}_K$  (see Sec. 7).

The Hamiltonian in Eq. (53) describes only the short-distance part of the  $\Delta S = 2$  amplitude. Long-distance contributions generated by the exchange of hadronic states are also present. These contributions break the OPE producing additional terms which are difficult to estimate. This is the case of the  $K^0 - \bar{K}^0$  mass difference  $\Delta M_K$  which therefore cannot be reliably predicted. On the other hand, the CP-violation parameter  $\epsilon_K$ , related to  $\text{Im}\langle \bar{K}^0 | \mathcal{H}_W^{\Delta S=2} | K^0 \rangle$ , is short-distance dominated and thus calculable.

Concerning  $\Delta B = 2$  transitions, namely the  $B_d^0 - \bar{B}_d^0$  and  $B_s^0 - \bar{B}_s^0$  mixing amplitudes, virtual top exchange gives the dominant contributions in the SM. Therefore these amplitudes are short-distance dominated and described by matrix elements of the Hamiltonian

$$\mathcal{H}_W^{\Delta B=2} = \frac{G_F^2}{4\pi^2} M_W^2 (\lambda_t^q)^2 \eta_2 S_0(x_t) \hat{Q}_b^q \tag{55}$$

where

$$Q_b^q = \bar{b}_L \gamma_\mu q_L \bar{b}_L \gamma^\mu q_L, \quad q = \{d, s\}, \tag{56}$$

and  $\hat{Q}_b^q$  is defined similarly to the  $\Delta S = 2$  case in terms of the bag-parameter  $\hat{Q}_b^q$  (see Sec. 7).

249 At present,  $\Delta F = 2$  effective Hamiltonians are known at the NLO in the strong  
250 coupling constants [33–35].

251 It is worth noting that, unlike  $\Delta F = 1$  Hamiltonians, generic new physics contributions  
252 to  $\Delta F = 2$  transitions generate few additional operators allowing for model-independent  
253 studies of  $\Delta F = 2$  processes where the Wilson coefficients at the matching scale are used  
254 as new physics parameters [36].

255 Finally, we mention that the absorptive part of  $\Delta F = 2$  amplitudes, related to the  
256 neutral mesons width differences, can also be calculated using an OPE applied to the  
257 rates rather than to the amplitudes. We refer the interested reader to Sec. 7. for details  
258 on this calculation.

## 259 2.2. Factorization

260 In the previous section it was shown how to integrate out physics at the electroweak  
261 scale, resulting in 10 four-fermion operators  $O_1$ - $O_{10}$ . In order to measure the decay rates  
262 or CP-asymmetries in non-leptonic decays of a  $B$  meson to two light pseudoscalar mesons  
263 (either  $\pi$  or  $K$ ), one needs information about the matrix elements of these operators  
264 between the initial  $B$  meson and the given final state. The nature of the strong interaction  
265 implies that these matrix elements can not be calculated perturbatively, and one either  
266 has to resort to non-perturbative methods to calculate these matrix elements or extract  
267 them from data.

268 In order to determine the required matrix elements from data and still obtain infor-  
269 mation about the electroweak physics requires to have more experimental input than  
270 unknown matrix elements. It has been known for a long time that in the  $B \rightarrow \pi\pi$  system  
271 there are more measurements than non-perturbative parameters, which allows to mea-  
272 sure some fundamental parameters of the CKM matrix [37]. However, of the 8 possible  
273 measurements, only 6 have been made to this point, one of which still has very large  
274 uncertainties. Thus, in practice, even in the  $\pi\pi$  system some additional information is re-  
275 quired in order to have detailed information about the electroweak phases. The situation  
276 is worse once we include Kaons in the final state, and without using additional theoretical  
277 information, there are more unknown parameters than there are measurements.

278 Factorization utilizes an expansion in  $\Lambda_{\text{QCD}}/m_b$  in order to simplify the required matrix  
279 elements, resulting in new relations in the limit  $\Lambda_{\text{QCD}}/m_b \rightarrow 0$ . Theoretically, this limit  
280 can be taken using diagrammatic factorization techniques (QCD factorization) [38–40]  
281 or, equivalently, soft-collinear effective theory (SCET) [41–44], together with heavy quark  
282 effective theory (HQET). Before we explain in detail factorization theorems arise in this  
283 effective field theory approach, we will first give a simple physical picture for factorization,  
284 known as color transparency.

285 As discussed above, the decay  $B \rightarrow M_1 M_2$  is described by the matrix element of local  
286 four-fermion operators, allowing the  $b$  quark to decay to three light quarks. Two of these  
287 two light quarks will form the meson  $M_1$ , while the meson  $M_2$  is formed from the third  
288 light quark together with the spectator quark of the  $B$  meson. The dominant contribution  
289 to a given decay arises from operators for which the two light quark forming  $M_1$  are in  
290 a color singlet configuration. These two quarks in a color singlet configuration will only  
291 interact non-perturbatively with the remaining system once their separation is of order  
292  $1/\Lambda_{\text{QCD}}$ . Due to the large energy  $E \sim m_b/2$  of the light mesons, this separation only

293 occurs when the two quarks are a distance  $d \sim E_\pi/\Lambda_{\text{QCD}}^2$  from the origin of the decay,  
 294 and therefore out of the reach  $d \sim 1/\Lambda_{\text{QCD}}$  of the non-perturbative physics of the  $B$   
 295 meson. Thus, the non-perturbative dynamics of one of the two mesons is independent of  
 296 the rest of the system. Since the second light meson requires the spectator quark of the  
 297  $B$  meson, no such factorization should be expected.

298 Using effective field theory methods allows to prove this intuitive result rigorously,  
 299 while at the same time allowing in principle to go beyond the leading order result in  
 300  $\Lambda_{\text{QCD}}/m_b$ . The first step in the factorization proof is to separate the different energy  
 301 scales in the system, by constructing the correct effective field theory. In the rest frame  
 302 of the  $B$  meson, the two light mesons decay back-to-back with energy  $m_B/2$ , and we  
 303 label the directions of the two mesons by four-vectors  $n$  and  $\bar{n}$ . To describe these two  
 304 energetic mesons we require collinear quark and gluon fields which are labeled by the  
 305 direction of flight  $n$  or  $\bar{n}$  of the meson. We will call the collinear quark fields  $\chi_{n/\bar{n}}$  and  
 306  $A_{n/\bar{n}}$ , respectively. In order to describe the heavy  $B$  meson, we require soft heavy quark  
 307 and soft light quark and gluon fields, which we call  $h_s$ ,  $q_s$  and  $A_s$ , respectively. Since it  
 308 is the two light quarks in the  $n$  direction that form the meson  $M_1$ , we will also write  
 309  $M_n \equiv M_1$  and  $M_{\bar{n}} \equiv M_2$ .

The important property of SCET/HQET that allows to prove the factorization theorem  
 is that to leading order in  $\Lambda_{\text{QCD}}/m_b$  the collinear fields in the different directions do not  
 interact with one another. Furthermore, all interactions between collinear and soft fields  
 can be removed from the Lagrangian by redefining the collinear fields to be multiplied by  
 a soft Wilson line  $Y_n$ , which depends on the direction  $n$  of the collinear field it belongs  
 to. Since all interactions between the different sectors disappear at leading order, the  
 Lagrangian can be written as

$$\mathcal{L}_{\text{eff}} = \mathcal{L}_n + \mathcal{L}_{\bar{n}} + \mathcal{L}_s + \mathcal{O}(\Lambda_{\text{QCD}}/m_b). \quad (57)$$

The 4-quark operators  $O_i$  describing the decay of the heavy  $b$  quark are matched onto  
 operators in the effective field theory, which are constructed out of the collinear and soft  
 fields. This allows to write written as

$$O_i = C_i \otimes O_i^{n\bar{n}} = C_i \otimes [\bar{h}_s \Gamma_i Y_{\bar{n}} \chi_{\bar{n}}] [\bar{\chi}_n Y_n^\dagger \Gamma_i Y_n \chi_n]. \quad (58)$$

Here  $C_i$  denotes the Wilson coefficient of the operators and describes the physics occur-  
 ring at the scale  $m_b$ , and the different operators are distinguished by their Dirac and  
 color structure  $\Gamma_i$ . The symbol  $\otimes$  denotes a convolution between the Wilson coefficients  
 and operators, which is due to the fact that the Wilson coefficients can depend on the  
 large energies of the light quarks. Note that if the two collinear quarks in the  $n$  direction  
 form a color singlet (meaning  $\Gamma_i$  is color singlet), then we can use the unitarity of Wilson  
 lines  $Y_n^\dagger Y_n = 1$  to write

$$O_i = C_i \otimes [\bar{h}_s \Gamma_i Y_{\bar{n}} \chi_{\bar{n}}] [\bar{\chi}_n \Gamma_i \chi_n]. \quad (59)$$

310 Since the Wilson lines  $Y_n$  describe the coupling of the collinear fields  $\chi_n$  to the rest of  
 311 the system, their cancellation is the field theoretical realization of the physical picture  
 312 given before.

313 The absence of interactions between the fields in the  $n$  direction from the rest of the  
 314 system can be used to separate the matrix element of the operators  $O_i$  as

$$\begin{aligned} \langle M_n M_{\bar{n}} | O_i | B_s \rangle &= C_i \otimes \langle M_n M_{\bar{n}} | O_i^{n\bar{n}} | B_s \rangle = C_i \otimes \langle M_n | \bar{\chi}_n \Gamma_i \chi_n | 0 \rangle \langle M_{\bar{n}} | h_s \Gamma_i Y_{\bar{n}} \chi_{\bar{n}} | B_s \rangle \\ &= C_i \otimes \phi_{M_n} \otimes \zeta_{B M_{\bar{n}}}. \end{aligned} \quad (60)$$

Table 1

Comparison of the different approaches to Factorization

	SCET	QCDF	PQCD
Expansion in $\alpha_s(\mu_i)$	No	Yes	Yes
Singular convolutions	N/A	New parameters	"Unphysical" $k_T$
Charm Loop	Non-perturbative	Perturbative	Perturbative
Number of parameters	Most	Middle	Least

315 Here  $\phi_M$  denotes the light cone distribution function of the meson  $M$ , while  $\zeta_{BM}$  denotes  
316 the matrix element describing the  $B \rightarrow M$  transition. Thus, the matrix element of  
317 the required operators factor into a convolution of a perturbatively calculable Wilson  
318 coefficient  $C_i$ , a matrix element describing the  $B \rightarrow M_2$  transition, as well as the wave  
319 function of the meson  $M_1$ . The wave functions of the light pseudoscalar mesons have  
320 been measured in the past and are known relatively well, and some of the  $B \rightarrow M_2$   
321 matrix elements can be measured in semileptonic  $B$  decays. Thus, much information for  
322 the matrix elements of the operators  $O_i$  can be measured in other processes, allowing to  
323 use the non-leptonic data on to extract information about the weak scale physics.

There are several different approaches to understanding factorization and they go by  
the names QCD Factorization (QCDF) [38–40], perturbative QCD (PQCD) [45–50] and  
soft-collinear effective theory (SCET) [51–53] in the literature. All three approaches agree  
with everything discussed up to this point, and the main differences arises when trying  
to factorize the matrix elements  $\zeta_{BM}$  further. This can be achieved by matching onto a  
second effective theory which integrates out physics at the scale  $\mu_i \sim \sqrt{\Lambda_{\text{QCD}} m_b}$ , which  
allows to write

$$\zeta_{BM} = J \otimes \phi_B \otimes \phi_M. \quad (61)$$

324 Here  $J$  is a matching coefficient that can be calculated perturbatively in an expansion in  
325  $\alpha_s(\mu_i)$ . A naive calculation of this function  $J$  unfortunately leads to a singular convolution  
326 with the wave functions  $\phi_M$  and  $\phi_B$ , and it is the resolution of this problem that separates  
327 the different approaches. The SCET approach to factorization simply never performs the  
328 second step of the factorization theorem and uses directly the results in Eq. (60) but  
329 requiring the most experimental information. The PQCD results regulate the singular  
330 convolution with an unphysical transverse momentum of the light meson. These results  
331 are therefore on less solid theoretical footing, but require the least amount of experimental  
332 input. QCDF uses a mixture of both approaches and only uses Eq. (61) in cases where  
333 no singular convolutions are obtained. Note however, that for power corrections included  
334 into QCDF a different logic is used and a new non-perturbative parameter is included to  
335 parameterize singular convolutions.

336 Besides the differences in the treatment of singular convolutions, there are also dif-  
337 ferences in how matrix elements of operators containing charm quarks are treated. The  
338 theoretical question is whether such contributions can be calculated perturbatively or  
339 if they lead to new non-perturbative effects. The SCET approach does not attempt to  
340 calculate these matrix elements perturbatively, while QCDF and PQCD do use perturba-  
341 tion theory. The differences between the different approaches are summarized in Tab. 1.

342

344 The tools explained in the previous two sections are used to separate the physical scales  
 345 of flavor physics into the weak scale, the heavy-quark scale, and the nonperturbative QCD  
 346 scale. At the short distances of the first two, QCD effects can be treated with perturbation  
 347 theory, as part of the evaluation of the Wilson coefficients. At longer distances, where  
 348 QCD confines, perturbative QCD breaks down: to obtain the hadronic matrix elements  
 349 of the operators, one must tackle nonperturbative QCD.

350 In some cases general features of field theory—symmetry, analyticity and unitarity,  
 351 the renormalization group—are enough. For example, using the fact that QCD preserves  
 352 CP one can show that the nonperturbative hadronic amplitude drops out of the CP  
 353 asymmetry for a process like  $B \rightarrow \psi K_S$ . Another set of examples entails using one  
 354 process to “measure” the hadronic matrix element, and then using this “measurement”  
 355 in other, more intriguing, processes.

356 In general, however, one would like to compute hadronic matrix elements. The end  
 357 objective is to see whether new physics lurks at short distances, so it is essential that  
 358 one start with the QCD Lagrangian. Any approach will involve some approximation and  
 359 compromise—QCD is too hard otherwise, so it is just as essential that any uncertainties  
 360 be systematically reducible and under quantifiable control.

One method that has these aims is based on lattice gauge theory, which provides a  
 mathematically sound definition of the gauge theory. In QCD, or any quantum field  
 theory, anything of interest can be related to a correlation function

$$\langle O_1(x_1)O_2(x_2)\cdots O_n(x_n)\rangle = \frac{1}{Z} \int \prod_{x,\mu} dA_\mu(x) \prod_x d\bar{q}(x)dq(x) O_1(x_1)O_2(x_2)\cdots O_n(x_n) e^{-S}, \quad (62)$$

361 where the  $O_i(x)$  are local, color singlet operators built out of quark fields  $q$ , antiquark  
 362 fields  $\bar{q}$ , and gluon fields  $A_\mu$ , and  $S$  is the classical action. The normalization factor  $Z$  is  
 363 defined so that  $\langle 1 \rangle = 1$ . For brevity, color, flavor, and (for  $q, \bar{q}$ ) Dirac indices are implied  
 364 but not written out. As it stands, Eq. (62) requires a definition of the products over  
 365 the continuous spacetime label  $x$ . A mathematically sound way to do so is to start with  
 366 a discrete spacetime variable, labeling the sites of a four-dimensional spacetime lattice.  
 367 The idea goes back to Heisenberg, but for QCD and other gauge theories, the key came  
 368 when Wilson showed how to incorporate local gauge invariance with the lattice [54]. If  
 369 the lattice has  $N_S^3 \times L_4$  sites, the spatial size of the finite volume is  $L = N_S a$ , where  $a$  is  
 370 the lattice spacing, and temporal extent  $L_4 = N_4 a$ .

371 The lattice regulates the ultraviolet divergences that appear in quantum field theory  
 372 and reduces the mathematical problem to one similar to statistical mechanics. Familiar  
 373 perturbation theory can be derived starting with lattice field theory, but many other  
 374 theoretical tools from condensed matter theory are available [55]. In the years after  
 375 Wilson’s paper there were, for example, many attempts to calculate hadron masses with  
 376 strong coupling expansions.

377 If the lattice has a finite extent, then the system defined by Eq. (62) has a finite, albeit  
 378 large, number of degrees of freedom. That means that the integrals can, in principle, be  
 379 evaluated on a computer. In the rest of this report all applications of lattice QCD use this  
 380 approach. In this section we provide a summary of the methods and a guide to estimate  
 381 the inevitable errors that enter when mounting large-scale computing.

To start, let us leave the quarks and antiquarks aside and consider how many gluonic integration variables are needed. One would like the lattice spacing  $a$  to be smaller than a hadron, and the spatial volume should be large enough to contain at least one hadron. A desirable target is then  $N_S = L/a = 32$ , which is typical by now, and some groups use even larger lattices. For reasons explained below, the temporal extent  $N_4$  is often taken to be 2 or 3 times larger than  $N_S$ . Taking the gluon's 8 colors and the 4-fold Lorentz index into account, the functional integral has  $8 \times 4 \times 32^3 \times 64 \sim 10^8$  dimensions. This is practical with Monte Carlo methods, generating an ensemble of random values of the fields and replacing the right-hand side of Eq. (62) with

$$\langle O_1(x_1)O_2(x_2)\cdots O_n(x_n) \rangle = \frac{1}{C} \sum_c w(A^{(c)}) O_1(x_1)O_2(x_2)\cdots O_n(x_n), \quad (63)$$

382 where the weight  $w$  for the  $c$ th configuration is specified below, and  $C$  is chosen so that  
 383  $\langle 1 \rangle = 1$ . If the weight  $e^{-S}$  in Eq. (62) is real and positive, then the random fields can be  
 384 generated with distribution  $e^{-S}$ , in which case the weights are field independent. This is  
 385 called importance sampling, and without it numerical lattice field theory is impractical.

386 In Minkowski space the weight is actually a phase factor  $e^{iS_M}$ . That means that  
 387 the weight fluctuates wildly, leading to enormous cancellations that are impossible to  
 388 deal with numerically. For that reason, numerical LQCD calculations are carried out in  
 389 Euclidean space or, equivalently, with imaginary time. With this restriction it remains  
 390 straightforward to compute hadron masses and many matrix elements. If, however, the  
 391 coordinates  $x_i$  in the original correlation function must have timelike or lightlike separa-  
 392 tion, then the function lies beyond current computational techniques.

Fermions, such as quarks, are special for several reasons. To impose the Pauli exclusion principle, the quark fields are Grassman numbers, *i.e.*, they anticommute with each other,  $q_i q_j = -q_j q_i (1 - \delta_{ij})$ . The integration is a formal procedure called Berezin integration. Fortunately, in cases of practical interest, the integration can be carried out by hand. The quark part of the action takes the form

$$S_{\bar{q}q} = \sum_{ij} \bar{q}_j M_{ji} q_i, \quad (64)$$

where  $i$  and  $j$  are multi-indices for spacetime, spin, color, and flavor. The matrix  $M$  is some lattice version of the Dirac operator. It is easy to show that

$$\int \prod_{ij} d\bar{q}_j dq_i e^{-S_{\bar{q}q}} = \det M. \quad (65)$$

393 Similarly, if quark fields appear in the operators, each instance of  $q_i \bar{q}_j$  is replaced, using  
 394 the Wick contraction, by the quark propagator  $M_{ij}^{-1}$ . The determinant and  $M^{-1}$  both  
 395 depend on the gauge field; we simply carry out the quark and antiquark integration by  
 396 hand and the gluon integration with the Monte Carlo, now with weight  $\det M e^{-S_{\text{gauge}}}$ .  
 397 The computation of  $M_{ij}^{-1}$  is demanding and the computation of  $\det M$  is very demanding.

398 Another peculiar feature of fermions is an obstacle to realizing chiral symmetry on  
 399 the lattice [56, 57], often called the fermion doubling problem, because a simple nearest-  
 400 neighbor version of the Dirac operator leads to a 16-fold duplication of states. As a  
 401 consequence, several formulations of lattice fermions are used in numerical lattice QCD.  
 402 With staggered fermions [58, 59] some of the doubling remains, but a subset of the chi-  
 403 ral symmetry is preserved. With Wilson fermions [60] all doubling is removed, but all



404 of the (softly broken) chiral symmetries are explicitly broken. The Ginsparg-Wilson  
 405 relation [61], which is derived from the renormalization group, shows how to preserve a  
 406 remnant of chiral symmetry. Specific solutions are the fixed-point action [62,63], domain-  
 407 wall fermions [64–67], and the overlap [68,69]. In the approaches satisfying the Ginsparg-  
 408 Wilson relation, the chiral transformation turns out to depend on the gauge field [70].  
 409 From a theoretical perspective these are the most attractive, but from a practical per-  
 410 spective the staggered and Wilson formulations are numerically faster.

To obtain a finite problem, numerical lattice QCD uses a finite spacetime volume, so  
 one must specify boundary conditions. In most cases, one identifies the field with itself,  
 up to a phase:

$$q(x + L_\mu e_\mu) = e^{i\theta_\mu} q(x), \quad (66)$$

where  $e_\mu$  is a unit vector and  $L_\mu$  is the total extent, both in the  $\mu$  direction. If  $\theta_\mu = 0$   
 this is called a periodic boundary condition; if  $\theta_\mu = \pi$  this is called an antiperiodic  
 boundary condition; and otherwise this is called a twisted boundary condition [71,72]  
 (although “twisted boundary condition” has other meanings too [73]). In a finite volume,  
 the spectrum is discrete. The allowed 3-momenta are

$$\mathbf{p} = \frac{\boldsymbol{\theta}}{L} + \frac{2\pi}{L} \mathbf{n}, \quad (67)$$

411 where  $\mathbf{n}$  is a vector of integers. One should bear in mind the discrete momentum fol-  
 412 lows from the finite volume, *not* the lattice itself. For one-particle states finite-volume  
 413 effects are exponentially suppressed in periodic and antiperiodic [74], as well as (par-  
 414 tially) twisted [75], boundary conditions. For multi-particle states the boundary effects  
 415 are larger and more interesting [76], as discussed for  $K \rightarrow \pi\pi$  in Ref. [77].

To determine the CKM matrix we need the matrix elements of the electroweak Hamil-  
 tonian derived in Sec. 2.1. In most cases, we are interested in transitions with at most  
 one hadron in the initial or final state. These quantities are determined from 2- and  
 3-point correlation functions, as follows. A first step is to determine the mass. Let  $O$   
 be an operator with the quantum numbers ( $J^{PC}$ , etc.) of the state of interest. For large  
 temporal extent  $L_4$ , and temporal separation  $x_4 > 0$ , the 2-point correlation function

$$\langle O(x)O^\dagger(0) \rangle = \langle 0|\hat{O}(x)\hat{O}^\dagger(0)|0\rangle, \quad (68)$$

where  $|0\rangle$  is the QCD vacuum state and the hat indicates an operator in Hilbert space.  
 Because these calculations are in Euclidean space, the time dependence of the annihilation  
 operator is

$$O(x) = e^{x_4\hat{H}}\hat{O}e^{-x_4\hat{H}}, \quad (69)$$

where  $\hat{H}$  is the Hamiltonian. In deriving Eq. (68) the eigenvalue of  $\hat{H}$  in  $|0\rangle$  is set to zero.  
 Inserting a complete set of eigenstates of  $\hat{H}$  into Eq. (68), one has

$$\langle O(x)O^\dagger(0) \rangle = \sum_n \langle 0|\hat{O}e^{-x_4\hat{H}}|n\rangle\langle n|\hat{O}^\dagger|0\rangle = \sum_n e^{-x_4E_n} |\langle n|\hat{O}^\dagger|0\rangle|^2, \quad (70)$$

416 where  $E_n$  is the energy of the  $n$ th state. If  $|n\rangle$  is a single-particle state with zero 3-  
 417 momentum, this energy is the mass. Taking  $x_4$  large enough the state with the lowest-  
 418 lying mass dominates, and this is how masses are computed in lattice QCD: evaluate the  
 419 left-hand side of Eq. (70) with Monte Carlo techniques, and fit the right-hand side to a  
 420 sum of exponentials.

Now suppose that one would like to consider the case where one is interested in a simple matrix element, one where an operator from the effective Hamiltonian annihilates the hadron. One can obtain the matrix element by computing another 2-point correlation function,

$$\langle J(x)O^\dagger(0) \rangle = \langle 0|\hat{J}(x)\hat{O}^\dagger(0)|0 \rangle = \sum_n e^{-x_4 E_n} \langle 0|\hat{J}|n \rangle \langle n|\hat{O}^\dagger|0 \rangle. \quad (71)$$

421 With the energies and overlaps  $\langle n|\hat{O}^\dagger|0 \rangle$  from the mass calculation, this calculation yields  
422 the transition matrix elements  $\langle 0|\hat{J}|n \rangle$ .

Most of the transitions of interest in flavor physics involve mesons, so it is worth illustrating how the quark propagators  $M^{-1}$  come in. For the charged Kaon, for example, we take the operator  $O = \bar{s}\gamma_5 u$ , and the 2-point function is computed via

$$\langle \bar{s}\gamma_5 u(x)\bar{u}\gamma_5 s(0) \rangle = -\langle \text{tr}[G_u(x,0)\gamma_5 G_s(0,x)\gamma_5] \rangle_A, \quad (72)$$

where the trace is over color and Dirac indices, the average on the right-hand side is over gluon fields, and the quark propagator  $G_f(x,y)$  is the solution of

$$\sum_x M(w,x)G_f(x,y) = \delta_{wy} \quad (73)$$

423 for flavor  $f$ , with color and Dirac indices implied. For the decay of a Kaon to leptons,  
424 the transition operator  $J = \bar{s}\gamma_4\gamma_5 u$ , and the computation of Eq. (71) simply replaces the  
425 first  $\gamma_5$  on both sides of Eq. (72) with  $\gamma_4\gamma_5$ .

In neutral meson mixing and in semileptonic and radiative decays one encounters hadronic matrix elements with one hadron in both the initial and final states. For these one computes a 3-point correlation function,

$$\langle O_f(x)J(y)O_i^\dagger(0) \rangle = \sum_{mn} e^{-(x_4-y_4)E_{fm}} e^{-y_4 E_{in}} \langle 0|\hat{O}_f|fm \rangle \langle fm|\hat{J}|in \rangle \langle in|\hat{O}_i^\dagger|0 \rangle. \quad (74)$$

426 The energies  $E_{fm}$ ,  $E_{in}$  and amplitudes  $\langle 0|\hat{O}_f|fm \rangle$ ,  $\langle in|\hat{O}_i^\dagger|0 \rangle$  are computed from 2-point  
427 functions, so the 3-point function yields  $\langle fm|\hat{J}|in \rangle$ . As before, for mesons (and baryons)  
428 the left-hand side is computed by contracting quark and antiquark fields in favor of quark  
429 propagators.

430 Hadron masses and decay amplitudes computed with lattice QCD depend on the bare  
431 gauge coupling and the bare quark masses,  $1 + n_f$  free parameters, if  $n_f$  flavors are  
432 relevant to the problem at hand. The bare gauge coupling is related to the lattice spacing  
433 via renormalization. Thus, all dimensional quantities are really ratios of the quantity of  
434 interest compared to some fiducial quantity with dimensions of mass. This standard mass  
435 should be one that is either not very sensitive to the quark masses, such as some of the  
436 mass splitting in quarkonium, or whose mass dependence is seen to be under good control,  
437 such as  $f_\pi$ . The bare quark masses are fixed through the simplest hadron masses:  $m_\pi^2$   
438 and  $m_K^2$  for the light and strange quarks, and the  $D_s$  and  $B_s$  or  $\eta_c$  and  $\Upsilon$  masses for  
439 charmed and bottom quarks.

440 In computational physics it is important to know how to estimate uncertainties. In  
441 lattice QCD uncertainties arise, in principal, from the nonzero lattice spacing and the  
442 finite volume. In practice, the algorithms for computing  $\det M$  and  $M^{-1}$  slow down as the  
443 quark masses are reduced. Consequently, the calculations cited elsewhere in this report  
444 are based on simulations with light quark masses that are higher than those of the up  
445 and down quarks in nature. Also in practice, one must be careful with heavy quarks,

446 because the ultraviolet cutoff of currently available lattices,  $1/a$  or  $\pi/a$ , is not (much)  
 447 higher than the  $b$ -quark mass.

448 Fortunately, all these uncertainties may be assessed and quantified with effective field  
 449 theories. (For a review of lattice QCD developed from this perspective, see [78].) For  
 450 the so-called chiral extrapolation, lattice practitioners use chiral perturbation theory  
 451 ( $\chi$ PT) to extend the reach from feasible light quark masses down to the physical up-  
 452 and down-quark masses. This is the same  $\chi$ PT discussed in Sec. 2.4, although some  
 453 practical considerations differ. Often applications of  $\chi$ PT to lattice QCD incorporate the  
 454 leading discretization effects of the lattice. A chiral extrapolation entails a fit to numerical  
 455 lattice-QCD data, and the associated uncertainty is estimated from a combination of  
 456 quantitative measures, like goodness of fit, and qualitative considerations, such as the  
 457 smallness of the quark mass and the effect of higher-order terms. In addition,  $\chi$ PT  
 458 can be used to estimate finite-size effects, because the largest ones typically stem from  
 459 processes in which a virtual pion is emitted, traverses the (periodic) boundary, and is  
 460 then reabsorbed [74, 79, 80].

Discretization effects can be understood and controlled with the Symanzik effective  
 field theory [81, 82]. The central Ansatz here is that lattice gauge theory is described by  
 a continuum effective field theory. For QCD

$$\mathcal{L}_{\text{LGT}} \doteq \mathcal{L}_{\text{QCD}} + \sum_i a^{\dim \mathcal{L}_i - 4} K_i \mathcal{L}_i, \quad (75)$$

461 where the sum runs over operators  $\mathcal{L}_i$  of dimension 5 or higher, and the power of  $a$   
 462 follows from dimensional analysis. The coefficient  $K_i$  subsumes short-distance effects,  
 463 analogously to the Wilson coefficients in Sec. 2.1. The right-hand side of Eq. (75) is a tool  
 464 to analyze the left-hand side or, more precisely, numerical data generated with the lattice  
 465 Lagrangian  $\mathcal{L}_{\text{LGT}}$ . If  $a$  is small enough, the higher dimensional operators may be treated  
 466 as perturbations, leading to two key insights. The first is to justify an extrapolation in  $a$   
 467 to the continuum limit. More powerfully, if one can show for any (expedient) observable  
 468 that, say, all the dimension-5  $K_i$  vanish, then one knows that they vanish for all processes.  
 469 The systematic reduction of the first several  $K_i$  is known as the Symanzik improvement  
 470 program. With chirally symmetric actions, the dimension-5  $K_i$  vanish by symmetry, so  
 471 these are automatically  $O(a)$  improved.

472 For heavy quarks it is often the case that  $m_Q a \not\ll 1$  and, hence, special care is needed.  
 473 It is often said that lattice gauge theory breaks down, but it is more accurate to say that  
 474 the most straightforward application of the Symanzik effective theory breaks down. For  
 475 most calculations relevant to the CKM unitarity triangle, it is simpler to use HQET as  
 476 a theory of cutoff effects [83–85]. This is possible because every (sensible) approach to  
 477 heavy quarks on the lattice enjoys the same static limit and heavy-quark symmetries. So  
 478 the same set-up as in Sec. 2.2 is possible, just with different short-distance structure—  
 479 because the lattice changes short distance. Analogously to Symanzik, one can set up  
 480 an improvement program. Now, however, the approach to the continuum limit is not so  
 481 simple as  $O(a)$  or  $O(a^2)$ . Nevertheless, most serious calculations with heavy-quarks use  
 482 this formalism, or something equivalent, to estimate heavy-quark discretization effects.  
 483 For further details on techniques for heavy quarks, see [86]. A more recent development  
 484 is to map out the  $m_Q a$  dependence in finite volume [87, 88], where both  $m_Q a \ll 1$  and  
 485  $m_Q a \approx 1$  are feasible (cf. Sec. 5).

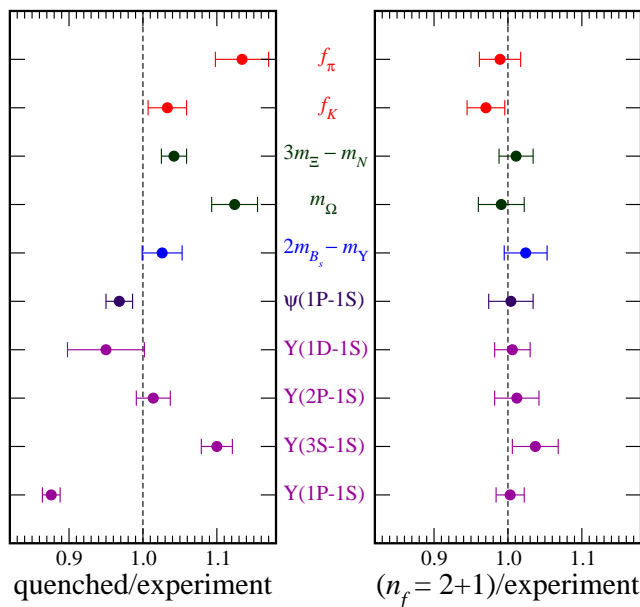


Fig. 3. Comparison of quenched and 2+1 flavor lattice QCD, plotting the ratio of calculated results to laboratory measurements [91]. The quenched results deviate by as much as 10–15%—not bad for a strongly-coupled field theory, but not good enough for flavor physics. With 2+1 flavors of sea quarks, however, the agreement is at the few-percent level.

486 One uncertainty that is not amenable to effective field theory (and is, therefore, devilish  
 487 to quantify) stems from the so-called quenched approximation [89, 90]. It corresponds to  
 488 replacing the computationally demanding  $\det M$  in the weight by 1 and attempting to  
 489 compensate by shifts in the bare gauge coupling and bare quark masses. Physically this  
 490 corresponds to keeping valence quarks but treating sea quarks as a dielectric medium.  
 491 This approximation is, by now, a historical artifact. All calculations that aspire to play  
 492 a role in flavor physics now have either  $n_f = 2$  or  $2 + 1$  flavors of sea quarks. In both  
 493 cases the 2 light quarks are taken as light as possible, as a basis for chiral extrapolation.  
 494 For  $2 + 1$  the third flavor is tuned to have the mass of the strange quark, whereas  $n_f = 2$   
 495 means that the strange quark is quenched. A comparison of quenched and 2+1 flavor  
 496 QCD is shown in Fig. 3, adapted from Ref. [91].

497 The results shown in Fig. 3, and many quoted in the rest of this report, have been  
 498 obtained with staggered sea quarks [92, 93], which provide the least computationally de-  
 499 manding method for computing  $\det M$  [94]. A drawback in this method is that staggered  
 500 quarks come in four species, and a single quark flavor is simulated with  $[\det_4 M]^{1/4}$  [95],  
 501 where the subscript emphasizes the number of species in the determinant. There are con-  
 502 cerns whether the fourth root really yields QCD in the continuum limit, although all pub-  
 503 lished criticisms [96–98] have been refuted [99, 100]. The theoretical arguments [101, 102]  
 504 in favor of this procedure are still being digested, although there is a significant body of  
 505 supporting circumstantial evidence [103–105]. Whatever one thinks of the rooted stag-  
 506 gered sea, it should be clear that these calculations should be confirmed. Other methods  
 507 for sea quarks are accumulating sufficiently high statistics, so one can anticipate compet-  
 508 itive results not only with staggered sea quarks [106], but also with Symanzik-improved

509 Wilson sea quarks [107, 108], twisted-mass Wilson sea quarks [109], domain-wall sea  
 510 quarks [110], and overlap sea quarks [111].

511 Calculations with 2 flavors of sea quarks have an uncertainty from quenching the  
 512 strange quark. The error incurred may be as large as 3–5%, but is again hard to pin  
 513 down. In many cases, for example the  $\Omega^-$  mass, no significant effect is seen. When using  
 514 2-flavor results in this report, we take the original authors' estimates of the error for  
 515 quenching the strange quark. If they have omitted this line from the error budget, we  
 516 then assign a conservative 5% error.

517 Numerical lattice QCD has developed over the past thirty years, and much of the  
 518 literature has aimed to develop numerical methods. Such work is not limited to algo-  
 519 rithm development, but also to demonstrate how a phenomenologically relevant calcula-  
 520 tion could or should be carried out. Inevitably, some papers straddle the middle ground  
 521 between development and mature results, with the consequence that some interesting  
 522 papers have incomplete error budgets. Where such results are used later in the report,  
 523 we try to account for omitted uncertainties in a rational way.

#### 524 2.4. Chiral Perturbation Theory

525 Chiral perturbation theory (ChPT) is the effective field theory describing strong and  
 526 electroweak interactions of the light pseudo-scalar mesons ( $\pi$ ,  $K$ ,  $\eta$ ) at low energy, in  
 527 a regime where standard perturbative methods are inapplicable [112–114]. ChPT relies  
 528 on our understanding of the chiral symmetry of QCD in the limit of massless light  
 529 quarks ( $m_u = m_d = m_s = 0$ ), its spontaneous symmetry breaking according to the  
 530 pattern  $SU(3)_L \times SU(3)_R \rightarrow SU(3)_V$  and its explicit breaking due to non-vanishing  
 531 quark masses.

In the massless limit  $m_q = 0$ , the QCD Lagrangian for light quarks ( $q^\top = (u, d, s)$ )

$$\mathcal{L}_{\text{QCD}} = -\frac{1}{4} G_{\mu\nu}^a G_a^{\mu\nu} + i \bar{q}_L \gamma^\mu D_\mu q_L + i \bar{q}_R \gamma^\mu D_\mu q_R - \bar{q}_L m_q q_R - \bar{q}_R m_q q_L \quad (76)$$

532 is invariant under global independent  $SU(3)_L \times SU(3)_R$  transformations of the left-  
 533 and right-handed quarks in flavor space:  $q_{L,R} \rightarrow g_{L,R} q_{L,R}$ ,  $g_{L,R} \in SU(3)_{L,R}$ . The  
 534 absence of  $SU(3)$  multiplets of opposite parity in the hadronic spectrum suggests that  
 535 the chiral group  $G = SU(3)_L \times SU(3)_R$  is spontaneously broken to the diagonal subgroup  
 536  $H = SU(3)_V$ , i.e. the symmetry is realized à la Nambu-Goldstone [115–117]. According  
 537 to Goldstone's theorem [115] then, the spectrum of QCD should contain an octet of  
 538 pseudoscalar massless bosons, in one to one correspondence to the broken symmetry  
 539 generators. These are identified with the  $\pi$ ,  $K$ , and  $\eta$  mesons, which would be massless  
 540 in the exact chiral limit of  $m_{u,d,s} = 0$ , but acquire a finite mass in the real world due  
 541 to explicit chiral symmetry breaking induced by  $m_q \neq 0$ . Pions, Kaons, and eta remain,  
 542 however, the lowest lying hadronic excitations. The existence of a gap separating  $\pi$ ,  $K$ ,  $\eta$   
 543 from the rest of the spectrum makes it possible to build an effective theory involving  
 544 only Goldstone modes.

The basic building blocks of the effective theory are the Goldstone fields  $\varphi$ . Intuitively,  
 the massless Goldstone modes describe excitations of the system along the directions  
 in field space that connect degenerate vacuum configurations (think about the circle of  
 minima in a "Mexican-hat" potential). Mathematically, this means that the Goldstone  
 fields parametrize the elements  $u(\varphi)$  of the coset space  $SU(3)_L \times SU(3)_R / SU(3)_V$  [118,

119]. The transformation of  $\varphi$  under  $G$  is determined by the action of  $G$  on the elements  $u(\varphi)$  of the coset space

$$u(\varphi) \rightarrow u(\varphi') = g_R u(\varphi) h(g, \varphi)^{-1} = h(g, \varphi) u(\varphi) g_L^{-1} \quad (77)$$

where  $g = (g_L, g_R) \in G$ . The explicit form of  $h(g, \varphi) \in SU(3)_V$  will not be needed here. An explicit parametrization of  $u(\varphi)$  is given by

$$u(\varphi) = \exp \left\{ \frac{i}{\sqrt{2}F} \varphi \right\}, \quad (78)$$

with

$$\varphi = \begin{pmatrix} \frac{1}{\sqrt{2}} \pi^0 + \frac{1}{\sqrt{6}} \eta_8 & \pi^+ & K^+ \\ \pi^- & -\frac{1}{\sqrt{2}} \pi^0 + \frac{1}{\sqrt{6}} \eta_8 & K^0 \\ K^- & \bar{K}^0 & -\frac{2}{\sqrt{6}} \eta_8 \end{pmatrix}.$$

The structure of the effective Lagrangian  $\mathcal{L}_{\text{eff}}$  is determined by chiral symmetry and the discrete symmetries of QCD.  $\mathcal{L}_{\text{eff}}$  has to be invariant under chiral transformations, up to explicit symmetry breaking terms that transform like the quark mass term in the QCD Lagrangian (76). As a consequence,  $\mathcal{L}_{\text{eff}}$  is organized as an expansion in powers of (i) derivatives (momenta) of the Goldstone fields and (ii) light quark masses ( $m_q$ ). Since the meson masses squared are proportional to the quark masses, the two expansions are related ( $m_q \sim O(M_M^2) \sim O(p^2)$ ) and the mesonic effective chiral Lagrangian takes the form

$$\mathcal{L}_{\text{eff}} = \sum_{n \geq 1} \mathcal{L}_{2n}, \quad \mathcal{L}_{2n} \sim O(p^{2n}). \quad (79)$$

The power counting parameter is given by the ratio  $p^2 \sim p_{\text{ext}}^2 / \Lambda_\chi^2$  of a typical external momentum (or quark mass) over the intrinsic scale  $\Lambda_\chi$ , set by the lightest non-Goldstone states ( $\Lambda_\chi \sim 1$  GeV). To each order in the expansion, the effective Lagrangian contains a number of low-energy constants (LECs) not fixed by symmetry consideration, encoding underlying QCD dynamics.

The leading order effective Lagrangian reads (in terms of  $U(\varphi) = u(\varphi)^2$ ),

$$\mathcal{L}_2 = \frac{F^2}{4} \text{Tr} \left[ \partial_\mu U \partial^\mu U + 2B m_q (U + U^\dagger) \right] \quad (80)$$

545 where  $m_q = \text{diag}(m_u, m_d, m_s)$  and the trace is performed over the  $SU(3)$  indices. The  
 546 dimensionful constants  $F$  and  $B$  are related to the pion decay constant and the quark  
 547 condensate by  $F_\pi = F(1 + O(m_q))$  and  $\langle 0 | \bar{u}u | 0 \rangle = -F^2 B(1 + O(m_q))$ .  $\mathcal{L}_2$  contains the  
 548 Gell-Mann-Oaks-Renner [120] and Gell-Mann-Okubo [121,122] mass relations and allows  
 549 one to calculate physical processes, such as  $\pi\pi$  scattering, to  $O(p^2)$  in terms of just  $F_\pi$   
 550 and  $M_M^2$  ( $M_\pi^2 = B(m_u + m_d)$ , ...).

551 The power of the effective field theory approach is that it allows to systematically  
 552 improve the calculations of low-energy processes by considering higher-order terms in  
 553 the momentum/light-quark-mass expansion. As shown by Weinberg [112], at any given  
 554 order in this expansion only a finite number of couplings in (79) appear. For instance at  
 555  $O(p^4)$  a given amplitude receives contributions only from: (i) tree-level diagrams with one  
 556 insertion from  $\mathcal{L}_4$ ; (ii) one-loop diagrams with all vertices from  $\mathcal{L}_2$ . The loop diagrams

557 perturbatively unitarize the theory and introduce physical infrared singularities due to  
 558 pseudoscalar meson intermediate states (the chiral logs,  $\sim m_q \log m_q$ ). However, loops  
 559 also introduce ultraviolet divergences. Using a regularization compatible with chiral sym-  
 560 metry, the counterterms necessary to absorb the divergences must have the same form  
 561 as the terms present in  $\mathcal{L}_4$ : thus, one loop divergences simply renormalize the LECs of  
 562  $O(p^4)$ . This argument generalizes to any order in the low-energy expansion: the effective  
 563 theory is renormalizable order by order in the low-energy expansion.

564 The finite parts of the LECs can be fitted to experiment or extracted by matching to  
 565 lattice QCD results (or other, less systematic approximations to non-perturbative QCD  
 566 dynamics). The accuracy of a given calculation is bounded by the size of higher order  
 567 terms in the low-energy expansion. State of the art calculations in the strong sector go  
 568 up to  $O(p^6)$  [123].

To illustrate the general features discussed above, we report here the expression of the  
 the pion decay constant to  $O(p^4)$  [114]

$$F_\pi = F \left[ 1 - 2\mu_\pi - \mu_K + \frac{8B}{F^2} \left( \hat{m} L_5^r(\mu) + (m_u + m_d + m_s) L_4^r(\mu) \right) \right]. \quad (81)$$

569 Here  $\mu_P = M_P^2 / (32\pi^2 F^2) \log(M_P^2 / \mu^2)$ ,  $M_\pi^2 = B(m_u + m_d)$ ,  $M_K = B(m_s + \hat{m})$ , and  
 570  $\hat{m} = 1/2(m_u + m_d)$ . Moreover,  $\mu$  is the renormalization scale and  $L_{4,5}^r(\mu)$  are two finite  
 571 scale-dependent LECs. This expression illustrates the appearance of calculable chiral log-  
 572 arithms (with unambiguous coefficients) as well as polynomial terms in the quark masses  
 573 multiplied by a priori unknown coefficients. Expressions of this type are used to extrapo-  
 574 late lattice QCD results from unphysical quark masses to the physical point. Nowadays,  
 575 this is one of the most relevant applications of ChPT in CKM physics. An important  
 576 recent development in this area is the use of  $SU(2)$  ChPT [110, 124], in which Kaons are  
 577 treated as external massive fields, to study the extrapolation of Kaon amplitudes in  $m_{u,d}$   
 578 (see Sec. 4.4.4 for discussion and applications)

579 The framework presented above describes the strong interactions of Goldstone modes.  
 580 It has been extended in several directions, highly relevant to CKM physics, to include:  
 581 – non-leptonic weak interactions of Goldstone modes ( $\Delta S = 1, 2$ ) [125–128];  
 582 – interactions of soft Goldstone modes with heavy particles (heavy mesons [129, 130] and  
 583 baryons [131, 132]);  
 584 – interaction of Goldstone modes with external electromagnetic fields and weak gauge  
 585 bosons (this is achieved by adding external sources that couple to quark bilinears in  
 586 the QCD Lagrangian [113, 114]);  
 587 – other dynamical fields in the low-energy theory, such as photons [133] and light lep-  
 588 tons [134] (the amplitudes are expanded to  $O(e^2 p^{2n})$ ,  $e$  being the electromagnetic  
 589 coupling).

## 590 2.5. Beyond the Standard Model

591 Despite its impressive phenomenological success, the SM should be regarded as a low-  
 592 energy effective theory. Viewing the SM as an effective theory poses two main questions:  
 593 which is the *energy scale* and which are the *interactions and symmetries properties* of the  
 594 new degrees of freedom. So far we have no unambiguous answer for both these questions;

595 however, a strong theoretical prejudice for new degrees of freedom around the TeV scale  
 596 follows from a natural stabilization of the mechanism of electroweak symmetry breaking.  
 597 In this perspective, low-energy flavor physics provide a powerful tool to address the second  
 598 question, and in particular to explore the symmetries properties of the new degrees of  
 599 freedom.

600 In order to describe New Physics (NP) effects in flavor physics we can follow two main  
 601 strategies, whose virtues and limitations can be summarised as follows:

602 – *Generic Effective Field Theory (EFT) approaches.*

603 Assuming the new degrees to be heavier than SM fields, we can integrate them out  
 604 and describe NP effects by means of a generalization of the Fermi Theory: the SM  
 605 Lagrangian becomes the renormalizable part of a more general local Lagrangian which  
 606 includes an infinite tower of higher-dimensional operators, constructed in terms of SM  
 607 fields and suppressed by inverse powers of an effective scale  $\Lambda_{\text{NP}} > M_W$ .

608 This general bottom-up approach allows us to analyse all realistic extensions of the SM  
 609 in terms of a limited number of parameters (the coefficients of the higher-dimensional  
 610 operators). The drawback of this method is the impossibility to establish correla-  
 611 tions of NP effects at low and high energies: the scale  $\Lambda_{\text{NP}}$  defines the cut-off of the  
 612 EFT. However, correlations among different low-energy processes can be established  
 613 implementing specific symmetry properties on the EFT, such as the Minimal Flavor  
 614 Violation hypothesis (see Sec. 2.5.1). The experimental tests of such correlations allow  
 615 us to test/establish general features of the new theory which holds independently of  
 616 the dynamical details of the model. In particular,  $B$ ,  $D$  and  $K$  decays are extremely  
 617 useful in determining the flavor-symmetry breaking pattern of the NP model.

618 – *Explicit Ultraviolet completions.*

619 The generic EFT approach is somehow the opposite of the standard top-down strat-  
 620 egy, where a given NP theory –and a specific set of parameters– are employed to  
 621 evaluate possible deviations from the SM. The top-down approach usually allows us to  
 622 establish several correlations, both at low energies and between low- and high-energy  
 623 observables. In the following we will discuss in some detail this approach in the case of  
 624 Minimal Supersymmetric extension of the SM (see Sec. 2.5.2). The price to pay of this  
 625 strategy is the loss of generality. This is quite a high price given our limited knowledge  
 626 about the physics above the electroweak scale.

### 627 2.5.1. *Model-independent approaches and the MFV hypothesis*

628 The NP contributions should naturally induce large effects in processes which are  
 629 severely suppressed in the SM, such as meson-antimeson mixing ( $\Delta F = 2$  amplitudes) or  
 630 flavor-changing neutral-current (FCNC) rare decays. Up to now there is no evidence of  
 631 deviations from the SM in these processes and this implies severe bounds on the effective  
 632 scale of various dimension-six operators in the EFT approach. For instance, the good  
 633 agreement between SM expectations and experimental determinations of  $K^0-\bar{K}^0$  mixing  
 634 leads to bounds above  $10^4$  TeV for the effective scale of  $\Delta S = 2$  operators, i.e. well above  
 635 the few TeV range suggested by a natural stabilization of the electroweak-symmetry  
 636 breaking mechanism.

637 The apparent contradiction between these two determinations of  $\Lambda$  is a manifestation  
 638 of what in many specific frameworks (supersymmetry, technicolor, etc.) goes under the  
 639 name of *flavor problem*: if we insist on the theoretical prejudice that new physics has to



640 emerge in the TeV region, we have to conclude that the new theory possesses a highly  
 641 non-generic flavor structure. Interestingly enough, this structure has not been clearly  
 642 identified yet, mainly because the SM (the low-energy limit of the new theory), doesn't  
 643 possess an exact flavor symmetry. Within a model-independent approach, we should  
 644 try to deduce this structure from data, using the experimental information on FCNC  
 645 transitions to constrain its form.

646 *2.5.1.1. Generic bounds on loop-mediated amplitudes.* In several realistic NP models we  
 647 can neglect non-standard effects in all cases where the corresponding effective operator  
 648 is generated at the tree-level within the SM. This general assumption implies that the  
 649 experimental determination of the CKM matrix via tree-level processes is free from the  
 650 contamination of NP contributions. Using this determination we can unambiguously  
 651 predict meson-antimeson mixing and FCNC amplitudes within the SM. Comparing these  
 652 predictions with data allows to derive general constraints on NP which holds in a wide  
 653 class of models.

654 The most constrained sector is the one of  $\Delta F = 2$  transitions, where almost all the  
 655 interesting amplitudes have been measured with good accuracy. An updated analysis of  
 656 the present constraints from these measurements will be presented in Sec. 10.2. The main  
 657 conclusions that can be drawn from this analysis can be summarized as follows:

- In all the three accessible short-distance amplitudes ( $K^0-\bar{K}^0$ ,  $B_d-\bar{B}_d$ , and  $B_s-\bar{B}_s$ )  
 the magnitude of the new-physics amplitude cannot exceed, in size, the SM short-  
 distance contribution. The latter is suppressed both by the GIM mechanism and by  
 the hierarchical structure of the CKM matrix. As a result, new-physics models with  
 TeV-scale flavored degrees of freedom and  $\mathcal{O}(1)$  flavor-mixing couplings are essentially  
 ruled out. For instance, considering a generic  $\Delta F = 2$  effective Lagrangian of the form

$$\mathcal{L}^{\Delta F=2} = \sum_{i \neq j} \frac{c_{ij}}{\Lambda^2} (\bar{d}_L^i \gamma^\mu d_L^j)^2, \quad (82)$$

658 where  $d^i$  denotes a generic down-type quark ( $i = 1, 2, 3$ ) and  $c_{ij}$  are dimensionless  
 659 couplings, the condition  $|\mathcal{A}_{\text{NP}}^{\Delta F=2}| < |\mathcal{A}_{\text{SM}}^{\Delta F=2}|$  implies

$$\Lambda < \frac{3.4 \text{ TeV}}{|V_{ti}^* V_{tj}|/|c_{ij}|^{1/2}} \approx \begin{cases} 9 \times 10^3 \text{ TeV} \times |c_{sd}|^{1/2} \\ 4 \times 10^2 \text{ TeV} \times |c_{bd}|^{1/2} \\ 7 \times 10^1 \text{ TeV} \times |c_{bs}|^{1/2} \end{cases} \quad (83)$$

- In the case of  $B_d-\bar{B}_d$  and  $K^0-\bar{K}^0$  mixing, which are both well measured, there is  
 still room for a new-physics contribution comparable to the SM one. However, this is  
 possible only if the new-physics contribution is aligned in phase with respect to the SM  
 amplitude. The situation is quite different in the case of  $B_s-\bar{B}_s$  mixing, where present  
 measurements allow a large non-standard CP violating phase.

665 As we will discuss in the following, a natural mechanism to reconcile the stringent bounds  
 666 in Eq. (83) with the expectation  $\Lambda \sim \text{few TeV}$  is obtained with the Minimal Flavor  
 667 Violation hypothesis.

668 *2.5.1.2. Minimal Flavor Violation.* A very reasonable, although quite pessimistic, so-  
 669 lution to the flavor problem is the so-called Minimal Flavor Violation (MFV) hypothesis.

670 Under this assumption, flavor-violating interactions are linked to the known structure  
671 of Yukawa couplings also beyond the SM. As a result, non-standard contributions in  
672 FCNC transitions turn out to be suppressed to a level consistent with experiments even  
673 for  $\Lambda \sim \text{few TeV}$ . One of the most interesting aspects of the MFV hypothesis is that it  
674 can naturally be implemented within the EFT approach to NP. The effective theories  
675 based on this symmetry principle allow us to establish unambiguous correlations among  
676 NP effects in various rare decays. These falsifiable predictions are the key ingredients to  
677 identify in a model-independent way which are the irreducible sources of flavor symmetry  
678 breaking.

The MFV hypothesis consists of two ingredients [135]: i) a *flavor symmetry* and ii) a set of *symmetry-breaking terms*. The symmetry is defined from the SM Lagrangian in absence of Yukawa couplings. This is invariant under a large global symmetry of flavor transformations:  $\mathcal{G}_q \otimes \mathcal{G}_\ell \otimes U(1)^5$ , where

$$\mathcal{G}_q = SU(3)_{Q_L} \otimes SU(3)_{U_R} \otimes SU(3)_{D_R} , \quad \mathcal{G}_\ell = SU(3)_{L_L} \otimes SU(3)_{E_R} . \quad (84)$$

679 The  $SU(3)$  groups refer to a rotation in flavor space (or a flavor mixing) among the  
680 three families of basic SM fields: the quark and lepton doublets,  $Q_L$  and  $L_L$ , and the  
681 three singlets  $U_R$ ,  $D_R$  and  $E_R$ . Two of the five  $U(1)$  groups can be identified with the  
682 total baryon and lepton number (not broken by the SM Yukawa interaction), while an  
683 independent  $U(1)$  can be associated to the weak hypercharge. Since hypercharge is gauged  
684 and involves also the Higgs field, it is more convenient not to include it in the flavour  
685 group, which would then be defined as  $\mathcal{G}_{\text{SM}} = \mathcal{G}_\ell \otimes U(1)^4$  [136].

Within the SM this large global symmetry, and particularly the  $SU(3)$  subgroups controlling flavor-changing transitions, is explicitly broken by the Yukawa interaction

$$\mathcal{L}_Y = \bar{Q}_L Y_D D_R H + \bar{Q}_L Y_U U_R H_c + \bar{L}_L Y_E E_R H + \text{h.c.} \quad (85)$$

The most restrictive hypothesis we can make to *protect* in a consistent way quark-flavor mixing beyond the SM is to assume that  $Y_D$  and  $Y_U$  are the only sources of  $\mathcal{G}_q$  breaking also in the NP model. To implement and interpret this hypothesis in a consistent way, we can assume that  $\mathcal{G}_q$  is a good symmetry, promoting  $Y_{U,D}$  to be non-dynamical fields (spurions) with non-trivial transformation properties under this symmetry

$$Y_U \sim (3, \bar{3}, 1)_{\mathcal{G}_q} , \quad Y_D \sim (3, 1, \bar{3})_{\mathcal{G}_q} . \quad (86)$$

686 If the breaking of the symmetry occurs at very high energy scales at low-energies we  
687 would only be sensitive to the background values of the  $Y$ , i.e. to the ordinary SM  
688 Yukawa couplings. Employing the effective-theory language, we then define that an effective theory satisfies the criterion of Minimal Flavor Violation in the quark sector if all higher-dimensional operators, constructed from SM and  $Y$  fields, are invariant under CP and (formally) under the flavor group  $\mathcal{G}_q$  [135].

692 According to this criterion one should in principle consider operators with arbitrary  
693 powers of the (dimensionless) Yukawa fields. However, a strong simplification arises by the observation that all the eigenvalues of the Yukawa matrices are small, but for the top one, and that the off-diagonal elements of the CKM matrix are very suppressed.  $Y$  As a consequence, in the limit where we neglect light quark masses, the leading  $\Delta F = 2$  and  $\Delta F = 1$  FCNC amplitudes get exactly the same CKM suppression as in the SM:

Table 2

Bounds on the scale of new physics for some representative  $\Delta F = 2$  [36] and  $\Delta F = 1$  [137] MFV operators (assuming effective coupling  $1/\Lambda^2$ ).

Operator	$A_i$ @95% prob. [TeV]	Observables
$H^\dagger (\bar{D}_R \lambda_d \lambda_{\text{FC}} \sigma_{\mu\nu} Q_L) (e F_{\mu\nu})$	6.1	$B \rightarrow X_s \gamma, B \rightarrow X_s \ell^+ \ell^-$
$\frac{1}{2} (\bar{Q}_L Y_U Y_U^\dagger \gamma_\mu Q_L)^2$	5.9	$\epsilon_K, \Delta m_{B_d}, \Delta m_{B_s}$
$(\bar{Q}_L \lambda_{\text{FC}} \gamma_\mu Q_L) (\bar{E}_R \gamma_\mu E_R)$	2.7	$B \rightarrow X_s \ell^+ \ell^-, B_s \rightarrow \mu^+ \mu^-$

$$\mathcal{A}(d^i \rightarrow d^j)_{\text{MFV}} = (V_{ti}^* V_{tj}) \mathcal{A}_{\text{SM}}^{(\Delta F=1)} \left[ 1 + a_1 \frac{16\pi^2 M_W^2}{\Lambda^2} \right], \quad (87)$$

$$\mathcal{A}(M_{ij} - \bar{M}_{ij})_{\text{MFV}} = (V_{ti}^* V_{tj})^2 \mathcal{A}_{\text{SM}}^{(\Delta F=2)} \left[ 1 + a_2 \frac{16\pi^2 M_W^2}{\Lambda^2} \right]. \quad (88)$$

698 where the  $\mathcal{A}_{\text{SM}}^{(i)}$  are the SM loop amplitudes and the  $a_i$  are  $\mathcal{O}(1)$  real parameters. The  $a_i$   
699 depend on the specific operator considered but are flavor independent. This implies the  
700 same relative correction in  $s \rightarrow d$ ,  $b \rightarrow d$ , and  $b \rightarrow s$  transitions of the same type.

701 As pointed out in Ref. [31], within the MFV framework several of the constraints used  
702 to determine the CKM matrix (and in particular the unitarity triangle) are not affected  
703 by NP. In this framework, NP effects are negligible not only in tree-level processes but  
704 also in a few clean observables sensitive to loop effects, such as the time-dependent CPV  
705 asymmetry in  $B_d \rightarrow J/\Psi K_{L,S}$ . Indeed the structure of the basic flavor-changing coupling  
706 in Eq. (88) implies that the weak CPV phase of  $B_d - \bar{B}_d$  mixing is  $\arg[(V_{td} V_{tb}^*)^2]$ , exactly  
707 as in the SM. This construction provides a natural (a posteriori) justification of why no  
708 NP effects have been observed in the quark sector: by construction, most of the clean  
709 observables measured at  $B$  factories are insensitive to NP effects in the MFV framework.

710 In Tab. 2 we report a few representative examples of the bounds on the higher-dimen-  
711 sional operators in the MFV framework. As can be noted, the built-in CKM suppression  
712 leads to bounds on the effective scale of new physics not far from the TeV region. These  
713 bounds are very similar to the bounds on flavor-conserving operators derived by precision  
714 electroweak tests. This observation reinforces the conclusion that a deeper study of rare  
715 decays is definitely needed in order to clarify the flavor problem: the experimental preci-  
716 sion on the clean FCNC observables required to obtain bounds more stringent than those  
717 derived from precision electroweak tests (and possibly discover new physics) is typically  
718 in the 1% – 10% range.

719 Although the MFV seems to be a natural solution to the flavor problem, it should be  
720 stressed that we are still very far from having proved the validity of this hypothesis from  
721 data.<sup>4</sup> A proof of the MFV hypothesis can be achieved only with a positive evidence of  
722 physics beyond the SM exhibiting the flavor-universality pattern (same relative correction  
723 in  $s \rightarrow d$ ,  $b \rightarrow d$ , and  $b \rightarrow s$  transitions of the same type) predicted by the MFV  
724 assumption.

725 The idea that the CKM matrix rules the strength of FCNC transitions also beyond the  
726 SM has become a very popular concept in the recent literature and has been implemented  
727 and discussed in several works. It is worth stressing that the CKM matrix represents  
728 only one part of the problem: a key role in determining the structure of FCNCs is

<sup>4</sup> In the EFT language we can say that there is still room for sizable new sources of flavour symmetry breaking beside the SM Yukawa couplings [138].

729 also played by quark masses, or by the Yukawa eigenvalues. In this respect, the MFV  
730 criterion illustrated above provides the maximal protection of FCNCs (or the minimal  
731 violation of flavor symmetry), since the full structure of Yukawa matrices is preserved.  
732 At the same time, this criterion is based on a renormalization-group-invariant symmetry  
733 argument, which can be implemented independently of any specific hypothesis about  
734 the dynamics of the new-physics framework. The only difference between weakly- and  
735 strongly-interacting theories at the TeV scale is that in the latter case the expansion in  
736 powers of the Yukawa spurions cannot be truncated to the first non-trivial terms [139,140]  
737 (leaving more freedom for non-negligible effects also in up-type FCNC amplitudes [140]).  
738 This model-independent structure does not hold in most of the alternative definitions of  
739 MFV models that can be found in the literature. For instance, the definition of Ref. [141]  
740 (denoted constrained MFV, or CMFV) contains the additional requirement that the  
741 effective FCNC operators playing a significant role within the SM are the only relevant  
742 ones also beyond the SM. This condition is realized only in weakly coupled theories at  
743 the TeV scale with only one light Higgs doublet, such as the MSSM with small  $\tan\beta$ . It  
744 does not hold in several other frameworks, such as Higgsless models, or the MSSM with  
745 large  $\tan\beta$ .

746 **2.5.1.3. MFV at large  $\tan\beta$ .** If the Yukawa Lagrangian contains only one Higgs field,  
747 we can still assume that the Yukawa couplings are the only irreducible breaking sources  
748 of  $\mathcal{G}_q$ , but we can change their overall normalization.

A particularly interesting scenario is the two-Higgs-doublet model where the two Higgses are coupled separately to up- and down-type quarks:

$$\mathcal{L}_Y^{2HDM} = \bar{Q}_L Y_D D_R H_D + \bar{Q}_L Y_U U_R H_U + \bar{L}_L Y_E E_R H_D + \text{h.c.} \quad (89)$$

749 This Lagrangian is invariant under an extra U(1) symmetry with respect to the one-  
750 Higgs Lagrangian in Eq. (85): a symmetry under which the only charged fields are  $D_R$   
751 and  $E_R$  (charge +1) and  $H_D$  (charge -1). This symmetry, denoted  $U_{PQ}$ , prevents tree-  
752 level FCNCs and implies that  $Y_{U,D}$  are the only sources of  $\mathcal{G}_q$  breaking appearing in  
753 the Yukawa interaction (similar to the one-Higgs-doublet scenario). Coherently with the  
754 MFV hypothesis, we can then assume that  $Y_{U,D}$  are the only relevant sources of  $\mathcal{G}_q$   
755 breaking appearing in all the low-energy effective operators. This is sufficient to ensure  
756 that flavor-mixing is still governed by the CKM matrix, and naturally guarantees a good  
757 agreement with present data in the  $\Delta F = 2$  sector. However, the extra symmetry of the  
758 Yukawa interaction allows us to change the overall normalization of  $Y_{U,D}$  with interesting  
759 phenomenological consequences in specific rare modes.

The normalization of the Yukawa couplings is controlled by the ratio of the vacuum expectation values (vev) of the two Higgs fields, or by the parameter  $\tan\beta = \langle H_U \rangle / \langle H_D \rangle$ . For  $\tan\beta \gg 1$  the smallness of the  $b$  quark and  $\tau$  lepton masses can be attributed to the smallness of  $1/\tan\beta$  rather than to the corresponding Yukawa couplings. As a result, for  $\tan\beta \gg 1$  we cannot anymore neglect the down-type Yukawa coupling. Moreover, the  $U(1)_{PQ}$  symmetry cannot be exact: it has to be broken at least in the scalar potential in order to avoid the presence of a massless pseudoscalar Higgs. Even if the breaking of  $U(1)_{PQ}$  and  $\mathcal{G}_q$  are decoupled, the presence of  $U(1)_{PQ}$  breaking sources can have important implications on the structure of the Yukawa interaction, especially if  $\tan\beta$  is large [135, 142–144]. We can indeed consider new dimension-four operators such as

$$\epsilon \bar{Q}_L Y_D D_R (H_U)^c \quad \text{or} \quad \epsilon \bar{Q}_L Y_U Y_U^\dagger Y_D D_R (H_U)^c, \quad (90)$$

where  $\epsilon$  denotes a generic MFV-invariant  $U(1)_{PQ}$ -breaking source. Even if  $\epsilon \ll 1$ , the product  $\epsilon \times \tan \beta$  can be  $\mathcal{O}(1)$ , inducing large corrections to the down-type Yukawa sector:

$$\epsilon \bar{Q}_L Y_D D_R (H_U)^c \xrightarrow{vev} \epsilon \bar{Q}_L Y_D D_R (H_U) = (\epsilon \times \tan \beta) \bar{Q}_L Y_D D_R (H_D). \quad (91)$$

760 Since the  $b$ -quark Yukawa coupling becomes  $\mathcal{O}(1)$ , the large- $\tan \beta$  regime is particularly  
761 interesting for helicity-suppressed observables in  $B$  physics.

762 One of the clearest phenomenological consequences is a suppression (typically in the  
763 10 – 50% range) of the  $B \rightarrow \ell \nu$  decay rate with respect to its SM expectation [145, 146].  
764 Potentially measurable effects in the 10 – 30% range are expected also in  $B \rightarrow X_s \gamma$  [147,  
765 148] and  $\Delta M_{B_s}$  [149, 150]. The most striking signature could arise from the rare decays  
766  $B_{s,d} \rightarrow \ell^+ \ell^-$  whose rates could be enhanced over the SM expectations by more than  
767 one order of magnitude [151–153]. An enhancement of both  $B_s \rightarrow \ell^+ \ell^-$  and  $B_d \rightarrow \ell^+ \ell^-$   
768 respecting the MFV relation  $\Gamma(B_s \rightarrow \ell^+ \ell^-) / \Gamma(B_d \rightarrow \ell^+ \ell^-) \approx |V_{ts} / V_{td}|^2$  would be an  
769 unambiguous signature of MFV at large  $\tan \beta$  [137].

### 770 2.5.2. The Minimal Supersymmetric extension of the SM (MSSM)

771 The MSSM is one of the most well-motivated and definitely the most studied extension  
772 of the SM at the TeV scale. For a detailed discussion of this model we refer to the  
773 specialised literature (see e.g. Ref. [154]). Here we limit our self to analyse some properties  
774 of this model relevant to flavor physics.

The particle content of the MSSM consist of the SM gauge and fermion fields plus a  
scalar partner for each quark and lepton (squarks and sleptons) and a spin-1/2 partner  
for each gauge field (gauginos). The Higgs sector has two Higgs doublets with the corre-  
sponding spin-1/2 partners (higgsinos) and a Yukawa coupling of the type in Eq. (89).  
While gauge and Yukawa interactions of the model are completely specified in terms  
of the corresponding SM couplings, the so-called soft-breaking sector<sup>5</sup> of the theory  
contains several new free parameters, most of which are related to flavor-violating ob-  
servables. For instance the  $6 \times 6$  mass matrix of the up-type squarks, after the up-type  
Higgs field gets a vev ( $H_U \rightarrow \langle H_U \rangle$ ), has the following structure

$$\tilde{M}_U^2 = \begin{pmatrix} \tilde{m}_{Q_L}^2 & A_U \langle H_U \rangle \\ A_U^\dagger \langle H_U \rangle & \tilde{m}_{U_R}^2 \end{pmatrix} + \mathcal{O}(m_Z, m_{\text{top}}), \quad (92)$$

775 where  $\tilde{m}_{Q_L}$ ,  $\tilde{m}_{U_R}$ , and  $A_U$  are  $3 \times 3$  unknown matrices. Indeed the adjective *minimal* in  
776 the MSSM acronyms refers to the particle content of the model but does not specify its  
777 flavor structure.

778 Because of this large number of free parameters, we cannot discuss the implications  
779 of the MSSM in flavor physics without specifying in more detail the flavor structure of  
780 the model. The versions of the MSSM analysed in the literature range from the so-called

<sup>5</sup> Supersymmetry must be broken in order to be consistent with observations (we do not observe degenerate spin partners in nature). The soft breaking terms are the most general supersymmetry-breaking terms which preserve the nice ultraviolet properties of the model. They can be divided into two main classes: i) mass terms which break the mass degeneracy of the spin partners (e.g. sfermion or gaugino mass terms); ii) trilinear couplings among the scalar fields of the theory (e.g. sfermion-sfermion-Higgs couplings).

781 Constrained MSSM (CMSSM), where the complete model is specified in terms of only  
 782 four free parameters (in addition to the SM couplings), to the MSSM without  $R$  parity  
 783 and generic flavor structure, which contains a few hundreds of new free parameters.

784 Throughout the large amount of work in the past decades it has become clear that  
 785 the MSSM with generic flavor structure and squarks in the TeV range is not compatible  
 786 with precision tests in flavor physics. This is true even if we impose  $R$  parity, the discrete  
 787 symmetry which forbids single s-particle production, usually advocated to prevent a too  
 788 fast proton decay. In this case we have no tree-level FCNC amplitudes, but the loop-  
 789 induced contributions are still too large compared to the SM ones unless the squarks  
 790 are highly degenerate or have very small intra-generation mixing angles. This is nothing  
 791 but a manifestation in the MSSM context of the general flavor problem illustrated in  
 792 Sec. 2.5.1.

793 The flavor problem of the MSSM is an important clue about the underlying mechanism  
 794 of supersymmetry breaking. On general grounds, mechanisms of SUSY breaking with  
 795 flavor universality (such as gauge mediation) or with heavy squarks (especially in the  
 796 case of the first two generations) tends to be favoured. However, several options are still  
 797 open. These range from the very restrictive CMSSM case, which is a special case of  
 798 MSSM with MFV, to more general scenarios with new small but non-negligible sources  
 799 of flavor symmetry breaking.

800 2.5.2.1. *Flavor Universality, MFV, and RGE in the MSSM.* Since the squark fields  
 801 have well-defined transformation properties under the SM quark-flavor group  $\mathcal{G}_q$ , the  
 802 MFV hypothesis can easily be implemented in the MSSM framework following the general  
 803 rules outlined in Sec. 2.5.1.2.

804 We need to consider all possible interactions compatible with i) softly-broken super-  
 805 symmetry; ii) the breaking of  $\mathcal{G}_q$  via the spurion fields  $Y_{U,D}$ . This allows to express the  
 806 squark mass terms and the trilinear quark-squark-Higgs couplings as follows [135, 155]:

$$\begin{aligned} \tilde{m}_{Q_L}^2 &= \tilde{m}^2 \left( a_1 \mathbb{1} + b_1 Y_U Y_U^\dagger + b_2 Y_D Y_D^\dagger + b_3 Y_D Y_D^\dagger Y_U Y_U^\dagger + b_4 Y_U Y_U^\dagger Y_D Y_D^\dagger + \dots \right) , \\ \tilde{m}_{U_R}^2 &= \tilde{m}^2 \left( a_2 \mathbb{1} + b_5 Y_U^\dagger Y_U + \dots \right) , \quad A_U = A \left( a_3 \mathbb{1} + b_6 Y_D Y_D^\dagger + \dots \right) Y_U , \end{aligned} \quad (93)$$

807 and similarly for the down-type terms. The dimensionful parameters  $\tilde{m}$  and  $A$ , expected  
 808 to be in the range few 100 GeV – 1 TeV, set the overall scale of the soft-breaking terms.  
 809 In Eq. (93) we have explicitly shown all independent flavor structures which cannot be  
 810 absorbed into a redefinition of the leading terms (up to tiny contributions quadratic in  
 811 the Yukawas of the first two families), when  $\tan \beta$  is not too large and the bottom Yukawa  
 812 coupling is small, the terms quadratic in  $Y_D$  can be dropped.

813 In a bottom-up approach, the dimensionless coefficients  $a_i$  and  $b_i$  should be considered  
 814 as free parameters of the model. Note that this structure is renormalization-group invari-  
 815 ant: the values of  $a_i$  and  $b_i$  change according to the Renormalization Group (RG) flow,  
 816 but the general structure of Eq. (93) is unchanged. This is not the case if the  $b_i$  are set to  
 817 zero, corresponding to the so-called hypothesis of *flavor universality*. In several explicit  
 818 mechanism of supersymmetry breaking, the condition of flavor universality holds at some  
 819 high scale  $M$ , such as the scale of Grand Unification in the CMSSM (see below) or the  
 820 mass-scale of the messenger particles in gauge mediation (see Ref. [156]). In this case  
 821 non-vanishing  $b_i \sim (1/4\pi)^2 \ln M^2/\tilde{m}^2$  are generated by the RG evolution. As recently

822 pointed out in Ref. [157, 158], the RG flow in the MSSM-MFV framework exhibit quasi  
 823 infra-red fixed points: even if we start with all the  $b_i = \mathcal{O}(1)$  at some high scale, the only  
 824 non-negligible terms at the TeV scale are those associated to the  $Y_U Y_U^\dagger$  structures.

825 If we are interested only in low-energy processes we can integrate out the supersym-  
 826 metric particles at one loop and project this theory into the general EFT discussed in  
 827 the previous sections. In this case the coefficients of the dimension-six effective operators  
 828 written in terms of SM and Higgs fields (see Tab. 2) are computable in terms of the  
 829 supersymmetric soft-breaking parameters. The typical effective scale suppressing these  
 830 operators (assuming an overall coefficient  $1/\Lambda^2$ ) is  $\Lambda \sim 4\pi\tilde{m}$ . Looking at the bounds  
 831 in Tab. 2, we then conclude that if MFV holds, the present bounds on FCNCs do not  
 832 exclude squarks in the few hundred GeV mass range, i.e. well within the LHC reach.

833 *2.5.2.2. The CMSSM framework.* The CMSSM, also known as mSUGRA, is the su-  
 834 persymmetric extension of the SM with the minimal particle content and the maximal  
 835 number of universality conditions on the soft-breaking terms. At the scale of Grand  
 836 Unification ( $M_{\text{GUT}} \sim 10^{16}$  GeV) it is assumed that there are only three independent  
 837 soft-breaking terms: the universal gaugino mass ( $\tilde{m}_{1/2}$ ), the universal trilinear term ( $A$ ),  
 838 and the universal sfermion mass ( $\tilde{m}_0$ ). The model has two additional free parameters in  
 839 the Higgs sector (the so-called  $\mu$  and  $B$  terms), which control the vacuum expectation  
 840 values of the two Higgs fields (determined also by the RG running from the unification  
 841 scale down to the electroweak scale). Imposing the correct  $W$ - and  $Z$ -boson masses allow  
 842 us to eliminate one of these Higgs-sector parameters, the remaining one is usually chosen  
 843 to be  $\tan\beta$ . As a result, the model is fully specified in terms of the three high-energy  
 844 parameters  $\{\tilde{m}_{1/2}, \tilde{m}_0, A\}$ , and the low-energy parameter  $\tan\beta$ .<sup>6</sup> This constrained ver-  
 845 sion of the MSSM is an example of a SUSY model with MFV. Note, however, that the  
 846 model is much more constrained than the general MSSM with MFV: in addition to be  
 847 flavor universal, the soft-breaking terms at the unification scale obey various additional  
 848 constraints (e.g. in Eq. (93) we have  $a_1 = a_2$  and  $b_i = 0$ ).

849 In the MSSM with  $R$  parity we can distinguish five main classes of one-loop diagrams  
 850 contributing to FCNC and CP violating processes with external down-type quarks. They  
 851 are distinguished according to the virtual particles running inside the loops:  $W$  and  
 852 up-quarks (i.e. the leading SM amplitudes), charged-Higgs and up-quarks, charginos  
 853 and up-squarks, neutralinos and down-squarks, gluinos and down-squarks. Within the  
 854 CMSSM, the charged-Higgs and chargino exchanges yield the dominant non-standard  
 855 contributions.

856 Given the low number of free parameters, the CMSSM is very predictive and phe-  
 857 nomenologically constrained by the precision measurements in flavor physics. The most  
 858 powerful low-energy constraint comes from  $B \rightarrow X_s \gamma$ . For large values of  $\tan\beta$ , strong  
 859 constraints are also obtained from  $B_s \rightarrow \mu^+ \mu^-$ ,  $\Delta M_s$  and from  $B(B \rightarrow \tau \nu)$ . If these  
 860 observables are within the present experimental bounds, the constrained nature of the  
 861 model implies essentially no observable deviations from the SM in other flavor-changing  
 862 processes. Interestingly enough, the CMSSM satisfy at the same time the flavor con-

---

<sup>6</sup> More precisely, for each choice of  $\{\tilde{m}_{1/2}, \tilde{m}_0, A, \tan\beta\}$  there is a discrete ambiguity related to the sign of the  $\mu$  term.

863 straints and those from electroweak precision observables for squark masses below 1 TeV  
 864 (see e.g. [159, 160]).

865 In principle, within the CMSSM the relative phases of the free parameters leads to  
 866 two new observable CP-violating phases (beside the CKM phase). However, these phases  
 867 are flavor-blind and turn out to be severely constrained by the experimental bounds on  
 868 the electric dipole moments. In particular, the combination of neutron and electron edms  
 869 forces these phases to be at most of  $\mathcal{O}(10^{-2})$  for squark masses below 1 TeV.  
 870 Once this constraints are satisfied, the effects of these new phases in the  $B$ ,  $D$  and  $K$   
 871 systems are negligible.

872 *2.5.2.3. The Mass Insertion Approximation in the general MSSM.* Flavor universality  
 873 at the GUT scale is not a general property of the MSSM, even if the model is embedded  
 874 in a Grand Unified Theory. If this assumption is relaxed, new interesting phenomena  
 875 can occur in flavor physics. The most general one is the appearance of gluino-mediated  
 876 one-loop contributions to FCNC amplitudes [161, 162].

877 The main problem when going beyond simplifying assumptions, such as flavor univer-  
 878 sality of MFV, is the proliferation in the number of free parameters. A useful model-  
 879 independent parameterization to describe the new phenomena occurring in the gen-  
 880 eral MSSM with R parity conservation is the so-called mass insertion (MI) approxima-  
 881 tion [163]. Selecting a flavor basis for fermion and sfermion states where all the couplings  
 882 of these particles to neutral gauginos are flavor diagonal, the new flavor-violating effects  
 883 are parametrized in terms of the non-diagonal entries of the sfermion mass matrices.  
 884 More precisely, denoting by  $\Delta$  the off-diagonal terms in the sfermion mass matrices (i.e.  
 885 the mass terms relating sfermions of the same electric charge, but different flavor), the  
 886 sfermion propagators can be expanded in terms of  $\delta = \Delta/\tilde{m}^2$ , where  $\tilde{m}$  is the average  
 887 sfermion mass. As long as  $\Delta$  is significantly smaller than  $\tilde{m}^2$  (as suggested by the ab-  
 888 sence of sizable deviations from the SM), one can truncate the series to the first term  
 889 of this expansion and the experimental information concerning FCNC and CP violating  
 890 phenomena translates into upper bounds on these  $\delta$ 's [164].

891 The major advantage of the MI method is that it is not necessary to perform a full  
 892 diagonalization of the sfermion mass matrices, obtaining a substantial simplification  
 893 in the comparison of flavor-violating effects in different processes. There exist four type  
 894 of mass insertions connecting flavors  $i$  and  $j$  along a sfermion propagator:  $(\Delta_{ij})_{LL}$ ,  $(\Delta_{ij})_{RR}$ ,  
 895  $(\Delta_{ij})_{LR}$  and  $(\Delta_{ij})_{RL}$ . The indices  $L$  and  $R$  refer to the helicity of the fermion partners.

896 In most cases the leading non-standard amplitude is the gluino-exchange one, which  
 897 is enhanced by one or two powers of the ratio  $(\alpha_{\text{strong}}/\alpha_{\text{weak}})$  with respect to neutralino-  
 898 or chargino-mediated amplitudes. When analysing the bounds, it is customary to con-  
 899 sider one non-vanishing MI at a time, barring accidental cancellations. This procedure  
 900 is justified a posteriori by observing that the MI bounds have typically a strong hierar-  
 901 chy, making the destructive interference among different MIs rather unlikely. The bound  
 902 thus obtained from recent measurements in  $B$  and  $K$  physics<sup>7</sup> are reported in Tab. 3.<sup>8</sup>

<sup>7</sup> The bounds on the 1-2 sector are obtained from the measurements of  $\Delta M_K$ ,  $\varepsilon$  and  $\varepsilon'/\varepsilon$ . In particular  $\Delta M_K$  and  $\varepsilon$  bound the real and imaginary part of the product  $(\delta_{12}^d \delta_{12}^d)$ , while  $\varepsilon'/\varepsilon$  puts a bound on  $\text{Im}(\delta_{12}^d)$ . The bounds on the 1-3 sector are obtained from  $\Delta M_{B_d}$  (modulus) and the CP violating asymmetry in  $B \rightarrow J/\Psi K$  (phase). The bounds on the 2 – 3 sector are derived mainly from  $\Delta M_{B_s}$ ,  $B \rightarrow X_s \gamma$  and  $B \rightarrow X_s \ell^+ \ell^-$ .

<sup>8</sup> The leading  $\Delta F = 1$  and  $\Delta F = 2$  gluino-mediated amplitudes in the MI approximation can be



Table 3

Upper bounds at 95% C.L. on the dimensionless down-type mass-insertion parameters (see text) for squark and gluino masses of 350 GeV (from Ref. [167]).

$$\begin{array}{l}
 |(\delta_{12}^d)_{LL,RR}| < 1 \cdot 10^{-2} \quad |(\delta_{12}^d)_{LL=RR}| < 2 \cdot 10^{-4} \quad |(\delta_{12}^d)_{LR}| < 5 \cdot 10^{-4} \quad |(\delta_{12}^d)_{RL}| < 5 \cdot 10^{-4} \\
 \hline
 |(\delta_{13}^d)_{LL,RR}| < 7 \cdot 10^{-2} \quad |(\delta_{13}^d)_{LL=RR}| < 5 \cdot 10^{-3} \quad |(\delta_{13}^d)_{LR}| < 1 \cdot 10^{-2} \quad |(\delta_{13}^d)_{RL}| < 1 \cdot 10^{-2} \\
 \hline
 |(\delta_{23}^d)_{LL}| < 2 \cdot 10^{-1} \quad |(\delta_{23}^d)_{RR}| < 7 \cdot 10^{-1} \quad |(\delta_{23}^d)_{LL=RR}| < 5 \cdot 10^{-2} \quad |(\delta_{23}^d)_{LR,RL}| < 5 \cdot 10^{-3}
 \end{array}$$

903 The bounds mainly depend on the gluino and on the average squark mass, scaling as  
 904 the inverse mass (the inverse mass square) for bounds derived from  $\Delta F = 2$  ( $\Delta F = 1$ )  
 905 observables.

906 The only clear pattern emerging from these bounds is that there is no room for siz-  
 907 able new sources of flavor-symmetry breaking. However, it is too early to draw definite  
 908 conclusions since some of the bounds, especially those in the 2-3 sector, are still rather  
 909 weak. As suggested by various authors (see e.g. ), the possibility of sizable deviations  
 910 from the SM in the 2-3 sector could fit well with the large 2-3 mixing of light neutrinos,  
 911 in the context of a unification of quark and lepton sectors [168, 169].

### 912 2.5.3. *Non-supersymmetric extensions of the Standard Model*

913 We conclude this chapter outlining two of the general features of flavor physics ap-  
 914 pearing in non-supersymmetric extensions of the Standard Model, without entering the  
 915 details of specific theories.

In models with generic flavor structure, the most stringent constraints on the new flavor-violating couplings are typically derived from Kaon physics (as it also happens for the bounds in Tab. 3). This is a consequence of the high suppression, within the SM, of short-distance dominated FCNC amplitudes between the first two families:

$$\mathcal{A}(s \rightarrow d)_{\text{SM}} = \mathcal{O}(\lambda^5), \quad \mathcal{A}(b \rightarrow d)_{\text{SM}} = \mathcal{O}(\lambda^3), \quad \mathcal{A}(b \rightarrow s)_{\text{SM}} = \mathcal{O}(\lambda^2). \quad (94)$$

916 As a result, a natural place to look for sizable deviations from the SM are rare decays  
 917  $K \rightarrow \pi \nu \bar{\nu}$  and  $K_L \rightarrow \pi^0 \ell^+ \ell^-$  (see for instance the expectations for these decays in the  
 918 *Littlest Higgs model* without [170] and with [171–174]) T-parity. These decays allow us  
 919 to explore the sector of  $\Delta F = 1$   $s \rightarrow d$  transitions, that so far is only loosely tested.

920 An interesting alternative to MFV, which naturally emerges in models with *Extra*  
 921 *Space-time Dimensions* (or models with strongly interacting dynamics at the TeV scale),  
 922 is the hypothesis of hierarchical fermion profiles [175–179] (which is equivalent to the  
 923 hypothesis of hierarchical kinetic terms [180]). Contrary to MFV, this hypothesis (often  
 924 denoted as NMFV or RS-GIM mechanism) is not a symmetry principle but a dynamical  
 925 argument: light fermions are weakly coupled to the new TeV dynamics, with a strength  
 926 inversely proportional to their Yukawa coupling (or better the square root of their SM  
 927 Yukawa coupling). Also in the case the most significant constraints are derived from  
 928 Kaon physics. However, in this case the stringent constraints from  $\epsilon_K$  and  $\epsilon'_K$  prevent  
 929 visible effects in other observables. Despite quite general, this mechanism is not a general  
 930 feature of models with extra dimensions: as discussed in [181–183], also in this context

---

found in Ref. [164]. In the  $\Delta F = 2$  case also the NLO QCD corrections to effective Hamiltonian are known [165]. A more complete set of supersymmetric amplitudes in the MI approximation, including chargino-mediated relevant in the large- $\tan \beta$  limit, can be found in Ref. [166].

931 is possible to postulate the existence of additional symmetries and, for instance, obtain  
932 a MFV structure.

### 933 3. Experimental Primers

934 This section contains all the relevant information on experiments and experimental  
935 techniques which are needed throughout the report.

#### 936 3.1. Overview of experiments

##### 937 3.1.1. Kaon experiments

938 In recent years, many experiments have been performed to precisely measure many  
939 Kaon decay parameters. Branching ratios (BR's) for main, subdominant, and rare decays,  
940 lifetimes, parameters of decay densities, and charge asymmetries have been measured  
941 with unprecedented accuracy for  $K_S$ ,  $K_L$ , and  $K^\pm$ . Different techniques have been used,  
942 often allowing careful checks of the results from experiments with independent sources  
943 of systematic errors.

944 In the approach of NA48 [184] at the CERN SPS and KTeV [185] at the Fermilab  
945 Tevatron, Kaons were produced by the interactions of intense high-energy proton beams  
946 on beryllium targets (see Tab. 4). Both experiments were designed to measure the direct  
947 CP violation parameter  $\text{Re}(\varepsilon'/\varepsilon)$  via the double ratio of branching fractions for  $K_S$   
948 and  $K_L$  decays to  $\pi^+\pi^-$  and  $\pi^0\pi^0$  final states. In order to confirm or disprove the  
949 conflicting results of the former-generation experiments, NA31 [186] and E-731 [187], the  
950 goal was to reach an uncertainty of a few parts in  $10^4$ . This not only requires intense  $K_L$   
951 beams, so as to guarantee the observation of at least  $10^8$  decays of the rarest of the four  
952 modes, i.e.,  $K_L \rightarrow \pi^0\pi^0$ ; it also made it necessary to achieve a high level of cancelation  
953 of the systematic uncertainties for  $K_L$  and  $K_S$  detection, separately for neutral and  
954 charged decay modes, as well as rejection of the order of  $10^6$  for the most frequent  $K_L$   
955 backgrounds,  $K_L \rightarrow 3\pi^0$  and  $K_L \rightarrow \pi\ell\nu$ .

956 In both setups, the target producing the  $K_L$  beam is the origin of coordinates.  $K_L$ 's  
957 are transported by a  $\sim 100$ -m long beam line, with magnetic filters to remove unwanted  
958 particles and collimators to better define the Kaon-beam direction, to a fiducial decay  
959 volume (FV). The FV is surrounded by veto detectors, for rejecting decay products  
960 emitted at large angles and therefore with relatively low energy; this is particularly  
961 useful for the rejection of  $K_L \rightarrow 3\pi^0$  background. The FV is followed by a tracker to  
962 measure the charge, multiplicity, and momentum of charged decay products, and by a fast  
963 scintillator hodoscope to provide the first-level trigger and determine the event time. The  
964 tracking resolution  $\sigma_p/p$  is  $(4 \oplus p[\text{GeV}]/11) \times 10^{-3}$  for NA48 and  $(1.7 \oplus p[\text{GeV}]/14) \times 10^{-3}$   
965 for KTeV. In the downstream (forward) region, both experiments use fine-granularity,  
966 high-efficiency calorimeters to accurately measure multiplicity and energy of photons and  
967 electrons for the identification of  $K_L \rightarrow 2\pi^0$ . The KTeV calorimeter is made of pure CsI,  
968 while the NA48 calorimeter is made of liquid krypton. The energy resolution  $\sigma_E/E$  is  
969  $3.2\%/\sqrt{E[\text{GeV}]} \oplus 9\%/E[\text{GeV}] \oplus 0.42\%$  for NA48 and  $2\%/\sqrt{E[\text{GeV}]} \oplus 0.4\%$  for KTeV.  
970 Behind the calorimeter, the detectors are completed by calorimeters for muon detection.  
971 Different methods are used for the production of a  $K_S$  beam. In NA48, a channeling  
972 crystal bends a small and adjustable fraction of protons that do not interact in the  $K_L$

973 target to a dedicated beam line; these protons are then transported and collimated to  
 974 interact with a second target located few meters before the FV, thus producing a  $K_S/K_L$   
 975 beam with momentum and direction close to those of the  $K_L$  beam, so that most of  $K_S$   
 976 decays are in the FV.  $K_S$  decays are identified by tagging protons on the secondary beam  
 977 line using time of flight. In KTeV, two  $K_L$  beams are produced at the first target, with  
 978 opposite transverse momenta in the horizontal direction, and a thick regenerator is placed  
 979 in one of the two beams to produce  $K_S$ , again a few meters before the FV.  $K_S$  and  $K_L$   
 980 decays are distinguished by their different transverse position on the detector. In both  
 981 setups, one measures decays from a  $K_L$  beam with  $< \sim 10^{-6}$  contamination from  $K_S$ ,  
 982 and from an enriched- $K_S$  beam contaminated by a  $K_L$  component, which is determined  
 983 very precisely during analysis.

Table 4

Typical beam parameters for  $K$  production in the NA48, KTeV, ISTRA+, and E787/E949 experiments.

Experiment	proton energy (GeV)	$K$ , spill/cycle	$K$ momentum	Beam type
NA48	450	$1.5 \times 10^{12}$ , 2.4 s/14.4 s	(70–170) GeV	$K_S$ – $K_L$
NA48/1	400	$5 \times 10^{10}$ , 4.8 s/16.2 s	(70–170) GeV	$K_S$
NA48/2	400	$7 \times 10^{11}$ , 4.8 s/16.8 s	60 GeV	$K^\pm$
KTeV	450–800	$3 \times 10^{12}$ , 20 s/60 s	(40–170) GeV	$K_S$ – $K_L$ , $K_L$
ISTRA+	70	$3 \times 10^6$ , 1.9 s/9.7 s	25 GeV	$K^-$
E787	24	$4$ – $7 \times 10^6$ , 1.6 s/3.6 s	710/730/790 MeV, stopped	$K^+$
E949	21.5	$3.5 \times 10^6$ , 2.2 s/5.4 s	710 MeV, stopped	$K^+$

984 The KTeV experiment at Fermilab underwent different phases. The E-799 KTeV phase-  
 985 I used the apparatus of the E-731 experiment [187], upgraded to handle increased  $K_L$   
 986 fluxes and to study multibody rare  $K_L$  and  $\pi^0$  decays. In phase-II of E-799, a new beam  
 987 line and a new detector were used, including a new CsI calorimeter and a new tran-  
 988 sition radiation detector, thus allowing a sensitivity of  $10^{-11}$  on the BR of many  $K_L$   
 989 decay channels and improving by large factors the accuracy on the ratio of BR’s of all of  
 990 the main  $K_L$  channels. Finally, using the E-832 experimental configuration  $\text{Re}(\epsilon'/\epsilon)$  was  
 991 measured to few parts in  $10^{-4}$  [185]. The NA48 program involved different setups as well.  
 992 After operating to simultaneously produce  $K_L$ ’s and  $K_S$ ’s, the beam parameters were  
 993 optimized in the NA48/1 phase to produce a high-intensity  $K_S$  beam for the study of  
 994 rare  $K_S$  decays, reaching the sensitivity of  $10^{-10}$  for some specific channels and especially  
 995 improving knowledge on those with little background from the accompanying  $K_L$  decay  
 996 to the same final state. Subsequent beam and detector upgrades, including the inser-  
 997 tion of a Cerenkov beam counter (“NA48/2 setup”) allowed production of simultaneous  
 998 unseparated charged Kaon beams for the measurement of CP violation from the charge  
 999 asymmetry in the Dalitz densities for three-pion decays [188]. The NA48/2 phase allowed  
 1000 the best present sensitivities for many rare  $K^\pm$  decays to be reached, with BR’s as low  
 1001 as  $10^{-8}$  and improved precision for the ratios of BR’s of the main  $K^\pm$  channels. A recent  
 1002 run made in 2007 by the NA62 collaboration using the NA48/2 setup was dedicated to  
 1003 a precision measurement of the ratio  $\Gamma(K_{e2})/\Gamma(K_{\mu2})$ . A future experiment is foreseen at  
 1004 the CERN SPS for the measurement of the ultra-rare decay  $K^+ \rightarrow \pi^+ \nu \bar{\nu}$  with a 10%  
 1005 accuracy [189, 190].

1006 An unseparated charged Kaon beam was also exploited for study of charged Kaon  
 1007 decay parameters with the ISTRAP detector [191] at the U-70 proton synchrotron in  
 1008 IHEP, Protvino, Russia. A beam (see Tab. 4), with  $\sim 3\%$   $K^-$  abundance is analyzed by  
 1009 a magnetic spectrometer with four proportional chambers and a particle identification is  
 1010 provided by three Cerenkov counters. The detector concept is similar to those presented  
 1011 above, with the tracking of charged decay products provided by drift chambers, drift  
 1012 tubes, and proportional chambers and with the calorimetry for photon vetoing at large  
 1013 angle or energy measurement at low angle performed by lead-glass detectors.

1014 A different approach for the study of the ultra-rare  $K \rightarrow \pi\nu\bar{\nu}$  decay and the search  
 1015 for lepton-flavor violating transitions was taken by the E787 [192–194] and E949 [195]  
 1016 experiments at the Alternating Gradient Synchrotron (AGS) of the Brookhaven National  
 1017 Laboratory. Charged Kaons were produced by 24-GeV protons interacting on a fixed  
 1018 target. A dedicated beam line transported, purified and momentum selected Kaons. The  
 1019 beam (see Tab. 4) had adjustable momenta from 670 MeV to 790 MeV and a ratio of  
 1020 Kaons to pions of  $\sim 4/1$ .

1021 The detector design was optimized to reach sensitivities of the order of  $10^{-10}$  on the  
 1022 BR's for decays of  $K^\pm$  to charged particles, especially lepton-flavor violating decays, such  
 1023 as  $K \rightarrow \pi\mu e$ : for this purpose, redundant and independent measurements for particle  
 1024 identification and kinematics were provided, as well as efficient vetoing for photons. The  
 1025 beam was first analyzed by Cerenkov and wire-chamber detectors, and later slowed down  
 1026 by a passive BeO degrader and an active lead-glass radiator, the Cerenkov light of which  
 1027 was used to veto pions and early  $K$  decays. Kaons were then stopped inside an active  
 1028 target made of scintillating fibers. The charged decay products emitted at large angle  
 1029 were first analyzed in position, trajectory, and momentum by a drift chamber; their range  
 1030 and kinetic energy was then measured in a Range Stack alternating plastic scintillator  
 1031 with passive material. The readout of the Range Stack photomultipliers was designed to  
 1032 record times and shapes of pulses up to  $6.4 \mu\text{s}$  after the trigger, thus allowing the entire  
 1033 chain of  $\pi \rightarrow \mu \rightarrow e$  decays to be detected and allowing clean particle identification. The  
 1034 detector was surrounded by electromagnetic calorimeters for hermetic photon vetoing: a  
 1035 lead/scintillator barrel and two CsI-crystal endcaps. Two lead/scintillating-fiber collars  
 1036 allowed vetoing of charged particles emitted at small angles. Using this setup, the best  
 1037 sensitivity to date was obtained for the BR for  $K \rightarrow \pi\nu\nu$ , reaching the  $10^{-10}$  level.

1038 Precision studies of  $K_S$ ,  $K_L$ , and  $K^\pm$  main and subdominant decays were performed  
 1039 with a different setup using the KLOE detector at the DAΦNE. DAΦNE, the Frascati  
 1040  $\phi$  factory, is an  $e^+e^-$  collider working at  $\sqrt{s} \sim m_\phi \sim 1.02 \text{ GeV}$ .  $\phi$  mesons are produced  
 1041 essentially at rest with a visible cross section of  $\sim 3.1 \mu\text{b}$  and decay into  $K_S K_L$  and  
 1042  $K^+ K^-$  pairs with BR's of  $\sim 34\%$  and  $\sim 49\%$ , respectively. During KLOE data taking,  
 1043 which started in 2001 and concluded in 2006, the peak luminosity of DAΦNE improved  
 1044 continuously, reaching  $\sim 2.5 \times 10^{32} \text{ cm}^{-2} \text{ s}^{-1}$  at the end. The total luminosity integrated  
 1045 at the  $\phi$  peak is  $\sim 2.2 \text{ fb}^{-1}$ , corresponding to  $\sim 2.2$  ( $\sim 3.3$ ) billion  $K^0 \bar{K}^0$  ( $K^+ K^-$ ) pairs.

1046 Kaons get a momentum of  $\sim 100 \text{ MeV}/c$  which translates into a low speed,  $\beta_K \sim 0.2$ .  
 1047  $K_S$  and  $K_L$  can therefore be distinguished by their mean decay lengths:  $\lambda_S \sim 0.6 \text{ cm}$   
 1048 and  $\lambda_L \sim 340 \text{ cm}$ .  $K^+$  and  $K^-$  decay with a mean length of  $\lambda_\pm \sim 90 \text{ cm}$  and can be  
 1049 distinguished from their decays in flight to one of the two-body final states  $\mu\nu$  or  $\pi\pi^0$ .

1050 The Kaon pairs from  $\phi$  decay are produced in a pure  $J^{PC} = 1^{--}$  quantum state, so  
 1051 that observation of a  $K_L$  ( $K^+$ ) in an event signals, or tags, the presence of a  $K_S$  ( $K^-$ )  
 1052 and vice versa; highly pure and nearly monochromatic  $K_S$ ,  $K_L$ , and  $K^\pm$  beams can thus

1053 be obtained and exploited to achieve high precision in the measurement of absolute BR's.

1054 The analysis of Kaon decays is performed with the KLOE detector, consisting essen-  
1055 tially of a drift chamber, DCH, surrounded by an electromagnetic calorimeter, EMC. A  
1056 superconducting coil provides a 0.52 T magnetic field. The DCH [196] is a cylinder of  
1057 4 m in diameter and 3.3 m in length, which constitutes a fiducial volume for  $K_L$  and  $K^\pm$   
1058 decays extending for  $\sim 0.5\lambda_L$  and  $\sim 1\lambda_\pm$ . The momentum resolution for tracks at large  
1059 polar angle is  $\sigma_p/p \leq 0.4\%$ . The invariant mass reconstructed from the momenta of the  
1060 two pion tracks of a  $K_S \rightarrow \pi^+\pi^-$  decay peaks around  $m_K$  with a resolution of  $\sim 800$  keV,  
1061 thus allowing clean  $K_L$  tagging. The c.m. momenta reconstructed from identification of  
1062 1-prong  $K^\pm \rightarrow \mu\nu, \pi\pi^0$  decay vertices in the DC peak around the expected values with  
1063 a resolution of 1–1.5 MeV, thus allowing clean and efficient  $K^\mp$  tagging.

1064 The EMC is a lead/scintillating-fiber sampling calorimeter [197] consisting of a barrel  
1065 and two endcaps, with good energy resolution,  $\sigma_E/E \sim 5.7\%/\sqrt{E(\text{GeV})}$ , and excellent  
1066 time resolution,  $\sigma_T = 54 \text{ ps}/\sqrt{E(\text{GeV})} \oplus 50 \text{ ps}$ . About 50% of the  $K_L$ 's produced reach  
1067 the EMC, where most interact. A signature of these interactions is the presence of an  
1068 high-energy cluster not connected to any charged track, with a time corresponding to  
1069 a low velocity: the resolution on  $\beta_K$  corresponds to a resolution of  $\sim 1$  MeV on the  
1070  $K_L$  momentum. This allows clean  $K_S$  tagging. The timing capabilities of the EMC are  
1071 exploited to precisely reconstruct the position of decay vertices of  $K_L$  and  $K^\pm$  to  $\pi^0$ 's  
1072 from the cluster times of the emitted photons, thus allowing a precise measurement of  
1073 the  $K_L$  and  $K^\pm$  lifetimes.

1074 With this setup, KLOE reached the best sensitivity for absolute BR's of the main  
1075  $K^\pm$ ,  $K_L$ , and  $K_S$  channels (dominating world data in the latter case) and improved the  
1076 knowledge of semileptonic decay rate densities and lifetimes for  $K^\pm$  and  $K_L$ .

### 1077 3.1.2. *B* Factories

1078 The high statistics required to perform precise flavor physics with *B* mesons has been  
1079 accomplished by B-Factories colliding electrons and positrons at the energy of the  $\Upsilon(4S)$   
1080 resonance ( $e^+e^- \rightarrow \Upsilon(4S)B\bar{B}$ ): CESR at LEPP (Cornell, USA), PEP-II [198] at SLAC  
1081 (Stanford, USA) and KEK-B [199] at KEK (Tsukuba, Japan). Measurements that ex-  
1082 ploit the evolution of the observables with the decay time of the mesons also require  
1083 asymmetric beams in order to ensure a boost to the produced mesons.

1084 To this aim PEP-II (KEK-B) collide 3.1 (3.5) GeV positrons on 9.0 (8.0) GeV electrons,  
1085 thus achieving a boost  $\beta\gamma = 0.56(0.43)$ . The other design parameters of the B-Factories  
1086 are listed in Tab: 5. The design instantaneous luminosities were  $10^{33}$ ,  $3 \times 10^{33}$ , and  
1087  $1 \times 10^{34} \text{ cm}^{-2} \text{ s}^{-1}$  for CESR, PEP-II and KEK-B, respectively.

1088 The accelerator performances have actually overcome the design: CESR has ceased its  
1089 operations as B-Factory in 1999 with a peak luminosity  $\mathcal{L} = 1.2 \times 10^{33} \text{ cm}^{-2} \text{ s}^{-1}$ , PEP-II  
1090 has ended its last run in April 2008 with a peak luminosity of  $12 \times 10^{33} \text{ cm}^{-2} \text{ s}^{-1}$  and  
1091 KEK-B, which is still operational and awaits an upgrade (Super-KEK-B), has achieved  
1092 a luminosity as high as  $1.7 \times 10^{34} \text{ cm}^{-2} \text{ s}^{-1}$ . The total collected luminosities are 15.5,  
1093 553 and 895  $\text{fb}^{-1}$  for CESR, PEP-II and KEK-B, respectively.

1094 The detectors installed on these accelerators, CLEO-II/II.V/III<sup>9</sup> [200–204] at CESR,

---

<sup>9</sup> The detector went through several major upgrades during its lifetime. In this section only the final configuration, CLEO-III, is described. The size of the  $\Upsilon(4S)$  data-sets collected were 4.7  $\text{fb}^{-1}$ , 9.0  $\text{fb}^{-1}$ , 9.1  $\text{fb}^{-1}$  with CLEO-II, CLEO-II.V and CLEO-III, respectively.

Table 5

Accelerator parameters of the B-Factories. The design parameters are given for PEP-II and KEK-B. The final running parameters for CESR are given.

	CESR	KEK-B		PEP-II	
		LER	HER	LER	HER
Energy ( GeV )	5.29	3.5	8.0	3.1	9.0
Collision mode	2 mrad	11mrad		Head-on	
Circumference ( m )	768	3018		2199	
$\beta_x^*/\beta_y^*$ ( cm )	100/1.8	100/1	100/1	37.5/1.5	75/3
$\xi_x^*/\xi_y^*$	0.03/0.06	0.05/0.05		0.03/0.03	
$\epsilon_x^*/\epsilon_y^*$ ( $\pi$ rad – nm )	210/1	19/0.19	19/0.19	64/2.6	48.2/1.9
relative energy spread ( $10^{-4}$ )	6.0	7.7	7.2	9.5	6.1
Total Current ( A )	0.34	2.6	1.1	2.14	0.98
number of bunches	45	5120		1658	
RF Frequency ( <i>MHz</i> ) / Voltage ( <i>MV</i> )	500/5	508/22	508/48	476/9.5	476/17.5
number of cavities	4	28	60	10	20

1095 BaBar [205] at PEP-II and Belle [206] at KEK-B, are multipurpose and require exclusive  
 1096 and hermetic reconstruction of the decay products of all generated particles. To this  
 1097 aim the following requirements must be met: (1) accurate reconstruction of charged-  
 1098 particle trajectories; (2) precise measurement of neutral particle energies; and (3) good  
 1099 identification of photons, electrons, muons, charged Kaons,  $K_S^0$  mesons and  $K_L^0$  mesons.

1100 The most challenging experimental requirement is the detection of the decay points of  
 1101 the short-lived B mesons. CLEO, BaBar and Belle use double-sided silicon-strip detectors  
 1102 allowing full tracking of low-momentum tracks. Four, three and five cylindrical layers are  
 1103 used at CLEO, Belle and BaBar, respectively. To minimize the contribution of multiple  
 1104 scattering, these detectors are located at small radii close to the interaction point. For  
 1105 tracking outside the silicon detector, and the measurement of momentum, all experiments  
 1106 use conventional drift chambers with a helium-based gas mixture to minimize multiple  
 1107 scattering and synchrotron radiation backgrounds.

1108 The other difficult requirement for the detectors is the separation of Kaons from pi-  
 1109 ons. At high momentum, this is needed to distinguish topologically identical final states  
 1110 such as  $B^0 \rightarrow \pi^+\pi^-$  and  $B^0 \rightarrow K^+\pi^-$  from one another. At lower momenta, particle  
 1111 identification is essential for B flavor tagging.

1112 Three different approaches to high-momentum particle identification have been imple-  
 1113 mented, all of which exploit Cerenkov radiation. At CLEO a proximity focusing RICH  
 1114 with  $\text{CH}_4/\text{TEA}$  as the photosensitive medium and LiF as the radiator. The system relies  
 1115 on an expansion gap between the radiator and photon detector to separate the Cherenkov  
 1116 light without the use of additional focusing elements. The RICH has good  $K-\pi$  separa-  
 1117 tion for charged tracks above 700 MeV/c; below this momenta  $dE/dx$  measurements in  
 1118 the drift chamber are used for particle identification.

1119 At Belle, aerogel is used as a radiator. Blocks of aerogel are read out directly by  
 1120 fine-mesh phototubes that have high gain and operate reliably in a 1.5-Tesla magnetic  
 1121 field. Because the threshold momentum for pions in the aerogel is 1.5 GeV/c, below this

Table 6  
Accelerator parameters of  $\tau$ -charm factories.

	BEPC	CESR-c	BEPC-II
Max. energy (GeV)	2.2	2.08	2.3
Collision mode	Head-on	$\pm 3.3$ mrad	22 mrad
Circumference (m)	240	768	240
$\beta_x^*/\beta_y^*$ (cm)	120/5	94/1.2	100/1.5
$\xi_x^*/\xi_y^*$ ( $10^{-4}$ )	350/350	420/280	400/400
$\epsilon_x^*/\epsilon_y^*$ ( $\pi$ rad - nm)	660/28	120/3.5	144/2.2
relative energy spread ( $10^{-4}$ )	5.8	8.2	5.2
Total Current (A)	0.04	0.072	0.91
number of bunches	1	24	93
RF Frequency (MHz)/ Voltage (MV)	200/0.6-1.6	500/5	500/1.5
number of cavities	4	4	2

1122 momentum  $K/\pi$  separation is carried out using high-precision time-of-flight (TOF) scin-  
 1123 tillators with a resolution of 95 ps. The aerogel and TOF counter system is complemented  
 1124 by  $dE/dx$  measurements in the central drift chamber. The  $dE/dx$  system provides  $K/\pi$   
 1125 separation below 0.7 GeV/ $c$  and above 2.5 GeV/ $c$  in the relativistic rise region.

1126 At BaBar, Cerenkov light is produced in quartz bars and then transmitted by total  
 1127 internal reflection to the outside of the detector through a water tank to a large array  
 1128 of phototubes where the ring is imaged. The detector is called DIRC (Detector of In-  
 1129 ternally Reflected Cerenkov light). It provides particle identification for particles above  
 1130 700 MeV/ $c$ . Additional particle identification is provided by  $dE/dx$  measurements in the  
 1131 drift chamber and the five-layer silicon detector.

1132 To detect photons and electrons, all detectors use large arrays of CsI(Tl) crystals  
 1133 located inside the coil of the magnet. In BABAR and Belle, another novel feature is the  
 1134 use of resistive plate chambers (RPC) inserted into the steel return yoke of the magnet.  
 1135 This detector system is used for both muon and  $K_L^0$  detection. At CLEO the iron return  
 1136 yoke of the solenoid is instrumented with plastic streamer counters to identify muons.

1137 To read out the detectors, BABAR uses electronics based on digital pipelines and  
 1138 incurs little or no dead-time. Belle uses charge-to-time (Q-to-T) converters that are then  
 1139 read out by multihit time-to-digital counters (TDCs). This allows a uniform treatment of  
 1140 timing and charge signals. Details of the CLEO data-acquisition system can be found in  
 1141 Ref. [202]; the system can handle trigger rates of 1 kHz well above the normal operating  
 1142 conditions (100 Hz).

### 1143 3.1.3. $\tau$ -charm Factories

1144 Recently there have been two accelerators that have been operating near the  $\tau$ -charm  
 1145 threshold: BEPC at IHEP (Beijing, China) and CESR-c [207] at LEPP (Cornell, USA).  
 1146 The center-of-mass-energy ranges covered are 3.7 – 5.0 GeV and 3.97 – 4.26 GeV by  
 1147 BEPC and CESR-c, respectively. The peak instantaneous luminosities achieved are  $12.6 \times$   
 1148  $10^{30}$   $\text{cm}^{-2} \text{s}^{-1}$  and  $76 \times 10^{30}$   $\text{cm}^{-2} \text{s}^{-1}$ . The other parameters of BEPC and CESR-c  
 1149 are given in Tab. 6.

1150 At CESR-c the CLEO-III detector, described in Sec. 3.1.2, was modified for lower en-  
 1151 ergy data-taking and renamed CLEO-c [207]. The principal differences were the reduction  
 1152 of the magnetic field from 1.5 T to 1 T and the replacement of the silicon vertex detector  
 1153 by a six-layer inner drift chamber. Both these modifications improved the reconstruction  
 1154 of low momentum tracks. CLEO-c collected 27 million  $\psi(2S)$  events,  $818 \text{ pb}^{-1}$  of  
 1155 integrated luminosity at the  $\psi(3770)$  and  $602 \text{ pb}^{-1}$  of integrated luminosity at a center-  
 1156 of-mass energy of 4.17 GeV. The latter data set includes a over half a million  $D_s\bar{D}_s^*$   
 1157 events.

1158 The most recent detector installed on BEPC is BES-II [208, 209]. BES-II collected  
 1159 samples of 58 million  $J/\psi$  and 14 million  $\psi(2S)$  events. In addition, an energy scan was  
 1160 performed between center-of-mass energies 3.7 to 5.0 GeV to determine both  $R$  and  
 1161 the resonances parameters of the higher-mass charmonium states. BES-II tracking was  
 1162 performed by a drift chamber surrounding a straw tube vertex detector.<sup>10</sup> A scintillating  
 1163 time-of-flight detector with 180 ps resolution is used for particle identification along with  
 1164  $dE/dx$  measurements in the drift chamber. There are sampling electromagnetic-shower  
 1165 counters in the barrel and endcap made from layers of streamer tubes sandwiched between  
 1166 lead absorbers. Outside the 0.4 T solenoid the iron flux return is instrumented with  
 1167 proportional tubes to detect muons.

1168 BEPC and BES-III have recently undergone significant upgrades (see for example  
 1169 [210]). The BEPC-II accelerator has a design luminosity 100 times greater than BEPC  
 1170 with a peak of  $10^{33} \text{ cm}^{-2} \text{ s}^{-1}$ . The other parameters of BEPC-II are given in Tab. 6. The  
 1171 BES-III detector has the following components: a He-based drift-chamber, a time-of-flight  
 1172 system with  $\sim 100$  ps resolution, a CsI(Tl) crystal calorimeter, a 1 T superconducting  
 1173 solenoid and the return yoke is instrumented with RPCs for muon identification. BES-  
 1174 III began taking data in the summer of 2008 and a  $\psi(2S)$  data sample of  $10 \text{ pb}^{-1}$  has  
 1175 already been collected. The collection of unprecedented samples of  $J/\psi$ ,  $\psi(2S)$  and  $D$   
 1176 mesons produced just above open-charm threshold are expected in the coming years.

#### 1177 3.1.4. Hadron Colliders

1178 High energy proton-(anti)proton collisions offer superb opportunities for beauty and  
 1179 charm physics due to large production cross section and, in contrast to electron-positron  
 1180 colliders running at the  $\Upsilon(4S)$ , the possibility of studying all species of  $b$ -mesons and  
 1181 baryons. Present generation experiments, CDF and D0 operate at the Fermilab Tevatron  
 1182 providing  $p\bar{p}$  collisions at  $\sqrt{s} = 1.96 \text{ TeV}$  in the Run II started in 2002, while experiments  
 1183 at the soon to be operated LHC collider at CERN will study proton-proton collisions  
 1184 at  $\sqrt{s} = 14 \text{ TeV}$ . The Tevatron collides  $p\bar{p}$  bunches every 396 ns, corresponding to an  
 1185 average of 2 inelastic collisions per crossing at a luminosity of  $\mathcal{L} = 1 \times 10^{32} \text{ cm}^{-2} \text{ s}^{-1}$ ,  
 1186 typical of the data used to produce the physics results discussed here. More recently  
 1187 Tevatron provided peak luminosities in excess of  $3 \times 10^{32} \text{ cm}^{-2} \text{ s}^{-1}$ , and delivered in total  
 1188  $6.5 \text{ fb}^{-1}$  as of this writing.

1189 The cross section for centrally produced  $b$ -hadrons has been measured with a variety  
 1190 of techniques at Tevatron and found to be consistent with NLO theoretical calculations:  
 1191 an early measurement using inclusive  $J/\psi$  down to  $P_T = 0$  in the rapidity range  $|y| < 0.6$   
 1192 found  $\sigma(p\bar{p} \rightarrow b + X) = 17.6 \pm 0.4(\text{stat.}) \pm_{2.3}^{2.5}(\text{sys.}) \mu\text{b}$  [211], while a more recent one using

<sup>10</sup>The vertex detector was originally operated at Mark III.



1193 fully reconstructed  $B^+ \rightarrow J/\psi K^+$  measured  $\sigma(p\bar{p} \rightarrow B^+ + X, P_T > 6 \text{ GeV}/c, |y| \leq 1) =$   
 1194  $2.78 \pm 0.24 \mu\text{b}$  [212] which gives more of an idea of the usable cross-section for central  
 1195 detectors like CDFII and D0. The fragmentation fraction of b-quarks in  $B_{u,d}$  and  $B_s$   
 1196 mesons has been measured to be consistent at Tevatron and at LEP, with roughly 1  $B_s$   
 1197 meson produced every 4  $B^+$  or  $B^0$ , while the rate of b-baryons has been reported to be  
 1198 higher at Tevatron with a possible mild  $P_T$  dependence [213].

1199 The huge production rate for heavy flavored particles has to be contrasted, however,  
 1200 with the overwhelming inelastic proton-(anti)proton interaction rate which is typically  
 1201 three order of magnitudes higher. This poses a fundamental experimental challenge for  
 1202 detectors at hadron colliders, which needs to devise trigger strategies in order to be able  
 1203 to record as pure a signal as possible while discarding uninteresting events.

1204 The Tevatron experiments exploit conceptually similar, multi-purpose central detectors  
 1205 with a cylindrical symmetry around the beam axis, in contrast the dedicated future  
 1206 experiment at LHC collider (LHCb) employs a radically different forward geometry, in  
 1207 order to exploit the rapidly increasing  $b\bar{b}$  cross section at high rapidity.

1208 Key elements in the design of detectors for heavy flavor physics at hadron colliders  
 1209 are: large magnetic spectrometers for charged particle momentum measurements; pre-  
 1210 cision vertex detectors for proper decay time determination and signal separation, low  
 1211 energy electron and muon identification for triggering, flavor tagging, and identification  
 1212 of rare leptonic decays; high rate capability for data acquisition and trigger systems.  
 1213 Additionally  $\pi$ -K identification is crucial for flavor tagging and signal separation, and,  
 1214 thus, a significant part of the design of the dedicated LHCb detector, while in central  
 1215 multi-purpose detectors limited particle id is available with the exception of CDF-II which  
 1216 benefits from dE/dx and TOF measurements. In the following we will briefly describe  
 1217 the CDF [211] and D0 [214] detectors relevant for the experimental results discussed in  
 1218 this report.

#### 1219 **CDF and D0 detectors**

1220 The CDF-II detector spectrometer is built around an axially symmetric Central Outer  
 1221 Tracker (COT), a open-cell drift chamber that provides charged track identification  
 1222 and measurement of the momentum transverse to the  $p\bar{p}$  beams ( $p_T$ ) in the central  
 1223 region ( $|\eta| \leq 1.2$ ) for tracks with  $p_T > 400 \text{ MeV}/c$ . The active volume of the COT covers  
 1224 extends from a radius of 40 to 140 cm, with up to 96 axial and stereo measurement points  
 1225 inside a superconducting solenoid that provides a 1.4 T axial magnetic field. D0 Central  
 1226 Fiber Tracker fills a significant smaller space inside a 2 T solenoid, 20 to 50 cm, with  
 1227 16000 channel organized in 8 alternating axial and stereo layers each providing a doublet  
 1228 of measurement points. The  $p_T$  resolution is found to be  $\delta_{p_T}/p_T \sim 0.001 \cdot p_T (\text{GeV}/c)$   
 1229 in the CDF tracker. This results in precise invariant mass reconstruction which provides  
 1230 excellent signal-to-background ratio for fully reconstructed  $B$  and  $D$  decay modes.

1231 Tracks found in the central tracker are extrapolated inward and matched to hits in  
 1232 silicon microvertex detectors in both CDF and D0. The CDF detector (SVX II + ISL)  
 1233 uses double sided silicon microstrip technology providing tracking information in the  $r$ - $\phi$   
 1234 and  $r$ - $z$  planes in the pseudo-rapidity range  $|\eta| < 2$ . The detector has up to 7 layers of  
 1235 double-sided silicon at radial distances ranging from 2.5 cm to 28 cm from the beamline.

1236 Within the SVX is the innermost single-sided, radiation hard silicon layer (Layer 00),  
 1237 which is mounted directly onto the beam pipe at a radius of 1.35 to 1.62 cm [215]. The  
 1238 impact parameter resolution of the tracking system with, and without, the inclusion of  
 1239 Layer 00 is shown in Figure 4. The impact parameter resolution for high  $p_T$  charged

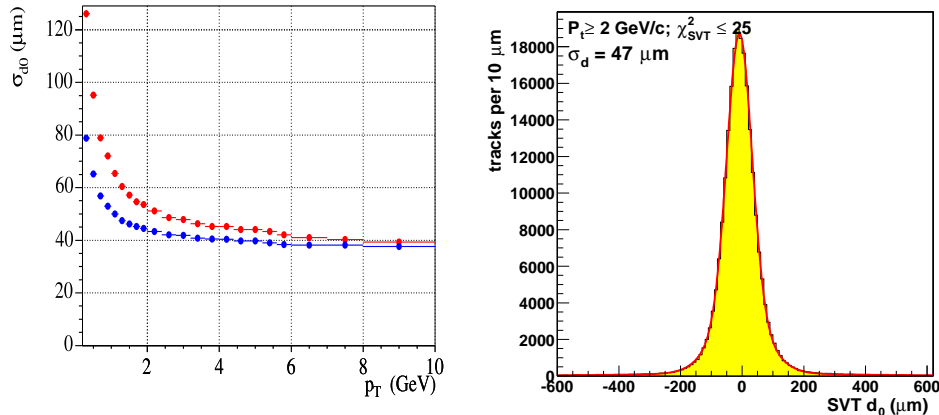


Fig. 4. CDF impact parameter resolution tracking tracks with Layer 00 hits (blue points) and without Layer 00 hits (red points.) a) and Silicon Vertex Trigger (SVT) impact parameter distribution for a generic sample of tracks b).

1240 tracks is  $\sim 25\mu m$  taking in to account the  $32\mu m$  contribution from the transverse size of  
 1241 the interaction region [215].

1242 D0 silicon microstrip tracker (SMT) is composed of cylindrical barrels with 4 layers of  
 1243 double-sided detectors interspersed with disks in the central part, and complemented with  
 1244 large forward disk at both ends, a design optimized for tracking up to  $|\eta| < 3$ . In addition,  
 1245 in 2006 a new innermost layer (Layer 0) was installed inside the existing detector. This  
 1246 has improved the impact parameter resolution and will prevent the expected performance  
 1247 degradation due to radiation damage of the innermost SMT layer during the rest of the  
 1248 Tevatron run [216].

1249 The silicon vertex detectors are crucial for precise decay length determination of  $b$  decays  
 1250 in time dependent measurement. Moreover the 3D vertex reconstruction allowed by  
 1251 the combined  $r$ - $\phi$  and  $r$ - $z$  measurements provides efficient background rejection against  
 1252 the large background of prompt events.

1253 Particle identification in CDF is provided by  $dE/dx$  in the central drift chamber and a  
 1254 time-of-flight (TOF) system consisting of 216 scintillator bars located between the COT  
 1255 and the solenoid [217]. The TOF, with a resolution of around 110 ps, provides at least  
 1256  $2\sigma$   $K/\pi$  separation for  $p_T < 1.5$  GeV/c. For  $p_T > 2.0$  GeV/c, the separation provided by  
 1257  $dE/dx$  between pions and Kaons is equivalent to  $1.4\sigma$  between two Gaussians while the  
 1258 separation for pions and electrons is  $2.5\sigma$  at  $p_T = 1.5$  GeV/c.

1259 Outside the solenoid are electromagnetic and hadronic calorimeters covering the pseudo-  
 1260 rapidity region  $|\eta| < 3.5$  in CDF and up to  $|\eta| < 4.0$  in D0.

1261 Muon detectors are located behind the hadron calorimeters, The CDF muon systems  
 1262 are segmented into four components, the Central Muon system (CMU) provides coverage  
 1263 for  $|\eta| < 0.6$  and  $p_T > 1.5$  GeV/c and sits behind  $\sim 5.5$  interaction lengths ( $\lambda$ ) of material  
 1264 primarily consisting of the iron of the hadronic calorimeter. The Central Muon upgrade  
 1265 (CMP) sits behind an additional 60 cm,  $\sim 3\lambda$  of steel, providing identification for muons  
 1266 with  $p_T > 3.0$  GeV/c in  $|\eta| < 0.6$ , with higher purity than muons identified only in  
 1267 the CMU. The Central Muon extension (CMX) consists of eight layers drift chambers

1268 arranged in conic sections and provides coverage for  $0.6 < |\eta| < 1.1$  and  $p_T > 2.0$  GeV/ $c$ ,  
 1269 and is located behind absorber material corresponding to  $\sim 6$  up to  $\sim 10$  interaction  
 1270 lengths. The D0 muon system sits outside of a thick absorber ( $> 10 \lambda$ ), and consists of  
 1271 a layer of tracking detectors and scintillation trigger counters inside a 1.8 T iron toroid,  
 1272 followed by two additional layers outside the toroid. The muon coverage extends to  
 1273  $|\eta| = 2$ . Magnet polarities are regularly reversed during data collection, thus providing  
 1274 an important way to control charge dependent effects in muon reconstruction that might  
 1275 affect semileptonic asymmetry measurement.

### 1276 Triggers

1277 Data acquisition and trigger system for experiments at hadron colliders have to sustain  
 1278 an extremely high collision rate, 7.6(40) MHz at Tevatron(LHC), and reduce it to ap-  
 1279 proximately 100-1000 Hz of interesting events that can be saved permanently for physics  
 1280 analysis, thus providing rejection factor  $> 10^4$  against uninteresting proton-(anti)proton  
 1281 collisions. The most straightforward way to achieve such a goal is to design electron and  
 1282 muon based triggers, using single or multi-lepton signatures, that allow to select signif-  
 1283 icantly pure samples of heavy flavor decays thanks to the large semileptonic branching  
 1284 ratios, or by isolating final states containing e.g.  $J/\psi$ . Rate is controlled primarily with  
 1285 lepton transverse momentum requirement, that has to be kept as low as possible in order  
 1286 to maximize signal efficiency. Inclusive electron and muon selection with a threshold of  
 1287 6-8 GeV/ $c$  are typical at Tevatron. Much lower thresholds are possible for events with two  
 1288 leptons, approaching the minimum detectable transverse momentum in each detector (  
 1289 2 GeV/ $c$  at Tevatron).

1290 This strategy has been implemented by all the present and forthcoming experiments  
 1291 and provided the majority of the result for rare decays and lifetime measurements at  
 1292 Tevatron in the last decade. A clear limitation of this approach is that it lacks the ability  
 1293 to select fully hadronic decays of b-hadrons. In the context of CKM-related physics the  
 1294 latter are important for the study of either 2 body charmless decays, or  $B \rightarrow DK$  decays  
 1295 involved in the measurement of the angle  $\gamma$  in tree processes, and, most importantly,  
 1296 for selecting large samples of fully reconstructed  $\bar{B}_s \rightarrow D_s^+ \pi^-$  and  $\bar{B}_s \rightarrow D_s^+ \pi^+ \pi^- \pi^+$   
 1297 that lead to the first observation of  $B_s^0 - \bar{B}_s^0$  mixing in 2006 [218]. To overcome this  
 1298 limitation the CDF collaboration pioneered the technique of online reconstruction of  
 1299 charged tracks originating from decay vertexes far from the collision point due to the  
 1300 significant boost and lifetime of B-mesons produced at high energy hadron colliders. The  
 1301 key innovation introduced for Run II in the CDF trigger was in fact the Silicon Vertex  
 1302 Trigger (SVT) [219] processor. At the second level of the trigger system, information from  
 1303 the silicon vertex detector is combined with tracks reconstructed at the first level trigger  
 1304 in the drift chamber. High resolution SVT-tracks are then provided within the latency  
 1305 of  $\approx 20 \mu s$ , and are used to select events characterized by two tracks with high impact  
 1306 parameter and vertex decay length greater than 200  $\mu m$ , thus providing a rejection  
 1307 factor of 100-1000 while maintaining a significant efficiency for B decays. The impact  
 1308 parameter resolution of the SVT, shown in Figure 4, is approximately 50  $\mu m$ , which  
 1309 includes a contribution of 32  $\mu m$  from the width of the  $p\bar{p}$  interaction region. It has to be  
 1310 noted, however, that selecting events based upon decay length information, introduces  
 1311 an important inefficiency at small values of proper decay time. We will describe how this  
 1312 bias has been incorporated in the analysis in Section 3.2.3.

1313 3.2. Common experimental tools

1314 In the following the most relevant experimental techniques for flavor physics will be  
 1315 briefly discussed. Time dependent measurements require excellent vertexing and flavor  
 1316 tagging capabilities, crucial in the latter case is particle identification and  $\pi$ -K separation.  
 1317 Finally noise suppression, recoil tagging technique and Dalitz-plot analysis techniques will  
 1318 be discussed.

1319 3.2.1. Time-dependent measurements

It is possible to measure phases of the CKM matrix elements, and therefore CP violating quantities, by exploiting the different time evolution of the two mass eigenstates of the  $B_0$  meson system,  $B_L$  and  $B_H$ . At B-Factories, where a  $B_0$  meson is produced coherently with its antiparticle, the probability density function of observing a  $B$  decay into a flavor eigenstate (called  $B_{tag}$ ) and for whom  $\eta = -1(+1)$  if  $B^0$  ( $\bar{B}^0$ ) and the other one, called  $B_{reco}$ , in a given final state  $f$  at times that differ by  $\Delta t$  is

$$f_\eta(\Delta t) = \frac{\Gamma}{4} e^{-\Gamma|\Delta t|} \{1 + \eta [S \sin \Delta m \Delta t - C \cos \Delta m \Delta t]\}, \quad (95)$$

1320 where the decay width difference between the two mass eigenstates is neglected,  $\Delta m$  is  
 1321 the mass difference,

$$S = \frac{2Im\lambda}{1 + |\lambda|^2} \quad C = \frac{1 - |\lambda|^2}{1 + |\lambda|^2}, \quad (96)$$

and

$$\lambda = - \frac{\langle B^0 | \mathcal{H}_{\Delta B=2} | \bar{B}^0 \rangle \langle f | \mathcal{H}_{\Delta B=1} | \bar{B}^0 \rangle}{\langle B^0 | \mathcal{H}_{\Delta B=2} | \bar{B}^0 \rangle \langle f | \mathcal{H}_{\Delta B=1} | B^0 \rangle}. \quad (97)$$

1322 Depending on the choice of the final state  $f$ ,  $S$  can be related to different phases of the  
 1323 CKM matrix elements. In particular if  $f$  is a flavor eigenstate then  $\lambda = 0$  and  $C = 1$  and  
 1324  $S = 0$ , no phase can be measured but there is sensitivity to  $\Delta m$ ; likewise if  $f$  is a CP  
 1325 eigenstate,  $\lambda$  is a pure phase and this is usually the cleanest configuration to measure  
 1326 CP violation parameters, although all non-zero values of  $\lambda$  allow such measurements.

1327 At hadron colliders the same considerations apply, a part from the fact that  $\Delta t$  mea-  
 1328 sures the time between the  $B$  meson production and its decay and that  $\eta = -1(+1)$  for  
 1329 an initially produced  $B^0$  ( $\bar{B}^0$ ). The initial  $B$  flavor can be measured either by observ-  
 1330 ing the decay products of the other hadron with a  $b$  quark in the event, or by utilizing  
 1331 information on the jet of particles the  $B$  meson is contained into.

1332 There are therefore three key ingredients in these measurements: the identification of  
 1333 the flavor of the meson produced in association with the one reconstructed in the channel  
 1334  $f$  (the so-called  $B$ -tagging), the measurement of  $\Delta t$  which requires the reconstruction of  
 1335 the decay vertex of at least one  $B$  meson (both mesons in the case of  $B$ -factories), and  
 1336 the reconstruction of the  $B$  meson in the final state  $f$  with the least possible background.

The experimental uncertainties on these quantities alter the probability density function of the measured quantities, function which is used in the likelihood fits implemented to perform these measurements. Instead of Eq. 95 one can then write

$$f_\eta(\Delta t) = \frac{\Gamma}{4} e^{-\Gamma|\Delta t_{true}|} \{1 + \eta \mathcal{D} [S \sin \Delta m \Delta t_{true} - C \cos \Delta m \Delta t_{true}]\} \otimes \mathcal{R}(\Delta t - \Delta t_{true}) + f_\eta^{bkg}(\Delta t), \quad (98)$$

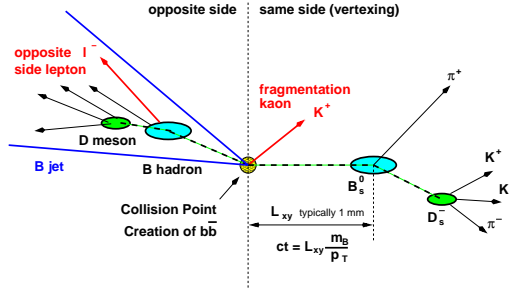


Fig. 5. Sketch of typical  $b\bar{b}$  event indicating several  $B$  flavor tagging techniques.

1337 where  $\otimes$  indicates the convolution,  $\mathcal{D} = 1 - p_w$  is the tagging dilution ( $p_w$  is the probability  
 1338 of incorrectly tagging a meson),  $R$  is the vertexing resolution function, and  $f_\eta^{bkg}$  is the  
 1339 probability density function for the background.

1340 The next sections describe the techniques adopted for tagging, vertexing reconstruction  
 1341 and background rejection and the means available to estimate the quantities that enter  
 1342 into Eq. 98.

### 1343 3.2.2. $B$ Flavor Tagging

1344 One of the key components in the measurement of neutral  $B$  meson flavor oscillations  
 1345 or time dependent CP asymmetries is identifying the flavor of the  $B$  meson (containing a  
 1346  $\bar{b}$  antiquark) or  $\bar{B}$  meson (containing a  $b$  quark) at production, in the case of incoherent  
 1347 mixing at hadronic colliders, or at the moment the other  $b$ -meson decays in the case of  
 1348  $B^0\bar{B}^0$  from  $\Upsilon(4S)$ . We refer to this method of identifying the  $B$  hadron flavor as “ $B$  flavor  
 1349 tagging”. The figure of merit to compare different tagging methods or algorithms is the  
 1350 so-called effective tagging power  $\varepsilon\mathcal{D}^2 = \varepsilon(1 - 2p_W)^2$ , where the efficiency  $\varepsilon$  represents the  
 1351 fraction of events for which a flavor tag exists and  $p_W$  is the mistag probability indicating  
 1352 the fraction of events with a wrong flavor tag. The mistag probability is related to the  
 1353 dilution:  $\mathcal{D} = 1 - 2p_W$ . The experimentally observed mixing or CP asymmetries are, in  
 1354 fact, proportional to the dilution  $\mathcal{D}$ . A flavor tag which always returns the correct tag  
 1355 has a dilution of 1, while a random tag yielding the correct flavor 50% of the time has a  
 1356 dilution of zero.

1357 Several methods to tag the initial  $b$  quark flavor have been used both at B-factories and  
 1358 hadron collider experiments. The flavor tagging methods can be divided into two groups,  
 1359 those that identify the flavor of the other  $b$ -hadron produced in the same event (opposite  
 1360 side tag - OST), and those that tag the initial flavor of the  $B$  candidates itself (same  
 1361 side tag - SST). The latter, being based on charge correlation between initial  $b$  quark  
 1362 and fragmentation particles is only possible at hadron colliders or Z-pole experiments.

1363 Fig. 5 is a sketch of a  $b\bar{b}$  event showing the  $B$  and  $\bar{B}$  mesons originating from the  
 1364 primary  $p\bar{p}$  interaction vertex and decaying at a secondary vertex indicating possible  
 1365 flavor tags on the decay vertex side (SST) as well as opposite side tags.

1366 In the following the main aspects of the opposite side taggers used at both Tevatron  
 1367 and B-Factories and of the SST used for the  $B_s^0\bar{B}_s^0$  oscillation observation and in the  
 1368 first  $\phi_s$  determination at Tevatron will be briefly discussed.

#### 1369 Opposite Side Tags

1370 Both experiments at hadron colliders and B-Factories exploit three feature of  $B$  decays

1371 to estimate the flavour of the opposite  $B$  meson.

1372 The “lepton tagging” looks for an electron or muon from the semileptonic decay of the  
1373 opposite side  $B$  hadron in the event. The charge of this lepton is correlated with the flavor  
1374 of the  $B$  hadron: an  $\ell^-$  comes from a  $b \rightarrow c \ell^- \bar{\nu} X$  transition, while an  $\ell^+$  originates from  
1375 a  $\bar{b}$  quark. Since the semileptonic  $B$  branching fraction is small,  $\mathcal{B}(B \rightarrow \ell X) \sim 20\%$ ,  
1376 lepton tags are expected to have low efficiency but high dilution because of the high  
1377 purity of lepton identification.

1378 The strangeness of Kaons or  $\Lambda$  from the subsequent charm decay  $c \rightarrow s X$  is also  
1379 correlated with the  $B$  flavor, e.g. a  $K^-$  results from the decay chain  $b \rightarrow c \rightarrow s$  while  
1380 a  $K^+$  signals a  $\bar{b}$  flavor. Searching for a charged Kaon from the opposite side  $B$  hadron  
1381 decay is referred to as “Kaon tagging”. This method is expected to have high efficiency  
1382 but low dilution at hadron colliders since the challenge is to first identify Kaons among  
1383 a vast background of pions through particle-id techniques, and then to discriminate the  
1384  $B$  decay Kaon candidates from all prompt Kaons produced in the collision by relying  
1385 on Kaon impact parameter and reconstruction of secondary vertexes in the opposite  
1386 side [220].

1387 Finally all other information carried by the tracks among the decays of the  $B$  mesons  
1388 constitutes the third large tagging category. On average in fact the most energetic charged  
1389 decay product carries the charge of the original  $b$  quark. At Tevatron the “jet charge  
1390 tagging” exploits the fact that the sign of the momentum weighted sum of the particle  
1391 charges of the opposite side secondary vertex from  $b$  (D0 [221]) or  $b$  jet (CDF [222]) is  
1392 correlated to the charge of the  $b$  quark. Jet charge tags can reach very high efficiency  
1393 but with low dilution. Furthermore, more than 20% of  $B$  decays contain charged  $D^*$   
1394 mesons which decay 66% of the times into a soft pion with the same charge. Soft pions  
1395 can therefore also have a high charge correlation with the original  $b$  quark. The Belle  
1396 and BaBar experiments input to multivariate tagging algorithms the charge of all tracks,  
1397 with special treatment for the softest in the event to take into account this effect.

1398 The algorithms to combine all the information use multivariate technique either ex-  
1399 ploiting directly the available output of the various tagging algorithms or starting by  
1400 assigning each track candidate of coming from the “tagging”  $B$  meson into one category  
1401 between lepton, kaon, soft pion (only for B-Factories) or generic track. Each experiment  
1402 then has a different approach to exploit the information.

1403 The BaBar experiment uses one Neural Network (NN) per category with different  
1404 quantities in input depending on the category (see Ref. [223] for details): for instance the  
1405 “Lepton” category would contain lepton identification quantities and the momentum.  
1406 The output of these NNs based on single-particle information are themselves combined  
1407 into several event-by-event NNs, that assess the likelihood of the flavor assignment. The  
1408 tagging categories are mutually exclusive and for each event only one NN is evaluated.  
1409 The algorithm of the Belle experiment is similar but exploits likelihood instead of NNs  
1410 and has a single output (called  $r$ ). In both cases the algorithms are tuned on MC, but  
1411 the mistag probability is estimated on data control samples.

1412 The experimental sensitivity is maximized upon using the expected dilution on an event  
1413 by event basis, employing parameterizations derived by a combination of simulation and  
1414 real data. As an example, the dilution of the lepton tagging is parameterized as a function  
1415 of the lepton identification quality and of the  $p_T^{\text{rel}}$  of the tagging lepton (CDF [224, 225])  
1416 or of the lepton jet-charge (D0 [221]). The quantity  $p_T^{\text{rel}}$  is defined as the magnitude  
1417 of the component of the tagging-lepton momentum that is perpendicular to the axis of

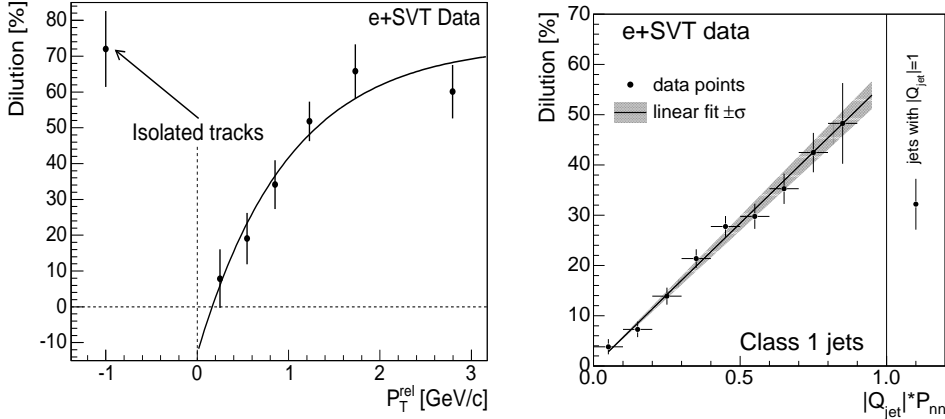


Fig. 6. Variation of dilution of the electron tags with  $p_T^{\text{rel}}$  (left). Dilution as a function of  $|Q_{\text{jet}}| \cdot \mathcal{P}_{\text{nn}}$  for "jet-charge" tagging algorithm (right).

1418 the jet associated with the lepton tag. Variation of the dilution as a function of  $p_T^{\text{rel}}$  is  
 1419 shown left side of Fig. 6 for electron tags in CDF. The dilution is lower for low  $p_T^{\text{rel}}$   
 1420 because fake leptons and leptons from sequential semileptonic decay ( $b \rightarrow c \rightarrow \ell^+$ ) tend  
 1421 to have relatively low  $p_T^{\text{rel}}$  values. Also, to maximize the tagging power the dilution  
 1422 of the jet charge tags can be calculated separately for different quality of the opposite  
 1423 side secondary vertex information and parametrized as a linear function in the quantity  
 1424  $|Q_{\text{jet}}| \cdot \mathcal{P}_{\text{nn}}$ , where  $\mathcal{P}_{\text{nn}}$  expresses a probability for the jet to be a  $b$  jet, as displayed  
 1425 in Fig. 6 for jets containing a well separated secondary vertex in the CDF case. Flavor  
 1426 misidentification can occur because the jet charge does not reflect perfectly the true  
 1427 charge of the original  $b$  quark, due e.g. to mixing. In addition, the selected tagging jet  
 1428 may contain only a few or no tracks from the actual opposite side  $B$  hadron decay.

1429 At Tevatron, the typical flavor tagging power of a single tagging algorithm is  $\mathcal{O}(1\%)$ .  
 1430 Limitations in opposite side tagging algorithms arise because the second bottom hadron  
 1431 is inside the detector acceptance in less than 40% of the time or it is possible that the  
 1432 second  $B$  hadron is a neutral  $B$  meson that mixed into its antiparticle. For example, the  
 1433 low efficiency of an opposite side lepton tag of  $\sim 20\%$  from the semileptonic  $B$  hadron  
 1434 branching fraction together with a dilution of  $\sim 30\%$  results in an estimated  $\varepsilon \mathcal{D}^2 \sim$   
 1435  $0.4 \times 0.2 \times 0.3^2 \sim 0.01$ . At B-factories, better hermeticity of detectors, enhanced particle  
 1436 identification capability, and the absence of incoherent mixing as a source of dilution  
 1437 makes it possible to reach combining all the information together an effective tagging  
 1438 power  $\varepsilon \mathcal{D}^2 \sim 0.30$  in both Belle and Babar. As an example of tagging performances for  
 1439 each experiment considered here, the obtained efficiencies  $\varepsilon$ , effective dilutions  $\langle \mathcal{D} \rangle$ , and  
 1440 effective tagging powers  $\varepsilon \mathcal{D}^2$  are shown in Table 7.

1441 In the case of opposite side flavor tags, the dilution is expected to be independent of  
 1442 the type of  $B$  meson ( $B^0, B^+, B_s$ ) under study, hence can be studied on large inclusive  
 1443 semileptonic samples (CDF) or on  $B^0$  or  $B^+$  samples (D0) and then applied in  $B_s$  related  
 1444 measurement. The final calibration of the opposite side tagging methods come from a  
 1445 measurement of the  $B^0$  oscillation frequency  $\Delta m_d$  in hadronic and semileptonic samples  
 1446 of  $B$  mesons at both B-factories and Tevatron experiments. A perfectly calibrated tagging

Table 7

Tagging performances of the opposite side tagging algorithms at BaBar [226], Belle [227], D0 [221], and CDF [228]. Note that the individual tagger performance in the latter case are determined in non-exclusive sample so their sum is greater than the neural network (NN) based combined opposite side tagging for CDF. All errors given are statistical.

Category		Efficiency $\varepsilon$ [%]		Effect. dilution $\langle \mathcal{D} \rangle$ [%]		Tagging Power $\varepsilon \mathcal{D}^2$ [%]	
BaBar	Belle ( $r \in$ )	BaBar	Belle	BaBar	Belle	BaBar	Belle
Lepton	0.875-1	8.96±0.07	14.4±0.9	99.4±0.3	97.0±0.5	7.98±0.11	13.5±0.9
Kaon I	0.75-0.875	10.82±0.07	9.8±0.7	89.4±0.3	78.2±0.9	8.65±0.3	6.0±0.5
Kaon II	0.625-0.75	17.19±0.09	10.7±0.8	71.0±0.4	68.4±1.0	8.68±0.17	5.0±0.5
Kaon-Pion	0.5-0.625	13.67±0.08	10.8±0.8	53.4±0.4	55.0±1.1	3.91±0.12	3.3±0.4
Pion	0.25-0.5	14.18±0.08	14.6±0.9	35.0±0.4	36.0±0.8	1.73±0.09	1.9±0.2
Other	0-0.25	9.54±0.07	39.7±1.5	17.0±0.5	7.2±0.7	0.27±0.04	0.2±0.1
Total Tagging Power						31.2±0.3	29.9±1.2
		CDF	D0	CDF	D0	CDF	D0
Muon		5.5 ± 0.1	6.6 ± 0.1	35.3 ± 1.1	47.3 ± 2.7	0.68 ± 0.05	1.48 ± 0.17
Electron		3.1 ± 0.1	1.8 ± 0.1	30.7 ± 1.1	34.1 ± 5.8	0.29 ± 0.01	0.21 ± 0.07
Jet Charge		90.5 ± 0.1	2.8 ± 0.1	9.5 ± 0.5	42.4 ± 4.8	0.80 ± 0.05	0.50 ± 0.11
Kaon		18.1 ± 0.1	N/A	11.1 ± 0.9	N/A	0.23 ± 0.02	N/A
Total Tagging Power						1.81±0.10	2.19±0.22

1447 method applied to a large sample of  $\bar{B}^0$  mesons should result in a precise measurement  
 1448 of  $\Delta m_d$ . In turn one can use the well known world average value of  $\Delta m_d$  to check and  
 1449 re-calibrate the predicted dilutions of the opposite side tagging algorithms.

1450

### 1451 Same Side Flavor Tagging

1452 The initial flavor of a  $B$  meson can additionally be tagged by exploiting correlations  
 1453 of the  $B$  flavor with the charge of particles produced in association with it (SST). Such  
 1454 correlations arise from  $b$  quark hadronization and from  $B^{**}$  decays. In the case of a  $B^-$   
 1455 or  $\bar{B}^0$  mesons, the fragmentation particles are mainly pions while  $\bar{B}_s$  meson are primarily  
 1456 accompanied by fragmentation Kaons. In the  $\bar{B}_s$  meson case we thus refer to this method  
 1457 as “same side Kaon tagging” (SSKT). In the simplest picture, where only pseudo-scalar  
 1458 mesons are produced directly by the fragmentation process, the following charged stable  
 1459 mesons are expected: a  $\bar{B}^0$  will be produced along with  $\pi^-$ , a  $B^-$  will be produced with  
 1460 a  $\pi^+$  or a  $K^+$ , and a  $\bar{B}_s$  will be produced with a  $K^-$ . Corresponding relations are true  
 1461 for the charge conjugated  $B$  mesons. The idea of the same side tagging algorithm is to  
 1462 identify the leading fragmentation track charge and to determine the  $B$  initial flavor  
 1463 accordingly.

1464 Several advantages compared to the opposite side tagging algorithms are worth men-  
 1465 tioning. The SST shows a high efficiency since the leading fragmentation track is in the  
 1466 same detector region as the signal  $B$  hadron, thus, within the detector acceptance, and  
 1467 there are also no limitations due to branching ratios. The search region for same side  
 1468 tagging tracks is limited near the signal  $B$  direction. Due to this geometrical restriction,  
 1469 the SST is robust against background from the underlying event or multiple interac-



1470 tions. Finally neutral meson mixing does not dilute the useful charge correlation. These  
 1471 advantages are reflected in an higher flavor tagging dilution.

1472 Unlike the opposite side flavor tagging algorithms, the performance of the same side algo-  
 1473 rithm cannot easily be quantified using data. Since SST is based on information from  
 1474 the signal  $B$  fragmentation process, its performance depends on the signal  $B$  species.  
 1475 Therefore,  $B^+$  and  $B^0$  modes can not be used to calibrate the same side tagging per-  
 1476 formance for  $B_s$  mesons. Instead, prior to the actual observation of  $B_s$  mixing, the  
 1477 experiments had to rely upon Monte Carlo simulation to quantify the performance of  
 1478 same side tagging for  $B_s$  mesons. High statistics  $B^+$  and  $B^0$  modes have been used to  
 1479 verify that specifically tuned Monte Carlo program accurately model the fragmentation  
 1480 process.

1481 The CDF algorithm [229] starts selecting charged tracks with  $p_T \geq 450 \text{ MeV}/c$ , good  
 1482 momentum and impact parameter resolution as potential tagging tracks. Fragmentation  
 1483 tracks originate from the primary vertex, therefore an impact parameter significance  
 1484 less than 4 is required. To reject background from multiple interactions, the tracks are  
 1485 required to be close to the  $B_s$  candidates both along the beam direction and in  $\Delta R =$   
 1486  $\sqrt{\Delta\eta^2 + \Delta\phi^2} \leq 0.7$ .

1487 About 60% of the tagged events have one and only one tagging track. Of the remaining  
 1488 events approximately one-third have all tagging tracks with the same charge. Therefore,  
 1489 the subsequent tagging algorithm makes a choice between multiple, oppositely charged  
 1490 tracks in about one-fourth of all tagged events. Several variables have been employed.  
 1491 The most sensitive was found to be the maximum longitudinal component of the tagging  
 1492 tracks with respect to the  $B$  momentum, and after that the largest likelihood to be a Kaon  
 1493 based on TOF and  $dE/dx$  measurements. A neural network is finally used to combine  
 1494 the available information. Examples of the dependence of the dilution on the variables  
 1495 discussed above are given in Fig. 7 for the subsample with only one tagging track.

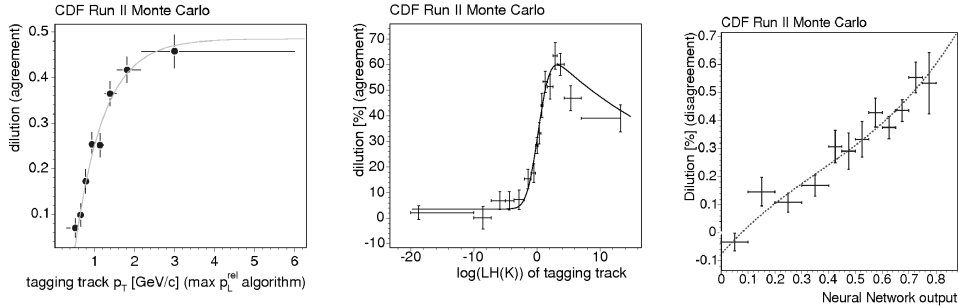


Fig. 7. (Left panel) Dilution of the maximum  $p_L^{rel}$  algorithm as a function of tagging track  $p_T$ . (Middle panel) Dilution for the Kaon identification based algorithm as function of Kaon likelihood. (Right panel) Dilution of the NN algorithm as a function of NN variable. The dots represent Monte Carlo data, the line is the parametrization, which has been used to determine the event-by-event dilution. Events with only one tagging track candidate around the  $B_s$  meson are displayed.

1496 The performance of the SSKT algorithm has been evaluated for  $B^+$ ,  $B^0$  and  $B_s$  modes  
 1497 on several decay channels (see Table 8). The agreement between simulation and data in  
 1498  $B^+$  and  $B^0$  modes suggests that the simulation can predict the tagger performance across  
 1499 all  $B$  species. The measured differences are used to evaluate a systematic uncertainty on  
 1500 SSKT for  $B_s$  mesons. Since the algorithm rely on the number of Kaons produced in the

1501 fragmentation process leading to the production of  $B_s$  mesons an additional important  
 1502 uncertainty is derived by the difference in data and simulation of the number of Kaons  
 1503 around the  $B_s$  direction of flight. Smaller systematic uncertainties arise considering  $b$ -  
 1504 quark production mechanism, fragmentation models,  $B^{**}$  rate and event pile-up.

Table 8  
 Performance of the NN based algorithm in data and Monte Carlo. Only statistical uncertainties are quoted.

[%]		$B^- \rightarrow D^0 \pi^-$	$\bar{B}^0 \rightarrow D^+ \pi^-$	$\bar{B}_s \rightarrow D_s^+ \pi^-$
MC	$\epsilon$	$55.9 \pm 0.1$	$56.6 \pm 0.1$	$52.1 \pm 0.3$
	$\langle \mathcal{D} \rangle$	$26.8 \pm 0.2$	$16.1 \pm 0.6$	$29.2 \pm 0.7$
data (1 fb $^{-1}$ )	$\epsilon$	$58.2 \pm 0.3$	$57.2 \pm 0.3$	$49.3 \pm 1.3$
	$\langle \mathcal{D} \rangle$	$26.4 \pm 0.8$	$15.2 \pm 1.7$	—

1505 The tagging dilution evaluated for the  $\bar{B}_s \rightarrow D_s^+ \pi^-$  sample using the event-by-event  
 1506 predicted dilution derived from Monte Carlo yields  $\langle \mathcal{D} \rangle = 24.9 - 29.3_{-4.3}^{+3.3}\%$  (for compar-  
 1507 ison using the maximum  $p_L^{rel}$  only gives  $\langle \mathcal{D} \rangle = 23.7_{-4.5}^{+2.6}\%$ ). The overall SSKT tagging  
 1508 figure of merit is  $\epsilon \langle \mathcal{D} \rangle^2 = 3.1 - 4.3_{-1.4}^{+1.0}$ , including statistical and systematic uncertainties  
 1509 (the given range reflect the performance of the CDF TOF system in different data taking  
 1510 periods). This result can be compared to the overall OST  $\epsilon \mathcal{D}^2 = 1.8 \pm 0.1\%$  for oppo-  
 1511 site side tagging on the same channel (note the significant channel dependence of the  
 1512 measured  $\epsilon \mathcal{D}^2$ , mostly related to the  $B$  meson  $p_T$  spectrum of the reconstructed decays).

1513 Also the D0 experiment recently introduced a same side tagger [230]. The track with  
 1514  $p_T > 500$  MeV/ $c$  closest in  $\Delta R$  to the  $B_s$  candidate flight direction is selected for tagging.  
 1515 Dilution is studied as a function of the product of the tagging track charge and  $\Delta R$ , as  
 1516 well as forming a same side jet charge from the transverse momentum weighted sum of all  
 1517 tracks within a narrow cone around the  $B_s$  flight direction. The combined  $\epsilon \mathcal{D}^2$  from OST  
 1518 and SST quoted by the D0 collaboration is  $4.68 \pm 0.54\%$  to be compared to  $2.48 \pm 0.22\%$   
 1519 from the OST alone.

### 1520 3.2.3. Vertexing

1521 For time dependent measurements determining the elapsed times ( $\Delta t$  in Sec. 3.2.1)  
 1522 is crucial. This is obtained by first measuring a length  $L$  and then computing  $\Delta t =$   
 1523  $L/(c \beta \gamma)$ . The vertexing techniques utilized to measure  $L$  are significantly different at B-  
 1524 Factories and hadron colliders because of the different boost and because time dependent  
 1525 measurements have two different needs: measure the difference in time between the two  $B$   
 1526 mesons in an event at the B-Factories and measure the time of flight since the production  
 1527 of the  $B$  meson of interest at the hadron colliders. The two approaches are therefore  
 1528 described separately in the following.

#### 1529 **Vertex reconstruction at B-Factories**

1530 The  $B_{reco}$  vertex is reconstructed from charged tracks and photon candidates that  
 1531 are combined to make up intermediate mesons (e.g.,  $J/\psi$ ,  $D$ ,  $K_s^0$ ) and then treated as  
 1532 virtual particles. The trajectory of these virtual particles is computed from those of their  
 1533 decay particles, and, when appropriate, mass constraints are imposed to improve the  
 1534 knowledge of the kinematics. In the case of charmonium states such as  $J/\psi K_s^0$ , Belle  
 1535 uses only the dileptons from the  $J/\psi$  decay. In Belle, the vertex of the signal candidate

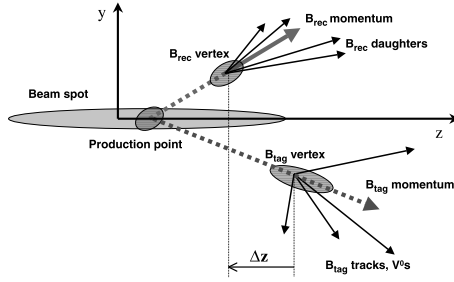


Fig. 8. Schematic view of the vertexing algorithm at B-Factories.

1536 is constrained to come from the beam-spot in the x-y plane and convolved with the  
 1537 finite B-meson lifetime. BABAR uses the beam-spot information only in the tag vertex  
 1538 reconstruction. The resulting spatial resolution depends on the final state; it is typically  
 1539  $65 \mu\text{m}$  in BABAR and  $75 \mu\text{m}$  in Belle.

1540 BABAR determines the Btag vertex by exploiting the knowledge of the center-of-  
 1541 mass four-momentum and an estimate of the interaction point or beam-spot position.  
 1542 This information, along with the measured three-momentum of the fully reconstructed  
 1543 Breco candidate, its decay vertex, and its error matrix, permits calculation of the Btag  
 1544 production point and three-momentum, with its associated error matrix (see Fig. 8). All  
 1545 tracks that are not associated with the Breco reconstruction are considered;  $K_s^0$  and  $\Lambda$   
 1546 candidates are used as input to the fit in place of their daughters, but tracks consistent  
 1547 with photon conversions are excluded. To reduce the bias from charm decay products,  
 1548 the track with the largest  $\chi^2$  vertex contribution if greater than 6 is removed and the fit  
 1549 is iterated until no track fails this requirement.

1550 Belle reconstructs the Btag vertex from well-reconstructed tracks that have hits in  
 1551 the silicon vertex detector and are not assigned to the Breco vertex. Tracks from K0S  
 1552 candidates and tracks farther than 1.8 mm in z or  $500 \mu\text{m}$  in r from the Breco vertex are  
 1553 excluded. An iterative fit to these tracks is performed with the constraint that the vertex  
 1554 position be consistent with the beam spot. If the overall  $\chi^2$  is poor, the track with the  
 1555 worst  $\chi^2$  contribution is removed, unless it is identified as a high-momentum lepton. In  
 1556 this case, the lepton is retained and the track with the second-largest  $\chi^2$  is removed.

1557 The resolution on  $\Delta z$  is dominated by the Btag vertex reconstruction and therefore is  
 1558 nearly independent of the reconstructed CP decay mode. Based on Monte Carlo simula-  
 1559 tion, it is estimated to be  $190 \mu\text{m}$ . The  $\Delta z$  measurement is converted to a  $\Delta t$  measure-  
 1560 ment, and the corresponding resolution is 1.1 ps in BABAR and 1.43 ps in Belle because  
 1561 of the different center-of-mass boosts.

### 1562 Decay Length Measurements at Tevatron

1563 In the Tevatron detectors, with a central geometry, the decay length is best measured  
 1564 in the transverse plane, the proper time  $t$  is computed from the flight distance in the  
 1565 transverse plane,  $L_{xy}$ . Thus, the expression for  $t$  and its resolution are:

$$1566 \quad t = \frac{L}{c\beta\gamma} = L_{xy} \frac{m_B}{c p_T} \quad ; \quad \sigma_t = \sigma_{L_{xy}} \frac{m_B}{c p_T} \oplus \frac{\sigma_{p_T}}{p_T} t \quad (99)$$

1567 For fully reconstructed decays, the only significant uncertainty is from the decay dis-  
 1568 tance measurement. Partially reconstructed decays have an additional term from  $p_T$   
 1569 uncertainty which grows linearly with  $t$ .

1569 The transverse flight distance of the  $B$ -meson,  $L_{xy}$ , is given by the transverse distance  
 1570 between the location of  $p\bar{p}$  interaction, the Primary Vertex (PV), and the Secondary  
 1571 Vertex (SV), i.e. the decay point of the  $B$ -meson. The position of the PV is determined  
 1572 for each event by fitting the tracks in the underlying event to a common origin, excluding  
 1573 the tracks belonging to the  $B$  candidate.

1574 The secondary vertex is determined by fitting to a common vertex the  $B$  daughter  
 1575 charged tracks, considering tertiary vertex from charm decay, and mass constraints on  
 1576 intermediate resonances where applicable. The error estimate on  $L_{xy}$  is obtained by  
 1577 combining the PV uncertainty with that provided by the SV fit. A gaussian resolution  
 1578 function is normally a good approximation but the error estimate from the vertex fit needs  
 1579 to be multiplied by a scale factor for a correct measurement. This rescaling is typically  
 1580 calculated from the lifetime distribution of prompt background (e.g. from prompt  $J/\psi$   
 1581 and underlying event tracks for decays involving  $J/\psi$ , or from prompt charm production  
 1582 and fake leptons for semileptonic decays). A peculiar situation arise when data biased in  
 1583 lifetime, due e.g. to trigger requirements, are used. In this case special samples can be  
 1584 manufactured combining a prompt charm meson with a randomly selected charged track,  
 1585 consistent with coming from the PV. The pseudo-decay length of this events is expected  
 1586 to peak at 0 and can be used to measure the decay length resolution scale factor.

1587 The proper decay time resolution for fully reconstructed  $\bar{B}_s \rightarrow D_s^+ \pi^-$  and  $\bar{B}_s \rightarrow$   
 1588  $D_s^+ \pi^+ \pi^- \pi^+$  decays with the CDF detector is shown in Fig. 9 (left). The mean proper  
 1589 decay time uncertainty corresponds to 86 fs, which has to be compared with the oscillation  
 1590 period for  $B_s$  mesons  $\approx 350$  fs, and shows the ability of the current Tevatron experiment  
 1591 vertex detectors to resolve the fast  $B_s$  oscillations.

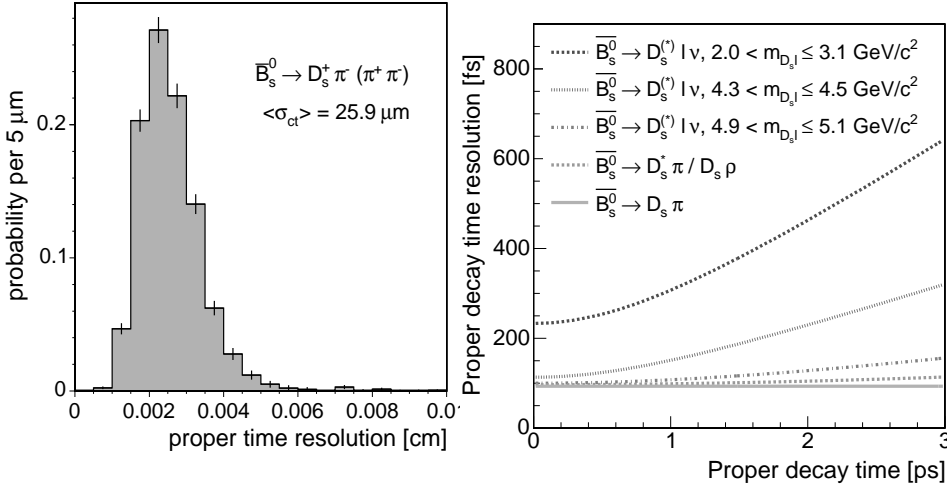


Fig. 9. The decay time resolution for fully reconstructed  $B_s$  decays in CDF (left) and the effective resolution for different values of missing (unreconstructed) semileptonic mass, as a function of the proper decay time (right).

1592 For partially reconstructed decays, like semileptonic decays, there is an important addi-  
 1593 tional uncertainty in the decay time due to the incompletely measured  $p_T$  of the  $B$  meson  
 1594 (Eq. 99). The distribution  $F(k)$  of the fractional missing momentum  $k = p_T^{\text{obs}}/p_T(B)$  is  
 1595 extracted from Monte Carlo simulations and is rather wide with a typical RMS of 10

1596 to 20%. The gaussian resolution function has to be convoluted with the distribution of  
 1597 this  $k$  factor in any time dependent measurement involving partially reconstructed or  
 1598 semi-leptonic decays. In semileptonic decays the missing neutrino momentum is corre-  
 1599 lated with the visible mass  $D + \ell$ ,  $M_{D\ell}$ , hence it is useful to divide the data in bins of  
 1600  $M_{D\ell}$  taking advantage of the narrower width of  $F(k)$  for higher  $M_{D\ell}$  as shown in Fig. 9  
 1601 (right).

1602 An important complication in time dependent measurement is introduced by recon-  
 1603 struction or trigger bias on proper time (see e.g. section 3.1.4). To take in to account this  
 1604 effect a function  $\xi(t)$ , that describes the acceptance as a function of proper decay time  
 1605 and is derived from simulations, multiply proper time related terms in the likelihood  
 1606 fits. To derive it CDF assumes that for each accepted event  $i$ , the expected  $ct$  distribu-  
 1607 tion without any bias is an exponential smeared by the experimental resolution function,  
 1608 where the width is the  $ct$  error ( $\sigma_{ct_i}$ ) of that event. The denominator is the sum of the  
 1609  $N$  expected distributions without any bias,

$$\xi(ct) \equiv \frac{\text{reconstructed } ct \text{ after trigger + selection}}{\sum_{i=1}^N \frac{1}{\tau} \exp\left(-\frac{ct}{c\tau}\right) \otimes G(ct; \sigma_{ct_i}) \otimes_k \mathcal{F}(k)}, \quad (100)$$

1610 where the smearing with the  $k$ -factor distribution  $\mathcal{F}(k)$  has to be included for incom-  
 1611 pletely reconstructed decays. The shape of the proper decay length efficiency curve is  
 1612 parametrized using analytically integrable functions and used to multiply proper time  
 1613 related terms in the likelihood fits. Fig. 10 shows a representative example of the proper  
 1614 time efficiency from the CDF experiment. The rapid turn-on of the curve is due to  
 1615 minimum impact parameter and  $L_{xy}$  significance requirements at the trigger and recon-  
 1616 struction level, while the turn-off at larger proper decay length is due to upper cut on  
 1617 impact parameter at the trigger level. Because each  $B$  decay mode has its own kine-  
 1618 matic characteristics and selection requirements, an efficiency curve has to be derived  
 1619 separately for each channel.

1620 The method has been extensively validated with Tevatron data, measuring  $B^0$ ,  $B^+$   
 1621 and  $B_s$  and  $\Lambda_b$  lifetime a variety of fully adronic modes. As an example, a recent prelim-  
 1622 inary determination of the  $B_s$  lifetime in the  $\bar{B}_s \rightarrow D_s^+ \pi^-$  channel is shown in Fig. 10  
 1623 right [231], giving  $c\tau(B_s) = 455.0 \pm 12.2_{\text{st}} \pm 8.2_{\text{sy}} \mu\text{m}$ , in good agreement with PDG  
 1624 averages.

### 1625 3.2.4. Charged Particle Identification

1626 Identification (ID) of charged particles ( $e$ ,  $\mu$ ,  $\pi$ ,  $K$ ,  $p$ ) plays a crucial role in flavor  
 1627 physics, in many cases  $\pi/K$  separation being both the most important and experimentally  
 1628 challenging. Some of the most important PID techniques are sensitive to the particle's  
 1629 velocity; working in tandem with tracking, which provides a measurement of the particle's  
 1630 momentum, they separate the particles by mass. Other techniques exploit the unique  
 1631 interaction properties of specific particles.

1632 The purpose of this primer is to describe conceptually the PID techniques employed  
 1633 in the detector experiments that provided the results included in this report. For a  
 1634 more general discussion, please see Chapters "Passage of particles through matter" and  
 1635 "Particle Detectors" in Ref. [4].

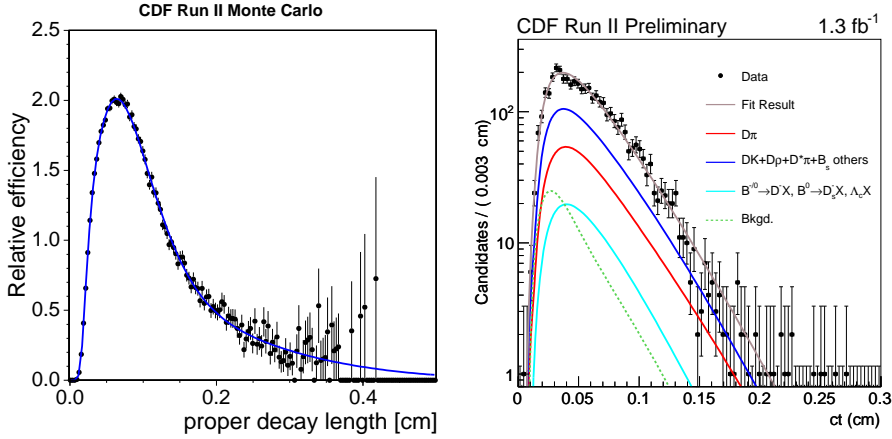


Fig. 10. A representative example of the dependence of trigger and selection efficiency on proper decay time from the displaced track trigger in CDF, vertical scale in arbitrary units (left). Lifetime fit to  $\overline{B}_s \rightarrow D_s^+ \pi^-$  sample from CDF (right)

1636 At the track momenta relevant to flavor physics, the rate of **ionization energy loss**,  
 1637 usually denoted  $dE/dx$ , to a good approximation is a constant for  $e^\pm$  and a function  
 1638 only of the particle's velocity (but not its type) for the others. Measurements of  $dE/dx$   
 1639 are naturally provided by nearly all types of tracking detectors. The type of information  
 1640 provided is either the collected charge or time-over-threshold for each of the detector  
 1641 elements crossed by the track (which typically number from 8–10 to a few dozen). The  
 1642 truncated-mean algorithm, which discards a fixed fraction (typically  $\sim 30\%$ ) of the sam-  
 1643 ples with the highest  $dE/dx$  values, is usually used to mitigate the effect of the long tail  
 1644 of the Landau–Vavilov distribution of the individual  $dE/dx$  samples.

1645 As a function of particle's velocity, the  $dE/dx$  truncated mean reaches a minimum at  
 1646  $\beta\gamma = p/m \approx 3.5\text{--}4.5$  and rises rapidly as the particle's velocity decreases ( $dE/dx \propto 1/\beta^2$   
 1647 for  $\beta\gamma \lesssim 1$ ). For this reason,  $dE/dx$  is the most useful for  $\mu/\pi/K/p$  separation at the  
 1648 momenta where for at least one of the particle types being separated  $p/m \lesssim 1.4$  (e.g., at  
 1649  $p \lesssim 0.7$  GeV/c for  $K/\pi$  separation). At  $\beta\gamma \gtrsim 6$ , the  $dE/dx$  truncated mean experiences  
 1650 a “relativistic rise”, which is mild in gases, allowing weak (1-2  $\sigma$ )  $\pi/K$  separation at  
 1651  $p \gtrsim 1.4$  GeV/c, but nearly non-existent in liquids and solids. Depending on the detec-  
 1652 tor and the environment, measurements of  $dE/dx$  can be affected by a large variety of  
 1653 sizable systematic effects, including aging, and thus development of a  $dE/dx$  calibration  
 1654 technique that can reliably predict the  $dE/dx$  mean value and resolution for a particle  
 1655 of a given type anywhere in the detector can be a great challenge, particularly when one  
 1656 wishes to exploit for PID the  $dE/dx$  “relativistic rise” in a gaseous tracking system.

1657 Examples of  $dE/dx$  use in PID include the drift chambers in *BABAR* [205,232], *Belle* [233],  
 1658 *BESII* [209], *CDF* [234], *CLEO-II* [201], *CLEO-III* and *CLEO-c* [203], and *KLOE* [235].  
 1659 In *BABAR* and *Belle*,  $dE/dx$   $K/\pi$  separation at low momenta is very important to  $B$  flavor  
 1660 tagging, and in *CDF* the  $dE/dx$  “relativistic rise” is critically important to the study  
 1661 of  $B^0$ ,  $B_s$ ,  $A_b \rightarrow h^+ h'^-$  ( $h = \pi, K, p$ ) decays. The *BABAR* silicon vertex tracker [205],

1662 with its 5 double-sided Si layers, is unique among Si vertex detectors at  $e^+e^-$  machines  
 1663 in its ability to provide useful  $dE/dx$  information, which is particularly valuable for  $\pi/e$   
 1664 separation at  $p \lesssim 0.2 \text{ GeV}/c$  (e.g., in charm physics).

1665 **Time-of-flight (TOF)** PID systems combine knowledge of the particle’s creation time  
 1666 and trajectory with a high-precision measurement of its arrival time at the TOF detector,  
 1667 thus proving a measurement of its velocity. Given the time resolution of the currently  
 1668 deployed TOF detectors ( $\sim 100\text{-}200 \text{ ps}$ ), they are limited in  $\pi/K$  separation of at least  
 1669  $2\sigma$  to  $p \lesssim 1.5 \text{ GeV}/c$ . Examples include the TOF systems at Belle [236], BESII [209],  
 1670 CDF [217], and KLOE [235]. Complementarity of TOF and  $dE/dx$  measurements is  
 1671 evident from the fact that  $dE/dx$  separation in gas vanishes for  $\pi/K$  at  $1.1 \text{ GeV}/c$ , for  
 1672  $e/\pi$  at  $0.16 \text{ GeV}/c$ , for  $e/K$  at  $0.63 \text{ GeV}/c$ , and for  $e/p$  at  $1.2 \text{ GeV}/c$ .

1673 Detectors that exploit the **Cherenkov–Vavilov** radiation by charged particles moving  
 1674 faster than  $v_{\text{crit}} = c/n$ , where  $n$  is the refraction coefficient of a solid, liquid or gaseous  
 1675 radiator, tend to provide the best velocity-based PID at  $p \gtrsim 1 \text{ GeV}/c$ . The cheapest  
 1676 and most simple are Cherenkov threshold detectors, where the refraction index of the  
 1677 radiator is chosen in such a way that in the kinematic range of interest the lighter of  
 1678 the two particle types being distinguished would be superluminal while the other one  
 1679 would not; additional information may be provided by comparing the observed number  
 1680 of Cherenkov photons with the one expected for each of the particle types. Belle employs  
 1681 silica aerogel with refraction indices varying from 1.01 to 1.03 [237].

1682 Since Cherenkov radiation is emitted in a cone with an opening angle  $\theta_C = \cos^{-1} \frac{1}{n\beta}$ ,  
 1683 the particle’s velocity can be determined by measuring the cone’s opening angle. The most  
 1684 common, moderately expensive such technology is RICH (Ring-Imaging Cherenkov),  
 1685 where the cone is produced in a transparent solid, liquid or gaseous radiator (LiF in  
 1686 CLEO-III and CLEO-*c*, [204]) and projected onto a planar photon detector a certain dis-  
 1687 tance away. Another, more expensive but space-saving ring-imaging technology is DIRC,  
 1688 used in *BABAR* [238], where the cone of Cherenkov light is produced and captured within  
 1689 a bar of synthetic fused silica running the length of the *BABAR* detector. The  $\pi/K$  separa-  
 1690 tion achieved in  $B \rightarrow Xh^\pm$  decays in *BABAR* by the DIRC (DCH  $dE/dx$ ) varies from  $13\sigma$   
 1691 ( $1.0\sigma$ ) at  $1.5 \text{ GeV}/c$  to  $2.5\sigma$  ( $1.9\sigma$ ) at  $4.5 \text{ GeV}/c$  [239]. However, due to the DIRC’s me-  
 1692 chanical complexity about 18% of reconstructed high-momentum tracks in *BABAR* miss  
 1693 the DIRC; similar coverage limitations are usually suffered by RICH and TOF systems  
 1694 as well.

1695 For dedicated  $e^\pm$  ID, the most distinctive and frequently used feature of their in-  
 1696 teractions with matter is the development of electromagnetic (EM) showers in thick  
 1697 absorbers. **EM calorimeters** seek to contain and measure the total shower energy  $E_{\text{cal}}$ .  
 1698 For  $e^\pm$ , the ratio  $E_{\text{cal}}/p$  is close to 1, while for the other charged particles the  $E_{\text{cal}}/p$   
 1699 ratio will be either much smaller than 1 (“minimum-ionizing”), have a broad distribu-  
 1700 tion mostly below 1 for those that shower hadronically, or have a poorly defined broad  
 1701 distribution for the antiprotons that annihilate in the calorimeter. Since the shapes of  
 1702 the EM showers produced by high-energy  $e^\pm$  and photons are quite similar, the match-  
 1703 ing of calorimeter clusters to tracks extrapolated from the tracking system is of critical  
 1704 importance. The materials used in EM calorimeters the most frequently are blocks of  
 1705 heavy inorganic scintillators with no longitudinal segmentation. Thallium-doped CsI is  
 1706 used in *BABAR* [205], Belle [206, 240], CLEO [241], and BESIII. Even in the absence of  
 1707 longitudinal segmentation, limited information on the longitudinal shower shape (which  
 1708 is different for  $e/\mu/\pi/K/p$ ) can be obtained for particles of sufficiently low momenta

1709 (which enter the calorimeter at an angle sufficiently different from  $90^\circ$ ) by combining  
1710 tracking and lateral cluster-shape information with a technique recently introduced in  
1711 *BABAR* [242]. KLOE has a lead-scintillating fiber sampling EM calorimeter [243], which,  
1712 thanks to its longitudinal segmentation, also provides good muon-hadron separation.

1713 Unlike the other long-lived charged particles, muons do not shower. Hence, dedicated  
1714 **muon ID** relies on muons' long path length in absorber thick enough to stop hadronic  
1715 showers (5-8 hadronic interaction lengths is common). Instrumentation of the magnet's  
1716 iron flux return with several layers of charged-particle detectors is a good approach since it  
1717 allows monitoring of hadron-shower development (which also enables  $K_L^0$  ID) and precise  
1718 matching of tracks with hits in the muon system. This approach is used in *BABAR* [205],  
1719 Belle [244], BESII [209], and CLEO [201, 245].

1720 Response of the detector as a whole, and each of the subdetectors individually, to  
1721 the passage of charged particles of a given type can be studied with high-purity, high-  
1722 statistics calibration samples selected on the basis of the physics and kinematics of certain  
1723 decays, with PID applied to the other particles in the decay to further enhance purity. In  
1724 calibrating the PID response of a given subdetector, PID information from the rest of the  
1725 detector can be used as well. Examples of calibration samples used in  $e^+e^- B$  factories  
1726 include protons from  $\Lambda \rightarrow p\pi^-$ , pions and Kaons from  $D^{*+} \rightarrow D^0\pi^+$  ( $D^0 \rightarrow K^-\pi^+$ ),  
1727 pions from  $K_S^0 \rightarrow \pi^+\pi^-$ , electrons and muons from  $e^+e^- \rightarrow \ell^+\ell^-\gamma$ .

1728 The best PID performance is achieved by combining information from all subdetectors.  
1729 The TOF,  $dE/dx$  and ring-imaging Cherenkov measurements can be conveniently repre-  
1730 sented in the form of probability-distribution functions (PDFs), which makes likelihood-  
1731 based hadron ID quite close to optimal. On the other hand, the calorimeter and muon-  
1732 system quantities, which are more numerous and can be highly correlated, are either very  
1733 difficult or impossible to adequately describe with PDFs. For this reason, the best PID  
1734 performance can be achieved by advanced multivariate techniques such as neural nets  
1735 and bagged decision trees.

### 1736 3.2.5. *Background suppression*

1737 The isolation of signal events in the presence of significant sources of backgrounds is  
1738 critical for almost all measurements. This usually is achieved by an optimization of the  
1739 event selection process designed to maximize the experimental sensitivity by suppressing  
1740 the backgrounds effectively while retaining a sizable fraction of the signal. The choice  
1741 of the method depends on both the nature of the signal and background events, and  
1742 critically on the signal over background ratio which may vary from more than 100 to  
1743  $10^{-6}$  or less.

1744 The separation of signal and background processes relies both on the detector perfor-  
1745 mance as well as kinematics of the final state produced. Large acceptance and the high  
1746 resolution and efficiencies for the reconstruction of charged and neutral particles and the  
1747 identification of leptons and hadrons over a wide range of energies are very important.  
1748 A low rate of the misidentification of charged hadrons as leptons is critical, in particular  
1749 for rare processes involving leptons.

1750 Though the cross sections for heavy flavor particle production in hadronic interactions  
1751 exceed the cross sections at  $e^+e^-$  colliders by several orders of magnitude, their fraction  
1752 of the total interaction rate is small. Furthermore, the multiplicity of the final states  
1753 is very large, and thus the combinatorial background to charm and beauty particles is



1754 extremely large for experiments at hadron colliders and for fixed-target experiments in  
 1755 high momentum hadron beams. Typical event triggers rely on the detection of charged  
 1756 hadrons and leptons of large transverse momentum and in some cases also on the isolation  
 1757 of decay vertices that are displaced from the primary interaction point. The analyses often  
 1758 focus on decays involving two- or three-body decays to intermediate states of narrow  
 1759 width, for instance  $J/\psi$ ,  $D$  or  $D^*$  mesons. Because of the very large momenta of these  
 1760 intermediate states, the identification of particles that do not originate from the primary  
 1761 interaction point is a very powerful tool to suppress backgrounds.

1762 Background conditions for the detection of charm and beauty particles at  $e^+e^-$  colliders  
 1763 are markedly different. There are two dominant sources of background, the so-called  
 1764 continuum background and combinatorial background from other particles in the final  
 1765 states from decays of resonances under study, for instance  $J/\psi$ ,  $\psi(3770)$ , or  $\Upsilon(nS)$  mesons.  
 1766 Two types of processes contribute to continuum background, QED processes,  $e^+e^- \rightarrow$   
 1767  $\ell^+\ell^-(\gamma)$  with  $\ell = e, \mu$ , or  $\tau$ , and quark-pair production,  $e^+e^- \rightarrow q\bar{q}$  with  $q = u, d, s, (c)$ .  
 1768 Both of these processes are impacted by energy losses due to initial state radiation.

1769 At  $e^+e^-$  colliders operating near kinematic thresholds for pair production of charm or  
 1770 beauty particles, for instance the B Factories at  $\Upsilon(4S)$  and the Charm Factories at the  
 1771  $\psi(3770)$  or above, the primary particles pairs are produced at very low momenta, leading  
 1772 to event topologies that are spherical, not jet-like.

1773 Continuum background is characterized by lower multiplicities and higher momenta of  
 1774 charged and neutral particles. To suppress QED background, selected events are usually  
 1775 required to have at least three reconstructed charged particles. At sufficiently high c.m.  
 1776 energies, the fragmentation of the light quarks leads to a two-jet topology. Such events  
 1777 are characterized by variables that measure the alignment of particles within an event  
 1778 along a common axis. Among the variables that show sharply peaked distributions for  
 1779 jet-like events are:

- 1780 – thrust, the maximum sum of the longitudinal momenta of all particles relative to a  
 1781 chosen axis; the thrust distribution peaks at or just below 1.0 for two-body final states  
 1782 and two-jet events;
- 1783 –  $\cos \Delta\theta_{thrust}$ , where  $\Delta\theta_{thrust}$  is the angle between the thrust axis of one or the sum  
 1784 of all particles associated with the signal candidate and the thrust axis of the rest of  
 1785 the event; this distribution is flat for signal events and peaked near 1.0 for continuum  
 1786 background;
- 1787 – the energy flow in conical shells centered on the thrust axis, typically nine double cones  
 1788 of 10 degrees; for continuum events most of the energy is contained in the inner cones,  
 1789 while for the more spherical signal events the energy is shared more uniformly among  
 1790 all cones;
- 1791 – normalized Legendre moments can be viewed as continuous generalizations of the en-  
 1792 ergy cones, typically the first and second of these moments are used,  $L_j = \sum_i p_i |\cos \theta_i|^j$   
 1793 with  $j = 0$  or  $j = 2$ , where  $p_i$  and  $\theta_i$  are the momentum and angle of any particles,  
 1794 except those related to the signal decay, relative to the thrust axis of the signal decay.  
 1795 In many cases these moments provide better discrimination of continuum events than  
 1796 the energy cones.
- 1797 –  $R_2 = H_2/H_0$ , the ratio of second to zeroth Fox-Wolfram moments, with  $H_2 =$   
 1798  $\sum_{i,j} |p_i||p_j| L_2(\cos \theta_{ij})$ , calculated for all particles in the event, charged and neutral.  
 1799 The  $n$ th Fox-Wolfram moment is the momentum-weighted sum of Legendre polynomial  
 1800 of the  $n$ th order, computed for the cosine of the angles between all pairs of particles;

1801 the ratio  $R_2$  peaks close to 1.0 for jet-like continuum events.  
 1802 In practice the suppression of the continuum background is achieved by imposing restric-  
 1803 tion on many of these variables, either as sequential individual cuts, or by constructing  
 1804 a multivariable discriminant, a decision tree, or employing a neural network.

1805 Fig. 11 shows examples of distributions for two of these variables for selected  $B\bar{B}$   
 events.

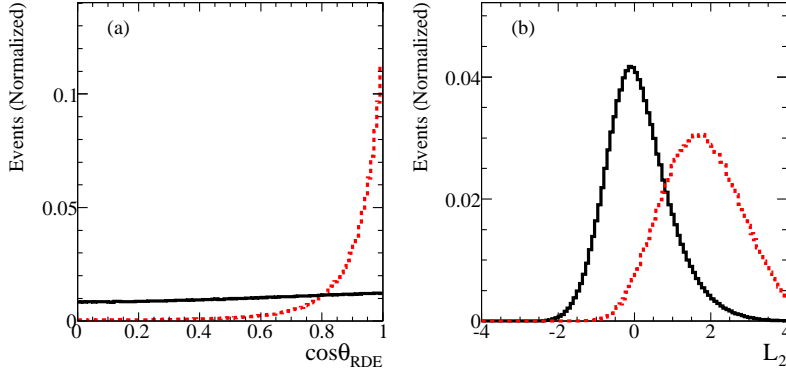


Fig. 11. Distribution of variables used to suppress continuum background in selected candidates for  $B^0 \rightarrow K^- \pi^+ \pi^0$  decays [246] a)  $\cos \Delta\theta_{thrust}$ , b) the normalized Legendre moments  $L_2$ . The solid lines show the expectation for continuum background, the dotted lines represent the background distributions.

1806

For the isolation of exclusive decays of  $B$  or  $D$  mesons that are pair-produced at Beauty or Charm Factories two kinematic variables are commonly used to separate signal from background events. These variables make optimum use of the measured beam energies and are largely uncorrelated. The difference of the reconstructed and expected energy for the decay of a meson  $M$  is defined as  $\Delta E = (q_M q_0 - s/2)/\sqrt{s}$ , where  $\sqrt{s} = 2E_{beam}^*$  is the total energy of the colliding beams in the c.m. frame, and  $q_M$  and  $q_0$  are the Lorentz vectors representing the momentum of the candidate  $M$  and of the  $e^+e^-$  system,  $q_0 = q_{e^-} + q_{e^+}$ . In the c.m. system,

$$\Delta E = E_M^* - E_{beam}^*, \quad (101)$$

1807 where  $E_M^*$  is the energy of the reconstructed meson  $M$ .

The second variable is often referred to as the energy-substituted mass,  $m_{ES}$ . In the laboratory frame, it can be determined from the measured three-momentum,  $\mathbf{p}_M$ , of the candidate  $M$ , without explicit knowledge of the masses of the decay products,  $m_{ES} = \sqrt{(s/2 + \mathbf{p}_M \cdot \mathbf{p}_0)^2/E_0^2 - \mathbf{p}_M^2}$ . In the c.m. frame ( $\mathbf{p}_0 = 0$ ), this variable takes the familiar form,

$$m_{ES} = \sqrt{E_{beam}^{*2} - \mathbf{p}_M^{*2}}, \quad (102)$$

1808 where  $\mathbf{p}_M^*$  is the c.m. momentum of the meson  $M$ , derived from the momenta of its decay  
 1809 products, and its energy is substituted by  $E_{beam}^*$ .

1810 An example of  $\Delta E$  and  $m_{ES}$  distributions is given in Fig. 12 for a selected sample  
 1811 of rare  $B$  decays.  $\Delta E$  is centered on zero and the  $m_{ES}$  distribution peaks at the  $B$ -  
 1812 meson mass. While resolution in  $\Delta E$  is dominated by detector resolution, the resolution  
 1813 in  $m_{ES}$  is determined by the spread in the energy of the colliding beams, typically a  
 1814 few MeV. The flat background is composed of both continuum and  $B\bar{B}$  events, its size

1815 depends on the decay mode under study and the overall event selection. There is a small  
 1816 component of peaking background due to backgrounds with kinematics very similar to  
 1817 the true decays.

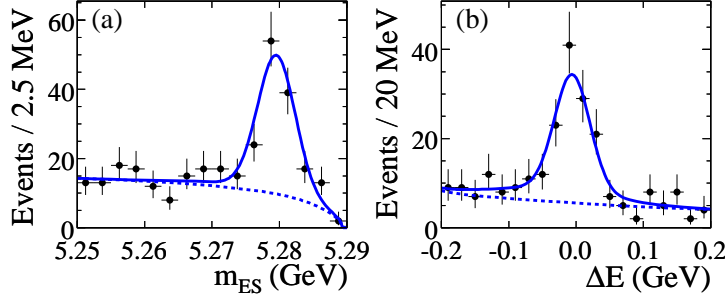


Fig. 12. Distributions of a)  $\Delta E$  and b)  $m_{ES}$  for a sample of  $B^0 \rightarrow \omega K_S^0$  candidates [247]. The solid line represents the result of the fit to the data, the dotted line marks the background contributions.

For decays that cannot be fully reconstructed because of an undetected neutrino or  $K_L^0$ , the separation of signal and backgrounds is more challenging. The energy and momentum of the missing particle can be inferred from the measurement of all other particles in the event and the total energy and momentum of the colliding beams,

$$(E_{miss}, \mathbf{p}_{miss}) = (E_0, \mathbf{p}_0) - \left( \sum_i E_i, \sum_i \mathbf{p}_i \right). \quad (103)$$

1818 If the only missing particle in the event is a neutrino or  $K_L^0$ , the missing mass should be  
 1819 close to zero or the Kaon mass and the missing momentum should be non-zero. Fig. 13a  
 1820 shows an example of a missing mass squared distribution,  $E_{miss}^2 - |\mathbf{p}_{miss}|^2$  for  $B^- \rightarrow$   
 1821  $D^0 \ell^- \bar{\nu}$  decays, selected in  $B\bar{B}$  events tagged by a hadronic decay of the second  $B$  meson  
 1822 in the event. There is a narrow peak at zero for events in which the only missing particle  
 1823 is the neutrino, and a broad enhancement due to  $B^- \rightarrow D^{*0} \ell^- \bar{\nu}$  decays, in which the low  
 1824 energy pion or photon from the decay  $D^{*0} \rightarrow D^0 \pi^0$  or  $D^{*0} \rightarrow D^0 \gamma$  escaped detection.  
 1825 Since the second  $B$  is fully reconstructed, there is very little combinatorial background.

For semileptonic  $B$  or  $D$  decays,  $M \rightarrow H \ell \nu$ , a variable first introduced by the CLEO Collaboration is used to suppress background,

$$\cos \theta_{BY} = \frac{(2E_B E_Y - M_M^2 - M_Y^2)}{2|\mathbf{p}_M||\mathbf{p}_Y|}. \quad (104)$$

1826 For a true semileptonic decay in which the only missing particle is the neutrino,  $\theta_{BY}$   
 1827 is the angle between the momentum vectors  $\mathbf{p}_M$  and  $\mathbf{p}_Y = \mathbf{p}_H + \mathbf{p}_\ell$ , and the condi-  
 1828 tion  $|\cos \theta_{BY}| \leq 1.0$  should be fulfilled, while for background events or incompletely  
 1829 reconstructed semileptonic decays the distribution extends to much larger values, thus  
 1830 enabling a clear separation from the signal decays (see Fig. 13b).

### 1831 3.2.6. Recoil Tagging Technique

1832 At  $e^+e^-$  colliders charged leptons and heavy flavor particles are produced in pairs, thus  
 1833 the detection of one member of the pair can be used to tag the presence of the other. In  
 1834 particular at Charm and  $B$  at B-Factories, operating at or near the threshold for charm or  
 1835 beauty particles tagging techniques not only identify the second member of the pair, they

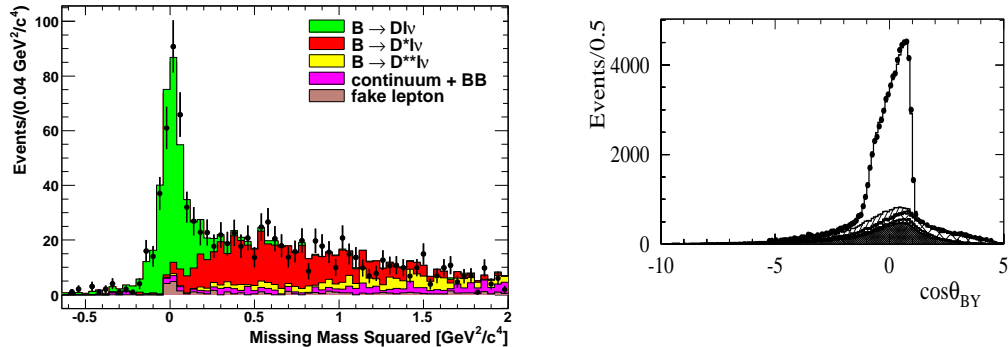


Fig. 13. Distributions of the a) the missing mass squared for selected  $B \rightarrow D\ell\nu$  candidates, in  $B\bar{B}$  events tagged by a hadronic decay of the second  $B$  meson in the event [248], b)  $\cos\theta_{BY}$ , for a sample of  $\bar{B}^0 \rightarrow D^{*+}\ell^-\bar{\nu}$  candidates [249]. Here the unshaded histogram indicates the signal distribution, on top of background contributions, mostly from other semileptonic  $B$  decays.

1836 also can be used to measure their momentum and energy and uniquely determine their  
 1837 charge and flavor quantum numbers. Furthermore, near threshold, there are no other  
 1838 particle produced, and therefore the combinatorial background is significantly reduced.  
 1839 In addition, the kinematics of the final state are constrained such that given a fully  
 1840 reconstructed tag of one decays, the presence of a missing or undetectable particle like  
 1841  $\nu$  or  $K_L^0$  meson can be identified from the missing momentum and missing energy of the  
 1842 whole event (see for example [250]).

1843 The tagging technique for  $\psi(3770) \rightarrow D\bar{D}$  events was first developed by the Mark III  
 1844 collaboration [251] at SLAC, and has since been exploited in many analyses based on  
 1845 data from by  $CLEO_c$ ,  $BES$ ,  $KLOE$ , and the  $B$  Factories. For  $\psi(3770) \rightarrow D^0\bar{D}^0$  events  
 1846 there are several tag modes, which can be divided into three categories: pure flavor tags  
 1847 such as  $D^0 \rightarrow K^-e^+\nu_e$  and  $D^0 \rightarrow \pi^-\mu^+\nu_\mu$ ; quasi-flavor tags for neutral mesons, such as  
 1848  $D^0 \rightarrow K^-\pi^+$ ,  $D^0 \rightarrow K^-\pi^+\pi^0$  and  $D^0 \rightarrow K^-\pi^+\pi^+\pi^-$ , for which there is a small doubly-  
 1849 Cabibbo-suppressed contribution, and tags for CP-eigenstates such as  $D^0 \rightarrow K^+K^-$  and  
 1850  $K_L^0\pi^0$ . The quasi-flavor tags can be used to make precision measurements of branching  
 1851 fractions [252] and partial rates [253]. The three decays listed correspond to 25% of the  
 1852 total branching fraction. Since the  $\psi(3770)$  is a  $C = -1$  state, the detection of a tag  
 1853 with definite CP means that the other  $D$  meson in the event must be of opposite CP.  
 1854 Studies combined flavor and CP-tagged samples of  $K\pi$  events [254] and  $K_s^0\pi^+\pi^-$  [255]  
 1855 have resulted in the determination of the strong-phase parameters in  $D$  decay. Using low-  
 1856 multiplicity decays, such as  $D^+ \rightarrow K^-\pi^+\pi^+$  and  $D^+ \rightarrow K_s^0\pi^+\pi^+$  has resulted in extremely  
 1857 clean samples, even for rare signal decays, and thus precise branching fraction and partial  
 1858 rate measurements.

1859 Single-tag efficiencies and purities vary considerably depending on the number of tracks  
 1860 and neutrals in the decay. For example,  $D^0 \rightarrow K^-\pi^+$  and  $D^+ \rightarrow K_s^0\pi^+\pi^0$  tags have  
 1861 efficiencies of 65% and 22% and sample purities of  $\sim 5\%$  and  $\sim 50\%$ , respectively. For  
 1862 fully reconstructed hadronic tags the discriminating variable (shown in Fig. 14) is the  
 1863 beam-constrained mass (see Sec. 3.2.5 and Eq. 102).

1864 The recoil technique has also been used successfully in  $e^+e^- \rightarrow D_s^+D_s^{*-}$  events at  
 1865 CLEO-c to measure branching fractions ([256]). Tag decays include  $D_s^- \rightarrow K^+K^-\pi^-$ ,

1866  $D_s^- \rightarrow K_s^0 K^-$ ,  $D_s^- \rightarrow K^+ K^- \pi^- \pi^0$  and  $D_s^- \rightarrow \pi^+ \pi^- \pi^-$  and correspond to approxi-  
 1867 mately 20% of the total  $D_s^-$  branching fraction. The  $D_s^{*-} \rightarrow D_s^- \gamma / \pi^0$  candidates are  
 1868 identified with or without the explicit reconstruction of the photon or  $\pi^0$ .

1869 At the  $\Upsilon(4S)$  resonance, the higher mass of the  $b$  mesons lead to much smaller individ-  
 1870 ual branching fractions for individual decays, which means that the achievable tagging  
 1871 efficiencies are much lower. Nevertheless, both *BABAR* and *Belle* have developed and em-  
 1872 ployed several tagging techniques. The cleanest samples are possible for tree-mediated  
 1873 hadronic decays of the form  $B \rightarrow D^{(*)} X$ , where  $X$  refers a hadronic state of one or  
 1874 more hadrons, up to five charged mesons (pions or Kaons), up to two neutral pions or a  
 1875  $K_s^0$ , and the  $D^{0,(*)}$ ,  $D^{+,(*)}$  or  $D_s^{+,(*)}$  mesons are reconstructed in many different decays  
 1876 modes. The kinematic variables  $\Delta E$  and  $m_{ES}$ , introduced in Sec. 3.2.5, are used to iso-  
 1877 late the true tag decays from combinatorial background and to estimate the purity of  
 1878 the tag samples. The purity of a given tag mode is used to separate the cleaner samples  
 1879 from those with high background, the actual choice usually depends on the signal mode  
 1880 under study. The tag efficiency is typically 0.3% and has a signal-to-noise ratio of 0.5  
 1881 (see Fig. 14).

1882 Significantly higher tag efficiencies can be obtained for semileptonic  $B$  decays, for  
 1883 instance  $B \rightarrow D^{(*)} \ell \nu$  ( $\ell = e, \mu$ ), with a branching fraction of more than 7% for each  
 1884 lepton. For  $D$  mesons the same decays listed above are used, are reconstructed and for  
 1885 the  $D^*$  mesons the decays are  $D^{*+} \rightarrow D^0 \pi^+$ ,  $D^+ \pi^0$  and  $D^{*0} \rightarrow D^0 \pi^0, D^0 \gamma$ . Due to the  
 1886 very small mass difference of the  $D^*$  and  $D$  mesons, the pions and photons from its  
 1887 decay are of low energy, and thus the mass difference  $\Delta M = m(D\pi) - m(D)$  can be  
 1888 very well measured. The presence of a neutrino in the decay can be checked using the  
 1889 variable  $\cos\theta_{BY}$  defined in Eq. 104. As for hadronic tags, tag selection and its efficiency  
 1890 and purity are strongly dependent on the signal decay recoiling against the tag. Typical  
 1891 efficiencies are of order 0.5-1%.

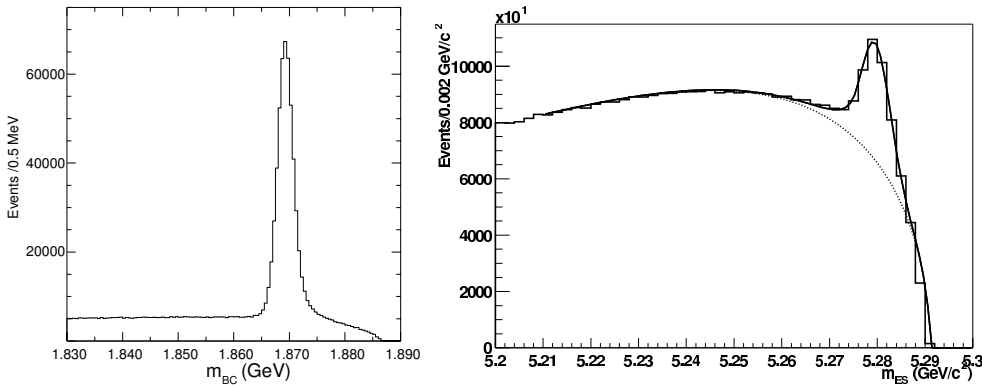


Fig. 14. Distribution of the energy substituted mass for selected hadronic tag decays a) for  $D$  mesons in  $\psi(3770)$  events at *CLEO*, and b) for  $B$  mesons in  $\Upsilon(4S)$  decays at *BABAR*.

1892 The biggest advantage of the hadronic  $B$  tags over the semileptonic  $B$  tags is the  
 1893 better measurement of the reconstructed  $B$  momentum. This permits constraints on the  
 1894 signal decays in the recoil and precise reconstruction of the kinematic variables even in  
 1895 decays with a neutrino or missing neutral Kaon. Otherwise the two tags have similar  
 1896 performance. They are completely orthogonal samples and thus can be combined .

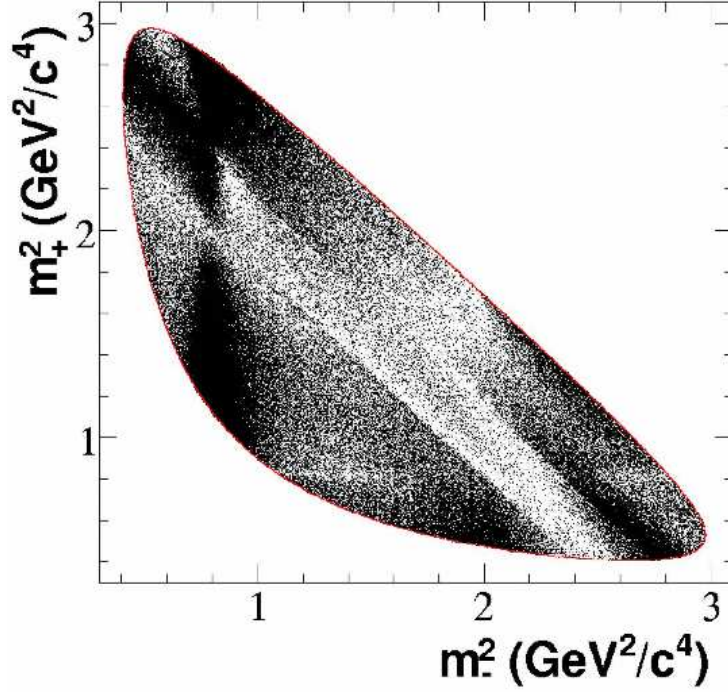


Fig. 15. Dalitz plot distribution of a high purity sample of  $D^0 \rightarrow K_S \pi^+ \pi^-$ , with  $m_-^2 = |p_{K_S} + p_{\pi^-}|^2$  and  $m_+^2 = |p_{K_S} + p_{\pi^+}|^2$  from [258]. The most visible features are described by a  $K^{*-}$ (892) resonance (vertical band with two lobes) and a  $\rho(770)$  resonance (diagonal band with two lobes). Interferences between resonances are distorting the distribution. The contours (solid red line) represent the kinematic limits of the decay.

### 1897 3.2.7. Dalitz Plot Analysis

1898 The partial decay rate of a particle into a multi-body final state depends on the square  
 1899 of a Lorentz invariant matrix element  $\mathcal{M}$ . Such matrix element can be independent of  
 1900 the specific kinematic configuration of the final state or otherwise reveal a non-trivial  
 1901 structure in the dynamics of the decay. In the case, for instance, of a three-body decay  
 1902  $P \rightarrow 123$ , invariant masses of pair of particles can be defined as  $m_{ij}^2 = |p_i + p_j|^2$  where  
 1903  $p_j$  ( $j=1,2,3$ ) are the four-momenta of the final states particle. A plot of  $m_{ij}^2$  versus  $m_{ik}^2$   
 1904 is commonly referred as Dalitz plot [257].

1905 Dalitz plots distributions have been used since several decades to study the strong  
 1906 interaction dynamics in particle decays or in scattering experiment. In a three body  
 1907 decay of a meson, the underlying dynamics can be therefore represented by intermediate  
 1908 *resonances*. As an example in Fig.15 a Dalitz plot for the decay  $D^0 \rightarrow K_S \pi^+ \pi^-$  is shown:  
 1909 there are several visible structures due to competing and interfering resonances.

1910 It is therefore a common practice to parameterize the matrix element as a coherent  
 1911 sum of two-body amplitudes (subscript  $r$ ) [259],

$$\mathcal{M} \equiv \sum_r a_r e^{i\phi_r} \mathcal{A}_r(m_{13}^2, m_{23}^2) \quad (105)$$

1912 An additional constant "non-resonant" term  $a_{\text{NR}}e^{i\phi_{\text{NR}}}$  is sometimes included.

1913 The parameters  $a_r$  and  $\phi_r$  are the magnitude and phase of the amplitude for the  
 1914 component  $r$ . In the case of a  $D^0$  decay the function  $\mathcal{A}_r = F_D \times F_r \times T_r \times W_r$  is a  
 1915 Lorentz-invariant expression where  $F_D$  ( $F_r$ ) is the Blatt-Weisskopf centrifugal barrier  
 1916 factor for the  $D$  (resonance) decay vertex [260]  $T_r$  is the resonance propagator, and  $W_r$   
 1917 describes the angular distribution in the decay.

1918 For  $T_r$  a relativistic Breit-Wigner (BW) parameterization with mass-dependent width  
 1919 is commonly used (for definitions see review in [259]). BW mass and width values are  
 1920 usually taken from scattering experiment or world averages provided by Particle Data  
 1921 Group.

1922 The angular dependence  $W_r$  reflects the spin of the resonance and is described using  
 1923 either Zemach tensors [261–263] where transversality is enforced or the helicity formal-  
 1924 ism [264,265] when a longitudinal component in the resonance propagator is allowed (see  
 1925 Ref. [259] for a comprehensive summary).

1926 Alternative parameterizations have been used especially to represent spin zero (S-wave)  
 1927 resonances. For this component the presence of several broad and overlapping resonances  
 1928 makes a simple BW model not adequate. For instance, K-matrix formalism with the P-  
 1929 vector approximation [266,267] was used for  $\pi\pi$  S-wave components.

1930 In the context of flavor physics Dalitz model have been used as effective parameteriz-  
 1931 ations to derive strong phase dependence. The knowledge of strong phases is relevant  
 1932 for analysis where the extraction of weak phases can be obtained through interferences  
 1933 between different resonances. Moreover, in the case of neutral meson decays the interfe-  
 1934 rence between flavor mixing and decay leads to time-dependent analyses (either for CP or  
 1935 flavor mixing measurements). For this reason Dalitz models have been included in such  
 1936 analyses (that are frequently referred for short as *time-dependent* Dalitz analyses).

#### 1937 4. Determination of $|V_{ud}|$ and $|V_{us}|$ .

1938 Unitarity of the bare (unrenormalized) CKM [1,2]  $3 \times 3$  quark mixing matrix  $V_{ij}^0$ ,  
 1939  $i = u, c, t$   $j = d, s, b$  implies the orthonormal tree level relations

$$\sum_i V_{ij}^{0*} V_{ik}^0 = \sum_i V_{ji}^{0*} V_{ki}^0 = \delta_{jk} \quad (106)$$

1940 Standard Model quantum loop effects are important and corrected for such that  
 1941 Eq. (106) continues to hold at the renormalized level [268]. That prescription gener-  
 1942 ally involves normalization of all charged current semileptonic amplitudes relative to the  
 1943 Fermi constant

$$G_\mu = 1.166371(6) \times 10^{-5} \text{GeV}^{-2} \quad (107)$$

1944 obtained from the precisely measured (recently improved) muon lifetime [269]

$$\tau_\mu = \Gamma^{-1}(\mu^+ \rightarrow e^+ \nu_e \bar{\nu}_\mu(\gamma)) = 2.197019(21) \times 10^{-6} \text{sec} \quad (108)$$

1945 In all processes, Standard Model  $\text{SU}(3)_C \times \text{SU}(2)_L \times \text{U}(1)_Y$  radiative corrections are  
 1946 explicitly accounted for [270].

1947 Of particular interest here is the first row constraint

$$|V_{ud}|^2 + |V_{us}|^2 + |V_{ub}|^2 = 1 \quad (109)$$

1948 An experimental deviation from that prediction would be evidence for “new physics”  
 1949 beyond Standard Model expectations in the form of tree or loop level contributions to  
 1950 muon decay and/or the semileptonic processes from which the  $V_{ij}$  are extracted. Of  
 1951 course, if Eq. (109) is respected at a high level of certainty, it implies useful constraints  
 1952 on various “new physics” scenarios.

#### 1953 4.1. $V_{ud}$ from nuclear decays

1954 Nuclear beta decays between  $0^+$  states sample only the vector component of the  
 1955 hadronic weak interaction. This is important because the conserved vector current (CVC)  
 1956 hypothesis protects the vector coupling constant  $G_V$  from renormalization by background  
 1957 strong interactions. Thus, the  $G_V$  that occurs in nuclei should be the same as the one  
 1958 that operates between free up and down quarks. In that case, one can write  $G_V = G_F V_{ud}$ ,  
 1959 which means that a measurement of  $G_V$  in nuclei, when combined with a measurement  
 1960 of the Fermi constant  $G_F$  in muon decay, yields the value of the CKM matrix element  
 1961  $V_{ud}$ . To date, precise measurements of the beta decay between isospin analog states of  
 1962 spin,  $J^\pi = 0^+$ , and isospin,  $T = 1$ , provide the most precise value of  $V_{ud}$ .

1963 A survey of the relevant experimental data has recently been completed by Hardy  
 1964 and Towner [271]. Compared to the previous survey [272] in 2005 there are 27 new  
 1965 publications, many with unprecedented precision. In some cases they have improved  
 1966 the average results by tightening their error assignments and in others by changing their  
 1967 central values. Penning-trap measurements of decay energies have been especially effective  
 1968 in this regard.

For each transition, three experimental quantities have to be determined: the decay energy,  $Q_{ec}$ ; the half-life of the decaying state,  $t_{1/2}$ ; and the branching ratio,  $R$ , for the particular transition under study. The decay energy is used to calculate the phase space integral,  $f$ , where it enters as the fifth power. Thus, if  $f$  is required to have 0.1% precision then the decay energy must be known to 0.02% – a demand that is currently being surpassed by Penning-trap devices. The partial half-life is defined as  $t = t_{1/2}/R$  and the product  $ft$  is

$$ft = \frac{K}{G_F^2 V_{ud}^2 \langle \tau_+ \rangle^2}, \quad (110)$$

where  $K/(\hbar c)^6 = 2\pi^3 \hbar \ln 2 / (m_e c^2)^5 = 8120.2787(11) \times 10^{-10} \text{ GeV}^{-4} \text{ s}$ . When isospin is an exact symmetry the initial and final states, being isospin analogs, are identical except that a proton has switched to a neutron. Since the operator describing the transition is simply the isospin ladder operator,  $\tau_+$ , its matrix element,  $\langle \tau_+ \rangle$ , is independent of nuclear structure and is given by an isospin Clebsch-Gordan coefficient, which for isospin  $T = 1$  states has the value  $\sqrt{2}$ . Hence,

$$ft = \frac{K}{2 G_F^2 V_{ud}^2}, \quad (111)$$

and according to CVC the  $ft$  value is a constant independent of the nucleus under study. In practice, however, isospin is always a broken symmetry in nuclei, and beta decay occurs in the presence of radiative corrections, so a ‘corrected’  $ft$  value is defined by



Table 9

Experimental  $ft$  values for  $0^+ \rightarrow 0^+$  superallowed Fermi beta decays, the trivial nucleus-dependent component of the radiative correction,  $\delta'_R$ , the nuclear-structure dependent isospin-symmetry-breaking and radiative correction taken together,  $\delta_C - \delta_{NS}$ , and the corrected  $\mathcal{F}t$  values. The last line gives the average  $\mathcal{F}t$  value and the  $\chi^2$  of the fit.

Parent	$ft(s)$	$\delta'_R(\%)$	$\delta_C - \delta_{NS}(\%)$	$\mathcal{F}t(s)$
$^{10}\text{C}$	$3041.7 \pm 4.3$	$1.679 \pm 0.004$	$0.520 \pm 0.039$	$3076.7 \pm 4.6$
$^{14}\text{O}$	$3042.3 \pm 2.7$	$1.543 \pm 0.008$	$0.575 \pm 0.056$	$3071.5 \pm 3.3$
$^{22}\text{Mg}$	$3052.0 \pm 7.2$	$1.466 \pm 0.017$	$0.605 \pm 0.030$	$3078.0 \pm 7.4$
$^{26}\text{Al}^m$	$3036.9 \pm 0.9$	$1.478 \pm 0.020$	$0.305 \pm 0.027$	$3072.4 \pm 1.4$
$^{34}\text{Cl}$	$3049.4 \pm 1.2$	$1.443 \pm 0.032$	$0.735 \pm 0.048$	$3070.6 \pm 2.1$
$^{34}\text{Ar}$	$3052.7 \pm 8.2$	$1.412 \pm 0.035$	$0.845 \pm 0.058$	$3069.6 \pm 8.5$
$^{38}\text{K}^m$	$3051.9 \pm 1.0$	$1.440 \pm 0.039$	$0.755 \pm 0.060$	$3072.5 \pm 2.4$
$^{42}\text{Sc}$	$3047.6 \pm 1.4$	$1.453 \pm 0.047$	$0.630 \pm 0.059$	$3072.4 \pm 2.7$
$^{46}\text{V}$	$3050.3 \pm 1.0$	$1.445 \pm 0.054$	$0.655 \pm 0.063$	$3074.1 \pm 2.7$
$^{50}\text{Mn}$	$3048.4 \pm 1.2$	$1.444 \pm 0.062$	$0.695 \pm 0.055$	$3070.9 \pm 2.8$
$^{54}\text{Co}$	$3050.8 \pm 1.3$	$1.443 \pm 0.071$	$0.805 \pm 0.068$	$3069.9 \pm 3.3$
$^{62}\text{Ga}$	$3074.1 \pm 1.5$	$1.459 \pm 0.087$	$1.52 \pm 0.21$	$3071.5 \pm 7.2$
$^{74}\text{Rb}$	$3084.9 \pm 7.8$	$1.50 \pm 0.12$	$1.71 \pm 0.31$	$3078 \pm 13$
Average $\overline{\mathcal{F}t}$				$3072.14 \pm 0.79$
$\chi^2/\nu$				0.31

$$\mathcal{F}t \equiv ft(1 + \delta'_R)(1 - (\delta_C - \delta_{NS})) = \frac{K}{2G_F^2 V_{ud}^2 (1 + \Delta_R^V)}; \quad (112)$$

1969 so it is this corrected  $\mathcal{F}t$  that is a constant. Here the radiative correction has been  
1970 separated into three components: (i)  $\Delta_R^V$  is a nucleus-independent part that includes  
1971 the universal short-distance component  $S_{EW}$  affecting all semi-leptonic decays, defined  
1972 later in Eq. (128). Being a constant,  $\Delta_R^V$  is placed on the right-hand-side of Eq. (112);  
1973 (ii)  $\delta'_R$  is transition dependent, but only in a trivial way, since it just depends on the  
1974 nuclear charge,  $Z$ , and the electron energy,  $E_e$ ; while  $\delta_{NS}$  is a small nuclear-structure  
1975 dependent term that requires a shell-model calculation for its evaluation. (iii) Lastly,  $\delta_C$   
1976 is an isospin-symmetry breaking correction, typically of order 0.5%, that also requires a  
1977 shell-model calculation for its evaluation.

In Tab. 9 are listed the experimental  $ft$  values from the survey of Hardy and Towner [271] for 13 transitions, of which 10 have an accuracy at the 0.1% level, and three at up to the 0.4% level. Also listed are the theoretical corrections,  $\delta'_R$  and  $\delta_C - \delta_{NS}$ , taken from Ref. [273], and the corrected  $\mathcal{F}t$  values. This data set is sufficient to provide a very demanding test of the CVC assertion that the  $\mathcal{F}t$  values should be constant for all nuclear superallowed transitions of this type. In Fig. 16 the uncorrected  $ft$  values in the upper panel show considerable scatter, the lowest and highest points differing by 50 parts in 3000. This scatter is completely absent in the corrected  $\mathcal{F}t$  values shown in the

lower panel of Fig. 16, an outcome principally due to the nuclear-structure-dependent corrections,  $\delta_C - \delta_{NS}$ , thus validating the theoretical calculations at the level of current experimental precision. The data in Tab. 9 and Fig. 16 are clearly satisfying the CVC test. The weighted average of the 13 data is

$$\overline{\mathcal{F}t} = 3072.14 \pm 0.79 \text{ s}, \quad (113)$$

1978 with a corresponding chi-square per degree of freedom of  $\chi^2/\nu = 0.31$ . Eq. (113) confirms  
1979 the constancy of  $G_V$  – the CVC hypothesis – at the level of  $1.3 \times 10^{-4}$ .

1980 Before proceeding to a determination of  $V_{ud}$  it has to be noted that the isospin-  
1981 symmetry-breaking correction,  $\delta_C$ , is taken from Towner and Hardy [273] who calculated  
1982 proton and neutron radial functions as eigenfunctions of a Saxon-Woods potential. An  
1983 alternative procedure used in the past by Ormand and Brown [274–276] takes the radial  
1984 functions as eigenfunctions of a Hartree-Fock mean-field potential. The corrections ob-  
1985 tained by Ormand and Brown were consistently smaller than the Saxon-Woods values  
1986 and this difference was treated as a systematic error in previous surveys. In their most  
1987 recent survey, though, Hardy and Towner [271] repeated the Hartree-Fock calculations,  
1988 but with a change in the calculational procedure, and obtained results that were closer  
1989 to the Saxon-Woods values. Even so, when these Hartree-Fock  $\delta_C$  values are used in  
1990 Eq. (112) the  $\chi^2$  of the fit to  $\mathcal{F}t = \text{constant}$  becomes a factor of three larger. This in  
1991 itself might be sufficient reason to reject the Hartree-Fock values, but to be safe an aver-  
1992 age of the Hartree-Fock and Saxon-Woods  $\overline{\mathcal{F}t}$  values was adopted and a systematic error  
1993 assigned that is half the spread between the two values. This leads to

$$\begin{aligned} \overline{\mathcal{F}t} &= 3071.83 \pm 0.79_{\text{stat}} \pm 0.32_{\text{syst}} \text{ s} \\ &= 3071.83 \pm 0.85 \text{ s}. \end{aligned} \quad (114)$$

1994 In the second line the two errors have been combined in quadrature.

1995 Recently, Miller and Schwenk [277] have explored the formally complete approach to  
1996 isospin-symmetry breaking, but produced no numerical results. The Towner-Hardy [271]  
1997 values quoted here are based on a model whose approximations can be tested for  $A = 10$   
1998 by comparing with the large no-core shell-model calculation of Caurier *et al* [278], which  
1999 is as close to an exact calculation as is currently possible. The agreement between the  
2000 two suggests that any further systematic error in the isospin-breaking correction is likely  
2001 to be small.

The CKM matrix element  $V_{ud}$  is then obtained from

$$V_{ud}^2 = \frac{K}{2G_F^2(1 + \Delta_R^V)\overline{\mathcal{F}t}}, \quad (115)$$

where  $\Delta_R^V$  is the nucleus-independent radiative correction taken from Marciano and Sirlin [279]: *viz.*

$$\Delta_R^V = (2.631 \pm 0.038)\%. \quad (116)$$

With  $\overline{\mathcal{F}t}$  obtained from Eq. (114), the value of  $V_{ud}$  becomes

$$V_{ud} = 0.97425 \pm 0.00022. \quad (117)$$

2002 Compared to the Hardy-Towner survey [272] of 2005, which obtained  $V_{ud} = 0.97380(40)$ ,  
2003 the central value has shifted by about one standard deviation primarily as a result of  
2004 Penning-trap decay-energy measurements and a reevaluation of the isospin-symmetry

2005 breaking correction in 2007 [273]. The error is dominated by theoretical uncertainties;  
 2006 experiment only contributes 0.00008 to the error budget. Currently the largest contribu-  
 2007 tion to the error budget comes from the nucleus-independent radiative correction  $\Delta_R^V$  –  
 2008 recently reduced by a factor of two by Marciano and Sirlin [279]. Further improvements  
 2009 here will need some theoretical breakthroughs. Second in order of significance are the  
 2010 nuclear-structure-dependent corrections  $\delta_C$  and  $\delta_{NS}$ . So long as  $0^+ \rightarrow 0^+$  nuclear decays  
 2011 provide the best access to  $V_{ud}$ , these corrections will need to be tested and honed. Here  
 2012 is where nuclear experiments will continue to play a critical role.

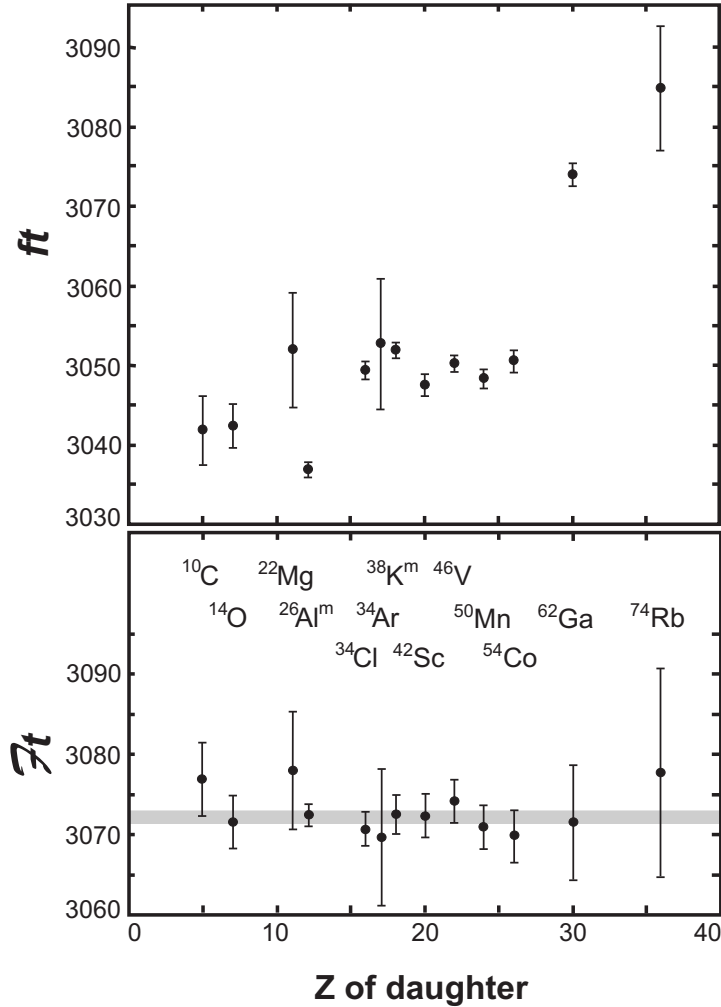


Fig. 16. In the top panel are plotted the uncorrected experimental  $ft$  values as a function of the charge on the daughter nucleus. In the bottom panel, the corresponding  $Ft$  values as defined in Eq. (112) are given. The horizontal grey band in the bottom panel gives one standard deviation around the average  $Ft$ .

2014 Although the result is not yet competitive, to extract  $V_{ud}$  from neutron  $\beta$ -decay is  
 2015 appealing because it does not require the application of corrections for isospin-symmetry  
 2016 breaking effects,  $\delta_C$ , or nuclear-structure effects,  $\delta_{NS}$ , as defined in the previous section  
 2017 on nuclear  $\beta$ -decay. However, it should be noted that the transition-dependent radiative  
 2018 correction,  $\delta'_R$ , and the nucleus-independent radiative correction,  $\Delta_R^V$ , must still be ap-  
 2019 plied to neutron  $\beta$ -decay observables; and the latter is, in fact, the largest contributor to  
 2020 the uncertainty in the nuclear value for  $V_{ud}$ .

2021 In contrast to nuclear  $\beta$ -decays between  $0^+$  states, which sample only the weak vector  
 2022 interaction, neutron  $\beta$ -decay proceeds via a mixture of the weak vector and axial-vector  
 2023 interactions. Consequently, three parameters are required for a description of neutron  
 2024  $\beta$ -decay:  $G_F$ , the fundamental weak interaction constant;  $\lambda \equiv g_A/g_V$ , the ratio of the  
 2025 weak axial-vector and vector coupling constants; and the parameter of interest,  $V_{ud}$ .  
 2026 Thus, measurements of at least two observables (treating  $G_F$  as an input parameter) are  
 2027 required for a determination of  $V_{ud}$ .

A value for  $\lambda$  can be extracted from measurements of correlation coefficients in po-  
 larized neutron  $\beta$ -decay. Assuming time-reversal invariance, the differential decay rate  
 distribution of the electron and neutrino momenta and the electron energy for polarized  
 $\beta$ -decay is of the form [280]

$$\frac{dW}{dE_e d\Omega_e d\Omega_\nu} \propto p_e E_e (E_0 - E_e)^2 \left[ 1 + a \frac{\mathbf{p}_e \cdot \mathbf{p}_\nu}{E_e E_\nu} + \langle \boldsymbol{\sigma}_n \rangle \cdot \left( A \frac{\mathbf{p}_e}{E_e} + B \frac{\mathbf{p}_\nu}{E_\nu} \right) \right], \quad (118)$$

where  $E_e$  ( $E_\nu$ ) and  $\mathbf{p}_e$  ( $\mathbf{p}_\nu$ ) denote, respectively, the electron (neutrino) energy and  
 momentum;  $E_0$  ( $= 782 \text{ keV} + m_e$ ) denotes the  $\beta$ -decay endpoint energy, with  $m_e$  the  
 electron mass; and  $\langle \boldsymbol{\sigma}_n \rangle$  denotes the neutron polarization. Neglecting recoil-order correc-  
 tions, the correlation coefficients  $a$  (the  $e$ - $\bar{\nu}_e$ -asymmetry),  $A$  (the  $\beta$ -asymmetry), and  $B$   
 (the  $\bar{\nu}_e$ -asymmetry) can be expressed in terms of  $\lambda$  as [281, 282]

$$a = \frac{1 - \lambda^2}{1 + 3\lambda^2}, \quad A = -2 \frac{\lambda^2 + \lambda}{1 + 3\lambda^2}, \quad B = 2 \frac{\lambda^2 - \lambda}{1 + 3\lambda^2}. \quad (119)$$

2028 At present, these correlation parameters have values  $a = -0.103 \pm 0.004$ ,  $A = -0.1173 \pm$   
 2029  $0.0013$ , and  $B = 0.983 \pm 0.004$  [283]. Although  $B$  has been measured to the highest  
 2030 precision (0.41%), the sensitivity of  $B$  to  $\lambda$  is a factor  $\sim 10$  less than that of  $a$  and  $A$ .  
 2031 Thus, the neutron  $\beta$ -asymmetry  $A$  yields the most precise result for  $\lambda$ .

A second observable is the neutron lifetime,  $\tau_n$ , which can be written in terms of the  
 above parameters as [279, 284, 285]

$$\frac{1}{\tau_n} = \frac{G_F^2 m_e^5}{2\pi^3} |V_{ud}|^2 (1 + 3\lambda^2) f (1 + \text{RC}). \quad (120)$$

Here,  $f = 1.6887 \pm 0.00015$  is a phase space factor, which includes the Fermi function  
 contribution [281], and  $(1 + \text{RC}) = 1.03886 \pm 0.00039$  denotes the total effect of all  
 electroweak radiative corrections [279, 284]. After insertion of the numerical factors in  
 Eq. (120), a value for  $V_{ud}$  can be determined from  $\tau_n$  and  $\lambda$  according to [279, 284]

$$|V_{ud}|^2 = \frac{4908.7 \pm 1.9 \text{ s}}{\tau_n (1 + 3\lambda^2)}. \quad (121)$$

2032 The current status of a neutron-sector result for  $V_{ud}$  is summarized in Fig. 17, where  $|\lambda|$   
 2033 is plotted on the horizontal axis, and  $V_{ud}$  on the vertical axis. At present, the Particle Data  
 2034 Group [283] averages the four most recent measurements of the neutron  $\beta$ -asymmetry,  
 2035  $A$ , performed with beams of polarized cold neutrons [286–289], and one combined mea-  
 2036 surement of  $A$  and  $B$  [290], to obtain their recommended value of  $\lambda = -1.2695 \pm 0.0029$   
 2037 (shown as the vertical error band). It should be noted that the error on the PDG average  
 2038 for  $\lambda$  (0.23%) is greater than that of the most precise individual result (0.15%) [289],  
 2039 because the error on the average has been increased by a  $\sqrt{\chi^2/(N-1)}$  scale factor of  
 2040 2.0 to account for the spread among the individual data points. Constraints between the  
 2041 values for  $V_{ud}$  and  $\lambda$ , computed according to Eq. (121) for two different values for the  
 2042 neutron lifetime, are shown as the angled error bands. The band labeled “PDG 2008”  
 2043 represents the PDG’s recommended value for  $\tau_n = 885.7 \pm 0.8$  s, whereas the other band  
 2044 relies solely on the most recent result reported for  $\tau_n$  of  $878.5 \pm 0.7 \pm 0.3$  s [291], which  
 2045 disagrees by  $6\sigma$  with the PDG average. Note that the PDG deliberately chose not to  
 2046 include this discrepant result in their most recent averaging procedure.

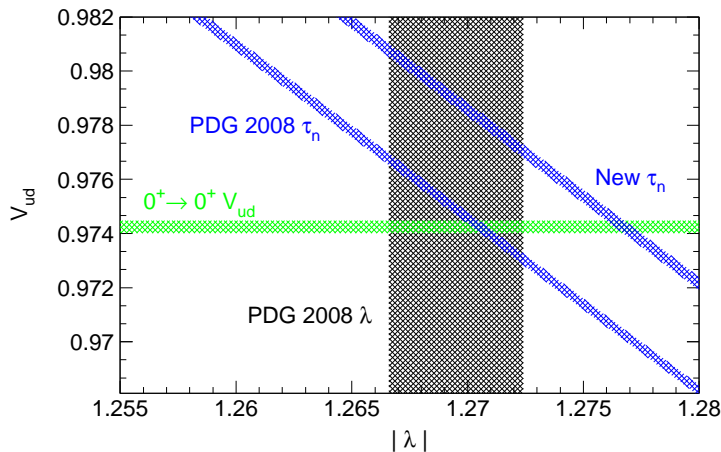


Fig. 17. Current status of  $V_{ud}$  from neutron  $\beta$ -decay. The vertical error band indicates the current PDG error on  $\lambda$ . The angled error bands show the constraints between  $V_{ud}$  and  $\lambda$  for two values of the neutron lifetime: the PDG recommended value, and that from a recent  $6\sigma$ -discrepant result. For comparison, the horizontal error band denotes the value of  $V_{ud}$  from  $0^+$  nuclear  $\beta$ -decays discussed in the previous section.

The intersection of the error band for  $\lambda$  with the error band defined by the neutron lifetime determines the value for  $V_{ud}$ . Assuming the PDG value of  $\tau_n = 885.7 \pm 0.8$  s yields [283]

$$V_{ud} = 0.9746 \pm 0.0004_{\tau_n} \pm 0.0018_{\lambda} \pm 0.0002_{RC}, \quad (122)$$

2047 where the subscripts denote the error sources. If the discrepant neutron lifetime result of  
 2048  $878.5 \pm 0.7 \pm 0.3$  s were employed instead, it would suggest a considerably larger value,  
 2049  $V_{ud} = 0.9786 \pm 0.0004_{\tau_n} \pm 0.0018_{\lambda} \pm 0.0002_{RC}$ . For comparison, the value for  $V_{ud}$  from  
 2050 nuclear  $\beta$ -decay discussed in the previous section is shown as the horizontal band. The  
 2051 neutron  $\beta$ -decay result derived from the PDG’s recommended values for  $\tau_n$  and  $\lambda$  is seen  
 2052 to be in excellent agreement with that from nuclear  $\beta$ -decay, albeit with an error bar  
 2053 that is a factor  $\sim 7$ – $8$  larger.

2054 An ongoing series of precision measurements of neutron  $\beta$ -decay observables aims to  
 2055 reduce the error on  $\lambda$  and resolve the lifetime discrepancy. The goal of two currently  
 2056 running experiments, the PERKEO III experiment at the Institut Laue-Langevin [285]  
 2057 (using a beam of cold neutrons) and the UCNA experiment at Los Alamos National  
 2058 Laboratory [292] (using stored ultracold neutrons), are sub-0.5% measurements of the  
 2059 neutron  $\beta$ -asymmetry,  $A$ . Since these two experiments employ different experimental  
 2060 approaches, they are sensitive to different systematic uncertainties. The combination of  
 2061 their results will reduce the  $\lambda$ -induced uncertainty for  $V_{ud}$  by up to a factor of  $\sim 3$ .

2062 Finally, although the error on  $\tau_n$  is not the dominant uncertainty, the  $6\sigma$  discrepancy  
 2063 between the PDG average and the most recent result is clearly unsatisfactory. Indeed,  
 2064 multiple groups are now attempting to measure  $\tau_n$  to a level of precision ranging between  
 2065 1 s and 0.1 s. Hence, the next round of experiments should reach sufficient precision to  
 2066 definitively discriminate between the PDG average and the recent discrepant result.

### 2067 4.3. $V_{ud}$ from pionic beta decay

$V_{ud}$  can also be obtained from the pion beta decay,  $\pi^+ \rightarrow \pi^0 e^+ \nu_e [\gamma]$ , which is a pure  
 vector transition between two spin-zero members of an isospin triplet and is therefore  
 analogous to the superallowed nuclear decays. Like neutron decay, it has the advantage  
 that there are no nuclear-structure dependent corrections to be applied. Its major dis-  
 advantage, however, is that it is a very weak branch,  $\mathcal{O}(10^{-8})$ , in the decay of the pion.  
 The corresponding decay width can be decomposed as

$$\Gamma_{\pi e 3} = \frac{G_F^2 M_{\pi^\pm}^5}{64\pi^3} S_{EW} \left| V_{ud} f_+(0) \right|^2 I_0^{\pi\pi} (1 + \delta_{EM}) . \quad (123)$$

2068 In the above equation  $S_{EW}$  represents the universal short-distance electroweak correction  
 2069 (Eq. 128),  $f_+(0)$  is the vector form-factor at zero momentum transfer,  $I_0^{\pi\pi}$  the phase  
 2070 space factor, and  $\delta_{EM}$  the long-distance electromagnetic correction. As far as the strong  
 2071 interaction is concerned, the Ademollo-Gatto theorem [293] requires the deviation of  
 2072  $f_+(0)$  from its value 1 in the isospin limit to be quadratic in the quark mass difference  
 2073  $m_d - m_u$ . This results in a very tiny correction  $f_+(0) - 1 = -7 \times 10^{-6}$  at one-loop [294] and  
 2074 leads to the expectation that higher order strong interaction corrections will not disturb  
 2075 this nice picture. The corrections in (123) are therefore dominated by electromagnetic  
 2076 contributions. The long-distance electromagnetic corrections can be separated into a  
 2077 shift to the phase space integral  $\delta I^{\pi\pi} / I_0^{\pi\pi} = 1.09 \times 10^{-3}$  as well as a structure dependent  
 2078 term [294]

$$\begin{aligned} \frac{1}{2} \cdot \delta_{EM} \Big|_{\text{str.dep.}} &= -4\pi\alpha \left\{ \frac{2}{3} X_1 + \frac{1}{2} X_6^{\text{phys}}(\mu) + \frac{1}{32\pi^2} \left( 3 + \log \frac{m_e^2}{M_{\pi^\pm}^2} + 3 \log \frac{M_{\pi^\pm}^2}{\mu^2} \right) \right\} \\ &= (5.11 \pm 0.25) \times 10^{-3} , \end{aligned} \quad (124)$$

where we have used the recent results of [295] for the electromagnetic coupling constants  
 $X_{1,6}$  entering in (124) (with a fractional uncertainty of 100%) to update the numerical  
 result of Ref. [294]. Higher order corrections are expected to be strongly suppressed by  
 $\sim (M_\pi/4\pi f_\pi)^2$ . Combining the updated theory with the branching fraction  $BR(\pi^+ \rightarrow$   
 $\pi^0 e^+ \nu_e [\gamma]) = (1.040 \pm 0.004(\text{stat}) \pm 0.004(\text{syst})) \times 10^{-8}$  from the PIBETA experiment [296],  
 we find:

$$V_{ud} = 0.9741(2)_{\text{th}}(26)_{\text{exp}}. \quad (125)$$

2079  $V_{ud}$  from pion beta decay is in agreement with the more precise result, Eq. (117), from nu-  
 2080 clear decays. A tenfold improvement on the experimental measurement would be needed  
 2081 to make this extraction competitive with nuclear decays.

#### 2082 4.4. Determination of $|V_{us}|$ from $K_{\ell 2}$ and $K_{\ell 3}$

2083 Here we discuss the determination of  $|V_{us}|$  from the combination of leptonic pion and  
 2084 Kaon decay and from semileptonic Kaon decay. We start with the status of the theoretical  
 2085 description of leptonic pion and Kaon decays and of semileptonic Kaon decays within  
 2086 the SM, and the report on the status of the experimental results, particularly for the  
 2087 semileptonic decay.

##### 2088 4.4.1. $P_{\ell 2}$ ( $P = \pi, K$ ) rates within the SM

2089 Including all known short- and long-distance electroweak corrections, and parame-  
 2090 terizing the hadronic effects in terms of a few dimensionless coefficients, the inclusive  
 2091  $P \rightarrow \ell \bar{\nu}_\ell(\gamma)$  decay rate can be written as [297, 298]

$$\begin{aligned} \Gamma_{P_{\ell 2}(\gamma)} = \Gamma_{P_{\ell 2}}^{(0)} S_{\text{EW}} \left\{ 1 + \frac{\alpha}{\pi} F(m_\ell^2/M_P^2) \right\} \left\{ 1 - \frac{\alpha}{\pi} \left[ \frac{3}{2} \log \frac{M_\rho}{M_P} + c_1^{(P)} \right. \right. \\ \left. \left. + \frac{m_\ell^2}{M_\rho^2} \left( c_2^{(P)} \log \frac{M_\rho^2}{m_\ell^2} + c_3^{(P)} + c_4^{(P)}(m_\ell/M_P) \right) \right. \right. \\ \left. \left. - \frac{M_P^2}{M_\rho^2} \tilde{c}_2^{(P)} \log \frac{M_\rho^2}{m_\ell^2} \right] \right\}, \quad (126) \end{aligned}$$

where the decay rate in the absence of radiative corrections is given by

$$\Gamma_{P_{\ell 2}}^{(0)} = \frac{G_F^2 |V_P|^2 f_P^2}{4\pi} M_P m_\ell^2 \left( 1 - \frac{m_\ell^2}{M_P^2} \right)^2, \quad V_\pi = V_{ud}, \quad V_K = V_{us}. \quad (127)$$

The factor  $S_{\text{EW}}$  describes the short-distance electromagnetic correction [299, 300] which is universal for all semileptonic processes. To leading order it is given by

$$S_{\text{EW}} = 1 + \frac{2\alpha}{\pi} \log \frac{M_Z}{M_\rho}. \quad (128)$$

2092 Including also the leading QCD corrections [297], it assumes the numerical value  
 2093  $S_{\text{EW}} = 1.0232$ . The first term in curly brackets is the universal long-distance correc-  
 2094 tion for a point-like meson. The explicit form of the one-loop function  $F(x)$  can be found  
 2095 in [297]. The structure dependent coefficients  $c_1^{(P)}$  are independent of the lepton mass  
 2096  $m_\ell$  and start at order  $e^2 p^2$  in chiral perturbation theory. The other coefficients appear  
 2097 only at higher orders in the chiral expansion. The one-loop result (order  $e^2 p^2$ ) for  $c_1^{(P)}$  is  
 2098 given by [134],

$$c_1^{(\pi)} = -4\pi^2 E^r(M_\rho) - \frac{1}{2} + \frac{Z}{4} \left( 3 + 2 \log \frac{M_\pi^2}{M_\rho^2} + \log \frac{M_K^2}{M_\rho^2} \right), \quad (129)$$

$$c_1^{(K)} = -4\pi^2 E^r(M_\rho) - \frac{1}{2} + \frac{Z}{4} \left( 3 + 2 \log \frac{M_K^2}{M_\rho^2} + \log \frac{M_\pi^2}{M_\rho^2} \right), \quad (130)$$

where the electromagnetic low-energy coupling  $Z$  arising at order  $e^2 p^0$  can be expressed through the pion mass difference by the relation

$$M_{\pi^\pm}^2 - M_{\pi^0}^2 = 8\pi\alpha Z f_\pi^2 + \dots \quad (131)$$

The quantity  $E^r(M_\rho)$ , being a certain linear combination of  $e^2 p^2$  low-energy couplings [134], cancels in the ratio  $\Gamma_{K\ell 2(\gamma)}/\Gamma_{\pi\ell 2(\gamma)}$ . As suggested by Marciano [301], a determination of  $|V_{us}/V_{ud}|$  can be obtained by combining the experimental values for the decay rates with the lattice determination of  $f_K/f_\pi$  via

$$\frac{|V_{us}|f_K}{|V_{ud}|f_\pi} = 0.23872(30) \left( \frac{\Gamma_{K\ell 2(\gamma)}}{\Gamma_{\pi\ell 2(\gamma)}} \right)^{1/2}. \quad (132)$$

2099 The small error is an estimate of unknown electromagnetic contributions arising at order  
2100  $e^2 p^4$ .

In the standard model, the ratios  $R_{e/\mu}^{(P)} = \Gamma_{P \rightarrow e\bar{\nu}_e(\gamma)}/\Gamma_{P \rightarrow \mu\bar{\nu}_\mu(\gamma)}$  are helicity suppressed as a consequence of the  $V - A$  structure of the charged currents, constituting sensitive probes of new physics. In a first systematic calculation to order  $e^2 p^4$ , the radiative corrections to  $R_{e/\mu}^{(P)}$  have been obtained with an unprecedented theoretical accuracy [298, 302]. The two-loop effective theory results were complemented with a matching calculation of an associated counterterm, giving

$$R_{e/\mu}^{(\pi)} = (1.2352 \pm 0.0001) \times 10^{-4}, \quad R_{e/\mu}^{(K)} = (2.477 \pm 0.001) \times 10^{-5}. \quad (133)$$

2101 The central value of  $R_{e/\mu}^{(\pi)}$  agrees with the results of a previous calculations [297, 303],  
2102 pushing the theoretical uncertainty below the 0.1 per mille level. The discrepancy with  
2103 a previous determination of  $R_{e/\mu}^{(K)}$  can be traced back to inconsistencies in the analysis  
2104 of [303].

#### 2105 4.4.2. $K_{\ell 3}$ rates within the SM

The photon-inclusive  $K_{\ell 3}$  decay rates are conveniently decomposed as [283]

$$\Gamma_{K_{\ell 3(\gamma)}} = \frac{G_F^2 M_K^5}{192\pi^3} C_K^2 S_{EW} \left| V_{us} f_+^{K^0\pi^-}(0) \right|^2 I_K^\ell(\lambda_{+,0}) \left( 1 + \delta_{EM}^{K\ell} + \delta_{SU(2)}^{K\pi} \right), \quad (134)$$

2106 where  $C_K^2 = 1$  (1/2) for the neutral (charged) Kaon decays,  $S_{EW}$  is the short distance  
2107 electroweak correction,  $f_+^{K^0\pi^-}(0)$  is the  $K \rightarrow \pi$  vector form factor at zero momentum  
2108 transfer, and  $I_K^\ell(\lambda_{+,0})$  is the phase space integral which depends on the (experimentally  
2109 accessible) slopes of the form factors (generically denoted by  $\lambda_{+,0}$ ). Finally,  $\delta_{EM}^{K\ell}$  represent  
2110 channel-dependent long distance radiative corrections and  $\delta_{SU(2)}^{K\pi}$  is a correction induced  
2111 by strong isospin breaking.



2112 *Electromagnetic effects in  $K_{\ell 3}$  decays*

The results of the most recent calculation [304] of the four channel-dependent long-distance electromagnetic corrections  $\delta_{\text{EM}}^{K\ell}$  are shown in Tab. 10. The values given here were obtained to leading nontrivial order in chiral effective theory, working with a fully inclusive prescription of real photon emission. For the electromagnetic low-energy couplings appearing in the structure dependent contributions, the recent determinations of [295,305] were employed. The errors in Tab. 10 are estimates of (only partially known)

Table 10

Summary of the electromagnetic corrections to the fully-inclusive  $K_{\ell 3(\gamma)}$  rate [304].

	$\delta_{\text{EM}}^{K\ell}(\%)$
$K_{e3}^0$	$0.99 \pm 0.22$
$K_{e3}^{\pm}$	$0.10 \pm 0.25$
$K_{\mu 3}^0$	$1.40 \pm 0.22$
$K_{\mu 3}^{\pm}$	$0.016 \pm 0.25$

higher order contributions. The associated correlation matrix was found [304]

$$\begin{pmatrix} 1.0 & 0.081 & 0.685 & -0.147 \\ & 1.0 & -0.147 & 0.764 \\ & & 1.0 & 0.081 \\ & & & 1.0 \end{pmatrix}. \quad (135)$$

2113 It is also useful to record the uncertainties on the linear combinations of  $\delta_{\text{EM}}^{K\ell}$  that are  
2114 relevant for lepton universality and strong isospin-breaking tests [304]:

$$\delta_{\text{EM}}^{K^0 e} - \delta_{\text{EM}}^{K^0 \mu} = (-0.41 \pm 0.17)\% \quad (136)$$

$$\delta_{\text{EM}}^{K^{\pm} e} - \delta_{\text{EM}}^{K^{\pm} \mu} = (0.08 \pm 0.17)\% \quad (137)$$

$$\delta_{\text{EM}}^{K^{\pm} e} - \delta_{\text{EM}}^{K^0 e} = (-0.89 \pm 0.32)\% \quad (138)$$

$$\delta_{\text{EM}}^{K^{\pm} \mu} - \delta_{\text{EM}}^{K^0 \mu} = (-1.38 \pm 0.32)\% . \quad (139)$$

2115 The corresponding electromagnetic corrections to the Dalitz plot densities can also be  
2116 found in [304]. It is important to notice that the corrections to the Dalitz distributions  
2117 can be locally large (up to  $\sim 10\%$ ) with considerable cancellations in the integrated  
2118 electromagnetic corrections.

2119 *Isospin breaking correction in  $K_{\ell 3}$  decays*

In (134), the same form factor  $f_+^{K^0 \pi^-}(0)$  (at zero-momentum transfer) is pulled out for all decay channels, where

$$\delta_{\text{SU}(2)}^{K^0 \pi^-} = 0, \quad \delta_{\text{SU}(2)}^{K^{\pm} \pi^0} = \left( \frac{f_+^{K^{\pm} \pi^0}(0)}{f_+^{K^0 \pi^-}(0)} \right)^2 - 1. \quad (140)$$

Note that the form factors denote the pure QCD quantities plus the electromagnetic contributions to the meson masses and to  $\pi^0$ - $\eta$  mixing. The isospin breaking parameter  $\delta_{\text{SU}(2)}^{K^{\pm} \pi^0}$  is related to the  $\pi^0$ - $\eta$  mixing angle via [306]

$$\delta_{\text{SU}(2)}^{K^\pm\pi^0} = 2\sqrt{3}\left(\varepsilon^{(2)} + \varepsilon_{\text{S}}^{(4)} + \varepsilon_{\text{EM}}^{(4)} + \dots\right) \quad (141)$$

The dominant lowest-order contribution can be expressed in terms of quark masses [307]:

$$\varepsilon^{(2)} = \frac{\sqrt{3}}{4} \frac{m_d - m_u}{m_s - \widehat{m}}, \quad \widehat{m} = \frac{m_u + m_d}{2}. \quad (142)$$

The explicit form of the strong and electromagnetic higher-order corrections in Eq. (141) can be found in [306]. The required determination of the quark mass ratio

$$R = \frac{m_s - \widehat{m}}{m_d - m_u} \quad (143)$$

uses the fact that the double ratio

$$Q^2 = \frac{m_s^2 - \widehat{m}^2}{m_d^2 - m_u^2} = R \frac{m_s/\widehat{m} + 1}{2} \quad (144)$$

can be expressed in terms of pseudoscalar masses and a purely electromagnetic contribution [307]:

$$Q^2 = \frac{\Delta_{K\pi} M_K^2 (1 + \mathcal{O}(m_q^2))}{M_\pi^2 [\Delta_{K^0 K^+} + \Delta_{\pi^+ \pi^0} - (\Delta_{K^0 K^+} + \Delta_{\pi^+ \pi^0})_{\text{EM}}]} , \quad \Delta_{PQ} = M_P^2 - M_Q^2. \quad (145)$$

2120 Due to Dashen's theorem [308], the electromagnetic term vanishes to lowest order  $e^2 p^0$ .  
2121 At next-to-leading order it is given by [133, 309]

$$\begin{aligned} (\Delta_{K^0 K^+} + \Delta_{\pi^+ \pi^0})_{\text{EM}} = e^2 M_K^2 \left[ \frac{1}{4\pi^2} \left( 3 \ln \frac{M_K^2}{\mu^2} - 4 + 2 \ln \frac{M_K^2}{\mu^2} \right) + \frac{4}{3} (K_5 + K_6)^r(\mu) \right. \\ \left. - 8(K_{10} + K_{11})^r(\mu) + 16ZL_5^r(\mu) \right] + \mathcal{O}(e^2 M_\pi^2). \quad (146) \end{aligned}$$

Based on their estimates for the electromagnetic low-energy couplings entering in (146), Ananthanarayan and Moussallam [305] found a rather large deviation from Dashen's limit,  $(\Delta_{K^0 K^+} + \Delta_{\pi^+ \pi^0})_{\text{EM}} = -1.5 \Delta_{\pi^+ \pi^0}$ , which corresponds to [310]  $Q = 20.7 \pm 1.2$  (the error accounts for the uncertainty due to higher order corrections). Such a small value for  $Q$  (compared to  $Q_{\text{Dashen}} = 24.2$ ) is also supported [311–313] by previous studies<sup>11</sup>. Together with [310]  $m_s/\widehat{m} = 24.7 \pm 1.1$  (see also [315]) one finds  $R = 33.5 \pm 4.3$  and finally, together with a determination of  $\varepsilon_{\text{S}}^{(4)}$  and  $\varepsilon_{\text{EM}}^{(4)}$ , the result [310]

$$\delta_{\text{SU}(2)}^{K^\pm\pi^0} = 0.058(8). \quad (147)$$

#### 2122 4.4.3. $K_{\ell 3}$ form factors

The hadronic  $K \rightarrow \pi$  matrix element of the vector current is described by two form factors (FFs),  $f_+(t)$  and  $f_-(t)$

$$\langle \pi^-(p_\pi) | \bar{s} \gamma^\mu u | K^0(p_K) \rangle = (p_K + p_\pi)^\mu f_+(t) + (p_K - p_\pi)^\mu f_-(t) \quad (148)$$

<sup>11</sup>Note however that a recent analysis of  $\eta \rightarrow 3\pi$  at the two-loop level [314] favors the value  $Q = 23.2$ .

where  $t = (p_K - p_\pi)^2 = (p_\ell + p_\nu)^2$ . The vector form factor  $f_+(t)$  represents the P-wave projection of the crossed channel matrix element  $\langle 0 | \bar{s} \gamma^\mu u | K \pi \rangle$  whereas the S-wave projection is described by the scalar form factor defined as

$$f_0(t) = f_+(t) + \frac{t}{m_K^2 - m_\pi^2} f_-(t). \quad (149)$$

2123 By construction,  $f_0(0) = f_+(0)$ .

In order to compute the phase space integrals appearing in Eq. (134) we need experimental or theoretical inputs about the  $t$ -dependence of  $f_{+,0}(t)$ . In principle, chiral perturbation theory (ChPT) and lattice QCD are useful tools to set theoretical constraints. However, in practice the  $t$ -dependence of the FFs at present is better determined by measurements and by combining measurements and dispersion relations. To that aim, we introduce the normalized FFs

$$\tilde{f}_+(t) = \frac{f_+(t)}{f_+(0)}, \quad \tilde{f}_0(t) = \frac{f_0(t)}{f_0(0)}, \quad \tilde{f}_+(0) = \tilde{f}_0(0) = 1. \quad (150)$$

2124 Whereas  $\tilde{f}_+(t)$  is accessible in the  $K_{e3}$  and  $K_{\mu 3}$  decays,  $\tilde{f}_0(t)$  is more difficult to measure  
2125 since it is only accessible in  $K_{\mu 3}$  decays, being kinematically suppressed in  $K_{e3}$  decays,  
2126 and is strongly correlated with  $\tilde{f}_+(t)$ .

Moreover, measuring the scalar form factor is of special interest due to the existence of the Callan-Treiman (CT) theorem [316] which predicts the value of the scalar form factor at the so-called CT point, namely  $t \equiv \Delta_{K\pi} = m_K^2 - m_\pi^2$ ,

$$C \equiv \tilde{f}_0(\Delta_{K\pi}) = \frac{f_K}{f_\pi} \frac{1}{f_+(0)} + \Delta_{CT}, \quad (151)$$

where  $\Delta_{CT} \sim \mathcal{O}(m_{u,d}/4\pi F_\pi)$  is a small correction. ChPT at NLO in the isospin limit [307] gives

$$\Delta_{CT} = (-3.5 \pm 8) \times 10^{-3}, \quad (152)$$

2127 where the error is a conservative estimate of the higher order corrections [317]. A complete  
2128 two-loop calculation of  $\Delta_{CT}$  [318], as well as a computation at  $\mathcal{O}(p^4, e^2 p^2, (m_d - m_u))$   
2129 [310], consistent with this estimate, have been recently presented.

2130 The measurement of  $C$  provide a powerful consistency check of the lattice QCD cal-  
2131 culations of  $f_K/f_\pi$  and  $f_+(0)$ , as will be discussed in Sec. 4.6.2.

2132 Another motivation to measure the shape of the scalar form factor very accurately is  
2133 that knowing the slope and the curvature of the scalar form factor allows one to perform  
2134 a matching with the 2-loop ChPT calculations [319] and then determine fundamental  
2135 constants of QCD such as  $f_+(0)$  or the low-energy constants (LECs)  $C_{12}$ ,  $C_{34}$  which  
2136 appear in many ChPT calculations.

### 2137 *Parametrization of the form factors and dispersive approach*

2138 To determine the FF shapes, different experimental analyses of  $K_{\ell 3}$  data have been  
2139 performed in the last few years, by KTeV, NA48, and KLOE for the neutral mode and  
2140 by ISTRA+ for the charged mode.

Among the different parameterizations available, one can distinguish two classes [320]. The class called class II in this reference contains parameterizations based on mathematical rigorous expansions where the slope, the curvature and all the higher order terms of the expansion are free parameters of the fit. In this class, one finds the Taylor expansion

$$\tilde{f}_{+,0}^{Tayl}(t) = 1 + \lambda'_{+,0} \frac{t}{M_\pi^2} + \frac{1}{2} \lambda''_{+,0} \left( \frac{t}{m_\pi^2} \right)^2 + \frac{1}{6} \lambda'''_{+,0} \left( \frac{t}{m_\pi^2} \right)^3 + \dots, \quad (153)$$

2141 where  $\lambda'_{+,0}$  and  $\lambda''_{+,0}$  are the slope and the curvature of the FFs respectively, but also the  
2142 so-called z-parametrization [321].

As for parameterizations belonging to class I, they correspond to parameterizations for which by using physical inputs, specific relations between the slope, the curvature and all the higher order terms of the Taylor expansion, Eq. (153) are imposed. This allows to reduce the correlations between the fit parameters since only one parameter is fitted for each FF. In this class, one finds the pole parametrization

$$\tilde{f}_{+,0}^{Pole}(t) = \frac{M_{V,S}^2}{M_{V,S}^2 - t}, \quad (154)$$

2143 in which dominance of a single resonance is assumed and its mass  $M_{V,S}$  is the fit pa-  
2144 rameter. Whereas for the vector FF a pole parametrization with the dominance of the  
2145  $K^*(892)$  ( $M_V \sim 892$  MeV) is in good agreement with the data, for the scalar FF there  
2146 is no such obvious dominance. One has thus to rely, at least for  $\tilde{f}_0(t)$ , on a dispersive  
2147 parametrization. In such a construction, in addition to guarantee the good properties of  
2148 analyticity and unitarity of the FFs, physical inputs such as the low energy  $K\pi$  data  
2149 and, in the case of the vector form factor, the dominance of  $K^*(892)$  resonance are used.

The vector and scalar form factors are analytic functions in the complex  $t$ -plane, except for a cut along the positive real axis, starting at the first physical threshold where they develop discontinuities. They are real for  $t < t_{th} = (m_K + m_\pi)^2$ . Cauchy's theorem implies that  $\tilde{f}_{+,0}(t)$  can be written as a dispersive integral along the physical cut

$$\tilde{f}_{+,0}(t) = \frac{1}{\pi} \int_{t_{th}}^{\infty} ds' \frac{\text{Im} \tilde{f}_{+,0}(s')}{(s' - t - i0)} + \text{subtractions}, \quad (155)$$

2150 where all the possible on-shell states contribute to its imaginary part  $\text{Im} \tilde{f}_{+,0}(s')$ . A  
2151 number of subtractions is needed to make the integral convergent.

A particularly appealing dispersive parametrization for the scalar form factor is the one proposed in Ref. [322]. Two subtractions are performed, one at  $t = 0$  where by definition  $\tilde{f}_0(0) = 1$ , see Eq. (150), and the other one at the CT point. This leads to

$$\tilde{f}_0^{Disp}(t) = \exp \left[ \frac{t}{\Delta_{K\pi}} (\ln C - G(t)) \right], \quad (156)$$

with

$$G(t) = \frac{\Delta_{K\pi}(\Delta_{K\pi} - t)}{\pi} \int_{(m_K + m_\pi)^2}^{\infty} \frac{ds}{s} \frac{\phi_0(s)}{(s - \Delta_{K\pi})(s - t - i\epsilon)}, \quad (157)$$

2152 assuming that the scalar FF has no zero. In this case the only free parameter to be  
2153 determined from a fit to the data is  $C$ .  $\phi_0(s)$  represents the phase of the form factor.  
2154 According to Watson's theorem [323], this phase can be identified in the elastic region  
2155 with the S-wave,  $I = 1/2$   $K\pi$  scattering phase. The fact that two subtractions have  
2156 been made in writing Eq. (156) allows to minimize the contributions from the unknown  
2157 high-energy phase in the dispersive integral. The resulting function  $G(t)$ , Eq. (157), does  
2158 not exceed 20% of the expected value of  $\ln C$  limiting the theoretical uncertainties which  
2159 represent at most 10% of the value of  $G(t)$  [322].

A dispersive representation for the vector FF has been built in a similar way [324]. Since there is no analog of the CT theorem, in this case, the two subtractions are performed at  $t = 0$ . Assuming that the vector FF has no zero, one gets

$$\tilde{f}_+^{Disp}(t) = \exp\left[\frac{t}{m_\pi^2} (\Lambda_+ + H(t))\right], \quad H(t) = \frac{m_\pi^2 t}{\pi} \int_{(m_K+m_\pi)^2}^{\infty} \frac{ds}{s^2} \frac{\phi_+(s)}{(s-t-i\epsilon)}. \quad (158)$$

with  $\Lambda_+ \equiv m_\pi^2 d\tilde{f}_+(t)/dt|_{t=0}$  is the fit parameter and  $\phi_+(s)$  the phase of the vector form factor. Here, in the elastic region,  $\phi_+(t)$  equals the  $I = 1/2$ , P-wave  $K\pi$  scattering phase according to Watson's theorem [323]. Similarly to what happens for  $G$ , the two subtractions minimize the contribution coming from the unknown high energy phase resulting in a relatively small uncertainty on  $H(t)$ . Since the dispersive integral  $H(t)$  represents at most 20% of the expected value of  $\Lambda_+$ , the latter can then be determined with a high precision knowing  $H(t)$  much less precisely. For more details on the dispersive representations and a detailed discussion of the different sources of theoretical uncertainties entering the dispersive parametrization via the function  $G$  and  $H$ , see [322] and [324].

Using a class II parametrization for the FFs in a fit to  $K_{\ell 3}$  decay distribution, only two parameters ( $\lambda'_+$  and  $\lambda''_+$  for a Taylor expansion, Eq. (153)) can be determined for  $\tilde{f}_+(t)$  and only one parameter ( $\lambda'_0$  for a Taylor expansion) for  $\tilde{f}_0(t)$ . Moreover these parameters are strongly correlated. It has also been shown in Ref. [322] that in order to describe the FF shapes accurately in the physical region, one has to go at least up to the second order in the Taylor expansion. Neglecting the curvature in the parametrization of  $\tilde{f}_0(t)$  generates a bias in the extraction of  $\lambda'_0$  which is then overestimated [322]. Hence, using a class II parametrization for  $\tilde{f}_0(t)$  doesn't allow it to be extrapolated from the physical region ( $m_\ell^2 < t < t_0 = (m_K - m_\pi)^2$ ) up to the CT point with a reliable precision. To measure the FF shapes from  $K_{\ell 3}$  decays with the precision demanded in the extraction of  $|V_{us}|$ , it is preferable to use a parametrization in class I.

#### 2180 4.4.4. Lattice determinations of $f_+(0)$ and $f_K/f_\pi$

2181 In this section we summarize the status of results of lattice QCD simulations for the  
2182 semileptonic Kaon decay form factor  $f_+(0)$  and for the ratio of Kaon and pion leptonic  
2183 decay constants,  $f_K/f_\pi$ . For a brief introduction to lattice QCD we refer the reader to  
2184 section 2.3.

#### 2185 *Theoretical estimates of $f_+(0)$*

The vector form factor at zero-momentum transfer,  $f_+(0)$ , is the key hadronic quantity required for the extraction of the CKM matrix element  $|V_{us}|$  from semileptonic  $K_{\ell 3}$  decays (cf. equation (134)). Within SU(3) ChPT one can perform a systematic expansion of  $f_+(0)$  of the type

$$f_+(0) = 1 + f_2 + f_4 + \dots, \quad (159)$$

where  $f_n = \mathcal{O}[M_{K,\pi}^n/(4\pi f_\pi)^n]$  and the first term is equal to unity due to the vector current conservation in the SU(3) limit. Because of the Ademollo-Gatto (AG) theorem [293], the first non-trivial term  $f_2$  does not receive contributions from the local operators of the effective theory and can be computed unambiguously in terms of the Kaon and pion masses ( $M_K$  and  $M_\pi$ ) and the pion decay constant  $f_\pi$ . It takes the value  $f_2 = -0.023$  at the physical point [325]. The task is thus reduced to the problem of finding a prediction for the quantity  $\Delta f$ , defined as

$$\Delta f \equiv f_4 + f_6 + \dots = f_+(0) - (1 + f_2) , \quad (160)$$

2186 which depends on the low-energy constants (LECs) of the effective theory and cannot be  
2187 deduced from other processes.

The original estimate made by Leutwyler and Roos [325] was based on the quark model yielding  $\Delta f = -0.016(8)$ . More recently other analytical approaches have tried to determine the next-to-next-to-leading order (NNLO) term  $f_4$  by writing it as

$$f_4 = L_4(\mu) + f_4^{loc}(\mu) , \quad (161)$$

2188 where  $\mu$  is the renormalization scale,  $L_4(\mu)$  is the loop contribution computed in Ref. [326]  
2189 and  $f_4^{loc}(\mu)$  is the  $\mathcal{O}(p^6)$  local contribution. For the latter various models have been  
2190 adopted, namely the quark model in Ref. [326], the dispersion relations in Ref. [327] and  
2191 the  $1/N_c$  expansion in Ref. [328], obtaining  $\Delta f = 0.001(10)$ ,  $-0.003(11)$ ,  $0.007(12)$ ,  
2192 respectively. These values are compatible with zero within the uncertainties and are  
2193 significantly larger than the LR estimate, leading to smaller SU(3)-breaking effects on  
2194  $f_+(0)$ .

2195 Notice that in principle the next-to-next-to-leading order (NNLO) term  $f_4$  may be  
2196 obtained from the slope and the curvature of the scalar form factor  $f_0(q^2)$ , but present  
2197 data from  $K \rightarrow \pi \mu \bar{\nu}_\mu$  decays are not precise enough for an accurate determination.

2198 A precise evaluation of  $f_+(0)$ , or equivalently  $\Delta f$ , requires the use of non-perturbative  
2199 methods based on the fundamental theory of the strong interaction, such as lattice  
2200 QCD simulations. Such determinations started recently with the quenched simulations of  
2201 Ref. [329], where it was shown that  $f_+(0)$  can be determined at the physical point with  
2202 a  $\simeq 1\%$  accuracy. The findings of Ref. [329] triggered various unquenched calculations of  
2203  $f_+(0)$ , namely those of Refs. [330–332] with  $N_f = 2$  with pion masses above  $\simeq 500$  MeV  
2204 and two very recent ones from Ref. [333] with  $N_f = 2 + 1$  and Ref. [334] with  $N_f = 2$ .  
2205 In the former the simulated pion masses start from 330 MeV, while in the latter, they  
2206 start from 260 MeV. In both cases the error associated with the chiral extrapolation was  
2207 significantly reduced with respect to previous works thanks to the lighter pion masses.

2208 In Ref. [334] the chiral extrapolation was performed using both SU(3) and SU(2)  
2209 ChPT for  $f_2$  (see Ref. [335]). In the latter case the Kaon field is integrated out and  
2210 the effects of the strange quark are absorbed into the LECs of the new effective theory.  
2211 The results obtained using SU(2) and SU(3) ChPT are found to be consistent within  
2212 the uncertainties, giving support to the applicability of chiral perturbation theory at  
2213 this order. We note that since no predictions in chiral perturbation theory for  $\Delta f$  as a  
2214 function of the quark masses exists in a closed form, the lattice data for  $\Delta f$  is currently  
2215 extrapolated to the physical point using phenomenologically motivated ansätze.

2216 The results for  $f_+(0)$  and  $\Delta f$  are summarized in Tab. 11, together with some relevant  
2217 details concerning the various lattice set-ups, and those of  $f_+(0)$  are shown in Fig. 18. It  
2218 can be seen that:

- 2219 i) all lattice results suggest a negative, sizable value for  $\Delta f$  in agreement with the LR  
2220 estimate, but at variance with the results of the analytical approaches of Refs. [326–  
2221 328], and
- 2222 ii) the two recent lattice calculations of Refs. [333, 334] have reached an encouraging  
2223 precision of  $\simeq 0.5\%$  on the determination of  $f_+(0)$ .

2224 Since simulations of lattice QCD are carried out in a finite volume, the momentum  
2225 transfer  $q^2$  for the conventionally used periodic fermion boundary conditions takes values  
2226 corresponding to the Fourier modes of the Kaon or pion. Using a phenomenological

Table 11

Summary of model and lattice results for  $f_+(0)$  and  $\Delta f$ . The lattice errors include both statistical and systematic uncertainties.

Ref.	Model/Lattice	$f_+(0)$	$\Delta f$	$M_\pi$ (MeV)	$M_\pi L$	$a$ (fm)	$N_f$
[325]	<i>LR</i>	0.961 ( 8)	-0.016 ( 8)				
[326]	<i>ChPT + LR</i>	0.978 (10)	+0.001 (10)				
[327]	<i>ChPT + disp.</i>	0.974 (11)	-0.003 (11)				
[328]	<i>ChPT + 1/<math>N_c</math></i>	0.984 (12)	+0.007 (12)				
[329]	<i>SPQ<sub>cdR</sub></i>	0.960 ( 9)	-0.017 ( 9)	$\gtrsim 500$	$\gtrsim 5$	$\simeq 0.07$	0
[330]	<i>JLQCD</i>	0.967 ( 6)	-0.010 ( 6)	$\gtrsim 550$	$\gtrsim 5$	$\simeq 0.09$	2
[331]	<i>RBC</i>	0.968 (12)	-0.009 (12)	$\gtrsim 490$	$\gtrsim 6$	$\simeq 0.12$	2
[332]	<i>QCDSF</i>	0.965 ( ?)	-0.012 ( ?)	$\gtrsim 590$	$\gtrsim 6$	$\simeq 0.08$	2
[334]	<i>ETMC</i>	0.956 ( 8)	-0.021 ( 8)	$\gtrsim 260$	$\gtrsim 4$	$\simeq 0.07$	2
[333]	<i>RBC + UKQCD</i>	0.964 ( 5)	-0.013 ( 5)	$\gtrsim 330$	$\gtrsim 4$	$\simeq 0.11$	2 + 1

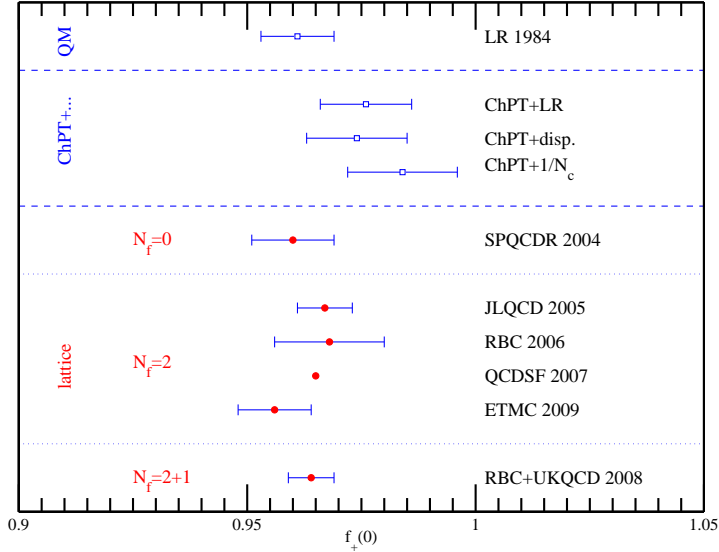


Fig. 18. Results of model (squares) and lattice (dots) calculations of  $f_+(0)$ .

2227 ansatz for the  $q^2$ -dependence of the form factor one interpolates to  $q^2 = 0$  where  $f_+(0)$  is  
 2228 extracted, thereby introducing a major systematic uncertainty. A new method based on  
 2229 the use of partially twisted boundary conditions (cf. section 2.3) has been developed [336]  
 2230 which allows this uncertainty to be entirely removed by simulating directly at the desired  
 2231 kinematic point  $q^2 = 0$ .

2232 Although the impact of discretization effects is expected to be small<sup>12</sup>, we emphasize

<sup>12</sup>The analysis from ETM [334], with fixed simulated quark mass, confirms that discretization effects are small with respect to present uncertainty.

2233 that all available lattice calculations have been carried out at a single lattice spacing.

2234 A systematic study of the scaling behavior of  $f_+(0)$ , using partially twisted boundary  
 2235 conditions and the extension of the simulations to lighter pion masses in order to improve  
 2236 the chiral extrapolation will be the priorities for the upcoming lattice studies of  $K_{\ell 3}$   
 2237 decays.

2238 *Theoretical estimates of  $f_K/f_\pi$*

2239 As was pointed out in Ref. [301], an alternative to  $K_{\ell 3}$  decays for obtaining a precise  
 2240 determination of  $|V_{us}|$  is provided by the Kaon(pion) leptonic decays  $K(\pi) \rightarrow \mu\bar{\nu}_\mu(\gamma)$ . In  
 2241 this case, the key hadronic quantity is the ratio of the Kaon and pion decay constants,  
 2242  $f_K/f_\pi$ .

2243 In contrast to  $f_+(0)$ , the pseudoscalar decay constants are not protected by the AG  
 2244 theorem [293] against corrections linear in the SU(3) breaking. Moreover the first non-  
 2245 trivial term (of order  $\mathcal{O}(p^4)$ ) in the chiral expansion of  $f_K/f_\pi$  depends on the LECs and  
 2246 therefore it cannot be predicted unambiguously within ChPT. This is the reason why  
 2247 the most precise determinations of  $f_K/f_\pi$  come from lattice QCD simulations.

2248 During the recent years various collaborations have provided new results for  $f_K/f_\pi$   
 2249 using unquenched gauge configurations with both 2 and 2+1 dynamical flavors. They  
 2250 are summarized in Tab. 12, together with some relevant details concerning the various  
 2251 lattice set-ups. They are shown graphically in Fig. 19.

Table 12  
 Summary of lattice results for  $f_K/f_\pi$ . The errors include both statistical and systematic uncertainties.

Ref.	Collaboration	$f_K/f_\pi$	$M_\pi$ (MeV)	$M_\pi L$	$a$ (fm)	$N_f$
[106, 337]	<i>MILC</i>	$1.197^{+7}_{-13}$	$\gtrsim 240$	$\gtrsim 4$	$\rightarrow 0$	2+1
[338]	<i>HPQCD</i>	1.189 ( 7)	$\gtrsim 250$	$\gtrsim 4$	$\rightarrow 0$	2+1
[339]	<i>BMW</i>	1.185 (15)	$\gtrsim 190$	$\gtrsim 5$	$\rightarrow 0$	2+1
[340]	<i>Aubin et al.</i>	1.191(23)	$\gtrsim 240$	$\gtrsim 3.8$	$\rightarrow 0$	2+1
[341]	<i>ETMC</i>	1.210 (18)	$\gtrsim 260$	$\gtrsim 4$	$\rightarrow 0$	2
[342]	<i>NPLQCD</i>	$1.218^{+11}_{-24}$	$\gtrsim 290$	$\gtrsim 4$	$\simeq 0.13$	2+1
[110]	<i>RBC/UKQCD</i>	1.205 (65)	$\gtrsim 330$	$\gtrsim 4$	$\simeq 0.11$	2+1
[107]	<i>PACS - CS</i>	1.189 (20)	$\gtrsim 160$	$\gtrsim 2$	$\simeq 0.09$	2+1

2252 A few comments are in order:

- 2253 i) finite size effects are kept under good control by the constraint  $M_\pi L \gtrsim 4$ , which is  
 2254 adopted by all collaborations except Ref. [107];
- 2255 ii) the continuum extrapolation, which allows discretization effects to be safely removed,  
 2256 has been performed by several collaborations;
- 2257 iii) the convergence of the SU(3) chiral expansion for  $f_K/f_\pi$  appears to be questionable,  
 2258 mainly because large NLO corrections are already required to account for the large  
 2259 difference between the experimental value of  $f_\pi$  and the value of the decay constant in  
 2260 the massless SU(3) limit;
- 2261 iv) the convergence of the SU(2) chiral expansion is much better and thanks to the light  
 2262 pion masses reached in the recent lattice calculations, the uncertainty related to the



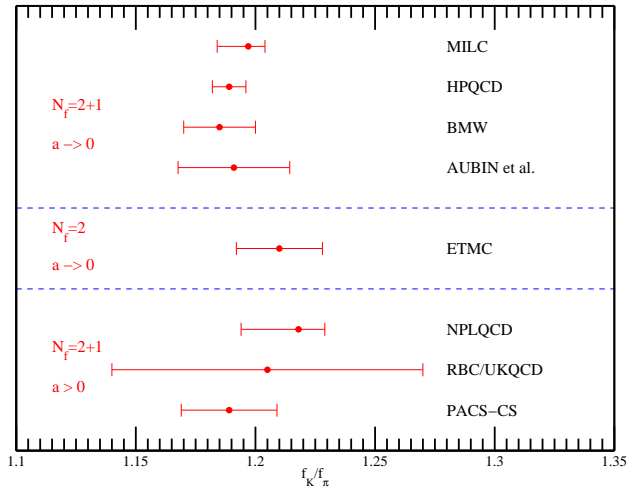


Fig. 19. Results of lattice calculations of  $f_K/f_\pi$ .

- 2263 chiral extrapolation to the physical point is kept to the percent level [110];  
2264 v) little is known about the details of the chiral and continuum extrapolation in Ref. [338]  
2265 (HPQCD) which is currently the most precise lattice prediction for  $f_K/f_\pi$ ; in particular  
2266 about the priors on many parameters that have been introduced;  
2267 vi) It is worth repeating (cf. section 2.3) that there exist conceptional concerns about  
2268 the staggered fermion formulation - the results by MILC, HPQCD, Aubin *et al.* and  
2269 NPLQCD use staggered fermions and need to be confirmed by conceptually clean  
2270 fermion formulations.

#### 2271 *Summary of lattice results*

2272 We note that the Flavia Net Lattice Averaging Group (FLAG) has just started to pe-  
2273 riodically compile and publish (web and journal) lattice QCD results for SM observables  
2274 and parameters. In addition, averages will be computed where feasible and a classifica-  
2275 tion of the quality of lattice results by means of a simple color coding will be provided  
2276 in order to facilitate understanding of lattice results for non-experts. For a first status  
2277 report see [343].

2278 Hence, no average over lattice results will be provided here. We merely identify those  
2279 results that have a good control over systematic uncertainties and have been published  
2280 in journals and refer the reader to the forthcoming FLAG document for averages.

2281 For  $f_+(0)$  the 2+1 flavor result by the RBC+UKQCD [333] collaboration is the most  
2282 advanced calculation,

$$f_+(0) = 0.964(5) \quad N_f = 2 + 1. \quad (162)$$

while for 2 flavors it is the result by ETM [334],

$$f_+(0) = 0.956(8) \quad N_f = 2. \quad (163)$$

For  $f_K/f_\pi$  with  $N_f = 2 + 1$  dynamical quarks, the currently most precise predictions are by MILC [106]

$$f_K/f_\pi = 1.197^{(+7)}_{(-13)} \quad N_f = 2 + 1, \quad (164)$$

and HPQCD [338]

$$f_K/f_\pi = 1.189(7) \quad N_f = 2 + 1, \quad (165)$$

both using the same set of staggered sea quark configurations.

For illustrative purposes the latter result will be used later in section 4.6. We also emphasize the currently most precise result with  $N_f = 2$  dynamical quarks by the ETM collaboration [341]:

$$f_K/f_\pi = 1.210(18) \quad (N_f = 2). \quad (166)$$

At the current level of precision the comparison of the  $N_f = 2$  and  $N_f = 2 + 1$  result indicates a rather small contribution of the strange sea quarks to the ratio of decay constants.

#### 4.4.5. Data Analysis

We perform fits to world data on the BRs and lifetimes for the  $K_L$  and  $K^\pm$ , with the constraint that BRs add to unity. This is the correct way of using the new measurements. A detailed description of the fit is given in Ref [344]. The present version of our fits uses only published measurements.

#### $K_L$ leading branching ratios and $\tau_L$

Numerous measurements of the principal  $K_L$  BRs, or of various ratios of these BRs, have been published recently. For the purposes of evaluating  $|V_{us}|f_+(0)$ , these data can be used in a PDG-like fit to the  $K_L$  BRs and lifetime, so all such measurements are interesting.

KTeV has measured five ratios of the six main  $K_L$  BRs [345]. The six channels involved account for more than 99.9% of the  $K_L$  width and KTeV combines the five measured ratios to extract the six BRs. We use the five measured ratios in our analysis:  $\mathcal{B}(K_{\mu 3})/\mathcal{B}(K_{e 3}) = 0.6640(26)$ ,  $\mathcal{B}(\pi^+\pi^-\pi^0)/\mathcal{B}(K_{e 3}) = 0.3078(18)$ ,  $\mathcal{B}(\pi^+\pi^-)/\mathcal{B}(K_{e 3}) = 0.004856(28)$ ,  $\mathcal{B}(3\pi^0)/\mathcal{B}(K_{e 3}) = 0.4782(55)$ , and  $\mathcal{B}(2\pi^0)/\mathcal{B}(3\pi^0) = 0.004446(25)$ . The errors on these measurements are correlated; this is taken into account in our fit.

NA48 has measured the ratio of the BR for  $K_{e 3}$  decays to the sum of BRs for all decays to two tracks, giving  $\mathcal{B}(K_{e 3})/(1 - \mathcal{B}(3\pi^0)) = 0.4978(35)$  [346].

Using  $\phi \rightarrow K_L K_S$  decays in which the  $K_S$  decays to  $\pi^+\pi^-$ , providing normalization, KLOE has directly measured the BRs for the four main  $K_L$  decay channels [347]. The errors on the KLOE BR values are dominated by the uncertainty on the  $K_L$  lifetime  $\tau_L$ ; since the dependence of the geometrical efficiency on  $\tau_L$  is known, KLOE can solve for  $\tau_L$  by imposing  $\sum_x \mathcal{B}(K_L \rightarrow x) = 1$  (using previous averages for the minor BRs), thereby greatly reducing the uncertainties on the BR values obtained. Our fit makes use of the KLOE BR values before application of this constraint:  $\mathcal{B}(K_{e 3}) = 0.4049(21)$ ,  $\mathcal{B}(K_{\mu 3}) = 0.2726(16)$ ,  $\mathcal{B}(3\pi^0) = 0.2018(24)$ , and  $\mathcal{B}(\pi^+\pi^-\pi^0) = 0.1276(15)$ . The dependence of these values on  $\tau_L$  and the correlations between the errors are taken into account. KLOE has also measured  $\tau_L$  directly, by fitting the proper decay time distribution for  $K_L \rightarrow 3\pi^0$  events, for which the reconstruction efficiency is high and uniform over a fiducial volume of  $\sim 0.4\lambda_L$ . They obtain  $\tau_L = 50.92(30)$  ns [348].

Table 13

Results of fit to  $K_L$  BRs and lifetime.

Parameter	Value	$S$
$\mathcal{B}(K_{e3})$	0.4056(9)	1.3
$\mathcal{B}(K_{\mu 3})$	0.2704(10)	1.5
$\mathcal{B}(3\pi^0)$	0.1952(9)	1.2
$\mathcal{B}(\pi^+\pi^-\pi^0)$	0.1254(6)	1.1
$\mathcal{B}(\pi^+\pi^-)$	$1.967(7) \times 10^{-3}$	1.1
$\mathcal{B}(\pi^+\pi^-\gamma)$	$4.15(9) \times 10^{-5}$	1.6
$\mathcal{B}(\pi^+\pi^-\gamma)$ DE	$2.84(8) \times 10^{-5}$	1.3
$\mathcal{B}(2\pi^0)$	$8.65(4) \times 10^{-4}$	1.4
$\mathcal{B}(\gamma\gamma)$	$5.47(4) \times 10^{-4}$	1.1
$\tau_L$	51.16(21) ns	1.1

2317 There are also two recent measurements of  $\mathcal{B}(\pi^+\pi^-)/\mathcal{B}(K_{\ell 3})$ , in addition to the KTeV  
2318 measurement of  $\mathcal{B}(\pi^+\pi^-)/\mathcal{B}(K_{e3})$  discussed above. The KLOE collaboration obtains  
2319  $\mathcal{B}(\pi^+\pi^-)/\mathcal{B}(K_{\mu 3}) = 7.275(68) \times 10^{-3}$  [349], while NA48 obtains  $\mathcal{B}(\pi^+\pi^-)/\mathcal{B}(K_{e3}) =$   
2320  $4.826(27) \times 10^{-3}$  [350]. All measurements are fully inclusive of inner bremsstrahlung.  
2321 The KLOE measurement is fully inclusive of the direct-emission (DE) component, DE  
2322 contributes negligibly to the KTeV measurement, and a residual DE contribution of  
2323 0.19% has been subtracted from the NA48 value to obtain the number quoted above.

2324 We fit the 13 recent measurements listed above, together with eight additional ratios of  
2325 the BRs for subdominant decays. The complete list of 21 inputs is given in Table 14. As  
2326 free parameters, our fit has the seven largest  $K_L$  BRs (those to  $K_{e3}$ ,  $K_{\mu 3}$ ,  $3\pi^0$ ,  $\pi^+\pi^-\pi^0$ ,  
2327  $\pi^+\pi^-$ ,  $\pi^0$  and  $\gamma\gamma$ ) and the  $K_L$  lifetime, as well as two additional parameters necessary for  
2328 the treatment of the direct emission (DE) component in the radiation-inclusive  $\pi^+\pi^-$   
2329 decay width. Our definition of  $\mathcal{B}(\pi^+\pi^-)$  is now fully inclusive of inner bremsstrahlung (IB),  
2330 but exclusive of the DE component. The fit also includes  $\mathcal{B}(\pi^+\pi^-\gamma)$  and  $\mathcal{B}(\pi^+\pi^-\gamma_{\text{DE}})$ ,  
2331 the branching ratios for decays to states with a photon with  $E_\gamma^* > 20$  MeV, and with a  
2332 photon from DE with  $E_\gamma^* > 20$  MeV, respectively. Other parameterizations are possible,  
2333 but this one most closely represents the input data set and conforms to recent PDG  
2334 usage. With 21 input measurements, 10 free parameters, and the constraint that the sum  
2335 of the BRs (except for  $\mathcal{B}(\pi^+\pi^-\gamma)$ , which is entirely included in the sum of  $\mathcal{B}(\pi^+\pi^-)$   
2336 and  $\mathcal{B}(\pi^+\pi^-\gamma_{\text{DE}})$ ) equal unity, we have 12 degrees of freedom. The fit gives  $\chi^2 = 19.8$   
2337 ( $P = 7.1\%$ ).

2338 The evolution of the average values of the BRs for  $K_{L\ell 3}$  decays and for the important  
2339 normalization channels is shown in Fig. 21.

#### 2340 $K_S$ leading branching ratios and $\tau_S$

2341 KLOE has measured the ratio  $\text{BR}(K_S \rightarrow \pi e \nu)/\text{BR}(K_S \rightarrow \pi^+\pi^-)$  with 1.3% preci-  
2342 sion [351], making possible an independent determination of  $|V_{us}| f_+(0)$  to better than  
2343 0.7%. In [352], KLOE combines the above measurement with their measurement  $rm\mathcal{B}(K_S \rightarrow$   
2344  $\pi^+\pi^-)/rm\mathcal{B}(K_S \rightarrow \pi^0\pi^0) = 2.2459(54)$ . Using the constraint that the  $K_S$  BRs sum to  
2345 unity and assuming the universality of lepton couplings, they determine the BRs for

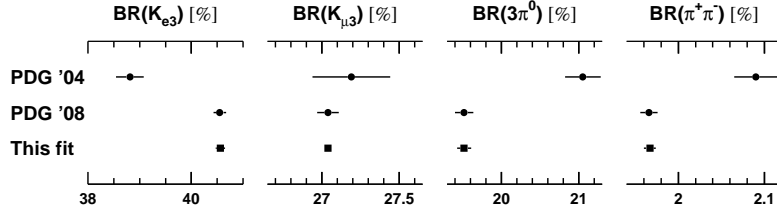


Fig. 20. Evolution of average values for main  $K_L$  BRs.

Table 14

Input data used for the fit to  $K_L$  BRs and lifetime (all the references refer to PDG08 [283]).

Parameter	Value	Source
$\tau_{K_L}$	50.92(30) ns	Ambrosino 05C
$\tau_{K_L}$	51.54(44) ns	Vosburgh 72
$\mathcal{B}K_{e3}$	0.4049(21)	Ambrosino 06
$\mathcal{B}K_{\mu 3}$	0.2726(16)	Ambrosino 06
$\mathcal{B}K_{\mu 3}/\mathcal{B}K_{e3}$	0.6640(26)	Alexopoulos 04
$\mathcal{B}3\pi^0$	0.2018(24)	Ambrosino 06
$\mathcal{B}3\pi^0/\mathcal{B}K_{e3}$	0.4782(55)	Alexopoulos 04
$\mathcal{B}\pi^+\pi^-\pi^0$	0.1276(15)	Ambrosino 06
$\mathcal{B}\pi^+\pi^-\pi^0/\mathcal{B}K_{e3}$	0.3078(18)	Alexopoulos 04
$\mathcal{B}\pi^+\pi^-/\mathcal{B}K_{e3}$	0.004856(29)	Alexopoulos 04
$\mathcal{B}\pi^+\pi^-/\mathcal{B}K_{e3}$	0.004826(27)	Lai 07
$\mathcal{B}\pi^+\pi^-/\mathcal{B}K_{\mu 3}$	0.007275(68)	Ambrosino 06F
$\mathcal{B}K_{e3}/\mathcal{B}2$ tracks	0.4978(35)	Lai 04B
$\mathcal{B}\pi^0\pi^0/\mathcal{B}3\pi^0$	0.004446(25)	Alexopoulos 04
$\mathcal{B}\pi^0\pi^0/\mathcal{B}\pi^+\pi^-$	0.4391(13)	PDG etafit [283]
$\mathcal{B}\gamma\gamma/\mathcal{B}3\pi^0$	0.00279(3)	Adinolfi 03
$\mathcal{B}\gamma\gamma/\mathcal{B}3\pi^0$	0.00281(2)	Lai 03
$\mathcal{B}\pi^+\pi^-/\mathcal{B}\pi^+\pi^-(\gamma)$	0.0208(3)	Alavi-Harati 01B
$\mathcal{B}\pi^+\pi^-\gamma_{DE}/\mathcal{B}\pi^+\pi^-\gamma$	0.689(21)	Abouzaid 06A
$\mathcal{B}\pi^+\pi^-\gamma_{DE}/\mathcal{B}\pi^+\pi^-\gamma$	0.683(11)	Alavi-Harati 01B
$\mathcal{B}\pi^+\pi^-\gamma_{DE}/\mathcal{B}\pi^+\pi^-\gamma$	0.685(41)	Ramberg 93

2346  $\pi^+\pi^-$ ,  $\pi^0\pi^0$ ,  $K_{e3}$ , and  $K_{\mu 3}$  decays.

2347 Our fit is an extension of the analysis in [352]. We perform a fit to the data on the  $K_S$

2348 BRs to  $\pi^+\pi^-$ ,  $\pi^0\pi^0$ , and  $K_{e3}$  that uses, in addition to the above two measurements:

2349 – the measurement from NA48,  $\Gamma K_S \rightarrow \pi e \nu / \Gamma K_L \rightarrow \pi e \nu$  [353], where the denominator

2350 is obtained from the results of our  $K_L$  fit;

2351 – the measurement of  $\tau_S$  (not assuming  $CPT$ ) from NA48 [283], 89.589(70) ps;

Table 15

Results of fit to  $K_S$  BRs and lifetime

Parameter	Value	$S$
$\mathcal{B}\pi^+\pi^-$	0.6920(5)	1.0
$\mathcal{B}\pi^0\pi^0$	0.3069(5)	1.0
$\mathcal{B}K_{e3}$	$7.05(8) \times 10^{-4}$	1.0
$\mathcal{B}K_{\mu 3}$	$4.66(6) \times 10^{-4}$	1.0
$\tau_S$	$4.66(6) \times 10^{-4}$	1.0

2352 – the measurement of  $\tau_S$  (not assuming  $CPT$ ) from KTeV [283], 89.58(13) ps;  
2353 – the result  $\text{BR}K_{\mu 3}/\text{BR}K_{e3} = 0.66100(214)$ , obtained from the assumption of universal  
2354 lepton couplings, the values of the quadratic (vector) and linear (scalar) form-factor  
2355 parameters from our fit to form-factor data, and the long-distance electromagnetic  
2356 corrections discussed in Sec. 4.4.2.  
2357 The free parameters are the four BRs listed above plus  $\tau_S$ . With six inputs and one  
2358 constraint (on the sum of the BRs), the fit has one degree of freedom and gives  $\chi^2 =$   
2359 0.0038 ( $P = 95\%$ ). The results of the fit are listed in Table 15.

2360  $K^\pm$  leading branching ratios and  $\tau^\pm$

2361 There are several new results providing information on  $K_{\ell 3}^\pm$  rates. The NA48/2 collab-  
2362 oration has published measurements of the three ratios  $\mathcal{B}(K_{e3}/\pi\pi^0)$ ,  $\mathcal{B}(K_{\mu 3}/\pi\pi^0)$ , and  
2363  $\mathcal{B}(K_{\mu 3}/K_{e3})$  [354]. These measurements are not independent; in our fit, we use the values  
2364  $\mathcal{B}(K_{e3}/\pi\pi^0) = 0.2470(10)$  and  $\mathcal{B}(K_{\mu 3}/\pi\pi^0) = 0.1637(7)$  and take their correlation into  
2365 account.

2366 KLOE has measured the absolute BRs for the  $K_{e3}$  and  $K_{\mu 3}$  decays [355]. In  $\phi \rightarrow$   
2367  $K^+K^-$  events,  $K^+$  decays into  $\mu\nu$  or  $\pi\pi^0$  are used to tag a  $K^-$  beam, and vice versa.  
2368 KLOE performs four separate measurements for each  $K_{\ell 3}$  BR, corresponding to the  
2369 different combinations of Kaon charge and tagging decay. The final averages are  $\mathcal{B}(K_{e3}) =$   
2370  $4.965(53)(38)\%$  and  $\mathcal{B}(K_{\mu 3}) = 3.233(29)(26)\%$ . KLOE has also measured the absolute  
2371 branching ratio for the  $\pi\pi^0$  [356] and  $\mu\nu$  decay [357].

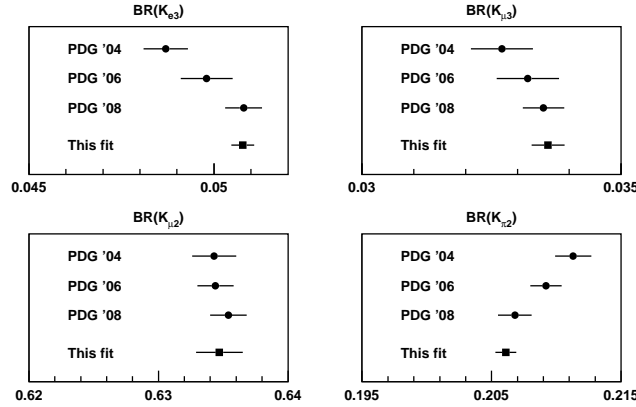
2372 Our fit takes into account the correlation between these values, as well as their de-  
2373 pendence on the  $K^\pm$  lifetime. The world average value for  $\tau_\pm$  is nominally quite precise.  
2374 However, the PDG error is scaled by 2.1; the confidence level for the average is 0.17%.  
2375 It is important to confirm the value of  $\tau_\pm$ . The new measurement from KLOE,  $\tau_\pm =$   
2376  $12.347(30)$  ns, agrees with the PDG average.

2377 Our fit for the six largest  $K^\pm$  branching ratios and lifetime uses the measurements in  
2378 Table 17, including the six measurements noted above. We have recently carried out a  
2379 comprehensive survey of the  $K^\pm$  data set, which led to the elimination of 11 measure-  
2380 ments currently in the 2008 PDG fit. Finally, we note that after the elimination of the  
2381 1970 measurement of  $\Gamma(\pi^\pm\pi^\pm\pi^\mp)$  from Ford et al. (Ford70 in Ref. [283]), the input data  
2382 set provides no strong constraint on the  $\pi^\pm\pi^\pm\pi^\mp$  branching ratio, which increases the  
2383 uncertainties on the resulting BR values. The fit uses 17 input measurements, seven free  
2384 parameters, and one constraint, giving 11 degrees of freedom. We obtain the results in  
2385 Table 16. The fit gives  $\chi^2 = 25.8$  ( $P = 0.69\%$ ). The comparatively low  $P$ -value reflects  
2386 some tension between the KLOE and NA48/2 measurements of the  $K_{\ell 3}$  branching ratios.

Table 16

Results of fit to  $K^\pm$  BRs and lifetime.

Parameter	Value	$S$
$\mathcal{B}(K_{\mu 2})$	63.47(18)%	1.3
$\mathcal{B}(\pi\pi^0)$	20.61(8)%	1.1
$\mathcal{B}(\pi\pi\pi)$	5.573(16)%	1.2
$\mathcal{B}(K_{e3})$	5.078(31)%	1.3
$\mathcal{B}(K_{\mu 3})$	3.359(32)%	1.9
$\mathcal{B}(\pi\pi^0\pi^0)$	1.757(24)%	1.0
$\tau_\pm$	12.384(15) ns	1.2

Fig. 21. Evolution of average values for main  $K^\pm$  BRs.

2387 Both the significant evolution of the average values of the  $K_{\ell 3}$  BRs and the effect of  
 2388 the correlations with  $\mathcal{B}(\pi\pi^0)$  are evident in Fig. 21.

2389 *Measurement of  $BR(K_{e2})/BR(K_{\mu 2})$*

Experimental knowledge of  $K_{e2}/K_{\mu 2}$  was poor until recently. The current world average  $R_K = \mathcal{B}(K_{e2})/\mathcal{B}(K_{\mu 2}) = (2.45 \pm 0.11) \times 10^{-5}$  dates back to three experiments of the 1970s [283] and has a precision of about 5%. Two new measurements were reported recently by NA62 and KLOE (see Tab. 18). A preliminary result based on about 14,000  $K_{e2}$  events, was presented at the 2009 winter conferences by the KLOE collaboration [358]. Preliminary result from NA62, based on about 50,000  $K_{e2}$  events from the 2008 data set was presented in at KAON 2009 [359]. Both the KLOE and the NA62 measurements are inclusive with respect to final state radiation contribution due to bremsstrahlung. The small contribution of  $K_{l2\gamma}$  events from direct photon emission from the decay vertex was subtracted by each of the experiments. Combining these new results with the current PDG value yields a current world average of

$$R_K = (2.498 \pm 0.014) \times 10^{-5}, \quad (167)$$

Table 17

Input data used for the fit to  $K^\pm$  BRs and lifetime (all the references refer to PDG08 [283]). The two 1995 values of the  $K^\pm$  lifetime from Koptev et al. are averaged with  $S = 1.6$  before being included in the fit as a single value.

Parameter	Value	Source
$\tau_{K^\pm}$	12.368(41) ns	Koptev 95 (*)
$\tau_{K^\pm}$	12.380(16) ns	Ott 71
$\tau_{K^\pm}$	12.443(38) ns	Fitch 65B
$\tau_{K^\pm}$	12.347(30) ns	Ambrosino 08
$\mathcal{B}K_{\mu 2}$	0.6366(17)	Ambrosino 06A
$\mathcal{B}\pi\pi^0$	0.2066(11)	[356]
$\mathcal{B}\pi\pi^0/\mathcal{B}K_{\mu 2}$	0.3329(48)	Usher 92
$\mathcal{B}\pi\pi^0/\mathcal{B}K_{\mu 2}$	0.3355(57)	Weissenberg 76
$\mathcal{B}\pi\pi^0/\mathcal{B}K_{\mu 2}$	0.3277(65)	Auerbach 67
$\mathcal{B}K_{e3}$	0.04965(53)	Ambrosino 08A
$\mathcal{B}K_{e3}/\mathcal{B}\pi\pi^0 + K_{\mu 3} + \pi 2\pi^0$	0.1962(36)	Sher 03
$\mathcal{B}K_{e3}/\mathcal{B}\pi\pi^0$	0.2470(10)	Batley 07A
$\mathcal{B}K_{\mu 3}$	0.03233(39)	Ambrosino 08A
$\mathcal{B}K_{\mu 3}/\mathcal{B}\pi\pi^0$	0.1636(7)	Batley 07A
$\mathcal{B}K_{\mu 3}/\mathcal{B}K_{e3}$	0.671(11)	Horie 01
$\mathcal{B}\pi\pi^0\pi^0$	0.01763(26)	Aloisio 04A
$\mathcal{B}\pi\pi^0\pi^0/\mathcal{B}\pi\pi\pi$	0.303(9)	Bisi 65

Table 18

Results and prediction for  $R_K = \mathcal{B}(K_{e2})/\mathcal{B}(K_{\mu 2})$ .

	$R_K [10^{-5}]$
PDG	$2.45 \pm 0.11$
NA48/2	$2.500 \pm 0.016$
KLOE	$2.493 \pm 0.031$
SM prediction	$2.477 \pm 0.001$

2390 in good agreement with the SM expectation [298] and, with a relative error of 0.56%, an  
 2391 order of magnitude more precise than the previous world average.

### 2392 *Measurements of $\mathbf{K}_{\ell 3}$ slopes*

2393 For  $K_{e3}$  decays, recent measurements of the quadratic slope parameters of the vector  
 2394 form factor ( $\lambda'_+, \lambda''_+$ ), see Eq. 153 are available from KTeV [360], KLOE [361], ISTR+  
 2395 [362], and NA48 [363].

2396 We show the results of a fit to the  $K_L$  and  $K^-$  data in the first column of Tab. 19,  
 2397 and to only the  $K_L$  data in the second column. With correlations correctly taken into  
 2398 account, both fits give good values of  $\chi^2/\text{ndf}$ . The significance of the quadratic term is

Table 19

Average of quadratic fit results for  $K_{e3}$  slopes.

	$K_L$ and $K^-$ data	$K_L$ data only
	4 measurements	3 measurements
	$\chi^2/\text{ndf} = 5.3/6$ (51%)	$\chi^2/\text{ndf} = 4.7/4$ (32%)
$\lambda'_+ \times 10^3$	$25.2 \pm 0.9$	$24.9 \pm 1.1$
$\lambda''_+ \times 10^3$	$1.6 \pm 0.4$	$1.6 \pm 0.5$
$\rho(\lambda'_+, \lambda''_+)$	-0.94	-0.95
$I(K_{e3}^0)$	0.15463(21)	0.15454(29)
$I(K_{e3}^\pm)$	0.15900(22)	0.15890(30)

Table 20

Pole fit results for  $K_{e3}^0$  slopes.

Experiment	$M_V$ (MeV)	$\langle M_V \rangle = 875 \pm 5$ MeV
KLOE	$870 \pm 6 \pm 7$	$\chi^2/\text{ndf} = 1.8/2$
KTeV	$881.03 \pm 7.11$	$\lambda'_+ \times 10^3 = 25.42(31)$
NA48	$859 \pm 18$	$\lambda''_+ = 2 \times \lambda'^2_+$
		$I(K_{e3}^0) = 0.15470(19)$

2399  $4.2\sigma$  from the fit to all data, and  $3.5\sigma$  from the fit to  $K_L$  data only.

2400 Including or excluding the  $K^-$  slopes has little impact on the values of  $\lambda'_+$  and  $\lambda''_+$ ; in  
 2401 particular, the values of the phase-space integrals change by just 0.07%. The errors on  
 2402 the phase-space integrals are significantly smaller when the  $K^-$  data are included in the  
 2403 average.

2404 KLOE, KTeV, and NA48 also quote the values shown in Tab. 20 for  $M_V$  from pole  
 2405 (see Eq. 154) fits to  $K_L e3$  data. The average value of  $M_V$  from all three experiments is  
 2406  $M_V = 875 \pm 5$  MeV with  $\chi^2/\text{ndf} = 1.8/2$ . The three values are quite compatible with each  
 2407 other and reasonably close to the known value of the  $K^{\pm*}(892)$  mass ( $891.66 \pm 0.26$  MeV).  
 2408 The values for  $\lambda'_+$  and  $\lambda''_+$  from expansion of the pole parametrization are qualitatively  
 2409 in agreement with the average of the quadratic fit results. More importantly, for the  
 2410 evaluation of the phase-space integrals, using the average of quadratic or pole fit results  
 2411 gives values of  $I(K_{e3}^0)$  that differ by just 0.03%.

2412 For  $K_{\mu 3}$  decays, recent measurements of the slope parameters ( $\lambda'_+, \lambda''_+, \lambda_0$ ) are available  
 2413 from KTeV [360], KLOE [364], ISTRA+ [365], and NA48 [366]. We will not use the  
 2414 ISTRA+ result for the average because systematic errors have not been provided. We  
 2415 use the  $K_{e3} - K_{\mu 3}$  averages provided by the experiments for KTeV and KLOE. NA48  
 2416 does not provide such an average, so we calculate it for inclusion in the fit.

2417 We have studied the statistical sensitivity of the form-factor slope measurements using  
 2418 Monte Carlo techniques. The conclusions of this study are a) that neglecting a quadratic  
 2419 term in the parametrization of the scalar form factor when fitting results leads to a shift  
 2420 of the value of the linear term by about 3.5 times the value of the quadratic term; and b)  
 2421 that because of correlations, it is impossible to measure the quadratic slope parameter  
 2422 from quadratic fits to the data at any plausible level of statistics. The use of the linear  
 2423 representation of the scalar form factor is thus inherently unsatisfactory. The effect is



Table 21

Averages of quadratic fit results for  $K_{e3}$  and  $K_{\mu3}$  slopes.

$\chi^2/\text{ndf}$	29/8 ( $3 \times 10^{-4}$ )
$\lambda'_+ \times 10^3$	$24.5 \pm 0.9$ ( $S = 1.1$ )
$\lambda''_+ \times 10^3$	$1.8 \pm 0.4$ ( $S = 1.3$ )
$\lambda_0 \times 10^3$	$11.7 \pm 1.4$ ( $S = 1.9$ )
$\rho(\lambda'_+, \lambda''_+)$	-0.94
$\rho(\lambda'_+, \lambda_0)$	+0.44
$\rho(\lambda''_+, \lambda_0)$	-0.52
$I(K_{e3}^0)$	0.15449(20)
$I(K_{e3}^\pm)$	0.15885(21)
$I(K_{\mu3}^0)$	0.10171(32)
$I(K_{\mu3}^\pm)$	0.10467(33)
$\rho(I_{e3}, I_{\mu3})$	+0.53

2424 relevant when testing the CT theorem Eq. (151) discussed in section 4.6.2.

2425 The results of the combination are listed in Tab. 21.

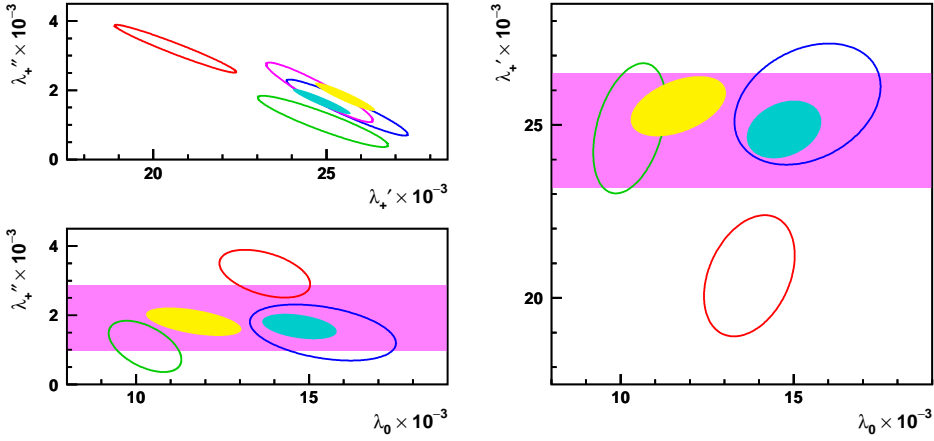


Fig. 22.  $1\text{-}\sigma$  contours for  $\lambda'_+$ ,  $\lambda''_+$ ,  $\lambda_0$  determinations from KLOE(blue ellipse), KTeV(red ellipse), NA48(green ellipse), and world average with(filled yellow ellipse) and without(filled cyan ellipse) the NA48  $K_{\mu3}$  result.

2426 The value of  $\chi^2/\text{ndf}$  for all measurements is terrible; we quote the results with scaled  
 2427 errors. This leads to errors on the phase-space integrals that are  $\sim 60\%$  larger after  
 2428 inclusion of the new  $K_{\mu3}$  NA48 data.

The evaluations of the phase-space integrals for all four modes are listed in each case. Correlations are fully accounted for, both in the fits and in the evaluation of the integrals. The correlation matrices for the integrals are of the form

$$\begin{array}{cccc}
+1 & +1 & \rho & \rho \\
+1 & +1 & \rho & \rho \\
\rho & \rho & +1 & +1 \\
\rho & \rho & +1 & +1
\end{array}$$

2429 where the order of the rows and columns is  $K_{e3}^0$ ,  $K_{e3}^\pm$ ,  $K_{\mu3}^0$ ,  $K_{\mu3}^\pm$ , and  $\rho = \rho(I_{e3}, I_{\mu3})$  as  
2430 listed in the table.

2431 Adding the  $K_{\mu3}$  data to the fit does not cause drastic changes to the values of the  
2432 phase-space integrals for the  $K_{e3}$  modes: the values for  $I(K_{e3}^0)$  and  $I(K_{e3}^\pm)$  in Tab. 21 are  
2433 qualitatively in agreement with those in Tab. 19. As in the case of the fits to the  $K_{e3}$   
2434 data only, the significance of the quadratic term in the vector form factor is strong ( $3.6\sigma$   
2435 from the fit to all data).

#### 2436 4.5. $|V_{us}|$ determination from tau decays

2437 A very precise determination of  $V_{us}$  can be obtained from the semi-inclusive hadronic  
2438 decay width of the  $\tau$  lepton into final states with strangeness [367, 368]. The ratio of the  
2439 Cabibbo-suppressed and Cabibbo-allowed  $\tau$  decay widths directly measures  $(V_{us}/V_{ud})^2$ ,  
2440 up to very small SU(3)-breaking corrections which can be theoretically estimated with  
2441 the needed accuracy.

The inclusive character of the total  $\tau$  hadronic width renders possible an accurate  
calculation of the ratio [369–373]

$$R_\tau \equiv \frac{\Gamma[\tau^- \rightarrow \nu_\tau \text{ hadrons}(\gamma)]}{\Gamma[\tau^- \rightarrow \nu_\tau e^- \bar{\nu}_e(\gamma)]} = R_{\tau,V} + R_{\tau,A} + R_{\tau,S}, \quad (168)$$

2442 using analyticity constraints and the operator product expansion. One can separately  
2443 compute the contributions associated with specific quark currents:  $R_{\tau,V}$  and  $R_{\tau,A}$  corre-  
2444 spond to the Cabibbo-allowed decays through the vector and axial-vector currents, while  
2445  $R_{\tau,S}$  contains the remaining Cabibbo-suppressed contributions.

To a first approximation the Cabibbo mixing can be directly obtained from experimen-  
tal measurements, without any theoretical input. Neglecting the small SU(3)-breaking  
corrections from the  $m_s - m_d$  quark-mass difference, one gets:

$$|V_{us}|^{\text{SU}(3)} = |V_{ud}| \left( \frac{R_{\tau,S}}{R_{\tau,V+A}} \right)^{1/2} = 0.210 \pm 0.003. \quad (169)$$

2446 We have used  $|V_{ud}| = 0.97425 \pm 0.00022$  (cf. Eq. (117)),  $R_\tau = 3.640 \pm 0.010$  and the  
2447 value  $R_{\tau,S} = 0.1617 \pm 0.0040$  [368], which results from the recent BaBar [374] and Belle  
2448 [375] measurements of Cabibbo-suppressed tau decays [376]. The new branching ratios  
2449 measured by BaBar and Belle are all smaller than the previous world averages, which  
2450 translates into a smaller value of  $R_{\tau,S}$  and  $|V_{us}|$ . For comparison, the previous value  
2451  $R_{\tau,S} = 0.1686 \pm 0.0047$  [377] resulted in  $|V_{us}|^{\text{SU}(3)} = 0.215 \pm 0.003$ .

This rather remarkable determination is only slightly shifted by the small SU(3)-  
breaking contributions induced by the strange quark mass. These corrections can be  
theoretically estimated through a QCD analysis of the difference [367, 368, 378–385]

$$\delta R_\tau \equiv \frac{R_{\tau,V+A}}{|V_{ud}|^2} - \frac{R_{\tau,S}}{|V_{us}|^2}. \quad (170)$$

Since the strong interactions are flavor blind, this quantity vanishes in the SU(3) limit. The only non-zero contributions are proportional to the mass-squared difference  $m_s^2 - m_d^2$  or to vacuum expectation values of SU(3)-breaking operators such as  $\delta O_4 \equiv \langle 0 | m_s \bar{s}s - m_d \bar{d}d | 0 \rangle = (-1.4 \pm 0.4) \cdot 10^{-3} \text{ GeV}^4$  [367, 378]. The dimensions of these operators are compensated by corresponding powers of  $m_\tau^2$ , which implies a strong suppression of  $\delta R_\tau$  [378]:

$$\delta R_\tau \approx 24 S_{\text{EW}} \left\{ \frac{m_s^2(m_\tau^2)}{m_\tau^2} (1 - \epsilon_d^2) \Delta(\alpha_s) - 2\pi^2 \frac{\delta O_4}{m_\tau^4} Q(\alpha_s) \right\}, \quad (171)$$

2452 where  $\epsilon_d \equiv m_d/m_s = 0.053 \pm 0.002$  [315]. The perturbative QCD corrections  $\Delta(\alpha_s)$  and  
2453  $Q(\alpha_s)$  are known to  $O(\alpha_s^3)$  and  $O(\alpha_s^2)$ , respectively [378, 385].

The theoretical analysis of  $\delta R_\tau$  involves the two-point vector and axial-vector correlators, which have transverse ( $J = 1$ ) and longitudinal ( $J = 0$ ) components. The  $J = 0$  contribution to  $\Delta(\alpha_s)$  shows a rather pathological behavior, with clear signs of being a non-convergent perturbative series. Fortunately, the corresponding longitudinal contribution to  $\delta R_\tau$  can be estimated phenomenologically with a much better accuracy,  $\delta R_\tau|^L = 0.1544 \pm 0.0037$  [367, 386], because it is dominated by far by the well-known  $\tau \rightarrow \nu_\tau \pi$  and  $\tau \rightarrow \nu_\tau K$  contributions [387]. To estimate the remaining  $L + T$  component, one needs an input value for the strange quark mass. Taking the range  $m_s(m_\tau) = (100 \pm 10) \text{ MeV}$  [ $m_s(2 \text{ GeV}) = (96 \pm 10) \text{ MeV}$ ], which includes the most recent determinations of  $m_s$  from QCD sum rules and lattice QCD [386], one gets finally  $\delta R_{\tau,th} = \delta R_\tau|^L + \delta R_\tau|^L + T = 0.216 \pm 0.016$ , which implies [368]

$$|V_{us}| = \left( \frac{R_{\tau,S}}{\frac{R_{\tau,V+A}}{|V_{ud}|^2} - \delta R_{\tau,th}} \right)^{1/2} = 0.2165 \pm 0.0026_{\text{exp}} \pm 0.0005_{\text{th}}. \quad (172)$$

2454 A larger central value,  $|V_{us}| = 0.2212 \pm 0.0031$ , is obtained with the old world average  
2455 for  $R_{\tau,S}$ .

2456 Notice that the theoretical input only appears through the quantity  $\delta R_{\tau,th}$ , which is  
2457 one order of magnitude smaller than the ratio  $R_{\tau,V+A}/|V_{ud}|^2 = 3.665 \pm 0.012$ . Theo-  
2458 retical uncertainties are thus very suppressed, although a number of issues deserve fur-  
2459 ther investigation. These include (i) an assessment of the uncertainty due to different  
2460 prescriptions (Contour Improved Perturbation Theory versus Fixed Order Perturbation  
2461 Theory) for the slow-converging  $D = 2$ , L+T correlator series, which could shift  $|V_{us}|$  by  
2462 up to  $\sim 0.0020$  [388]; (ii) addressing the stability of the extracted  $|V_{us}|$  by using alter-  
2463 nate sum rules that involve different weights,  $w(s)$ , and/or spectral integral endpoints  
2464  $s_0 < m_\tau/2$  [382, 389]. With theory errors at the level of Eq. (172), experimental errors  
2465 would dominate, in contrast to the situation encountered in  $K_{\ell 3}$  decays.

2466 The phenomenological determination of  $\delta R_\tau|^L$  contains a hidden dependence on  $V_{us}$   
2467 through the input value of the Kaon decay constant  $f_K$ . Although the numerical impact of  
2468 this dependence is negligible, it can be taken explicitly into account. Using the measured  
2469  $K^-/\pi^- \rightarrow \bar{\nu}_\mu \mu^-$  decay widths and the  $\tau$  lifetime [283], one can determine the Kaon and  
2470 pion contributions to  $R_\tau$  with better accuracy than the direct  $\tau$  decay measurements, with  
2471 the results  $R_\tau|^{\tau^- \rightarrow \nu_\tau K^-} = (0.04014 \pm 0.00021)$  and  $R_\tau|^{\tau^- \rightarrow \nu_\tau \pi^-} = (0.6123 \pm 0.0025)$ . The

2472 corresponding longitudinal contributions are just given by  $R_\tau|_{L^{\tau^- \rightarrow \nu_\tau P^-}} \equiv R_\tau|_{L^{\tau^- \rightarrow \nu_\tau P^-}} -$   
 2473  $R_\tau|_{L+T}^{\tau^- \rightarrow \nu_\tau P^-} = -2(m_P^2/m_\tau^2)R_\tau|_{L^{\tau^- \rightarrow \nu_\tau P^-}} (P = K, \pi).$

Subtracting the longitudinal contributions from Eq. (172), one gets an improved formula to determine  $V_{us}$  with the best possible accuracy [368]:

$$|V_{us}|^2 = \frac{\tilde{R}_{\tau,S}}{\frac{\tilde{R}_{\tau,V+A}}{|V_{ud}|^2} - \delta\tilde{R}_{\tau,\text{th}}} \equiv \frac{R_{\tau,S} - R_\tau|_{L^{\tau^- \rightarrow \nu_\tau K^-}}}{\frac{R_{\tau,V+A} - R_\tau|_{L^{\tau^- \rightarrow \nu_\tau \pi^-}}{|V_{ud}|^2} - \delta\tilde{R}_{\tau,\text{th}}}, \quad (173)$$

2474 where  $\delta\tilde{R}_{\tau,\text{th}} \equiv \delta\tilde{R}_\tau|_{L^{\tau^- \rightarrow \nu_\tau P^-}} + \delta R_{\tau,\text{th}}|_{L+T}^{\tau^- \rightarrow \nu_\tau P^-} = (0.033 \pm 0.003) + (0.062 \pm 0.015) = 0.095 \pm 0.015.$   
 2475 The subtracted longitudinal correction  $\delta\tilde{R}_\tau|_{L^{\tau^- \rightarrow \nu_\tau P^-}}$  is now much smaller because it does not  
 2476 contain any pion or Kaon contribution. Using the same input values for  $R_{\tau,S}$  and  $R_{\tau,V+A}$ ,  
 2477 one recovers the  $V_{us}$  determination obtained before in Eq. (172), with an error of  $\pm 0.0030.$

2478 Sizable changes on the experimental determination of  $R_{\tau,S}$  are to be expected from  
 2479 the full analysis of the huge BaBar and Belle data samples. In particular, the high-  
 2480 multiplicity decay modes are not well known at present and their effect has been just  
 2481 roughly estimated or simply ignored. Thus, the result (172) could easily fluctuate in the  
 2482 near future. However, it is important to realize that the final error of the  $V_{us}$  determi-  
 2483 nation from  $\tau$  decay is likely to remain dominated by the experimental uncertainties. If  
 2484  $R_{\tau,S}$  is measured with a 1% precision, the resulting  $V_{us}$  uncertainty will get reduced to  
 2485 around 0.6%, i.e.  $\pm 0.0013$ , making  $\tau$  decay the competitive source of information about  
 2486  $V_{us}.$

2487 An accurate measurement of the invariant-mass distribution of the final hadrons in  
 2488 Cabibbo-suppressed  $\tau$  decays could make possible a simultaneous determination of  $V_{us}$   
 2489 and the strange quark mass, through a correlated analysis of several SU(3)-breaking  
 2490 observables constructed with weighted moments of the hadronic distribution [367, 378,  
 2491 379]. However, the extraction of  $m_s$  suffers from theoretical uncertainties related to the  
 2492 convergence of the associated perturbative QCD series. A better understanding of these  
 2493 QCD corrections is needed in order to improve the present determination of  $m_s$  [367,  
 2494 378, 382–385].

#### 2495 4.6. Physics Results

2496 In this section we summarize the results for  $|V_{us}|$  discussed in the previous sections and  
 2497 based on these results we give constraints on physics beyond the SM. Instead of averages  
 2498 for lattice results for  $f_K/f_\pi$  we use  $f_K/f_\pi = 1.189(7)$  by HPQCD [338] for illustrative  
 2499 purposes (cf. the discussion at the end of section 4.4.4).

##### 2500 4.6.1. Determination of $|V_{us}| \times f_+(0)$ and $|V_{us}|/|V_{ud}| \times f_K/f_\pi$

2501 This section describes the results that are independent of the theoretical parameters  
 2502  $f_+(0)$  and  $f_K/f_\pi.$

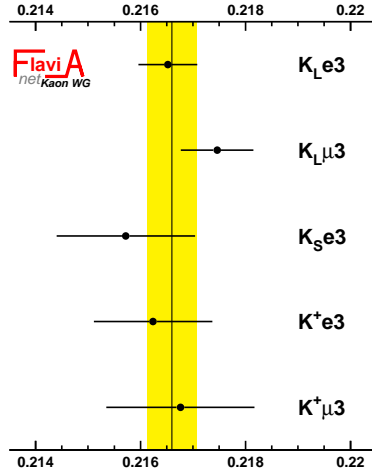
##### 2503 Determination of $|V_{us}| \times f_+(0)$

2504 The value of  $|V_{us}| \times f_+(0)$  has been determined from (134) using the world average  
 2505 values reported in section 4.4.5 for lifetimes, branching ratios and phase space integrals,  
 2506 and the radiative and SU(2) breaking corrections discussed in section 4.4.2.

Table 22

Summary of  $|V_{us}| \times f_+(0)$  determination from all channels.

mode	$ V_{us}  \times f_+(0)$	% err	BR	$\tau$	$\Delta$	Int
$K_L \rightarrow \pi e \nu$	0.2165(5)	0.26	0.09	0.20	0.11	0.06
$K_L \rightarrow \pi \mu \nu$	0.2175(6)	0.32	0.15	0.18	0.15	0.16
$K_S \rightarrow \pi e \nu$	0.2157(13)	0.61	0.60	0.03	0.11	0.06
$K^\pm \rightarrow \pi e \nu$	0.2162(11)	0.52	0.31	0.09	0.41	0.06
$K^\pm \rightarrow \pi \mu \nu$	0.2168(14)	0.65	0.47	0.08	0.42	0.16
average	0.2166(5)					

Fig. 23. Display of  $|V_{us}| \times f_+(0)$  for all channels.

The results are given in Tab. 22, and are shown in Fig. 23 for  $K_L \rightarrow \pi e \nu$ ,  $K_L \rightarrow \pi \mu \nu$ ,  $K_S \rightarrow \pi e \nu$ ,  $K^\pm \rightarrow \pi e \nu$ ,  $K^\pm \rightarrow \pi \mu \nu$ , and for the combination. The average,

$$|V_{us}| \times f_+(0) = 0.2166(5), \quad (174)$$

has an uncertainty of about of 0.2%. The results from the five modes are in good agreement, the fit probability is 55%. In particular, comparing the values of  $|V_{us}| \times f_+(0)$  obtained from  $K_{\ell 3}^0$  and  $K_{\ell 3}^\pm$  we obtain a value of the SU(2) breaking correction

$$\delta_{SU(2)_{exp.}}^K = 5.4(8)\%$$

2507 in agreement with the CHPT calculation reported in Eq. 147:  $\delta_{SU(2)}^K = 5.8(8)\%$ .

#### 2508 4.6.2. A test of lattice calculation: the Callan-Treiman relation

2509 As described in Sec. 4.4.3 the Callan-Treiman relation fixes the value of scalar form  
2510 factor at  $t = m_K^2 - m_\pi^2$  (the so-called Callan-Treiman point) to the ratio  $(f_K/f_\pi)/f_+(0)$ .

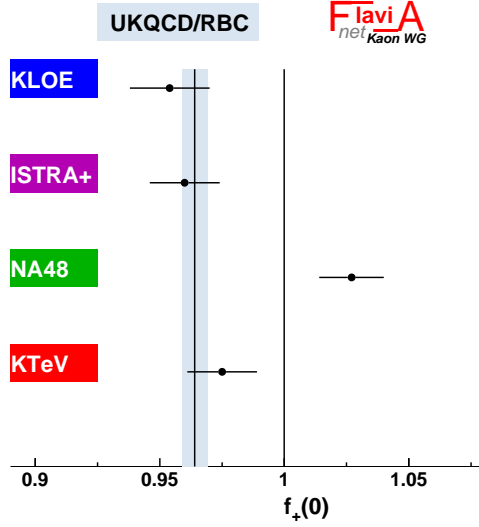


Fig. 24. Values for  $f_+(0)$  determined from the scalar form factor slope using the Callan-Treiman relation and  $f_K/f_\pi = 1.189(7)$ . The UKQCD/RBC result  $f_+(0) = 0.964(5)$  is also shown.

2511 The dispersive parametrization for the scalar form factor proposed in [322] and dis-  
 2512 cussed in Sec. 4.4.3 allows the available measurements of the scalar form factor to be  
 2513 transformed into a precise information on  $(f_K/f_\pi)/f_+(0)$ , completely independent of the  
 2514 lattice estimates.

2515 Very recently KLOE [390], KTeV [391], ISTRA+ [392], and NA48 [366] have produced  
 2516 results on the scalar FF behavior using the dispersive parametrization. The results are  
 2517 given in Tab. 23 for all four experiments.

Table 23

Experimental results for  $\log(C)$ .

Experiment	$\log(C)$	mode
KTeV	0.195(14)	$K_{L\mu 3}$
KLOE	0.217(16)	$K_{L\mu 3}$ and $K_{Le 3}$
NA48	0.144(14)	$K_{L\mu 3}$
ISTRA+	0.211(13)	$K_{\mu 3}^-$

2518 Fig. 24 shows the values for  $f_+(0)$  determined from the scalar form factor slope mea-  
 2519 surements obtained using the Callan-Treiman relation and  $f_K/f_\pi = 1.189(7)$ . The value  
 2520 of  $f_+(0) = 0.964(5)$  from UKQCD/RBC is also shown. As already noted in Sec. 4.4.5,  
 2521 the NA48 result is difficult to accommodate. Here one can see that this results is also  
 2522 inconsistent with the theoretical estimates of  $f_+(0)$ . In particular, it violates the Fubini-  
 2523 Furlan bound  $f_+(0) < 1$  [393]. For this reason, the NA48 result will be excluded when  
 2524 using the Callan-Treiman constraint.

2525 We combine the average of the above results,  $\log C = 0.207 \pm 0.008$ , with the lattice  
 2526 determinations of  $f_K/f_\pi = 1.189(7)$  and  $f_+(0) = 0.964(5)$  using the constraint given by  
 the Callan-Treiman relation. The results of the combination are given in Tab. 24. The fit

Table 24

Results from the form factor fit.

$\log C$	$f_+(0)$	$f_K/f_\pi$
0.204(6)	0.964(4)	1.187(6)
correlation matrix		
1.	-0.44	0.52
	1.	0.28
		1.

2527

2528 probability is 99%, confirming the agreement between experimental measurements and  
 2529 lattice determinations. The accuracies of  $f_K/f_\pi$  and  $f_+(0)$  are also slightly improved,  
 2530 and this effect can be better seen in the ratio  $f_+(0)/(f_K/f_\pi)$ , which is directly related  
 2531 to the Callan-Treiman constraint.

2532 *Determination of  $|V_{us}|/|V_{ud}| \times f_K/f_\pi$*

2533 An independent determination of  $|V_{us}|$  is obtained from  $K_{\ell 2}$  decays. The most impor-  
 2534 tant mode is  $K^+ \rightarrow \mu^+ \nu$ , which has been measured by KLOE with a relative uncertainty  
 2535 of about 0.3%. Hadronic uncertainties are minimized by making use of the ratio  $\Gamma(K^+ \rightarrow$   
 2536  $\mu^+ \nu)/\Gamma(\pi^+ \rightarrow \mu^+ \nu)$ .

Using the world average values of  $\text{BR}(K^\pm \rightarrow \mu^\pm \nu)$  and of  $\tau^\pm$  given in Sec. 4.4.5 and  
 the value of  $\Gamma(\pi^\pm \rightarrow \mu^\pm \nu) = 38.408(7) \mu\text{s}^{-1}$  from [283] we obtain:

$$|V_{us}|/|V_{ud}| \times f_K/f_\pi = 0.2758 \pm 0.0007 . \quad (175)$$

#### 2537 4.6.3. Test of Cabibbo Universality or CKM unitarity

2538 To determine  $|V_{us}|$  and  $|V_{ud}|$  we use the value  $|V_{us}| \times f_+(0) = 0.2166(5)$  reported in  
 2539 Tab. 22, the result  $|V_{us}|/|V_{ud}|f_K/f_\pi = 0.2758(7)$  discussed in Sec. 4.6.2,  $f_+(0) = 0.964(5)$ ,  
 2540 and  $f_K/f_\pi = 1.189(7)$ . From the above we find:

$$|V_{us}| = 0.2246 \pm 0.0012 \quad [K_{\ell 3} \text{ only}] , \quad (176)$$

$$|V_{us}|/|V_{ud}| = 0.2319 \pm 0.0015 \quad [K_{\ell 2} \text{ only}] . \quad (177)$$

A slightly less precise determination of  $|V_{us}|/|V_{ud}| = 0.2304^{(+0.0026)}_{(-0.0015)}$  is obtained using  
 the value of  $f_K/f_\pi$  from MILC [106]. These determinations can be used in a fit together  
 with the the evaluation of  $|V_{ud}|$  from  $0^+ \rightarrow 0^+$  nuclear beta decays quoted in section 4.1:  
 $|V_{ud}| = 0.97425 \pm 0.00022$ . The global fit gives

$$|V_{ud}| = 0.97425(22) \quad |V_{us}| = 0.2252(9) \quad [K_{\ell 3, \ell 2} + 0^+ \rightarrow 0^+] , \quad (178)$$

with  $\chi^2/\text{ndf} = 0.52/1$  (47%). This result does not make use of CKM unitarity. If the  
 unitarity constraint is included, the fit gives

$$|V_{us}| = \sin \theta_C = \lambda = 0.2253(6) \quad [\text{with unitarity}] \quad (179)$$

2541 Both results are illustrated in Fig. 25.

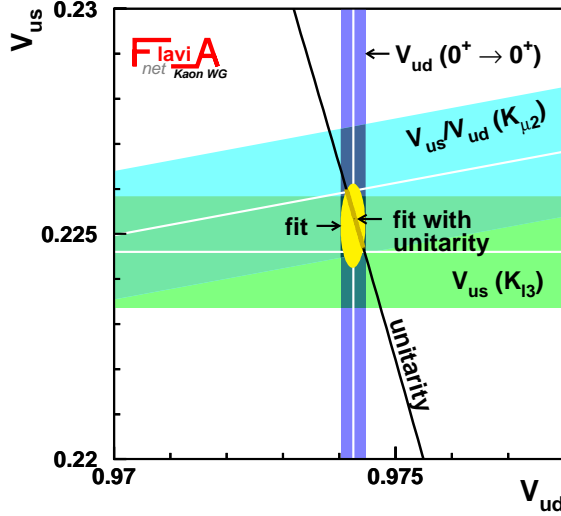


Fig. 25. Results of fits to  $|V_{ud}|$ ,  $|V_{us}|$ , and  $|V_{us}|/|V_{ud}|$ .

2542 Using the (rather negligible)  $|V_{ub}|^2 \simeq 1.5 \times 10^{-5}$  in conjunction with the above results  
 2543 leads to

$$|V_{ud}|^2 + |V_{us}|^2 + |V_{ub}|^2 = 0.9999(4)_{V_{ud}}(4)_{V_{us}} = 0.9999(6) \quad (180)$$

2544 The outstanding agreement with unitarity provides an impressive confirmation of Stan-  
 2545 dard Model radiative corrections [279,284](at about the 60 sigma level!). It can be used  
 2546 to constrain “new physics” effects which, if present, would manifest themselves as a  
 2547 deviation from 1, *i.e.* what would appear to be a breakdown of unitarity.

2548 We will give several examples of the utility Eq. (180) provides for constraining “new  
 2549 physics”. Each case is considered in isolation, *i.e.* it is assumed that there are no accidental  
 2550 cancellations.

### 2551 *Exotic Muon Decays*

2552 If the muon can undergo decay modes beyond the Standard Model  $\mu^+ \rightarrow e^+ \nu_e \bar{\nu}_\mu$  and  
 2553 its radiative extensions, those exotic decays will contribute to the muon lifetime. That  
 2554 would mean that the “real” Fermi constant,  $G_F$ , is actually smaller than the value in  
 2555 Eq. (107) and we should be finding

$$|V_{ud}|^2 + |V_{us}|^2 + |V_{ub}|^2 = 1 - BR(\text{exotic muon decays}) \quad (181)$$

2556 A unitarity sum below 1 could be interpreted as possible evidence for such decays.  
 2557 Alternatively, Eq. (180) provides at (one-sided) 95% CL

$$BR(\text{exotic muon decays}) < 0.001 \quad (182)$$

2558 That is, of course, not competitive with, for example, the direct bound  $BR(\mu^+ \rightarrow$   
 2559  $e^+ \gamma) < 1 \times 10^{-11}$  [283]. However, for decays such as  $\mu^+ \rightarrow e^+ \bar{\nu}_e \nu_\mu$  (wrong neutrinos),  
 2560 Eq. (182) is about a factor of 10 better than the direct constraint [283]  $BR(\mu^+ \rightarrow$



2561  $e^+\bar{\nu}_e\nu_\mu) < 0.012$ . That constraint is useful for possible future neutrino factories where  
 2562 the neutrino beams originate from muon decays. If such a decay were to exist, it would  
 2563 provide a background to neutrino oscillations.

2564 Another way to illustrate the above constraint is to extract the Fermi constant from  
 2565 nuclear,  $K$  and  $B$  decays assuming the validity of CKM unitarity without employing  
 2566 muon decay. Values in Eq. 178 give

$$G_F^{\text{CKM}} = 1.166279(261) \times 10^{-5} \text{GeV}^{-2} \quad \text{CKM Unitarity} \quad (183)$$

2567 which is in fact the second best determination of  $G_F$ , after Eq. (107). The comparison  
 2568 between  $G_\mu$  in Eq. (107) and  $G_F^{\text{CKM}}$  in Eq. (183) is providing the constraints on “new  
 2569 physics”, if it affects them differently. So far, they are equal to within errors.

### 2570 *Heavy Quarks and Leptons*

2571 As a second example, consider the case of new heavy quarks or leptons that couple to  
 2572 the ordinary 3 generations of fermions via mixing [268]. For a generic heavy charge  $-1/3$   
 2573  $D$  quark from a 4th generation, mirror fermions,  $SU(2)_L$  singlets etc., one finds at the  
 2574 one-sided 95% CL

$$|V_{uD}| \leq 0.03 \quad (184)$$

2575 Considering that  $|V_{ub}| \simeq 0.004$ , such an indirect constraint appears not to be very  
 2576 stringent but it can be useful in some models to rule out large loop induced effects from  
 2577 mixing. In the case of heavy neutrinos with  $m_N > m_\mu$ , one finds similarly

$$|V_{\ell N}| < 0.03 \quad , \quad \ell = e, \mu \quad (185)$$

### 2578 *Four Fermion Operators*

2579 If there are induced dim. 6 four fermion operators of the form

$$\mp i \frac{2\pi}{\Lambda^2} \bar{u} \gamma_\mu d \bar{e}_L \gamma^\mu \nu_e \quad (186)$$

2580 where  $\Lambda$  is a high effective mass scale due to compositeness, leptoquarks, excited  $W^*$   
 2581 bosons (*e.g.* extra dimensions) or even heavy loop effects, they will interfere with the  
 2582 Standard Model beta decay amplitudes and give  $G_F^{\text{CKM}} = G_\mu \left(1 \pm \frac{\sqrt{2}\pi}{G_\mu \Lambda^2}\right)$ . One finds at  
 2583 90%CL

$$\Lambda > 30 \text{ TeV} \quad (187)$$

2584 Similar constraints apply to new 4 fermion lepton operators that contribute to  $\mu^+ \rightarrow$   
 2585  $e^+\nu_e\bar{\nu}_\mu$ . Of course, in some cases there can be a cancellation between semileptonic and  
 2586 purely leptonic effects and no bound results.

2587 The high scale bounds in Eq. (187) apply most directly to compositeness because no  
 2588 coupling suppression was assumed. For leptoquarks,  $W^*$  bosons etc. the bounds should  
 2589 be about an order of magnitude smaller due to weak couplings. A  $m_{W^*}$  bound of about  
 2590 4~6 TeV results if we assume it affects leptonic and semileptonic decays very differently;  
 2591 but that assumption may not be valid and may need to be relaxed (see below). In the  
 2592 case of new loop effects, those bounds should be further reduced by another order of

2593 magnitude. For example, we next consider the effect of heavy  $Z'$  bosons in loops that  
 2594 enter muon and charged current semileptonic decays differently where a bound of about  
 2595 400 GeV is obtained.

2596 *Additional  $Z'$  Gauge Bosons*

2597 As next example, we consider the existence of additional  $Z'$  bosons that influence  
 2598 unitarity at the loop level by affecting muon and semi-leptonic beta decays differently  
 2599 [394]. In general, we found that the unitarity sum was predicted to be greater than one  
 2600 in most scenarios. In fact, one expects

$$|V_{ud}|^2 + |V_{us}|^2 + |V_{ub}|^2 = 1 + 0.01\lambda\ell n X/(X-1)$$

$$X = m_{Z'}^2/m_W^2 \quad (188)$$

2601 where  $\lambda$  is a model dependent quantity of  $O(1)$ . It can have either sign, but generally  
 2602  $\lambda > 0$ .

2603 In the case of SO(10) grand unification  $Z' = Z_\chi$  with  $\lambda \simeq 0.5$ , one finds at one-sided  
 2604 90% CL

$$m_{Z_\chi} > 400\text{GeV} \quad (189)$$

2605 That bound is somewhat smaller than tree level bounds on  $Z'$  bosons from atomic  
 2606 parity violation and polarized Moller scattering [395, 396] as well as the direct collider  
 2607 search bounds [283]  $m_{Z_\chi} > 720$  GeV.

2608 *Charged Higgs Bosons*

A particularly interesting test is the comparison of the  $|V_{us}|$  value extracted from the  
 helicity-suppressed  $K_{\ell 2}$  decays with respect to the value extracted from the helicity-  
 allowed  $K_{\ell 3}$  modes. To reduce theoretical uncertainties from  $f_K$  and electromagnetic  
 corrections in  $K_{\ell 2}$ , we exploit the ratio  $Br(K_{\ell 2})/Br(\pi_{\ell 2})$  and we study the quantity

$$R_{l23} = \left| \frac{V_{us}(K_{\ell 2})}{V_{us}(K_{\ell 3})} \times \frac{V_{ud}(0^+ \rightarrow 0^+)}{V_{ud}(\pi_{\ell 2})} \right|. \quad (190)$$

2609 Within the SM,  $R_{l23} = 1$ , while deviation from 1 can be induced by non-vanishing scalar-  
 2610 or right-handed currents. Notice that in  $R_{l23}$  the hadronic uncertainties enter through  
 2611  $(f_K/f_\pi)/f_+(0)$ .

Effects of scalar currents due to a charged Higgs give [344]

$$R_{l23} = \left| 1 - \frac{m_{K^+}^2}{M_{H^+}^2} \left( 1 - \frac{m_d}{m_s} \right) \frac{\tan^2 \beta}{1 + \epsilon_0 \tan \beta} \right|, \quad (191)$$

whereas for right-handed currents we have

$$R_{l23} = 1 - 2 (\epsilon_s - \epsilon_{ns}) . \quad (192)$$

In the case of scalar densities (MSSM), the unitarity relation between  $|V_{ud}|$  extracted  
 from  $0^+ \rightarrow 0^+$  nuclear beta decays and  $|V_{us}|$  extracted from  $K_{\ell 3}$  remains valid as soon  
 as form factors are experimentally determined. This constrain together with the experi-  
 mental information of  $\log C^{MSSM}$  can be used in the global fit to improve the accuracy  
 of the determination of  $R_{l23}$ , which in this scenario turns to be

$$R_{l23}|_{\text{scalar}}^{\text{exp}} = 1.004 \pm 0.007 . \quad (193)$$

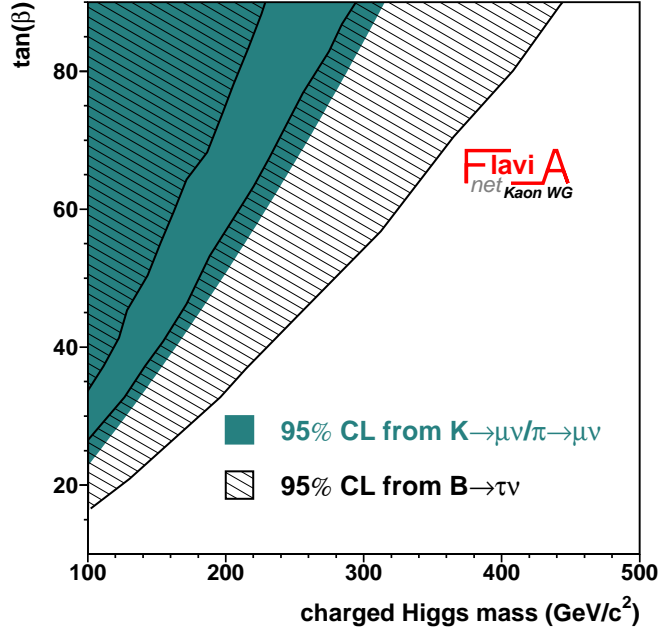


Fig. 26. Excluded region in the charged Higgs mass- $\tan\beta$  plane. The region excluded by  $B \rightarrow \tau\nu$  is also indicated.

2612 Here  $(f_K/f_\pi)/f_+(0)$  has been fixed from lattice. This ratio is the key quantity to be  
 2613 improved in order to reduce present uncertainty on  $R_{l23}$ .

2614 The measurement of  $R_{l23}$  above can be used to set bounds on the charged Higgs mass  
 2615 and  $\tan\beta$ . Fig. 26 shows the excluded region at 95% CL in the  $M_H$ - $\tan\beta$  plane (setting  
 2616  $\epsilon_0 = 0.01$ ). The measurement of  $\text{BR}(B \rightarrow \tau\nu)$  [145, 146, 397] can be also used to set a  
 2617 similar bound in the  $M_H$ - $\tan\beta$  plane. While  $B \rightarrow \tau\nu$  can exclude quite an extensive  
 2618 region of this plane, there is an uncovered region in the exclusion corresponding to a  
 2619 destructive interference between the charged-Higgs and the SM amplitude. This region  
 2620 is fully covered by the  $K \rightarrow \mu\nu$  result.

In the case of right-handed currents [322],  $R_{l23}$  can be obtained from a global fit to  
 the values of eqs. (174) and (175). Here  $\log C^{\text{exp}}$  is free of new physics effects and can be  
 also used to constrain  $(f_K/f_\pi)/f_+(0)$  together with lattice results (namely the values in  
 Tab. 24). The result is

$$R_{l23}|_{\text{RHcurr.}}^{\text{exp}} = 1.004 \pm 0.006 . \quad (194)$$

2621 In addition, interesting unitarity constraints can be placed on supersymmetry [398–400]  
 2622 where SUSY loops affect muon and semileptonic decays differently. Again, one expects  
 2623 constraints up to mass scales of  $O(500 \text{ GeV})$ , depending on the degree of cancellation  
 2624 between squark and slepton effects.

2625 In the future, the unitarity constraint could improve from  $\pm 0.0006$  to  $\pm 0.0004$  if  $f_+(0)$   
 2626 and  $f_K/f_\pi$  errors as well as uncertainties from radiative corrections can be reduced. Such  
 2627 an improvement will be difficult, but particularly well motivated if an apparent violation

2628 starts to emerge or the LHC makes a relevant “new physics” discovery.

2629 As an added comment, we again mention that eqs. (107) and (183) represent our two  
 2630 best measurements of the Fermi constant. Their agreement reinforces the validity of using  
 2631  $G_\mu$  to normalize electroweak charged and neutral current amplitudes in other precision  
 2632 searches for “new physics”. In fact, either  $G_\mu$  or  $G_F^{\text{CKM}}$  could be used without much  
 2633 loss of sensitivity, since all other experiments are currently less precise than both. For  
 2634 example, one of the next best determinations of the Fermi constant (which is insensitive  
 2635 to  $m_t$ ) comes from [284]

$$G_F^{(2)} = \frac{\pi\alpha}{\sqrt{2}m_W^2 \sin^2 \theta_W(m_Z)_{\overline{MS}}(1 - \Delta r(m_Z)_{\overline{MS}})} \quad (195)$$

2636 where

$$\alpha^{-1} = 137.035999084(51) \quad (196a)$$

$$m_W = 80.398(25) \text{ GeV} \quad (196b)$$

$$\sin^2 \theta_W(m_Z)_{\overline{MS}} = 0.23125(16) \quad (196c)$$

$$\Delta r(m_Z)_{\overline{MS}} = 0.0696(2) \quad (196d)$$

2637 One finds

$$G_F^{(2)} = 1.165629(1100) \times 10^{-5} \text{ GeV}^{-2} \quad (197)$$

2638 with an uncertainty about 180 times larger than  $G_\mu$  and about 4 times larger than  
 2639  $G_F^{\text{CKM}}$ . The value in Eq. (197) is, nevertheless, very useful for constraining “new physics”  
 2640 that affects it differently than  $G_\mu$  or  $G_F^{\text{CKM}}$ . Perhaps the two best examples are the  $S$   
 2641 parameter [401, 402]

$$S \simeq \frac{1}{6\pi} N_D \quad (198)$$

2642 which depends on the number of new heavy  $\text{SU}(2)_L$  doublets (e.g.  $N_D = 4$  in the case  
 2643 of a 4th generation) and a generic  $W^*$  Kaluza-Klein excitation associated with extra  
 2644 dimensions [284] that has the same quark and lepton couplings. Either would contribute  
 2645 to  $G_\mu$  or  $G_F^{\text{CKM}}$  but not to  $G_F^{(2)}$ . Therefore, one has the relation

$$G_\mu \simeq G_F^{\text{CKM}} \simeq G_F^{(2)}(1 + 0.0085S + \mathcal{O}(1)\frac{m_W^2}{m_{W^*}^2}) \quad (199)$$

2646 The good agreement among all three Fermi constants then suggests  $m_{W^*} > 2$   
 2647  $\sim 3$  TeV and  $S \simeq 0.1 \pm 0.1$  (consistent with zero). Those constraints are similar to  
 2648 what is obtained from global fits to all electroweak data. Taken at face value they sug-  
 2649 gest any “new physics” near the TeV scale that we hope to unveil at the LHC is hiding  
 2650 itself quite well from us in precision low energy data. It will be interesting to see what  
 2651 the LHC finds.

#### 2652 4.6.4. Tests of Lepton Flavor Universality in $K_{\ell 2}$ decays

The ratio  $R_K = \Gamma(K_{\mu 2})/\Gamma(K_{e 2})$  can be precisely calculated within the Standard Model. Neglecting radiative corrections, it is given by

$$R_K^{(0)} = \frac{m_e^2}{m_\mu^2} \frac{(m_K^2 - m_e^2)^2}{(m_K^2 - m_\mu^2)^2} = 2.569 \times 10^{-5}, \quad (200)$$

and reflects the strong helicity suppression of the electron channel. Radiative corrections have been computed with effective theories [298], yielding the final SM prediction

$$\begin{aligned} R_K^{\text{SM}} &= R_K^{(0)} (1 + \delta R_K^{\text{rad.corr.}}) \\ &= 2.569 \times 10^{-5} \times (0.9622 \pm 0.0004) = (2.477 \pm 0.001) \times 10^{-5}. \end{aligned} \quad (201)$$

Because of the helicity suppression within the SM, the  $K_{e2}$  amplitude is a prominent candidate for possible sizable contributions from physics beyond the SM. Moreover, when normalizing to the  $K_{\mu 2}$  rate, we obtain an extremely precise prediction of the  $K_{e2}$  width within the SM. In order to be visible in the  $K_{e2}/K_{\mu 2}$  ratio, the new physics must violate lepton flavor universality.

Recently it has been pointed out that in a supersymmetric framework sizable violations of lepton universality can be expected in  $K_{l2}$  decays [403]. At the tree level, lepton flavor violating terms are forbidden in the MSSM. However, these appear at the one-loop level, where an effective  $H^+ l \nu_\tau$  Yukawa interaction is generated. Following the notation of Ref. [403], the non-SM contribution to  $R_K$  can be written as

$$R_K^{\text{LFV}} \approx R_K^{\text{SM}} \left[ 1 + \left( \frac{m_K^4}{M_{H^\pm}^4} \right) \left( \frac{m_\tau^2}{m_e^2} \right) |\Delta_{13}|^2 \tan^6 \beta \right]. \quad (202)$$

The lepton flavor violating coupling  $\Delta_{13}$ , being generated at the loop level, could reach values of  $\mathcal{O}(10^{-3})$ . For moderately large  $\tan \beta$  values, this contribution may therefore enhance  $R_K$  by up to a few percent. Since the additional term in Eq. 202 goes with the fourth power of the meson mass, no similar effect is expected in  $\pi_{l2}$  decays.

The world average result for  $R_K$  presented in Sec. 4.4.5 gives strong constraints for  $\tan \beta$  and  $M_{H^\pm}$ , as shown in Fig. 27. For values of  $\Delta_{13} \approx 10^{-3}$  and  $\tan \beta > 50$  the charged Higgs masses is pushed above 1000 GeV/ $c^2$  at 95% CL.

## 5. Semileptonic $B$ and $D$ decays: $|V_{cx}|$ and $|V_{ub}|$

In this section, we address semileptonic decays that proceed at the tree level of the weak interaction. We focus on decays of the lightest pseudoscalar mesons,  $D$  for charm and  $B$  for bottom, because higher excitations decay hadronically (or, in case of the  $B^*$ , radiatively) to the  $D$  and  $B$  and thus have negligibly small semileptonic partial widths. The amplitude for quark flavor change in these processes is proportional to a CKM matrix element, providing a direct way to “measure” the CKM matrix.

Purely leptonic decays of pseudoscalars are, of course, also directly sensitive to the CKM matrix, but they require a spin flip. Their rate is, hence, helicity suppressed by a factor  $(m_\ell/m_P)^2$ , where  $m_P$  is the pseudoscalar meson mass and  $m_\ell$  the mass of the daughter lepton. This suppression makes purely leptonic decays more sensitive to non-Standard processes, and therefore less reliable channels for the determination of CKM matrix elements than semileptonic decays.

As with the determination of  $|V_{us}|$  in the semileptonic decay  $K \rightarrow \pi \ell \nu$ , discussed in Sec. 4, one can determine  $|V_{cs}|$  from  $D \rightarrow K \ell \nu$ ,  $|V_{cd}|$  from  $D \rightarrow \pi \ell \nu$ ,  $|V_{ub}|$  from  $B \rightarrow \pi \ell \nu$ , and  $|V_{cb}|$  from  $B \rightarrow D^{(*)} \ell \nu$ , by combining measurements of the differential decay

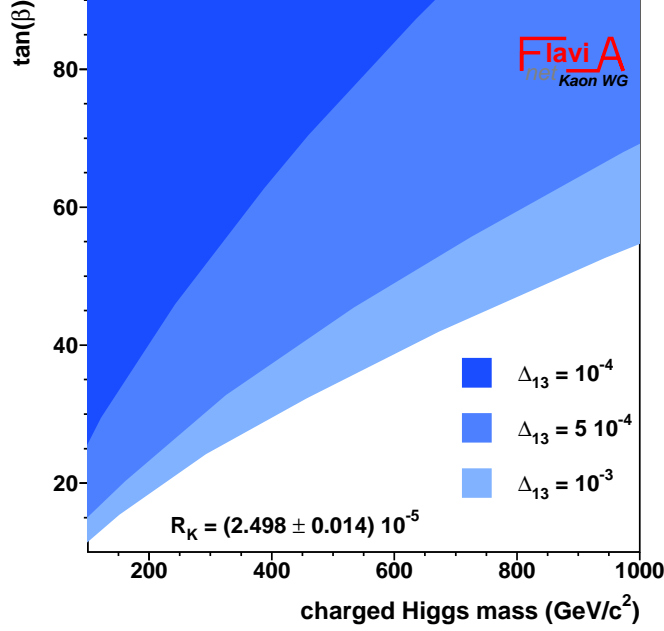


Fig. 27. Exclusion limits at 95% CL on  $\tan\beta$  and the charged Higgs mass  $M_{H\pm}$  from  $R_K$  for different values of  $\Delta_{13}$ .

2683 rate with lattice-QCD calculations for the hadronic part of the transition, commonly  
 2684 described with form factors. This section starts with the three heavy-to-light decays,  
 2685 and then proceeds to heavy-to-heavy decays for which heavy-quark symmetry plays a  
 2686 crucial role.  $|V_{cb}|$  and  $|V_{ub}|$  can also be determined from *inclusive* semileptonic  $B$  decays,  
 2687 because the large energy scale  $m_b$  and the inclusion of all final-state hadrons makes  
 2688 these processes amenable to the operator-product expansion (OPE). Within the OPE  
 2689 the short-distance QCD can be calculated in perturbation theory, and the long-distance  
 2690 QCD can be measured from kinematic distributions. While this is rather straightforward  
 2691 for  $|V_{cb}|$  it is more subtle  $|V_{ub}|$  so these two topics are treated in separate subsections.

## 2692 5.1. Exclusive semileptonic $B$ and $D$ decays to light mesons $\pi$ and $K$

### 2693 5.1.1. Theoretical Background

2694 Heavy-to-light semileptonic decays, in which a  $B$  or  $D$  meson decays into a light  
 2695 pseudoscalar or vector meson (such as a pion or  $\rho$  meson), are sensitive probes of quark  
 2696 flavor-changing interactions. The decay rate for  $H \rightarrow P\ell\nu$  semileptonic decay is given by

$$\frac{d\Gamma}{dq^2} = \frac{G_F^2 |V_{qQ}|^2 (q^2 - m_\ell^2)^2 \sqrt{E_P^2 - m_P^2}}{24\pi^3 q^4 m_H^2} \left\{ \left( 1 + \frac{m_\ell^2}{2q^2} \right) m_H^2 (E_P^2 - m_P^2) [f_+(q^2)]^2 + \frac{3m_\ell^2}{8q^2} (m_H^2 - m_P^2)^2 [f_0(q^2)]^2 \right\}, \quad (203)$$

where  $q \equiv p_H - p_P$  is the momentum transferred to the lepton pair and  $|V_{qQ}|$  is the relevant CKM matrix element. The form factors,  $f_+(q^2)$  and  $f_0(q^2)$ , parametrize the hadronic matrix element of the heavy-to-light vector current,  $V^\mu \equiv i\bar{q}\gamma^\mu Q$ :

$$\langle P|V^\mu|H\rangle = f_+(q^2) \left( p_H^\mu + p_P^\mu - \frac{m_H^2 - m_P^2}{q^2} q^\mu \right) + f_0(q^2) \frac{m_H^2 - m_P^2}{q^2} q^\mu, \quad (204)$$

where  $E_P = (m_H^2 + m_P^2 - q^2)/2m_H$  is the energy of the light meson in the heavy meson's rest frame. The kinematics of semileptonic decay require that the form factors are equal at zero momentum-transfer,  $f_+(0) = f_0(0)$ . In the limit  $m_\ell \rightarrow 0$ , which is a good approximation for  $\ell = e, \mu$ , the form factor  $f_0(q^2)$  drops out and the expression for the decay rate simplifies to

$$\frac{d\Gamma}{dq^2} = \frac{G_F^2 |V_{qQ}|^2}{192\pi^3 m_H^3} [(m_H^2 + m_P^2 - q^2)^2 - 4m_H^2 m_P^2]^{3/2} |f_+(q^2)|^2. \quad (205)$$

2697 Using the above expression, a precise experimental measurement of the decay rate, in  
2698 combination with a controlled theoretical calculation of the form factor, allows for a clean  
2699 determination of the CKM matrix element  $|V_{qQ}|$ .

### 2700 Analyticity and unitarity

2701 It is well-established that the general properties of analyticity and unitarity largely  
2702 constrain the shapes of heavy-to-light semileptonic form factors [404–408]. All form fac-  
2703 tors are analytic in  $q^2$  except at physical poles and threshold branch points. Because  
2704 analytic functions can always be expressed as convergent power series, this allows the  
2705 form factors to be written in a particularly useful manner.

Consider a change of variables that maps  $q^2$  in the semileptonic region onto a unit circle:

$$z(q^2, t_0) = \frac{\sqrt{1 - q^2/t_+} - \sqrt{1 - t_0/t_+}}{\sqrt{1 - q^2/t_+} + \sqrt{1 - t_0/t_+}}, \quad (206)$$

where  $t_+ \equiv (m_H + m_P)^2$ ,  $t_- \equiv (m_H - m_P)^2$ , and  $t_0$  is a constant to be discussed later. In terms of this new variable,  $z$ , the form factors have a simple form:

$$P(q^2)\phi(q^2, t_0)f(q^2) = \sum_{k=0}^{\infty} a_k(t_0)z(q^2, t_0)^k. \quad (207)$$

In order to preserve the analytic structure of  $f(q^2)$ , the function  $P(q^2)$  vanishes at poles below the  $H$ - $P$  pair-production threshold that contribute to  $H$ - $P$  pair-production as virtual intermediate states. For example, in the case of  $B \rightarrow \pi\ell\nu$  decay,  $P(q^2)$  incorporates the location of the  $B^*$  pole:

$$P_+^{B \rightarrow \pi\ell\nu}(q^2) = z(q^2, m_{B^*}). \quad (208)$$

2706 For the case of  $D$  meson semileptonic decays, the mass of the  $D^*$  meson is above the  
2707  $D$ - $\pi$  production threshold, but the  $D_s^*$  is below  $D$ - $K$  production threshold. Hence

$$P_+^{D \rightarrow \pi\ell\nu}(q^2) = 1, \quad (209)$$

$$P_+^{D \rightarrow K\ell\nu}(q^2) = z(q^2, m_{D_s^*}). \quad (210)$$

2708 In the expression for  $f(q^2)$ , Eq. (207),  $\phi(q^2, t_0)$  is any analytic function. It can be chosen,  
2709 however, to make the unitarity constraint on the series coefficients have a simple form.  
2710 The standard choice for  $\phi_+(q^2, t_0)$ , which enters the expression for  $f_+(q^2)$ , is [408]:

Table 25

Physical region in terms of the variable  $z$  for various semileptonic decays given the choice  $t_0 = 0.65t_-$ .

$$\underline{\underline{B \rightarrow \pi l \nu \quad -0.34 < z < 0.22}}$$

$$D \rightarrow \pi l \nu \quad -0.17 < z < 0.16$$

$$\underline{\underline{D \rightarrow K l \nu \quad -0.04 < z < 0.06}}$$

$$\begin{aligned} \phi_+(q^2, t_0) = & \sqrt{\frac{3}{96\pi\chi_J^{(0)}}} \left( \sqrt{t_+ - q^2} + \sqrt{t_+ - t_0} \right) \left( \sqrt{t_+ - q^2} + \sqrt{t_+ - t_-} \right)^{3/2} \\ & \times \left( \sqrt{t_+ - q^2} + \sqrt{t_+} \right)^{-5} \frac{(t_+ - q^2)}{(t_+ - t_0)^{1/4}}, \end{aligned} \quad (211)$$

2711 where  $\chi_J^{(0)}$  is a numerical factor that can be calculated using perturbation theory and  
 2712 the operator product expansion. A similar function can be derived for the irrelevant form  
 2713 factor  $f_0(q^2)$ .

Given the above choices for  $P(q^2)$  and  $\phi(q^2, t_0)$ , unitarity constrains the size of the series coefficients:

$$\sum_{k=0}^N a_k^2 \lesssim 1, \quad (212)$$

where this holds for any value of  $N$ . In the case of the  $B \rightarrow \pi l \nu$  form factor, the sizes of the series coefficients ( $a_k$ s) turn out to be much less than 1 [409]. Becher and Hill recently pointed out that this is due to the fact that the  $b$ -quark mass is so large, and used heavy-quark power-counting to derive a tighter constraint on the  $a_k$ s:

$$\sum_{k=0}^N a_k^2 \leq \left( \frac{\Lambda}{m_Q} \right)^3, \quad (213)$$

2714 where  $\Lambda$  is a typical hadronic scale [410]. The above expression suggests that the series  
 2715 coefficients should be larger for  $D$ -meson form factors than for  $B$ -meson form factors.  
 2716 This, however, has not been tested.

2717 In order to accelerate the convergence of the power-series in  $z$ , the free parameter  
 2718  $t_0$  in Eq. (206) can be chosen to make the range of  $|z|$  as small as possible. For the  
 2719 value  $t_0 = 0.65t_-$  used in Ref. [408], the ranges of  $|z|$  for some typical heavy-to-light  
 2720 semileptonic decays are given in Tab. 25. The tight heavy-quark constraint on the size of  
 2721 the coefficients in the  $z$ -expansion, in conjunction with the small value of  $|z|$ , ensures that  
 2722 only the first few terms in the series are needed to describe heavy-to-light semileptonic  
 2723 form factors to a high accuracy.

2724 Other model-independent parameterizations of heavy-to-light semileptonic form fac-  
 2725 tors base on analyticity and unitarity have been proposed and applied to the case of  $B \rightarrow$   
 2726  $\pi l \nu$  decay by Bourrely, Caprini, and Lellouch [411] and by Flynn and Nieves [412, 413].  
 2727 Bourrely *et al.* use the series expansion in  $z$  described above, but choose simpler outer  
 2728 function,  $\phi(q^2, t_0) = 1$ . This leads, however, to a more complicated constraint on the  
 2729 series coefficients, which is no longer diagonal in the series index  $k$ . Flynn and Nieves use  
 2730 multiply-subtracted Omnès dispersion relations to parametrize the form factor shape in  
 2731 terms of the elastic  $B$ - $\pi$  scattering phase shift and the value of  $f_+(q^2)$  at a few subtraction  
 2732 points below the  $B$ - $\pi$  production threshold.

## 2733 Lattice QCD



In lattice-QCD calculations and in heavy-quark effective theory (HQET), it is easier to work with a different linear combination of the form factors:

$$\langle P|V^\mu|H\rangle = \sqrt{2m_H} [v^\mu f_{\parallel}(E_P) + p_{\perp}^\mu f_{\perp}(E_P)], \quad (214)$$

where  $v^\mu = p_H^\mu/m_H$  is the velocity of the heavy meson,  $p_{\perp}^\mu = p_P^\mu - (p_P \cdot v)v^\mu$  is the component of the light meson momentum perpendicular to  $v$ , and  $E_P = p_P \cdot v = (m_H^2 + m_P^2 - q^2)/(2m_H)$  is the energy of the light meson in the heavy meson's rest frame. In the heavy meson's rest frame, the form factors  $f_{\parallel}(E_P)$  and  $f_{\perp}(E_P)$  are directly proportional to the hadronic matrix elements of the temporal and spatial vector current:

$$f_{\parallel}(E_P) = \frac{\langle P|V^0|H\rangle}{\sqrt{2m_H}} \quad (215)$$

$$f_{\perp}(E_P) = \frac{\langle P|V^i|H\rangle}{\sqrt{2m_H}} \frac{1}{p_P^i}. \quad (216)$$

Lattice QCD simulations therefore typically determine  $f_{\parallel}(E_P)$  and  $f_{\perp}(E_P)$ , and then calculate the form factors that appear in the heavy-to-light decay width using the following equations:

$$f_0(q^2) = \frac{\sqrt{2m_H}}{m_H^2 - m_P^2} [(m_H - E_P)f_{\parallel}(E_P) + (E_P^2 - m_P^2)f_{\perp}(E_P)], \quad (217)$$

$$f_+(q^2) = \frac{1}{\sqrt{2m_H}} [f_{\parallel}(E_P) + (m_H - E_P)f_{\perp}(E_P)]. \quad (218)$$

These expressions automatically satisfy the kinematic constraint  $f_+(0) = f_0(0)$ .

The goal is to evaluate the hadronic matrix elements on the right-hand side of Eqs.(215) and (216) via numerical simulations in lattice QCD. Such simulations are carried out with operators,  $V_\mu^L$ , written in terms of the lattice heavy and light quark fields appearing in the lattice actions. Hence, an important step in any lattice determination of hadronic matrix elements is the matching between continuum operators such as  $V_\mu$  and their lattice counterparts. The matching takes the form

$$\langle P|V_\mu|H\rangle = Z_{V_\mu}^{Qq} \langle P|V_\mu^L|H\rangle. \quad (219)$$

For heavy-light currents with dynamical (as opposed to static) heavy quarks, the matching factors  $Z_{V_\mu}^{Qq}$  have been obtained to date either through a combination of perturbative and nonperturbative methods or via straight one-loop perturbation theory. Uncertainties in  $Z_{V_\mu}^{Qq}$  can be a major source of systematic error in semileptonic form factor calculations and methods are being developed for complete nonperturbative determinations in order to reduce such errors in the future.

Another important feature of lattice simulations is that calculations are carried out at nonzero lattice spacings and with *up*- and *down*-quark masses  $m_q$  that are larger than in the real world. Results are obtained for several lattice spacings and for a sequence of  $m_q$  values and one must then extrapolate to both the continuum and the physical quark mass limits. These two limits are intimately connected to each other, and it is now standard to use chiral perturbation theory ( $\chi$ Pt) that has been adapted to include discretization effects [414–419].

The initial pioneering work on  $B$  and  $D$  meson semileptonic decays on the lattice were all carried out in the quenched approximation [420–424]. This approximation which

2758 ignores effects of sea quark-antiquark pairs has now been overcome and most recent  
 2759 lattice calculations include vacuum polarization from  $N_f = 2 + 1$  or  $N_f = 2$  dynamical  
 2760 light quark flavors. Unquenched calculations of  $B \rightarrow \pi \ell \nu$  semileptonic decays have been  
 2761 carried out by the Fermilab/MILC and the HPQCD collaborations using the MILC  
 2762 collaboration  $N_f = 2 + 1$  configurations [409, 425, 426]. Both collaborations use improved  
 2763 staggered (AsqTad) quarks for light valence and sea quarks. They differ, however, in their  
 2764 treatment of the heavy  $b$  quark. Fermilab/MILC employs the heavy clover action and  
 2765 HPQCD the nonrelativistic NRQCD action. The dominant errors in both calculations are  
 2766 due to statistics and the chiral extrapolation. The next most important error stems from  
 2767 discretization corrections for the Fermilab/MILC and operator matching for the HPQCD  
 2768 collaborations, respectively. It is important that simulations based on other light quark  
 2769 lattice actions be pursued in the future as a cross check.

2770 In the case of  $D \rightarrow K$  and  $D \rightarrow \pi$  semileptonic decays, there exists to-date only one  
 2771  $N_f = 2 + 1$  calculation, again based on AsqTad light and clover heavy quarks, by the  
 2772 Fermilab Lattice and MILC collaborations [425]. Recently two groups have initiated  $N_f =$   
 2773  $2$  calculations, and their results are still at a preliminary stage. The ETM collaboration  
 2774 uses “twisted mass” light and charm quarks at maximal twist [427], whereas Bećirević,  
 2775 Haas and Mescia use improved Wilson quarks and configurations created by the QCDSF  
 2776 collaboration [428, 429]. The latter group employs double ratio methods and twisted  
 2777 boundary conditions to allow more flexibility in picking out many values of  $q^2$ . There has  
 2778 also been a recent exploratory study with improved Wilson quark action which, although  
 2779 still quenched, is at a very small lattice spacing of around 0.04 fm [430]. These authors  
 2780 have considered both  $B$  and  $D$  decays.

### 2781 Light-cone QCD Sum Rules

2782 Light-cone sum rules (LCSR) [431–433] combine the idea of the original QCD sum  
 2783 rules [434, 435] with the elements of the theory of hard exclusive processes. LCSR are  
 2784 used in a wide array of applications (for a review, see [436]), in particular, for calculating  
 2785  $B \rightarrow \pi, K, \eta, \rho, K^*$  and  $D \rightarrow \pi, K$  form factors [437–447]. The starting point is a specially  
 2786 designed correlation function where the product of two currents is sandwiched between  
 2787 the vacuum and an on-shell state. In the case of  $\bar{B}^0 \rightarrow \pi^+$  form factor

$$\begin{aligned}
 F_\mu(p, q) &= i \int d^4x e^{iqx} \langle \pi^+(p) | T \{ \bar{u} \gamma_\mu b(x), m_b \bar{b} i \gamma_5 d(0) \} | 0 \rangle \\
 &= \left( \frac{2f_B f_{B\pi}^+(q^2) m_B^2}{m_B^2 - (p+q)^2} + \sum_{B_h} \frac{2f_{B_h} f_{B_h\pi}^+(q^2) m_{B_h}^2}{m_{B_h}^2 - (p+q)^2} \right) p_\mu + O(q_\mu), \quad (220)
 \end{aligned}$$

2788 where the factor proportional to  $p_\mu$  is transformed into a hadronic sum by inserting a  
 2789 complete set of hadronic states between the currents. This sum also represents, schemat-  
 2790 ically, a dispersion integral over the hadronic spectral density. The lowest-lying  $B$ -state  
 2791 contribution contains the desired  $B \rightarrow \pi$  form factor multiplied by the  $B$  decay constant.

At spacelike  $(p+q)^2 \ll m_b^2$  and at small and intermediate  $q^2 \ll m_b^2$ , the time ordered  
 product in Eq. (220) may also be expanded near the light-cone  $x^2 \sim 0$ , thereby resumming  
 local operators into distribution amplitudes:

$$F((p+q)^2, q^2) = \sum_{t=2,3,4} \int D u_i \sum_{k=0,1} \left( \frac{\alpha_s}{\pi} \right)^k T_k^{(t)}((p+q)^2, q^2, u_i, m_b, \mu) \varphi_\pi^{(t)}(u_i, \mu). \quad (221)$$

2792 This generic expression is a convolution (at the factorization scale  $\mu$ ) of calculable short-  
2793 distance coefficient functions  $T_k^{(t)}$  and universal pion light-cone distribution amplitudes  
2794 (DA's)  $\varphi_\pi^{(t)}(u_i, \mu)$  of twist  $t \geq 2$ . The integration goes over the pion momentum fractions  
2795  $u_i = u_1, u_2, \dots$  distributed among quarks and gluons. Importantly, the contributions  
2796 to Eq. (221) corresponding to higher twist and/or higher multiplicity pion DA's are  
2797 suppressed by inverse powers of the  $b$ -quark virtuality  $((p+q)^2 - m_b^2)$ , allowing one to  
2798 retain a few low twist contributions in this expansion. Currently, analyses of Eq. (220)  
2799 can include all LO contributions of twist 2,3,4 quark-antiquark and quark-antiquark-  
2800 gluon DA's of the pion and the  $O(\alpha_s)$  NLO corrections to the twist 2 and 3 two-particle  
2801 coefficient functions.

Furthermore, one uses quark-hadron duality to approximate the sum over excited  $B_h$  states in Eq. (220) by the result from the perturbative QCD calculation introducing the effective threshold parameter  $s_0^B$ . The final step involves a Borel transformation  $(p+q)^2 \rightarrow M^2$ , where the scale of the Borel parameter  $M^2$  reflects the characteristic virtuality at which the correlation function is calculated. The resulting LCSR for the  $B \rightarrow \pi$  form factor has the following form

$$f_{B\pi}^+(q^2) = \frac{e^{m_B^2/M^2}}{2m_B^2 f_B} \frac{1}{\pi} \int_{m_b^2}^{s_0^B} ds \operatorname{Im} F^{(OPE)}(s, q^2) e^{-s/M^2}, \quad (222)$$

2802 where  $\operatorname{Im} F^{(OPE)}$  is directly calculated from the double expansion (221). The intrinsic  
2803 uncertainty introduced by the quark-hadron duality approximation is minimized by cal-  
2804 culating the  $B$  meson mass using the derivative of the same sum rule. The main input  
2805 parameters, apart from  $\alpha_s$  and  $b$  quark mass (taken in the  $\overline{\text{MS}}$  scheme), include the non-  
2806 perturbative normalization constants and nonasymptotic coefficients for each given twist  
2807 component, e.g., for the twist-2 pion DA  $\varphi_\pi$  these are  $f_\pi$  and the Gegenbauer moments  
2808  $a_i$ . For twist-3,4 the recent analysis can be found in Ref. [448]. For the  $B$ -meson decay  
2809 constant entering LCSR (222) one usually employs the conventional QCD sum rule for  
2810 the two-point correlator of  $\bar{b}i\gamma_5 q$  currents with  $O(\alpha_s)$  accuracy (the most complete sum  
2811 rule in  $\overline{\text{MS}}$ -scheme is presented in [449]). More details on the numerical results, sources  
2812 of uncertainties and their estimates can be found in the recent update [446]. Further  
2813 improvement of the LCSR calculation of heavy-to-light form factors is possible, if one  
2814 gets a better understanding of the quark-hadron duality approximation in  $B$  channel,  
2815 and a more accurate estimation of nonperturbative parameters of pion DA's.

2816 Despite their intrinsically approximate nature, LCSRs represent a useful analytic  
2817 method providing a unique possibility to calculate both hard and soft contributions to  
2818 the transition form factors. Different versions of LCSR employing  $B$ -meson distribution  
2819 amplitudes [450] as well as the framework of SCET [451, 452] have also been introduced.

### 2820 5.1.2. Measurements of $D$ Branching Fractions and $q^2$ Dependence

2821 In the last few years, a new level of precision has been achieved in measurements of  
2822 branching fractions and hadronic form factors for exclusive semileptonic  $D$  decays by the  
2823 Belle, BaBar, and CLEO collaborations. In this section, we focus on semileptonic decays,  
2824  $D \rightarrow P\ell\nu_\ell$ , where  $D$  represents a  $D^0$  or  $D^+$ ,  $P$  a pseudoscalar meson, charged or neutral,  
2825 either  $\pi$  or  $K$ , and  $\ell$  a muon or electron. In addition, we also present a BaBar analysis  
2826 of  $D_s^+ \rightarrow K^+ K^- \ell^+ \nu_\ell$ , which provided first evidence of an S-wave contribution.

2827 The results from the  $B$ -Factories (Babar and Belle) are based on very large samples of  
 2828  $D$  mesons produced via the process  $e^+e^- \rightarrow c\bar{c}$  recorded at about 10.58 GeV c.m. energy.  
 2829 CLEO-c experiment relies on a sample of  $\psi(3770) \rightarrow D\bar{D}$  events, which is smaller, but  
 2830 allows for very clean tags and excellent  $q^2$  resolution. Two of the four recent analyses tag  
 2831 events by reconstructing a hadronic decay of one of the  $D$  mesons in the event, in addition  
 2832 to the semileptonic decay of the other. The total number of tagged events serves as a  
 2833 measure of the total sample of  $D$  mesons and thus provides the absolute normalization for  
 2834 the determination of the semileptonic branching fractions. Untagged analyses typically  
 2835 rely on the relative normalization to a sample of  $D$  decays with a well measured branching  
 2836 fraction. The analyses use sophisticated techniques for background suppression (Fisher  
 2837 discriminants) and resolution enhancement (kinematic fits). The neutrino momentum  
 2838 and energy is equated with the reconstructed missing momentum and energy relying  
 2839 on energy-momentum conservation. The detailed implementation and resolution varies  
 2840 significantly among the measurements and cannot be presented here in detail.

2841 The BaBar Collaboration reports a study of  $D^0 \rightarrow K^-e^+\nu_e$  based on a luminosity of  
 2842  $75 \text{ fb}^{-1}$  [453]. They analyze  $D^{*+} \rightarrow D^0\pi^+$  decays, with  $D^0 \rightarrow K^-e^+\nu_e$ . The analysis  
 2843 exploits the two-jet topology of  $e^+e^- \rightarrow c\bar{c}$  events. The events are divided by the plane  
 2844 perpendicular to the event thrust axis into two halves, each equivalent to a jet produced  
 2845 by  $c$ - or  $\bar{c}$ -quark fragmentation. The energy of each jet is estimated from its measured  
 2846 mass and the total c.m. energy. To determine the momentum of the  $D$  and the energy of  
 2847 the neutrino a kinematic fit is performed to the total event, constraining the invariant  
 2848 mass of the  $K^-e^+\nu_e$  candidate to the  $D^0$  mass. The  $D$  direction is approximated by  
 2849 the direction opposite the vector sum of the momenta of all other particles in the event,  
 2850 except the Kaon and lepton associated with the signal candidate. The neutrino energy is  
 2851 estimated as the difference between the total energy of the jet containing the Kaon and  
 2852 charged lepton and the sum of the particle energies in that jet. To suppress combinatorial  
 2853 background each  $D^0$  candidate is combined with a  $\pi^+$  of the same charge as the lepton and  
 2854 the mass difference is required to be small,  $\delta M = M(D^0\pi^+) - M(D^0) < 0.160 \text{ GeV}$ . The  
 2855 background-subtracted  $q^2$  distribution is corrected for efficiency and detector resolution  
 2856 effects.

2857 For BaBar's analysis [453], the normalization of the form factor at  $q^2 = 0$  is  $f_+^K(0) =$   
 2858  $0.727 \pm 0.007 \pm 0.005 \pm 0.007$ , where the first error is statistical, the second systematic,  
 2859 and the third due to uncertainties of external input parameters. In addition to the tradi-  
 2860 tional parametrization of the form factors as a function of  $q^2$  using pole approximations,  
 2861 BaBar also performed a fit in terms of the expansion in the parameter  $z$ . The results are  
 2862 presented in Fig. 28. A fit to a polynomial shows that data are compatible with a linear  
 2863 dependence, which is fully consistent with the modified pole ansatz for  $f_+(q^2)$ .

2864 BaBar also reports the branching fraction for  $D^0 \rightarrow K^-e^+\nu_e$ . To obtain the nor-  
 2865 malization for the signal sample, they perform a largely identical analysis to isolate  
 2866 a sample of  $D^0 \rightarrow K^-\pi^+$  decays, and combine it with the world average  $\mathcal{B}(D^0 \rightarrow$   
 2867  $K^-\pi^+) = (3.80 \pm 0.07)\%$ . The result, the ratio of branching fractions,  $R_D = \mathcal{B}(D^0 \rightarrow$   
 2868  $K^-e^+\nu_e)/\mathcal{B}(D^0 \rightarrow K^-\pi^+) = 0.927 \pm 0.007 \pm 0.012$ , translates to  $\mathcal{B}(D^0 \rightarrow K^-e^+\nu_e) =$   
 2869  $(3.522 \pm 0.027 \pm 0.045 \pm 0.065)\%$ , where the last error represents the uncertainty of  
 2870  $\mathcal{B}(D^0 \rightarrow K^-\pi^+)$ .

2871 The Belle Collaboration has analyzed a sample of  $282 \text{ fb}^{-1}$ , recorded at or just below  
 2872 the  $\Upsilon(4S)$  resonance [454]. They search for the process,  $e^+e^- \rightarrow c\bar{c} \rightarrow D_{\text{tag}}^{(*)}D_{\text{sig}}^{*+}X$ , with

2873  $D_{\text{sig}}^{*+} \rightarrow D^0 \pi_{\text{soft}}^+$  [454]. Here  $X$  represents additional particles from  $c$ -quark fragmentation.  
 2874 The  $D_{\text{tag}}$  is reconstructed as a  $D^0$  or  $D^+$ , in decay modes  $D \rightarrow K(n\pi)$  with  $n =$   
 2875  $1, 2, 3$ . In events that contain a  $D_{\text{sig}}^{*+}$ , the recoil of the  $D_{\text{tag}}^{(*)} X \pi_{\text{soft}}^+$  provides an estimate  
 2876 of the signal  $D^0$ -meson energy and momentum vector. Figure 29 shows the invariant  
 2877 mass spectrum as derived from the  $D_{\text{tag}}^{(*)} X \pi_{\text{soft}}^+$  system. This distribution determines the  
 2878 number of  $D^0$ 's in the candidate sample and provides an absolute normalization. In this  
 2879 sample a search for semileptonic decays  $D^0 \rightarrow \pi^- \ell^+ \nu_\ell$  or  $D^0 \rightarrow K^- \ell^+ \nu_\ell$  is performed;  
 2880 here the charged lepton is either an electron or muon. Pairs of a hadron and a lepton of  
 2881 opposite sign are identified and the neutrino four-momentum is obtained from energy-  
 2882 momentum conservation. Fig. 30 shows the distribution for the missing mass squared,

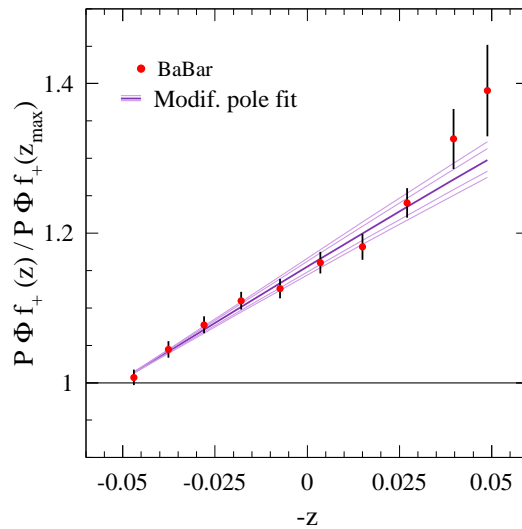


Fig. 28. Babar analysis of  $D^0 \rightarrow K^- e^+ \nu_e$  [453]: Measured values for  $P \times \Phi \times f_+$  versus  $-z$ , normalized to 1.0 at  $z = z_{\text{max}}$ . The straight lines represent the expectation from the fit to the modified pole ansatz, the result in the center, as well as the statistical and total uncertainties on either side.

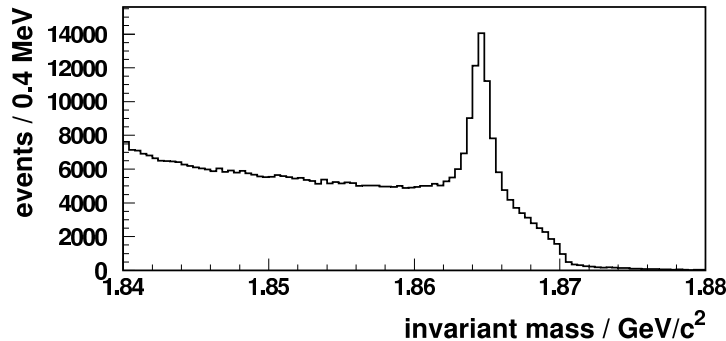


Fig. 29. Belle experiment [454]: Invariant mass distribution for  $D_{\text{sig}}^0$  candidates.

2883  $M_\nu^2$ , which for signal events is required to be consistent with zero,  $< 0.05 \text{ GeV}^2/c^4$ .  
 2884 The resulting branching fractions are  $\mathcal{B}(D^0 \rightarrow K^- \ell^+ \nu_\ell) = (3.45 \pm 0.07 \pm 0.20)\%$  and  
 2885  $\mathcal{B}(D^0 \rightarrow \pi^- \ell^+ \nu_\ell) = (0.255 \pm 0.019 \pm 0.016)\%$ . The measured form factors as a function  
 2886 of  $q^2$  are also included in Fig. 33 for both decay modes. The normalization of the form  
 2887 factors at  $q^2 = 0$  are  $f_+^K(0) = 0.695 \pm 0.007 \pm 0.022$  and  $f_+^\pi(0) = 0.624 \pm 0.020 \pm 0.030$ .

2888 The CLEO Collaboration analyzed data recorded at the mass at the  $\psi(3770)$  resonance,  
 2889 which decays exclusively to  $D\bar{D}$  pairs. They report measurements of semileptonic decays  
 2890 of both  $D^0$  and  $D^+$ , for both untagged and tagged events. For the untagged analysis [456]  
 2891 the normalization of  $D\bar{D}$  pairs is based on a separate analysis [252]. Individual hadrons,  
 2892  $\pi^-$ ,  $\pi^0$ ,  $K^-$ , or  $K_S$ , are paired with an electron and the missing momentum and energy  
 2893 of the entire event are used to estimate the neutrino four-momentum. The missing mass  
 2894 squared is required to be consistent with zero. Additionally, the four-momentum of the  
 2895 signal candidates, i.e., the sum of the hadron, lepton and neutrino energies must be  
 2896 consistent with the known energy and mass of the  $D$  meson. The yield of  $D$  mesons  
 2897 is extracted in five  $q^2$  bins. The CLEO Collaboration reports the branching fractions,  
 2898  $\mathcal{B}(D^0 \rightarrow K^- e^+ \nu_e) = (3.56 \pm 0.03 \pm 0.09)\%$ ,  $\mathcal{B}(D^0 \rightarrow \pi^- e^+ \nu_e) = (0.299 \pm 0.011 \pm 0.09)\%$ ,  
 2899  $\mathcal{B}(D^+ \rightarrow \bar{K}^0 e^+ \nu_e) = (8.53 \pm 0.13 \pm 0.23)\%$ , and  $\mathcal{B}(D^+ \rightarrow \pi^0 e^+ \nu_e) = (0.373 \pm 0.022 \pm$   
 2900  $0.013)\%$ . Figure 33 includes the CLEO-c untagged results for  $f_+(q^2)$  versus  $q^2$ .

2901 Recent results of the CLEO-c tagged analysis [253] were reported for the first time at  
 2902 this workshop. This analysis is based on a luminosity of  $281 \text{ pb}^{-1}$ . To tag events, all events  
 2903 are required to have a hadronic  $D$  decay, fully reconstructed in one of eight channels for  
 2904  $D^0$  and one of six channels for  $D^+$ . Since the  $D\bar{D}$  system is produced nearly at rest, the  
 2905  $D$  candidate should have an energy consistent with the beam energy. The beam-energy  
 2906 substituted mass,  $m_{ES}$ , is required to be consistent with the known  $D$  mass. For this  
 2907 sample of events, an electron is paired with a hadron,  $\pi^-$ ,  $\pi^0$ ,  $K^-$ , or  $K_S$ . In  $D\bar{D}$  events  
 2908 with a signal semileptonic decay, the only unidentified particle is the neutrino. Its energy  
 2909 and momentum are derived from the missing energy and momentum. The measured  
 2910 difference of these two quantities,  $U = E_\nu - P_\nu$ , is used to discriminate signal from  
 2911 background. Fig. 31 shows the  $U$  distribution for the four semileptonic decay modes.  
 2912 The requirement of a hadronic tag results in extremely pure samples. For the decay  
 2913  $D^0 \rightarrow K^- e^+ \nu_e$  the signal-to-noise ratio is about 300. Based on these selected samples  
 2914 CLEO-c reports the branching fractions,  $\mathcal{B}(D^0 \rightarrow K^- e^+ \nu_e) = (3.61 \pm 0.05 \pm 0.05)\%$ ,  
 2915  $\mathcal{B}(D^0 \rightarrow \pi^- e^+ \nu_e) = (0.314 \pm 0.013 \pm 0.004)\%$ ,  $\mathcal{B}(D^+ \rightarrow \bar{K}^0 e^+ \nu_e) = (8.90 \pm 0.17 \pm 0.21)\%$ ,  
 2916 and  $\mathcal{B}(D^+ \rightarrow \pi^0 e^+ \nu_e) = (0.384 \pm 0.027 \pm 0.023)\%$ . Figure 33 shows the CLEO-c results

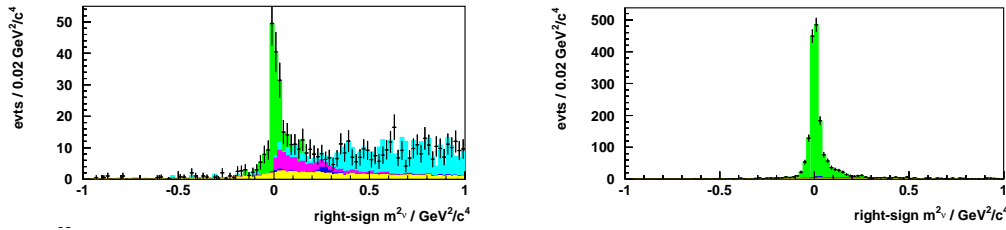


Fig. 30. Belle experiment [454, 455]: Missing mass squared distribution for  $D_{\text{sig}}^0$  candidates. Left:  $D^0 \rightarrow \pi^- \ell^+ \nu_\ell$ ; right:  $D^0 \rightarrow K^- \ell^+ \nu_\ell$ . The  $D^0 \rightarrow K^- \ell^+ \nu_\ell$  and fake  $D^0$  backgrounds are derived from data and are shown in magenta and yellow respectively. The cyan histogram shows the contribution from  $D^0 \rightarrow K^*/\rho \ell^+ \nu_\ell$  as determined from simulation.

Table 26

CLEO-c: Absolute branching fractions for tagged, untagged and averaged results.

	Tagged	Untagged	Average
$\pi^- e^+ \nu_e$	$0.308 \pm 0.013 \pm 0.004$	$0.299 \pm 0.011 \pm 0.008$	$0.304 \pm 0.011 \pm 0.005$
$\pi^0 e^+ \nu_e$	$0.379 \pm 0.027 \pm 0.002$	$0.373 \pm 0.022 \pm 0.013$	$0.378 \pm 0.020 \pm 0.012$
$K^- e^+ \nu_e$	$3.60 \pm 0.05 \pm 0.05$	$3.56 \pm 0.03 \pm 0.09$	$3.60 \pm 0.03 \pm 0.06$
$\bar{K}^0 e^+ \nu_e$	$8.87 \pm 0.17 \pm 0.21$	$8.53 \pm 0.13 \pm 0.23$	$8.69 \pm 0.12 \pm 0.19$

2917 for  $f_+(q^2)$  versus  $q^2$ .

2918 The CLEO Collaboration has computed the average of the untagged and tagged re-  
 2919 sults, taking into account all correlations. The results for the branching fractions are  
 2920 shown in Tab. 26. The untagged analysis contains about 2.5 times more events but has  
 2921 larger backgrounds and different systematic uncertainties. The product of the form fac-  
 2922 tor  $f_+(0)$  and the CKM matrix element is extracted from the combined measurements,  
 2923  $f_+^K(0)|V_{cs}| = 0.744 \pm 0.007 \pm 0.005$  and  $f_+^\pi(0)|V_{cd}| = 0.143 \pm 0.005 \pm 0.002$ .

2924 Since the time that the above results were reported at CKM2008, CLEO collabora-  
 2925 tion has completed a new tagged analysis which is based on the entire  $818 \text{ pb}^{-1}$  of  
 2926 data recorded at the  $\psi(3770)$  resonance [457]. The results for the most recent branch-  
 2927 ing fraction measurements are,  $\mathcal{B}(D^0 \rightarrow K^- e^+ \nu_e) = (3.50 \pm 0.03 \pm 0.04)\%$ ,  $\mathcal{B}(D^0 \rightarrow$   
 2928  $\pi^- e^+ \nu_e) = (0.288 \pm 0.008 \pm 0.003)\%$ ,  $\mathcal{B}(D^+ \rightarrow \bar{K}^0 e^+ \nu_e) = (8.83 \pm 0.10 \pm 0.20)\%$ , and  
 2929  $\mathcal{B}(D^+ \rightarrow \pi^0 e^+ \nu_e) = (0.405 \pm 0.016 \pm 0.009)\%$ . The measured form factors as a function  
 2930 of  $q^2$  for this analysis are shown at the bottom of Fig. 33. The product of the form fac-  
 2931 tor  $f_+(0)$  and the CKM matrix element is extracted from an isospin-combined fit which  
 2932 yields  $f_+^K(0)|V_{cs}| = 0.719 \pm 0.006 \pm 0.005$  and  $f_+^\pi(0)|V_{cd}| = 0.150 \pm 0.004 \pm 0.001$ . The new  
 2933 CLEO-c results are consistent with the previous CLEO-c measurements and supersede  
 2934 those measurements.

At this conference BaBar reported a measurement of  $D_s^+ \rightarrow K^+ K^- \ell^+ \nu_\ell$  decays [458].

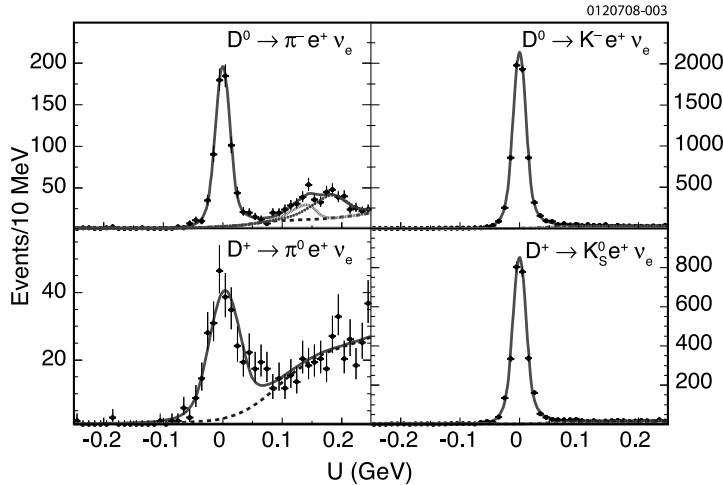


Fig. 31. CLEO-c tagged analysis [253]: Signal distributions ( $U = E_\nu - P_\nu$ ) for the four semileptonic  $D$  decay channels.

Events with a  $K^+K^-$  mass in the range  $1.01 - 1.03 \text{ GeV}/c^2$  are selected, corresponding to  $\phi \rightarrow K^+K^-$  decays, except for a small S-wave contribution which is observed for the first time. Since the final state meson is a vector, the decay rate depends on five variables, the mass squared of the  $K^+K^-$  pair,  $q^2$  and three decay angles, and on three form factors,  $A_1$ ,  $A_2$  and  $V$ , for which the  $q^2$  dependence is assumed to be dominated by a single pole,

$$V(q^2) = \frac{V(0)}{1 - q^2/m_V^2}, \quad A_{1,2}(q^2) = \frac{A_{1,2}(0)}{1 - q^2/m_A^2}, \quad (223)$$

2935 with a total of five parameters, the normalizations  $V(0)$ ,  $A_1(0)$ ,  $A_2(0)$  and the pole masses  
 2936  $m_V$  and  $m_A$ . In a data sample of  $214 \text{ fb}^{-1}$ , the BaBar Collaboration selects about 25,000  
 2937 signal decays, about 50 times more than the earlier analysis by FOCUS [459]. The signal  
 2938 yield and the form factor ratios are extracted from a binned maximum likelihood fit to the  
 2939 four-dimensional decay distribution,  $r_2 = A_2(0)/A_1(0) = 0.763 \pm 0.071 \pm 0.065$  and  $r_V =$   
 2940  $V(0)/A_1(0) = 1.849 \pm 0.060 \pm 0.095$ , as well as the pole mass  $m_A = 2.28_{-0.18}^{+0.23} \pm 0.18 \text{ GeV}/c^2$ .  
 2941 The sensitivity to  $m_V$  is weak and therefore this parameter is fixed to  $2.1 \text{ GeV}/c^2$ . The  
 2942 result of the fit is shown in Fig. 32. The small S-wave contribution, which can be asso-  
 2943 ciated with  $f_0 \rightarrow K^+K^-$  decays, corresponds to  $(0.22_{-0.08}^{+0.12} \pm 0.03)\%$  of the  $K^+K^-e^+\nu_e$   
 2944 decay rate. The  $D_s^+ \rightarrow K^+K^-e^+\nu_e$  branching fraction is measured relative to the de-  
 2945 cay  $D_s^+ \rightarrow K^+K^-\pi^+$ , resulting in  $\mathcal{B}(D_s^+ \rightarrow K^+K^-e^+\nu_e)/\mathcal{B}(D_s^+ \rightarrow K^+K^-\pi^+) =$   
 2946  $0.558 \pm 0.007 \pm 0.016$ , from which the absolute total branching fraction  $\mathcal{B}(D_s^+ \rightarrow \phi e^+\nu_e) =$   
 2947  $(2.61 \pm 0.03 \pm 0.08 \pm 0.15)\%$  is obtained. By comparing this quantity with the predicted  
 2948 decay rate, using the fitted parameters for the form factors, the absolute normalization  
 2949  $A_1(0) = 0.607 \pm 0.011 \pm 0.019 \pm 0.018$  was determined for the first time. The third error

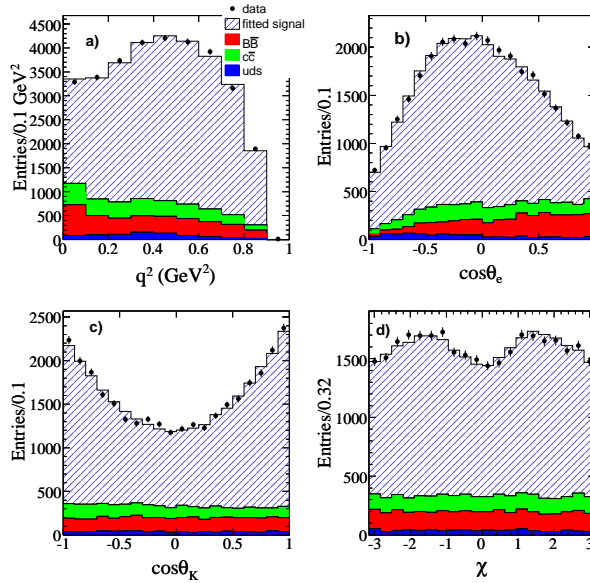


Fig. 32. BaBar [458]: Projected distributions of the four kinematic variables. The data (points with statistical errors) are compared to the sum of four contributions: the fitted signal (hatched histograms) and the estimated background contributions (different colored histograms) from  $B\bar{B}$ ,  $c\bar{c}$ , and the sum of  $u\bar{u}$ ,  $d\bar{d}$ , and  $s\bar{s}$  events.



2950 stated here refers to the combined uncertainties from various external inputs, namely  
 2951 branching fractions for  $D_s^+$ , and  $\phi$ , the  $D_s^+$  lifetime and  $|V_{cs}|$ . Lattice QCD calculations  
 2952 for this decay have been performed only in the quenched approximation. They agree with  
 2953 the experimental results for  $A_1(0)$ ,  $r_2$  and  $m_A$ , but are lower than the measured value  
 2954 of  $r_V$ . It would be interesting to see if unquenched calculations are in better agreement  
 2955 with experimental results.

2956 In summary, BaBar, Belle and CLEO-c have measured  $D$  meson semileptonic branching  
 2957 fractions and hadronic form factors in a variety of decay modes, using complementary  
 2958 experimental approaches. The results from the experiments are highly consistent. With  
 2959 lattice QCD prediction for the form factors, these results will allow a precise determina-  
 2960 tion of  $V_{cs}$  and  $V_{cd}$ . Fig. 33 shows a compilation of all form factor measurements,  $f_+(q^2)$   
 2961 versus  $q^2$ . All analyses presented here have performed studies of the  $q^2$  parameterizations  
 2962 and extractions of the associated parameters. A summary of these measurements is given  
 2963 in Tabs. 27 and 28, as well as the values obtained by lattice QCD computation [461].  
 2964 The reader is referred to the references for more details.

2965 Measurements of  $D \rightarrow \pi \ell \nu_\ell$  and  $D \rightarrow V \ell \nu_\ell$  will benefit from the increased data sam-  
 2966 ples expected in the near future. Of particular interest is the anticipated  $\psi(3770)$  running  
 2967 of BES-III. The BES-III Collaboration began data accumulation in July of 2008. The

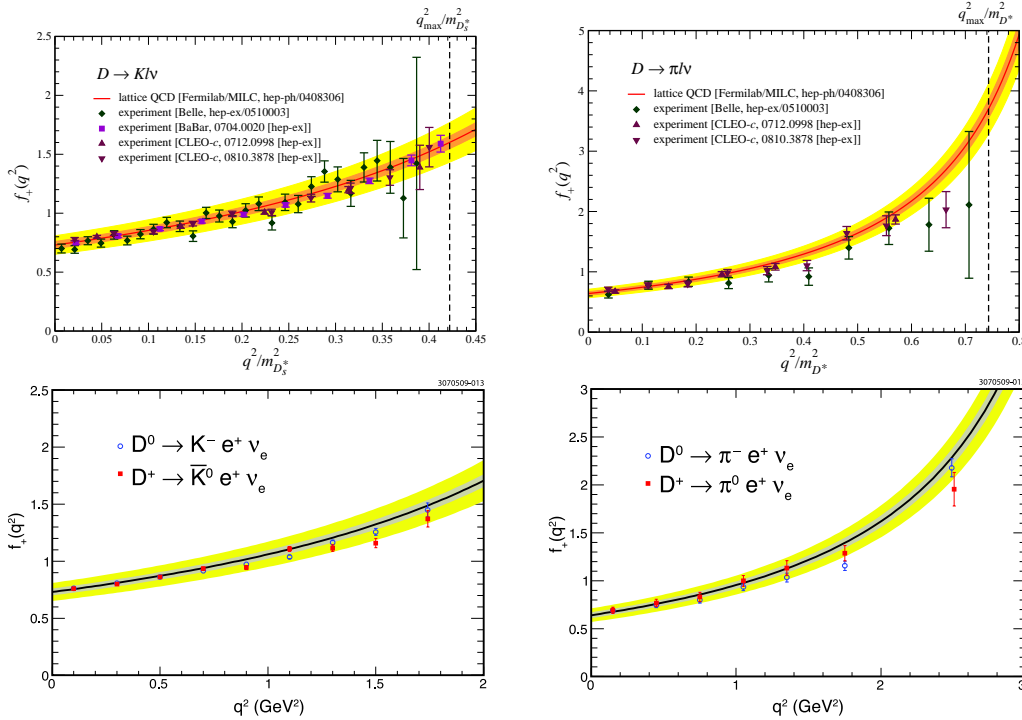


Fig. 33. Compilation of the form factor  $f_+(q^2)$  versus  $q^2$  for the semileptonic  $D$  decays with a Kaon (left) and pion (right). Top plots, adapted from Ref. [460], include measurements through the end of 2008. Bottom plots show results of a recent CLEO-c analysis [457]. In all plots the lines are the LQCD results of Ref. [461]; the inner band represents statistical uncertainty and the outer band includes the systematic uncertainty.

Table 27

Summary of the form factors parameters obtained by the different experiments for  $D \rightarrow K$  semileptonic decays. The first column gives the simple pole mass, the second the parameter  $\alpha$  used in the modified pole model, and the third the normalization.

	$M_{\text{pole}}[\text{GeV}/c^2]$	$\alpha$	$f_+(0)$
Belle [454]	$1.82 \pm 0.04 \pm 0.03$	$0.52 \pm 0.08 \pm 0.06$	$0.695 \pm 0.007 \pm 0.022$
BaBar [453]	$1.884 \pm 0.012 \pm 0.015$	$0.38 \pm 0.02 \pm 0.03$	$0.727 \pm 0.007 \pm 0.005 \pm 0.007$
CLEO-c [457]	$1.93 \pm 0.02 \pm 0.01$	$0.30 \pm 0.03 \pm 0.01$	$0.739 \pm 0.007 \pm 0.005$
LQCD [461]		$0.50 \pm 0.04 \pm 0.07$	$0.73 \pm 0.03 \pm 0.07$

Table 28

Summary of the form factors parameters obtained by the different experiments for  $D \rightarrow \pi$  semileptonic decays. The first column gives the simple pole mass, the second the parameter  $\alpha$  used in the modified pole model, and the third the normalization.

	$M_{\text{pole}}[\text{GeV}/c^2]$	$\alpha$	$f_+(0)$
Belle [454]	$1.97 \pm 0.08 \pm 0.04$	$0.10 \pm 0.21 \pm 0.10$	$0.624 \pm 0.020 \pm 0.030$
CLEO-c [457]	$1.91 \pm 0.02 \pm 0.01$	$0.21 \pm 0.07 \pm 0.02$	$0.666 \pm 0.019 \pm 0.004 \pm 0.003$
LQCD [461]		$0.44 \pm 0.04 \pm 0.07$	$0.64 \pm 0.03 \pm 0.06$

2968 experiment is comparable to CLEO-c in detector design but has superior muon identifi-  
 2969 cation performance, but worse performance for hadron identification, and is expected to  
 2970 accumulate at least an order of magnitude more data. The muon identification will allow  
 2971 access to all the semileptonic modes covered in this section from a single experiment.

### 2972 5.1.3. Measurements of $B$ branching fractions and $q^2$ dependence

2973 Exclusive semileptonic decays  $B \rightarrow X_u \ell \nu$ , where  $X_u$  denotes a charmless hadronic  
 2974 final state, have been reported by the CLEO, BaBar, and Belle collaborations [462–  
 2975 471]. The specification of the final state provides good kinematic constraints and an  
 2976 effective background rejection, but results in lower signal yields compared with inclusive  
 2977 measurements. Three experimental techniques that differ in the way the second  $B$  meson  
 2978 in the  $B\bar{B}$  event is treated have been employed in these measurements. The second  $B$   
 2979 meson is either fully reconstructed in a hadronic decay mode (“hadronic tags”), partially  
 2980 reconstructed in a semileptonic decay mode (“semileptonic tags”) or not reconstructed  
 2981 at all (“untagged”). The tagged and untagged methods differ greatly in terms of signal  
 2982 efficiency and purity.

#### 2983 $B \rightarrow \pi \ell \nu$

2984 The  $B \rightarrow \pi \ell \nu$  decay is the most promising decay mode for a precise determination of  
 2985  $|V_{ub}|$ , both for experiment and for theory. A number of measurements with different tag-  
 2986 ging techniques exist, but at present the untagged analyses, which were first performed  
 2987 by the CLEO collaboration [463], still provide the most precise results. In untagged anal-  
 2988 yses, the momentum of the neutrino is inferred from the missing energy and momentum  
 2989 in the whole event. The neutrino is combined with a charged lepton and a pion to form  
 2990 a  $B \rightarrow \pi \ell \nu$  candidate. The biggest experimental challenge is the suppression of the  
 2991  $B \rightarrow X_c \ell \nu$  background. Additional background sources are  $e^+e^- \rightarrow q\bar{q}$  ( $q = u, d, s, c$ )  
 2992 continuum events, which dominate at low  $q^2$ , and feed-down from other  $B \rightarrow X_u \ell \nu$

2993 decays, which dominate at high  $q^2$ .

2994 The BaBar experiment has measured the  $B \rightarrow \pi\ell\nu$  branching fraction and  $q^2$  spec-  
 2995 trum with a good accuracy [464]. In this analysis, the signal yields are extracted from a  
 2996 maximum-likelihood fit to the two-dimensional  $\Delta E$  vs.  $m_{\text{ES}}$  distribution of the signal  $B$   
 2997 meson in twelve bins of  $q^2$  (see Fig. 34). This fit allows for an extraction of the  $q^2$  depen-  
 2998 dence of the form factor  $f_+(q^2)$ . The shape of the measured spectrum is compatible with  
 2999 the ones predicted from LQCD [425, 426] and LCSR [442] calculations, but incompatible  
 3000 with the ISGW2 quark model [472]. A fit to the  $q^2$  spectrum using the Becirevic-Kaidalov  
 3001 (BK) parametrization yields a shape parameter  $\alpha = 0.52 \pm 0.05 \pm 0.03$  with a goodness-  
 3002 of-fit of  $P(\chi^2) = 0.65$ . Other parameterizations, e.g. the  $z$ -expansion, have been used  
 3003 in a simultaneous fit of the BaBar data and LQCD calculations [409]. The measured  
 3004 partial branching fractions are extrapolated to the full decay rate and, in combination  
 3005 with recent form-factor calculations, used to determine  $|V_{ub}|$

3006 The leading experimental systematic uncertainties are associated with the reconstruc-  
 3007 tion of charged and neutral particles, which impact the modeling of the missing momen-  
 3008 tum reconstruction, and with backgrounds from continuum events at low  $q^2$  and from  
 3009  $B \rightarrow X_u\ell\nu$  decays at high  $q^2$ . Due to the feed-down from  $B \rightarrow \rho\ell\nu$  decays, the uncer-  
 3010 tainties on the branching fraction and form factors for this decay mode contribute to the  
 3011 systematic uncertainty. A simultaneous measurement of  $B \rightarrow \pi\ell\nu$  and  $B \rightarrow \rho\ell\nu$  decays  
 3012 can reduce this uncertainty.

3013 Recently several tagged measurements have appeared [465, 466, 469, 470]. They have  
 3014 led to a simpler and more precise reconstruction of the neutrino momentum and have low  
 3015 backgrounds and a uniform acceptance in  $q^2$ . This is achieved, however, at the expense of  
 3016 much smaller signal samples which limit the statistical precision of the form-factor mea-  
 3017 surement. Semileptonic-tag measurements have a signal-to-background ratio of around  
 3018 1–2 and yield  $\sim 0.5$  signal decays per  $\text{fb}^{-1}$ . The signal is extracted from the distribution  
 3019 of events in  $\cos^2\phi_B$ , where  $\phi_B$  is the angle between the direction of either  $B$  meson and

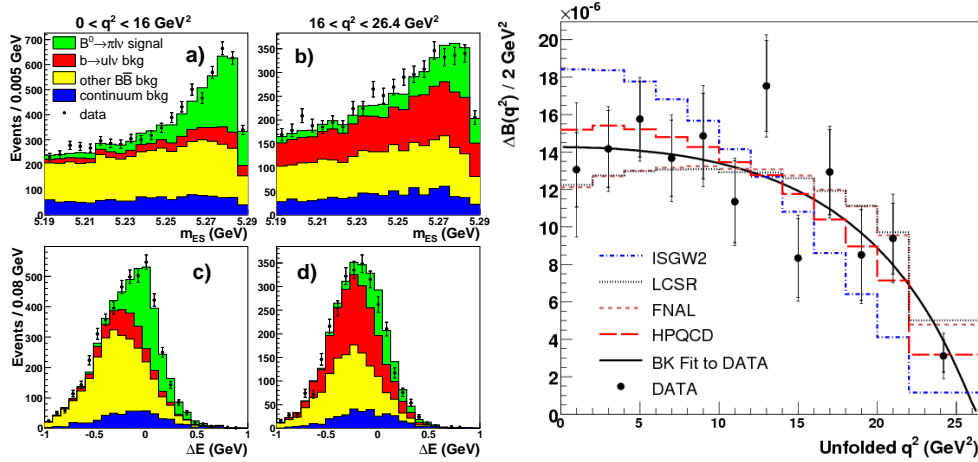


Fig. 34. Untagged  $B \rightarrow \pi\ell\nu$  measurement from BaBar [464]. Left:  $\Delta E$  and  $m_{\text{ES}}$  projections for  $q^2 < 16 \text{ GeV}^2$  and  $q^2 > 16 \text{ GeV}^2$ . Right: Measured  $q^2$  spectrum compared with a fit of the BK parametrization and with theory predictions from LQCD [425, 426], LCSR [442] and the ISGW2 quark model [472].

Table 29

Total and partial branching fractions for  $B^0 \rightarrow \pi^- \ell^+ \nu$  with statistical and systematic uncertainties. Measurements of  $\mathcal{B}(B^+ \rightarrow \pi^0 \ell^+ \nu)$  have been multiplied by a factor  $2\tau_{B^0}/\tau_{B^+}$ .

	$\mathcal{L}(\text{fb}^{-1})$	$\mathcal{B} \times 10^4$	$\Delta\mathcal{B}(q^2 < 16) \times 10^4$	$\Delta\mathcal{B}(q^2 > 16) \times 10^4$
BaBar no tag ( $\pi^-$ ) [464]	206	$1.45 \pm 0.07 \pm 0.11$	$1.08 \pm 0.06 \pm 0.09$	$0.38 \pm 0.04 \pm 0.05$
CLEO no tag ( $\pi^-, \pi^0$ ) [462]	16	$1.38 \pm 0.15 \pm 0.11$	$0.97 \pm 0.13 \pm 0.09$	$0.41 \pm 0.08 \pm 0.04$
BaBar sl. tag ( $\pi^-$ ) [465]	348	$1.39 \pm 0.21 \pm 0.08$	$0.92 \pm 0.16 \pm 0.05$	$0.46 \pm 0.13 \pm 0.03$
Belle sl. tag ( $\pi^-$ ) [469]	253	$1.38 \pm 0.19 \pm 0.15$	$1.02 \pm 0.16 \pm 0.11$	$0.36 \pm 0.10 \pm 0.04$
BaBar sl. tag ( $\pi^0$ ) [465]	348	$1.80 \pm 0.28 \pm 0.15$	$1.38 \pm 0.23 \pm 0.11$	$0.45 \pm 0.17 \pm 0.06$
Belle sl. tag ( $\pi^0$ ) [469]	253	$1.43 \pm 0.26 \pm 0.15$	$1.05 \pm 0.23 \pm 0.12$	$0.37 \pm 0.15 \pm 0.04$
BaBar had. tag ( $\pi^-$ ) [466]	211	$1.07 \pm 0.27 \pm 0.19$	$0.42 \pm 0.18 \pm 0.06$	$0.65 \pm 0.20 \pm 0.13$
Belle had. tag ( $\pi^-$ ) [470]	605	$1.12 \pm 0.18 \pm 0.05$	$0.85 \pm 0.16 \pm 0.04$	$0.26 \pm 0.08 \pm 0.01$
BaBar had. tag ( $\pi^0$ ) [466]	211	$1.54 \pm 0.41 \pm 0.30$	$1.05 \pm 0.36 \pm 0.19$	$0.49 \pm 0.23 \pm 0.12$
Belle had. tag ( $\pi^0$ ) [470]	605	$1.24 \pm 0.23 \pm 0.05$	$0.85 \pm 0.16 \pm 0.04$	$0.41 \pm 0.11 \pm 0.02$
Average		$1.36 \pm 0.05 \pm 0.05$	$0.94 \pm 0.05 \pm 0.04$	$0.37 \pm 0.03 \pm 0.02$

3020 the plane containing the momentum vectors of the tag-side  $D^* \ell$  system and the signal-  
3021 side  $\pi \ell$  system [465]. Hadronic-tag measurements reach signal-to-background ratios of up  
3022 to  $\sim 10$  and yield  $\sim 0.1$  signal decays per  $\text{fb}^{-1}$ . Here the signal is extracted from the  
3023 missing-mass squared distribution (see Fig. 35).

3024 Tab. 29 summarizes all  $B \rightarrow \pi \ell \nu$  branching-fraction measurements; shown are the  
3025 total branching fraction as well as the partial branching fractions for  $q^2 < 16 \text{ GeV}^2$  and  
3026  $q^2 > 16 \text{ GeV}^2$  with statistical and systematic uncertainties. The measurements agree well  
3027 among each other. A combination of all measurements results in an average branching  
3028 fraction of  $1.34 \times 10^{-4}$  with a precision of 6% (4% statistical and 4% systematic).

### 3029 $B \rightarrow \eta/\eta'/\rho/\omega \ell \nu$

3030 In addition to  $B \rightarrow \pi \ell \nu$ , the experiments have measured other semileptonic final states  
3031 with a pseudoscalar meson,  $\eta$  [463, 465, 467, 473] or  $\eta'$  [462, 465, 473], or a vector meson,  
3032  $\rho$  [462, 463, 468–470] or  $\omega$  [467, 471]. They are important ingredients to the determination  
3033 of the composition of the inclusive  $B \rightarrow X_u \ell \nu$  rate. They may also help to further  
3034 constrain theoretical form-factor calculations and provide valuable cross-checks for the  
3035 determination of  $|V_{ub}|$  from  $B \rightarrow \pi \ell \nu$ . The LQCD calculations for these final states are  
3036 challenging. For the flavor-neutral final-state mesons,  $\eta$ ,  $\eta'$  and  $\omega$ , the matrix element  
3037 contains contributions from quark-disconnected diagrams. For the  $\rho$  final state, the large  
3038 width of the  $\rho$  resonance complicates the calculations.

3039 The  $\eta$  and  $\eta'$  modes have been measured by the CLEO and BaBar collaboration.  
3040 The limit on  $\mathcal{B}(B \rightarrow \eta' \ell \nu)$  published by BaBar [465] agrees only marginally with the  
3041 CLEO result [462] (at the  $2.6\sigma$  level). Further measurements are needed to resolve this  
3042 discrepancy. In the future, a measurement of the ratio  $R_{\eta'\eta} = \mathcal{B}(B \rightarrow \eta' \ell \nu)/\mathcal{B}(B \rightarrow \eta \ell \nu)$   
3043 would be interesting to constrain the gluonic singlet contribution to the  $B \rightarrow \eta^{(\prime)}$  form  
3044 factor, as proposed in [445].

3045 The  $B \rightarrow \rho \ell \nu$  decay has a larger rate than charmless semileptonic decays into pseu-  
3046 doscalar mesons, but one must deal with the non-resonant  $\pi\pi$  contribution, which leads  
3047 to a sizable systematic uncertainty. The kinematics of decays with vector mesons are  
3048 described by three form factors. The statistical precision in current analyses is still too  
3049 low to measure these form factors. As an example, Fig. 35 shows the missing-mass and  
3050  $q^2$  spectra of  $B \rightarrow \rho \ell \nu$  and  $B \rightarrow \omega \ell \nu$  decays measured by the Belle collaboration in  
3051 a hadronic-tag analysis [470]. Tab. 30 summarizes the most precise branching fraction

Table 30

Total branching fractions for exclusive  $B \rightarrow X_u \ell \nu$  decays with  $X_u = \eta, \eta', \rho, \text{ or } \omega$ . <sup>†</sup>The BaBar collaboration reports an upper limit of  $\mathcal{B}(B^+ \rightarrow \eta' \ell^+ \nu) < 0.47$  at 90% CL [465].

Decay mode	$\mathcal{B} \times 10^4 \sigma_{stat} \times 10^4 \sigma_{syst} \times 10^4$		
$B^+ \rightarrow \eta \ell^+ \nu$ (BaBar average) [467]	0.37	0.06	0.07
$B^+ \rightarrow \eta' \ell^+ \nu$ (CLEO no tag) [462] <sup>†</sup>	2.66	0.80	0.56
$B^0 \rightarrow \rho^- \ell^+ \nu$ (average)	2.80	0.18	0.16
$B^+ \rightarrow \omega \ell^+ \nu$ (BaBar no tag) [467]	1.14	0.16	0.08

3052 results for semileptonic  $B$  decays to low-mass charmless hadrons heavier than the pion.

### 3053 Prospects for exclusive charmless decays

3054 The outlook for further improvements in these measurements for the full  $B$ -factory  
 3055 datasets and for a Super  $B$  factory is good. It can be expected that for  $B \rightarrow \pi \ell \nu$   
 3056 the untagged measurements will remain the most precise up to integrated luminosities  
 3057 of several  $\text{ab}^{-1}$ . To reduce the systematic uncertainties of untagged measurements, a  
 3058 better knowledge of inclusive  $B \rightarrow X_u \ell \nu$  decays is important, since they are the biggest  
 3059 limitation in the high- $q^2$  region where LQCD calculations exist. In addition, a significant  
 3060 fraction of the  $B\bar{B}$  background comes from events, where the signal  $B$  meson has been  
 3061 wrongly reconstructed by assigning one or more particles from the decay of the other  $B$   
 3062 meson to the signal decay. To reduce this uncertainty, much effort is needed to improve  
 3063 the simulation of generic  $B$ -meson decays. With the full  $B$ -factory dataset, a precision  
 3064 of about 4-5% should be achievable for the total  $B \rightarrow \pi \ell \nu$  branching fraction.

3065 The tagged measurements in particular will improve with larger data samples. The  
 3066 systematic uncertainties in these measurements have a significant statistical component  
 3067 and thus the total experimental error is expected to fall as  $1/\sqrt{N}$ . For the higher-mass  
 3068 states, the tagged measurements should soon give the most precise branching-fraction  
 3069 results. However, the larger data samples from untagged analyses will be needed to

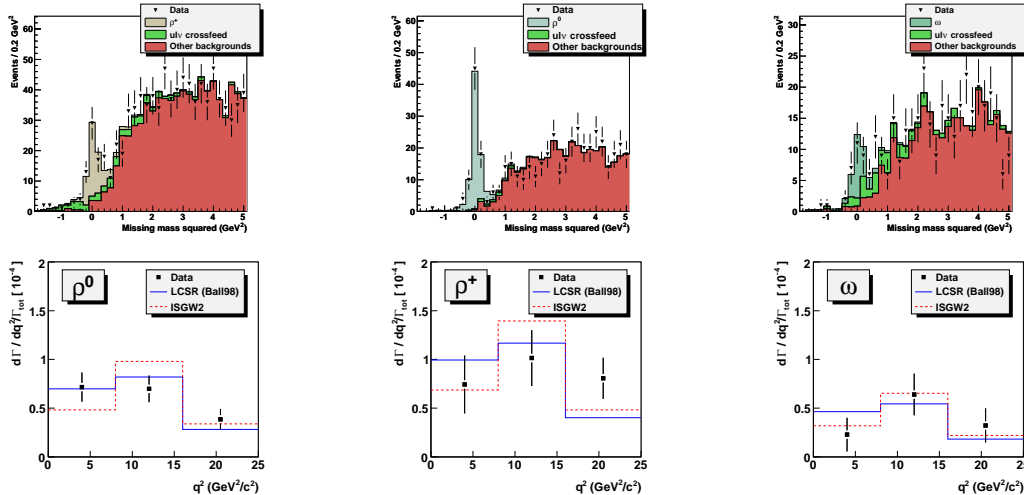


Fig. 35. Belle hadronic-tag measurements [470]: Missing-mass squared distributions and  $q^2$  spectra for  $B \rightarrow \rho \ell \nu$  and  $B \rightarrow \omega \ell \nu$  decays.

3070 extract information on the three form factors involved in decays with a vector meson.  
 3071 For an integrated luminosity of  $1\text{--}2 \text{ ab}^{-1}$ , several thousand  $B \rightarrow \rho \ell \nu$  and  $B \rightarrow \omega \ell \nu$   
 3072 decays can be expected. These signal samples will allow us to obtain some information  
 3073 on the form factors or ratios of form-factors through a simultaneous fit of the  $q^2$  spectrum  
 3074 and decay-angle distributions, similar to the study of  $B \rightarrow D^* \ell \nu$  decays. A measurement  
 3075 of all three form factors will most likely not be feasible with the current  $B$ -factory data  
 3076 samples.

3077 5.1.4. *Determination of  $|V_{cs}|$ ,  $|V_{cd}|$ ,  $|V_{ub}|$*

3078 Once both the form factor  $|f_+(q^2)|^2$  and the experimental decay width  $\Gamma(q_{\min})$  are  
 3079 known, the CKM matrix element  $|V_{qQ}|$  can be determined in several ways. We briefly  
 3080 describe the two most common methods below.

Until recently the standard procedure used to extract CKM matrix elements from  
 exclusive semileptonic decays has been to integrate the theoretically determined form  
 factor over a region of  $q^2$  and then combine it with the experimentally measured decay  
 rate in this region:

$$\frac{\Gamma(q_{\min})}{|V_{qQ}|^2} = \frac{G_F^2}{192\pi^3 m_H^3} \int_{q_{\min}^2}^{q_{\max}^2} dq^2 [(m_H^2 + m_P^2 - q^2)^2 - 4m_H^2 m_P^2]^{3/2} |f_+(q^2)|^2. \quad (224)$$

3081 The integration requires a continuous parametrization of the form factor between  $q_{\min}^2$   
 3082 and  $q_{\max}^2$  that is typically obtained by fitting the theoretical form factor result to a model  
 3083 function such as the Bećirević-Kaidalov (BK) [474] or Ball-Zwicky (BZ) parametriza-  
 3084 tion [442]. The three-parameter BK Ansatz,

$$f_+(q^2) = \frac{f_+(0)}{(1 - q^2/m_{B^*}^2)(1 - \alpha q^2/m_{B^*}^2)}, \quad (225)$$

$$f_0(q^2) = \frac{f_+(0)}{(1 - q^2/\beta m_{B^*}^2)}, \quad (226)$$

3085 incorporates many essential features of the form factor shape such as the kinematic  
 3086 constraint at  $q^2 = 0$ , heavy-quark scaling, and the location of the  $B^*$  pole. The four-  
 3087 parameter BZ Ansatz extends the BK expression for  $f_+(q^2)$  by including an additional  
 3088 pole to capture the effects of multiparticle states.

3089 In general, the use of a model function to parametrize the form factor introduces  
 3090 assumptions that make it difficult to quantify the agreement between theory and exper-  
 3091 iment and gives rise to a systematic uncertainty in the CKM matrix element  $|V_{qQ}|$  that  
 3092 is hard to estimate. It is likely that this error can be safely neglected when interpolating  
 3093 between data points. Thus the choice of fit function should have only a slight impact on  
 3094 the exclusive determinations of  $|V_{cs}|$  and  $|V_{cd}|$  because lattice-QCD calculations and exper-  
 3095 imental measurements possess a large region of overlap in  $q^2$ . It is less clear, however,  
 3096 how well the BK and BZ Ansätze can be trusted to extrapolate the form factor shape  
 3097 beyond the reach of the numerical lattice-QCD data or the experimental data. Thus one  
 3098 should be cautious in using them for the exclusive determination of  $|V_{ub}|$  via Eq. (224),  
 3099 since an extrapolation in  $q^2$  is necessary both for lattice QCD, which is most accurate  
 3100 at high  $q^2$ , and for experimental measurements, which are most precise at low values of  
 3101  $q^2$ . In particular, comparisons of lattice and experimental determinations of BK or BZ

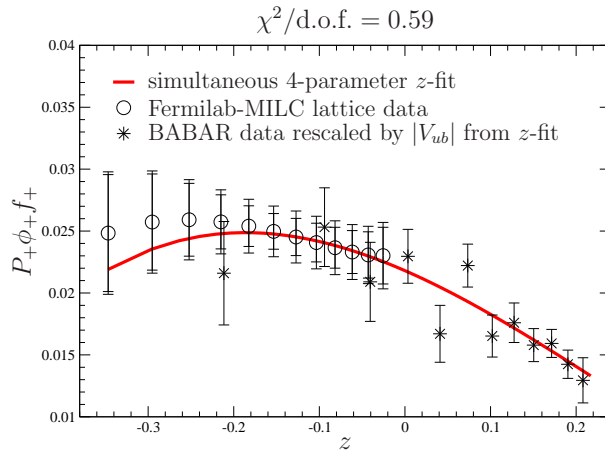


Fig. 36. Model-independent determination of  $|V_{ub}|$  from a simultaneous fit of lattice and experimental  $B \rightarrow \pi \ell \nu$  semileptonic form factor data to the  $z$ -parametrization [409]. Inclusion of terms in the power-series through  $z^3$  yields the maximum uncertainty in  $|V_{ub}|$ ; the corresponding 4-parameter  $z$ -fit is given by the red curve in both plots. The circles denote the Fermilab-MILC lattice-QCD calculation [409], while the stars indicate the 12-bin Babar data [464], rescaled by the value of  $|V_{ub}|$  determined in the simultaneous  $z$ -fit.

3102 fit parameters are potentially misleading, because apparent inconsistencies could simply  
 3103 be due to the inadequacy of the parametrization.

3104 Recently, several groups have begun to use model-independent parameterizations for  
 3105 the exclusive determination of  $|V_{ub}|$  [408–413, 475]. This avoids the concerns about the  
 3106 BK and BZ Ansätze outlined above, and should become the standard method for deter-  
 3107 mining  $|V_{ub}|$  and other CKM matrix elements from semileptonic decays in the near  
 3108 future. For concreteness, here we focus on the  $z$ -expansion given in Eq. (207), but the  
 3109 procedure for determining  $|V_{ub}|$  outlined here should apply to other model-independent  
 3110 parameterizations. Because the  $z$ -expansion relies only on analyticity and unitarity, it can  
 3111 be trusted to extrapolate the form factor shape in  $q^2$  beyond the reach of the data. One  
 3112 can easily check for consistency between theory and experiment using this parametriza-  
 3113 tion by fitting the data separately and comparing the slope ( $a_1/a_0$ ), curvature ( $a_2/a_0$ ),  
 3114 and so forth. Finally, because as many terms can be added to the convergent series as are  
 3115 needed to describe the  $B \rightarrow \pi \ell \nu$  form factor to the desired accuracy, the parametrization  
 3116 can be systematically improved as theoretical and experimental data get better.

3117 Once the shapes of the theoretical and experimental form factor data are determined  
 3118 to be consistent, the CKM matrix element  $|V_{ub}|$  is given simply by the ratio of the nor-  
 3119 malizations,  $|V_{ub}| = a_0^{\text{exp}}/a_0^{\text{theo}}$ . The total uncertainty in  $|V_{ub}|$  can be reduced, however,  
 3120 by fitting the theoretical and experimental data simultaneously, leaving the relative nor-  
 3121 malization as a free parameter to be determined [409]. The combined fit incorporates  
 3122 all of the available data, thereby allowing the numerical lattice QCD data primarily to  
 3123 dictate the shape at high  $q^2$  and the experimental data largely to determine the shape at  
 3124 low  $q^2$ . Although the theoretical and experimental data are uncorrelated, it is important  
 3125 to include the correlations between experiments or between theoretical calculations, de-  
 3126 spite the fact that they can be difficult to ascertain. Fig. 36 shows an example combined  
 3127 fit to the model-independent  $z$ -parametrization that uses 2+1 flavor lattice QCD results  
 3128 from Fermilab/MILC [409] and experimental data from BABAR [464].

3129 Combining the most recent experimental measurements of  $D \rightarrow K\ell\nu$  and  $D \rightarrow \pi\ell\nu$   
 3130 form factors with the 2+1 flavor lattice QCD calculations from the Fermilab/MILC  
 3131 collaboration [283, 461], CLEO finds [457]

$$|V_{cd}| = 0.234 \pm 0.007 \pm 0.025, \quad (227)$$

$$|V_{cs}| = 0.985 \pm 0.012 \pm 0.103, \quad (228)$$

3132 where the errors are experimental and theoretical, respectively. These determinations  
 3133 rely upon the BK parametrization, both to parametrize the theoretical  $D \rightarrow \pi\ell\nu$  and  
 3134  $D \rightarrow K\ell\nu$  form factor shapes for use in Eq. (224) and within the lattice QCD calculation  
 3135 itself. Although this is unlikely to introduce a significant systematic error, use of one of  
 3136 the many model-independent functional forms available would be preferable. The largest  
 3137 uncertainties in both  $|V_{cs}|$  and  $|V_{cd}|$  are from discretization errors in the lattice QCD  
 3138 calculation, and can be reduced by simulating at a finer lattice spacing. Because the  
 3139 lattice calculations of the  $D \rightarrow \pi\ell\nu$  and  $D \rightarrow K\ell\nu$  form factors can improved in a  
 3140 straightforward manner, without requiring new techniques, we expect the errors in both  
 3141  $|V_{cd}|$  and  $|V_{cs}|$  to decrease significantly in the near future.

3142 Most recent exclusive determinations of  $|V_{ub}|$  rely upon the 2+1 flavor lattice QCD  
 3143 calculations of the  $B \rightarrow \pi\ell\nu$  form factor of the HPQCD and Fermilab/MILC collabora-  
 3144 tions [283, 425, 426]. Those which use model-independent parameterizations of the form  
 3145 factor shape often incorporate additional theoretical points from light cone sum rules,  
 3146 soft collinear effective theory, and chiral perturbation theory [408, 410, 411, 413]. All of  
 3147 the results for  $|V_{ub}|$  are consistent within uncertainties. We show a representative sample  
 3148 of these results, along with two model-dependent determinations that rely on the BK  
 3149 and BZ parameterizations for comparison, in Fig. 37. Below we quote the most recent  
 3150 calculation by Fermilab/MILC because this is the only one to use a model-independent  
 3151 parametrization along with the full correlation matrices, derived directly from the data,  
 3152 for both theory and experiment [409]:

$$|V_{ub}| = (3.38 \pm 36) \times 10^{-3}, \quad (229)$$

3153 where the total uncertainty is the sum of statistical, systematic, and experimental errors  
 3154 added in quadrature. The dominant theoretical uncertainty in  $|V_{ub}|$  comes from statistics  
 3155 and the extrapolation to the physical up and down quark masses and to the continuum.  
 3156 The sub-dominant uncertainties, which are of comparable size, are due to the perturbative  
 3157 renormalization of the heavy-light vector current and heavy-quark discretization errors  
 3158 in the action and current. All of these errors can be reduced by increasing statistics and  
 3159 simulating at a finer lattice spacing. We therefore expect the total uncertainty in  $|V_{ub}|$   
 3160 determined from  $B \rightarrow \pi\ell\nu$  semileptonic decay to decrease in the next few years.

## 3161 5.2. $B \rightarrow D^{(*)}\ell\nu$ decays for $|V_{cb}|$

### 3162 5.2.1. *Theoretical background: HQS and HQET*

3163 The matrix elements of semileptonic decays can be related to a set of form factors. In  
 3164 the conventions of refs. [476–478], the matrix elements relevant for  $B \rightarrow D^{(*)}\ell\nu$  decays  
 3165 are



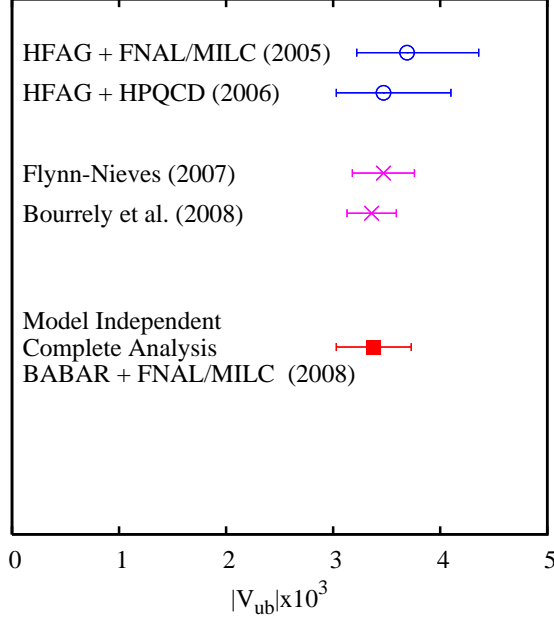


Fig. 37. Determinations of  $|V_{ub}|$  that rely upon 2+1 flavor lattice QCD calculations. The upper two results use the BK and BZ parameterizations, respectively, to describe the the  $B \rightarrow \pi \ell \nu$  form factor, while the lower three results use different model-independent parameterizations.

$$\frac{\langle D | \mathcal{V}^\mu | B \rangle}{\sqrt{m_B m_D}} = (v_B + v_D)^\mu h_+ + (v_B - v_D)^\mu h_-, \quad (230)$$

$$\frac{\langle D_\alpha^* | \mathcal{V}^\mu | B \rangle}{\sqrt{m_B m_{D^*}}} = \varepsilon^{\mu\nu\rho\sigma} v_B^\nu v_{D^*}^\rho \epsilon_\alpha^{*\sigma} h_V, \quad (231)$$

$$\frac{\langle D_\alpha^* | \mathcal{A}^\mu | B \rangle}{\sqrt{m_B m_{D^*}}} = i \epsilon_\alpha^{*\nu} [h_{A_1} (1+w) g^{\mu\nu} - (h_{A_2} v_B^\mu + h_{A_3} v_{D^*}^\mu) v_B^\nu], \quad (232)$$

where  $m_B$  and  $m_{D^{(*)}}$  are the masses of the  $B$  and  $D^{(*)}$  mesons, respectively,  $v_{B,D^{(*)}} = p_{B,D^{(*)}}/m_{B,D^{(*)}}$  is the 4-velocity of the mesons,  $\varepsilon^{\mu\nu\rho\sigma}$  is the totally antisymmetric tensor in 4 dimensions, and  $\epsilon_\alpha^\mu$  is the polarization vector of  $D_\alpha^*$ , with

$$\sum_{\alpha=1}^3 \epsilon_\alpha^{*\mu} \epsilon_\alpha^\nu = -g^{\mu\nu} + v_{D^*}^\mu v_{D^*}^\nu. \quad (233)$$

The form factors depend on the heavy-light meson masses, and on the velocity transfer from initial to final state  $w = v_B \cdot v_{D^{(*)}}$ . The values of  $w$  are constrained by kinematics to fall in the range

$$1 \leq w \leq \frac{m_B^2 + m_{D^{(*)}}^2}{2m_B m_{D^{(*)}}}, \quad (234)$$

with the largest value of  $w$  around 1.5. The usual invariant  $q^2 = m_B^2 + m_{D^{(*)}}^2 - 2w m_B m_{D^{(*)}}$ .

The differential rate for the decay  $B \rightarrow D \ell \nu$  is

$$\frac{d\Gamma(B \rightarrow D \ell \nu)}{dw} = \frac{G_F^2}{48\pi^3} m_D^3 (m_B + m_D)^2 (w^2 - 1)^{3/2} |V_{cb}|^2 |\mathcal{G}(w)|^2, \quad (235)$$

with

$$\mathcal{G}(w) = h_+^{B \rightarrow D}(w) - \frac{m_B - m_D}{m_B + m_D} h_-^{B \rightarrow D}(w). \quad (236)$$

The differential rate for the semileptonic decay  $\bar{B} \rightarrow D^* \ell \bar{\nu}_\ell$  is

$$\frac{d\Gamma(B \rightarrow D^* \ell \nu)}{dw} = \frac{G_F^2}{4\pi^3} m_{D^*}^3 (m_B - m_{D^*})^2 \sqrt{w^2 - 1} |V_{cb}|^2 \chi(w) |\mathcal{F}(w)|^2, \quad (237)$$

3167 where  $\chi(w) |\mathcal{F}_{B \rightarrow D^*}(w)|^2$  contains a combination of four form factors that must be cal-  
 3168 culated nonperturbatively. At zero recoil  $\chi(1) = 1$ , and  $\mathcal{F}(1)$  reduces to a single form  
 3169 factor,  $h_{A_1}(1)$ . At non-zero recoil, all four form factors contribute, yielding

$$\chi(w) = \frac{w+1}{12} \left( 5w + 1 - \frac{8w(w-1)m_B m_{D^*}}{(m_B - m_{D^*})^2} \right), \quad (238)$$

$$\mathcal{F}(w) = h_{A_1}(w) \frac{1+w}{2} \sqrt{\frac{H_0^2(w) + H_+^2(w) + H_-^2(w)}{3\chi(w)}}, \quad (239)$$

3170 with

$$H_0(w) = \frac{w - m_{D^*}/m_B - (w-1)R_2(w)}{1 - m_{D^*}/m_B}, \quad (240)$$

$$H_\pm(w) = t(w) \left[ 1 \mp \sqrt{\frac{w-1}{w+1}} R_1(w) \right], \quad (241)$$

$$t^2(w) = \frac{m_B^2 - 2wm_B m_{D^*} + m_{D^*}^2}{(m_B - m_{D^*})^2}, \quad (242)$$

$$R_1(w) = \frac{h_V(w)}{h_{A_1}(w)}, \quad (243)$$

$$R_2(w) = \frac{h_{A_3}(w) + (m_{D^*}/m_B)h_{A_2}(w)}{h_{A_1}(w)}. \quad (244)$$

3171 Eqs. (235) and (237) hold for vanishing lepton mass, and there are corrections analo-  
 3172 gous to those in Eq. (203). For semimuonic decays, these effects are included in recent  
 3173 experimental analyses.

3174 In the limit of infinite heavy-quark mass, all heavy quarks interact in the same way  
 3175 in heavy light mesons. This phenomenon is known as heavy quark symmetry (HQS).  
 3176 For example, given that a heavy quark has spin quantum number 1/2, the quark has  
 3177 a chromomagnetic moment  $g/(2m_Q)$ , which vanishes as the heavy quark  $m_Q$  goes to  
 3178 infinity. Thus, in a meson, the interaction between the spin of the heavy quark and the  
 3179 light degrees of freedom is suppressed. The heavy-light meson is then symmetric under  
 3180 a change in the  $z$ -component of the heavy-quark spin, and this is known as heavy-quark  
 3181 spin symmetry.

3182 In the heavy-quark limit we have that the velocity of the heavy quark is conserved  
 3183 in soft processes. Thus, the mass-dependent piece of the momentum operator can be  
 3184 removed by a field redefinition,

$$h_Q(v, x) = \frac{1 + \not{v}}{2} e^{im_Q v \cdot x} Q(x), \quad (245)$$

3185 where  $(1 + \not{v})/2$  is a projection operator, and  $Q(x)$  is the conventional quark field in QCD.  
 3186 If the quark has a total momentum  $P^\alpha$ , the new field carries a residual momentum  $k^\alpha =$   
 3187  $P^\alpha - m_Q v^\alpha$ . In the limit  $m_Q \rightarrow \infty$ , the effective Lagrangian for heavy quarks interacting  
 3188 via QCD becomes

$$\mathcal{L}_{\text{HQET}} = \bar{h}_Q i v \cdot D h_Q, \quad (246)$$

3189 where  $D^\alpha = \partial^\alpha - ig_s t_a A_a^\alpha$  is the covariant derivative. For large but finite  $m_Q$ , this  
 3190 Lagrangian receives corrections from terms of higher-dimension proportional to inverse  
 3191 powers of  $m_Q$ . These corrections break the HQS of the leading order Lagrangian, but  
 3192 are well-defined at each order of the expansion, and can be included in a systematic way.  
 3193 The resulting Lagrangian is known as the Heavy-Quark Effective Theory (HQET). The  
 3194 higher-dimension operators in the HQET come with coefficients that are determined by  
 3195 matching to the underlying, fundamental theory, namely QCD.

3196 In lattice simulations, it is not possible to treat quarks where the mass in lattice units  
 3197  $am_Q$  is large compared to 1 using conventional light-quark methods. All lattice heavy-  
 3198 quark methods make use of HQET in order to avoid the large discretization effects that  
 3199 would result from such a naive treatment. For lattices currently in use,  $am_c \sim 0.5 - 1.0$   
 3200 and  $am_b \sim 2 - 3$ , so HQET methods are essential for precision calculations. For a technical  
 3201 review of these methods, see Ref. [86].

3202 One approach consists in simulating a discrete version of the HQET action, introduced  
 3203 in Ref. [479], by treating the sub-leading operators as insertions in correlation functions.  
 3204 The matching procedure is particularly complicated on the lattice because of the presence  
 3205 of power divergences that arise as a consequence of the mixing of operators of lower  
 3206 dimensions with the observable of interest, but it can be carried out with non-perturbative  
 3207 accuracy [480] by means of a finite volume technique (see also [481] for a review of the  
 3208 subject).

3209 The Fermilab approach makes use of the fact that the Wilson fermion action reproduces  
 3210 the static quark action in the infinite mass limit. Higher dimension operators can then  
 3211 be adjusted in a systematic way. Each higher dimension operator has a counterpart in  
 3212 HQET, and once the coefficients of the new operators are tuned to the appropriate  
 3213 values, the lattice action gives the continuum result, to a given order in HQET. To order  
 3214  $\Lambda_{\text{QCD}}/2m_Q$ , the only new operator is a single dimension 5 term, and this is the same  
 3215 term that is added to the Wilson fermion action to improve it in the light quark sector.  
 3216 (The power of 2 is a combinatoric factor appropriate to the HQET expansion.) This  
 3217 improved action is known as the Sheikholeslami-Wohlert action [482], and the tunings of  
 3218 the parameters in this action appropriate to heavy quarks is the Fermilab method now  
 3219 in common use [83, 483]. Higher order improvement to the Fermilab method, including  
 3220 operators of even higher dimension, has been proposed in Ref. [484].

3221 Another approach to handle with heavy quarks on the lattice is the so-called “step-  
 3222 scaling method” [485]. Within the step-scaling method the dynamics of the heavy quarks  
 3223 is resolved by making simulations on small volumes ( $L \simeq 0.5$  fm) without recurring to  
 3224 any approximation but introducing, at intermediate stages, finite volume effects. These  
 3225 are subsequently accounted for by performing simulations on progressively larger volumes  
 3226 and by relying on the observation that sub-leading operators enter the HQET expansion  
 3227 of finite volume effects multiplied by inverse powers of  $Lm_Q$ . The success of this approach  
 3228 depends on the possibility of computing the finite volume observable, finite volume effects

3229 and their product with smaller errors and systematics with respect to the ones that would  
 3230 be obtained by a direct calculation. The strength of the method is a great freedom in the  
 3231 definition of the observable on finite volumes provided that its physical value is recovered  
 3232 at the end of the procedure.

The Fermilab Lattice Collaboration introduced a double ratio in order to compute  $h_+$  at zero-recoil [486]

$$\frac{\langle D|\bar{c}\gamma_4 b|\bar{B}\rangle\langle\bar{B}|\bar{b}\gamma_4 c|D\rangle}{\langle D|\bar{c}\gamma_4 c|D\rangle\langle\bar{B}|\bar{b}\gamma_4 b|\bar{B}\rangle} = |h_+(1)|^2. \quad (247)$$

3233 This double ratio has the advantage that the statistical errors and many of the systematic  
 3234 errors cancel. The discretization errors are suppressed by inverse powers of heavy-quark  
 3235 mass as  $\alpha_s(\Lambda_{\text{QCD}}/2m_Q)^2$  and  $(\Lambda_{\text{QCD}}/2m_Q)^3$  [83], and much of the current renormaliza-  
 3236 tion cancels, leaving only a small correction that can be computed perturbatively [85].  
 3237 The extra suppression of discretization errors by a factor of  $\Lambda_{\text{QCD}}/2m_Q$  occurs at zero-  
 3238 recoil for heavy-to-heavy transitions, and is a consequence of Luke's Theorem [487].

In order to obtain  $h_-$ , it is necessary to consider non-zero recoil momenta. In this case, Luke's theorem does not apply, and the HQET power counting leads to larger heavy-quark discretization errors. However, this is mitigated by the small contribution of  $h_-$  to the branching fraction. The form factor  $h_-$  can be determined from the double ratio [486]

$$\frac{\langle D|\bar{c}\gamma_j b|\bar{B}\rangle\langle D|\bar{c}\gamma_4 c|D\rangle}{\langle D|\bar{c}\gamma_4 b|\bar{B}\rangle\langle D|\bar{c}\gamma_j b|D\rangle} = \left[1 - \frac{h_-(w)}{h_+(w)}\right] \left[1 + \frac{h_-(w)}{2h_+(w)}(w-1)\right], \quad (248)$$

which can be extrapolated to the zero-recoil point  $w = 1$ . Using the double ratios of Eqs. (247) and (248) the latest (preliminary) unquenched determinations of  $h_+(1)$  and  $h_-(1)$  from the Fermilab Lattice and MILC Collaborations combine to give [488]

$$\mathcal{G}(1) = 1.074(18)(16), \quad (249)$$

3239 where the first error is statistical and the second is the sum of all systematic errors in  
 3240 quadrature.

The form factor at zero-recoil needed for  $B \rightarrow D^* \ell \nu$  has been computed by the Fermilab Lattice and MILC Collaborations using the double ratio [489]

$$\frac{\langle D^*|\bar{c}\gamma_j\gamma_5 b|\bar{B}\rangle\langle\bar{B}|\bar{b}\gamma_j\gamma_5 c|D^*\rangle}{\langle D^*|\bar{c}\gamma_4 c|D^*\rangle\langle\bar{B}|\bar{b}\gamma_4 b|\bar{B}\rangle} = |h_{A_1}(1)|^2, \quad (250)$$

where again, the discretization errors are suppressed by inverse powers of heavy-quark mass as  $\alpha_s(\Lambda_{\text{QCD}}/2m_Q)^2$  and  $(\Lambda_{\text{QCD}}/2m_Q)^3$ , and much of the current renormalization cancels, leaving only a small correction that can be computed perturbatively [85]. They extrapolate to physical light quark masses using the appropriate rooted staggered chiral perturbation theory [490]. Including a QED correction of 0.7% [300], they obtain [489]

$$\mathcal{F}(1) = 0.927(13)(20), \quad (251)$$

3241 where the first error is statistical and the second is the sum of systematic errors in  
 3242 quadrature.

3243 Because of the kinematic suppression factors  $(w^2 - 1)^{3/2}$  and  $(w^2 - 1)^{1/2}$  appearing  
 3244 in Eqs. (235) and (237), respectively, the experimental decay rates at zero recoil must  
 3245 be obtained by extrapolation. The extrapolation is guided by theory, where Ref. [491]  
 3246 have used dispersive constraints on the form factor shapes, together with heavy-quark

Table 31

Quenched results for  $\mathcal{G}(w)$  and  $\Delta(w)$  at non zero recoil [476, 477]. The notation “(q)” stays for the unknown systematics coming from the quenching approximation. QED corrections not included.

$w$	$\mathcal{G}(w)$	$\Delta(w)$
1.000	1.026(17)(q)	0.466(26)(q)
1.030	1.001(19)(q)	0.465(25)(q)
1.050	0.987(15)(q)	0.464(24)(q)
1.100	0.943(11)(q)	0.463(24)(q)
1.200	0.853(21)(q)	0.463(23)(q)

Table 32

Quenched results for  $\mathcal{F}(w)$  and  $\mathcal{F}(w)/\mathcal{G}(w)$  at non zero recoil [478]. The notation “(q)” stands for the unknown systematics coming from the quenching approximation. QED corrections not included.

$w$	$\mathcal{F}(w)$	$\mathcal{F}(w)/\mathcal{G}(w)$
1.000	0.917(08)(05)(q)	0.878(10)(04)(q)
1.010	0.913(09)(05)(q)	0.883(09)(04)(q)
1.025	0.905(10)(05)(q)	0.891(09)(04)(q)
1.050	0.892(13)(04)(q)	0.905(10)(04)(q)
1.070	0.880(17)(04)(q)	0.914(12)(05)(q)
1.075	0.877(18)(04)(q)	0.916(12)(05)(q)
1.100	0.861(23)(04)(q)	0.923(16)(05)(q)

3247 symmetry to provide simple, few parameter, extrapolation formulas expanded about the  
3248 zero-recoil point,

$$h_{A_1}(w) = h_{A_1}(1) [1 - 8\rho_{D^*}^2 z + (53\rho_{D^*}^2 - 15)z^2 - (231\rho_{D^*}^2 - 91)z^3], \quad (252)$$

$$R_1(w) = R_1(1) - 0.12(w - 1) + 0.05(w - 1)^2, \quad (253)$$

$$R_2(w) = R_2(1) + 0.11(w - 1) - 0.06(w - 1)^2, \quad (254)$$

$$\mathcal{G}(w) = \mathcal{G}(1) [1 - 8\rho_D^2 z + (51\rho_D^2 - 10)z^2 - (252\rho_D^2 - 84)z^3], \quad (255)$$

with

$$z = \frac{\sqrt{w+1} - \sqrt{2}}{\sqrt{w+1} + \sqrt{2}}. \quad (256)$$

3249 This approach is employed below to determine  $\mathcal{G}(1)|V_{cb}|$  and  $\mathcal{F}(1)|V_{cb}|$ .

3250 These extrapolations introduce a systematic error into the extraction of  $|V_{cb}|$  that,  
3251 although mild for  $B \rightarrow D^* \ell \nu$ , can be eliminated by calculating the form factors at  
3252 non zero recoil. A first step on this route has been done by applying the step scaling  
3253 method to calculate, in the *quenched* approximation,  $\mathcal{G}(w)$  and  $\mathcal{F}(w)$  for values of  $w$   
3254 where experimental data are directly available. The form factors have been defined on  
3255 the lattice entirely in terms of ratios of three-point correlation functions, analogously to  
3256 the double ratios discussed above, obtaining in such a way a remarkable statistical and (a  
3257 part from quenching) systematic accuracy. All the details of the calculations, including  
3258 chiral and continuum extrapolations and discussions on the sensitiveness of finite volume  
3259 effects on the heavy quark masses, can be found in refs. [476–478]. The results are shown in  
3260 Tab. 31 and Tab. 32. The quantity  $\Delta(w)$  appearing in Tab. 31 is required to parametrize  
3261 the decay rate  $B \rightarrow D \tau \nu_\tau$  and its knowledge with non perturbative accuracy opens the  
3262 possibility to perform lepton-flavor universality checks on the extraction of  $|V_{cb}|$  from  
3263 this channel. On the one hand, the phenomenological relevance of the results of Tab. 31

3264 and Tab. 32 is limited by the quenching uncertainty that cannot be reliably quantified.  
 3265 On the other hand, these results shed light on the systematics on  $|V_{cb}|$  coming from the  
 3266 extrapolation of the experimental decay rates at zero recoil. The agreement at zero recoil  
 3267 with the full QCD results, Eqs. (249) and (251), suggests that the unestimated quenching  
 3268 error may be comparable to the present statistical error.

### 3269 5.2.2. *Measurements and Tests*

3270 Measurements of the partial decay widths  $d\Gamma/dw$  for the decays  $B \rightarrow D^{(*)}\ell\nu$  have been  
 3271 performed for more than fifteen years on data recorded at the  $\Upsilon(4S)$  resonance (CLEO,  
 3272 Babar, Belle), and at LEP. Though this review will cover only the most recent measure-  
 3273 ments, it will offer an almost complete overview of the analysis techniques employed so  
 3274 far.

3275 A semileptonic decay is reconstructed by combining a charged lepton,  $\ell$ , either an  
 3276 electron or a muon, and a charm meson of the appropriate charge and flavor. To reject  
 3277 non- $B\bar{B}$  background, only leptons with momentum  $p_\ell < 2.3$  GeV/ $c$  are accepted. To  
 3278 suppress fake leptons and leptons from secondary decays, a lower bound  $p_\ell$  is usually  
 3279 applied, in the range from 0.6 to 1.2 GeV/ $c$ , depending on the analysis.  $D$  mesons are fully  
 3280 reconstructed in several hadronic decay channels. Charged and neutral  $D^*$  are identified  
 3281 by their decays to  $D\pi$ . In  $\Upsilon(4S)$  decays, the energy and momentum of the  $B$  mesons,  $E_B$   
 3282 and  $|\mathbf{p}_B|$ , are well known<sup>13</sup>. Since the neutrino escapes detection, the  $B$  decay usually  
 3283 is not completely reconstructed. However, kinematic constraints can be applied to reject  
 3284 background. In particular, if the massless neutrino is the only unobserved particle, the  
 3285  $B$ -meson direction is constrained to lie on a cone centered along the  $D^{(*)}\ell$  momentum  
 3286 vector,  $\mathbf{p}_{D^{(*)}\ell}$ , with an opening angle  $\theta_{BY}$  bounded by the condition  $|\cos\theta_{BY}| \leq 1$  (see  
 3287 Eq. 104 for the exact definition). Background events from random  $D^{(*)}\ell$  combinations are  
 3288 spread over a much larger range in  $\cos\theta_{BY}$  and decays of the type  $B \rightarrow D^{(*)}\pi\pi\ell\nu$ , where  
 3289 the additional pions are not reconstructed, accumulate mainly below  $\cos\theta_{BY} = -1$ .

3290 The differential decay rate  $d^4\Gamma/dwd\cos\theta_\ell d\cos\theta_V d\chi$  depends on four variables:  $w =$   
 3291  $v_B \cdot v_{D^{(*)}}$ ,  $\theta_\ell$ , the angle between the lepton direction in the virtual  $W$  rest frame and the  
 3292  $W$  direction in the  $B$  rest frame,  $\theta_V$ , the angle between the  $D$ -meson direction in the  
 3293  $D^*$  rest frame and the  $D^*$  direction in the  $B$  rest frame, and  $\chi$ , the angle between the  
 3294 plane determined from the  $D^*$  decay products and the plane defined by the two leptons.  
 3295 In HQET, the decay rate is parametrized in term of four quantities: the normalization  
 3296  $\mathcal{F}(1)|V_{cb}|$ , the slope  $\rho_{D^*}^2$ , and the form-factor ratios  $R_1(1)$  and  $R_2(1)$ . Many measurements  
 3297 of  $\mathcal{F}(1)|V_{cb}|$  and  $\rho_{D^*}^2$  rely on the differential decay rates, integrated over the three angles,  
 3298  $d\Gamma(B \rightarrow D^*\ell\nu)/dw$  and thus require external knowledge of  $R_1(1)$  and  $R_2(1)$ .

3299 Following the first measurement by CLEO [492], the Babar [249], and Belle [493]  
 3300 Collaborations have employed much larger samples of reconstructed neutral  $B$  mesons  
 3301 to determine  $R_1(1)$  and  $R_2(1)$  from a fit to the four-dimensional differential decay rate.  
 3302 Figure 38 shows a comparison of the data and the fit results from the recent Belle  
 3303 analysis, for the projections of the four kinematic variables. Tab. 33 lists the results of  
 3304 the fully-differential measurements from Babar and Belle.

<sup>13</sup>In LEP experiments the direction of the  $B$  meson is obtained from the vector joining the primary vertex to the  $B$  decay vertex, the neutrino energy is computed from the missing energy in the event. A missing energy technique is also applied by  $\Upsilon(4S)$  experiments to improve background rejection in  $B \rightarrow D\ell\nu$  measurements.

Table 33

Summary of the  $B$ -factories results on form factors and  $|V_{cb}|$  from semileptonic  $B$  decays.

Mode	Ref.	$\mathcal{F}(1) V_{cb}  \cdot 10^3$	$\rho_{D^*}^2$	$R_1$	$R_2$
$B^- \rightarrow D^{*0}\ell^- \bar{\nu}$ [494]		$35.9 \pm 0.6 \pm 1.4$	$1.16 \pm 0.06 \pm 0.08$	-	-
$\bar{B}^0 \rightarrow D^{*+}\ell^- \bar{\nu}$ [493]		$34.4 \pm 0.2 \pm 1.0$	$1.29 \pm 0.05 \pm 0.03$	$1.50 \pm 0.05 \pm 0.06$	$0.84 \pm 0.03 \pm 0.03$
$\bar{B}^0 \rightarrow D^{*+}\ell^- \bar{\nu}$ [249]		$34.4 \pm 0.3 \pm 1.1$	$1.19 \pm 0.05 \pm 0.03$	$1.43 \pm 0.06 \pm 0.04$	$0.83 \pm 0.04 \pm 0.02$
$B \rightarrow D^{(*)}\ell^- \bar{\nu}$ [495]		$35.9 \pm 0.2 \pm 1.2$	$1.22 \pm 0.02 \pm 0.07$	-	-

Mode	Ref.	$\mathcal{G}(1) V_{cb}  \cdot 10^3$	$\rho_D^2$
$B \rightarrow D\ell^- \bar{\nu}$ [495]		$43.1 \pm 0.8 \pm 2.3$	$1.20 \pm 0.04 \pm 0.07$
$B \rightarrow D\ell^- \bar{\nu}$ [248]		$43.0 \pm 1.9 \pm 1.4$	$1.20 \pm 0.09 \pm 0.04$

3305 In a recent Babar analysis [494] a sample of about 23,500  $B^- \rightarrow D^{*0}\ell^- \bar{\nu}$  decays has  
 3306 been selected from about  $2 \times 10^7 \Upsilon(4S) \rightarrow B\bar{B}$  events. The signal yield is determined in  
 3307 ten bins in  $w$  to measure  $d\Gamma(B^- \rightarrow D^{*0}\ell^- \bar{\nu})/dw$  with minimal model dependence. The  
 3308 fitted values of  $\mathcal{F}(1)|V_{cb}|$  and  $\rho_{D^*}^2$  are given in Tab. 33.

3309 The large integrated luminosities and the deeper understanding of  $B$  mesons properties  
 3310 accumulated in recent years have allowed  $B$ -factories to perform new measurements of  
 3311 semileptonic decays based on innovative approaches. Babar has recently published results  
 3312 on  $\mathcal{G}(w)|V_{cb}|$  and  $\mathcal{F}(w)|V_{cb}|$ , based on an inclusive selection of  $B \rightarrow D\ell\nu X$  decays, where  
 3313 only the  $D$  meson and the charged lepton are reconstructed [495]. To reduce background  
 3314 from  $D^{*}\ell\nu$  decays and other background sources, the lepton momentum is restricted

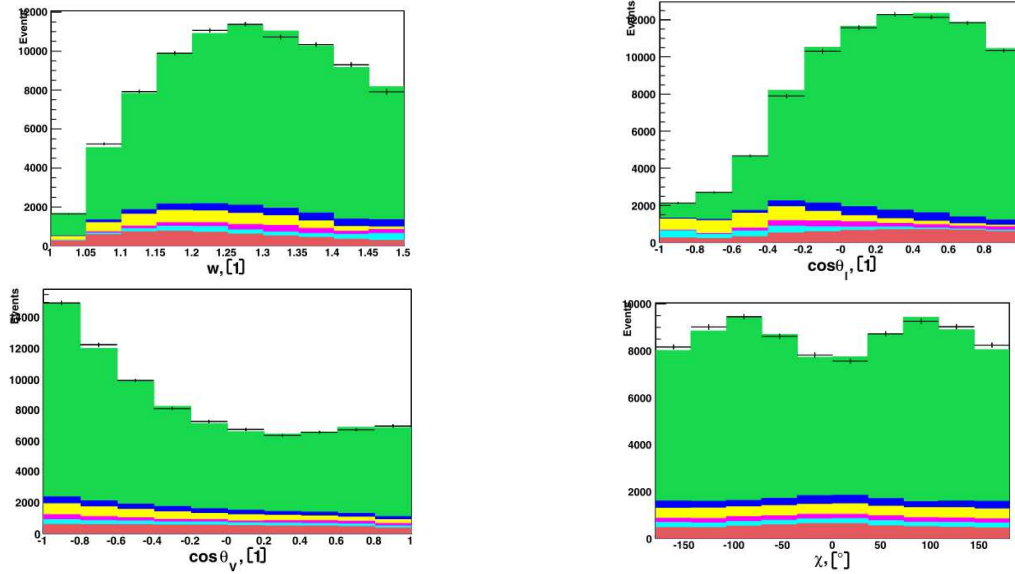


Fig. 38. Belle [493]: Results of the four-dimensional fit to the  $B^0 \rightarrow D^{*+}\ell\nu$  decay rate in terms one one-dimensional projections:  $w$  (top-left),  $\cos\theta_\ell$  (top-right),  $\cos\theta_\nu$  (bottom left) and  $\chi$  (bottom right). The data (points) are compared to the sum of the fitted contribution, signal (green) and several background sources (in different colors).

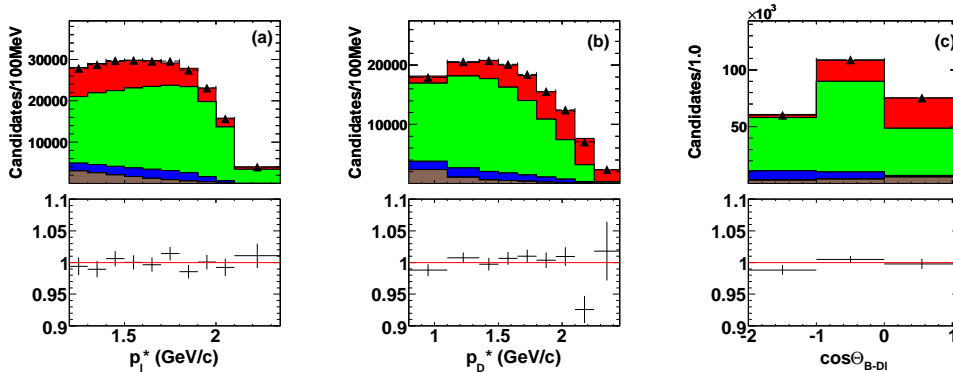


Fig. 39. BaBar [495]: Projected distributions for selected  $B \rightarrow D^0 e^- \bar{\nu}_e X$  events a)  $p_\ell$ , (b)  $p_D$ , and (c)  $\cos\theta_{BY}$ . The data (points) are compared to the fit result, showing contributions from  $D\ell\nu$  (red),  $D^*\ell\nu$  (green),  $D^{**}\ell\nu$  (blue) decays, and residual background (taupe).

3315  $p_\ell > 1.2 \text{ GeV}/c$ , and the  $D$  mesons are reconstructed only in the two simplest and cleanest  
 3316 decay modes,  $D^0 \rightarrow K^- \pi^+ \pi^+$  and  $D^+ \rightarrow K^- \pi^+ \pi^+$ .

3317 Signal decays with  $D$  and  $D^*$  mesons in the final states are separated from background  
 3318 processes (mainly semileptonic decays involving higher mass charm mesons,  $D^{**}$ ) on a  
 3319 statistical basis. The  $V - A$  structure of the weak decays favors larger values of  $p_\ell$  for  
 3320 the vector meson  $D^*$  than for the scalar  $D$ . using the three-dimensional distributions of  
 3321 the lepton momentum  $p_\ell$ , the  $D$  momentum  $p_D$ , and  $\cos\theta_{BY}$ .

3322 The signal and background yields, the values of  $\rho_D^2$ ,  $\rho_{D^*}^2$ ,  $\mathcal{G}(1)|V_{cb}|$  and  $\mathcal{F}(1)|V_{cb}|$   
 3323 are obtained from a binned  $\chi^2$  fit to the three-dimensional distributions of the lepton  
 3324 momentum  $p_\ell$ , the  $D$  momentum  $p_D$ , and  $\cos\theta_{BY}$ , separately for the  $D^0\ell$  and  $D^+\ell$   
 3325 samples. The contribution from neutral and charged  $B$  decays in each sample are obtained  
 3326 from the ratio of measured branching fractions of  $\Upsilon(4S) \rightarrow B^+ B^-$ ,  $\Upsilon(4S) \rightarrow B^0 \bar{B}^0$ , the  
 3327 branching fractions for charged and neutral  $D^*$  mesons to  $D$  mesons, and by imposing  
 3328 equal semileptonic decay rates for charged and neutral  $B$  mesons. As an example, Fig. 39  
 3329 shows the results of the fit in one-dimensional projections for the  $D^0 e^- \bar{\nu}_e X$  sample. An  
 3330 alternative fit with  $R_1(1)$  and  $R_2(1)$  as free parameters gives results consistent with the  
 3331 fully differential measurements cited above, albeit with larger statistical and systematic  
 3332 errors.

3333 Since the  $D\ell\nu$  and  $D^*\ell\nu$  decays are measured simultaneously, the comparison of their  
 3334 form factors to validate the QCD predictions is straightforward. The measured form  
 3335 factor ratio at zero recoil  $\mathcal{G}(1)/\mathcal{F}(1) = 1.23 \pm 0.09$  confirms the lattice QCD prediction of  
 3336  $1.16 \pm 0.04$ . The difference of the slope parameters  $\rho_D^2 - \rho_{D^*}^2 = 0.01 \pm 0.04$  is consistent  
 3337 with zero, as predicted [496].

3338 The large luminosity accumulated in the  $B$ -factories permits the use of tagged event  
 3339 samples, for which one of the two  $B$  mesons is fully reconstructed in an hadronic final  
 3340 state (more than 1000 modes are considered) and a semileptonic decay of the other  $B$   
 3341 is reconstructed from the remaining particles in the event. Since the momentum of the  
 3342 tagged  $B$  is measured, the kinematic properties of the semileptonic  $B$  are fully deter-  
 3343 mined. This technique results in a sizable background reduction and thus a much lower  
 3344 bound on the lepton momentum ( $p_\ell > 0.6 \text{ GeV}/c$ ), a much more precise determination



3345 of  $w$ , and therefore a remarkable reduction of the systematic error, at the cost of an increase in the statistical error (the tagging efficiency does not exceed 0.5%). While several  
 3346 measurements of semileptonic branching fractions exist to date, only BaBar has presented a form factor determination,  $\mathcal{G}(1)|V_{cb}|$  and  $\rho_D^2$ , with a tagged sample of  $B \rightarrow D\ell\nu$   
 3347 decays [248].  
 3348  
 3349

3350 The yield of signal events in ten equal size  $w$  bins is obtained from a fit to the distribution of the missing mass squared,  $\mathcal{M}_\nu^2 = (P_B - P_D - P_\ell)^2$ . An example is shown in  
 3351 Fig. 40. A fit to the background-subtracted and efficiency-corrected signal yield, summed over charged and neutral  $B$  decays, is used to extract the form-factor parameters, the  
 3352 normalization  $\mathcal{G}|V_{cb}|$ , and the slope,  $\rho_D^2$ . The signal yield and the fitted form factor as a function of  $w$  are shown in Fig. 40. The results of this measurement, and of all the others  
 3353 discussed so far, are reported in Tab. 33. There is very good consistency among all of the most recent measurements.  
 3354  
 3355  
 3356  
 3357

3358 By integrating the differential decays rates the branching fractions for  $B \rightarrow D^\ell\nu$  and  
 3359  $B \rightarrow D^*\ell\nu$  decays can be determined with good precision. However, there has been a long standing problem with the measured semileptonic branching fractions. The sums of the  
 3360 branching fractions for  $B \rightarrow D\ell^-\bar{\nu}$ ,  $B \rightarrow D^*\ell^-\bar{\nu}$  and  $B \rightarrow D^{(*)}\pi\ell^-\bar{\nu}$  decays [497, 498],  $9.5 \pm 0.3\%$  for  $B^+$  and  $8.9 \pm 0.2\%$  for  $B^0$ , are significantly smaller than the measured  
 3361 inclusive  $B \rightarrow X_c\ell\nu$  branching fractions of  $10.89 \pm 0.16\%$  and  $10.15 \pm 0.16\%$  for  $B^+$  and  $B^0$ , respectively. Branching fractions for  $B \rightarrow D^{**}\ell\nu$  decay are still not well known, and  
 3362 furthermore, the assumption that the four  $D^{**}$  mesons decay exclusively to  $D\pi$  and  $D^*\pi$  final states is largely untested experimentally. And even among the measured values for  
 3363 the single largest  $B$  branching fraction,  $\mathcal{B}(B \rightarrow D^*\ell\nu)$ , there is a spread that exceeds the stated errors significantly.  
 3364  
 3365  
 3366  
 3367  
 3368

### 3369 5.2.3. Determination of Form Factors and $|V_{cb}|$

3370 Fig. 41 shows the one sigma contour plots for all the measurements of  $\mathcal{G}(w)|V_{cb}|$  and  
 3371  $\mathcal{F}(w)|V_{cb}|$  performed so far. While there is a good agreement among the five measurements of  $B \rightarrow D\ell\nu$  decays, there is less consistency among the ten  $D^*$  results, specifically  
 3372 two of the older measurements differ significantly from the recent, more precise measurements. Tab. 34 shows the averages of form factor measurements. Using the values of  $\mathcal{G}(1)$   
 3373 and  $\mathcal{F}(1)$  reported in Eqs. (249) and (251) we obtain  
 3374  
 3375

$$|V_{cb}| = (39.4 \pm 1.4 \pm 0.9) \times 10^{-3} \text{ from } B \rightarrow D\ell\nu, \quad (257)$$

$$|V_{cb}| = (38.28 \pm 0.71 \pm 0.99) \times 10^{-3} \text{ from } B \rightarrow D^*\ell\nu, \quad (258)$$

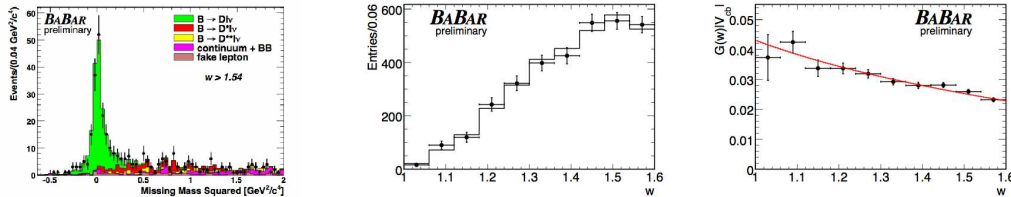


Fig. 40. BaBar analysis of tagged  $B \rightarrow D\ell\mu$  decays [248] Data (points) compared to fit results, left:  $\mathcal{M}_\nu^2$  for  $w > 1.54$ , center: signal event yield for the sum of charged and neutral  $B$  decays, right:  $\mathcal{G}(w)$  vs  $w$ , as obtained from efficiency-corrected yields (data points) and the result of the form factor fit (solid line).

Table 34

Averages for form factors extrapolations and slopes.

Process	$\mathcal{G}(1) V_{cb} , \mathcal{F}(1) V_{cb} $	$\rho_{D^{(*)}}^2$
$B \rightarrow D\ell\nu$	$42.4 \pm 1.6$	$1.19 \pm 0.05$
$B \rightarrow D^*\ell\nu$	$35.41 \pm 0.52$	$1.16 \pm 0.05$

where the first error is from experiment and the second from unquenched lattice QCD. The two results agree well. It is not straightforward for combine these two results, because the correlations between the two sets of measurements and two calculations have not been analyzed. Assuming a correlation of 50% for both, we obtain the average value from exclusive decays

$$|V_{cb}| = (38.6 \pm 1.1) \times 10^{-3}, \quad (259)$$

3376 where experimental and lattice-QCD errors have been added in quadrature.

### 3377 5.3. Inclusive CKM-favored $B$ decays

#### 3378 5.3.1. Theoretical Background

3379 The inclusive  $\bar{B} \rightarrow X_c \ell \bar{\nu}$  decay rate can be calculated using the operator product  
 3380 expansion (OPE). Applied to heavy quark decays, the OPE amounts to an expansion in  
 3381 inverse powers of the heavy quark mass and is often referred to as heavy-quark expansion  
 3382 (HQE). Using this technique, the non-perturbative input needed to predict the rate is  
 3383 reduced to a few matrix elements of local operators in HQET. Together with  $|V_{cb}|$ ,  $m_b$ ,  
 3384 and  $m_c$ , these heavy-quark parameters can be extracted from a moment analysis, i.e. by  
 3385 fitting the theoretical predictions for the decay rate and moments of decay spectra to the  
 3386 available experimental results.

3387 The application of the OPE to semileptonic heavy hadron decays was developed quite  
 3388 some time ago [499–502]. A detailed discussion of the technique can, for example, be  
 3389 found in the textbook [503]. For a review focusing on the extraction of  $|V_{cb}|$  and the heavy  
 3390 quark parameters, see [504] and the PDG review [283]. In the following, we briefly recall  
 3391 some of the basic concepts, review recent progress in evaluating higher-order perturbative  
 3392 corrections, and briefly discuss possible limitations of the approach. After this, we review  
 3393 the available experimental data and the results of the moment analysis.

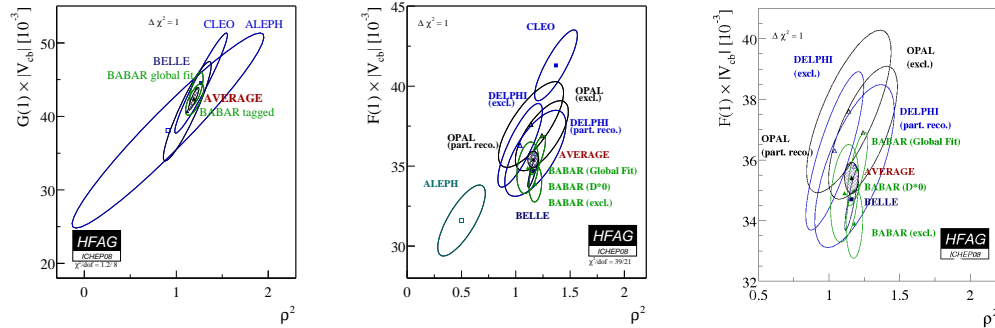


Fig. 41. HFAG: One sigma contour plots for all measurements of  $\mathcal{G}(1)|V_{cb}|$  (left),  $\mathcal{F}(1)|V_{cb}|$  (center), and  $\mathcal{F}(1)|V_{cb}|$  with the two measurements that are least consistent with the average removed (right).

The  $\bar{B} \rightarrow X_c \ell \bar{\nu}$  decay is mediated by the effective Hamiltonian

$$\mathcal{H}_{\text{eff}} = \frac{G_F}{\sqrt{2}} V_{cb} J^\mu J_\mu^\ell = \frac{G_F}{\sqrt{2}} V_{cb} \bar{c} \gamma^\mu (1 - \gamma_5) b \bar{\ell} \gamma_\mu (1 - \gamma_5) \nu. \quad (260)$$

Neglecting electromagnetic corrections, the decay rate factors into a product of a leptonic tensor  $L_{\mu\nu}$  and a hadronic tensor  $W_{\mu\nu}$ , which are given by the matrix elements of two leptonic and two hadronic currents. Using the optical theorem, the hadronic tensor can be obtained from the imaginary part of the forward matrix element of the product  $\mathbf{T}_{\mu\nu}$  of two weak currents,  $2M_B W_{\mu\nu} = -2 \text{Im} \langle B(p_B) | \mathbf{T}_{\mu\nu} | B(p_B) \rangle$ . The OPE expands the time-ordered product  $\mathbf{T}_{\mu\nu}$  into a sum of local HQET operators  $O_i$  of increasing dimension

$$\mathbf{T}_{\mu\nu} = -i \int d^4 x e^{-iqx} \mathbf{T} [J_\mu^\dagger(x) J_\nu(0)] = \sum_i C_{\mu\nu}^i(v \cdot q, q^2, m_b, m_c) O_i(0). \quad (261)$$

3394 In order to perform the expansion, a velocity vector  $v^\mu$ , with  $v^2 = 1$ , is introduced to  
 3395 split the  $b$ -quark momentum into  $p_b^\mu = m_b v^\mu + r^\mu$ , where the components of the residual  
 3396 momentum  $r^\mu$  are independent of the  $b$ -quark mass. It is usually chosen to be the meson  
 3397 velocity,  $v^\mu = p_B^\mu / M_B$ . Because Eq. (261) is an operator relation, it holds for arbitrary  
 3398 matrix elements. To determine the Wilson coefficients  $C_{\mu\nu}^i$  one considers partonic matrix  
 3399 elements of Eq. (261) in perturbation theory.

3400 The OPE separates the physics associated with large scales such as  $m_b$ , which enter  
 3401 the Wilson coefficients  $C_{\mu\nu}^i$ , from the non-perturbative dynamics entering the matrix  
 3402 elements of the operators  $O_i$ . In this context, it is important that the operators on the  
 3403 right-hand side of Eq. (261) are defined in HQET so that their matrix elements are inde-  
 3404 pendent of  $m_b$  up to power corrections and are governed by non-perturbative dynamics  
 3405 associated with the scale  $\Lambda_{\text{QCD}}$ . Since the Wilson coefficients of higher dimensional oper-  
 3406 ators in Eq. (261) contain inverse powers of  $m_b$ , their contributions to the rate are  
 3407 suppressed by powers of  $\Lambda_{\text{QCD}}/m_b$ . The leading operator in Eq. (261) has dimension  
 3408 three and is given by a product of two HQET heavy quark fields  $O_3 = \bar{h}_v h_v$ . Up to  
 3409 power corrections, its  $B$ -meson matrix element is one. Dimension four operators can be  
 3410 eliminated using the equation of motion and the leading power corrections arise from  
 3411 two dimension five operators: the kinetic operator  $O_{\text{kin}}$  and the chromomagnetic oper-  
 3412 ator  $O_{\text{mag}}$ , whose  $B$ -meson matrix elements are denoted by  $\lambda_1$  and  $\lambda_2$  [505] or  $\mu_\pi^2$  and  
 3413  $\mu_G^2$  [501]. Different schemes are used to define these parameters, but to leading order and  
 3414 leading power they are given by

$$\begin{aligned} \langle O_{\text{kin}} \rangle &\equiv \frac{1}{2M_B} \langle \bar{B}(p_B) | \bar{h}_v (iD)^2 h_v | \bar{B}(p_B) \rangle = -\mu_\pi^2 = \lambda_1, \\ \langle O_{\text{mag}} \rangle &\equiv \frac{1}{2M_B} \langle \bar{B}(p_B) | \frac{g}{2} \bar{h}_v \sigma_{\mu\nu} G^{\mu\nu} h_v | \bar{B}(p_B) \rangle = \mu_G^2 = 3\lambda_2. \end{aligned} \quad (262)$$

In order for the OPE to converge, it is necessary that the scales entering the Wilson coefficients are all larger than  $\Lambda_{\text{QCD}}$ . This condition is violated in certain regions of phase-space. In order to get reliable predictions, one needs to consider sufficiently inclusive quantities such as the total rate, which takes the form [499–502]

$$\Gamma(\bar{B} \rightarrow X_c \ell \bar{\nu}) = \frac{G_F^2 |V_{cb}|^2 m_b^5}{192\pi^3} \left\{ f(\rho) + k(\rho) \frac{\mu_\pi^2}{2m_b^2} + g(\rho) \frac{\mu_G^2}{2m_b^2} \right\}, \quad (263)$$

up to corrections suppressed by  $(\Lambda_{\text{QCD}}/m_b)^3$ , and with  $\rho = m_c^2/m_b^2$ . The Wilson coefficients  $f(\rho)$ ,  $k(\rho)$  and  $g(\rho)$  can be calculated in perturbation theory. They are obtained by taking the imaginary part of  $C_{\mu\nu}^i$ , contracting with the lepton tensor  $L^{\mu\nu}$  and integrating over the leptonic phase space. We have written the expansion in inverse powers of  $m_b$ , but it is the energy release  $\Delta E \sim m_b - m_c$  which dictates the size of higher order corrections. Other suitable inclusive observables include the spectral moments

$$\langle E_\ell^n E_X^m (M_X^2)^l \rangle = \frac{1}{\Gamma_0} \int_{E_0}^{E_{\text{max}}} dE_\ell \int dE_X \int dM_X^2 \frac{d\Gamma}{dE_X dM_X^2 dE_\ell} E_\ell^n E_X^m (M_X^2)^l, \quad (264)$$

3415 with  $\Gamma_0 = \Gamma(E_\ell > E_0)$  for low values of  $n$ ,  $m$ , and  $l$ , with a moderate lepton energy cut  
 3416  $E_0$ . The OPE for the moments Eq. (264) depends on the *same* operator matrix elements  
 3417 as the rate Eq. (263), but the calculable Wilson coefficients  $f(\rho)$ ,  $g(\rho)$ , and  $k(\rho)$  will be  
 3418 different for each moment. Note that the coefficient  $k(\rho)$  of the kinetic operator is linked  
 3419 to the leading power coefficient  $f(\rho)$ , for example  $k(\rho) = -f(\rho)$  for the total rate. The  
 3420 corresponding relations for the moments are given in [506].

3421 By measuring the rate and several spectral moments Eq. (264), and fitting the theo-  
 3422 retical expressions to the data, one can simultaneously extract  $|V_{cb}|$ , the quark masses  
 3423  $m_b$  and  $m_c$ , as well as the heavy quark parameters such as  $\mu_\pi$  and  $\mu_G$ . Two independent  
 3424 implementations of this moment analysis are currently used [507, 508] and [509] (based  
 3425 on [504, 510]). Both groups include terms up to third order in  $\Lambda_{\text{QCD}}/m_b$  [511] and eval-  
 3426 uate leading order Wilson coefficients to one-loop accuracy [512–518]. In addition, they  
 3427 also include the part of the two-loop corrections which is proportional  $\beta_0$  [510, 519–524].  
 3428 However, the two fits use different schemes for the masses and heavy quark parameters.  
 3429 The analysis of [509] is performed in the kinetic scheme [525], while [507, 508] adopt the  
 3430  $1S$ -scheme [526] as their default choice. Both schemes, as well as others, such as the  
 3431 potential-subtracted [527] and the shape-function scheme [528], are designed to improve  
 3432 the perturbative behavior by reducing the large infrared sensitivity inherent in the pole  
 3433 scheme. Two-loop formulae for the conversion among the different schemes can be found  
 3434 in [529].

3435 It has been noticed that the two-loop terms appearing in the conversion of  $m_b$  among  
 3436 schemes were in some cases larger than the uncertainties quoted after fitting in a given  
 3437 scheme [530]. This indicates that higher-order corrections to the Wilson coefficients can  
 3438 no longer be neglected. Recently, a number of new perturbative results for the Wilson  
 3439 coefficients have become available, however, they have not yet been implemented into  
 3440 the moment analysis. The Wilson coefficient of the leading order operator  $O_3$  has been  
 3441 evaluated to two-loop accuracy [531, 532]. The numerical technique used in [531] allows  
 3442 for the calculation of arbitrary moments and its results are confirmed by an independent  
 3443 analytical calculation of the rate and the first few  $E_\ell$  and  $E_X$  moments [532]. An earlier  
 3444 estimate of the two-loop corrections [533] needed to be revised in view of the new results  
 3445 [534]. At the same accuracy, one should also include the one-loop corrections to the  
 3446 coefficients of the kinetic and chromomagnetic operators. So far, only the corrections  
 3447 for the kinetic operator are available [506]. Furthermore, the tree-level OPE has been  
 3448 extended to fourth order in  $\Lambda_{\text{QCD}}/m_b$  [535].

3449 In addition to perturbative and non-perturbative corrections, the hadronic decay rates  
 3450 will contain terms which are not captured by the OPE. While such terms are expo-  
 3451 nentially suppressed in completely Euclidean situations, they are not guaranteed to be  
 3452 negligible for the semileptonic rate and its moments [536]. These violations of quark-

3453 hadron duality are difficult to quantify. Model estimates seem to indicate that the effects  
 3454 on the rate are safely below the 1% level for the total rate [537,538], but they could be  
 3455 larger for the spectral moments. Other issues studied in the recent literature concern the  
 3456 role of the charm quarks [539,540] and potential new physics effects [541,542].

### 3457 5.3.2. *Measurements of Moments*

3458 Measurements of the semileptonic  $B$  branching fraction and inclusive observables in  
 3459  $B \rightarrow X_c \ell \nu$  decays relevant to the determination of the heavy quark parameters in the  
 3460 OPE have been obtained by the BaBar [543–545], Belle [546,547], CDF [548], CLEO [549]  
 3461 and DELPHI [550] Collaborations. The photon-energy spectrum in  $B \rightarrow X_s \gamma$  decays,  
 3462 which is particularly sensitive to the  $b$ -quark mass,  $m_b$ , has been studied by BaBar [551,  
 3463 552], Belle [553,554] and CLEO [555]. In this section, we briefly review new or updated  
 3464 measurements of  $B \rightarrow X_c \ell \nu$  decays.

3465 BaBar has updated their previous measurement of the hadronic mass moments  $\langle M_X^{2n} \rangle$   
 3466 [544] and obtained preliminary results based on a dataset of  $210 \text{ fb}^{-1}$  taken at the  
 3467  $\Upsilon(4S)$  resonance [545]. In this analysis, the hadronic decay of one  $B$  meson in  $\Upsilon(4S) \rightarrow$   
 3468  $B\bar{B}$  is fully reconstructed ( $B_{\text{tag}}$ ) and the semileptonic decay of the second  $B$  is inferred  
 3469 from the presence of an identified lepton ( $e$  or  $\mu$ ) among the remaining particles in the  
 3470 event ( $B_{\text{sig}}$ ). This fully reconstructed tag provides a significant reduction in combinatorial  
 3471 backgrounds and results in a sample of semileptonic decays with a purity of about 80%.  
 3472 Particles that are not used in the reconstruction of  $B_{\text{tag}}$  and are not identified as the  
 3473 charged lepton are assigned to the  $X_c$  system, and its mass  $M_X$  is calculated using some  
 3474 kinematic constraints for the whole event.

3475 From the  $M_X$  spectrum, BaBar calculates the hadronic mass moments  $\langle M_X^n \rangle$ ,  $n =$   
 3476  $1, \dots, 6$  as a function of a lower limit on the lepton momenta in the center-of-mass (c.m.)  
 3477 frame ranging from 0.8 to 1.9 GeV/ $c$ . These moments are distorted by acceptance and  
 3478 finite resolution effects and an event-by-event correction is derived from Monte Carlo  
 3479 (MC) simulated events. These corrections are approximated as linear functions of the  
 3480 observed mass with coefficients that depend on the lepton momentum, the multiplicity  
 3481 of the  $X_c$  system and  $E_{\text{miss}} - c|\mathbf{p}_{\text{miss}}|$ , where  $E_{\text{miss}}$  and  $\mathbf{p}_{\text{miss}}$  are the missing energy and  
 3482 3-momentum in the event, respectively. Note that in this analysis mixed mass and c.m.  
 3483 energy moments  $\langle N_X^{2n} \rangle$ ,  $n = 1, 2, 3$ , with  $N_X = M_X^2 c^4 - 2\tilde{\Lambda}E_X + \tilde{\Lambda}^2$  and  $\tilde{\Lambda} = 0.65 \text{ GeV}$   
 3484 are measured in addition to ordinary hadronic mass moments. These mixed moments  
 3485 are expected to better constrain some heavy quark parameters, though they are not yet  
 3486 used in global fit analyses.

3487 Belle has recently measured the c.m. electron energy [546] and the hadronic mass [547]  
 3488 spectra in  $B \rightarrow X_c \ell \nu$  decays, based on  $140 \text{ fb}^{-1}$  of  $\Upsilon(4S)$  data. The experimental pro-  
 3489 cedure is very similar to the BaBar analysis, *i.e.*, the hadronic decay of one  $B$  meson  
 3490 in the event is fully reconstructed. The main difference to the BaBar analysis is that  
 3491 detector effects in the spectra are removed by unfolding using the Singular Value De-  
 3492 composition (SVD) algorithm [556] with a detector response matrix determined by MC  
 3493 simulation. The moments are calculated from the unfolded spectra. Belle measures the  
 3494 partial semileptonic branching fraction and the c.m. electron energy moments  $\langle E_e^n \rangle$ ,  $n =$   
 3495  $1, \dots, 4$ , for minimum c.m. electron energies ranging from 0.4 to 2.0 GeV. In the hadronic  
 3496 mass analysis [547] the first and second moments of  $M_X^2$  are measured for minimum c.m.  
 3497 lepton energies between 0.7 and 1.9 GeV.

Table 35

Results of the global fit analyses by BaBar and Belle in terms of  $|V_{cb}|$  and the  $b$ -quark mass  $m_b$ , including the  $\chi^2$  of the fit over the number of degrees of freedom. Note that the fit results for  $m_b$  in the kinetic and 1S schemes can be compared only after scheme translation.

	$ V_{cb} $ ( $10^{-3}$ )	$m_b$ (GeV)	$\chi^2/\text{ndf.}$
BaBar kinetic [545]	$41.88 \pm 0.81$	$4.552 \pm 0.055$	$8/(27 - 7)$
Belle kinetic [553]	$41.58 \pm 0.90$	$4.543 \pm 0.075$	$4.7/(25 - 7)$
Belle 1S [553]	$41.56 \pm 0.68$	$4.723 \pm 0.055$	$7.3/(25 - 7)$

3498 Another interesting analysis of inclusive  $B \rightarrow X_c \ell \nu$  decays comes from the DELPHI  
 3499 experiment [550] operating at LEP. In this study, the  $b$ -frame lepton energy  $\langle E_\ell^n \rangle$ ,  $n =$   
 3500  $1, 2, 3$ , and the hadronic mass  $M_X^{2n}$ ,  $n = 1, \dots, 5$ , moments are measured without applying  
 3501 any selection on the lepton energy in the  $b$ -frame. This is possible because DELPHI  
 3502 measures decays of  $b$ -hadrons in  $Z^0 \rightarrow b\bar{b}$  events.  $b$ -hadrons are produced with significant  
 3503 kinetic energy in the laboratory frame, so that charged leptons produced at rest in the  
 3504  $b$ -frame can be observed in the detector.

### 3505 5.3.3. Global Fits for $|V_{cb}|$ and $m_b$

3506 The OPE calculation of the  $B \rightarrow X_c \ell \nu$  weak decay rate depends on a set of heavy  
 3507 quark parameters that contain the soft QCD contributions. These parameters can be  
 3508 determined from other inclusive observables in  $B$  decays, namely the lepton energy  $\langle E_\ell^n \rangle$   
 3509 and hadronic mass moments  $\langle M_X^{2n} \rangle$  in  $B \rightarrow X_c \ell \nu$  and the photon energy moments  $\langle E_\gamma^n \rangle$   
 3510 in  $B \rightarrow X_s \gamma$ . Once these parameters are known,  $|V_{cb}|$  can be determined from mea-  
 3511 surements of the semileptonic  $B$  branching fraction. This is the principle of the global fit  
 3512 analyses for  $|V_{cb}|$ . On the theory side, these analyses require OPE predictions of the afore-  
 3513 mentioned inclusive observables, in addition to a calculation of the semileptonic width.  
 3514 At present, two independent sets of theoretical formulae have been derived including  
 3515 non-perturbative corrections up to  $\mathcal{O}(1/m_b^3)$ , referred to as the kinetic [504, 510, 557] and  
 3516 the 1S scheme [508], according to the definition of the  $b$ -quark mass used.

3517 Tab. 35 summarizes the results of the global fit analyses performed by BaBar [545] and  
 3518 Belle [553] in terms of  $|V_{cb}|$  and the  $b$ -quark mass  $m_b$ . BaBar uses 27 and Belle 25 mea-  
 3519 surements of the partial  $B \rightarrow X_c \ell \nu$  branching fraction and the moments in  $B \rightarrow X_c \ell \nu$   
 3520 and  $B \rightarrow X_s \gamma$  decays. Measurements at different thresholds in the lepton or photon  
 3521 energy are highly correlated. Correlations between measurements and between their the-  
 3522 oretical predictions must therefore be accounted for in the definition of the  $\chi^2$  of the fit.  
 3523 The BaBar analysis performs a fit in the kinetic mass scheme only. In this framework,  
 3524 the free parameters are:  $|V_{cb}|$ ,  $m_b(\mu)$ ,  $m_c(\mu)$ ,  $\mu_\pi^2(\mu)$ ,  $\mu_G^2(\mu)$ ,  $\rho_D^3(\mu)$  and  $\rho_{LS}^3(\mu)$ , where  $\mu$   
 3525 is the scale taken to be 1 GeV. In addition, Belle fits their data also in the 1S scheme.  
 3526 Here, the free parameters are:  $|V_{cb}|$ ,  $m_b$ ,  $\lambda_1$ ,  $\rho_1$ ,  $\tau_1$ ,  $\tau_2$  and  $\tau_3$ . The only external input in  
 3527 these analyses is the average  $B$  lifetime  $\tau_B = (1.585 \pm 0.006)$  ps [558].

3528 HFAG has combined the available  $B \rightarrow X_c \ell \nu$  and  $B \rightarrow X_s \gamma$  data from different  
 3529 experiments to extract  $|V_{cb}|$  and  $m_b$ . Using 64 measurements in total (Tab. 36), the  
 3530 analysis is carried out in the kinetic scheme. The procedure is very similar to the analyses  
 3531 of the  $B$ -factory datasets described above. The results for  $|V_{cb}|$ ,  $m_b$  and  $\mu_\pi^2$  are quoted  
 3532 in Tab. 37 and Fig. 42. Recently, concerns have been raised about the inclusion of  $B \rightarrow$   
 3533  $X_s \gamma$  moments, because their prediction is not based on pure OPE but involves modeling

Table 36

Measurements of the lepton energy  $\langle E_\ell^n \rangle$  and hadronic mass moments  $\langle M_X^{2n} \rangle$  in  $B \rightarrow X_c \ell \nu$  and the photon energy moments  $\langle E_\gamma^n \rangle$  in  $B \rightarrow X_s \gamma$  used in the combined HFAG fit.

Experiment	$\langle E_\ell^n \rangle$	$\langle M_X^{2n} \rangle$	$\langle E_\gamma^n \rangle$
BaBar	$n = 0, 1, 2, 3$ [543]	$n = 1, 2$ [545]	$n = 1, 2$ [551, 552]
Belle	$n = 0, 1, 2, 3$ [546]	$n = 1, 2$ [547]	$n = 1, 2$ [554]
CDF		$n = 1, 2$ [548]	
CLEO		$n = 1, 2$ [549]	$n = 1$ [555]
DELPHI	$n = 1, 2, 3$ [550]	$n = 1, 2$ [550]	

Table 37

Combined HFAG fit to all experimental data (Tab. 36). In the last column we quote the  $\chi^2$  of the fit over the number of degrees of freedom.

Dataset	$ V_{cb} $ ( $10^{-3}$ )	$m_b$ (GeV)	$\mu_\pi^2$ ( $\text{GeV}^2$ )	$\chi^2/\text{ndf}$ .
$X_c \ell \nu$ and $X_s \gamma$	$41.54 \pm 0.73$	$4.620 \pm 0.035$	$0.424 \pm 0.042$	26.4/(64 - 7)
$X_c \ell \nu$ only	$41.31 \pm 0.76$	$4.678 \pm 0.051$	$0.410 \pm 0.046$	20.3/(53 - 7)

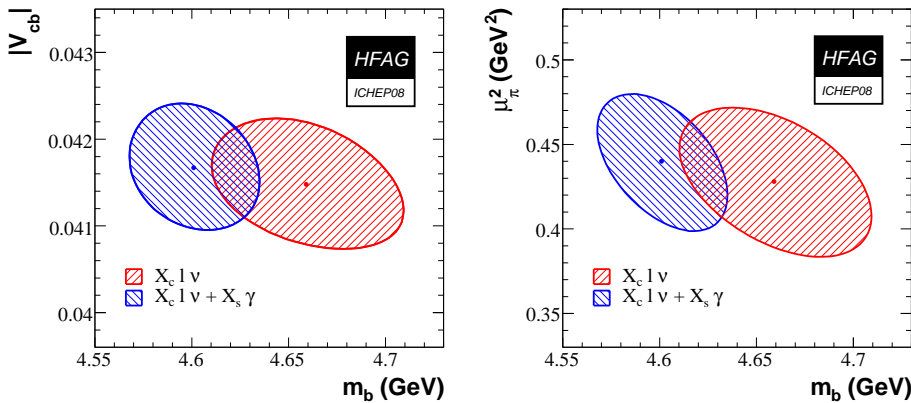


Fig. 42.  $\Delta\chi^2 = 1$  contours for the HFAG fit for  $|V_{cb}|$  and  $m_b$  in the  $(m_b, |V_{cb}|)$  and  $(m_b, \mu_\pi^2)$  planes, with and without  $B \rightarrow X_s \gamma$  data.

3534 of non-OPE contributions using a shape function. We therefore also quote the results of  
 3535 a fit without the  $B \rightarrow X_s \gamma$  data (53 measurements).

The current result for  $|V_{cb}|$  based on fits to lepton-energy, hadronic-mass, and photon-energy moments by HFAG is

$$|V_{cb}| = (41.54 \pm 0.73) \times 10^{-3}, \quad (265)$$

3536 where theoretical and experimental uncertainties have been combined. This value differs  
 3537 from the exclusive determination of  $|V_{cb}|$ , Eq. (259), at the  $2\sigma$  level. Note that the inclusive  
 3538 fits lead to values  $\chi^2$  that are substantially smaller than should be expected, which may  
 3539 point to a problem with the input errors or correlations. The determination of  $m_b$  and  
 3540  $m_c$  will be further discussed in Sec. 5.4.2.

3541 5.4. *Inclusive CKM-suppressed B decays*

3542 5.4.1. *Theoretical Overview*

3543 The inclusive semileptonic B decays into charmless final states are described by the  
 3544 same local OPE we have considered above for the CKM favored ones. The relevant non-  
 3545 perturbative matrix elements are those measured in the fit to the moments discussed in  
 3546 Sec. 5.3. In the total width there is one additional contribution from a four-quark operator  
 3547 related to the Weak Annihilation (WA) between the  $b$  quark and a spectator [559],  
 3548 whose analogue in the CKM favored decay is suppressed by the large charm mass. In an  
 3549 arbitrary, properly defined scheme the total semileptonic width is through  $O(1/m_b^3, \alpha_s^2)$

$$\Gamma[\bar{B} \rightarrow X_u e \bar{\nu}] = \frac{G_F^2 m_b^5}{192\pi^3} |V_{ub}|^2 \left[ 1 + \frac{\alpha_s}{\pi} p_u^{(1)} + \frac{\alpha_s^2}{\pi^2} p_u^{(2)} - \frac{\mu_\pi^2}{2m_b^2} - \frac{3\mu_G^2}{2m_b^2} + \left( \frac{77}{6} + 8 \ln \frac{\mu_{\text{WA}}}{m_b^2} \right) \frac{\rho_D^3}{m_b^3} + \frac{3\rho_{LS}^3}{2m_b^3} + \frac{32\pi^2}{m_b^3} B_{\text{WA}}(\mu_{\text{WA}}) \right], \quad (266)$$

3550 where  $B_{\text{WA}}$  is the  $B$  meson matrix element of the WA operator evaluated at the scale  
 3551  $\mu_{\text{WA}}$ . Since  $B_{\text{WA}}$  vanishes in the factorization approximation, WA is phenomenologically  
 3552 important only to the extent factorization is violated at  $\mu_{\text{WA}}$ . We therefore expect it  
 3553 to contribute less than 2-3% to the difference between  $B^0$  and  $B^+$  widths and, due to  
 3554 its isosinglet component, to the total width of both neutral and charged  $B$  [560, 561].  
 3555 The latter and the  $\ln \mu_{\text{WA}}$  in the coefficient of  $\rho_D^3$  originate in the mixing between WA  
 3556 and Darwin operators [562]. The dominant parametric uncertainty on the total width  
 3557 currently comes from  $m_b$ , due to the  $m_b^5$  dependence. The theoretical uncertainty from  
 3558 missing higher order corrections has been estimated to be at most 2% in the kinetic  
 3559 scheme [560]. Assuming 35 MeV precision on  $m_b$ ,  $|V_{ub}|$  could presently be extracted from  
 3560 the total decay rate with a theoretical error smaller than 2.5%.

3561 Unfortunately, most experimental analyses apply severe cuts to avoid the charm back-  
 3562 ground. The cuts limit the invariant mass of the hadronic final state,  $X$ , and destroy the  
 3563 convergence of the local OPE introducing a sensitivity to the effects of Fermi motion of  
 3564 the heavy quark inside the  $B$  meson. These effects are not suppressed by powers of  $1/m_b$   
 3565 in the restricted kinematic regions. The Fermi motion is inherently non-perturbative;  
 3566 within the OPE it can be described by a nonlocal distribution function, called the shape  
 3567 function (SF) [563, 564], whose lowest integer moments are given by the same expecta-  
 3568 tion values of local operators appearing in Eq.(266). In terms of light-cone momenta  
 3569  $P^\pm = E_X \mp p_X$ , a typical event in the SF region has  $P^+ \ll P^- = O(m_b)$ , with  $P^+$  not  
 3570 far above the QCD scale. The emergence of the SF is also evident in perturbation theory:  
 3571 soft-gluon resummation gives rise to a  $b$  quark SF when supplemented by an internal re-  
 3572 summation of running coupling corrections, see e.g. [565–568]. This SF has the required  
 3573 support properties, namely it extends the kinematic ranges by energies of  $O(\Lambda_{QCD})$ , and  
 3574 it is stable under higher order corrections. The quark SF can therefore be predicted under  
 3575 a few assumptions, as we will see below. The inclusion of power corrections related to the  
 3576 difference between  $b$  quark and  $B$  meson SFs and the proper matching to the OPE are  
 3577 important issues in this context. An alternative possibility is to give up predicting the  
 3578 SF. Since the OPE fixes the first few moments of the SF, one can parametrize it in terms  
 3579 of the known non-perturbative quantities employing an ansatz for its functional form.  
 3580 The uncertainty due to the functional form can be evaluated by varying it, a process that



3581 has been recently systematized [569]. Finally, one can exploit the universality of the SF,  
 3582 up to  $1/m_b$  corrections, and extract it from the photon spectrum of  $B \rightarrow X_s \gamma$ , which  
 3583 is governed by the same dynamics as inclusive semileptonic decays [563, 564, 570, 571].  
 3584 Notice that rates in restricted phase space regions always show increased sensitivity to  
 3585  $m_b$ , up to twice that in Eq.(266).

3586 Subleading contributions in  $1/m_b$  are an important issue, and acquire a different char-  
 3587 acter depending on the framework in which they are discussed. For instance, if one  
 3588 expands in powers of the heavy quark mass the non-local OPE that gives rise to the  
 3589 SF, the first subleading order sees the emergence of many largely unconstrained *sub-*  
 3590 *leading SFs* [572–574] that break the universality noted above. An alternative procedure  
 3591 has been developed in [575], where the only expansion in  $1/m_b$  is at the level of local  
 3592 OPE. A single *finite*  $m_b$  distribution function has been introduced for each of the three  
 3593 relevant structure functions at fixed  $q^2$ . All power-suppressed terms are taken into ac-  
 3594 count in the OPE relations for the integer moments of the SFs, which are computed, like  
 3595 Eq.(266) through  $O(\Lambda^3)$ . Finally, in the context of resummed perturbation theory, power  
 3596 corrections appear in moment space and can be parametrized.

3597 Perturbative corrections also modify the physical spectra: the complete  $O(\alpha_s)$  and  
 3598  $O(\beta_0 \alpha_s^2)$  corrections to the triple differential spectrum [576, 577] are available, while the  
 3599  $O(\alpha_s^2)$  have been recently computed in the SF region only [578–581]. There is a clear  
 3600 interplay between perturbative corrections and the proper definition of the SF beyond  
 3601 lowest order, a problem that has been addressed in different ways, see below.

3602 The experimental cuts can aggravate the uncertainty due to WA. Indeed, WA effects  
 3603 are expected to manifest themselves only at maximal  $q^2$  and lead to an uncertainty that  
 3604 depends strongly on the cuts employed. In the experimental analyses the high- $q^2$  region  
 3605 could therefore either be excluded or used to put additional constraints on the WA matrix  
 3606 element [562, 582, 583]. Moreover, the high- $q^2$  spectrum is not properly described by the  
 3607 OPE (see [575] and references therein) and should be modeled, while its contribution to  
 3608 the integrated rate can be parametrized by the WA matrix element  $B_{\text{WA}}$ . In particular,  
 3609 at  $\mu_{\text{WA}} = 1\text{GeV}$ , the positivity of the  $q^2$  spectrum implies a positive value of  $B_{\text{WA}}(1\text{GeV})$ ,  
 3610 leading to a decrease in the extracted  $|V_{ub}|$  [575].

3611 All the problems outlined above have been extensively discussed in the literature. We  
 3612 will now consider four practical implementations, briefly discussing their basic features.

3613 **DGE** The approach of Refs. [565–568] uses resummed perturbation theory in moment-  
 3614 space to compute the on-shell decay spectrum in the entire phase space; non-perturbative  
 3615 effects are taken into account as power corrections in moment space. Resummation is ap-  
 3616 plied to both the ‘jet’ and the ‘soft’ (quark distribution or SF) subprocesses at NNLL<sup>14</sup>,  
 3617 dealing directly with the double hierarchy of scales ( $\Lambda \ll \sqrt{\Lambda m_b} \ll m_b$ ) characterizing  
 3618 the decay process. Consequently, the shape of the spectrum in the kinematic region where  
 3619 the final state is jet-like is largely determined by a calculation, and less by parametriza-  
 3620 tion. The resummation method employed, Dressed Gluon Exponentiation (DGE), is a  
 3621 general resummation formalism for inclusive distributions near a threshold [585]. It goes  
 3622 beyond the standard Sudakov resummation by incorporating an internal resummation  
 3623 of running-coupling corrections (renormalons) in the exponent and has proved effective  
 3624 in a range of applications [585]. DGE adopts the Principal Value procedure to regularize

<sup>14</sup>The ‘jet’ logarithms are similar to those resummed in the approach of Ref. [584]; there however ‘soft’ logarithms are not resummed.

3625 the Sudakov exponent and thus *define* the non-perturbative parameters. In particular,  
 3626 this definition applies to the would-be  $1/m_b$  ambiguity of the ‘soft’ Sudakov factor, which  
 3627 cancels exactly [586] against the pole–mass renormalon when considering the spectrum  
 3628 in physical hadronic variables. The same regularization used in the Sudakov exponent  
 3629 must be applied in the computation of the regularized  $b$  pole mass from the input  $m_b^{\overline{\text{MS}}}$ .  
 3630 This makes DGE calculation consistent with the local OPE up to  $\mathcal{O}(\Lambda^2/m_b^2)$ .

3631 **ADFR** In this model based on perturbative resummation [587] the integral in the  
 3632 Sudakov exponent is regulated by the use of the *analytic coupling* [588], which is finite in  
 3633 the infrared and is meant to account for all non-perturbative effects. The resummation is  
 3634 performed at NNLL, while the non-logarithmic part of the spectra is computed at  $\mathcal{O}(\alpha_s)$   
 3635 in the on-shell scheme, setting the pole  $b$  mass numerically equal to  $M_B$ . In contrast  
 3636 with DGE, this procedure does not enforce the cancellation of the renormalon ambiguity  
 3637 associated with  $m_b$ , and thus it violates the local OPE at  $\mathcal{O}(\Lambda/m_b)$ , resulting in an  
 3638 uncontrolled  $\mathcal{O}(\Lambda)$  shift of the  $P^+$  spectrum. The model reproduces  $b$  fragmentation  
 3639 data and the photon spectrum in  $B \rightarrow X_s \gamma$ , but does not account for  $\mathcal{O}(\Lambda/m_b)$  power  
 3640 corrections relating different processes. The normalization (total rate) is fixed by the  
 3641 total width of  $B \rightarrow X_c \ell \nu$ , avoiding the  $m_b^5$  dependence, but introducing a dependence  
 3642 on  $m_c$ .

**BLNP** The SF approach of Ref. [584] employs a modified expansion in inverse powers  
 of  $m_b$ , where at each order the dynamical effects associated with soft gluons,  $k^+ \sim P^+ \sim$   
 $\Lambda$  are summed into non-perturbative shape functions. As mentioned above, at leading  
 power there is one such function; beyond this order there are several different functions.  
 To extend the calculation beyond this particular region, the expansion is designed to  
 match the local OPE when integrated over a significant part of the phase space. In this  
 way two systematic expansions in inverse powers of the mass are used together. In this  
*multiscale* OPE, developed following SCET methodology (cf. Sec. 2.2), the differential  
 width is given by

$$\frac{d\Gamma}{dP^+ dP^- dE_l} = HJ \otimes S + \frac{1}{m_b} H'_i J_i \otimes S'_i + \dots \quad (267)$$

3643 where soft (S), jet (J), and hard (H) functions depend on momenta  $\sim \Lambda, \sqrt{\Lambda m_b}, m_b$ ,  
 3644 respectively. The jet and hard functions are computed perturbatively at  $\mathcal{O}(\alpha_s)$  in the  
 3645 *shape function scheme*, resumming Sudakov logs at NNLL, while the soft functions are  
 3646 parametrized at an intermediate scale,  $\mu \sim 1.5$  GeV, using the local OPE constraints on  
 3647 their first moments computed at  $\mathcal{O}(1/m_b^2)$  and a set of functional forms. Although the  
 3648 subleading SFs are largely unconstrained, BLNP find that the experimentally-relevant  
 3649 partial branching fractions remain under good control: the largest uncertainty in the  
 3650 determination of  $|V_{ub}|$  is due to  $m_b$ .

**GGOU** The kinetic scheme used in Sec. 5.3 to define the OPE parameters, is employed  
 in [575] to introduce the distribution functions through a factorization formula for the  
 structure functions  $W_i$ ,

$$W_i(q_0, q^2) \propto \int dk_+ F_i(k_+, q^2, \mu) W_i^{\text{pert}} \left[ q_0 - \frac{k_+}{2} \left( 1 - \frac{q^2}{m_b M_B} \right), q^2, \mu \right], \quad (268)$$

3651 where the distribution functions  $F_i(k_+, q^2, \mu)$  depend on the light-cone momentum  $k_+$ ,  
 3652 on  $q^2$  (through subleading effects) and on the infrared cutoff  $\mu$  [575]. As the latter inhibits  
 3653 soft gluon emission, the spectrum has only collinear singularities whose resummation is

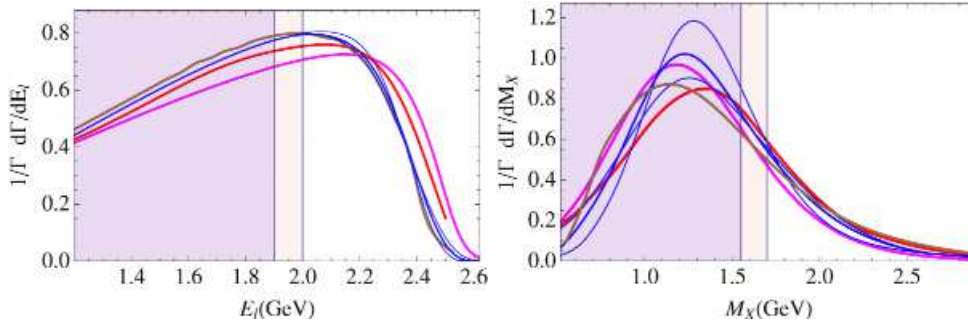


Fig. 43. Comparison of different theoretical treatments of inclusive  $b \rightarrow u$  transitions: (a)  $E_l$  spectrum; (b)  $M_X$  spectrum. Red, magenta, brown and blue lines refer, respectively, to DGE, ADFR, BLNP, GGOU with a sample of three different functional forms. The actual experimental cuts at  $E_l = 1.9, 2.0$  GeV and  $M_X = 1.55, 1.7$  GeV are also indicated.

3654 numerically irrelevant. The perturbative corrections in  $W_i^{\text{pert}}$  include  $O(\alpha_s^2 \beta_0)$  contribu-  
 3655 tions, which alone decrease the value of  $|V_{ub}|$  by about 5%. The functions  $F_i(k_+, q^2, \mu)$   
 3656 are constrained by the local OPE expressions for their first moments at fixed  $q^2$  and  
 3657  $\mu = 1$  GeV, computed including all  $1/m_b^3$  corrections. A vast range of functional forms is  
 3658 explored, leading to a 1-2% uncertainty on  $|V_{ub}|$  [575].

3659 Although conceptually quite different, the above approaches generally lead to roughly  
 3660 consistent results when the same inputs are used and the theoretical errors are taken into  
 3661 account. In Fig. 43(a) we show the normalized electron energy spectrum computed in the  
 3662 latest implementations of the four approaches. Except in ADFR, the spectrum depends  
 3663 sensitively on  $m_b$ . An accurate measurement of the electron spectrum can discriminate  
 3664 between at least some of the methods. The same applies to the  $M_X$  spectrum, which is  
 3665 shown in Fig. 43(b) for  $E_l > 1$  GeV.

#### 3666 5.4.2. Review of $m_b$ determinations

3667 As we have just seen, theoretical predictions of inclusive B decays can depend strongly  
 3668 on  $m_b$ . Thus, uncertainties in the knowledge of  $m_b$  can affect the determination of other  
 3669 parameters. To achieve the high precision in the theoretical predictions required by ex-  
 3670 perimental data it is important to avoid the  $O(\Lambda_{\text{QCD}})$  renormalon ambiguities related  
 3671 to the pole mass parameter and to consider the quark masses as renormalization scheme  
 3672 dependent couplings of the Standard Model Lagrangian that have to be determined from  
 3673 processes that depend on them. Thus having precise control over the scheme-dependence  
 3674 of the bottom quark mass parameters is as important as reducing their numerical uncer-  
 3675 tainty.

3676 Predictions for  $B$  meson decays also suffer from renormalon ambiguities of order  
 3677  $\Lambda_{\text{QCD}}^2/m_b$  or smaller. These ambiguities cannot in general be removed solely by a partic-  
 3678 ular choice of a bottom mass scheme. Additional subtractions in connection with fixing  
 3679 specific schemes for higher order non-perturbative matrix element in the framework of  
 3680 the OPE are required to remove these ambiguities. Some short-distance bottom mass  
 3681 schemes have been proposed together with additional subtractions concerning the kin-  
 3682 etic operator  $\lambda_1$  or  $\mu_\pi^2$ . In the following we briefly review the prevalent perturbative  
 3683 bottom mass definitions which were employed in recent analyses of inclusive  $B$  decays.  
 3684 A more detailed review on quark mass definitions including analytic formulae has been

3685 given in the CKM 2003 Report [589].

3686  **$\overline{\text{MS}}$  mass:** The most common short-distance mass parameter is the  $\overline{\text{MS}}$  mass  $\overline{m}_b(\mu)$ ,  
 3687 which is defined by regularizing QCD with dimensional regularization and subtracting  
 3688 the UV divergences in the  $\overline{\text{MS}}$  scheme. As a consequence the  $\overline{\text{MS}}$  mass depends on the  
 3689 renormalization scale  $\mu$ . Since the UV subtractions do not contain any infrared sensitive  
 3690 terms, the  $\overline{\text{MS}}$  mass is only sensitive to scales of order or larger than  $m_b$ . The  $\overline{\text{MS}}$  mass  
 3691 is therefore disfavored for direct use in the theoretical description of inclusive  $B$  decays.  
 3692 However, it is still useful as a reference mass. The relation between the pole mass and the  
 3693  $\overline{\text{MS}}$  mass is known to  $\mathcal{O}(\alpha_s^3)$  [590–592], see Sec. 2.1 of the 2003 report [589] for analytic  
 3694 formulae.

3695 **Threshold masses** The shortcomings of the  $\overline{\text{MS}}$  masses in describing inclusive  $B$   
 3696 decays can be resolved by so-called threshold masses [593]. The prevalent threshold mass  
 3697 definitions are the kinetic, the shape function and the 1S mass schemes. They are free of  
 3698 an ambiguity of order  $\Lambda_{\text{QCD}}$  through in general scale-dependent subtractions.

3699 The *kinetic mass* is defined as [594, 595]

$$m_{b,\text{kin}}(\mu_{\text{kin}}) = m_{b,\text{pole}} - [\bar{A}(\mu_{\text{kin}})]_{\text{pert}} - \left[ \frac{\mu_{\pi}^2(\mu_{\text{kin}})}{2m_{b,\text{pole}}} \right]_{\text{pert}}, \quad (269)$$

3700 where  $[\bar{A}(\mu_{\text{kin}})]_{\text{pert}}$  and  $[\mu_{\pi}^2(\mu_{\text{kin}})]_{\text{pert}}$  are perturbative evaluations of HQET matrix  
 3701 elements that describe the difference between the pole and the  $B$  meson mass. The  
 3702 term  $\mu_{\text{kin}}$  is the subtraction scale. To avoid the appearance of large logarithmic terms  
 3703 it should be chosen somewhat close to the typical momentum fluctuations within the  $B$   
 3704 meson. The relation between the kinetic mass and the pole mass is known to  $\mathcal{O}(\alpha_s^2)$  and  
 3705  $\mathcal{O}(\alpha_s^3 \beta_0^2)$  [596, 597], see the 2002 report [589] for analytic formulae.

3706 The *shape function mass* [528, 529] is defined from the condition that the OPE for the  
 3707 first moment of the leading order shape function for the  $B \rightarrow X_u \ell \nu$  and  $B \rightarrow X_s \gamma$  decays  
 3708 in the endpoint regions vanishes identically. The relation between the shape function mass  
 3709 and the pole mass is known at  $\mathcal{O}(\alpha_s^2)$  and reads

$$m_b^{\text{SF}}(\mu_{\text{SF}}, \mu) = m_{b,\text{pole}} - \mu_{\text{SF}} \frac{C_F \alpha_s(\mu)}{\pi} \left[ 1 - 2 \ln \frac{\mu_{\text{SF}}}{\mu} + \frac{\alpha_s(\mu)}{\pi} k_1(\mu_{\text{SF}}, \mu) \right] \\ - \frac{\mu_{\pi}^2(\mu_{\text{SF}}, \mu)}{3\mu_{\text{SF}}} \frac{C_F \alpha_s(\mu)}{\pi} \left[ 2 \ln \frac{\mu_{\text{SF}}}{\mu} + \frac{\alpha_s(\mu)}{\pi} k_2(\mu_{\text{SF}}, \mu) \right], \quad (270)$$

3710 where

$$k_1(\mu_{\text{SF}}, \mu) = \frac{47}{36} \beta_0 + \left( \frac{10}{9} - \frac{\pi^2}{12} - \frac{9}{4} \zeta_3 + \frac{\kappa}{8} \right) C_A + \left( -8 + \frac{\pi^2}{3} + 4\zeta_3 \right) C_F \\ + \left[ -\frac{4}{3} \beta_0 + \left( -\frac{2}{3} + \frac{\pi^2}{6} \right) C_A + \left( 8 - \frac{2\pi^2}{3} \right) C_F \right] \ln \frac{\mu_{\text{SF}}}{\mu} \\ + \left( \frac{1}{2} \beta_0 + 2C_F \right) \ln^2 \frac{\mu_{\text{SF}}}{\mu}, \quad (271)$$

$$k_2(\mu_{\text{SF}}, \mu) = -k_1(\mu_{\text{SF}}, \mu) + \frac{7}{6} \beta_0 + \left( \frac{1}{3} - \frac{\pi^2}{12} \right) C_A + \left( -5 + \frac{\pi^2}{3} \right) C_F \\ + \left( -\frac{1}{2} \beta_0 - C_F \right) \ln \frac{\mu_{\text{SF}}}{\mu}. \quad (272)$$

3711 The relation depends on the momentum cutoff  $\mu_{\text{SF}}$  which enters the definition of the  
3712 first moment and on the (non-perturbative and infrared subtracted) kinetic energy matrix  
3713 element  $\mu_\pi^2$  defined from the ratio of the second and zeroth moment of the shape function.  
3714 Since the shape function is renormalization scale dependent, the shape function mass  
3715 depends on also on the renormalization scale  $\mu$ . In practical applications the SF mass  
3716 has been considered for  $\mu = \mu_{\text{SF}}$ ,  $m_b^{\text{SF}}(\mu_{\text{SF}}) \equiv m_b^{\text{SF}}(\mu_{\text{SF}}, \mu_{\text{SF}})$ .

3717 The *1S mass* [526,598,599] is defined as one half of the perturbative series for the mass  
3718 of the  $n = 1$ ,  $^3S_1$  bottomonium bound state in the limit  $m_b \gg m_b v \gg m_b v^2 \gg \Lambda_{\text{QCD}}$ .  
3719 In contrast to the kinetic and shape-function masses, the subtraction scale involved in  
3720 the 1S mass is tied dynamically to the inverse Bohr radius  $\sim m_b \alpha_s$  of the bottomonium  
3721 ground state and therefore does not appear as an explicit parameter. The 1S mass scheme  
3722 is known completely to  $\mathcal{O}(\alpha_s^3)$ , see the 2003 report [589] for analytic formulae.

3723 In Tab. 38 the numerical values of the bottom quark kinetic, shape function and 1S  
3724 masses are provided for different values for the strong coupling taking the  $\overline{\text{MS}}$  mass  
3725  $\overline{m}_b(\overline{m}_b)$  as a the reference input. Each entry corresponds to the mass using the respec-  
3726 tive 1-loop/2-loop/3-loop relations as far as they are available and employing a common  
3727 renormalization scale for the strong coupling when the pole mass is eliminated. As the  
3728 renormalization scale we employed  $\mu = \overline{m}_b(\overline{m}_b)$  to minimize the impact of logarithmic  
3729 terms involving the cutoff scales  $\mu_{\text{kin,SF}}$  and the scale  $\overline{m}_b(\overline{m}_b)$  [600]. Numerical approxi-  
3730 mations for the conversion formulae at the respective highest available order accounting  
3731 in particular for the dependence on  $\alpha_s^{(n_f=5)}(M_Z)$  and the renormalization scale  $\mu$  read:

$$m_b^{1\text{S}} = 1.032 m_b^{\text{kin}}(1 \text{ GeV}) + 1.9 \Delta\alpha_s - 0.003 \Delta\mu, \quad (273)$$

$$m_b^{\text{SF}}(1.5 \text{ GeV}) = 1.005 m_b^{\text{kin}}(1 \text{ GeV}) + 0.9 \Delta\alpha_s - 0.006 \Delta\mu - 0.003 \Delta\mu_\pi^2, \quad (274)$$

$$m_b^{\text{SF}}(1.5 \text{ GeV}) = 0.976 m_b^{1\text{S}} - 0.9 \Delta\alpha_s + 0.001 \Delta\mu - 0.003 \Delta\mu_\pi^2, \quad (275)$$

$$\overline{m}_b(\overline{m}_b) = 0.917 m_b^{\text{kin}}(1 \text{ GeV}) - 8.2 \Delta\alpha_s + 0.005 \Delta\mu, \quad (276)$$

$$\overline{m}_b(\overline{m}_b) = 0.888 m_b^{1\text{S}} - 9.9 \Delta\alpha_s + 0.006 \Delta\mu, \quad (277)$$

$$\overline{m}_b(\overline{m}_b) = 0.916 m_b^{\text{SF}}(1.5 \text{ GeV}) - 8.0 \Delta\alpha_s + 0.017 \Delta\mu + 0.003 \Delta\mu_\pi^2, \quad (278)$$

3732 where  $\Delta\alpha_s = [\alpha_s^{(5)}(M_Z) - 0.118]$  GeV,  $\Delta\mu = (\mu - 4.2 \text{ GeV})$ ,  $\Delta\mu_\pi^2 = [\mu_\pi^2(1.5 \text{ GeV}) -$   
3733  $0.15 \text{ GeV}^2]$  GeV $^{-1}$ . The formulae agree with the respective exact relations to better  
3734 than 10 MeV (for  $3.7 \text{ GeV} < \mu < 4.7 \text{ GeV}$ ). The theoretical uncertainties from missing  
3735 higher order terms are reflected in the renormalization scale dependence of the conversion  
3736 formulae.

### 3737 **Bottom quark mass determinations**

3738 There are two major methods to determine the bottom mass with high precision:  
3739 spectral sum rules using data for the bottom production rate in  $e^+e^-$  collisions, and  
3740 fits to moments obtained from distributions of semileptonic  $B \rightarrow X_c \ell \nu$  and radiative  
3741  $B \rightarrow X_s \gamma$  decays. Both rely on the validity of the operator product expansion and the  
3742 input of higher order perturbative corrections. The results obtained from both methods  
3743 are compatible. Lattice determinations still have larger uncertainties and suffer from

Table 38

Numerical values of the bottom quark kinetic, 1S and shape function masses in units of GeV for a given  $\overline{\text{MS}}$  value  $\overline{m}_b(\overline{m}_b)$  using  $\mu = \overline{m}_b(\overline{m}_b)$ ,  $n_l = 4$  and three values of  $\alpha_s^{(5)}(m_Z)$ . Flavor matching was carried out at  $\mu = \overline{m}_b(\overline{m}_b)$ . For the shape function mass  $\mu_\pi^2(1.5 \text{ GeV}) = 0.15 \text{ GeV}^2$  was adopted. Numbers with an asterisk are given in the large- $\beta_0$  approximation.

$\overline{m}_b(\overline{m}_b)$	$m_{b,\text{kin}}(1 \text{ GeV})$	$m_{b,1\text{S}}$	$m_{b,\text{SF}}(1.5 \text{ GeV})$
$\alpha_s^{(5)}(m_Z) = 0.116$			
4.10	4.36/4.42/4.45*	4.44/4.56/4.60	4.34/4.44/-
4.15	4.41/4.48/4.50*	4.49/4.61/4.65	4.39/4.50/-
4.20	4.46/4.53/4.56*	4.54/4.66/4.71	4.45/4.55/-
4.25	4.52/4.59/4.61*	4.60/4.72/4.76	4.50/4.61/-
4.30	4.57/4.64/4.67*	4.65/4.77/4.81	4.56/4.66/-
$\alpha_s^{(5)}(m_Z) = 0.118$			
4.10	4.37/4.44/4.46*	4.45/4.57/4.62	4.35/4.46/-
4.15	4.42/4.49/4.52*	4.50/4.63/4.67	4.40/4.51/-
4.20	4.47/4.55/4.57*	4.55/4.68/4.73	4.46/4.57/-
4.25	4.52/4.60/4.63*	4.61/4.73/4.78	4.51/4.62/-
4.30	4.58/4.66/4.69*	4.66/4.79/4.84	4.56/4.68/-
$\alpha_s^{(5)}(m_Z) = 0.120$			
4.10	4.37/4.45/4.48*	4.46/4.59/4.64	4.36/4.48/-
4.15	4.43/4.51/4.54*	4.51/4.64/4.70	4.41/4.53/-
4.20	4.48/4.56/4.59*	4.56/4.70/4.75	4.47/4.59/-
4.25	4.54/4.62/4.65*	4.62/4.75/4.80	4.52/4.64/-
4.30	4.59/4.67/4.71*	4.67/4.81/4.86	4.57/4.70/-

3744 systematic effects, which need to be better understood to be competitive to the previous  
3745 two methods. A summary of recent bottom mass determinations is given in Tab. 39.

3746 **Spectral  $e^+e^-$  sum rules**

The spectral sum rules start from the correlator  $\Pi(q^2)$  of two electromagnetic bottom quark currents and are based on the fact that derivatives of  $\Pi$  at  $q^2 = 0$  are related to moments of the total cross section  $\sigma(e^+e^- \rightarrow b\bar{b})$ ,

$$\mathcal{M}_n = \frac{12\pi^2 Q_b^2}{n!} \left( \frac{d}{dq^2} \right)^n \Pi(q^2) \Big|_{q^2=0} = \int \frac{ds}{s^{n+1}} R(s), \quad (279)$$

3747 where  $R = \sigma(e^+e^- \rightarrow b\bar{b})/\sigma(e^+e^- \rightarrow \mu^+\mu^-)$ . From Eq. (279) it is possible to determine  
3748 the bottom quark mass using an operator product expansion [601,602]. One has to restrict  
3749 the moments to  $n \lesssim 10$  such that the momentum range contributing to the moment is  
3750 sufficient larger than  $\Lambda_{\text{QCD}}$  and the perturbative contributions dominate. Here the most  
3751 important non-perturbative matrix element is the gluon condensate, but its contribution  
3752 is very small.

3753 *Nonrelativistic  $e^+e^-$  sum rules:* For the large  $n$ ,  $4 \lesssim n \lesssim 10$ , the moments are domi-  
3754 nated by the bottomonium bound states region and the experimentally unknown parts

Table 39

Collection in historical order in units of GeV of recent bottom quark mass determinations from spectral sum rules and the  $\Upsilon(1S)$  mass. Only results where  $\alpha_s$  was taken as an input are shown. The uncertainties quoted in the respective references have been added quadratically. All numbers have been taken from the respective publications.

author	$\bar{m}_b(\bar{m}_b)$	other mass	comments, Ref.
nonrelativistic spectral sum rules			
Melnikov	98 $4.20 \pm 0.10$	$M_{\text{kin}}^{1\text{GeV}} = 4.56 \pm 0.06$	NNLO, $m_c = 0$ [597]
Hoang	99 $4.20 \pm 0.06$	$M_{1S} = 4.71 \pm 0.03$	NNLO, $m_c = 0$ [603]
Beneke	99 $4.26 \pm 0.09$	$M_{\text{PS}}^{2\text{GeV}} = 4.60 \pm 0.11$	NNLO, $m_c = 0$ [604]
Hoang	00 $4.17 \pm 0.05$	$M_{1S} = 4.69 \pm 0.03$	NNLO, $m_c \neq 0$ [605]
Eidemüller	02 $4.24 \pm 0.10$	$M_{\text{PS}}^{2\text{GeV}} = 4.56 \pm 0.11$	NNLO + $O(\alpha_s^2)$ , $m_c = 0$ [606]
Pineda	06 $4.19 \pm 0.06$	$M_{\text{PS}}^{2\text{GeV}} = 4.52 \pm 0.06$	NNLL partial, $m_c = 0$ [607]
relativistic spectral sum rules			
Kühn	01 $4.19 \pm 0.05$		$O(\alpha_s^2)$ [608]
Bordes	02 $4.19 \pm 0.05$		$O(\alpha_s^2)$ , finite energ. s.r. [609]
Corcella	02 $4.20 \pm 0.09$		$O(\alpha_s^2)$ , continuum err.incl. [610]
Hoang	04 $4.22 \pm 0.11$		$O(\alpha_s^2)$ , contour improved [611]
Boughezal	06 $4.21 \pm 0.06$		$O(\alpha_s^3)$ [612]
Kühn	07 $4.16 \pm 0.03$		$O(\alpha_s^3)$ [613]
moments from $B \rightarrow X_c \ell \nu$ and $B \rightarrow X_s \gamma$ distributions			
HFAG (ICHEP 08)	08 $4.28 \pm 0.07$	$M_{\text{kin}}^{1\text{GeV}} = 4.66 \pm 0.05$	$B \rightarrow X_c \ell \nu$ , $O(\alpha_s^2 \beta_0)$ [558]
		$4.23 \pm 0.05$	$M_{\text{kin}}^{1\text{GeV}} = 4.60 \pm 0.03$ $B \rightarrow X_c \ell \nu$ , $B \rightarrow X_s \gamma$ , $O(\alpha_s^2 \beta_0)$ [558]
		$4.17 \pm 0.04$	$M_{1S} = 4.70 \pm 0.03$ $B \rightarrow X_c \ell \nu$ & $B \rightarrow X_s \gamma$ , $O(\alpha_s^2 \beta_0)$ [558]
		$4.22 \pm 0.07$	$M_{1S} = 4.75 \pm 0.06$ $B \rightarrow X_c \ell \nu$ , $O(\alpha_s^2 \beta_0)$ [558]

of the  $b\bar{b}$  continuum cross section are suppressed. Depending on the moment the overall experimental uncertainties in the b quark mass are between 15 and 20 MeV. Sum rule analyses using threshold masses and based on NNLO fixed order computations in the framework of NRQCD [597, 603–605] yield consistent results but suffer from relatively large NNLO corrections to the normalization of the moments  $\mathcal{M}_n$ . Uncertainties in the bottom mass at the level of below 50 to 100 MeV were achieved by making assumptions on the behavior of higher order corrections. The use of renormalization group improved NRQCD computations in Ref. [607] yields an uncertainty of 60 MeV without making such assumptions. However, the analysis of Ref. [607] neglects known large NNLL order contributions to the anomalous dimension of the quark pair production currents [614].

*Relativistic sum rules:* For small  $n$ ,  $1 \leq n \lesssim 4$ , the experimentally unmeasured parts of the  $b\bar{b}$  continuum cross section above the  $\Upsilon$  resonance region constitute a substantial contribution to the spectral moments and uncertainties below the 100 MeV level are only possible using theory to predict the continuum contributions [610]. For the theoretical determination of the moments usual fixed order perturbation theory can be employed.

3770 The most recent bottom quark mass determinations [612,613] use perturbation theory  
 3771 at  $O(\alpha_s^3)$  and obtain  $\overline{m}_b(\overline{m}_b)$  with an uncertainty between 25 and 58 MeV.

3772 **Inclusive  $B$  decay moments**

3773 As already discussed in Sec. 5.3 the analysis of moments of lepton energy and hadron  
 3774 invariant mass moments obtained from spectra in the semileptonic decay  $B \rightarrow X_c \ell \nu$  and  
 3775 of radiative photon energy moments from  $B \rightarrow X_s \gamma$  allows to determine the bottom  
 3776 quark threshold masses. Currently the theoretical input for the moment computations  
 3777 includes  $O(\alpha_s)$  and  $\mathcal{O}(\alpha_s^2 \beta_0)$  corrections for the partonic contribution and tree-level Wil-  
 3778 son coefficients for the power corrections [508,510,524]; it would be desirable to include  
 3779 the known full  $O(\alpha_s^2)$  corrections into the analysis. For what concerns the determination  
 3780 of  $m_b$ , the results based on combined  $B \rightarrow X_c \ell \nu$  and  $B \rightarrow X_s \gamma$  data are in agreement  
 3781 with the  $e^+e^-$  sum rule determinations, while using only  $B \rightarrow X_c \ell \nu$  data leads to slightly  
 3782 larger  $m_b$  with larger error, which are, however, still compatible with the other deter-  
 3783 minations. In fact, the semileptonic moments are mostly sensitive to a combination of  
 3784  $m_b$  and  $m_c$ , as apparent from Fig.44, where various determinations of  $m_c$  and  $m_b$  are  
 3785 compared.

3786 **Lattice QCD**

3787 In principle, lattice QCD should provide sound ways of determining the quark masses:  
 3788 each bare mass is adjusted until one particular hadron mass agrees with experiment.  
 3789 In practice, there are several approaches. One is to convert the bare mass of the lat-

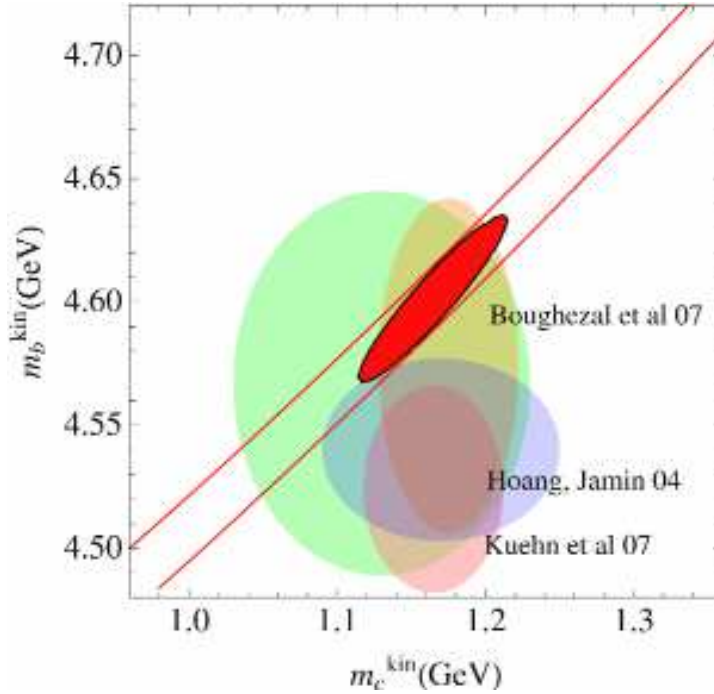


Fig. 44. Comparison of different determinations of  $m_c$  and  $m_b$  in the kinetic scheme. The red ellipse refers to the semileptonic fit discussed in Sec. 5.3, the large green ellipse to the 2007 PDG values, and the others to various  $e^+e^-$  sum rule determinations listed in Table 39, taking into account the sizable theoretical error in the change of scheme. Figure updated from [615].



3790 tice action to a more familiar renormalization scheme. Another is to define the mass via  
 3791 ratios of matrix elements derived from the CVC or PCAC relations. Finally, one can  
 3792 compute short-distance objects that are sensitive to the (heavy) quark masses, for which  
 3793 continuum perturbation theory can be used [616]. For the first two methods, a matching  
 3794 procedure is needed to relate the bare lattice mass, or currents, to a continuum scheme,  
 3795 such as  $\overline{\text{MS}}$ . The matching can be done in perturbation theory—the state of the art  
 3796 for light quarks is two-loop [617]—or via nonperturbative matching [481]. When con-  
 3797 sidering nonperturbatively matched results from lattice QCD, one should bear in mind  
 3798 that the match is to an RI-MOM scheme or to the renormalization-group independent  
 3799 (RGI) mass. Final conversion to the  $\overline{\text{MS}}$  scheme always entails perturbation theory, be-  
 3800 cause dimensional regulators, and hence their minimal subtractions, are defined only in  
 3801 perturbation theory.

3802 For bottom quarks, light-quark methods do not carry over straightforwardly [86]. Con-  
 3803 sequently, unquenched determinations of  $m_b$  have been limited to one-loop accuracy [618]  
 3804 while nonperturbatively matched determinations remain quenched [619]. They are, thus,  
 3805 not competitive with the other determinations of  $m_b$  discussed here. For charm the sit-  
 3806 uation is almost the same, except on the finest lattices with the most-improved actions.  
 3807 Then, as discussed below, it is possible to use moments of the charmonium correlator  
 3808 and continuum  $\mathcal{O}(\alpha_s^3)$  perturbation theory [620], or to employ two-loop matching, which  
 3809 is still in progress [621].

### 3810 Charm mass determinations

3811 Due to the increased precision in the data and in the theoretical description the charm  
 3812 quark mass is also an important input parameter in the analysis of inclusive  $B$  decays.  
 3813 Due to its low mass the use of threshold masses is not imperative for the charm quark,  
 3814 and the most common scheme is the  $\overline{\text{MS}}$  mass. The most precise measurements are  
 3815 obtained from  $e^+e^-$  sum rules. More recently, charm mass measurements with small  
 3816 uncertainties are also obtained from inclusive  $B$  decays. In the  $e^+e^-$  sum rule anal-  
 3817 yses of Refs. [612, 613] based on fixed order perturbation theory at  $\mathcal{O}(\alpha_s^3)$  the results  
 3818  $\overline{m}_c(\overline{m}_c) = 1.295 \pm 0.015$  GeV and  $1.286 \pm 0.013$  GeV, respectively, were obtained. In  
 3819 was, however, pointed out in Ref. [611] based on an  $\mathcal{O}(\alpha_s^2)$  analysis that carrying out  
 3820 the analysis in fixed-order perturbation theory might underestimate the theory error  
 3821 due to a discrepancy of the predictions in fixed-order and in contour-improved pertur-  
 3822 bation theory. In the analysis of Ref. [620] lattice calculations of moments of different  
 3823 current-current correlators, defined in analogy to Eq. (279), and  $\mathcal{O}(\alpha_s^3)$  fixed-order com-  
 3824 putations of these moments were combined and the result  $\overline{m}_c(\overline{m}_c) = 1.268 \pm 0.009$  GeV  
 3825 was obtained. This analysis avoids the usually large conversion uncertainties when lattice  
 3826 masses are converted to the  $\overline{\text{MS}}$  continuum mass, however, it might also suffer from the  
 3827 theory issue pointed out in Ref. [611]. Thus this issue certainly deserves further inves-  
 3828 tigation. More recently, measurement of the charm mass with small uncertainties were  
 3829 also obtained from fits to inclusive  $B$  decay spectra. In Refs. [622] and [509] the results  
 3830  $\overline{m}_c(\overline{m}_c) = 1.22 \pm 0.06$  GeV and  $1.24 \pm 0.09$  GeV, respectively, were obtained. These  
 3831 results are compatible with the  $e^+e^-$  sum rule analyses.

### 3832 5.4.3. Measurements and tests

3833 The experimental measurements of inclusive charmless semileptonic  $B$  decays are dom-  
 3834 inated by measurements at the  $\Upsilon(4S)$  resonance. They fall into two broad categories: so-

3835 called “tagged” measurements, in which the companion  $B$  meson is fully reconstructed  
3836 in a hadronic decay mode (see Sec. 3.2.6), which allows an unambiguous association  
3837 of particles with the semileptonic  $B$  decay and the determination of the  $B$  decay rest  
3838 frame; and untagged measurements, in which only a charged lepton and, in some cases,  
3839 the missing momentum vector for the event are measured.

3840 The untagged measurements tend to have high efficiency but poor signal to noise, and  
3841 are sensitive to  $e^+e^- \rightarrow q\bar{q}$  continuum background. The main source of background is  
3842 from  $b \rightarrow c\ell\bar{\nu}$  decays. Existing measurements all require the lepton momentum to exceed  
3843 1.9 GeV in the  $\Upsilon(4S)$  rest frame. Those analyses that utilize the missing momentum vec-  
3844 tor generally have improved background rejection, but also have additional uncertainties  
3845 due to the modeling of sources of missing momentum, such as imperfect track and cluster  
3846 reconstruction, the response to neutral hadrons and the presence of additional neutrinos.  
3847 The partial branching fraction in a specified kinematic region is determined in some  
3848 analyses by a cut-and-count method, and in others by a fit of the measured spectrum  
3849 to the predicted shapes of the signal and background components. In all cases the fits  
3850 use coarse binning in regions where the differential distributions are highly sensitive to  
3851 details of the shape function.

3852 The tagged measurements require the presence of an electron or muon with  $E_\ell >$   
3853 1.0 GeV amongst the particles not used in the reconstruction of the hadronic  $B$  de-  
3854 cay. These analyses provide measurements of the kinematic variables of the hadronic  
3855 system associated with the semileptonic decay, such as  $m_X$  and  $P_+$ , as well as of  $q^2$ .  
3856 They also provide additional handles for suppressing background, which comes predom-  
3857 inantly from the Cabibbo-favored decays  $b \rightarrow c\ell\bar{\nu}$ ; these include charge correlations  
3858 between the fully-reconstructed  $B$  meson and the lepton, the veto of Kaons from the  
3859 semileptonically-decaying  $\bar{B}$ , and constraints on the charge sum of reconstructed tracks  
3860 and on the reconstructed missing mass-squared in the event. This power has a cost; the  
3861 net selection efficiency is  $< 1\%$  relative to an untagged analysis, and is not well under-  
3862 stood in absolute terms due to incomplete knowledge of the decay modes that contribute  
3863 to the fully-reconstructed  $B$  meson sample. As a result, these analyses measure ratios  
3864 of branching fractions, usually relative to the inclusive semileptonic partial branching  
3865 fraction for  $E_e > 1.0$  GeV. Examples of measurements from these two categories are  
3866 shown in Figs. 45 and 46.

3867 The large  $b \rightarrow c\ell\bar{\nu}$  background is reduced in most analyses by making restrictive  
3868 kinematic cuts. The measured quantity is then a (sometimes small) fraction of the full  $b \rightarrow$   
3869  $u\ell\bar{\nu}$  rate. As discussed in section 5.4.1, these restrictions introduce sensitivity to the non-  
3870 perturbative shape function, and significantly increase the sensitivity to  $m_b$ . The choice  
3871 of kinematic cuts is a balance between statistical and systematic uncertainties, which  
3872 increase as kinematic cuts are relaxed, and theoretical and parametric uncertainties,  
3873 which decrease under these conditions.

3874 The best determinations to date of various  $b \rightarrow u\ell\bar{\nu}$  partial rates are given in Tab. 40.  
3875 The experimental systematic uncertainties affecting all analyses are due to track recon-  
3876 struction and electron identification. Untagged analyses are relatively more sensitive to  
3877 bremsstrahlung and radiative corrections. The tagged analyses have additional uncer-  
3878 tainties due to the determination of event yields via fits to the invariant mass spectra of  
3879 fully-reconstructed  $B$  candidates. Uncertainties due to the modeling of  $b \rightarrow c\ell\bar{\nu}$  decays  
3880 are correlated between measurements, but their magnitude varies depending on the cuts  
3881 applied and the analysis strategy; most analyses include some data-based evaluation of

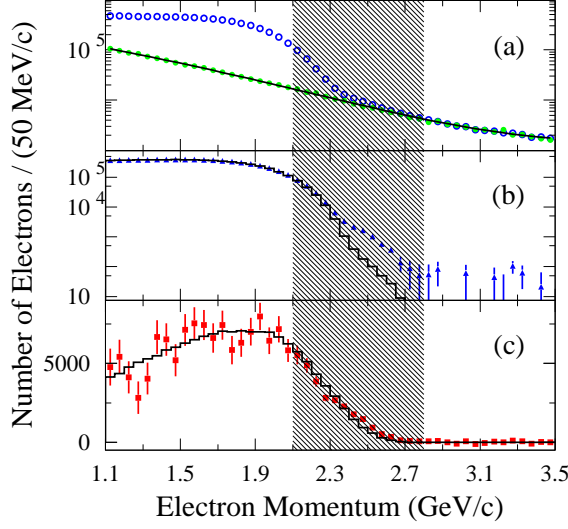


Fig. 45. The inclusive electron energy spectrum [623] from BaBar is shown for (a) on-peak data and  $q^2$  continuum (histogram); (b) data subtracted for non- $B\bar{B}$  contributions (points) and the simulated contribution from  $B$  decays other than  $b \rightarrow ul\nu$  (histogram); and (c) background-subtracted data (points) with a model of the  $b \rightarrow ul\nu$  spectrum (histogram).

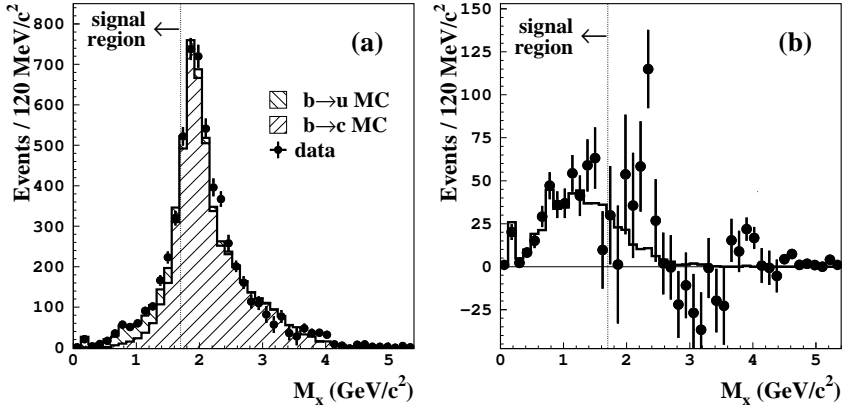


Fig. 46. The hadronic invariant mass spectrum [624] in Belle data (points) is shown in (a) with histograms corresponding to the fitted contributions from  $b \rightarrow cl\nu$  and  $b \rightarrow ul\nu$ . After subtracting the expected contribution from  $b \rightarrow cl\nu$ , the data (points) are compared to a model  $b \rightarrow ul\nu$  spectrum (histogram) in (b).

3882 the level of this background. The leading sources of uncertainty arise from uncertainties  
 3883 in the form factors for  $\bar{B} \rightarrow D^* \ell \bar{\nu}$  decays and limited knowledge of semileptonic decays to  
 3884 higher mass charm states. The modeling of  $b \rightarrow ul\nu$  decays is relevant to all analyses to  
 3885 the extent that the precise mix of exclusive states, which is not well measured, affects the  
 3886 acceptance and reconstruction efficiency. In some analyses an additional sensitivity arises

3887 due to the use of a  $b \rightarrow u\ell\bar{\nu}$  component in a fit to the measured kinematic observable;  
 3888 the shape of this component then affects the result. The sensitivity of each analysis to  
 3889 weak annihilation varies as a function of the acceptance cuts used.

3890 The larger data sets now available allow less restrictive kinematic cuts that encompass  
 3891 up to 90% or more of the total  $b \rightarrow u\ell\bar{\nu}$  rate, which significantly reduces the impact  
 3892 of theoretical uncertainties. A preliminary result from Belle [625] uses a multivariate  
 3893 analysis on a tagged sample to measure the full  $b \rightarrow u\ell\bar{\nu}$  rate for  $E_\ell > 1.0$  GeV, and  
 3894 quotes an experimental uncertainty of 6% on  $|V_{ub}|$  and smaller theoretical uncertainties  
 3895 than measurements made in more restrictive kinematic regions. Given the challenging  
 3896 nature of the measurements that include large regions dominated by  $b \rightarrow c\ell\bar{\nu}$  decays, it  
 3897 is valuable to have results based on complementary techniques. Untagged measurements  
 3898 of the fully inclusive electron spectrum can also be pushed further into the region domi-  
 3899 nated by  $b \rightarrow c\ell\bar{\nu}$  decays; there are prospects for pushing down to  $E_e > 1.6$  GeV while  
 3900 maintaining experimental errors at the  $< 5\%$  level on  $|V_{ub}|$ .

3901 The availability of measured partial rates in different kinematic regions allows a test of  
 3902 the theoretical predictions, as ratios of partial rates are independent of  $|V_{ub}|$ . One gauge of  
 3903 the consistency of the measured and predicted partial rates is the  $\chi^2$  of the  $|V_{ub}|$  average  
 3904 within each theoretical framework. These are given in Tab. 40 In each case a reasonable  
 3905  $\chi^2$  probability is obtained. One can also probe directly the ratios of particular partial  
 3906 rates.

#### 3907 5.4.4. Determination of $|V_{ub}|$

3908 As described in the previous section, the large background from the  $b \rightarrow c\ell\nu$  decays  
 3909 is the chief experimental limitation in the determination of the total branching fraction  
 3910 for  $b \rightarrow u\ell\nu$  decays. The different analyses are characterized by kinematic cuts applied  
 3911 on: the lepton energy ( $E_\ell$ ), the invariant mass of the hadron final state ( $M_X$ ), the light-  
 3912 cone component of the hadronic final state momentum along the jet direction ( $P^+$ ), the  
 3913 two dimensional distributions  $M_X$ - $q^2$  and  $E_\ell$ - $s^{\max}$ , where  $q^2$  is the squared transferred  
 3914 momentum to the lepton pair and  $s^{\max}$  is the maximal  $M_X^2$  at fixed  $q^2$  and  $E_\ell$ . Given  
 3915 the large variety of analyses performed, and the differences in background rejection cuts  
 3916 used in the different experimental techniques, each analysis measures a partial rate in a  
 3917 different phase-space region. The differential rates needed from the theory to extract  $|V_{ub}|$   
 3918 from the experimental results have been calculated using each theoretical approach. The  
 3919 challenge of averaging the  $|V_{ub}|$  measurements from the different analyses is due mainly to  
 3920 the complexity of combining measurements performed with different systematic assump-  
 3921 tions and with potentially-correlated systematic uncertainties. Different analyses often  
 3922 use a different decomposition of their systematic uncertainties, so achieving consistent  
 3923 definitions for any potentially correlated contributions requires close coordination with  
 3924 the experiments. Also, some tagged analyses produce partial rates in several kinematic  
 3925 variables, like  $M_X$ ,  $M_X$ - $q^2$  and  $P^+$ , based on the same data sample, so the statistical  
 3926 correlation among the analyses needs to be accounted for. As a result, only those analyses  
 3927 for which the statistical correlation is provided are included in the average. Systematic  
 3928 uncertainties that are uncorrelated with any other sources of uncertainty appearing in  
 3929 an average are lumped with the statistical error. Those systematic errors correlated with  
 3930 at least one other measurement are treated explicitly. Examples of correlated system-  
 3931 atic errors include uncertainties in the branching fractions for exclusive  $b \rightarrow c\ell\nu$  and

3932  $b \rightarrow ul\nu$  decay modes, the tracking, particle identification and luminosity uncertainties  
 3933 for analyses performed in the same experiment, etc.

3934 The theoretical errors for a given calculation are considered completely correlated  
 3935 among all the analyses. No uncertainty is assigned for possible duality violations.

3936 For BLNP, we have considered theoretical errors due to the HQE parameters  $m_b$  and  
 3937  $\mu_\pi^2$ , the functional form of the shape function, the subleading shape functions, the vari-  
 3938 ation of the matching scales, and weak annihilation.

3939 For DGE, the theoretical errors are due to the effect of the  $\alpha_s$  and  $m_b$  uncertainties on  
 3940 the prediction of the event fraction and the total rate, weak annihilation and the change  
 3941 and variation of the scale of the matching scheme.

3942 The theoretical errors for GGOU are from the value of  $\alpha_s$ ,  $m_b$  and non-perturbative  
 3943 parameters, higher order perturbative and non-perturbative corrections, the modeling  
 3944 of the  $q^2$  tail, the weak annihilation matrix element and the functional form of the  
 3945 distribution functions at fixed  $q^2$  and  $\mu = 1$  GeV.

3946 Finally, the theoretical errors considered for ADFR are related to the uncertainties on  
 3947  $\alpha_s$ ,  $|V_{cb}|$ ,  $m_c$ , and the semileptonic branching fraction. In addition, a different method to  
 3948 extract  $|V_{ub}|$  from the semileptonic rate is used, which does not depend on the inclusive  
 3949 semileptonic charm rate, and pole quark masses are employed instead of the  $\overline{\text{MS}}$  ones.

3950 The theoretical errors are all characterized by uncertainties whose size and derivative  
 3951 as a function of the rate are different, affecting in different ways the  $|V_{ub}|$  averages.

3952 The methodology and the results provided by the Heavy Flavor Averaging Group  
 3953 (HFAG) are presented in this section. To meaningfully combine the different analyses, the  
 3954 central values and errors are rescaled to a common set of input parameters. Specifically  
 3955 for the  $b \rightarrow ul\nu$  analyses, the average  $B$  lifetime used for the measurements is  $(1.573 \pm$   
 3956  $0.009)$  ps. Moreover, a rescaling factor to account for final state radiation is applied to  
 3957 the partial branching fractions used for the CLEO and Belle endpoint measurements.

3958 The fit performed to obtain the value of the  $b$  quark mass is described in Sec. 5.3. The  
 3959 value of  $m_b$  from the global fit in the kinetic scheme is used for all the four frameworks  
 3960 for consistency, translated to the different mass schemes as needed. Note that the models  
 3961 depend strongly on the  $b$  quark mass, except for ADFR, so it is very important to use a  
 3962 precise determination of the  $b$  quark mass. The results obtained by these methods and  
 3963 the corresponding averages are shown in Tab. 40.

All the methods are consistent with the current data. Fig. 47 compares  $|V_{ub}|$  extracted  
 in each experimental analysis using different frameworks. The results of DGE, BLNP,  
 GGOU agree in all cases within theoretical non-parametric errors. We take as our eval-  
 uation of  $|V_{ub}|$  from inclusive semileptonic decays the arithmetic average of the values  
 and errors of these three determinations to find

$$|V_{ub}| = (411_{-28}^{+27}) \times 10^{-5}. \quad (280)$$

3964 Although in these three cases the  $\chi^2/\text{d.f.}$  reported in Tab. 40 is good, a small WA  
 3965 contribution can marginally improve it. Differences among these theory approaches can be  
 3966 uncovered by additional experimental information on the physical spectra. For instance,  
 3967 the endpoint analyses of *BABAR* and Belle already allow us to extract  $|V_{ub}|$  at values of  
 3968  $E_{\text{cut}}$  ranging from 1.9 to 2.3 GeV. The two plots in Fig 48 compare  $|V_{ub}|$  extracted in  
 3969 the four theory frameworks at various  $E_{\text{cut}}$ . *BABAR*'s more precise results lead to stable  
 3970 values of  $|V_{ub}|$  for  $E_{\text{cut}} \leq 2.2$  GeV in BLNP and GGOU, but it must be stressed that  
 3971 the shape of the spectrum strongly depends on  $m_b$  and no conclusion can presently be

Table 40

Partial branching fraction and  $|V_{ub}|$  from inclusive  $b \rightarrow u\ell\bar{\nu}$  measurements. The values determined using different theoretical calculations are given along with the corresponding theory uncertainty; the experimental error on  $|V_{ub}|$  is quoted separately. The  $f_u$  values are from BLNP. The ADFR values for the endpoint analyses refer to  $E_e > 2.3$  GeV.

Method (GeV)	$\Delta\text{BF} \times 10^5$	$f_u^{BLNP}$	$( V_{ub}  \times 10^5)$			
			BLNP	GGOU	DGE	ADFR
$E_e > 2.1$ [626]	$33 \pm 2 \pm 7$	0.20	$383 \pm 45^{+32}_{-33}$	$368 \pm 43^{+24}_{-38}$	$358 \pm 42^{+28}_{-25}$	$349 \pm 20^{+24}_{-24}$
$E_e - q^2$ [627]	$44 \pm 4 \pm 4$	0.20	$428 \pm 29^{+36}_{-37}$	not avail.	$404 \pm 27^{+28}_{-30}$	$390 \pm 26^{+23}_{-24}$
$m_X - q^2$ [628]	$74 \pm 9 \pm 13$	0.35	$423 \pm 45^{+29}_{-30}$	$414 \pm 44^{+33}_{-34}$	$420 \pm 44^{+23}_{-18}$	$397 \pm 42^{+23}_{-23}$
$E_e > 1.9$ [629]	$85 \pm 4 \pm 15$	0.36	$464 \pm 43^{+29}_{-31}$	$453 \pm 42^{+22}_{-30}$	$456 \pm 42^{+28}_{-24}$	$326 \pm 17^{+22}_{-22}$
$E_e > 2.0$ [623]	$57 \pm 4 \pm 5$	0.28	$418 \pm 24^{+29}_{-31}$	$405 \pm 23^{+22}_{-32}$	$406 \pm 27^{+27}_{-26}$	$346 \pm 14^{+24}_{-23}$
$m_X < 1.7$ [624]	$123 \pm 11 \pm 12$	0.69	$390 \pm 26^{+24}_{-26}$	$386 \pm 26^{+18}_{-21}$	$403 \pm 27^{+26}_{-20}$	$393 \pm 26^{+24}_{-24}$
$m_X < 1.55$ [630]	$117 \pm 9 \pm 7$	0.61	$402 \pm 19^{+27}_{-29}$	$398 \pm 19^{+26}_{-28}$	$423 \pm 20^{+21}_{-16}$	$404 \pm 19^{+25}_{-26}$
$m_X - q^2$ [630]	$77 \pm 8 \pm 7$	0.35	$432 \pm 28^{+29}_{-31}$	$422 \pm 28^{+33}_{-35}$	$426 \pm 28^{+23}_{-19}$	$415 \pm 27^{+24}_{-24}$
$P^+ < 0.66$ [630]	$94 \pm 9 \pm 8$	0.60	$365 \pm 24^{+25}_{-27}$	$343 \pm 22^{+28}_{-27}$	$370 \pm 24^{+31}_{-24}$	$356 \pm 23^{+23}_{-23}$
Average			$406 \pm 15^{+25}_{-27}$	$403 \pm 15^{+20}_{-25}$	$425 \pm 15^{+21}_{-17}$	$384 \pm 13^{+23}_{-20}$
$\chi^2/\text{d.f.}$			13.9/8	9.4/7	7.1/8	16.1/8

3972 drawn.

3973 As mentioned above, the leading shape function can also be measured in  $b \rightarrow s\gamma$  de-  
 3974 cays, and there are prescriptions that relate directly the partial rates for  $b \rightarrow s\gamma$  and  
 3975  $b \rightarrow u\ell\nu$  decays [570, 571, 631, 632], thus avoiding any parametrization of the shape  
 3976 function. However, uncertainties due to the sub-leading shape function remain. The  
 3977 BABAR measurement in Ref. [623] has been analyzed by in Ref. [633] to obtain  $|V_{ub}|$   
 3978  $= (4.28 \pm 0.29 \pm 0.29 \pm 0.26 \pm 0.28) \times 10^{-3}$  and  $|V_{ub}| = (4.40 \pm 0.30 \pm 0.41 \pm 0.23) \times 10^{-3}$   
 3979 using calculations from Refs. [632] and [570, 571], respectively. These results are consistent  
 3980 with the inclusive  $|V_{ub}|$  average.

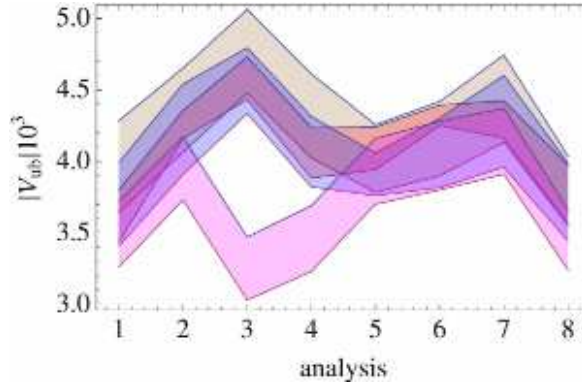


Fig. 47. Comparison of  $|V_{ub}|$  extracted from experiment as in Tab. 40 (with the exception of the second line) using the color code introduced in Fig. 43 for the four frameworks. The bands correspond to theory errors deparated of common parametric errors.

3981 Another approach is to measure  $b \rightarrow u\ell\nu$  transitions over the full phase space, thereby  
 3982 reducing theoretical uncertainties. In the first measurement of this type, *BABAR* [634]  
 3983 found  $|V_{ub}| = (4.43 \pm 0.45 \pm 0.29) \times 10^{-3}$ . A preliminary BELLE measurement of 90% of  
 3984 the full  $b \rightarrow u\ell\nu$  rate quotes  $|V_{ub}| \times 10^5$  as follows: [625]  $437 \pm 26^{+23}_{-21}$  (BLNP),  $446 \pm 26^{+15}_{-16}$   
 3985 (DGE),  $441 \pm 26^{+12}_{-22}$  (GGOU). The last error in each case combines uncertainties from  
 3986 theory and  $m_b$ , and is smaller than in less-inclusive measurements.

3987 The inclusive determinations of  $|V_{ub}|$  are about  $\sim 2\sigma$  larger than those obtained from  
 3988 exclusive  $B \rightarrow \pi\ell\nu$ . The estimated uncertainty on  $|V_{ub}|$  from inclusive decays is presently  
 3989 smaller than from exclusive decays. The value of  $|V_{ub}|$  predicted from the measured  $\sin 2\beta$   
 3990 value is closer to the exclusive result [635].

3991 The experimental results and theoretical computations presented in this chapter rep-  
 3992 resent an enormous effort, and their distillation into determinations of  $|V_{ub}|$  and  $|V_{cb}|$   
 3993 have required close communication among the participants.

## 3994 6. Rare decays and measurements of $|V_{td}/V_{ts}|$

### 3995 6.1. Introduction

3996 In this chapter we will discuss a particular subclass of  $B$ ,  $K$ , and  $D$  meson decays,  
 3997 so-called rare decays. These transitions have been the subject of a considerable number  
 3998 of experimental and theoretical investigations. Being rare processes mediated by loop  
 3999 diagrams in the SM, they all test the flavor structure of the underlying theory at the  
 4000 level of quantum corrections and provide information on the couplings and masses of  
 4001 heavy virtual particles appearing as intermediate states. The resulting sensitivity to  
 4002 non-standard contributions, such as charged Higgs bosons, SUSY particles, Kaluza-Klein  
 4003 (KK) excitations or other exotics arising in extensions of the SM, allows for an indirect  
 4004 observation of NP, a strategy complementary to the direct production of new particles.  
 4005 Whereas the latter option is reserved to the Tevatron and the LHC, the indirect searches  
 4006 performed by CLEO, *BABAR*, Belle, and other low-energy experiments already impose  
 4007 severe restrictions on the parameter space of a plethora of NP scenarios, while they do  
 4008 not exclude the possibility that CDF, D0, or LHC***b*** may find significant deviations from  
 4009 the SM expectations in certain rare processes, and thus evidence for NP, prior to a direct

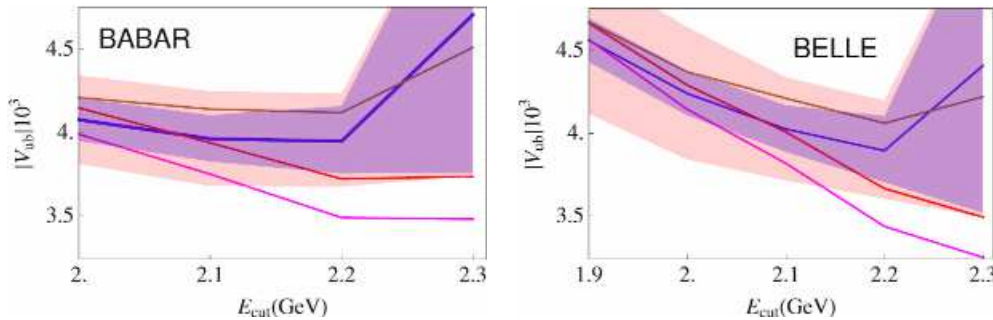


Fig. 48.  $|V_{ub}|$  extracted from the lepton endpoint by *BABAR* and Belle as a function of the cut on the lepton energy. The bands correspond to GGOU theory errors deparated of the parametric and WA error and to the latter combined with the experimental one.

4010 discovery of the associated new states by the high- $p_T$  experiments ATLAS and CMS.

4011 Among the rare decays, the radiative  $b \rightarrow (s, d)\gamma$  transitions play a special role. Pro-  
4012 ceeding at rates of order  $G_F^2\alpha$ , they are parametrically enhanced over all other loop-  
4013 induced, non-radiative rare decays that are proportional to  $G_F^2\alpha^2$ . The helicity violat-  
4014 ing  $b \rightarrow (s, d)\gamma$  amplitudes are dominated by perturbative QCD effects which replace  
4015 the quadratic GIM suppression present in the electroweak vertex by a logarithmic one.  
4016 This mild suppression of the QCD corrected amplitudes reduces the sensitivity of these  
4017 processes to high-scale physics, but makes them wonderful laboratories to study both  
4018 perturbative and non-perturbative strong-interaction phenomena. Since the  $b \rightarrow (s, d)\gamma$   
4019 transitions receive sizable contributions from top-quark loops involving the couplings  $|V_{ts}|$   
4020 or  $|V_{td}|$ , radiative  $B$ -meson decays may be in addition used to test the unitarity of the  
4021 CKM matrix and to over-constrain the Wolfenstein parameters  $\bar{\rho}$  and  $\bar{\eta}$ . The theoretical  
4022 and experimental status of both the inclusive  $B \rightarrow X_{s,d}\gamma$  and exclusive  $B \rightarrow (K^*, \rho, \omega)\gamma$   
4023 modes is reviewed in Sec.s 6.2 and 6.3.

4024 Useful complementary information on the chiral nature of the flavor structure of possible  
4025 non-standard interactions can be obtained from the studies of purely leptonic and  
4026 semileptonic rare decays. Tree-level processes like  $B \rightarrow \tau\nu$  or  $B \rightarrow D\tau\nu$  provide a  
4027 unique window on scalar interactions induced by charged Higgs bosons exchange, while  
4028 loop-induced decays such as  $B_{s,d} \rightarrow \mu^+\mu^-$  and  $B \rightarrow (X_s, K, K^*)\ell^+\ell^-$  also probe the  
4029 magnitude and phase of  $SU(2)$  breaking effects arising from  $Z$ -penguin and electroweak  
4030 box amplitudes. The latter contributions lead to a quadratic GIM mechanism in the  
4031 corresponding decay amplitudes and therefore to an enhanced sensitivity to the scale of  
4032 possible non-standard interactions. In contrast to the two-body decay modes  $B \rightarrow \tau\nu$   
4033 and  $B_{s,d} \rightarrow \mu^+\mu^-$ , the three-body decays  $B \rightarrow D\tau\nu$  and  $B \rightarrow (X_s, K, K^*)\ell^+\ell^-$  allow  
4034 one to study non-trivial observables beyond the branching fraction by kinematic mea-  
4035 surements of the decay products. In the presence of large statistics, expected from the  
4036 LHC and a future super flavor factor, angular analyses of the  $b \rightarrow c\tau\nu$  and  $b \rightarrow s\ell^+\ell^-$   
4037 channels will admit model-independent extractions of the coupling constants multiply-  
4038 ing the effective interaction vertices. The recent progress achieved in the field of purely  
4039 leptonic and semileptonic rare decays is summarized in Sec.s 6.4 to 6.6.

4040 Our survey is rounded off in Sec.s 6.7 and 6.8 with concise discussions of various  
4041 rare  $K$  and  $D$  meson decays. In the former case, the special role of the  $K \rightarrow \pi\nu\bar{\nu}$  and  
4042  $K_L \rightarrow \pi^0\ell^+\ell^-$  modes is emphasized, which due to their theoretical cleanliness and their  
4043 enhanced sensitivity to both non-standard flavor and CP violation, are unique tools to  
4044 discover or, if no deviation is found, to set severe constraints on non-MFV physics where  
4045 the hard GIM cancellation present in the SM and MFV is not active.

## 4046 6.2. Inclusive $B \rightarrow X_{s,d}\gamma$

### 4047 6.2.1. Theory of inclusive $B \rightarrow X_{s,d}\gamma$

4048 The inclusive decay  $B \rightarrow X_s\gamma$  is mediated by a FCNC and is loop suppressed within  
4049 the SM. Comparing the experimentally measured branching fraction with that obtained  
4050 in the SM puts constraints on all NP models which alter the strength of FCNCs. These  
4051 constraints are quite stringent, because theory and experiment show good agreement  
4052 within errors that amount to roughly 10% on each side. To reach this accuracy on the  
4053 theory prediction requires to include QCD corrections to NNLO in perturbation theory.



4054 In this section we describe the SM calculation of the branching fraction to this order,  
 4055 elaborate on some theoretical subtleties related to experimental cuts on the photon en-  
 4056 ergy, and give examples of the implications for NP models. We also summarize the status  
 4057 of  $B \rightarrow X_d \gamma$  decays, for which experimental results have recently become available.

The calculation of QCD corrections to the  $B \rightarrow X_s \gamma$  branching fraction is compli-  
 cated by the presence of widely separated mass scales, ranging from the mass of the top  
 quark and the electroweak gauge bosons to those of the bottom and charm quarks. A  
 straightforward expansion in powers of  $\alpha_s$  leads to terms of the form  $\alpha_s \ln(M_W/m_b) \sim 1$   
 at each order in perturbation theory, so fixed-order perturbation theory is inappropriate.  
 One uses instead the EFT techniques discussed in Sec. 2.1, to set up an expansion in RG  
 improved perturbation theory. After integrating out the top quark and the electroweak  
 gauge bosons, the leading-power effective Lagrangian reads

$$\mathcal{L}_{\text{eff}} = \mathcal{L}_{\text{QCD} \times \text{QED}} + \frac{G_F}{\sqrt{2}} \sum_{q=u,c} V_{qs}^* V_{qb} \left[ C_1(\mu) Q_1^q + C_2(\mu) Q_2^q + \sum_{i=3}^8 C_i(\mu) Q_i \right]. \quad (281)$$

4058 The Wilson coefficients  $C_i$  are obtained at a high scale  $\mu_0 \sim M_W$  as a series in  $\alpha_s$  by  
 4059 matching Green's functions in the SM with those in the EFT. They are then evolved  
 4060 down to a low scale  $\mu \sim m_b$  by means of the RG. Solving the RG equations requires  
 4061 the knowledge of the anomalous dimensions of the operators, and the counting in RG-  
 4062 improved perturbation theory is such that the anomalous dimensions must be known  
 4063 to one order higher in  $\alpha_s$  than the matching coefficients themselves. The Wilson coeffi-  
 4064 cients and anomalous dimensions to the accuracy needed for the NNLO calculation were  
 4065 obtained in [27, 28] and [24, 29, 30], respectively.

The final step in the calculation consists in the evaluation of the decay rate  $\Gamma(B \rightarrow$   
 $X_s \gamma)_{E_\gamma > E_0}$  using the effective Lagrangian (281). The cut on the photon energy is required  
 to suppress background in the experimental measurements. The rate is calculated in the  
 heavy-quark expansion, which uses that  $\Lambda_{\text{QCD}} \ll m_b, m_c$ . The leading-order result can  
 be written as

$$\Gamma(B \rightarrow X_s \gamma)_{E_\gamma > E_0} = \frac{G_F^2 \alpha m_b^5}{32\pi^4} |V_{ts}^* V_{tb}|^2 \sum_{i,j=1}^8 C_i(\mu) C_j(\mu) G_{ij}(E_0), \quad (282)$$

4066 where we have neglected contributions from  $Q_{1,2}^u$ , which are CKM suppressed. The func-  
 4067 tions  $G_{ij}$  can be calculated in fixed-order perturbation theory as long as  $\Lambda_{\text{QCD}} \ll$   
 4068  $m_b - 2E_0 = \Delta$ . In that case, they are obtained from the partonic matrix elements of  
 4069 the  $b \rightarrow X_s \gamma$  decay. Results at NLO in  $\alpha_s$  are known completely [636]. At NNLO, exact  
 4070 results are available only for  $G_{77}$  [637–639]. Concerning the NNLO corrections to the  
 4071 other elements  $G_{ij}$ , it is reasonable to focus on terms where  $i, j \in \{1, 2, 7, 8\}$ , since the  
 4072 Wilson coefficients  $C_{3-6}$  are small. For those terms, the set of NNLO diagrams generated  
 4073 by inserting a bottom, charm, or light-quark loop into the gluon lines of the NLO dia-  
 4074 grams are also known [640–643], with the exception of  $G_{18}$  and  $G_{28}$ . An estimate of the  
 4075 remaining NNLO corrections was performed in [644], by calculating the full corrections  
 4076 to the elements  $G_{ij}$  in the asymptotic limit  $m_c \gg m_b/2$ , and then interpolating them  
 4077 to three different boundary conditions at  $m_c = 0$  to find results at the physical value  
 4078  $m_c \approx m_b/4$ .

The results of the various NNLO corrections discussed above lead to the numerical  
 analysis of [645], which found

$$\mathcal{B}(B \rightarrow X_s \gamma)_{E_\gamma > 1.6 \text{ GeV}} = (3.15 \pm 0.23) \times 10^{-4}. \quad (283)$$

4079 The total error was obtained by adding in quadrature the uncertainties from hadronic  
 4080 power corrections (5%), parametric dependences (3%), and the interpolation in the charm  
 4081 quark mass (3%). The most significant unknown stems from hadronic power corrections  
 4082 scaling as  $\alpha_s A_{\text{QCD}}/m_b$  [646]. For the  $(Q_7, Q_8)$  interference, this involve hadronic ma-  
 4083 trix elements of four-quark operators with trilocal light-cone structure, which were esti-  
 4084 mated in the vacuum insertion approximation to change the branching fraction by about  
 4085  $-[0.3, 3.0]\%$ . Corrections of similar or larger size may arise from non-local  $\alpha_s A_{\text{QCD}}/m_b$   
 4086 corrections due to the  $(Q_{1,2}, Q_7)$  interference, but these have not yet been estimated.

4087 The fixed-order calculation relies on the parametric counting  $\Delta \sim m_b$ . However, mea-  
 4088 surements of the branching fractions are limited to values above a photon energy cut  
 4089  $E_0 = 1.6 \text{ GeV}$ , corresponding to  $\Delta \sim 1.4 \text{ GeV}$ , so it can be argued the counting  $A_{\text{QCD}} \ll$   
 4090  $\Delta \ll m_b$  is more appropriate. In that case, to properly account for the photon energy cut  
 4091 requires to separate contributions from a hard scale  $\mu_h \sim m_b$ , the soft scale  $\mu_s \sim \Delta$ , and  
 4092 an intermediate scale  $\mu_i \sim \sqrt{m_b \Delta}$ . An EFT approach able to separate these scales and  
 4093 to resum large logarithms of their ratios was developed in [647], and extended to NNLO  
 4094 in RG-improved perturbation theory in [648–650]. An approach which used the same  
 4095 factorization of scales, but a different approach to resummation, called dressed gluon  
 4096 exponentiation (DGE), was pursued in [565, 567]. Compared to [650], the DGE approach  
 4097 includes additional effects arising from the resummation of running-coupling corrections  
 4098 in the power-suppressed  $\Delta/m_b$  contributions.

4099 The consistency between the SM prediction (283) and the experimental world average  
 4100 as given in Tab. 41, provides strong constraints on many extensions of the SM. The prime  
 4101 example is the bound on the mass of the charged Higgs boson in the 2HDM of type II  
 4102 (2HDM-II) [651–653] that amounts to  $M_{H^+} > 295 \text{ GeV}$  at 95% CL [645], essentially  
 4103 independent of  $\tan \beta$ . This is much stronger than other available direct and indirect  
 4104 constraints on  $M_{H^+}$ .

4105 The inclusive  $b \rightarrow s \gamma$  transition has also received a lot of attention in SUSY extensions  
 4106 of the SM [147, 148, 653–655]. In the limit of  $M_{\text{SUSY}} \gg M_W$ , SUSY effects can be absorbed  
 4107 into the coupling constants of local operators in an EFT [135]. The Higgs sector of the  
 4108 MSSM is modified by these non-decoupling corrections and can differ notably from the  
 4109 native 2HDM-II model. Some of the corrections to  $B \rightarrow X_s \gamma$  in the EFT are enhanced  
 4110 by  $\tan \beta$ , as  $\alpha_s \tan \beta \sim 1$  for  $\tan \beta \gg 1$ , and need to be resummed if applicable. In the  
 4111 large  $\tan \beta$  regime the relative sign of the chargino contribution is given by  $-\text{sgn}(A_t \mu)$ .  
 4112 For  $\text{sgn}(A_t \mu) > 0$ , the chargino and charged Higgs boson contributions interfere con-  
 4113 structively with the SM amplitude and this tends to rule out large positive values of the  
 4114 product of the trilinear soft SUSY breaking coupling  $A_t$  and the Higgsino parameter  $\mu$ .  
 4115 In the MSSM with generic sources of flavor violation,  $B \rightarrow X_s \gamma$  implies stringent bounds  
 4116 on the flavor-violating entries in the down-squark mass matrix. In particular, for small  
 4117 and moderate values of  $\tan \beta$  all four mass insertions  $(\delta_{23}^d)_{AB}$  with  $A, B = L, R$  except for  
 4118  $(\delta_{23}^d)_{RR}$  are determined entirely by  $B \rightarrow X_s \gamma$  2.5.2.3. The bounds on  $|(\delta_{23}^d)_{AB}|$  amount  
 4119 to  $4 \times 10^{-1}$ ,  $6 \times 10^{-2}$ , and  $2 \times 10^{-2}$  for the  $LL$ ,  $LR$ , and  $RL$  insertion.

4120 In the portion of the SUSY parameter space with inverted scalar mass hierarchy, real-  
 4121 ized in the class of SUSY GUT scenarios, chargino contributions to  $b \rightarrow s \gamma$  are strongly  
 4122 enhanced. As a result, SUSY GUT models with third generation Yukawa unification and  
 4123 universal squark and gaugino masses at the GUT scale are unable to accommodate the

4124 value of the bottom-quark mass without violating either the constraint from  $B \rightarrow X_s \gamma$  or  
 4125  $B_s \rightarrow \mu^+ \mu^-$ , unless the scalar masses are pushed into the few TeV range [656]. A poten-  
 4126 tial remedy consists in relaxing Yukawa to  $b$ - $\tau$  unification, but even then the predictions  
 4127 for  $\mathcal{B}(B \rightarrow X_s \gamma)$  tend to be at the lower end of the range favored by experiment [657].

4128 In non-SUSY extensions of the SM, contributions due to Kaluza-Klein (KK) excita-  
 4129 tions in models with universal extra dimensions (UEDs) interfere destructively with the  
 4130 SM amplitude,  $B \rightarrow X_s \gamma$  leads to powerful bounds on the inverse compactification ra-  
 4131 dius  $1/R$ . Exclusion limits have been obtained in the five- and six-dimensional case and  
 4132 amount to  $1/R > 600$  GeV [658] and  $1/R > 650$  GeV [659] at 95% CL. These bounds  
 4133 exceed the limits that can be derived from any other direct measurement.

4134 The discussion so far dealt with  $B \rightarrow X_s \gamma$ . Recently, a first measurement of the  $B \rightarrow$   
 4135  $X_d \gamma$  branching fraction has been presented [660]. Compared to  $B \rightarrow X_s \gamma$ , the nominal  
 4136 theoretical difference is to replace  $s \rightarrow d$  in the effective Lagrangian (281), in which case  
 4137 the terms proportional to  $Q_{1,2}^u$  are no longer CKM suppressed. The implications of this  
 4138 have been studied in [661], where it was pointed out that the ratio  $\mathcal{B}(B \rightarrow X_s \gamma)/\mathcal{B}(B \rightarrow$   
 4139  $X_d \gamma)$  can be calculated with reduced theoretical uncertainty. This was used along with  
 4140 the experimental results to determine  $|V_{td}/V_{ts}|$  in [660]. A possible subtlety is that in [661]  
 4141 the total branching fraction has been calculated, whereas the experimental measurements  
 4142 are limited to the region  $M_{X_s} < 1.8$  GeV of hadronic invariant masses, where “shape-  
 4143 function” effects are expected to be important.

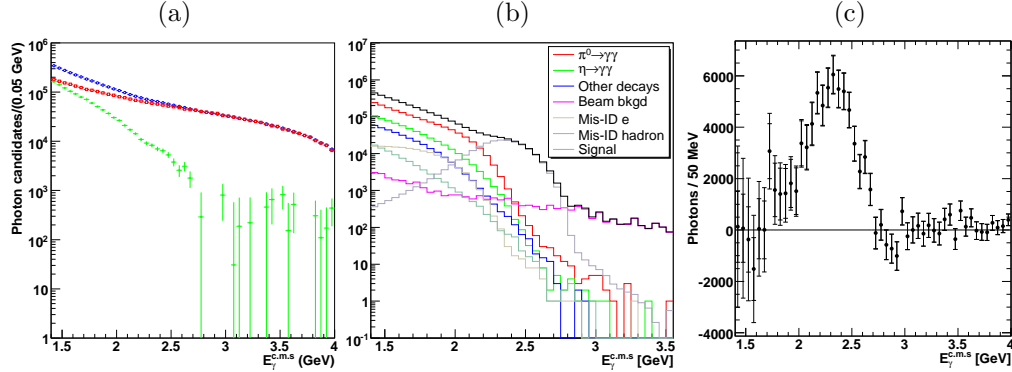
#### 4144 6.2.2. *Experimental methods and status of $B \rightarrow X_{s,d} \gamma$*

4145 The analysis of the inclusive  $B \rightarrow X_s \gamma$  decay at the  $B$  factories is rather complicated.  
 4146 The quantities to be measured are the differential decay rate, i.e., the photon energy  
 4147 spectrum as well as the total branching fraction. There are three methods for the inclusive  
 4148 analyses: fully inclusive, semi-inclusive, and  $B$  recoil.

4149 The idea of the fully inclusive method is to subtract the photon energy spectrum of  
 4150 the on-resonant  $e^+ e^- \rightarrow \Upsilon(4S) \rightarrow B \bar{B}$  events by that of the continuum  $e^+ e^- \rightarrow q \bar{q}$   
 4151 events. This method is free from the uncertainty of the final state, and can exploit the  
 4152 whole available statistics. However, the signal purity is very low, and the background  
 4153 suppression is a key issue. The photon energy is obtained in the  $\Upsilon(4S)$  rest frame and  
 4154 not in the  $B$  rest frame, since the momentum of the  $B$  is unknown.

4155 Panel (a) of Fig. 49 shows the photon energy spectrum after suppressing the contin-  
 4156 uum background, using event topology, and vetoing high energy photons from  $\pi^0$  or  $\eta$   
 4157 using the invariant mass of the candidate high energy photon, and of any other photons  
 4158 in the event. The largest background is from the continuum events, and is subtracted us-  
 4159 ing the continuum data. This subtraction requires correction due to small center-of-mass  
 4160 energy difference for the event selection efficiency, photon energy, and photon multiplic-  
 4161 ity between the on-resonant and continuum sample. As shown in panel (b) of Fig. 49,  
 4162 the subtracted spectrum still suffers from huge backgrounds from  $B$  decays, which are  
 4163 subtracted using the MC sample. Here, the MC sample needs to be calibrated with data  
 4164 using control samples to reproduce the yields of  $\pi^0$ ,  $\eta$ , etc. The final photon spectrum, ob-  
 4165 tained with the prescribed procedure, for  $b \rightarrow s \gamma$  events, is shown in panel (c) of Fig. 49.  
 4166 It can be seen that the errors increase rapidly for photon energies below 2 GeV due to  
 4167 the very large continuum background in that region. For this reason all measurements of  
 4168 the branching ratio introduce a cutoff  $E_\gamma^{\min}$  and then extrapolate to get  $\mathcal{B}(E_\gamma > 1.6$  GeV)

Fig. 49. (a) On-resonant data (open circle), scaled continuum data (open square) and continuum background subtracted (filled circle) photon energy spectrum. (b) The spectra of photons from  $B$  decays (MC). (c) The extracted photon spectrum for  $B \rightarrow X_s \gamma$ . The plots are taken from [662].



4169 which is compared to the theory prediction. Measurements by CLEO, *BABAR*, and Belle  
 4170 using the fully inclusive method are listed in Tab. 41. The results are consistent with the  
 4171 SM expectation (283).

4172 In the semi-inclusive method, also called “sum-of-exclusive” method, the reconstruction  
 4173 of the  $B \rightarrow X_s \gamma$  signal is performed by the sum of certain hadronic final states  $X_s$   
 4174 that are exclusively reconstructed. Typically,  $X_s$  is reconstructed from one Kaon plus  
 4175 up to four pions including up to one or two neutral pions, but also modes with three  
 4176 Kaons or an  $\eta$  are used. The advantage of this method is a better signal purity compared  
 4177 to the fully inclusive method. The background suppression is still important, but the  
 4178 detailed correction of the MC samples and the precise determination of the luminosity of  
 4179 the off-resonance sample, used in the fully inclusive method, are not necessary. Another  
 4180 advantage is that the photon energy in the  $B$  rest frame can be measured from the mass  
 4181 of the  $X_s$  system. However, this method can reconstruct only a part of the  $X_s$  system,  
 4182 and suffers from the large uncertainty in the fraction of the total width present in the  
 4183 exclusive modes that are reconstructed. The measurements from *BABAR* and Belle are  
 4184 listed in Tab. 41.

4185 It is also possible to measure the CP asymmetry,  $A_{CP}$ , of  $B \rightarrow X_s \gamma$  with the semi-  
 4186 inclusive method, since most of the final states provide flavor information. In the SM,  $A_{CP}$   
 4187 is predicted to be less than 1% [663,664], but some models beyond the SM predict much  
 4188 larger values of  $A_{CP}$  [663–666]. The measurement of *BABAR* leads to  $A_{CP} = -0.010 \pm$   
 4189  $0.030_{\text{stat}} \pm 0.014_{\text{syst}}$  for  $M_{X_s} < 2.8$  GeV [667] while Belle finds  $A_{CP} = 0.002 \pm 0.050_{\text{stat}} \pm$   
 4190  $0.030_{\text{syst}}$  for  $M_{X_s} < 2.1$  GeV [668].

4191 *BABAR* recently reported a first measurement of  $B \rightarrow X_d \gamma$  using the semi-inclusive  
 4192 approach [660]. In this analysis, seven exclusive final states in the range  $0.6$  GeV  $<$   
 4193  $M_{X_d} < 1.8$  GeV are reconstructed. Although the analysis suffers from a large background  
 4194 from continuum events, mis-reconstructed  $B \rightarrow X_s \gamma$  events, and an large uncertainty in  
 4195 missing modes, *BABAR* obtained the branching fraction in this mass range to be  $(7.2 \pm$   
 4196  $2.7_{\text{stat}} \pm 2.3_{\text{syst}}) \times 10^{-6}$ .

4197 In the  $B$  recoil method, one of the two produced  $B$  mesons is fully reconstructed in a  
 4198 hadronic mode, and an isolated photon is identified in the rest of the event. This method

Table 41

Inclusive branching fractions of radiative  $B$  decays.  $E_\gamma^{\min}$  and  $\mathcal{B}(E_\gamma > E_\gamma^{\min})$  are the minimum energy and branching fraction reported in the paper, while  $\mathcal{B}(E_\gamma > 1.6 \text{ GeV})$  is the rescaled branching fraction. The size of the data sets is given in units of  $\text{fb}^{-1}$  and the branching fractions are in units of  $10^{-6}$ .

Method	Data set	$E_\gamma^{\min}$	$\mathcal{B}(E_\gamma > E_\gamma^{\min})$	$\mathcal{B}(E_\gamma > 1.6 \text{ GeV})$	Ref.
CLEO fully inclusive	9	2.0	$305 \pm 41 \pm 26$	$329 \pm 53$	[555]
BABAR fully inclusive	82	1.9	$367 \pm 29 \pm 34 \pm 29$	$392 \pm 56$	[551]
BABAR semi-inclusive	82	1.9	$327 \pm 18^{+55}_{-40} +4_{-9}$	$349 \pm 57$	[552]
BABAR $B$ -recoil	210	1.9	$366 \pm 85 \pm 60$	$391 \pm 111$	[669]
Belle semi-inclusive	6	2.24	—	$369 \pm 94$	[670]
Belle fully inclusive	605	1.7	$332 \pm 16 \pm 37 \pm 1$	$337 \pm 43$	[662]
Average	—	—	—	$352 \pm 23 \pm 9$	
Theory prediction	—	—	—	$315 \pm 23$	[645]

4199 provides a very clean signal, and one obtains simultaneously the flavor, charge, and  
 4200 momentum of the  $B$  meson. The drawback is a very low efficiency. In the analysis with  
 4201  $210 \text{ fb}^{-1}$  by BABAR [669],  $6.8 \times 10^5$   $B$  mesons are tagged and  $119 \pm 27$  signal events are  
 4202 found. The result is limited by statistics and is not competitive with the other methods  
 4203 listed in Tab. 41. However, this method is promising for a future super flavor factory.

### 4204 6.2.3. Theory of photon energy spectrum and moments

4205 The basic motivation to study the photon energy spectrum in  $B \rightarrow X_s \gamma$  is the fact that  
 4206 backgrounds prohibit a measurement of the branching fraction for non-hard photons.  
 4207 Despite significant progress, the current measurements still have sizable errors below  
 4208  $E_\gamma \sim 2 \text{ GeV}$ . Raising the photon energy cut  $E_\gamma > E_0$  significantly increases the accuracy  
 4209 of the measurements, but requires an larger extrapolation to the “total” width, thereby  
 4210 introducing some model dependence.

4211 In contrast to the branching ratio, the photon energy spectrum is largely insensitive to  
 4212 NP [671]. It can thus be used for precision studies of perturbative and non-perturbative  
 4213 strong-interaction effects. In particular, the measured spectrum allows to extract the  
 4214 value of the mass of the bottom quark from its first moment  $\langle E_\gamma \rangle \sim m_b/2$ , its average  
 4215 kinetic energy  $\mu_\pi^2$  from its second moment, and gives direct information on the importance  
 4216 of the  $B$  meson “shape function” for different values of  $E_0$ . The measurements of  $m_b$  and  
 4217  $\mu_\pi^2$  using  $B \rightarrow X_s \gamma$  are complementary to the determinations using the inclusive moments  
 4218 of  $B \rightarrow X_c \ell \bar{\nu}$ . Fits to the measured moments [509, 553] based on the 1S [508] and the  
 4219 kinetic scheme [510, 564] have been very useful, and constitute today an important input  
 4220 to the determination of  $|V_{ub}|$  [558].

4221 The calculation of the  $B \rightarrow X_s \gamma$  photon spectrum is a complex theoretical problem.  
 4222 First of all, there is no unique way to define the total  $B \rightarrow X_s \gamma$  width owing to both  
 4223 the soft divergence of the  $(Q_7, Q_8)$  interference term and the possibility of secondary  
 4224 photon emission in non-radiative  $b \rightarrow s$  decays. Furthermore, the local OPE in  $B \rightarrow X_s \gamma$   
 4225 does not apply to contributions from operators other than  $Q_7$ , in which the photon  
 4226 couples to light quarks [672, 673]. In the case of the  $(Q_7, Q_8)$  interference, the resulting  
 4227  $\mathcal{O}(\alpha_s \Lambda_{\text{QCD}}/m_b)$  corrections to the total rate have been estimated in [646]. A detailed  
 4228 study of the impact of these and similar enhanced non-local power-corrections on the

4229 photon energy spectrum is in progress [].

4230 Even in the case of the  $Q_7$  self-interference, where an local OPE for the total width  
 4231 exists, the calculation of the spectrum is highly non-trivial. The main difficulty arises  
 4232 due to the jet-like structure of the decay process, where an energetic hadronic system,  
 4233  $E_{X_s} \sim E_\gamma \sim \mathcal{O}(m_b/2)$ , with a relatively small mass,  $\mathcal{O}(\sqrt{m_b}\Lambda_{\text{QCD}})$ , recoils against the  
 4234 photon.

4235 In the endpoint region, the  $B \rightarrow X_s\gamma$  spectrum can be computed as a convolution be-  
 4236 tween a perturbatively calculable coefficient function and the quark distribution function  
 4237  $S(l^+)$ . While the non-perturbative content of  $S(l^+)$  is in principle clear, a calculation by  
 4238 existing non-perturbative methods is not possible, so that in practice one must model  
 4239 the function  $S(l^+)$  using a suitable parametrization. Information on the corresponding  
 4240 model parameters can be obtained from the experimental measurements of the first few  
 4241 moments of inclusive decay spectra, which in turn determine the moments of the “shape  
 4242 function”.

Significant progress has been made since the first dedicated calculation of the spectrum  
 [671]. The state-of-the-art calculations are based on the factorization picture of inclusive  
 decays near the endpoint [674]. Consider for example the measurement of the partial  
 $B \rightarrow X_s\gamma$  width with  $E_\gamma > E_0$ . The key observation is that near the endpoint, i.e., for  
 $\Delta \ll m_b$ , and to leading order in  $\Lambda_{\text{QCD}}/m_b$  there are three separate dynamical processes  
 which are quantum mechanically incoherent. A soft subprocess,  $S$ , which is characterized  
 by soft gluons with momenta of order  $\Delta = m_b - 2E_\gamma$ , a jet subprocess,  $J$ , summing up  
 collinear hard radiation with virtualities of order of  $\sqrt{m_b}\Delta$ , and a hard function,  $H$ ,  
 associated with virtual gluons with momenta of order  $m_b$ . The factorized decay width  
 takes the form

$$\Gamma(\Delta) = H(m_b)J(\sqrt{m_b}\Delta) \otimes S(\Delta) + \mathcal{O}(\Lambda_{\text{QCD}}/m_b). \quad (284)$$

4243 This factorization formula, originally proposed in [674], was rederived in the framework  
 4244 of SCET [41, 528]. It serves as a basis for a range of approaches, facilitating the re-  
 4245 summation of large Sudakov logarithms associated with the double hierarchy of scales  
 4246  $m_b \gg \sqrt{m_b}\Delta \gg \Delta$ . This includes DGE [565–567, 586, 675] and a multi-scale OPE  
 4247 (MSOPE) [648–650, 676].

4248 Using SCET, it is possible to systematically define additional non-local operators that  
 4249 contribute to the decay spectra at subleading powers of  $\Lambda_{\text{QCD}}/m_b$  [677–679]. Unfortu-  
 4250 nately, the corresponding subleading “shape functions” are not well constrained since  
 4251 starting at  $\mathcal{O}(\Lambda_{\text{QCD}}/m_b)$  the number of functions exceeds the number of observables.  
 4252 Thus, estimating non-perturbative corrections to (284) remains a notoriously difficult  
 4253 task.

4254 While (284) only holds for  $\Delta \ll m_b$ , its use may vary depending on the extent at  
 4255 which effects on the lowest scale are described by perturbation theory. If  $\Delta \gg \Lambda_{\text{QCD}}$  it  
 4256 is useful to compute the quark distribution function perturbatively [586, 648] rather than  
 4257 to parametrize it. In contrast, when  $\Delta \sim \Lambda_{\text{QCD}}$  this function becomes non-perturbative.  
 4258 Two different approaches based on SCET have been developed to deal with these two  
 4259 regimes, MSOPE for the former and a formalism based on parametrization of the shape  
 4260 functions for the latter [528]. In contrast, DGE, which is at the outset derived in the  
 4261 regime  $\Delta \gg \Lambda_{\text{QCD}}$ , has been extended to the regime  $\Delta \sim \Lambda_{\text{QCD}}$  by constraining the  
 4262 Borel transform of  $S(l^+)$  and then parametrizing non-perturbative corrections depending  
 4263 on the soft scale in moment space.

4264 Beyond the conceptual issues discussed so far, much progress has been made on the  
 4265 calculation side. In particular, the  $Q_7$  self-interference part of the spectrum has been  
 4266 computed to NNLO accuracy [637, 680]. In addition, all the necessary ingredients for  
 4267 Sudakov resummation at NNLO of both the soft and the jet function are in place [586, 648,  
 4268 649, 681, 682]. Some additional higher-order corrections are known, in particular, running-  
 4269 coupling corrections [567, 640, 675], but unfortunately complete NNLO calculations of the  
 4270  $(Q_7, Q_{1,2})$  and  $(Q_{1,2}, Q_{1,2})$  interference terms are not available at present.

4271 Systematic NNLO analysis of the  $B \rightarrow X_s \gamma$  branching fraction and spectrum have  
 4272 been performed by three groups [567, 645, 650]. While the first analysis works at fixed-  
 4273 order in perturbation theory, the latter two articles are based on Sudakov resummation  
 4274 utilizing (284). The MSOPE result has been combined with the fixed-order predictions  
 4275 by computing the fraction of events  $1 - T$  that lies in the range  $E_0 = [1.0, 1.6]$  GeV. The  
 4276 analysis [650] finds  $1 - T = 0.07^{+0.03}_{-0.05_{\text{pert}}} \pm 0.02_{\text{hard}} \pm 0.02_{\text{pars}}$ , where the individual errors  
 4277 are perturbative, hadronic, and parametric. The quoted value is almost twice as large as  
 4278 the estimate  $1 - T = 0.04 \pm 0.01_{\text{pert}}$  obtained in fixed-order perturbation theory [645]. In  
 4279 contrast, in the DGE approach [567] one finds a much thinner tail of the photon energy  
 4280 spectrum at NNLO,  $1 - T = 0.016 \pm 0.003_{\text{pert}}$ , which is consistent with the result obtained  
 4281 in fixed order perturbation theory.

4282 Given the common theoretical basis for the resummation, the opposite conclusions  
 4283 drawn in [650] and [567] may look surprising. The main qualitative differences between the  
 4284 two calculations are as follows. First, the result [650] is plagued by a significant additional  
 4285 theoretical error related to low-scale,  $\mu \sim \Delta$ , perturbative corrections, indicating the  
 4286 presence of large subleading logarithmic corrections to the soft function. In contrast, the  
 4287 DGE approach [567] supplements Sudakov resummation with internal resummation of  
 4288 running-coupling corrections, which is necessary to cure the endpoint divergence of the  
 4289 fixed-logarithmic-accuracy expansion. Second, the MSOPE approach [650] identified a  
 4290 high sensitivity to the matching procedure, dealing with terms that are suppressed by  
 4291 powers of  $\Delta/m_b$  for  $E_\gamma \sim m_b/2$ , but are not small away from the endpoint [567, 683].  
 4292 The analysis [567], on the other hand, has used additional information on the small  $E_\gamma$   
 4293 behavior of the different interference terms, which is known to all orders in perturbation  
 4294 theory, to extend the range of applicability of resummation to the tail region.

4295 In conclusion, progress on the theory front, in particular in factorization and resum-  
 4296 mation of perturbation theory, and in explicit higher order calculations, significantly  
 4297 improved our knowledge of the photon energy spectrum in  $B \rightarrow X_s \gamma$ . Nevertheless,  
 4298 uncertainties of both perturbative and non-perturbative origin remain, which deserve  
 4299 further theoretical investigations.

#### 4300 6.2.4. *Experimental results of photon energy spectrum and moments*

4301 In the case of the semi-inclusive and  $B$  recoil methods, the photon energy spectrum  
 4302 can be measured directly in the  $B$  meson rest frame. The semi-inclusive method suffers  
 4303 from large uncertainty from the hadronic system, while the  $B$  recoil method requires  
 4304 much more statistics. Presently, precise measurements of the photon energy spectrum  
 4305 are therefore provided only with the fully inclusive method.

4306 In the fully inclusive method, it is not possible to know the momentum of the  $B$  meson  
 4307 for each photon, so only the photon energy distribution in the  $\Upsilon(4S)$  rest frame is directly  
 4308 measurable. As a result the raw photon energy spectrum has to be corrected not only for

4309 the photon detection efficiency of the calorimeter and other selection efficiency, but also  
 4310 for the smearing effect between the  $B$  meson and the  $\mathcal{T}(4S)$  frame. The energy spectrum is  
 4311 also smeared by the response of the calorimeter. The correction due to smearing, which  
 4312 is also referred to as “unfolding”, depends on the signal models and its parameters.  
 4313 CLEO [555] uses a signal model by Ali and Greub [684], while a model by Kagan and  
 4314 Neubert [671] is used by both *BABAR* [551] and Belle [662]. The latter collaboration also  
 4315 considers other models [557, 567, 570, 584].

4316 The photon energy spectrum is often represented in terms of the first two moments,  
 4317 i.e., mean and variance, above a certain energy threshold. For example, *BABAR* [551] ob-  
 4318 tains  $\langle E_\gamma \rangle = (2.346 \pm 0.032_{\text{stat}} \pm 0.011_{\text{syst}})$  GeV and  $\langle E_\gamma^2 \rangle - \langle E_\gamma \rangle^2 = (0.0226 \pm 0.0066_{\text{stat}} \pm$   
 4319  $0.0020_{\text{syst}})$  GeV<sup>2</sup> for  $E_\gamma > 2.0$  GeV, while Belle [662]  $\langle E_\gamma \rangle = (2.281 \pm 0.032_{\text{stat}} \pm 0.053_{\text{syst}} \pm$   
 4320  $0.002_{\text{boos}})$  GeV and  $\langle E_\gamma^2 \rangle - \langle E_\gamma \rangle^2 = (0.0396 \pm 0.0156_{\text{stat}} \pm 0.0214_{\text{syst}} \pm 0.0012_{\text{boos}})$  GeV<sup>2</sup>  
 4321 for  $E_\gamma > 1.7$  GeV, where the last errors in the Belle measurements are from the boost cor-  
 4322 rection. In these measurements, branching fractions and moments with different photon  
 4323 energy thresholds are also obtained. Parameters useful for the  $|V_{cb}|$  and  $|V_{ub}|$  determi-  
 4324 nations such as the bottom-quark mass  $m_b$  or its mean momentum squared  $\mu_\pi^2$  can be  
 4325 obtained by fitting the theoretical predictions to the measured moments. This is discussed  
 4326 in detail in Sec. 5.3.

4327 One of the challenges in the measurement is to lower the energy threshold of the photon.  
 4328 The contamination of the background from  $B$  decays becomes more severe rapidly, as  
 4329 the threshold is lowered, especially in the region below 2 GeV. So far, with growing data  
 4330 sets, measurements with lower photon energy threshold have been performed. However,  
 4331 the results with lower cut on the photon energy tend to give larger systematic, and model  
 4332 errors. This raises the question which threshold value is optimal to determine  $|V_{cb}|$  and  
 4333  $|V_{ub}|$ . Another issue is that the uncertainty of  $m_b$  is included in the signal model error for  
 4334 the measurements of the moments, but the measured moments themselves are used to  
 4335 determine  $m_b$ . The latter issue could probably be avoided by performing a simultaneous  
 4336 determination of the parameters in question from the raw photon energy spectrum.

### 4337 6.3. Exclusive $B \rightarrow V\gamma$ decays

#### 4338 6.3.1. Theory of exclusive $B \rightarrow V\gamma$ decays

4339 The exclusive decays  $B_{(s)} \rightarrow V\gamma$ , with  $V \in \{K^*, \rho, \omega, \phi\}$ , are mediated by FCNCs  
 4340 and thus test the flavor sector in and beyond the SM. After matching onto the effec-  
 4341 tive Lagrangian (281), the main theoretical challenge is to evaluate the hadronic matrix  
 4342 elements of the operators  $Q_{1-8}$ . QCDF is a model-independent approach based on the  
 4343 heavy-quark expansion [685–687], and the bulk of this section is devoted to describing  
 4344 this formalism. At the end of the section we briefly mention the “perturbative QCD”  
 4345 (pQCD) approach [688–690]. Although the hadronic uncertainties inherent to the exclu-  
 4346 sive decay modes are a barrier to precise predictions, we shall see that the exclusive decays  
 4347 nonetheless provide valuable information on the CKM elements  $|V_{td}/V_{ts}|$  and allow to  
 4348 put constraints on the chiral structure of possible non-standard interactions.

QCDF is the statement that in the heavy-quark limit the hadronic matrix element of  
 each operator in the effective Lagrangian can be written in the form

$$\langle V\gamma | Q_i | \bar{B} \rangle = T_i^I F^{B \rightarrow V_\perp} + \int_0^\infty \frac{d\omega}{\omega} \phi_+^B(\omega) \int_0^1 du \phi_\perp^V(u) T_i^{\text{II}}(\omega, u) + \mathcal{O}\left(\frac{\Lambda_{\text{QCD}}}{m_b}\right). \quad (285)$$



4349 The form factor  $F^{B \rightarrow V_\perp}$  and the light-cone distribution amplitudes (LCDAs)  $\phi_+^B, \phi_\perp^V$  are  
 4350 non-perturbative, universal objects. The hard-scattering kernels  $T_i^{I,II}$  can be calculated as  
 4351 a perturbative series in  $\alpha_s$ . The elements  $T_i^I$  ( $T_i^{II}$ ) are referred to as “vertex corrections”  
 4352 (“spectator corrections”). The hard-scattering kernels have been known completely at  
 4353 order  $\alpha_s$  (NLO) for some time [685–687], and recently some of the  $\alpha_s^2$  (NNLO) corrections  
 4354 have also been calculated [691].

4355 An all orders proof of the QCDF formula (285) was performed in [692], using the  
 4356 technology of SCET. The EFT approach also allows to separate physics from the two  
 4357 perturbative scales  $m_b$  and  $\sqrt{m_b \Lambda_{\text{QCD}}}$ , and to resum perturbative logarithms of their  
 4358 ratio using the RG. The numerical impact of this resummation has been investigated  
 4359 in [691, 692].

4360 The predictive power of QCDF is limited by hadronic uncertainties related to the  
 4361 LCDAs and QCD form factors, as well as by power corrections in  $\Lambda_{\text{QCD}}/m_b$ . For in-  
 4362 stance, the form factors  $F^{B \rightarrow V_\perp}$  can be calculated with QCD sum rules to an accuracy  
 4363 of about 15%, which implies an uncertainty of roughly 30% on the  $B \rightarrow V\gamma$  branching  
 4364 fractions. More troublesome is the issue of power corrections. A naive dimensional esti-  
 4365 mate indicates that these should be on the order of 10%, but this statement is hard to  
 4366 quantify. Since SCET is an effective theory which sets up a systematic expansion in  $\alpha_s$   
 4367 and  $\Lambda_{\text{QCD}}/m_b$ , it has the potential to extend the QCDF formalism to subleading order  
 4368 in  $\Lambda_{\text{QCD}}/m_b$ . However, in cases where power corrections have been calculated, the convo-  
 4369 lution integrals over momentum fractions do not always converge [693]. These “endpoint  
 4370 divergences” are at present a principle limitation on the entire formalism.

4371 Although a comprehensive theory of power corrections is lacking, it is nonetheless  
 4372 possible to estimate some of the corrections which are believed to be large, or which  
 4373 play an important role in phenomenological applications. One such correction stems  
 4374 from the annihilation topology, which has been shown to factorize at leading order in  
 4375  $\alpha_s$  [686]. Annihilation gives the leading contribution to isospin asymmetries, and is also  
 4376 important for  $B^\pm \rightarrow \rho^\pm \gamma$  branching fractions, where it is enhanced by a factor of  $C_{1,2}/C_7$ .  
 4377 The  $\Lambda_{\text{QCD}}/m_b$  corrections from annihilation have been included in all recent numerical  
 4378 studies [444, 694–696], and part of the  $\Lambda_{\text{QCD}}^2/m_b^2$  correction, so-called “long-distance  
 4379 photon emission”, has been calculated in [444]. Some additional  $\alpha_s \Lambda_{\text{QCD}}/m_b$  corrections  
 4380 from annihilation and spectator scattering needed to calculate isospin asymmetries were  
 4381 dealt with in [693]. Corrections from three-particle Fock states in the  $B$  and  $V$  mesons,  
 4382 most significant for indirect CP asymmetries, were estimated in [444].

We now give numerical results for some key observables in  $B \rightarrow V\gamma$  decays, and  
 compare them with experiment. The ratio of  $B \rightarrow K^*\gamma$  and  $B \rightarrow \rho\gamma$  branching fractions  
 is useful for the determination of  $|V_{td}/V_{ts}|$ . To understand why this is the case, consider  
 the expression

$$\frac{\mathcal{B}(B^0 \rightarrow \rho^0 \gamma)}{\mathcal{B}(B^0 \rightarrow K^{*0} \gamma)} = \frac{1}{2\xi^2} \left| \frac{V_{td}}{V_{ts}} \right|^2 \left[ 1 - 2R_{ut}\epsilon_0 \cos \alpha \cos \theta_0 + R_{ut}^2 \epsilon_0^2 \right]. \quad (286)$$

4383 Analogous expressions hold for charged decays and  $B \rightarrow \omega\gamma$ . The quantities  $\epsilon_0$  and  $\cos \theta_0$   
 4384 can be calculated in QCDF, and vanish at leading order in  $\Lambda_{\text{QCD}}/m_b$  and  $\alpha_s$ . Beyond  
 4385 leading order they are approximately 10%, but the factor inside the brackets remains  
 4386 close to unity, due to a additional suppression from the CKM factors  $\cos \alpha \sim 0.1$  and  
 4387  $R_{ut} = |(V_{ud}V_{ub})/(V_{td}V_{tb})| \sim 0.5$ . Therefore, by far, the dominant theoretical uncertainty  
 4388 is related to the form factor ratio  $\xi = F^{B \rightarrow K^*}/F^{B \rightarrow \rho}$ . The ratio of form factors can be

4389 calculated with better accuracy than the form factors themselves and has been estimated  
 4390 using light-cone sum rules to be  $1.17 \pm 0.09$  [444]. Extracting  $|V_{td}/V_{ts}|$  from (286) and  
 4391 averaging with determinations from the charged mode and the  $B \rightarrow \omega\gamma$  decay yields the  
 4392 results given in Sec. 6.3.3.

4393 Direct and isospin CP asymmetries,  $A_{\text{CP}}$  and  $A_{\text{I}}$ , provide useful tests of the SM and  
 4394 the QCDF approach. In QCDF, direct CP asymmetries in  $B \rightarrow V\gamma$  decays are suppressed  
 4395 by at least one power of  $\alpha_s$  and isospin asymmetries by at least one power of  $\Lambda_{\text{QCD}}/m_b$ ,  
 4396 so both of these are predicted to be small. We first consider  $B \rightarrow \rho\gamma$  decays. In that  
 4397 case the QCDF prediction for the direct CP asymmetry is about  $-10\%$  [695,696] and  
 4398 agrees well with the recent experimental results quoted in Sec. 6.3.2. The QCDF result  
 4399 for  $A_{\text{I}}$  depends strongly on  $\cos\alpha$ , but in the preferred range of  $\alpha$  near  $90^\circ$  is roughly  
 4400 between zero and  $-10\%$  [695,696]. Values closer to the central experimental value can be  
 4401 generated if one assumes a large contribution from non-perturbative charming penguins  
 4402 [697], which would be in contradiction with the power counting of QCDF. Given the large  
 4403 experimental errors it is not yet possible to draw a definite conclusion. For  $B \rightarrow K^*\gamma$   
 4404 decays, the direct CP asymmetries are strongly suppressed due to the CKM structure of  
 4405 the decay amplitude. The isospin asymmetry comes out to be  $(3 \pm 4)\%$  [558], which is  
 4406 compatible with predictions from QCDF [444,693–695]. This isospin asymmetry is very  
 4407 sensitive to the magnitude and sign of the ratio  $C_6/C_7$ .

4408 Finally, we consider indirect CP asymmetries. In the SM, these are suppressed by  
 4409 powers of  $m_{s,d}/m_b$  or arise from the presence of three-particle Fock states in the  $B$  and  $V$   
 4410 mesons, which are  $\Lambda_{\text{QCD}}/m_b$  corrections to the leading order factorization formula [698].  
 4411 A calculation performed in [444] indicates that the corrections from three-particle Fock  
 4412 states are much smaller than the generic size of a  $\Lambda_{\text{QCD}}/m_b$  power correction, so that the  
 4413 indirect CP asymmetries are estimated to be below the 3% level for all decay modes. The  
 4414 asymmetries could be much larger in extensions of the SM with altered chiral structure  
 4415 such as left-right symmetric models [444]. The current experimental results are within  
 4416 their large errors consistent with zero [699,700].

4417 A modified implementation of the heavy-quark expansion is provided by the pQCD  
 4418 approach [688–690]. The main difference compared to QCDF is that pQCD attempts  
 4419 to calculate the QCD form factors perturbatively. The assumptions required for such a  
 4420 treatment have been questioned in [701]. However, numerical results for most observ-  
 4421 ables are in rough agreement with those from QCDF. A recent comparison between the  
 4422 branching fractions, isospin and CP asymmetries obtained within the two theoretical  
 4423 setups can be found in [444].

### 4424 6.3.2. *Experimental results for exclusive $B \rightarrow V\gamma$ decays*

4425 The exclusive reconstruction of radiative  $B \rightarrow V\gamma$  decays or other multi-body decays  
 4426 such as  $B \rightarrow K\pi\gamma$  is usually straightforward. The dominant background originates from  
 4427 the continuum process  $e^+e^- \rightarrow q\bar{q}$ , which is experimentally suppressed by means of event  
 4428 shape variables.

4429 Vetoing high energetic photons from  $\pi^0$  or  $\eta$  is also useful. The background from  $B$   
 4430 decays is small in the low hadronic mass region, but becomes larger for higher hadronic  
 4431 mass, i.e., lower photon energy. Therefore, in the analysis of the exclusive final states  
 4432 with more than two particles, it is necessary to apply a cut on the hadronic mass, which  
 4433 is typically around 2 to 2.5 GeV. The contribution of the cross-feed from radiative  $B$

Table 42

Measured branching fractions of radiative  $B$  decays. Only modes with evidence are listed. The size of the data sets is given in the units of  $\text{fb}^{-1}$ .

Mode	Belle			BABAR		
	$\mathcal{B}$ ( $10^{-6}$ )	Data set	Ref.	$\mathcal{B}$ ( $10^{-6}$ )	Data set	Ref.
$B^0 \rightarrow K^{*0}\gamma$	$40.1 \pm 2.1 \pm 1.7$	78	[703]	$45.8 \pm 1.0 \pm 1.6$	347	[704]
$B^0 \rightarrow K^{*+}\gamma$	$42.5 \pm 3.1 \pm 2.4$	78	[703]	$47.3 \pm 1.5 \pm 1.7$	347	[704]
$B^+ \rightarrow K_1(1270)^+\gamma$	$43 \pm 9 \pm 9$	140	[705]	–	–	–
$B^0 \rightarrow K_2^*(1430)^0\gamma$	$13 \pm 5 \pm 1$	29	[706]	$12.2 \pm 2.5 \pm 1.0$	81	[707]
$B^+ \rightarrow K_2^*(1430)^+\gamma$	–	–	–	$14.5 \pm 4.0 \pm 1.5$	81	[707]
$B^+ \rightarrow K^+\eta\gamma$	$8.4 \pm 1.5 \begin{smallmatrix} +1.2 \\ -0.9 \end{smallmatrix}$	253	[708]	$7.7 \pm 1.0 \pm 0.4$	423	[709]
$B^0 \rightarrow K^0\eta\gamma$	$8.7 \begin{smallmatrix} +3.1 \\ -2.7 \end{smallmatrix} \begin{smallmatrix} +1.9 \\ -1.6 \end{smallmatrix}$	253	[708]	$7.1 \begin{smallmatrix} +2.1 \\ -2.0 \end{smallmatrix} \pm 0.4$	423	[709]
$B^+ \rightarrow K^+\eta'\gamma$	$3.2 \begin{smallmatrix} +1.2 \\ -1.1 \end{smallmatrix} \pm 0.3$	605	[710]	–	–	–
$B^+ \rightarrow K^+\phi\gamma$	$3.4 \pm 0.9 \pm 0.4$	90	[711]	$3.5 \pm 0.6 \pm 0.4$	211	[712]
$B^+ \rightarrow p\bar{A}\gamma$	$2.45 \begin{smallmatrix} +0.44 \\ -0.38 \end{smallmatrix} \pm 0.22$	414	[713]	–	–	–
$B^+ \rightarrow K^+\pi^-\pi^+\gamma$	$25.0 \pm 1.8 \pm 2.2$	140	[705]	$29.5 \pm 1.3 \pm 2.0$	211	[714]
$B^+ \rightarrow K^0\pi^+\pi^0\gamma$	–	–	–	$45.6 \pm 4.2 \pm 3.1$	211	[714]
$B^0 \rightarrow K^0\pi^+\pi^-\gamma$	$24.0 \pm 4.0 \pm 3.0$	140	[705]	$18.5 \pm 2.1 \pm 1.2$	211	[714]
$B^0 \rightarrow K^+\pi^-\pi^0\gamma$	–	–	–	$40.7 \pm 2.2 \pm 3.1$	211	[714]
$B_s^0 \rightarrow \phi\gamma$	$57 \begin{smallmatrix} +18 \\ -15 \end{smallmatrix} \begin{smallmatrix} +12 \\ -11 \end{smallmatrix}$	24	[715]	–	–	–
$B^+ \rightarrow \rho^+\gamma$	$0.87 \begin{smallmatrix} +0.29 \\ -0.27 \end{smallmatrix} \begin{smallmatrix} +0.09 \\ -0.11 \end{smallmatrix}$	605	[716]	$1.20 \begin{smallmatrix} +0.42 \\ -0.37 \end{smallmatrix} \pm 0.20$	423	[717]
$B^0 \rightarrow \rho^0\gamma$	$0.78 \begin{smallmatrix} +0.17 \\ -0.16 \end{smallmatrix} \begin{smallmatrix} +0.09 \\ -0.10 \end{smallmatrix}$	605	[716]	$0.97 \begin{smallmatrix} +0.24 \\ -0.22 \end{smallmatrix} \pm 0.06$	423	[717]
$B^0 \rightarrow \omega\gamma$	$0.40 \begin{smallmatrix} +0.19 \\ -0.17 \end{smallmatrix} \pm 0.13$	605	[716]	$0.50 \begin{smallmatrix} +0.27 \\ -0.23 \end{smallmatrix} \pm 0.09$	423	[717]

4434 decays to other final states also becomes a significant background in some modes.

4435 The first observation of radiative  $B$  decays has been established in 1993 by CLEO [702]  
4436 by a measurement of the  $B \rightarrow K^*\gamma$  mode. They found 13 events in the signal region  
4437 in a data sample of  $1.4 \text{ fb}^{-1}$ , and measured the branching fraction  $\mathcal{B}(B \rightarrow K^*\gamma) =$   
4438  $(45 \pm 15_{\text{stat}} \pm 3_{\text{syst}}) \times 10^{-6}$ . Now, the measurements by *BABAR* and Belle are based on  
4439 data set that are more than 100 times larger and start to be dominated by systematics, as  
4440 can be seen from Tab. 42. Unfortunately, it is not easy to predict the branching fractions  
4441 of exclusive modes precisely, and hence it is difficult to compare the results with theory.

What can be predicted more precisely are the direct CP or charge asymmetry  $A_{\text{CP}}$  and the isospin asymmetry  $A_{\text{I}}$ . They are defined as

$$A_{\text{CP}} = \frac{\Gamma(\bar{B} \rightarrow \bar{K}^*\gamma) - \Gamma(B \rightarrow K^*\gamma)}{\Gamma(\bar{B} \rightarrow \bar{K}^*\gamma) + \Gamma(B \rightarrow K^*\gamma)}, \quad (287)$$

$$A_{\text{I}} = \frac{\Gamma(B^0 \rightarrow K^{*0}\gamma) - \Gamma(B^+ \rightarrow K^{*+}\gamma)}{\Gamma(B^0 \rightarrow K^{*0}\gamma) + \Gamma(B^+ \rightarrow K^{*+}\gamma)},$$

4442 and similarly for the other decay modes. In the case of  $B \rightarrow K^*\gamma$ , *BABAR* obtained  $A_{\text{CP}} =$   
4443  $-0.009 \pm 0.017_{\text{stat}} \pm 0.011_{\text{syst}}$  and  $A_{\text{I}} = 0.029 \pm 0.019_{\text{stat}} \pm 0.016_{\text{syst}} \pm 0.018_{\text{prod}}$  [704] while  
4444 the results of Belle read  $A_{\text{CP}} = -0.015 \pm 0.044_{\text{stat}} \pm 0.012_{\text{syst}}$  and  $A_{\text{I}} = 0.034 \pm 0.044_{\text{stat}} \pm$

4445  $0.026_{\text{syst}} \pm 0.025_{\text{prod}}$  [703]. The last errors in  $A_I$  arise from the production ratio of  $B^0$   
4446 and  $B^+$  for which *BABAR* and Belle assume the values  $1.044 \pm 0.050$  and  $1.020 \pm 0.034$ ,  
4447 respectively. The direct CP asymmetry has also been measured in the  $B \rightarrow \rho\gamma$  system by  
4448 Belle which finds  $A_{\text{CP}} = -0.11 \pm 0.32_{\text{stat}} \pm 0.09_{\text{syst}}$  [716]. The corresponding experimental  
4449 results for the isospin asymmetry read  $A_I = -0.43^{+0.25}_{-0.22_{\text{stat}}} \pm 0.10_{\text{syst}}$  from *BABAR* [717]  
4450 and  $A_I = -0.48^{+0.21}_{-0.19_{\text{stat}}} \pm 0.08_{-0.09_{\text{syst}}}$  from Belle [716]. Within errors, the measured values of  
4451  $A_{\text{CP}}$  and  $A_I$  are consistent with the SM predictions discussed in Sec. 6.3.1.

4452 Another important variable is the time-dependent CP asymmetry. In the SM, the  
4453 photon from the  $b \rightarrow s\gamma$  process is almost polarized. Photons from  $B^0$  are right-handed,  
4454 while photons from  $\bar{B}^0$  are left-handed. So if the photon is completely polarized,  $B^0$  and  
4455  $\bar{B}^0$  cannot decay into a common final state, and mixing-induced CP violation does not  
4456 happen. Indeed, the time-dependent CP violation (tCPV) in radiative  $B$  decays  $B \rightarrow$   
4457  $f_{\text{CP}}\gamma$ , where  $f_{\text{CP}}$  denotes a CP eigenstate, is expected to be within a few percent even  
4458 when we consider the possible enhancement due to the strong interaction. Therefore, the  
4459 measurement of tCPV for  $b \rightarrow s\gamma$  is a probe of the photon polarization, and large values  
4460 of tCPV would be a signal of the presence of non-standard right-handed interactions.

4461 The final state in  $K^{*0} \rightarrow K_s^0\pi^0$  is a CP eigenstate, but it is not essential whether  
4462 the decay goes through  $K^{*0}$  or not. Actually, final states can be any of the type  $P_1P_2\gamma$ ,  
4463 where  $P_1$  and  $P_2$  are pseudoscalar mesons [718]. In consequence, the measurements have  
4464 been performed not only for  $B \rightarrow K^{*0}\gamma \rightarrow K_s^0\pi^0\gamma$  but also for the non-resonant mode  
4465  $B \rightarrow K_s^0\pi^0\gamma$ . In Tab. 43 we list the measured  $S$  terms of the various tCPV. Since the  
4466 final state  $K_s^0\pi^0\gamma$  does not include charged tracks that come from the  $B$  vertex, the  $B$   
4467 decay vertex has to be calculated using the  $K_s^0$  trajectory, which causes lower efficiency.  
4468 Although the error is still large, the result is consistent with vanishing CP asymmetry.

4469 Many other exclusive final states have also been found by *BABAR* and Belle. Tab. 42  
4470 shows the decays with experimental evidence and their branching fractions. Radiative  
4471 decays through kaonic resonances are observed for  $B \rightarrow K_2^*(1430)\gamma$  and  $B \rightarrow K_1(1270)\gamma$ ,  
4472 in addition to  $B \rightarrow K^*\gamma$ . The other listed modes are three- or four-body decays. Mea-  
4473 surements of these branching ratios provide a better understanding of the composition  
4474 of  $b \rightarrow s\gamma$  final states, and potentially reduce the systematic errors due to hadronization  
4475 in the inclusive analysis with the sum of exclusive method. Some exclusive modes can  
4476 also be used to study the tCPV. As shown in Tab. 43, *BABAR* has performed the first  
4477 measurement of tCPV for  $B^0 \rightarrow K_s^0\eta\gamma$ , while Belle has reported the first evidence of  
4478  $B^+ \rightarrow K^+\eta'\gamma$ , whose neutral mode is also usable for an tCPV analysis.

4479 Belle has recently reported the measurement of tCPV in  $B^0 \rightarrow K_s^0\rho^0\gamma \rightarrow K_s^0\pi^+\pi^-\gamma$  [719].  
4480 The advantage of this mode is that the  $B$  decay vertex can be determined from two  
4481 charged pions. On the other hand, there exists a contamination from other decays with  
4482 the same final state such as  $B^0 \rightarrow K^{*+}\pi^-\gamma$ . Since  $K_1(1270)$  and  $K^*(1680)$  have signifi-  
4483 cant branching fractions to  $K\rho$ , it is necessary to estimate the fraction of  $B \rightarrow K_1(1270)\gamma$   
4484 and  $B \rightarrow K^*(1680)\gamma$  in the entire  $B \rightarrow K\pi\pi\gamma$  decay. Belle uses the charged mode  $B^+ \rightarrow$   
4485  $K^+\pi^+\pi^-\gamma$  in order to disentangle the composition, and, assuming the isospin relation,  
4486 estimates the dilution factor to the effective  $S$  in the  $\rho^0$  mass window. The result listed  
4487 in Tab. 43 shows that the size of the error is competitive to those for  $B^0 \rightarrow K^{*0}\gamma$ .

Radiative decays of the  $B_s$  meson have been studied by Belle using the data taken at  
the  $\Upsilon(5S)$  center-of-mass energy, and the decay  $B_s \rightarrow \phi\gamma$  has been observed as shown  
in Tab. 42. LHCb is expected to perform the study of the time-dependent asymmetry of

Table 43

Measurements of tCPV of radiative  $B$  decays. Only the  $S$  terms are shown. The size of the data sets is given in units of  $\text{fb}^{-1}$ .

Mode	Belle			BABAR		
	$S$	Data set	Ref.	$S$	Data set	Ref.
$B^0 \rightarrow K^{*0}\gamma$	$-0.32^{+0.36}_{-0.33} \pm 0.05$	492	[699]	$-0.03 \pm 0.29 \pm 0.03$	423	[700]
$B^0 \rightarrow K_S^0\pi^0\gamma^\dagger$	$-0.10 \pm 0.31 \pm 0.07$	492	[699]	-	-	-
$B^0 \rightarrow K_S^0\pi^0\gamma^\ddagger$	-	-	-	$-0.78 \pm 0.59 \pm 0.09$	423	[700]
$B^0 \rightarrow K_S^0\eta\gamma$	-	-	-	$-0.18^{+0.49}_{-0.46} \pm 0.12$	423	[709]
$B^0 \rightarrow K_S^0\rho^0\gamma$	$0.11 \pm 0.33^{+0.05}_{-0.09}$	605	[719]	-	-	-

$\dagger M_{K\pi} < 1.8 \text{ GeV}$      $\ddagger 1.1 \text{ GeV} < M_{K\pi} < 1.8 \text{ GeV}$

this mode [720]. With respect to the  $B_d$  system, there is an additional observable  $A^\Delta$  in the formula of the asymmetry:

$$A_{\text{CP}}(t) = \frac{S \sin(\Delta m_s t) - C \cos(\Delta m_s t)}{\cosh(\Delta\Gamma_s t/2) - A^\Delta \sinh(\Delta\Gamma_s/2)}. \quad (288)$$

4488 The extra contribution  $A^\Delta$  parametrizes the fraction of wrongly polarized photons, and is  
 4489 sensitive to NP as well as the  $S$  term. According to the MC simulation, LHC***b*** is expected  
 4490 to reach sensitivities of  $\sigma(A^\Delta) \sim 0.22$  and  $\sigma(S) \sim 0.11$  for  $2 \text{ fb}^{-1}$ , which demonstrates  
 4491 that the prospects for a measurement of the photon polarization at LHC***b*** are promising.

### 4492 6.3.3. Determinations of $|V_{td}/V_{ts}|$ from $b \rightarrow (s, d)\gamma$

4493 Since the  $b \rightarrow d\gamma$  process is suppressed by a factor of  $|V_{td}/V_{ts}|$  compared to  $b \rightarrow s\gamma$ ,  
 4494 its branching fraction is useful to extract the ratio  $|V_{td}/V_{ts}|$  by means of (286). The  
 4495 exclusive modes to be studied in the case of  $b \rightarrow d\gamma$  are  $B \rightarrow (\rho, \omega)\gamma$ . Due to their small  
 4496 branching fractions, the continuum background suppression is a key issue in the analysis.  
 4497 In addition, the good particle identification of the BABAR and Belle detectors is essential  
 4498 to separate  $B \rightarrow \rho\gamma$  from  $B \rightarrow K^*\gamma$ . Both BABAR and Belle have observed clear signals  
 4499 of these modes. The current values of the branching fractions are given in Tab. 42.

4500 The input value for the extraction of  $|V_{td}/V_{ts}|$  is the branching ratio of  $B \rightarrow (\rho, \omega)\gamma$   
 4501 and  $B \rightarrow K^*\gamma$ . One can perform a simultaneous fit to  $B \rightarrow (\rho, \omega)\gamma$  and  $B \rightarrow K^*\gamma$   
 4502 or calculate the ratio from the individual fits to  $B \rightarrow (\rho, \omega)\gamma$  and  $B \rightarrow K^*\gamma$ , so as to  
 4503 cancel common systematic errors. In order to obtain the combined branching fraction  
 4504 of  $B \rightarrow (\rho, \omega)\gamma$ , one assumes the isospin relation  $\mathcal{B}(B \rightarrow (\rho, \omega)\gamma) = \mathcal{B}(B^+ \rightarrow \rho^+\gamma) =$   
 4505  $2(\tau_{B^+}/\tau_{B^0})\mathcal{B}(B^0 \rightarrow \rho^0\gamma) = 2(\tau_{B^+}/\tau_{B^0})\mathcal{B}(B^0 \rightarrow \omega\gamma)$ . From the combined branching  
 4506 fraction of  $B \rightarrow \rho^+\gamma$ ,  $B \rightarrow \rho^0\gamma$ , and  $B \rightarrow \omega\gamma$ , BABAR and Belle have extracted the  
 4507 values  $0.039 \pm 0.008$  and  $0.0284 \pm 0.0050_{\text{stat}}^{+0.0027}_{-0.0029_{\text{syst}}}$  for  $\mathcal{B}(B \rightarrow (\rho, \omega)\gamma)/\mathcal{B}(B \rightarrow K^*\gamma)$ ,  
 4508 respectively. These measurements translate into  $|V_{td}/V_{ts}| = 0.233^{+0.025}_{-0.024_{\text{expr}}} \pm 0.021_{\text{theo}}$   
 4509 for BABAR [717] and  $0.195^{+0.020}_{-0.019_{\text{expr}}} \pm 0.015_{\text{theo}}$  for Belle [716], where the first (second)  
 4510 error in  $|V_{td}/V_{ts}|$  is of experimental (theoretical) nature. The values extracted from the  
 4511 individual decay modes can also be found in the latter references.

4512 Future precise measurements of  $B \rightarrow X_d\gamma$  also provide a promising way to deter-  
 4513 mine the ratio  $|V_{td}/V_{ts}|$ . Using the value of  $\mathcal{B}(B \rightarrow X_d\gamma)$  as given in Sec. 6.2.2 leads to  
 4514  $|V_{td}/V_{ts}| = 0.177 \pm 0.043_{\text{expr}} \pm 0.001_{\text{theo}}$  [660]. Although the given theory error is likely

4515 to be underestimated, as it does not take into account an uncertainty due to the exper-  
 4516 imental cut on  $M_{X_d}$ , the quoted numbers make clear that determinations of  $|V_{td}/V_{ts}|$   
 4517 from  $B \rightarrow X_d \gamma$  are at the moment essentially only limited by experiment.

4518 So far, the central values of  $|V_{td}/V_{ts}|$  extracted from  $b \rightarrow (s, d) \gamma$  are compatible with  
 4519 the ones following from  $B_{d,s}$  mixing [218], although both the experimental and theo-  
 4520 retical uncertainties are significantly larger in the former case. While thus not suitable  
 4521 for a precise determination of  $|V_{td}/V_{ts}|$ , the  $b \rightarrow (s, d) \gamma$  results are complementary to  
 4522 those from neutral meson mixing, since they could be affected differently by NP. It is  
 4523 therefore worthwhile to try to improve the measurements of  $b \rightarrow (s, d) \gamma$  with one order  
 4524 of magnitude larger luminosities.

## 4525 6.4. Purely leptonic rare decays

### 4526 6.4.1. Theory of purely leptonic rare decays

The charged-current processes  $P \rightarrow \ell \nu$  are the simplest flavor-violating helicity sup-  
 pressed observables. Both in the SM and models of NP with an extended Higgs sector these  
 modes appear already at the tree level. The charged Higgs contribution is proportional  
 to the Yukawa couplings of quarks and leptons, but it can compete with the contribution  
 arising from  $W^\pm$ -boson exchange due to the helicity suppression of  $P \rightarrow \ell \nu$  [145]. Taking  
 into account the resummation of the leading  $\tan \beta = v_u/v_d$  corrections to all orders, the  
 $H^\pm$  contributions to the  $P \rightarrow \ell \nu$  amplitude within a MFV supersymmetric framework  
 leads to the following ratio [146, 397]

$$R_{P\ell\nu} = \frac{\mathcal{B}^{\text{SM}}(P \rightarrow \ell\nu)}{\mathcal{B}^{\text{SUSY}}(P \rightarrow \ell\nu)} = \left[ 1 - \left( \frac{m_P^2}{m_{H^\pm}^2} \right) \frac{\tan^2 \beta}{1 + \epsilon_0 \tan \beta} \right]^2, \quad (289)$$

4527 where  $\epsilon_0$  denotes the effective coupling which parametrizes the non-holomorphic correc-  
 4528 tions to the down-type Yukawa interaction. One typically has  $\epsilon_0 \sim 10^{-2}$ . For a natural  
 4529 choice of the MSSM parameters, the relation (289) implies a suppression with respect to  
 4530 the SM in the  $B \rightarrow \tau \nu$  decay of  $\mathcal{O}(10\%)$ , but an enhancement is also possible for very  
 4531 light  $M_{H^\pm}$ .

4532 Performing a global fit of the unitarity triangle, one obtains the following SM prediction  
 4533  $\mathcal{B}(B \rightarrow \tau \nu)_{\text{SM}} = (0.87 \pm 0.19) \times 10^{-4}$ . The major part of the total error stems from the  
 4534 uncertainty due to the  $B$ -meson decay constant  $f_B$ . The latter prediction is  $1.7\sigma$  below the  
 4535 current world average  $\mathcal{B}(B \rightarrow \tau \nu)_{\text{exp}} = (1.51 \pm 0.33) \times 10^{-4}$ . At the moment systematic  
 4536 errors in the lattice determinations of  $f_B$  in conjunction with the limited experimental  
 4537 statistics however do not allow to draw a clear-cut conclusion about the presence of  
 4538 beyond the SM physics in  $B \rightarrow \tau \nu$ .

4539 The expression for  $R_{K\mu\nu}$  is obtained from (289) by replacing  $m_B^2$  with  $m_K^2$ . Although  
 4540 the charged Higgs contributions are now suppressed by a factor  $m_K^2/m_B^2 \sim 1/100$ ,  $K \rightarrow$   
 4541  $\ell \nu$  is competitive with  $B \rightarrow \tau \nu$  due to the excellent experimental resolution [344] and  
 4542 the good theoretical control of the former. The best strategy to fully exploit the NP  
 4543 sensitivity of the  $K_{l2}$  system is to consider the observable  $R_{K\mu\nu}/R_{\pi\mu\nu}$  [146, 344] that  
 4544 is proportional to  $(f_K/f_\pi)^2$ . Once a well established unquenched lattice calculations of  
 4545  $f_K/f_\pi$  will be available,  $R_{K\mu\nu}/R_{\pi\mu\nu}$  will play a relevant role in both constraining and  
 4546 probing scenarios with an extended Higgs sector.

4547 The SM prediction for the  $B_s \rightarrow \mu^+\mu^-$  branching fraction is  $\mathcal{B}(B_s \rightarrow \mu^+\mu^-)_{\text{SM}} =$   
4548  $(3.37 \pm 0.31) \times 10^{-9}$  [721] while the current 95% CL upper bound from CDF reads  
4549  $\mathcal{B}(B_s \rightarrow \mu^+\mu^-)_{\text{exp}} < 5.8 \times 10^{-8}$  [722], which still leaves room for enhancements of  
4550 the branching fraction relative to the SM of more than factor of 10. In particular, the  
4551 MSSM with large  $\tan\beta$  provides a natural framework where large departures from the  
4552 SM expectations of  $\mathcal{B}(B_s \rightarrow \mu^+\mu^-)$  are allowed [153].

The important role of  $\mathcal{B}(B_{s,d} \rightarrow \ell^+\ell^-)$  in the large  $\tan\beta$  regime of the MSSM has been widely discussed in the literature. The leading non-SM contribution to  $B \rightarrow \ell^+\ell^-$  decays is generated by a single tree-level amplitude, i.e., the neutral Higgs exchange  $B \rightarrow A^0, H^0 \rightarrow \ell^+\ell^-$ . Since the effective FCNC coupling of the neutral Higgs bosons appears only at the quantum level, in this case the amplitude has a strong dependence on other MSSM parameters of the soft sector in addition to  $M_{A^0} \sim M_{H^0}$  and  $\tan\beta$ . In particular, a key role is played by the  $\mu$  term and the up-type trilinear soft-breaking term,  $A_U$ , which control the strength of the non-holomorphic terms. The leading parametric dependence of the scalar FCNC amplitude from these parameters is given by

$$\mathcal{A}(B_s \rightarrow \mu^+\mu^-) \propto \frac{m_b m_\mu}{M_{A^0}^2} \frac{\mu A_U}{M_{\tilde{q}}^2} \tan^3 \beta m_b (\bar{b}_{RS_L})(\bar{\mu}_L \mu_R). \quad (290)$$

More quantitatively, the pure SUSY contributions can be summarized by the approximate formula

$$\mathcal{B}(B_s \rightarrow \mu^+\mu^-) \simeq \frac{5 \times 10^{-8}}{\left(1 + 0.5 \frac{\tan\beta}{50}\right)^4} \left(\frac{\tan\beta}{50}\right)^6 \left(\frac{500\text{GeV}}{M_{A^0}}\right)^4 \left(\frac{\epsilon_Y}{3 \times 10^{-3}}\right)^2, \quad (291)$$

4553 where  $\epsilon_Y \sim 3 \times 10^{-3}$  holds in the limit of all the SUSY masses and  $A_U$  equal. The  
4554 approximation (291) shows that  $\mathcal{B}(B_s \rightarrow \mu^+\mu^-)$  already poses interesting constraints on  
4555 the MSSM parameter space, especially for light  $M_{A^0}$  and large values of  $\tan\beta$ . However,  
4556 given the specific dependence on  $\mu$  and  $A_U$ , the present  $\mathcal{B}(B_s \rightarrow \mu^+\mu^-)$  bound does not  
4557 exclude the large  $\tan\beta$  effects in  $P \rightarrow \ell\nu$  already discussed.

#### 4558 6.4.2. Experimental results on purely leptonic rare decays

4559 To measure the branching fraction for  $B \rightarrow \tau\nu$  is a big challenge as there are at  
4560 least three neutrinos in the final state. To get a sufficiently pure signal sample the recoil  
4561 technique discussed in Sec. 3.2.6 is used. On the tagging side a semi-leptonic or a fully  
4562 reconstructed hadronic state is required, and on the signal side the visible particles from  
4563 the  $\tau$  decay. On top of this the most powerful discriminating variable is excess energy in  
4564 the calorimeter.

4565 The first Belle analysis used fully hadronic tag decays and had a  $3.5\sigma$  signal with  
4566  $449 \times 10^6 B\bar{B}$  pairs [723]. BABAR used both hadronic and semileptonic tag decays and  
4567 had a  $2.6\sigma$  signal with  $383 \times 10^6 B\bar{B}$  pairs [724, 725]. The latest Belle analysis uses  
4568 semileptonic tag decays with one prong  $\tau$  decays and  $657 \times 10^6 B\bar{B}$  pairs. In this sample  
4569 they find 154 signal events with a significance of  $3.8\sigma$ . This results in a branching fraction  
4570 of  $(1.65_{-0.37}^{+0.38} \text{stat} \text{ } ^{+0.35}_{-0.37} \text{syst}) \times 10^{-4}$ . All the results are summarized in Tab. 44. Searches have  
4571 also been made for the decay  $B^+ \rightarrow \mu^+\nu_\mu$  where BABAR has set a 90% CL upper limit  
4572 of  $1.3 \times 10^{-6}$  [726] and Belle at  $1.7 \times 10^{-6}$  [727].

Table 44

Summary of the  $B \rightarrow \tau\nu_\tau$  measurements.

Experiment	Tagging method	Data set	Significance	$\mathcal{B}(10^{-4})$	Ref.
Belle	Hadronic	449M	$3.5\sigma$	$1.79_{-0.49-0.51}^{+0.56+0.46}$	[723]
BABAR	Semileptonic	383M	-	$0.9 \pm 0.6 \pm 0.1$	[724]
BABAR	Hadronic	383M	$2.2\sigma$	$1.8_{-0.8}^{+0.9} \pm 0.4$	[725]
Belle	Semileptonic	657M	$3.8\sigma$	$1.65_{-0.37-0.37}^{+0.38+0.35}$	[728]
Average				$1.51 \pm 0.33$	

4573 Searches for  $B_s \rightarrow \mu^+\mu^-$  are only carried out at hadron machines, whereas  $B_d \rightarrow \mu^+\mu^-$   
4574 is being searched for at the  $B$ -factories as well, even if the measurements are no longer  
4575 competitive with the Tevatron results. CDF and D0 build multivariate discriminants that  
4576 combine muon identification with kinematics and lifetime information. This keeps signal  
4577 efficiency high while rejecting  $\mathcal{O}(10^6)$  larger backgrounds including Drell-Yan continuum,  
4578 sequential  $b \rightarrow c \rightarrow s$  decays,  $b\bar{b} \rightarrow \mu^+\mu^- + X$  decays, and hadrons faking muons.  
4579 Background estimates are checked in multiple control regions, and then the signal-like  
4580 region of the discriminant output is inspected for excess of events clustering at the  $B$   
4581 mass. The overlap between  $B_s$  and  $B_d$  search regions, due to limited mass resolution, is  
4582 smaller at CDF allowing independent results on each mode. There is no evidence of a  
4583 signal and the best limit at 90% CL is  $\mathcal{B}(B_s \rightarrow \mu^+\mu^-) < 4.7 \times 10^{-8}$  [722].

4584 In the near future it is expected that both CDF and D0 will reach a limit of  $\mathcal{B}(B_s \rightarrow$   
4585  $\mu^+\mu^-)$  at  $2 \times 10^{-8}$  with  $8 \text{ fb}^{-1}$  of data. This is just a factor six above the SM expectation  
4586 and will set serious constraints on NP as outlined in the previous section. Assuming no  
4587 signal, LHCb will be able to exclude  $\mathcal{B}(B_s \rightarrow \mu^+\mu^-)$  to be above the SM level with just  
4588  $2 \text{ fb}^{-1}$  of data corresponding to one nominal year of data taking. A  $5\sigma$  discovery at the  
4589 SM level will require several years of data taking and all three LHC experiments are  
4590 competitive for this [729, 730].

4591 Other rare leptonic decay modes have been searched for including rare  $D^0$  decays and  
4592 the LFV decay  $B \rightarrow e\mu$ . All of these results are summarized in Tab. 45.

## 4593 6.5. Semileptonic modes

### 4594 6.5.1. $B \rightarrow D\tau\nu$ modes

4595 In the framework of the 2HDM-II, charged Higgs boson exchange contributes sig-  
4596 nificantly not only to  $B \rightarrow \tau\nu$  but also to  $B \rightarrow D\tau\nu$  decays already at tree level, if  
4597  $\tan\beta = \mathcal{O}(50)$ . Due to the recent data accumulated at the  $B$  factories, these channels  
4598 become a standard tool to constrain the effective coupling  $g_S$  of a charged Higgs boson  
4599 to right-handed down-type fermions [735–737].

4600 While  $\mathcal{B}(B \rightarrow \tau\nu)$  is more sensitive to charged-Higgs effects than  $\mathcal{B}(B \rightarrow D\tau\nu)$ , the  
4601 latter branching fraction has a much smaller theoretical uncertainty. The prediction for  
4602  $\mathcal{B}(B \rightarrow \tau\nu)$  involves the  $B$ -meson decay constant  $f_B$ , which is obtained from lattice  
4603 calculations, and the CKM element  $|V_{ub}|$ , both suffering from large errors,  $\delta(|V_{ub}|f_B) \sim$   
4604  $20\%$ . In contrast, the vector and scalar form factors  $F_V$  and  $F_S$  in  $B \rightarrow D\tau\nu$  are well  
4605 under control,  $\delta(|V_{cb}|F_V) < 4\%$  and  $\delta(|V_{cb}|F_S) < 7\%$ . First,  $|V_{cb}|F_V(q^2)$  is extracted from  
4606 the measured  $q^2$  spectrum in  $B \rightarrow D\ell\nu$  [558]. Second,  $F_S(q^2)$  is constrained by  $F_V$  at



Table 45

An overview of the limits set on the decays of the type  $B \rightarrow \ell^+ \ell^-$ .

Experiment	Decay	Data set	90% CL Limit ( $\times 10^8$ )	Ref.
D0	$B_s \rightarrow \mu^+ \mu^-$	$1.3 \text{ fb}^{-1}$	9.4	[731]
CDF	$B_s \rightarrow \mu^+ \mu^-$	$2.0 \text{ fb}^{-1}$	4.7	[722]
CDF	$B_s \rightarrow e^\pm \mu^\mp$	$2.0 \text{ fb}^{-1}$	20	[732]
CDF	$B_s \rightarrow e^+ e^-$	$2.0 \text{ fb}^{-1}$	28	[732]
CDF	$B_d \rightarrow \mu^+ \mu^-$	$2.0 \text{ fb}^{-1}$	1.5	[722]
CDF	$B_d \rightarrow e^\pm \mu^\mp$	$2.0 \text{ fb}^{-1}$	6.4	[732]
CDF	$B_d \rightarrow e^+ e^-$	$2.0 \text{ fb}^{-1}$	8.3	[732]
BABAR	$B_d \rightarrow \mu^+ \mu^-$	384M	11.3	[733]
BABAR	$B_d \rightarrow e^+ e^-$	384M	5.2	[733]
BABAR	$B_d \rightarrow e^\pm \mu^\mp$	384M	9.2	[733]
Belle	$B_d \rightarrow \mu^+ \mu^-$	85M	16	[734]
Belle	$B_d \rightarrow e^+ e^-$	85M	19	[734]
Belle	$B_d \rightarrow e^\pm \mu^\mp$	85M	17	[734]

4607  $q^2 = (p_B - p_D)^2 = 0$  and by heavy-quark symmetry at maximal  $q^2$ . Since two parameters  
4608 are sufficient to describe the  $B \rightarrow D$  form factors,  $F_S(q^2)$  is thus fixed [735, 738]. Thanks  
4609 to this good precision, present data on  $\mathcal{B}(B \rightarrow D\tau\nu)$  can almost completely exclude the  
4610 window around  $g_S = 2$  left by  $\mathcal{B}(B \rightarrow \tau\nu)$  at 95% CL [738].

4611 Since charged-Higgs effects exhibit a  $q^2$  dependence distinct from longitudinal  $W^\pm$ -  
4612 boson exchange, the differential distribution  $d\Gamma(B \rightarrow D\tau\nu)/dq^2$  is more sensitive than the  
4613 branching ratio  $\mathcal{B}(B \rightarrow D\tau\nu)$  [739]. Notice that in the differential distribution charged-  
4614 Higgs effects can be detected not only from the normalization of the decay mode, but  
4615 also from the shape of the spectrum.

4616 To further increase the sensitivity to charged Higgs boson exchange, one can include  
4617 information on the polarization of the  $\tau$  lepton. Though the latter is not directly accessible  
4618 at the  $B$  factories, in the decay chain  $B \rightarrow D\nu[\tau \rightarrow \pi\nu]$  the  $\tau$  spin is directly correlated  
4619 with the direction of the pion in the final state. To combine this correlation with the  
4620 sensitivity from the  $q^2$  distribution, an unbinned fit to the triple-differential distribution  
4621  $d\Gamma(B \rightarrow D\bar{\nu}[\tau^- \rightarrow \pi^-\bar{\nu}])/(dE_D dE_\pi d\cos\theta_{D\pi})$  should be performed [735]. Here  $E_D$ ,  $E_\pi$ ,  
4622 denote the energies of the mesons and  $\theta_{D\pi}$  is the angle between  $D$  and  $\pi^-$  in the  $B$  rest  
4623 frame. The exploration of both differential distributions in a comprehensive experimental  
4624 analysis makes the  $B \rightarrow D\tau\nu$  mode particularly well-suited to detect charged-Higgs  
4625 effects and to distinguish them from other possible NP contributions.

## 4626 6.6. Semileptonic neutral currents decays

### 4627 6.6.1. Theory of inclusive $B \rightarrow X_s \ell^+ \ell^-$

The study of  $b \rightarrow s \ell^+ \ell^-$  transitions can yield useful complementary information, when  
confronted with the less rare  $b \rightarrow s \gamma$  decays, in testing the flavor sector of the SM. In par-  
ticular, a precise measurement of the inclusive  $B \rightarrow X_s \ell^+ \ell^-$  decay distributions would be

welcome in view of NP searches, because they are amenable to clean theoretical descriptions for dilepton invariant masses in the ranges  $q^2 \in [1, 6] \text{ GeV}^2$  and  $q^2 > 14.4 \text{ GeV}^2$ . The inclusive  $B \rightarrow X_s \ell^+ \ell^-$  rate can be written as follows

$$\frac{d^2\Gamma}{dq^2 d\cos\theta_l} = \frac{3}{8} [(1 + \cos^2\theta_l) H_T(q^2) + 2 \cos\theta_l H_A(q^2) + 2(1 - \cos^2\theta_l) H_L(q^2)], \quad (292)$$

where  $q^2 = (p_\ell^+ + p_\ell^-)^2$  and  $\theta_l$  is the angle between the negatively charged lepton and the  $\bar{B}$  meson in the center-of-mass frame of the lepton pair. At leading order and up to an overall  $(m_b^2 - q^2)^2$  factor one has

$$\begin{aligned} H_T(q^2) &\propto 2q^2 \left[ \left( C_9 + 2C_7 \frac{m_b^2}{q^2} \right)^2 + C_{10}^2 \right], \\ H_A(q^2) &\propto -4q^2 C_{10} \left( C_9 + 2C_7 \frac{m_b^2}{q^2} \right), \\ H_L(q^2) &\propto [(C_9 + 2C_7)^2 + C_{10}^2]. \end{aligned}$$

4628 The coefficients  $H_i(q^2)$  are three independent functions of the Wilson coefficients of the  
 4629 effective Hamiltonian (281). Hence separate measurements of these three quantities  
 4630 lead to better constraints on the coefficients  $C_7$ ,  $C_9$ , and  $C_{10}$ . In terms of the functions  
 4631  $H_i(q^2)$  the total rate and the forward-backward asymmetry (FBA) are given by  $d\Gamma/dq^2 =$   
 4632  $H_T(q^2) + H_L(q^2)$  and  $dA_{\text{FB}}/dq^2 = 3/4 H_A(q^2)$ . The double differential rate (292) is known  
 4633 at NNLO in QCD [24, 27, 740–747] and at NLO in QED [746, 748, 749]. In addition non-  
 4634 perturbative corrections scaling as  $A_{\text{QCD}}^2/m_b^2$ ,  $A_{\text{QCD}}^3/m_b^3$ , or  $A_{\text{QCD}}^2/m_c^2$  [750–756] have  
 4635 been calculated.

4636 A comment on QED corrections is necessary. After inclusion of the NLO QED ma-  
 4637 trix elements, the electron and muon channels receive contributions proportional to  
 4638  $\ln(m_b^2/m_\ell^2)$ . These results correspond to the process  $B \rightarrow X_s \ell^+ \ell^-$  in which QED ra-  
 4639 diation is included in the  $X_s$  system and the dilepton invariant mass does not contain  
 4640 any photon. In the BABAR and Belle experiments the inclusive decay is measured as a  
 4641 sum over exclusive states. As a consequence the log-enhanced QED corrections are not  
 4642 directly applicable to the present experimental results and have to be modified [757]. We  
 4643 also add that potentially large corrections to  $R_K = \Gamma(B \rightarrow X_s \mu^+ \mu^-)_{q^2 \in [q_0^2, q_1^2]} / \Gamma(B \rightarrow$   
 4644  $X_s e^+ e^-)_{q^2 \in [q_0^2, q_1^2]}$ , which in the SM is to an excellent approximation equal to 1, can arise  
 4645 from collinear photon emission. Since the actual net effect of these corrections depends  
 4646 on the experimental cuts, an good understanding of this issue is crucial to put reliable  
 4647 bounds on possible NP effects from a measurement of  $R_K$ .

4648 Cuts on the dilepton and hadronic invariant masses are necessary to reject backgrounds  
 4649 from resonant charmonium production,  $B \rightarrow X_s \psi(c\bar{c}) \rightarrow X_s \ell^+ \ell^-$ , and double semilep-  
 4650 tonic decays,  $B \rightarrow X_c \ell^- \bar{\nu} \rightarrow X_s \ell^+ \ell^- \nu \bar{\nu}$ , respectively. The first cut, in particular, forces  
 4651 us to consider separately the low- and high- $q^2$  regions corresponding to dilepton invari-  
 4652 ant masses of  $q^2 \in [1, 6] \text{ GeV}^2$  and  $q^2 > 14.4 \text{ GeV}^2$ , respectively. In the low- $q^2$  region  
 4653 the OPE is well behaved and power corrections are small, but the effect of the  $M_{X_s}$  cut  
 4654 is quite important. The present experimental analyses correct for this effect utilizing a  
 4655 Fermi motion model [758]. In the high- $q^2$  region  $M_{X_s}$  cuts are irrelevant but the OPE

4656 itself breaks down, resulting in large  $\Lambda_{\text{QCD}}/m_b$  power corrections. Both these problems  
 4657 can be addressed as discussed at the very end of this subsection.

The most up-to-date SM predictions in the case of muons in the final state read

$$\begin{aligned}
 \mathcal{B}_{q^2 \in [1,6] \text{ GeV}^2} &= (1.59 \pm 0.11) \times 10^{-6}, \\
 \mathcal{B}_{q^2 > 14 \text{ GeV}^2} &= (2.42 \pm 0.66) \times 10^{-7}, \\
 q_0^2 &= (3.50 \pm 0.12) \text{ GeV}^2, \\
 \bar{\mathcal{A}}_{q^2 \in [1,3.5] \text{ GeV}^2} &= (-9.09 \pm 0.91)\%, \\
 \bar{\mathcal{A}}_{q^2 \in [3.5,6] \text{ GeV}^2} &= (7.80 \pm 0.76)\%,
 \end{aligned} \tag{293}$$

4658 where  $q_0^2$  denotes the location of the zero in the FBA spectrum and  $\bar{\mathcal{A}}_{\text{bin}}$  are the integrated  
 4659 FBA in the  $q^2 \in [1, 3.5] \text{ GeV}^2$  and  $q^2 \in [3.5, 6] \text{ GeV}^2$  bins. We emphasize that the quoted  
 4660 errors do not take into account uncertainties related to the presence of enhanced local  
 4661 power corrections scaling as  $\alpha_s \Lambda_{\text{QCD}}/m_b$ . Based on simple dimensional reasons these  
 4662 unknown corrections can be estimated to induce errors at the order of 5%.

4663 Finally, let us mention three possible improvements in the experimental analyses. First,  
 4664 a measurement of the low- $q^2$  rate normalized to the semileptonic  $B \rightarrow X_u \ell \nu$  rate with  
 4665 the same  $M_{X_s}$  cut would have a much reduced sensitivity to the actual  $M_{X_s}$  cut em-  
 4666 ployed [759]. Second, the convergence of the OPE is greatly enhanced for the high- $q^2$  rate  
 4667 normalized to the semileptonic  $B \rightarrow X_u \ell \nu$  rate with the same  $q^2$  cut [756], as can be seen  
 4668 by comparing the relative error in (293) with the SM prediction for this new ratio which  
 4669 reads  $\mathcal{R}_{q^2 > 14 \text{ GeV}^2} = (2.29 \pm 0.30) \times 10^{-3}$  [749]. Third, the angular decomposition of the  
 4670 rate and the separate extraction of  $H_T(q^2)$  and  $H_A(q^2)$  would result in much stronger  
 4671 constraints on the Wilson coefficients [760].

### 4672 6.6.2. *Experimental results on inclusive $B \rightarrow X_s \ell^+ \ell^-$*

4673 In a fully inclusive analysis of the rare electroweak penguin decay  $B \rightarrow X_s \ell^+ \ell^-$ , where  
 4674  $\ell^+ \ell^-$  is either  $e^+ e^-$  or  $\mu^+ \mu^-$ , some difficulties arise, since an abundant source of leptons  
 4675 is produced in semileptonic  $B$  and  $D$  decays. For example, the branching fraction for  
 4676 two semileptonic  $B$  decays,  $\mathcal{B}(B \rightarrow X_c \ell \nu) = (10.64 \pm 0.11)\%$  [558], is about four orders  
 4677 of magnitude larger than that of the signal. Since standard kinematic constraints like  
 4678 the the beam-energy-substituted mass,  $m_{\text{ES}}$ , or the difference between the reconstructed  
 4679  $B$  meson energy in the center-of-mass frame and its known value,  $\Delta E$ , cannot be used  
 4680 here, one needs to develop other analysis strategies. So far two alternative methods were  
 4681 developed that allows one to reduce these backgrounds. The first so-called recoil method  
 4682 is based on kinematic constraints of the  $\Upsilon(4S) \rightarrow B\bar{B}$  decays. By performing a complete  
 4683 reconstruction of the other  $B$  meson in a hadronic final state plus requiring a lepton pair  
 4684 the residual background consists of two consecutive semileptonic decays of the signal  $B$   
 4685 candidate. This is reduced by requirements on missing energy in the whole events, event  
 4686 shapes, and vertex information. Since the  $B$  reconstruction efficiency is of the order of  
 4687 0.1%, the present  $B\bar{B}$  sample are not sufficiently large to use this method. The second  
 4688 so-called semi-inclusive method consists of summing up exclusive final states.

Both *BABAR* and *Belle* focused on the second method. Using 89 (152) million  $B\bar{B}$   
 events *BABAR* (*Belle*) reconstructed final states from a  $K^+$  or a  $K_S^0$  and up to two (four)  
 pions recoiling against the lepton pair, where at most one  $\pi^0$  was accepted [761, 762].  
 In both analyses, event shape variables, kinematic variables, and vertex information

Table 46

*BABAR* and Belle measurements of the partial branching fractions for the  $B \rightarrow X_s \ell^+ \ell^-$  decay in different bins of  $q^2$ . The  $J/\psi$  and  $\psi(2S)$  veto regions differ for the  $e^+e^-$  and  $\mu^+\mu^-$  modes. The latter are shown in parentheses.

Experiment	$q^2$ [GeV <sup>2</sup> ]	$\mathcal{B}$ [ $10^{-7}$ ]
BaBar [761]	0.04–1.0	$0.8 \pm 3.6^{+0.7}_{-0.4}$
	1.0–4.0	$16 \pm 6 \pm 5$
	4.0–7.29 (7.84)	$18 \pm 8 \pm 4$
	10.56 (10.24)–11.90 (12.60)	$10 \pm 8 \pm 2$
	14.44–25.0	$6.4 \pm 3.2^{+1.2}_{-0.9}$
Belle [762]	0.04–1.0	$11.34 \pm 4.83^{+4.60}_{-2.71}$
	1.0–6.0	$14.93 \pm 5.04^{+4.11}_{-3.21}$
	6.0–7.27 (7.55) & 10.54 (10.22)– 11.81 (12.50) & 14.33 (14.33)–14.4	$7.32 \pm 6.14^{+1.84}_{-1.91}$
	14.4–25.0	$4.18 \pm 1.17^{+0.61}_{-0.68}$

are combined into likelihood functions for signal,  $B\bar{B}$  backgrounds, and  $e^+e^- \rightarrow q\bar{q}$  continuum backgrounds. The likelihood ratios are optimized to enhance signal-like events. The signal is extracted from an extended maximum likelihood fit to the  $m_{\text{ES}}$  distribution after selecting a signal-like region in  $\Delta E$ . Both analyses found significant event yields, measuring branching fractions of

$$\begin{aligned} \mathcal{B}(B \rightarrow X_s \ell^+ \ell^-) &= (5.6 \pm 1.5_{\text{stat}} \pm 0.6_{\text{syst}} \pm 1.1_{\text{mode}}) \times 10^{-6}, \\ \mathcal{B}(B \rightarrow X_s \ell^+ \ell^-) &= \left(4.11 \pm 0.83_{\text{stat}} \begin{smallmatrix} +0.85 \\ -0.81_{\text{syst}} \end{smallmatrix}\right) \times 10^{-6}, \end{aligned} \quad (294)$$

4689 where the  $J/\psi$  and  $\psi(2S)$  veto regions have been excluded and the third error of the  
4690 *BABAR* number corresponds to the uncertainty induced by the Fermi motion model [758].  
4691 The partial branching fractions in bins of  $q^2$  as measured by *BABAR* and Belle are summa-  
4692 rized in Tab. 46. *BABAR* also measured the direct CP asymmetry  $(N_{\bar{B}} - N_B)/(N_{\bar{B}} + N_B) =$   
4693  $-0.22 \pm 0.26 \pm 0.02$ , where  $N_{B(\bar{B})}$  are the signal yields for  $B(\bar{B}) \rightarrow X_s \ell^+ \ell^-$ . All results  
4694 are consistent with the SM predictions discussed in Sec. 6.6.1.

### 4695 6.6.3. Theory of exclusive $b \rightarrow s \ell^+ \ell^-$ modes

4696 The theoretical calculation of exclusive  $b \rightarrow s \ell^+ \ell^-$  amplitudes is complicated by the  
4697 fact that one encounters non-factorizable QCD dynamics. Some of these effects can be  
4698 estimated using perturbative methods based on the heavy-quark expansion. To be con-  
4699 crete, we focus on the decays  $B \rightarrow K^* \ell^+ \ell^-$  and comment on other decay modes at the  
4700 end of this section.

Assuming the  $K^*$  to be on the mass shell, the decay  $\bar{B}^0 \rightarrow \bar{K}^{*0}(\rightarrow K^- \pi^+) \ell^+ \ell^-$  is completely described by four independent kinematic variables; namely, the lepton-pair invariant mass,  $q^2$ , and the three angles  $\theta_l$ ,  $\theta_{K^*}$ ,  $\phi$ . The sign of the angles for the  $\bar{B}$  decay show great variation in the literature. Therefore we present here an explicit definition.  $\mathbf{p}$  denote three momentum vectors in the  $\bar{B}$  rest frame,  $\mathbf{q}$  the same in the di-muon rest frame, and  $\mathbf{r}$  in the  $\bar{K}^{*0}$  rest frame, the  $z$ -axis is defined as as the direction of the  $\bar{K}^{*0}$  in the  $\bar{B}$  rest frame. Three unit vectors are given in the following way: the first one is

in the direction of the  $z$ -axis where the  $\theta$  angles are measured with respect to, and the other two are perpendicular to the di-muon and  $\bar{K}^{*0}$  decay planes.

$$\mathbf{e}_z = \frac{\mathbf{p}_{K^-} + \mathbf{p}_{\pi^+}}{|\mathbf{p}_{K^-} + \mathbf{p}_{\pi^+}|}, \quad \mathbf{e}_l = \frac{\mathbf{p}_{\mu^-} \times \mathbf{p}_{\mu^+}}{|\mathbf{p}_{\mu^-} \times \mathbf{p}_{\mu^+}|}, \quad \mathbf{e}_K = \frac{\mathbf{p}_{K^-} \times \mathbf{p}_{\pi^+}}{|\mathbf{p}_{K^-} \times \mathbf{p}_{\pi^+}|}. \quad (295)$$

It follows for the  $\bar{B}$

$$\cos \theta_l = \frac{\mathbf{q}_{\mu^+} \cdot \mathbf{e}_z}{|\mathbf{q}_{\mu^+}|}, \quad \cos \theta_K = \frac{\mathbf{r}_{K^-} \cdot \mathbf{e}_z}{|\mathbf{r}_{K^-}|} \quad (296)$$

and

$$\sin \phi = (\mathbf{e}_l \times \mathbf{e}_K) \cdot \mathbf{e}_z, \quad \cos \phi = \mathbf{e}_K \cdot \mathbf{e}_l. \quad (297)$$

The angles are defined in the intervals

$$-1 \leq \cos \theta_l \leq 1, \quad -1 \leq \cos \theta_K \leq 1, \quad -\pi \leq \phi < \pi, \quad (298)$$

4701 where in particular it should be noted that the  $\phi$  angle is signed.

4702 In words, for the  $\bar{B}$  the angle  $\theta_l$  is measured as the angle between the  $\ell^+$  and the  $z$ -axis  
 4703 in the dimuon rest frame. As the  $\bar{B}$  flies in the direction of the  $z$ -axis in the dimuon rest  
 4704 frame this is equivalent to measuring  $\theta_l$  as the angle between the  $\ell^+$  and the  $\bar{B}$  in the  
 4705 di-lepton rest frame. The angle  $\theta_K$  is measured as the angle between the Kaon and the  
 4706  $z$ -axis measured in the  $\bar{K}^{*0}$  rest frame. Finally  $\phi$  is the angle between the normals to  
 4707 the planes defined by the  $K\pi$  system and the  $\mu^+\mu^-$  system in the rest frame of the  $\bar{B}$   
 4708 meson.

4709 For the  $B$  the definition is such that the angular distributions will stay the same as  
 4710 for the  $\bar{B}$  in the absence of  $CP$  violation. This means that for all the definitions above,  
 4711  $\ell^-$  is interchanged with  $\ell^+$ ,  $K^+$  with  $K^-$  and  $\pi^+$  with  $\pi^-$ .

Following [760], the doubly differential decay rate for  $\bar{B} \rightarrow \bar{K}^* \ell^+ \ell^-$  can be decomposed as in the inclusive case (292). Here the helicity amplitude  $H_T(q^2)$  determines the rate for transversely polarized  $K^*$  mesons,  $H_L(q^2)$  the longitudinal rate, and  $H_A(q^2)$  is responsible for the lepton FBA. In terms of transversity amplitudes, which are relevant for the angular analysis of  $B \rightarrow K^*(K\pi)\ell^+\ell^-$ , these functions read [763]

$$\begin{aligned} H_T(q^2) &= |A_{\perp L}|^2 + |A_{\perp R}|^2 + |A_{\parallel L}|^2 + |A_{\parallel R}|^2, \\ H_L(q^2) &= |A_{0L}|^2 + |A_{0R}|^2, \\ H_A(q^2) &= 2 \operatorname{Re} [A_{\parallel R} A_{\perp R}^* - A_{\parallel L} A_{\perp L}^*]. \end{aligned} \quad (299)$$

The transversity amplitudes themselves can be written as [685, 695, 763]

$$\begin{aligned} A_{\perp L,R} &\propto \left[ (C_9 \mp C_{10}) \frac{V(q^2)}{m_B + m_{K^*}} + \frac{2m_b}{q^2} \mathcal{T}_1(q^2) \right], \\ A_{\parallel L,R} &\propto \left[ (C_9 \mp C_{10}) \frac{A_1(q^2)}{m_B - m_{K^*}} + \frac{2m_b}{q^2} \mathcal{T}_2(q^2) \right], \\ A_{0L,R} &\propto \left[ (C_9 \mp C_{10}) \left\{ \frac{A_1(q^2)}{m_B - m_{K^*}} - \frac{m_B^2 - q^2}{m_B^2} \frac{A_2(q^2)}{m_B + m_{K^*}} \right\} \right. \\ &\quad \left. + \frac{2m_b}{m_B^2} \left\{ \mathcal{T}_2(q^2) - \frac{m_B^2 - q^2}{m_B^2} \mathcal{T}_3(q^2) \right\} \right]. \end{aligned} \quad (300)$$

Here we neglected some terms of order  $m_{K^*}^2/m_B^2$ , and did not show the kinematic normalization factors which can be found in [763]. The ingredients in (300) are: first, the

SM short-distance Wilson coefficients  $C_{9,10}$  of the  $b \rightarrow s\ell^+\ell^-$  operators in the weak effective Lagrangian (281), which are to be tested against NP.<sup>15</sup> Second, the vector- and axial-vector  $B \rightarrow K^*$  transition form factors  $V, A_{1,2}$  which have to be estimated by non-perturbative methods. Third, the  $q^2$ -dependent functions  $\mathcal{T}_i(q^2)$  that contain factorizable and non-factorizable effects from virtual photons via the operators  $Q_{1-8}$  in (281). In the “naive factorization approximation”, the functions  $\mathcal{T}_i(q^2)$  are again expressed in terms of short-distance Wilson coefficients,  $B \rightarrow K^*$  transition form factors, and quark-loop functions, which are perturbative if  $q^2$  lies outside the vector-resonance region. Corrections to “naive factorization” can and should be systematically computed in the  $m_b \rightarrow \infty$  limit, if we restrict ourselves<sup>16</sup> to the window  $q^2 \in [1, 6] \text{ GeV}^2$ . The QCDF theorem [685, 695] which can be further justified in SCET, takes the schematic form

$$\begin{aligned} \mathcal{T}_1(q^2) &\simeq \frac{m_B^2}{m_B^2 - q^2} \mathcal{T}_2(q^2) \\ \mathcal{T}_3(q^2) - \frac{m_B^2}{m_B^2 - q^2} \mathcal{T}_2(q^2) &\simeq \begin{cases} \xi_\perp(q^2) C_\perp(q^2) + \phi_B^\pm(\omega) \otimes \phi_{K^*}^\pm(u) \otimes T_\perp(\omega, u), \\ \xi_\parallel(q^2) C_\parallel(q^2) + \phi_B^\pm(\omega) \otimes \phi_{K^*}^\parallel(u) \otimes T_\parallel(\omega, u), \end{cases} \end{aligned} \quad (301)$$

4712 where  $\xi_{\perp,\parallel}$  are universal form factors arising in the combined heavy-quark-mass and  
4713 large-recoil-energy limit [765, 766],  $C_{\perp,\parallel}$  and  $T_{\perp,\parallel}$  are perturbative coefficient functions  
4714 including vertex corrections and spectator effects, respectively, and  $\phi_B$  and  $\phi_{K^*}$  denote  
4715 hadronic LCDAs which again have to be estimated from non-perturbative methods. On  
4716 the one hand, the reduction of form factors in the symmetry limit is a crucial ingredient  
4717 to obtain a precise estimate of the FBA [766–768]. On the other hand, observables like  
4718 the isospin asymmetry between charged and neutral decays are sensitive to  $A_{\text{QCD}}/m_b$   
4719 corrections to (301), which generally are small but difficult to estimate very precisely  
4720 [695, 769, 770].

To be concrete, let us quote some theoretical predictions for individual SM rates and asymmetries in the low- $q^2$  region, following the numerical analysis in [695] but using updated values for the  $B$  lifetimes. We first note that the hadronic uncertainties for the partial rates in that region are dominated by the form factor uncertainties, and therefore should be considered as less useful for precision tests of the SM. These uncertainties drop out to a large extent in the prediction for the FBA in particular in the vicinity of the zero of the FBA<sup>17</sup>. This is illustrated in panel (a) of Fig. 50. For the zero of the FBA one obtains

$$\begin{aligned} q_0^2(B^0 \rightarrow K^{*0}\ell^+\ell^-) &= (4.36_{-0.31}^{+0.33}) \text{ GeV}^2, \\ q_0^2(B^\pm \rightarrow K^{*\pm}\ell^+\ell^-) &= (4.15_{-0.27}^{+0.27}) \text{ GeV}^2. \end{aligned} \quad (302)$$

Considering the FBA for the partially integrated rates

$$A_{\text{FB}} = \frac{\int_0^1 \frac{d\Gamma}{d\cos\theta_l} d\theta_l - \int_{-1}^0 \frac{d\Gamma}{d\cos\theta_l} d\theta_l}{\int_0^1 \frac{d\Gamma}{d\cos\theta_l} d\theta_l + \int_{-1}^0 \frac{d\Gamma}{d\cos\theta_l} d\theta_l} \quad (303)$$

<sup>15</sup> NP contributions to the operators  $Q'_{7-10}$ , that are obtained from  $Q_{7-10}$  by exchanging left- by right-handed fields everywhere, can easily be included [763].

<sup>16</sup> In principle, the region  $4m_c^2 \ll q^2 \leq m_b^2$  can be treated in heavy hadron chiral perturbation theory [764].

<sup>17</sup> The form factor dependence could be further reduced by normalizing the FBA to the transverse rate, instead of the full rate.

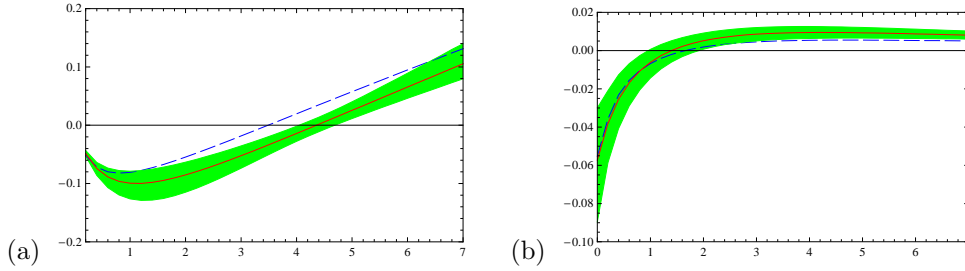


Fig. 50. (a) Theoretical estimate for differential FBA in  $B^0 \rightarrow K^{*0} \ell^+ \ell^-$ . (b) Estimate for differential isospin asymmetry. The dashed line denotes the LO result. The solid line with the error band the NLO prediction with parametric uncertainties.

one obtains

$$A_{\text{FB}}^{\text{low-}q^2} = \begin{cases} -0.033_{-0.016}^{+0.014}, & \text{for } B^0 \rightarrow K^{*0} \ell^+ \ell^-, \\ -0.062_{-0.023}^{+0.018}, & \text{for } B^\pm \rightarrow K^{*\pm} \ell^+ \ell^-. \end{cases} \quad (304)$$

The corresponding predictions for the isospin asymmetry are shown in panel (a) of Fig. 50, and the partially integrated isospin asymmetry is estimated as

$$A_1^{\text{low-}q^2} = \frac{\int d\Gamma^0 - \int d\Gamma^\pm}{\int d\Gamma^0 + \int d\Gamma^\pm} = 0.007_{-0.003}^{+0.003}. \quad (305)$$

4721 Notice that the perturbative errors can be reduced by resummation of large logarithms  
 4722 in SCET [771] or the computation of higher-order corrections, but irreducible systematic  
 4723 uncertainties from both higher-order  $\Lambda_{\text{QCD}}/m_b$  corrections, and the restricted precision  
 4724 of the form factor estimates from LCSR or LQCD remain.

4725 Let us finally consider further exclusive decay modes that can be used to test the  
 4726  $b \rightarrow s \ell^+ \ell^-$  transition. The decay into a pseudoscalar Kaon,  $B \rightarrow K \ell^+ \ell^-$ , is similar  
 4727 to the decay into a longitudinal vector meson [685, 772]. An interesting observable for  
 4728 the identification of NP is the ratio  $R_K$  already mentioned in Sec. 6.6.1. One should also  
 4729 mention the decay  $B_s \rightarrow \phi \ell^+ \ell^-$ , where a recent model-independent analysis of NP effects  
 4730 based on “naive” factorization has been given [773]. A SM analysis including NLO effects  
 4731 is straightforward and will be discussed elsewhere [774].

4732 A related process is  $B \rightarrow \rho \ell^+ \ell^-$  which probes the  $b \rightarrow d \ell^+ \ell^-$  transition in and beyond  
 4733 the SM. Due to the different CKM hierarchy it may show potentially larger isospin and  
 4734  $CP$ -violating effects than its counterparts in  $b \rightarrow s \ell^+ \ell^-$  [685]. It is also useful as a  
 4735 cross-check for the factorization approach.

#### 4736 6.6.4. Angular observables in $B \rightarrow K^* \ell^+ \ell^-$

Besides the branching fractions, the FBA and  $CP$ -violating observables, the exclusive decay  $\bar{B}^0 \rightarrow \bar{K}^{*0} \ell^+ \ell^-$  with an angular analysis of the subsequent  $\bar{K}^{*0} \rightarrow K^- \pi^+$  decay offers the possibility to further constrain NP [763, 770, 775–778]. The decay is described by 4 independent kinematic variables: the lepton-pair invariant mass squared,  $q^2$ , and the three angles  $\theta_l$ ,  $\theta_K$ ,  $\phi$ . Summing over final-state spins, the differential decay distribution can be expressed in terms of 9 independent functions [779–783], which are related to the transversity amplitudes<sup>18</sup> discussed around (299) and (300), and which are invariant

<sup>18</sup>Another transversity amplitude  $A_t$  does not contribute for massless leptons.

under the following symmetry transformations [778]

$$\begin{aligned}
A_{iL} &\rightarrow \cos\theta e^{+i\phi_L} A_{iL} - \sin\theta e^{-i\phi_R} A_{iR}^*, \\
A_{iR} &\rightarrow \sin\theta e^{-i\phi_L} A_{iL}^* + \cos\theta e^{+i\phi_R} A_{iR}, \\
A_{\perp L} &\rightarrow +\cos\theta e^{+i\phi_L} A_{\perp L} + \sin\theta e^{-i\phi_R} A_{\perp R}^*, \\
A_{\perp R} &\rightarrow -\sin\theta e^{-i\phi_L} A_{\perp L}^* + \cos\theta e^{+i\phi_R} A_{\perp R}.
\end{aligned} \tag{306}$$

4737 Here  $i = \parallel, 0$ . Any experimental observable constructed from the transversity amplitudes  
4738 thus has to be invariant under these symmetries or would require to measure the helicity  
4739 of the decay products which is not possible at LHC**b** or a super flavor factory. For  
4740 instance, this excludes the asymmetry  $A_T^{(1)}$  defined in [780], despite its very attractive  
4741 NP sensitivity [763, 776].

As it has been emphasized in [778], one can construct angular observables which simultaneously fulfill a number of requirements, namely: i) small theoretical uncertainties due to cancellations of form-factor dependencies, ii) good experimental resolution at LHC**b** and/or super flavor factory, iii) high sensitivity to NP effects, including contributions from new operators in the weak effective Hamiltonian. Focusing on the sensitivity to right-handed operator  $Q_7'$ , where one would encounter the combination of Wilson coefficients  $(C_7 + C_7')$  in  $A_{\perp L, R}$  and  $(C_7 - C_7')$  in  $A_{\parallel L, R}$  and  $A_{0L, R}$ , the authors of [778] identify the following three observables to satisfy the above criteria

$$A_T^{(2)} = \frac{|A_{\perp}|^2 - |A_{\parallel}|^2}{|A_{\perp}|^2 + |A_{\parallel}|^2}, \quad A_T^{(3)} = \frac{|A_0 A_{\parallel}^*|}{|A_0| |A_{\perp}|}, \quad A_T^{(4)} = \frac{|A_{0L} A_{\perp L}^* - A_{0R}^* A_{\perp R}|}{|A_0 A_{\parallel}^*|}, \tag{307}$$

4742 where  $A_i A_j^* = A_{iL} A_{jL}^* + A_{iR} A_{jR}^*$ . In particular, the dependence on the form factors  $\xi_{\perp, \parallel}$   
4743 drops out to first approximation if one neglects  $\alpha_s$  and  $\Lambda_{\text{QCD}}/m_b$  corrections.

4744 In Fig. 51, the theoretical estimates and experimental sensitivity for  $A_T^{(2)}$ ,  $A_T^{(3)}$ , and  
4745  $A_T^{(4)}$  are plotted as a function of  $q^2$ . In each theoretical plot on the left-hand side the  
4746 thin dark line is the central NLO result for the SM and the narrow inner dark (orange)  
4747 band corresponds to the related uncertainties due to both input parameters and per-  
4748 turbative scale dependence. Light gray (green) bands refer to  $\Lambda_{\text{QCD}}/m_b = \pm 5\%$  correc-  
4749 tions considered for each spin amplitude, while for the darker gray (green) one considers  
4750  $\Lambda_{\text{QCD}}/m_b = \pm 10\%$  corrections. The curves labeled (a) to (d) correspond to four different  
4751 benchmark points in the MSSM. For more details we refer to [778]. The experimental  
4752 sensitivity for a data set corresponding to  $10 \text{ fb}^{-1}$  of integrated luminosity at LHC**b** is  
4753 given in each figure on the right, assuming SM rates. Here the solid (red) line shows the  
4754 median extracted from the fit to the ensemble of data, and the dashed (black) line shows  
4755 the theoretical input distribution. The inner and outer bands correspond to  $1\sigma$  and  $2\sigma$   
4756 experimental errors.

4757 The observables  $A_T^{(3)}$  and  $A_T^{(4)}$  offer sensitivity to the longitudinal spin amplitude  $A_{0L, R}$   
4758 in a controlled way, i.e., the theoretical uncertainties from NLO corrections turn out to  
4759 be very small. Concerning the sensitivity to right-handed currents, one observes sizable  
4760 deviations from the SM for  $A_T^{(2)}$ ,  $A_T^{(3)}$ , and  $A_T^{(4)}$  in the 4 SUSY benchmark scenarios  
4761 studied in [778]. For a recent discussion of other NP scenarios we refer to [770]. Comparing  
4762 the theoretical and experimental figures, it can be seen that in particular  $A_T^{(3)}$  offers great  
4763 promise to distinguish between such NP models.



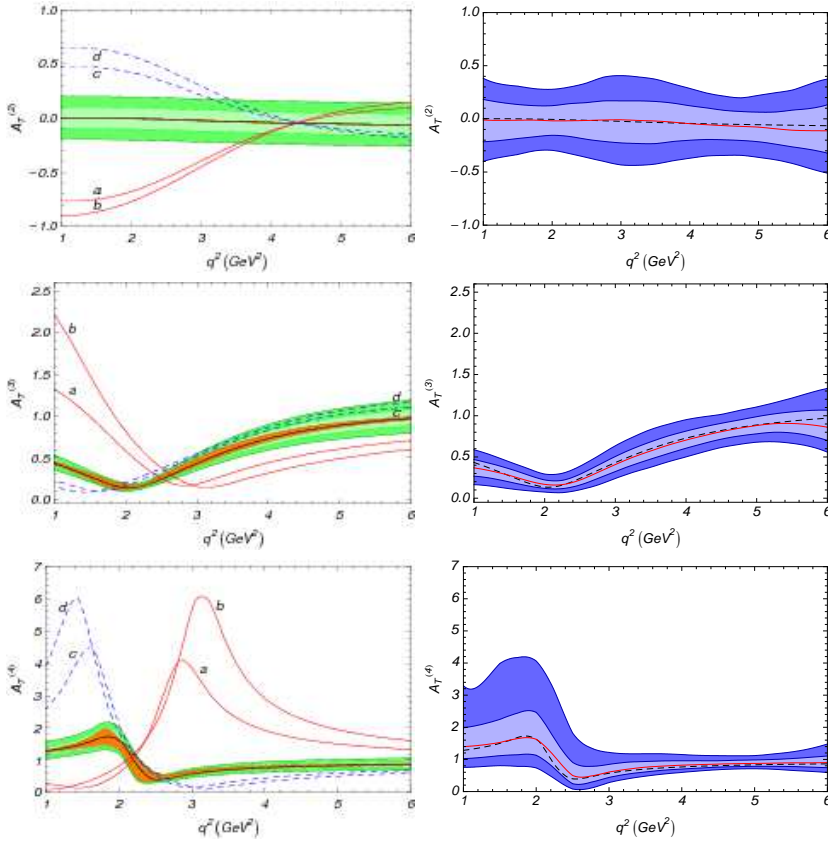


Fig. 51. The asymmetries  $A_T^{(2)}$ ,  $A_T^{(3)}$ , and  $A_T^{(4)}$  as a function of  $q^2$ , with theoretical errors (left panels), and experimental errors (right panels). See text for details. Figs taken from [778].

4764 6.6.5. *Experimental results on exclusive  $b \rightarrow (s, d)\ell^+\ell^-$*

4765 The exclusive electroweak decay  $B \rightarrow K\ell^+\ell^-$  is a  $b \rightarrow s$  transition that was first  
 4766 observed by Belle [784] in a sample of 31 million  $B\bar{B}$  events. Using 123 million  $B\bar{B}$   
 4767 events *BABAR* confirmed the observation and reported first evidence for  $B \rightarrow K^*\ell^+\ell^-$   
 4768 [785] which was confirmed later by Belle [786]. In the most recent studies *BABAR* and  
 4769 Belle have reconstructed ten final states consisting of  $K^\mp$ ,  $K_S^0(\rightarrow \pi^+\pi^-)$ ,  $K^\mp\pi^\pm$ ,  $K^\mp\pi^0$   
 4770 or  $K_S^0(\rightarrow \pi^+\pi^-)\pi^\mp$  besides the lepton pair using 384 million and 657 million  $B\bar{B}$  events,  
 4771 respectively [787–789]. The signal yields in individual final states are extracted from  
 4772 the  $m_{ES}$  and  $\Delta E$  distributions. The main background arises from random combinations  
 4773 of leptons from  $B$  and  $D$  decays. As in the semi-inclusive analysis this combinatorial  
 4774 background is suppressed by using event shape variables, kinematic variables, and vertex  
 4775 information that are combined into a neural network (*BABAR*) or a likelihood ratio (Belle).  
 4776 The multivariate observables are optimized separately for each mode, for each type of  
 4777 background,  $B\bar{B}$  or  $e^+e^- \rightarrow q\bar{q}$ , and each  $q^2$  region.

4778 Total branching fractions measured by *BABAR*, Belle, and CDF are in agreement with  
 4779 each other and the SM predictions [768, 790]. The interest, however, has shifted towards  
 4780 rate asymmetries, since many uncertainties in both predictions and measurements cancel

4781 as explained in Sec. 6.6.3. *BABAR* and Belle so far studied isospin asymmetries,  $A_I^{K^{(*)}}$ ,  
 4782 direct CP asymmetries,  $A_{\text{CP}}^{K^{(*)}}$ , and lepton forward-backward asymmetries,  $A_{\text{FB}}$ , as well as  
 4783 the  $K^*$  longitudinal polarization,  $F_L$ , and the ratio of rates to  $\mu^+\mu^-$  and  $e^+e^-$  final states,  
 4784  $R_{K^{(*)}}$ . With increased statistics both experiments started to explore the  $q^2$  dependence  
 4785 of these observables.

The CP-averaged isospin asymmetry and direct CP asymmetry are defined by

$$\begin{aligned}
 A_I^{K^{(*)}} &= \frac{\mathcal{B}(B^0 \rightarrow K^{(*)0}\ell^+\ell^-) - (\tau_0/\tau_+)\mathcal{B}(B^\pm \rightarrow K^{(*)\pm}\ell^+\ell^-)}{\mathcal{B}(B^0 \rightarrow K^{(*)0}\ell^+\ell^-) + (\tau_0/\tau_+)\mathcal{B}(B^\pm \rightarrow K^{(*)\pm}\ell^+\ell^-)}, \\
 A_{\text{CP}}^{K^{(*)}} &= \frac{\mathcal{B}(\overline{B} \rightarrow \overline{K}^{(*)}\ell^+\ell^-) - \mathcal{B}(B \rightarrow K^{(*)}\ell^+\ell^-)}{\mathcal{B}(\overline{B} \rightarrow \overline{K}^{(*)}\ell^+\ell^-) + \mathcal{B}(B \rightarrow K^{(*)}\ell^+\ell^-)},
 \end{aligned}
 \tag{308}$$

4786 where  $\tau_0$  and  $\tau_+$  are the  $B^0$  and  $B^+$  lifetimes, respectively.  $A_{\text{CP}}$  is predicted to be  
 4787  $\mathcal{O}(10^{-3})$  in the SM. NP at the electroweak scale, however, could produce a significant  
 4788 enhancement [777]. The ratios  $R_{K^{(*)}}$  are sensitive to the presence of a neutral SUSY Higgs  
 4789 boson [791]. In the SM,  $R_K$  is expected to be unity modulo a small correction accounting  
 4790 for differences in phase space [792] and possibly QED radiation. For  $m_{\ell^+\ell^-} \geq 2m_\mu$ ,  
 4791  $R_{K^*}$  should be also close to unity. Due to the  $1/q^2$  dependence of the photon penguin  
 4792 contribution, however, there is a significant rate enhancement in the  $B \rightarrow K^*e^+e^-$   
 4793 mode for  $m_{e^+e^-} < 2m_\mu$  decreasing the SM expectation of  $R_{K^*}$  to 0.75. New scalar and  
 4794 pseudoscalar contributions may modify this prediction. The possible size of these effects  
 4795 is however already bounded severely by the Tevatron limits on  $B_s \rightarrow \mu^+\mu^-$ .

4796 Present results of branching fractions, rate-based asymmetries, and lepton-flavor ratios  
 4797 are summarized in Tab.s 47 and 48. At the present level of precision branching fractions,  
 4798  $R_{K^{(*)}}$ , and  $A_{\text{CP}}$  are in good agreement with the SM. While  $A_I$  agrees with the SM for  
 4799 large values of  $q^2$ , the *BABAR* measurement of  $A_I$  in the low- $q^2$  region deviates from the  
 4800 SM expectation [769] by almost 4  $\sigma$  for the combination of the  $B \rightarrow K\ell^+\ell^-$  and  $B \rightarrow$   
 4801  $K^*\ell^+\ell^-$  modes. Though consistent with the SM expectation the Belle results support  
 4802 the *BABAR* observations at low  $q^2$ .

The angular distribution of  $B \rightarrow K^*\ell^+\ell^-$  depends on the three angles defined in  
 eqs. 296 and 297. The one-dimensional angular distributions in  $\cos\theta_K$  and  $\cos\theta_\ell$  simply  
 are

$$\begin{aligned}
 W(\theta_K) &= \frac{3}{2}F_L \cos^2\theta_K + \frac{3}{4}(1 - F_L)(1 - \cos^2\theta_K), \\
 W(\theta_\ell) &= \frac{3}{4}F_L(1 - \cos^2\theta_\ell) + \frac{3}{8}(1 - F_L)(1 + \cos^2\theta_\ell) + A_{\text{FB}} \cos\theta_\ell.
 \end{aligned}
 \tag{309}$$

4803 While  $W(\theta_K)$  depends only on  $F_L$ ,  $W(\theta_\ell)$  depends both on  $F_L$  and  $A_{\text{FB}}$ . The FBA  
 4804 is proportional to the difference of two interference terms that include products of the  
 4805 Wilson coefficients  $C_9C_{10}$  and  $C_7C_{10}$ . In the first term the main  $q^2$  dependence originates  
 4806 from the  $q^2$  dependence of  $C_9$  while in the second term it results from the  $1/q^2$  dependence  
 4807 of the photon penguin contribution.

4808 *BABAR* and Belle measured  $F_L$  and  $A_{\text{FB}}$  in different bins of  $q^2$ . After extracting the  
 4809 event yield from the  $m_{ES}$  distribution,  $F_L$  is determined first from a fit to  $W(\theta_K)$ . Then  
 4810  $A_{\text{FB}}$  is determined from a fit to  $W(\theta_\ell)$  for fixed signal yields and fixed  $F_L$ . The results are  
 4811 summarized in Tab. 49. The *BABAR* and Belle results for  $F_L$  and  $A_{\text{FB}}$  in comparison to  
 4812 their SM predictions and three scenarios, that result from changing the sign of the Wilson  
 4813 coefficients  $C_7$ , or  $C_9C_{10}$ , or both combinations with respect to the SM values are shown

Table 47

Measurements of the partial branching fractions and isospin asymmetries for the  $B \rightarrow K\ell^+\ell^-$  and  $B \rightarrow K^*\ell^+\ell^-$  decays in different bins of  $q^2$ .

Experiment	Mode	$q^2$ [GeV $^2$ ]	$\mathcal{B}$ [ $10^{-7}$ ]	$A_{\Gamma}$
BABAR [788]	$B \rightarrow K\ell^+\ell^-$	0.1–7.02	$0.181^{+0.39}_{-0.36} \pm 0.008$	$-1.43^{+0.56}_{-0.85} \pm 0.05$
		10.24–12.96 or >14.06	$0.135^{+0.040}_{-0.037} \pm 0.007$	$0.28^{+0.24}_{-0.30} \pm 0.03$
	$B \rightarrow K^*\ell^+\ell^-$	0.1–7.02	$0.43^{+0.11}_{-0.10} \pm 0.03$	$-0.56^{+0.17}_{-0.15} \pm 0.03$
		10.24–12.96 or >14.06	$0.42^{+0.10}_{-0.10} \pm 0.03$	$0.18^{+0.36}_{-0.28} \pm 0.04$
Belle [789]	$B \rightarrow K\ell^+\ell^-$	0.0–2.0	$0.81^{+0.18}_{-0.16} \pm 0.05$	$-0.33^{+0.33}_{-0.25} \pm 0.05$
		2.0–5.0	$0.58^{+0.16}_{-0.14} \pm 0.04$	$-0.49^{+0.45}_{-0.34} \pm 0.04$
		5.0–8.86	$0.86^{+0.18}_{-0.16} \pm 0.05$	$-0.19^{+0.26}_{-0.22} \pm 0.05$
		10.09–12.86	$0.55^{+0.16}_{-0.14} \pm 0.03$	$-0.29^{+0.37}_{-0.29} \pm 0.05$
		14.18–16.0	$0.38^{+0.19}_{-0.12} \pm 0.02$	$-0.40^{+0.61}_{-0.69} \pm 0.04$
		> 16.0	$0.98^{+0.20}_{-0.18} \pm 0.06$	$0.11^{+0.24}_{-0.21} \pm 0.05$
			1.0–6.0	$1.36^{+0.23}_{-0.21} \pm 0.08$
	$B \rightarrow K^*\ell^+\ell^-$	0.0–2.0	$1.46^{+0.40}_{-0.35} \pm 0.12$	$-0.67^{+0.18}_{-0.16} \pm 0.03$
		2.0–5.0	$1.29^{+0.38}_{-0.34} \pm 0.10$	$1.17^{+0.72}_{-0.82} \pm 0.02$
		5.0–8.86	$0.99^{+0.41}_{-0.36} \pm 0.08$	$-0.47^{+0.31}_{-0.29} \pm 0.04$
		10.09–12.86	$2.24^{+0.44}_{-0.40} \pm 0.18$	$0.00^{+0.20}_{-0.21} \pm 0.05$
		14.18–16.0	$1.05^{+0.29}_{-0.26} \pm 0.08$	$0.16^{+0.30}_{-0.35} \pm 0.05$
		> 16.0	$2.04^{+0.27}_{-0.24} \pm 0.16$	$-0.02^{+0.20}_{-0.21} \pm 0.05$
			1.0–6.0	$1.49^{+0.45}_{-0.40} \pm 0.12$
CDF [793]	$B^+ \rightarrow K^+\ell^+\ell^-$	<8.4 or 10.2–13.0 or >14.1	$5.9 \pm 1.5 \pm 0.4$	$-0.33^{+0.33}_{-0.25} \pm 0.05$
CDF [793]	$B^0 \rightarrow K^{*+}\ell^+\ell^-$	<8.4 or 10.2–13.0 or >14.1	$8.1 \pm 3.0 \pm 1.0$	

Table 48

BABAR and Belle measurements of total branching fractions, CP asymmetries, and lepton flavor ratios for the  $B \rightarrow K\ell^+\ell^-$  and  $B \rightarrow K^*\ell^+\ell^-$  decays. For  $B \rightarrow K^*\ell^+\ell^-$  the pole region,  $q^2 < m_{\mu}^2$ , is included in  $R_{K^{(*)}}$ . The CP asymmetries are given for  $B \rightarrow K^+\ell^+\ell^-$  and the combined  $B \rightarrow K^*\ell^+\ell^-$  modes.

Experiment	Mode	$\mathcal{B}$ [ $10^{-7}$ ]	$A_{CP}$	$R_{K^{(*)}}$
BABAR [788]	$B \rightarrow K\ell^+\ell^-$	$3.9^{+0.7}_{-0.7} \pm 0.2$	$-0.18^{+0.18}_{-0.18} \pm 0.01$	$0.96^{+0.44}_{-0.34} \pm 0.05$
	$B \rightarrow K^*\ell^+\ell^-$	$11.1^{+1.9}_{-1.8} \pm 0.7$	$0.01^{+0.16}_{-0.15} \pm 0.01$	$1.1^{+0.42}_{-0.32} \pm 0.07$
Belle [789]	$B \rightarrow K\ell^+\ell^-$	$4.8^{+0.5}_{-0.4} \pm 0.3$	$-0.04^{+0.1}_{-0.1} \pm 0.02$	$1.03^{+0.19}_{-0.19} \pm 0.06$
	$B \rightarrow K^*\ell^+\ell^-$	$10.8^{+1.1}_{-1.0} \pm 0.9$	$-0.10^{+0.10}_{-0.10} \pm 0.01$	$0.83^{+0.17}_{-0.17} \pm 0.08$

4814 in Fig. 52. At the present level of precision both  $F_L$  and  $A_{FB}$  are consistent with the  
4815 SM expectations. For  $B \rightarrow K\ell^+\ell^-$ , the measurement of  $A_{FB}$  is consistent with zero as  
4816 expected in the SM. It is important to emphasize, that models in which the sign of  $C_7$  is  
4817 reversed while  $C_{9,10}$  receive only small non-standard corrections are disfavored at the  $3\sigma$   
4818 level by the combination of the  $\mathcal{B}(B \rightarrow X_s\gamma)$  and  $\mathcal{B}(B \rightarrow X_s\ell^+\ell^-)$  measurements [794].  
4819 The hypothetical NP scenario corresponding to the green dashed curves in Fig. 52 is

Table 49

BABAR and Belle measurements of the  $K^*$  longitudinal polarizations and the lepton FBAs for the  $B \rightarrow K^* \ell^+ \ell^-$  decays in different bins of  $q^2$ .

Experiment	$q^2$ [GeV $^2$ ]	$F_L$	$A_{FB}$
BABAR [787]	0.1–6.25	$0.35^{+0.16}_{-0.16} \pm 0.04$	$0.24^{+0.18}_{-0.23} \pm 0.05$
	10.24–12.96 or >14.06	$0.71^{+0.20}_{-0.22} \pm 0.04$	$0.76^{+0.52}_{-0.32} \pm 0.07$
Belle [789]	0.0–2.0	$0.29^{+0.21}_{-0.18} \pm 0.02$	$0.47^{+0.26}_{-0.32} \pm 0.03$
	2.0–5.0	$0.75^{+0.21}_{-0.22} \pm 0.05$	$0.14^{+0.20}_{-0.26} \pm 0.07$
	5.0–8.86	$0.65^{+0.26}_{-0.27} \pm 0.06$	$0.47^{+0.16}_{-0.25} \pm 0.14$
	10.09–12.86	$0.17^{+0.17}_{-0.15} \pm 0.03$	$0.43^{+0.18}_{-0.20} \pm 0.03$
	14.18–16.0	$-0.15^{+0.27}_{-0.23} \pm 0.07$	$0.70^{+0.16}_{-0.22} \pm 0.10$
	> 16.0	$0.12^{+0.15}_{-0.13} \pm 0.02$	$0.66^{+0.11}_{-0.16} \pm 0.04$
	1.0–6.0	$0.67^{+0.23}_{-0.23} \pm 0.05$	$0.26^{+0.27}_{-0.30} \pm 0.07$

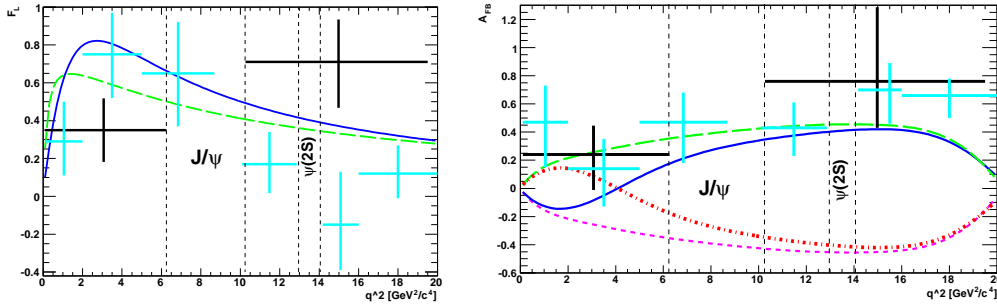


Fig. 52. Measurements of  $F_L$  (left) and of  $A_{FB}$  (right) as a function of  $q^2$  for  $B \rightarrow K^* \ell^+ \ell^-$  from BABAR (black points) and Belle (cyan points). The curves show predictions for four cases, the SM (blue solid curve), the flipped-sign  $C_7$  case (green dashed curve), the case of flipped-sign  $C_9 C_{10}$  (magenta dotted curve), and the case with both flipped-sign  $C_7$  and  $C_9 C_{10}$  (red dash-dotted curve).

4820 thus in variance with the available data on the inclusive  $b \rightarrow s \gamma, \ell^+ \ell^-$  transitions. This  
 4821 observation makes clear that to bound the values of the various Wilson coefficients one  
 4822 should exploit all the experimental information in the  $b \rightarrow s \gamma$  and  $b \rightarrow s \ell^+ \ell^-$  sector  
 4823 combining both inclusive and exclusive channels.

4824 The exclusive decays  $B \rightarrow \pi(\rho) \ell^+ \ell^-$  are the corresponding  $b \rightarrow d$  transitions that are  
 4825 suppressed with respect to the  $b \rightarrow s$  transitions by  $|V_{td}/V_{ts}|^2$ . BABAR [795] searched  
 4826 for  $B \rightarrow \pi \ell^+ \ell^-$  events using 230 million  $B\bar{B}$  events while Belle [796] searched for  $B \rightarrow$   
 4827  $(\pi, \rho, \omega) \ell^+ \ell^-$  modes using 657 million  $B\bar{B}$  events. The lowest branching fraction upper  
 4828 limit is set for the  $B \rightarrow \pi \ell^+ \ell^-$  mode by Belle yielding  $\mathcal{B}(B \rightarrow \pi \ell^+ \ell^-) < 4.9 \times 10^{-8}$  at  
 4829 90% CL which just lies a factor of around 1.5 above the central value of the SM prediction  
 4830 which reads  $\mathcal{B}(B \rightarrow \pi \ell^+ \ell^-) = (3.3 \pm 1.0) \times 10^{-8}$  [797].

4831 The LHCb experiment will collect  $\sim 7 \times 10^3$  fully reconstructed  $B^0 \rightarrow K^{*0} \mu^+ \mu^-$   
 4832 events per  $2 \text{ fb}^{-1}$  integrated luminosity [798]. At the LHC design luminosity, such an  
 4833 data-set will be acquired in a single year of data-taking. Before such conditions are  
 4834 achieved, with even the data from the LHC pilot run, a  $0.1 \text{ fb}^{-1}$  integrated luminosity  
 4835 would therefore give a comparable number of events to the final dataset expected from

4836 the B-factory experiments [787, 789] and CDF [793]. The branching ratio for this decay  
 4837 is already measured with a precision comparable to the level of theoretical uncertainties.  
 4838 LHC***b***'s experimental exploration will therefore focus on angular observables such as the  
 4839 forward-backward asymmetry  $A_{\text{FB}}$ .

4840 Given the background expected from simulation studies [798], LHC***b*** will be able to  
 4841 determine the zero-crossing point of this asymmetry by counting forward- and backward-  
 4842 events with a statistical precision of  $0.5 \text{ GeV}^2$  with  $2 \text{ fb}^{-1}$  integrated luminosity [799].  
 4843 Additional systematic contributions to this precision from e.g. the determination of ac-  
 4844 ceptance and trigger efficiencies are under study. A measurement with a statistical un-  
 4845 certainty at the level of present theoretical uncertainties on the zero-crossing point (see  
 4846 Sec. 6.6.3) will therefore require a  $10 \text{ fb}^{-1}$  integrated luminosity. However, using infor-  
 4847 mation from the  $\theta_K$  angular distribution, in particular, by making a simultaneous fit for  
 4848 both the  $A_{\text{FB}}$  and  $F_L$  observables, a factor  $\sim 2$  increase in the statistical precision can  
 4849 be obtained [800]. Adding the information from the angle  $\phi$ , a full angular fit will give  
 4850 a further  $\sim 30\%$  increase in the precision [801]. More significantly, such a full angular  
 4851 fit will give access to the underlying amplitudes, from which any observable can then be  
 4852 formed. As detailed in Sec. 6.6.4, LHC***b*** will be able to measure, with good precision,  
 4853 other theoretically well controlled observables such as  $A_T^{(2,3,4)}$  (see Eq 307), which will  
 4854 give very different new physics sensitivity to  $A_{\text{FB}}$ . Studies indicate that full angular fits  
 4855 can be made to converge with data-sets in excess of the expectation from  $2 \text{ fb}^{-1}$  inte-  
 4856 grated luminosity. In practise, performing such a fit will require excellent understanding  
 4857 of the trigger and detector efficiencies and will be a later LHC***b*** measurement.

#### 4858 6.6.6. Rare $K \rightarrow \pi \nu \bar{\nu}, \ell^+ \ell^-$ decays in and beyond the SM

4859 The rare decays  $K_L \rightarrow \pi^0 \nu \bar{\nu}$ ,  $K^+ \rightarrow \pi^+ \nu \bar{\nu}$ , and  $K_L \rightarrow \pi^0 \ell^+ \ell^-$  proceed dominantly  
 4860 through heavy-quark induced FCNC. Since their rates in the SM are predicted with high  
 4861 precision, they offer the cleanest and clearest window into the sector of  $s \rightarrow d$  transitions.  
 4862 Their study is thus complementary to  $B$  physics in searching for NP, and constraining  
 4863 the possible models.

4864 6.6.6.1. *Prediction within the SM.* The electroweak processes inducing the rare  $K$  de-  
 4865 cays are of three types:  $Z$  penguin and  $W^\pm$  boxes, single- and double-photon penguin.  
 4866 The former as well as the CP-violating single-photon penguin, are always dominated by  
 4867 short-distance physics, i.e., the top- and charm-quark contribution. On the other hand,  
 4868 the CP-conserving photon penguins are fully dominated by the long-distance up-quark  
 4869 contribution, in which case they get further enhanced by the  $\Delta I = 1/2$  rule. These  
 4870 contributions are to be evaluated in  $\chi$ PT, by relating them to other, well-measured ob-  
 4871 servables.

For  $K_L \rightarrow \pi^0 \nu \bar{\nu}$  and  $K^+ \rightarrow \pi^+ \nu \bar{\nu}$ , short-distance physics dominates because of the  
 absence of photon penguins and the quadratic GIM breaking exhibited in the  $Z$  penguin.  
 The calculation of the branching ratios can be split into several pieces. First, the top quark  
 contribution  $X_t$  is known including NLO QCD effects [802]. While NLO electroweak ef-  
 fects have been estimated in the large top-quark mass limit [803]. In the charm-quark  
 sector, the NNLO QCD [804, 805] and electroweak [806] corrections have been computed,  
 significantly reducing the scheme and scale ambiguities in the corresponding quantity  
 $P_C$ . For both these contributions, the matrix elements of the resulting dimension-six op-

erator, encoded in  $\kappa_L$  and  $\kappa_+$ , are obtained from the full set of  $K_{\ell 3}$  data, including isospin-breaking and long-distance QED corrections [807]. Higher-dimensional contributions for the charm quark, which are negligible in the case of the top quark since they are suppressed by  $m_K^2/m_t^2$ , as well as the residual up-quark contributions are parametrized by  $\delta P_{u,c}$ , which has been estimated using  $\chi$ PT [808]. The error on  $\delta P_{u,c}$  may be reduced through LQCD studies [809]. Finally, the rate for  $K_1 \approx K_S$  and  $K_2 \approx K_L$  are similar, and thus indirect CP-violation,  $K_L \rightarrow \varepsilon K_2 \rightarrow \pi^0 \nu \bar{\nu}$ , is below the percent level since the smallness of  $\varepsilon_K \sim 10^{-3}$  cannot be compensated [810]. Putting all these pieces together, the  $K \rightarrow \pi \nu \bar{\nu}$  rates are predicted with a high level of accuracy in the SM

$$\begin{aligned}\mathcal{B}(K_L \rightarrow \pi^0 \nu \bar{\nu}) &= (2.54 \pm 0.35) \times 10^{-11}, \\ \mathcal{B}(K^+ \rightarrow \pi^+ \nu \bar{\nu}) &= (8.51 \pm 0.73) \times 10^{-11}.\end{aligned}\tag{310}$$

4872 The composition of the quoted errors is as follows 69%<sub>CKM</sub>, 12%<sub>para</sub>, 15% <sub>$X_t$</sub> , 4% <sub>$\kappa_L$</sub>   
4873 and 52%<sub>CKM</sub>, 17%<sub>para</sub>, 12% <sub>$X_t$</sub> , 12% <sub>$\delta P_{u,c}$</sub> , 5% <sub>$P_c$</sub> , 2% <sub>$\kappa_+$</sub> , where the parametric uncertainty  
4874 combines the errors on  $m_t$ ,  $m_c$ , and  $\alpha_s$ .

For the  $K \rightarrow \pi \ell^+ \ell^-$  modes, besides the short-distance top- and charm-quark contributions, some long-distance effects arise due to the photon penguins. For the CP-odd  $K_2$ , the single-photon penguin is CP-violating, hence still short-distance dominated, and is known precisely [811]. On the other hand, the double-photon penguin is a purely long-distance CP-conserving contribution. It has been evaluated from  $K_L \rightarrow \pi^0 \gamma \gamma$  data, and turns out to be competitive in the muon case [812, 813]. For the  $K^+$  and the CP-even  $K_1$ , the CP-conserving single-photon penguin completely dominates, hence these modes do not give us access to the short-distance physics. Further, this photon penguin is large enough to compensate for  $\varepsilon_K \sim 10^{-3}$  in the indirect CP-violating  $K_L \rightarrow \varepsilon K_1 \rightarrow \pi^0 \gamma^* \rightarrow \pi^0 \ell^+ \ell^-$  contribution [814]. This piece can be brought under control thanks to the  $\mathcal{B}(K_S \rightarrow \pi^0 \ell^+ \ell^-)$  measurements, up to its interference sign [812, 815–817]. Nevertheless, the current experimental accuracy for  $\mathcal{B}(K_S \rightarrow \pi^0 \ell^+ \ell^-)$  still represents the largest source of uncertainty in the  $\mathcal{B}(K_L \rightarrow \pi^0 \ell^+ \ell^-)$  predictions, which are

$$\begin{aligned}\mathcal{B}(K_L \rightarrow \pi^0 e^+ e^-) &= 3.54_{-0.85}^{+0.98} (1.56_{-0.49}^{+0.62}) \times 10^{-11}, \\ \mathcal{B}(K_L \rightarrow \pi^0 \mu^+ \mu^-) &= 1.41_{-0.26}^{+0.28} (0.95_{-0.21}^{+0.22}) \times 10^{-11},\end{aligned}\tag{311}$$

4875 for constructive (destructive) interference.

4876 For the  $K_L \rightarrow \ell^+ \ell^-$  modes, though the short-distance top- and charm-quark contri-  
4877 butions are predicted with excellent accuracy [818], it is the long-distance two-photon  
4878 penguin which dominates. Its theoretical estimation is problematic because, contrary to  
4879  $K_L \rightarrow \pi^0 \gamma \gamma \rightarrow \pi^0 \ell^+ \ell^-$ , it i) diverges in  $\chi$ PT [819] and ii) produces the final lepton  
4880 pair in the same state as the short-distance processes, and hence interferes with them  
4881 with an unknown sign. Better measurements of  $K_S \rightarrow \pi^0 \gamma \gamma$  and  $K^+ \rightarrow \pi^+ \gamma \gamma$  could  
4882 settle this issue [820]. These two problems have, up to now, upset attempts to extract  
4883 the subleading short-distance top- and charm-quark components from the well-measured  
4884  $\mathcal{B}(K_L \rightarrow \mu^+ \mu^-)$ .

6.6.6.2. *Sensitivity to NP effects.* Rare  $K$  decays are ideally suited to search for NP effects. Indeed, besides the loop suppression of the underlying FCNC processes, they are significantly CKM suppressed. Compared to  $\mathcal{A}(b \rightarrow s, d)$ , the amplitudes in the  $s \rightarrow d$  sector scale as

$$\begin{aligned}
\mathcal{A}(s \rightarrow d) &\sim |V_{td}^* V_{ts}| \sim \lambda^5, \\
\mathcal{A}(b \rightarrow d) &\sim |V_{td}^* V_{tb}| \sim \lambda^3, \\
\mathcal{A}(b \rightarrow s) &\sim |V_{ts}^* V_{tb}| \sim \lambda^2,
\end{aligned}
\tag{312}$$

4885 with  $\lambda \sim 0.22$ . If NP is generic, i.e., it does not follow the CKM scaling (312), it is  
4886 clear that the constraints from rare  $K$  decays are typically the most stringent. Stated  
4887 differently, a measurement of  $K_L \rightarrow \pi^0 \nu \bar{\nu}$  close to its SM prediction is the most difficult  
4888 to reconcile with the existence of generic NP at a reasonably low scale around a TeV.

4889 NP models in which the CKM scalings (312) are preserved are referred to as of MFV  
4890 type [135]. When this is the case, NP can show up at a low scale without violating  
4891 experimental bounds, including those from rare  $K$  decays. In addition, when MFV is  
4892 enforced within a particular model like the MSSM, the effects are expected to be rather  
4893 small, often beyond the experimental sensitivity. This has been analyzed at moderate  
4894 [821] or large  $\tan \beta$  [144, 822, 823], without  $R$ -parity [824], or with MFV imposed at  
4895 the GUT scale [157, 158]. Turning this around, the rare  $K$  decays emerge as one of the  
4896 best places to look for deviations of the MFV hypothesis [137, 825, 826]. If the flavor-  
4897 breaking transitions induced by the NP particles are not precisely aligned with those of  
4898 the SM, large effects can show up. This is true even given the current measurement of  
4899 the  $K^+ \rightarrow \pi^+ \nu \bar{\nu}$  mode. The model-independent bound it implies on the  $K_L \rightarrow \pi^0 \nu \bar{\nu}$   
4900 mode is still about 30 times higher than the SM prediction [827].

4901 Each NP model affects the basic electroweak FCNC differently. If it enters into the  $Z$   
4902 penguin, the two  $K \rightarrow \pi \nu \bar{\nu}$  modes exhibit the best sensitivity. This happens for example  
4903 in the MSSM from chargino-squark loops at moderate  $\tan \beta$  [828–832] or charged-Higgs-  
4904 quark loops at large  $\tan \beta$  [823], with  $R$ -parity violation [833–835], in little Higgs models  
4905 without [170] and with [171–173, 836]  $T$ -parity, and in the presence of extra-dimensions  
4906 [659, 837, 838]. In most of these models, correlated changes to the short-distance photon  
4907 penguin are induced [839, 840], and these could then be probed and disentangled using the  
4908  $K_L \rightarrow \pi^0 \ell^+ \ell^-$  modes. Combined measurements of all the rare  $K$  decay modes can serve as  
4909 a powerful discriminator among models [813, 817]. Further, purely electromagnetic effects  
4910 could also be present, as in the electromagnetic operators, for which the  $K_L \rightarrow \pi^0 \ell^+ \ell^-$   
4911 modes are clean probes while  $e'$  is problematic [841].

4912 In addition, NP could occur with helicity-suppressed couplings proportional to the  
4913 fermion mass. Typical examples are the neutral Higgs-induced FCNC, as generated in  
4914 the MSSM at large  $\tan \beta$  [142, 144, 153, 822]. Obviously, the  $K_L \rightarrow \pi^0 \mu^+ \mu^-$  and  $K_L \rightarrow$   
4915  $\mu^+ \mu^-$  modes are the only available windows for such helicity-suppressed effects in the  
4916  $s \rightarrow d$  sector. Therefore, these effects can in principle be disentangled from NP in the  $Z$   
4917 or photon penguins by a combined analysis of all the rare  $K$  decay modes [817].

4918 In conclusion, the  $K \rightarrow \pi \nu \bar{\nu}$  modes offer one of the best opportunities to find a ir-  
4919 refutable signal of NP in the field of flavor physics. Furthermore, combining information  
4920 on the different  $K \rightarrow \pi \nu \bar{\nu}$  and  $K_L \rightarrow \pi^0 \ell^+ \ell^-$  channels allows one to probe and disen-  
4921 tangle NP effects in most of the different types of FCNC interactions. Being either free  
4922 of hadronic uncertainties, or these being under sufficiently good theoretical control, the  
4923 stage is set for a complete and detailed study of  $s \rightarrow d$  transitions.

#### 4924 6.6.7. *Experimental status of $K \rightarrow \pi \nu \bar{\nu}$ and $K_L \rightarrow \pi \ell^+ \ell^-$*

4925 The E787 and E949 experiments have established the feasibility of observing the  $K^+ \rightarrow$   
4926  $\pi^+ \nu \bar{\nu}$  decay using a stopped Kaon beam [195]. Observation of seven candidate events by

4927 E787 and E949 yields  $\mathcal{B}(K^+ \rightarrow \pi^+\nu\bar{\nu}) = (1.73_{-1.05}^{+1.15}) \times 10^{-10}$  when the relative acceptance  
4928 and measured background are taken into account with a likelihood method [842]. It  
4929 has been estimated that, assuming the SM decay rate, a stopped  $K^+$  experiment could  
4930 accumulate hundreds of  $K^+ \rightarrow \pi^+\nu\bar{\nu}$  events, using a copious proton source such as  
4931 Project-X at FNAL [843]. The NA62 experiment at CERN seeks to observe on the order  
4932 of a hundred  $K^+ \rightarrow \pi^+\nu\bar{\nu}$  decays using a decay-in-flight technique in an unseparated 75  
4933 GeV beam.

4934 The experiment E391a has set a limit of  $\mathcal{B}(K_L \rightarrow \pi^0\nu\bar{\nu}) < 670 \times 10^{-10}$  at 90% CL in  
4935 a sample of  $5.1 \times 10^9$   $K_L$  decays [844]. The experimental result is still larger than the  
4936 model-independent limit [827] of  $\mathcal{B}(K_L \rightarrow \pi^0\nu\bar{\nu}) < 14.6 \times 10^{-10}$  at 90% CL implied by  
4937 the  $K^+ \rightarrow \pi^+\nu\bar{\nu}$  results. E391a is currently analyzing an additional  $3.6 \times 10^9$   $K_L$  decays  
4938 and plans to implement an upgraded detector in the experiment E14 at JPARC that  
4939 would have a sensitivity comparable to the expected SM  $K_L \rightarrow \pi^0\nu\bar{\nu}$  decay rate.

4940 The experimental limits on  $K_L \rightarrow \pi^0 e^+ e^-$  and  $K_L \rightarrow \pi^0 \mu^+ \mu^-$  are  $2.8 \times 10^{-10}$  and  
4941  $3.8 \times 10^{-10}$  at 90% CL by the KTeV collaboration [4]. The  $K_L \rightarrow \pi^0 e^+ e^-$  mode suffers  
4942 from an irreducible background from  $K_L \rightarrow \gamma\gamma e^+ e^-$  decays,  $\mathcal{B}(K_L \rightarrow \gamma\gamma e^+ e^-) = (5.95 \pm$   
4943  $0.33) \times 10^{-7}$ , that can be suppressed by a precise diphoton mass resolution. There are  
4944 currently no experiments planned to continue the search for these decays.

## 4945 6.7. Rare $D$ meson decays

### 4946 6.7.1. Rare leptonic decays

4947 In the Standard Model (SM) flavor-changing neutral current (FCNC) decays of charm  
4948 hadrons are highly suppressed by the GIM mechanism [845]. In the process  $D^0 \rightarrow X_u \ell^+ \ell^-$   
4949 this leads to branching fractions of  $\mathcal{O}(10^{-8})$  [846]. However, this process can be enhanced  
4950 by the presence of long-distance contributions, increasing the branching fractions by  
4951 several orders of magnitude [846]. The effect of these long distance contributions from  
4952 intermediate resonances can be separated by examining the invariant mass of the lep-  
4953 ton pair (e.g.  $\phi \rightarrow \ell^+ \ell^-$ ). In radiative charm decays (e.g.  $c \rightarrow u\gamma$ ), the long distance  
4954 contributions are not so easily determined, making it increasingly difficult to study the  
4955 short-distance effects. The branching fractions of the  $D^0 \rightarrow \ell^+ \ell^-$  final state are predicted  
4956 to be  $\mathcal{O}(10^{-13})$  [846], including contributions from long distance processes.

4957 Lepton family-number violating (LFV), and lepton-number violating (LV) decays are  
4958 strictly forbidden in the SM. The processes are allowed in extensions to the SM with  
4959 non-zero neutrino mass but at a very low level [846]. The largest impact is expected to  
4960 come from R-parity violating super-symmetry. Depending on the size of the R-parity  
4961 violating couplings, branching fractions for these processes can be enhanced up to the  
4962  $\mathcal{O}(10^{-6})$  level for differing  $c \rightarrow u\ell^+ \ell^-$  processes.

4963 The search for FCNC processes in charm decays has not received the attention that  
4964 the  $K$  and  $B$  meson sectors have attracted. The current measurements of these decays  
4965 (Tab. 50-52) agree with SM predictions, and there are ongoing efforts to improve both  
4966 theoretical predictions and experimental limits. There is also ongoing effort to measure  
4967 new effects such as  $CP$  violation in these processes.

4968 Therefore, searching for FCNC, LFV, or LV modes in the charm sector is a relatively  
4969 inviting place to investigate new physics in the SM. Similar arguments hold for rare  
4970 decays in the  $K$  and  $B$  sector. However, the charm system is unique in that it couples



Table 50

90% confidence limits on Flavor-changing neutral current, (FCNC), lepton family-number (LFV) violating, or lepton-number (LV) violating decay modes of the  $D^+$  (left) and the  $D_s^+$  (right) [283].

Process	Decay type	Upper limit	Reference	Process	Decay type	Upper limit	Reference
$\pi^+ e^+ e^-$	FCNC	$< 7.4 \times 10^{-6}$	[847]	$\pi^+ e^+ e^-$	N/A <sup>a</sup>	$< 2.7 \times 10^{-4}$	[851]
$\pi^+ \mu^+ \mu^-$	FCNC	$< 3.9 \times 10^{-6}$	[848]	$\pi^+ \mu^+ \mu^-$	N/A <sup>a</sup>	$< 2.6 \times 10^{-5}$	[850]
$\rho^+ \mu^+ \mu^-$	FCNC	$< 5.6 \times 10^{-4}$	[849]	$K^+ e^+ e^-$	FCNC	$< 1.6 \times 10^{-3}$	[851]
$K^+ e^+ e^-$	N/A <sup>a</sup>	$< 6.2 \times 10^{-6}$	[847]	$K^+ \mu^+ \mu^-$	FCNC	$< 3.6 \times 10^{-5}$	[850]
$K^+ \mu^+ \mu^-$	N/A <sup>a</sup>	$< 9.2 \times 10^{-6}$	[850]	$K^{*-} \mu^+ \mu^-$	FCNC	$< 1.4 \times 10^{-3}$	[849]
$\pi^+ e^\pm \mu^\mp$	LFV	$< 3.4 \times 10^{-5}$	[851]	$\pi^+ e^\pm \mu^\mp$	LFV	$< 6.1 \times 10^{-4}$	[851]
$K^+ e^\pm \mu^\mp$	LFV	$< 6.8 \times 10^{-5}$	[851]	$K^+ e^\pm \mu^\mp$	LFV	$< 6.3 \times 10^{-4}$	[851]
$\pi^- e^+ e^+$	LV	$< 3.6 \times 10^{-6}$	[847]	$\pi^- e^+ e^+$	LV	$< 6.9 \times 10^{-4}$	[851]
$\pi^- \mu^+ \mu^+$	LV	$< 4.8 \times 10^{-6}$	[850]	$\pi^- \mu^+ \mu^+$	LV	$< 2.9 \times 10^{-5}$	[850]
$\pi^- e^+ \mu^+$	LV	$< 5.0 \times 10^{-5}$	[851]	$\pi^- e^+ \mu^+$	LV	$< 7.3 \times 10^{-4}$	[851]
$\rho^- \mu^+ \mu^+$	LV	$< 5.6 \times 10^{-4}$	[849]	$K^- e^+ e^+$	LV	$< 6.3 \times 10^{-4}$	[851]
$K^- e^+ e^+$	LV	$< 4.5 \times 10^{-6}$	[847]	$K^- \mu^+ \mu^+$	LV	$< 1.3 \times 10^{-5}$	[850]
$K^- \mu^+ \mu^+$	LV	$< 1.3 \times 10^{-5}$	[850]	$K^- e^+ \mu^+$	LV	$< 6.8 \times 10^{-4}$	[851]
$K^- e^+ \mu^+$	LV	$< 1.3 \times 10^{-4}$	[852]	$K^{*-} \mu^+ \mu^+$	LV	$< 1.4 \times 10^{-3}$	[849]
$K^{*-} \mu^+ \mu^+$	LV	$< 8.5 \times 10^{-4}$	[849]				

<sup>a</sup> These modes are not a useful test for FCNC, because both quarks must change flavor.

Table 51

90% confidence limits on flavor-changing neutral current (FCNC), or lepton-number (LV) violating decay modes of the  $A_c$  [283].

Process	Decay type	Upper limit	Reference
$p\mu^+\mu^-$	FCNC	$< 3.4 \times 10^{-4}$	[849]
$\Sigma^-\mu^+\mu^+$	LV	$< 7.0 \times 10^{-4}$	[849]

4971 an up-type quark to new physics.

4972 It is clear that due to the relatively little experimental progress in this area within the  
 4973 last decade and the large data sets from the flavor factories, that there is a several orders  
 4974 of magnitude in precision to be gained from re-analyzing these measurements with  
 4975 meaningful limits to be derived which may have the potential to constrain parameter  
 4976 space for many new physics models. At present the upper limits for branching fractions  
 4977 for those modes more recently measured [847,848,854] are starting to confine the allowed  
 4978 parameter space of R-parity violating super-symmetric models.

### 4979 6.7.2. $D$ and $D_s$ decay constants from lattice QCD

Quark confinement inside hadrons makes the direct experimental determination of how quarks change from one flavor to another via the weak interactions impossible. Instead we must study experimentally the decay of a hadron, calculate the effect of the strong force

Table 52

90% confidence limits on flavor-changing neutral current (FCNC), lepton family-number (LFV) violating, or lepton-number (LV) violating decay modes of the  $D^0$  [283].

Process	Decay type	Upper limit	Reference	Process	Decay type	Upper limit	Reference
$\gamma\gamma$	FCNC	$< 2.7 \times 10^{-5}$	[853]	$\bar{K}^{*0} \mu^+ \mu^-$	N/A <sup>a</sup>	$< 2.4 \times 10^{-5}$	[856]
$e^+ e^-$	FCNC	$< 1.2 \times 10^{-6}$	[854]	$\pi^+ \pi^- \pi^0 \mu^+ \mu^-$	FCNC	$< 8.1 \times 10^{-4}$	[849]
$\mu^+ \mu^-$	FCNC	$< 1.3 \times 10^{-6}$	[854]	$e^\pm \mu^\mp$	LFV	$< 8.1 \times 10^{-7}$	[854]
$\pi^0 e^+ e^-$	FCNC	$< 4.5 \times 10^{-5}$	[855]	$\pi^0 e^\pm \mu^\mp$	LFV	$< 8.6 \times 10^{-5}$	[855]
$\pi^0 \mu^+ \mu^-$	FCNC	$< 1.8 \times 10^{-4}$	[849]	$\eta e^\pm \mu^\mp$	LFV	$< 1.0 \times 10^{-4}$	[855]
$\eta e^+ e^-$	FCNC	$< 1.1 \times 10^{-4}$	[855]	$\pi^+ \pi^- e^\pm \mu^\mp$	LFV	$< 1.5 \times 10^{-5}$	[856]
$\eta \mu^+ \mu^-$	FCNC	$< 5.3 \times 10^{-4}$	[855]	$\rho^0 e^\pm \mu^\mp$	LFV	$< 4.9 \times 10^{-5}$	[855]
$\pi^+ \pi^- e^+ e^-$	FCNC	$< 3.73 \times 10^{-4}$	[856]	$\omega e^\pm \mu^\mp$	LFV	$< 1.2 \times 10^{-4}$	[855]
$\rho^0 e^+ e^-$	FCNC	$< 1.0 \times 10^{-4}$	[855]	$K^- K^+ e^\pm \mu^\mp$	LFV	$< 1.8 \times 10^{-4}$	[856]
$\pi^+ \pi^- \mu^+ \mu^-$	FCNC	$< 3.0 \times 10^{-5}$	[856]	$\phi e^\pm \mu^\mp$	LFV	$< 3.4 \times 10^{-5}$	[855]
$\rho^0 \mu^+ \mu^-$	FCNC	$< 2.2 \times 10^{-5}$	[856]	$\bar{K}^0 e^\pm \mu^\mp$	LFV	$< 1.0 \times 10^{-4}$	[855]
$\omega e^+ e^-$	FCNC	$< 1.8 \times 10^{-4}$	[855]	$K^- \pi^+ e^\pm \mu^\mp$	LFV	$< 5.53 \times 10^{-4}$	[855]
$\omega \mu^+ \mu^-$	FCNC	$< 8.3 \times 10^{-4}$	[855]	$\bar{K}^{*0} e^\pm \mu^\mp$	LFV	$< 8.3 \times 10^{-5}$	[856]
$K^+ K^- e^+ e^-$	FCNC	$< 3.15 \times 10^{-4}$	[856]	$\pi^- \pi^- e^+ e^+ + \text{c.c}$	LV	$< 1.12 \times 10^{-4}$	[856]
$\phi e^+ e^-$	FCNC	$< 5.2 \times 10^{-5}$	[855]	$\pi^- \pi^- \mu^+ \mu^+ + \text{c.c}$	LV	$< 2.9 \times 10^{-5}$	[856]
$K^+ K^- \mu^+ \mu^-$	FCNC	$< 3.3 \times 10^{-5}$	[856]	$K^- \pi^- e^+ e^+ + \text{c.c}$	LV	$< 2.06 \times 10^{-4}$	[856]
$\phi \mu^+ \mu^-$	FCNC	$< 3.1 \times 10^{-5}$	[856]	$K^- \pi^- \mu^+ \mu^+ + \text{c.c}$	LV	$< 3.9 \times 10^{-4}$	[856]
$\bar{K}^0 e^+ e^-$	N/A <sup>a</sup>	$< 1.1 \times 10^{-4}$	[855]	$K^- K^- e^+ e^+ + \text{c.c}$	LV	$< 1.52 \times 10^{-4}$	[856]
$\bar{K}^0 \mu^+ \mu^-$	N/A <sup>a</sup>	$< 2.6 \times 10^{-4}$	[849]	$K^- K^- \mu^+ \mu^+ + \text{c.c}$	LV	$< 9.4 \times 10^{-5}$	[856]
$K^- \pi^+ e^+ e^-$	FCNC	$< 3.85 \times 10^{-4}$	[856]	$\pi^- \pi^- e^+ \mu^+ + \text{c.c}$	LV	$< 7.9 \times 10^{-5}$	[856]
$\bar{K}^{*0} e^+ e^-$	N/A <sup>a</sup>	$< 4.7 \times 10^{-5}$	[856]	$K^- \pi^- e^+ \mu^+ + \text{c.c}$	LV	$< 2.18 \times 10^{-4}$	[856]
$K^+ \pi^+ \mu^+ \mu^-$	FCNC	$< 3.59 \times 10^{-4}$	[856]	$K^- K^- e^+ \mu^+ + \text{c.c}$	LV	$< 5.7 \times 10^{-5}$	[856]

<sup>a</sup> These modes are not a useful test for FCNC, because both quarks must change flavor.

on the quarks in the hadron and then correct for this to expose the quark interaction with the W boson. The simplest such hadron decay is annihilation of a charged pseudoscalar into a W and thence into a lepton and an antineutrino. The leptonic width of such a pseudoscalar meson,  $P$ , of quark content  $a\bar{b}$  (or  $\bar{a}b$ ) is given by:

$$\Gamma(P \rightarrow l\nu_l(\gamma)) = \frac{G_F^2 |V_{ab}|^2}{8\pi} f_P^2 m_l^2 m_P \left(1 - \frac{m_l^2}{m_P^2}\right)^2. \quad (313)$$

$V_{ab}$  is from the Cabibbo-Kobayashi-Maskawa (CKM) matrix element which encapsulates the Standard Model description of quark coupling to the W.  $f_P$ , the decay constant, parametrizes the amplitude for the meson annihilation to a W and is basically the probability for the quark and antiquark to be in the same place. It is defined by:

$$f_P m_P = \langle 0 | \bar{\psi}(x) \gamma_0 \gamma_5 \psi(x) | P(\mathbf{p} = 0) \rangle \quad (314)$$

4980 Note that  $f_P$  is a property of the meson in pure QCD. In the real world there is also elec-  
 4981 tromagnetism and so the experimental rate must be corrected for this. It is a small (1-2%)  
 4982 effect, except for very heavy mesons ( $B$ s) decaying to very light leptons (electrons) [259].  
 4983 If  $V_{ab}$  is known from elsewhere an experimental value for  $\Gamma$  gives  $f_P$ , to be compared to  
 4984 theory. If not, an accurate theoretical value for  $f_P$ , combined with experiment, can yield  
 4985 a value of  $V_{ab}$ .

4986 Accuracy in both experiment and theory is important for useful tests of the Standard  
 4987 Model. Here the numerical techniques of lattice QCD come to the fore for the theoretical  
 4988 calculation because it is now possible to do such calculations accurately [91] and the  
 4989 pseudoscalar decay constant is one of the simplest quantities to calculate in lattice QCD.

A lattice QCD calculation proceeds by splitting space-time up into a lattice of points  
 (with spacing  $a$ ) and generating sets of gluon fields on the lattice that are ‘typical snap-  
 shots of the vacuum’. For accurate calculations these snapshots need to include the effect  
 of quark-antiquark pairs, known as ‘sea’ quarks, generated by energy fluctuations in the  
 vacuum. The important sea quarks are those which cost little energy to make i.e. the  
 light  $u$ ,  $d$  and  $s$ . Unfortunately in lattice QCD it is numerically expensive to work with  
 sea  $u$  and  $d$  masses that are close to their physical values and we have to extrapolate to  
 the physical point from heavier values using chiral perturbation theory. Valence quarks  
 that make up a hadron are propagated through these gluon fields, allowing any number  
 of interactions. We tie together appropriate valence quark and antiquark propagators to  
 make, for example, a meson correlator which is then printed out as a function of lattice  
 time,  $t$  (we sum on spatial lattice sites to project on to zero spatial momentum). We fit  
 as a function of  $t$  to a multi-exponential form:

$$26 <0|H^\dagger(0)H(t)|0> = \sum_i A_i(e^{-E_i t} + e^{-E_i(T-t)}) \quad (315)$$

4990 where  $T$  is the time extent of the lattice. The smallest value of  $E_i$  (corresponding to  
 4991 the state that survives to large  $t$ ) is the ground state mass in that channel, and  $A_i$  is  
 4992 the square of the matrix element between the vacuum and  $P$  of the operator  $H$  used to  
 4993 create and destroy the hadron. If  $H$  is the local temporal axial current of equation 314  
 4994 (and this is the operator used if the valence quark and antiquark are simply tied together  
 4995 at the same start and end points matching colors and spins) then  $A_0$  will be directly  
 4996 related to the decay constant of the ground state pseudoscalar.

4997 For  $K$  and  $\pi$  mesons several very accurate decay constant determinations have been  
 4998 done now in lattice QCD including the full effect of  $u$ ,  $d$  and  $s$  quarks in the sea, and at  
 4999 several values of the lattice spacing. Extrapolations to the physical point in the  $u/d$  mass  
 5000 and  $a = 0$  have been done with a full error budget. The lattice value of  $f_K/f_\pi$  can be  
 5001 used to determine  $V_{us}$  to 1% accuracy. (\* This is presumably described in the subsection  
 5002 on strange physics, so you only need a reference to that here \*).

5003 For the charged charmed mesons  $D_d$  and  $D_s$  the lattice determination of the decay  
 5004 constant can be compared to an experimental one derived from the leptonic decay rate if  
 5005 values of  $V_{cd}$  and  $V_{cs}$  are assumed (usually  $V_{us} = V_{cd}$  and  $V_{ud} = V_{cs}$ ). This is an important  
 5006 test of modern lattice techniques, that can be used to calibrate lattice errors. The errors  
 5007 expected in the  $D/D_s$  case are similar to those for  $K/\pi$ . The statistical errors on the raw  
 5008 lattice numbers are similar, and the extrapolations that must be done in the  $u/d$  mass  
 5009 are less of an issue than for  $\pi$ . Indeed for the  $D_s$ , which has no valence  $u/d$  quark, there  
 5010 is very little dependence on the (sea)  $u/d$  mass and so very little extrapolation.

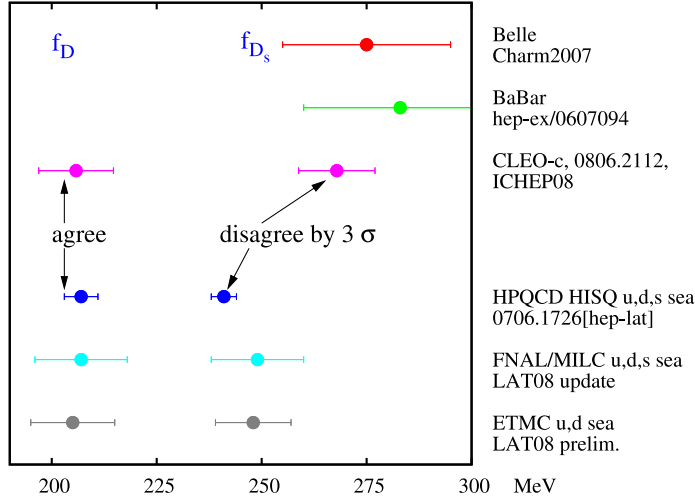


Fig. 53. A comparison of lattice results for the  $D$  and  $D_s$  decay constant [338,427,857] and experimental results obtained from the leptonic decay rate using CKM elements  $V_{cs}$  and  $V_{cd}$  from elsewhere [455,858–861]. There is agreement between lattice and experiment for  $f_D$ , but not for  $f_{D_s}$ .

The extrapolations to  $a = 0$  are worse for  $D/D_s$  than for  $K/\pi$  and the reason is that the charm quark mass in lattice units,  $m_c a$ , is relatively large. Typically a lattice result at non-zero lattice spacing will have a power series dependence on the lattice spacing with the scale of the  $a$ -dependent terms set by a typical momentum inside the bound state. Extrapolations to  $a = 0$  can then be done using this functional form, and the resulting error will depend on the size of the extrapolation. For charm physics the scale of the  $a$ -dependent terms is set by  $m_c$  and we expect

$$m = m_{a=0}(1 + A(m_c a)^2 + B(m_c a)^4 + \dots). \quad (316)$$

5011 The extrapolation can then be quite severe, and will determine the final error, if we do  
 5012 not take steps to control or eliminate terms in this series by improving the action.

5013 The Highly Improved Staggered Quark (HISQ) action for charm quarks [862] elimi-  
 5014 nates the  $(m_c a)^2$  term and results at three values of the lattice spacing then give an  
 5015 accurate extrapolation to  $a = 0$  with a 2% final error [338]. Alternatives to this are the  
 5016 ‘Fermilab interpretation’ of improved Wilson quarks [857] and the twisted mass formal-  
 5017 ism [427]. Both have larger errors than for HISQ at present. Improved Wilson quarks  
 5018 have discretization errors at  $\alpha_s(m_c a)$  in principle but the Fermilab interpretation re-  
 5019 moves the leading errors that come from the kinetic energy, and experience has shown  
 5020 that  $a$ -dependence is small in this formalism. However, relativity is given up and this  
 5021 means, for example, that the masses of mesons cannot be as accurately tuned and a  
 5022 renormalisation factor is needed to relate the decay constant on the lattice to a result  
 5023 appropriate to the real world (at  $a = 0$ ). The twisted mass formalism uses a relativistic  
 5024 framework with errors appearing first at  $(m_c a)^2$ . It has so far been applied at two values  
 5025 of the lattice spacing for gluon field configurations that do not include  $s$  sea quarks, so  
 5026 are not completely realistic.

5027 Fig. 53 shows a comparison of these lattice calculations to new experimental results  
 5028 from CLEO-c for both  $f_D$  and  $f_{D_s}$  (which appeared after [338,857]) and older results for  
 5029  $f_{D_s}$  from BaBar [861]. The good agreement between lattice and experiment for  $f_D$  (and

5030  $f_K$  and  $f_\pi$ ) contrasts with the  $3\sigma$  disagreement for  $f_{D_s}$  and it has been suggested that  
 5031 this is a harbinger of new physics [863]. Improved experimental errors for  $f_{D_s}$  will shed  
 5032 light on this. Meanwhile, lattice calculations and their systematic errors are also being  
 5033 tested against other quantities in charm physics [864].

### 5034 6.7.3. Experimental results on $f_D$

Fully leptonic decays of  $D_{(s)}^+$  mesons depend upon both the weak and strong interactions. The weak part is straightforward to describe in terms of the annihilation of the quark antiquark pair to a  $W^+$  boson. The strong interaction is required to describe the gluon exchange between the quark and antiquark. The strong interaction effects are parametrized by the decay constant,  $f_{D_{(s)}^+}$ , such that the total decay rate is given by

$$\Gamma(D_{(s)}^+ \rightarrow l^+\nu) = \frac{G_F^2}{8\pi} f_{D_{(s)}^+}^2 m_l^2 M_{D_{(s)}^+} [1 - \frac{m_l^2}{M_{D_{(s)}^+}^2}]^2 |V_{cd(s)}|^2,$$

5035 where  $G_F$  is the Fermi coupling constant,  $M_{D_{(s)}^+}$  and  $m_l$  are the  $D_{(s)}^+$  meson and final  
 5036 state lepton masses, respectively, and  $V_{cd(s)}$  is a Cabibbo-Kobayashi-Maskawa (CKM)  
 5037 matrix element. The values of  $V_{cd}$  and  $V_{cs}$  can be equated  $V_{us}$  and  $V_{ud}$ , which are well  
 5038 known. Therefore, within the standard model, measurements of the fully leptonic decay  
 5039 rates allow a determination of  $f_{D_{(s)}^+}$ .

5040 Measurements of  $f_{D_{(s)}^+}$  can be compared to calculations from theories of QCD, the most  
 5041 precise of which use unquenched lattice techniques (see for example Ref. [338]). Similar  
 5042 calculations of strong parameters in  $B$  meson decay are relied upon to extract CKM  
 5043 matrix elements, such as  $|V_{td}|/|V_{ts}|$  from the rates of  $B$  mixing. Therefore, comparing  
 5044 predictions for  $f_{D_{(s)}^+}$  to measurements is important for validating the QCD calculation  
 5045 techniques. Deviations of experimental measurements from theoretical predictions may  
 5046 be a consequence of non-SM physics (see for example Ref. [863]).

5047 CLEO-c provides the most precise experimental determinations of  $f_{D^+}$  [859] and  $f_{D_s^+}$   
 5048 [256, 865] to date. All measurements at CLEO-c exploit the recoil technique described in  
 5049 Sec. 3.2.6.

The determination of  $f_{D^+}$  uses six hadronic decays of the  $D^-$  as tags:  $K^+\pi^-\pi^-$ ,  
 $K^+\pi^-\pi^-\pi^0$ ,  $K_S^0\pi^-$ ,  $K_S^0\pi^-\pi^-\pi^+$ ,  $K_S^0\pi^-\pi^0$  and  $K^+K^-\pi^-$ . The analysis is performed on  
 818  $\text{pb}^{-1}$  of  $e^+e^- \rightarrow \psi(3770) \rightarrow D\bar{D}$  data. 460,000 tagged events are reconstructed. The  
 fully leptonic decay reconstructed is  $D^+ \rightarrow \mu^+\nu_\mu$ . Events are considered as signal if they  
 contain a single additional charged track of opposite charge to the fully reconstructed  
 tag decay. Events with additional neutral energy deposits in the calorimeter are vetoed.  
 The beam-energy constrained missing-mass squared,  $MM^2$  is computed:

$$MM^2 = (E_{beam} - E_{\mu^+})^2 - (-\mathbf{p}_{D^-} - \mathbf{p}_{\mu^+})^2,$$

5050 where  $E_{beam}$  is the beam energy,  $\mathbf{p}_{D^-}$  is the three-momentum of the fully reconstructed  
 5051  $D^-$  decay and  $E_{\mu^+}$  ( $\mathbf{p}_{\mu^+}$ ) is the energy (three-momentum) of the  $\mu^+$  candidate. For  
 5052 signal events the measured  $MM^2$  will be close to zero (the  $\nu$  mass).

5053 The sample of events is then divided depending upon whether the energy the  $\mu^+$   
 5054 candidate deposits in the electromagnetic calorimeter is more or less than 300 MeV;  
 5055 98.8% of  $\mu^+$  deposit less than 300 MeV. The yield of  $D^+ \rightarrow \mu^+\nu$  events is extracted by  
 5056 a fit to the  $MM^2$  distribution of  $\mu$  candidates depositing less than 300 MeV.

The fit to data produces the following results:

$$\mathcal{B}(D^+ \rightarrow \mu^+\nu) = (3.82 \pm 0.32 \pm 0.09) \times 10^{-4},$$

and

$$f_{D^+} = (205.8 \pm 8.5 \pm 2.5) \text{ MeV},$$

5057 where first uncertainty is statistical and the second uncertainty is systematic. Further-  
 5058 more, the ratio between  $\mu\nu$  and the small  $D^+ \rightarrow \tau^+(\pi^+\nu)\nu$  contribution has been fixed to  
 5059 the SM expectation. The systematic uncertainty contains significant contributions from  
 5060 radiative corrections, particle identification efficiency and background assumptions. The  
 5061 measurement is in good agreement with the theoretical prediction of Follana *et al.* [338]  
 5062 of  $f_{D^+} = (207 \pm 4) \text{ MeV}$ .

5063 The CLEO-c measurements of  $f_{D_s^+}$  are made with a data set corresponding to  $600 \text{ pb}^{-1}$   
 5064 of integrated luminosity collected at a center-of-mass energy of 4.170 GeV, which is close  
 5065 to the maximum of the  $D_s^+ D_s^{*-}$  production cross-section. One analysis reconstructs  
 5066  $D_s^+ \rightarrow \mu^+\nu$  and  $D_s^+ \rightarrow \tau^+(\pi^+\bar{\nu})\nu$  events [256] and the other reconstructs  $D_s^+ \rightarrow$   
 5067  $\tau^+(e^+\nu\bar{\nu})\nu$  events [865]. These are briefly reviewed in turn.

5068 The analysis of  $D_s^+ \rightarrow \mu^+\nu$  and  $D_s^+ \rightarrow \tau^+(\pi^+\bar{\nu})\nu$  reconstructs  $D_s^{*-} \rightarrow D_s^- \gamma$  tags  
 5069 in nine hadronic  $D_s^+$  decay modes. The number of tags reconstructed is approximately  
 5070 44,000. Signal candidates are reconstructed in an almost identical fashion to the mea-  
 5071 surements of  $f_{D^+}$  and the resulting  $MM^2$  distribution and fit are shown in Fig. 54 (a).  
 5072 The principal results from this analysis are:

$$\mathcal{B}(D_s^+ \rightarrow \mu^+\nu) = (0.591 \pm 0.037 \pm 0.018)\%,$$

$$\mathcal{B}(D_s^+ \rightarrow \tau^+\nu) = (6.42 \pm 0.81 \pm 0.18)\%,$$

and

$$f_{D_s^+} = (263.3 \pm 8.2 \pm 3.9) \text{ MeV}.$$

5073 The main systematic uncertainty is from the  $D_s^{*+}$  tag yields.

5074 The selection of  $D_s^+ \rightarrow \tau^+(e^+\nu\bar{\nu})\nu$  only uses three of the purest  $D_s^-$  tags:  $\phi\pi^-$ ,  $K^{*0}K^-$   
 5075 and  $K^-K_S^0$ . There are 26,300 tagged events reconstructed. Events with a single charged  
 5076 track of opposite sign, which is compatible with being an electron, are selected as signal  
 5077 candidates. The distribution of extra energy,  $E_{\text{extra}}$ , in these events, with the background  
 5078 evaluated in the tag  $D_s^-$  mass sidebands subtracted, is shown in Fig. 54 (a). The signal  
 5079 peaks close to 150 MeV, which is the energy of the photon in  $D_s^{*+} \rightarrow D_s^+ \gamma$  decays. A  
 5080 binned fit to this distribution gives the following results:

$$\mathcal{B}(D_s^+ \rightarrow \tau^+\nu) = (0.530 \pm 0.47 \pm 0.22)\%$$

and

$$f_{D_s^+} = (252.5 \pm 11.1 \pm 5.2) \text{ MeV}.$$

5081 The main systematic uncertainty is from the estimation of the  $D_s^+ \rightarrow K_L^0 e^+\nu$  peaking  
 5082 backgrounds.

The two results for  $f_{D_s^+}$  give an average value of

$$f_{D_s^+} = (259.5 \pm 6.6 \pm 3.1) \text{ MeV},$$

5083 which is  $2.3\sigma$  larger than the recent lattice calculation  $f_{D_s^+} = (241 \pm 3) \text{ MeV}$  [338].

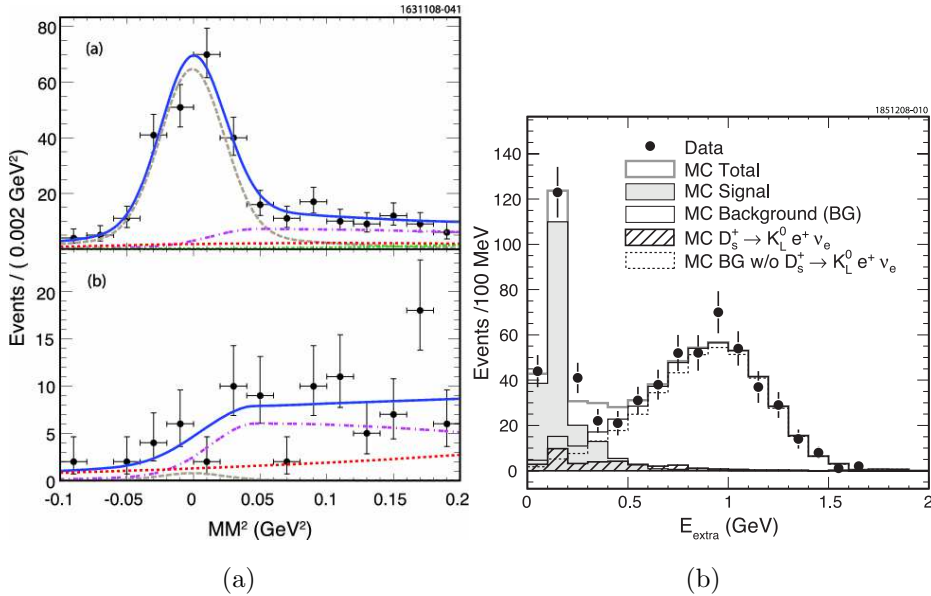


Fig. 54. Fits to the (a)  $MM^2$  and (b)  $E_{\text{extra}}$  distributions used to extract the  $D_s^+ \rightarrow l\nu$  yields at CLEO-c. In (a) the solid line is the total fit result, the dashed line is the  $\mu\nu$  component, the dot-dashed line is the  $\tau\nu$  component and the dotted line is background.

5084 *BABAR* [861] and Belle [454] have also measured  $f_{D_s^+}$ , but the results are much less  
 5085 precise than those from CLEO-c. However, these results were made with a fraction of  
 5086 their data sets and will be updated.

## 5087 7. Measurements of $\Gamma$ , $\Delta\Gamma$ , $\Delta m$ and mixing-phases in $K$ , $B$ , and $D$ meson 5088 decays

5089 The phenomenon of meson-antimeson oscillation, being a flavor changing neutral cur-  
 5090 rent (FCNC) process, is very sensitive to heavy degrees of freedom propagating in the  
 5091 mixing amplitude and, therefore, it represents one of the most powerful probes of New  
 5092 Physics (NP). In  $K$  and  $B_{d,s}$  systems the comparison of observed meson mixing with the  
 5093 Standard Model (SM) prediction has achieved a good accuracy and plays a fundamental  
 5094 role in constraining not only the Unitarity Triangle (UT) but also possible extensions of  
 5095 the SM. Very recently the evidence for flavor oscillation in the  $D$  system has been also  
 5096 revealed, providing complementary information with respect to the  $K$  and  $B_{d,s}$  systems,  
 5097 since it involves mesons with up-type quarks.

5098 We recall here the basic formalism of meson-antimeson mixing, starting from the  $K$   
 5099 system. In principle, one could describe neutral meson mixing with a unique formalism.  
 5100 However, we present different formalism for the  $K$  and  $B$  and  $D$  mixing to make contact  
 5101 with previous literature, considering also that different approximations are used.

The neutral Kaons  $K^0 = (\bar{s}d)$  and  $\bar{K}^0 = (s\bar{d})$  are flavor eigenstates which in the SM can mix via weak interactions through the box diagrams shown in Fig. 55. In the presence of flavor mixing the time evolution of the  $K^0$ - $\bar{K}^0$  system is described by

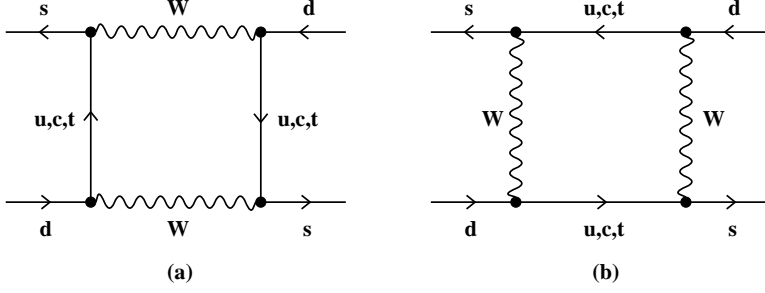


Fig. 55. Box diagrams contributing to  $K^0 - \bar{K}^0$  mixing in the SM.

$$i \frac{d}{dt} \begin{pmatrix} K^0(t) \\ \bar{K}^0(t) \end{pmatrix} = \hat{H} \begin{pmatrix} K^0(t) \\ \bar{K}^0(t) \end{pmatrix}, \quad (317)$$

5102 where the the Hamiltonian  $\hat{H}$  is a  $2 \times 2$  non-hermitian matrix which can be decomposed  
 5103 as  $\hat{H} = \hat{M} - i\hat{\Gamma}/2$ . The matrices  $\hat{M}$  and  $\hat{\Gamma}$  are hermitian and their elements respectively  
 5104 describe the dispersive and absorptive part of the time evolution of the Kaon states.

5105 We note that, in terms of  $K^0$  and  $\bar{K}^0$ , the CP eigenstates are given by<sup>19</sup>

$$K_{\pm} = \frac{1}{\sqrt{2}}(K^0 \pm \bar{K}^0), \quad CP|K_{\pm}\rangle = \pm|K_{\pm}\rangle. \quad (318)$$

The Hamiltonian eigenstates, called *short* and *long* due to the significant difference between their decay time, can be written as

$$K_S = \frac{K_+ + \bar{\epsilon} K_-}{\sqrt{(1 + |\bar{\epsilon}|^2)}}, \quad K_L = \frac{K_- + \bar{\epsilon} K_+}{\sqrt{(1 + |\bar{\epsilon}|^2)}}. \quad (319)$$

They coincide with CP eigenstates but for a small admixture governed by a small complex parameter  $\bar{\epsilon}$ , defined as

$$\frac{1 - \bar{\epsilon}}{1 + \bar{\epsilon}} = -\sqrt{\frac{M_{12}^* - i\Gamma_{12}^*/2}{M_{12} - i\Gamma_{12}/2}}. \quad (320)$$

5106

In the  $K$  system, the smallness of  $\bar{\epsilon} \simeq \mathcal{O}(10^{-3})$  implies  $\text{Im}M_{12} \ll \text{Re}M_{12}$  and  $\text{Im}\Gamma_{12} \ll \text{Re}\Gamma_{12}$ . Consequently, the mass difference between the mass eigenstates  $K_L$  and  $K_S$  can be well approximated by the simple expression:

$$\Delta M_K \equiv M_{K_L} - M_{K_S} = -2\text{Re}M_{12}, \quad (321)$$

where the off-diagonal element  $M_{12}$  is given by

$$M_{12} = \langle K^0 | \mathcal{H}_{eff}^{\Delta S=2} | \bar{K}^0 \rangle, \quad (322)$$

5107 with  $\mathcal{H}_{eff}^{\Delta S=2}$  being the effective Hamiltonian that describes  $\Delta S = 2$  transitions, defined in  
 5108 Sec. 2.1. Notice that Eq. (321) only gives the short-distance part of  $\Delta M_K$ . Long-distance  
 5109 contributions, however, are present due to the exchange of light meson states and are  
 5110 difficult to estimate. On the other hand, the imaginary part of the amplitudes discussed

<sup>19</sup>The phase convention is chosen so that  $CP|K^0\rangle = |\bar{K}^0\rangle$  and  $CP|\bar{K}^0\rangle = |K^0\rangle$ .



5111 below are not affected by these contributions, which have Cabibbo-suppressed imaginary  
 5112 part.

5113 We now discuss the parameters that in the  $K$  system are used to measure indirect and  
 5114 direct CP violations, which are  $\varepsilon_K$  and  $\varepsilon'_K/\varepsilon_K$ .

Since a two pion final state is CP even while a three pion final state is CP odd,  $K_S$   
 and  $K_L$  preferably decay to  $2\pi$  and  $3\pi$  respectively, via the following CP conserving  
 decay modes:  $K_L \rightarrow 3\pi$  (via  $K_2$ ),  $K_S \rightarrow 2\pi$  (via  $K_1$ ). However, since  $K_L$  and  $K_S$   
 are not CP eigenstates, they may decay with small branching fractions as follows:  $K_L \rightarrow 2\pi$   
 (via  $K_1$ ),  $K_S \rightarrow 3\pi$  (via  $K_2$ ). This CP violation is called indirect as it proceeds not  
 via explicit breaking of the CP symmetry in the decay itself but via the mixing of the  
 CP state with opposite CP parity to the dominant one. We note that  $\bar{\varepsilon}$  depends on  
 the phase convention of the  $K$  meson states and hence it is not measurable by itself. A  
 phase-independent parameter which provides a measure of the indirect CP violation is

$$\varepsilon_K = \frac{A(K_L \rightarrow (\pi\pi)_{I=0})}{A(K_S \rightarrow (\pi\pi)_{I=0})}, \quad (323)$$

which, using the already-mentioned approximations as well as  $\Delta M \simeq -\Delta\Gamma$  and  $\Gamma_{12} \simeq$   
 $(A_0^*)^2$ , is related to  $\bar{\varepsilon}$  by

$$\varepsilon_K = \bar{\varepsilon} + i\xi = \left( \frac{\text{Im}M_{12}}{2\text{Re}M_{12}} + \xi \right) \exp(i\phi_\varepsilon) \sin\phi_\varepsilon, \quad \text{with} \quad \xi = \frac{\text{Im}A_0}{\text{Re}A_0}, \quad (324)$$

5115 where the phase  $\phi_\varepsilon$  is measured to be  $(43.51 \pm 0.05)^\circ$  [4]. The amplitude  $A_0$  appearing  
 5116 in Eq. (324) is defined through

$$\begin{aligned} A(K^0 \rightarrow \pi^+\pi^-) &= \sqrt{\frac{2}{3}}A_0e^{i\delta_0} + \sqrt{\frac{1}{3}}A_2e^{i\delta_2}, \\ A(K^0 \rightarrow \pi^0\pi^0) &= \sqrt{\frac{2}{3}}A_0e^{i\delta_0} - 2\sqrt{\frac{1}{3}}A_2e^{i\delta_2}, \end{aligned} \quad (325)$$

5117 where the subscript  $I = 0, 2$  denotes states with isospin 0, 2, and  $\delta_{0,2}$  are the correspond-  
 5118 ing strong phases, while the weak CKM phases are contained in  $A_0$  and  $A_2$ .

While indirect CP violation reflects the fact that the mass eigenstates are not CP  
 eigenstates, so-called direct CP violation is realized via a direct transition of a CP odd  
 to a CP even state or vice-versa. A measure of the direct CP violation in  $K_L \rightarrow \pi\pi$  is  
 characterized by a complex parameter  $\varepsilon'_K$  defined as<sup>20</sup>

$$\varepsilon'_K = \frac{1}{\sqrt{2}}\text{Im}\left(\frac{A_2}{A_0}\right)e^{i\Phi}, \quad \Phi = \pi/2 + \delta_2 - \delta_0, \quad (326)$$

with the  $A_{0,2}$  amplitudes defined in Eq. (325). By extracting the strong phases  $\delta_{0,2}$   
 from  $\pi\pi$  scattering, it turns out that  $\Phi \approx \pi/4$ . Experimentally the ratio  $\varepsilon'_K/\varepsilon_K$  can be  
 determined by measuring the ratios

$$\eta_{00} = \frac{A(K_L \rightarrow \pi^0\pi^0)}{A(K_S \rightarrow \pi^0\pi^0)}, \quad \eta_{+-} = \frac{A(K_L \rightarrow \pi^+\pi^-)}{A(K_S \rightarrow \pi^+\pi^-)}. \quad (327)$$

In fact, from Eqs. (327) and (325), one finds

$$\eta_{00} \simeq \varepsilon_K - 2\varepsilon'_K, \quad \eta_{+-} \simeq \varepsilon_K + \varepsilon'_K, \quad (328)$$

<sup>20</sup> Actually direct CP violation is accounted for by  $\text{Re}(\varepsilon'_K)$ .

by exploiting the smallness of  $\varepsilon_K$  and  $\varepsilon'_K$ , using  $\text{Im}A_i \ll \text{Re}A_i$  and  $\omega = \text{Re}A_2/\text{Re}A_0 = 0.045 \ll 1$ , which corresponds to the  $\Delta I = 1/2$  rule. The ratio  $\varepsilon'_K/\varepsilon_K$  can then be measured from

$$\left| \frac{\eta_{00}}{\eta_{+-}} \right|^2 \simeq 1 - 6 \text{Re} \left( \frac{\varepsilon'_K}{\varepsilon_K} \right). \quad (329)$$

The formalism recalled in the case of the  $K$  system is basically the same for the  $B_d$  and  $B_s$  systems. There is however a notation difference for the neutral mass eigenstates, which are denoted *heavy* and *light* and are expressed in terms of the flavor eigenstates as

$$B_q^{L,H} = \frac{1}{\sqrt{(1 + |(q/p)_q|^2)}} (B_q \pm (q/p)_q \bar{B}_q), \quad (q = d, s) \quad (330)$$

5119 with  $(q/p)_q$  parameterizing indirect CP violation. This parameter is similar to  $\bar{\varepsilon}$  for  
5120 Kaons. Comparing Eqs. (319) and (330), one finds  $q/p = (1 - \bar{\varepsilon})/(1 + \bar{\varepsilon})$ .

5121 Similarly to the Kaon case, the phase of  $(q/p)_q$  depends on the phase convention of the  
5122  $B$  meson states. However the absolute value  $|(q/p)_q|$  can be measured. Further interesting  
5123 experimental observables in the  $B_d$  and  $B_s$  systems are the mass and width differences:  
5124  $\Delta M_{B_q} \equiv M_{B_H} - M_{B_L}$  and  $\Delta \Gamma_{B_q} \equiv \Gamma_{B_L} - \Gamma_{B_H}$ . They can be written in terms of the  
5125 dispersive,  $M_{12}^q$ , and absorptive,  $\Gamma_{12}^q$ , matrix elements as

$$\begin{aligned} (\Delta M_{B_q})^2 - \frac{1}{4}(\Delta \Gamma_{B_q})^2 &= 4|M_{12}^q|^2 - |\Gamma_{12}^q|^2, \\ \Delta M_{B_q} \Delta \Gamma_{B_q} &= -4\text{Re}(M_{12}^q \Gamma_{12}^{q*}), \quad |(q/p)_q| = \left| \sqrt{\frac{2M_{12}^{q*} - i\Gamma_{12}^{q*}}{2M_{12}^q - i\Gamma_{12}^q}} \right|. \end{aligned} \quad (331)$$

The dispersive element  $M_{12}^q$  is related to the matrix element of the effective  $\Delta B = 2$  Hamiltonian, defined in Sec. 2.1, as it can be straightforwardly derived from Eq. (322). The absorptive matrix element  $\Gamma_{12}^q$  can be written as

$$\Gamma_{12}^q = \frac{1}{2M_{B_q}} \text{Disc} \langle B_q | i \int d^4x \mathcal{T} (\mathcal{H}_{eff}^{\Delta B=1}(x) \mathcal{H}_{eff}^{\Delta B=1}(0)) | \bar{B}_q \rangle, \quad (332)$$

5126 where “Disc” picks up the discontinuities across the physical cut in the time-ordered  
5127 product of the  $\Delta B = 1$  Hamiltonians, defined in Sec. 2.1.

The relations in Eq. (331) can be simplified by exploiting the smallness of the ratio  $\Gamma_{12}^q/M_{12}^q \sim \mathcal{O}(m_b^2/m_t^2) \sim 10^{-3}$  that allows to neglect  $\mathcal{O}(m_b^4/m_t^4)$  terms, so that one can write

$$\Delta M_{B_q} = 2|M_{12}^q|, \quad \Delta \Gamma_{B_q} = -\Delta M_{B_q} \text{Re} \left( \frac{\Gamma_{12}^q}{M_{12}^q} \right), \quad |(q/p)_q| = 1 - \frac{1}{2} \text{Im} \left( \frac{\Gamma_{12}^q}{M_{12}^q} \right). \quad (333)$$

Other important CP-violating observables, associated in the CKM phase convention to the phases of the  $B_q$  mixing amplitudes, are the CKM angles

$$\beta = \arg \left( -\frac{V_{cb}^* V_{cd}}{V_{tb}^* V_{td}} \right), \quad \beta_s = \arg \left( -\frac{V_{tb}^* V_{ts}}{V_{cb}^* V_{cs}} \right). \quad (334)$$

5128 Note that  $V_{cb}^* V_{cd}$  and  $V_{cb}^* V_{cs}$  are approximately real in the CKM phase convention so  
5129 that  $M_{12}^d \simeq |M_{12}^d| e^{2i\beta}$  and  $M_{12}^s \simeq |M_{12}^s| e^{-2i\beta_s}$ . Moreover, the two angles have different  
5130 size: we have  $\beta \sim 1$  and  $\beta_s \sim \lambda^2 \sim \mathcal{O}(10^{-2})$ .

The angle  $\beta$  can be measured, for instance, in the time-dependent CP asymmetry of  $b \rightarrow c\bar{c}s$  transitions. In particular, considering the golden channel  $B_d \rightarrow J/\psi K_S$  and neglecting doubly Cabibbo-suppressed contributions to the decay amplitudes, one obtains

$$a_{CP}^{B \rightarrow J/\psi K_S}(t) = \sin(2\beta) \sin(\Delta M_{B_d} t). \quad (335)$$

We refer the reader to Sec. 7.2.3 for more details. Similarly the angle  $\beta_s$  can be extracted from the decay  $B_s \rightarrow J/\psi \phi$ . In this case, however, a time-dependent angular analysis is required to separate CP-odd and CP-even contributions. This provides a joint measurement of  $\Gamma_s$ ,  $\Delta\Gamma_s$  and  $\beta_s$  in the SM. Details on the experimental measurements can be found in Sec. 7.2.4. Notice that the time-dependent angular analysis of  $B_s \rightarrow J/\psi \phi$  actually measures  $\phi_s = \arg(\lambda_{J/\psi \phi})$  with  $\lambda_{J/\psi \phi} = (q/p)_s A(\bar{B}_s \rightarrow J/\psi \phi)/A(B_s \rightarrow J/\psi \phi)$ , namely it determines the phase of the mixing amplitude also in the presence of new physics, provided that the amplitude ratio  $\bar{A}/A$  is real (in the CKM phase convention), namely that Cabibbo-suppressed contributions are neglected. In the same approximation,  $\phi_s = 2\beta_s$  in the SM. An alternative definition is  $\phi'_s = \arg(-M_{12}^s/\Gamma_{12}^s)$ , from which one can write

$$\Delta\Gamma_{B_s} = 2|\Gamma_{12}^s| \cos \phi'_s, \quad a_{\text{fs}}^s = \frac{|\Gamma_{12}^s|}{|M_{12}^s|} \sin \phi'_s. \quad (336)$$

5131 Similarly to the case of  $\phi_s$ ,  $\phi'_s$  coincides with the phase of the mixing amplitude if  
 5132 Cabibbo-suppressed terms in  $\Gamma_{12}^s$  are neglected also beyond the SM. In the SM case and  
 5133 with the same approximation,  $\phi'_s \simeq -2\beta_s + \pi$ .

Finally, the study of mixing and CP violation in the  $D$  system is based on the same formalism as for  $B$  mesons. A peculiarity of  $D$  mesons is that CP violation in mixing is strongly suppressed within the SM by the CKM combination  $V_{cb}V_{ub}^*$ , so that the matrix elements  $M_{12}^D$  and  $\Gamma_{12}^D$  of the  $\Delta C = 2$  effective Hamiltonian (see Sec. 2.1) are real to a good approximation. Even more than in the case of  $\Delta M_K$ , long-distance contributions which cannot be accounted for by the effective Hamiltonian, plague computations of  $D$ - $\bar{D}$  mixing observables. Yet the short-distance (SD) part of the mass and width differences can be computed. It is given by

$$\Delta M_D^{\text{SD}} = 2M_{12}^D, \quad \Delta\Gamma_D^{\text{SD}} = 2\Gamma_{12}^D. \quad (337)$$

Notice that, for the  $D$  system, the experimental information on the mass and width differences is provided by the time-integrated observables

$$x_D = \frac{\Delta M_D}{\Gamma_D}, \quad y_D = \frac{\Delta\Gamma_D}{2\Gamma_D}. \quad (338)$$

## 5134 7.1. The $K$ -meson system

### 5135 7.1.1. Theoretical prediction for $\Delta M_K$ , $\varepsilon_K$ , and $\varepsilon'_K/\varepsilon_K$

5136 The expression for the mass difference  $\Delta m_K$  has been given in Eq. (321). The short-  
 5137 distance contributions, which are represented by the real parts of the box diagrams (see  
 5138 Fig. 55) with charm quark and top quark exchanges, are known at NLO in QCD [34].  
 5139 The dominant contribution is represented by charm exchanges, due to the smallness of  
 5140 the real parts of the CKM top quark couplings, which is not compensated by the effect  
 5141 of having heavier quarks running in the loop. Non-negligible contribution comes from  
 5142 the box diagrams with simultaneous charm and top exchanges. In spite of the accuracy

5143 achieved in the short-distance part, a reliable theoretical prediction of  $\Delta m_K$  is prevented  
 5144 by relevant long-distance contributions which are difficult to estimate. The calculated  
 5145 short-distance part leads in fact to a value of  $\sim 80\%$  [866] of the experimentally observed  
 5146 mass difference between the neutral Kaon states of  $\Delta m_K = (3.483 \pm 0.006) \cdot 10^{-12}$  MeV [4].

Theoretical predictions for the parameter of indirect CP violation  $\varepsilon_K$  have been so far  
 obtained from the expression (324) by neglecting the term  $\xi$ , which constitutes a small  
 contribution, and approximating the phase  $\phi_\varepsilon$  to  $\pi/4$ , so that  $|\varepsilon_K|$  can be written as:

$$|\varepsilon_K| = C_\varepsilon \hat{B}_K A^2 \lambda^6 \bar{\eta} \left\{ -\eta_1 S_0(x_c) \left(1 - \frac{\lambda^2}{2}\right) + \eta_3 S_0(x_c, x_t) + \eta_2 S_0(x_t) A^2 \lambda^4 (1 - \bar{\rho}) \right\}, \quad (339)$$

where  $C_\varepsilon = \frac{G_F^2 f_K^2 M_K M_W^2}{6\sqrt{2}\pi^2 \Delta m_K}$ . However, it has been recently pointed out [867, 868] that the  
 adopted approximations might no longer be justified, due to the improved theoretical ac-  
 curacy in both perturbative and non-perturbative contributions. In Eq. (339) the Inami-  
 Lim functions  $S_0(x_{c,t})$  and  $S_0(x_c, x_t)$  [869] contain the box-contributions from the charm  
 and top-quark exchange with  $x_i = m_i^2/M_W^2$ , while  $\eta_i$  ( $i = 1, 2, 3$ ) describe (perturbative)  
 short-distance QCD-corrections [33–35]. The Kaon bag parameter  $\hat{B}_K$  measures the de-  
 viation of the  $\Delta S = 2$  hadronic matrix element from its value in the vacuum saturation  
 approach:

$$\hat{B}_K = \frac{\langle \bar{K}^0 | \hat{Q}^{\Delta S=2} | K^0 \rangle}{\frac{8}{3} f_K^2 m_K^2}. \quad (340)$$

5147 Therefore,  $\hat{B}_K$  contains all the non-perturbative QCD contributions for  $\varepsilon_K$ . Currently the  
 5148 best determination of this parameter is available from lattice simulations of QCD with  
 5149 either 2+1 or 2 dynamical quark flavors, which avoid the systematic uncertainty due to  
 5150 “quenching” in earlier lattice studies done without dynamical quarks (cf. Sec. 2.3). At  
 5151 this time, the most accurate results (obtained independently with 2+1 dynamical quark  
 5152 flavors) by RBC/UKQCD [870] and Aubin et al. [871] quote a combined statistical and  
 5153 systematic uncertainty of 5.4 and 4.0 per cent for  $\hat{B}_K$ , respectively. That means that the  
 5154 contribution from  $\hat{B}_K$  to the total uncertainty in  $\varepsilon_K$  is now comparable to the second  
 5155 biggest contribution, which originates from  $|V_{cb}|$ . This CKM-matrix element is nowadays  
 5156 known with 2.3 per cent accuracy [4] but enters  $\varepsilon_K$  in the fourth power.

5157 In most current lattice calculations, due to algorithmic and computational limitations,  
 5158 the simulated up- and down-quark masses are heavier than their physical values, thus  
 5159 requiring an extrapolation for  $\hat{B}_K$  to those light quark masses guided by chiral pertur-  
 5160 bation theory (ChPT, see Sec. 2.4). Fig. 56 summarizes the currently available lattice  
 5161 results with either  $N_f = 2 + 1$  or 2 dynamical quarks. The RBC/UKQCD [110, 870] and  
 5162 the HPQCD [872] results both were obtained with  $N_f = 2 + 1$ , where the former used  
 5163 the domain-wall and the latter the staggered fermion formulation. The work by Aubin et  
 5164 al. [871] used a mixed action approach, where domain-wall valence fermions have been  
 5165 calculated on a 2+1 flavor background of dynamical staggered quarks. In case of the  
 5166 RBC/UKQCD result, crucial ingredients for obtaining a small uncertainty in the final  
 5167 number were the use of Kaon SU(2)-ChPT to extrapolate to light physical quark masses  
 5168 and the use of a non-perturbative renormalization technique. The HPQCD result was  
 5169 obtained using degenerate Kaons (made of two quarks of mass  $m_s/2$ ) and used a pertur-  
 5170 bative renormalization technique. Results with  $N_f = 2$  are available from JLQCD [873]

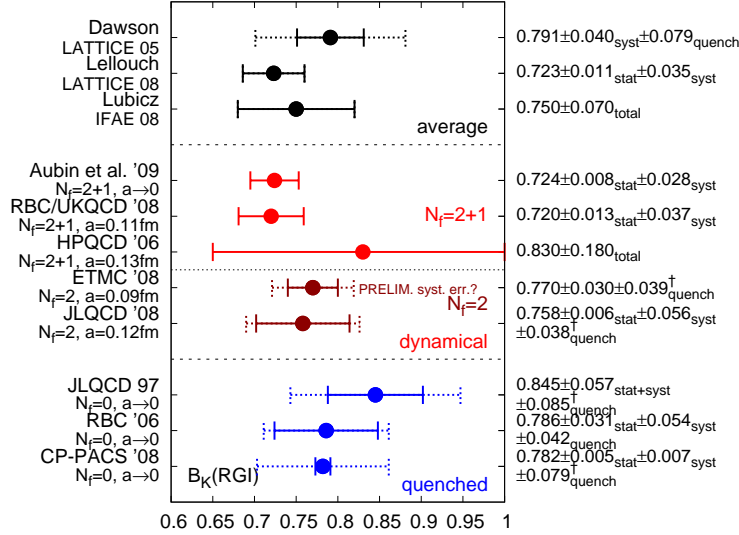


Fig. 56. Summary of lattice results for  $\hat{B}_K$ : included are recent results from dynamical  $N_f = 2 + 1$  [110, 870–872] and  $N_f = 2$  [873, 874] simulations. Also shown are quenched ( $N_f = 0$ ) results from JLQCD [877], RBC [878], and CP-PACS [879]. For comparison, the figure includes the old lattice average from the Lattice 2005 conference [880] and two recently published averages [881, 882], too. *Solid errorbars* do not include the error due to quenching, which is added in the *dashed errorbars*.

<sup>†</sup> A (conservative) quenching error of 5% or 10% has been assigned to  $N_f = 2$  or quenched results, respectively, where no estimate for this systematic error has been provided (see Sec. 2.3).

5171 using dynamical overlap fermions and from ETMC [874] using twisted mass fermions<sup>21</sup>,  
5172 both with non-perturbative renormalization. While ETMC also used Kaon SU(2)-ChPT,  
5173 the JLQCD result was extrapolated using NLO SU(3)-ChPT with analytic NNLO-terms  
5174 added. All these dynamical results except the one from Aubin et al. were obtained at a  
5175 single value for the finite lattice spacing  $a$  (values indicated in Fig. 56), meaning that a  
5176 continuum extrapolation is still missing. But the RBC/UKQCD and the HPQCD results  
5177 account for this fact in the systematic error estimate. For the near future, one should  
5178 expect updates to these results, containing, e.g. simulations at finer lattice spacings and  
5179 lighter dynamical quark masses and therefore further increasing the accuracy of the value  
5180  $\hat{B}_K$  obtained from lattice calculations.

5181 Estimates of the Kaon bag parameter in the chiral limit ( $m_u, m_d, m_s \rightarrow 0$ ) are avail-  
5182 able from lattice simulations [110], large  $N_C$  approximation [875] or the QCD-hadronic  
5183 duality [876].

5184 As far as indirect CP violation is concerned, the parameter  $\varepsilon'_K/\varepsilon_K$  can be written  
5185 by using the operator-product expansion (OPE) as an expression involving the hadronic

<sup>21</sup> The ETMC result is still preliminary. No systematic errors are included yet.

5186  $K \rightarrow (\pi\pi)$  operators  $Q_6$  and  $Q_8$  given in Eq. (44) of Sec. 2.1, see e.g. [883]. Here  $\varepsilon'_K$  can be  
5187 expressed in terms of isospin amplitudes and is an experimentally measurable (complex)  
5188 parameter. The hadronic matrix elements  $Q_6$ ,  $Q_8$  contribute most to the uncertainties in  
5189 the theoretical prediction for  $\varepsilon'_K/\varepsilon_K$ . On the lattice, usually an indirect approach [884]  
5190 is pursued, which measures  $K \rightarrow \pi$  and  $K \rightarrow$  vacuum operators instead and relates  
5191 those via chiral perturbation to the wanted  $K \rightarrow (\pi\pi)$  operators. For quenched studies  
5192 see [885,886], for recent work using dynamical domain-wall fermions see [887]. The latter  
5193 work raises some doubts about the applicability of this approach, which is based on  
5194 SU(3)-ChPT to be valid around the strange quark mass. A different technique, based on  
5195 the calculation of finite volume correlation functions, is described in [77], which might  
5196 turn out to be more successful in the future. See also [888] for an alternative approach,  
5197 i.e. to study  $\varepsilon'_K/\varepsilon_K$  in the small box approach ( $\epsilon$ -regime).

### 5198 7.1.2. *Experimental methods and results*

5199 The Kaon system was the first playground for the understanding of the violation of the  
5200 CP symmetry. In the years before the  $B$  system was investigated all forms of CP violation  
5201 had been observed: in the Kaon mixing, with the measurement of  $\text{Re}(\varepsilon_K)$ , in the direct  
5202 decay, providing a non-null result on  $\text{Re}(\varepsilon'_K/\varepsilon_K)$  and in the interference between mixing  
5203 and decay, through the determination of the  $\eta_{+-}$  phase,  $\phi_{+-}$ . CP violation has been  
5204 observed in the  $K_L$  decay to the CP-even eigenstate of two pions, in the time-integrated  
5205 charge asymmetry of the  $K_L$  semileptonic decay rates, in the  $K_L \rightarrow \pi^+\pi^-\gamma$  channel, and  
5206 in the angular asymmetry of the  $K_L \rightarrow e^+e^-\pi^+\pi^-$  decays.

5207 Direct CP violation through  $\Delta S=1$  processes has been measured as a tiny difference  
5208 in the ratios of the branching ratios of the  $K_L$  to the CP-even eigenstates,  $K_L \rightarrow \pi^+\pi^-$   
5209 and  $K_L \rightarrow \pi^0\pi^0$ , normalized to the  $K_S$  branching ratio for the same final state (Eq. 329).

5210 Precise measurements in the Kaon sector have been obtained with different techniques  
5211 by the present generation of experiments (KTeV, NA48 and KLOE). The results on all of  
5212 the major branching ratios, the lifetimes and the  $K_L$  mass are summarized in Sec. 4.4.5,  
5213 where analyses of interest for the  $|V_{us}|$  determination are discussed. Several of these new  
5214 measurements are not in good agreement with the average of older data. This is the  
5215 case of the CP-violating decays,  $K_L \rightarrow \pi^+\pi^-$ ,  $K_L \rightarrow \pi^0\pi^0$ , whose branching ratios as  
5216 measured by KTeV [345] in year 2004 are 5% and 8% lower, respectively, than previous  
5217 world averages. KLOE and NA48 recently confirmed [349,350] the KTeV result on the  
5218  $\text{BR}(K_L \rightarrow \pi^+\pi^-)$ .

5219 KTeV has measured the  $\text{BR}(K_L \rightarrow \pi^+\pi^-)$  and the  $\text{BR}(K_L \rightarrow \pi^0\pi^0)$  [345] from the  
5220 analysis of all of the main  $K_L$  decay channels, as described in Sec. 4.4.5. The CP-violating  
5221 charged channel was selected among the events not satisfying the criteria for the semilep-  
5222 tonic and the  $\pi^+\pi^-\pi^0$  decays imposing cuts on the  $m_{\pi\pi}$  invariant mass and on the  
5223 two-track transverse momentum-squared. The  $K_L \rightarrow \pi^0\pi^0$  events are identified by the  
5224 reconstruction of exactly four clusters in the calorimeter. The photons are paired to have  
5225 two pions pointing to a single decay vertex and the pion invariant mass is required to be  
5226 consistent with the Kaon mass. Major systematic uncertainties come from the precision  
5227 on the knowledge of the efficiency reconstruction and to a less extent from radiative  
5228 corrections to charged modes, Monte Carlo statistics and background subtraction.

5229 The KLOE measurement [349] has been obtained from the relative ratio of  $K_L \rightarrow$   
5230  $\pi^+\pi^-$  and  $K_L \rightarrow \pi\mu\nu$  decays, the absolute semileptonic branching ratio  $\text{BR}(K_L \rightarrow \pi\mu\nu)$

5231 being previously determined [347] from the measurement of all the major decay modes,  
 5232 using the tagging technique to obtain the absolute branching fractions and imposing the  
 5233 constraint on the sum of the branching fractions to solve the dependence on the  $K_L$   
 5234 lifetime. The  $K_L$  sample at KLOE, operating at the Frascati  $\phi$  factory, is tagged by  
 5235 the reconstruction of the  $K_S \rightarrow \pi^+\pi^-$  decays, giving a precise determination of the  $K_L$   
 5236 momentum. In order to minimize the difference on trigger efficiency between the two  
 5237 selected channels, the pions from  $K_S$  decay are requested to release in the calorimeter  
 5238 energy enough to trigger the data acquisition system.

5239 The CP-violating channel was selected by a fit with a linear combination of MonteCarlo  
 5240 shapes for signal and background to the  $\sqrt{E_{miss}^2 + |p_{miss}^2|}$  distribution, where  $E_{miss}$  is  
 5241 the missing energy in the hypothesis of the two charged pion decay. The precision is  
 5242 dominated by the accuracy on tagging and tracking efficiency, depending on the correc-  
 5243 tions applied to the MonteCarlo sample for getting rid of small discrepancies between  
 5244 the MonteCarlo-predicted distributions and those obtained from data control samples.

5245 NA48 measured the relative decay widths  $\Gamma(K_L \rightarrow \pi^+\pi^-)/\Gamma(K_L \rightarrow \pi e \nu)$  [350]  
 5246 from a sample of two-track events selected for the analysis giving the semileptonic Ke3  
 5247 branching ratio normalized to all of the two-track modes [346]. The CP-violating channel  
 5248 was selected by cuts on the  $m_{\pi\pi}$  invariant mass, on the Kaon transverse momentum-  
 5249 squared, on the ratio of the reconstructed energy and the particle momentum, E/P, very  
 5250 effective in separating electrons from  $\mu$  and  $\pi$ , and finally using the muon veto system  
 5251 for  $K\mu 3$  rejection. Systematic uncertainties are due to the knowledge of Kaon spectrum,  
 5252 background contamination from  $K\mu 3$  decays, and to a less extent radiative corrections,  
 5253 trigger efficiencies and MonteCarlo statistics.

5254 The branching fractions obtained are summarized in Tab. 53, together with the CP-  
 5255 violation parameter  $|\eta_{+-}|$ , defined in Eq. 327, and  $\text{Re}(\varepsilon_K)$ .

Table 53

$K_L \rightarrow \pi^+\pi^-$  branching ratios as measured by KTeV [345], KLOE [349] and NA48 [350], compared with  
 previous world average [889]. For  $\text{Re}(\varepsilon_K)$ , the average value of  $\phi_{+-} = (43.4 \pm 0.7)^\circ$  and  $\text{Re}(\varepsilon'_K/\varepsilon_K) =$   
 $(16.5 \pm 2.6) \times 10^{-4}$  have been used.

Source	$\text{BR}(K_L \rightarrow \pi^+\pi^-)$	$ \eta_{+-} $	$\text{Re}(\varepsilon_K)$
PDG 04	$(20.90 \pm 0.25)10^{-4}$ [889]	$(22.88 \pm 0.14)10^{-4}$	$(16.6 \pm 0.2)10^{-4}$
KTeV 04	$(19.75 \pm 0.12)10^{-4}$ [345]	$(22.28 \pm 0.10)10^{-4}$	$(16.1 \pm 0.2)10^{-4}$
KLOE 06	$(19.63 \pm 0.21)10^{-4}$ [349]	$(22.19 \pm 0.13)10^{-4}$	$(16.1 \pm 0.2)10^{-4}$
NA48 07	$(19.69 \pm 0.19)10^{-4}$ [350]	$(22.23 \pm 0.12)10^{-4}$	$(16.1 \pm 0.2)10^{-4}$

5256 Direct CP violation has been established by the precision measurements from NA48  
 5257 [890] and KTeV [185], giving  $\text{Re}(\varepsilon'_K/\varepsilon_K) = (14.7 \pm 2.2) \times 10^{-4}$  and  $\text{Re}(\varepsilon'_K/\varepsilon_K) = (20.7 \pm$   
 5258  $2.8) \times 10^{-4}$ , respectively.

The measurements hitherto summarized are used in the fit procedure described in the  
 “CP violation in Klong decays” Review of [283] to obtain the value of

$$|\varepsilon_K| = (2 \cdot |\eta_{+-}| + |\eta_{00}|)/3 = (2.229 \pm 0.012) \times 10^{-3} \quad (341)$$

5259 The KTeV collaboration recently announced the final result on  $\text{Re}(\varepsilon'_K/\varepsilon_K)$ , obtained  
 5260 with an improved analysis of the entire data set [891, 892].

5261 Systematic error was reduced from  $2.4 \times 10^{-4}$  to  $1.8 \times 10^{-4}$  and the statistical uncer-  
5262 tainty from  $1.5 \times 10^{-4}$  to  $1.1 \times 10^{-4}$ , giving  $Re(\varepsilon'_K/\varepsilon_K) = (19.2 \pm 1.1_{stat} \pm 1.8_{syst}) \times 10^{-4}$ .  
5263 The results from the two experiments are consistent within  $1.7 \sigma$ .

5264 The new average, scaling the errors to take into account the consistency level of the  
5265 measurements and including also contributions not present in Eq.323, from  $\Delta I=3/2$  am-  
5266 plitudes [893], is  $Re(\varepsilon'_K/\varepsilon_K) = (16.4 \pm 1.9) \times 10^{-4}$ .

5267 The KTeV experiment measured also the phase of the CP-violating decays. In fact,  
5268 they used the simultaneous measurements of events from two nearly parallel Kaon beams,  
5269 with one of the beams passing through a thick regenerator, for the precise determination  
5270 of the acceptances and the contamination for both, the charged ( $\pi^+\pi^-$ ) and the neutral  
5271 ( $\pi^0\pi^0$ ) modes. To reduce systematic uncertainties the regenerator positions were alter-  
5272 nated between the two beams once per minute.  $Re(\varepsilon'_K/\varepsilon_K)$  has been obtained by a fit to  
5273 the vacuum-to-regenerator ratio for charged and neutral modes, taking into account the  
5274  $K_L$ - $K_S$  interference pattern in the regenerator sample [185]. Together with  $Re(\varepsilon'_K/\varepsilon_K)$ ,  
5275 the fit provides the best results on  $\phi_{00} - \phi_{+-} = (0.29 \pm 0.31)^\circ$ ,  $\Delta M_K = M_{K_L} - M_{K_S} =$   
5276  $3.465(7)10^{-12}$  MeV and the  $K_S$  lifetime,  $\tau_S = 89.62(5)10^{-12}$  s.

5277 The unitarity relation applied to time evolution of the neutral Kaon state leads to the  
5278 Bell-Steinberger relation expressing CP and CPT violation parameters in terms of Kaon  
5279 decay widths.

$$\begin{aligned} & \left[ \frac{\Gamma_S + \Gamma_L}{\Gamma_S - \Gamma_L} + i \tan \phi_{sw} \right] \times \left[ \frac{\text{Re}(\epsilon)}{1 + |\epsilon|^2} - i \text{Im}(\delta) \right] \\ &= \frac{1}{\Gamma_S - \Gamma_L} \sum_f \mathcal{A}_L(f) \mathcal{A}_S^*(f), \end{aligned} \quad (342)$$

where

$$\phi_{sw} = \arctan \left( \frac{2\Delta M_K}{\Gamma_S - \Gamma_L} \right). \quad (343)$$

5280 Besides testing CPT symmetry, the unitarity constraint for the neutral Kaon system,  
5281 that receives relevant contributions only from few final states, really improves the pre-  
5282 cision on the  $Re(\varepsilon_K)$  parameter. The measurements of the  $K_L$ ,  $K_S$  branching fractions  
5283 and lifetimes, together with the KLOE upper limit on the  $K_S \rightarrow \pi^0\pi^0\pi^0$  mode [894], on  
5284 the time-integrated charge asymmetry of the  $K_S$  semileptonic decay [351], and the new  
5285 result on  $\phi_{+-}$  announced by KTeV [891,892], have improved the accuracy on both, CP-  
5286 and CPT-violation parameters,  $Re(\varepsilon_K)$  and  $Im(\delta)$ . The results published in Ref. [895]  
5287 were mostly based on the KLOE measurements. They have been revised for the ‘‘CPT  
5288 invariance tests in neutral Kaon decay’’ Review in [283] using the entire set of published  
5289 data from KTeV and NA48, and then updated by the FlaviaNet Kaon Working Group to  
5290 include the preliminary results on the  $\eta_{\pi\pi}$  phases from the KTeV experiment [891,892].  
5291 They are summarized in Tab. 54.

5292 Overall, the measurements in the Kaon sector to date constitute a precise data set con-  
5293 sistent with CPT symmetry and unitarity. The comparison with CP-violation parameters  
5294 in the B sector confirms that the CKM mechanism is the major source of CP-violation  
5295 in meson decays.

5296 Still, Kaon physics has to meet the challenging experimental program on CP violation  
5297 in very rare, and especially  $K_L \rightarrow \pi\nu\nu$ , decays which is extremely promising for con-  
5298 straining the CKM parameters and the physics beyond the SM as discussed in Sec. 6.6.6.



Table 54

CP and CPT violation parameters from the unitarity constraint (Bell-Steinberger relation).

Source	$\text{Re}(\varepsilon_K)$	$\text{Im}(\delta)$	Ref.
KLOE 06	$(15.96 \pm 0.13)10^{-4}$	$(0.04 \pm 0.21)10^{-4}$	[895]
PDG 08	$(16.12 \pm 0.06)10^{-4}$	$(-0.06 \pm 0.19)10^{-4}$	[283]
FlaviaNet 08	$(16.12 \pm 0.06)10^{-4}$	$(-0.01 \pm 0.14)10^{-4}$	

5299 7.2. The  $B$ -meson system5300 7.2.1. Lifetimes,  $\Delta\Gamma_{B_q}$ ,  $A_{SL}^q$  and  $\Delta M_{B_q}$ 5301 **Theory predictions**

5302 Heavy meson mixing plays a particularly important role in placing constraints on NP,  
5303 since this loop process can be computed quite reliably using the heavy-quark expansion  
5304 (HQE). Similarly, the hierarchy of lifetimes of heavy hadrons can be understood in the  
5305 HQE, which makes use of the disparity of scales present in the decays of hadrons con-  
5306 taining b-quarks. HQE predicts the ratios of lifetimes of beauty mesons [896–899], which  
5307 now agree with the experimental observations within experimental and theoretical uncer-  
5308 tainties. The most recent theoretical predictions show evidence of excellent agreement of  
5309 theoretical and experimental results [900–905]. This agreement also provides us with some  
5310 confidence that quark-hadron duality, which states that smeared partonic amplitudes can  
5311 be replaced by the hadronic ones, is expected to hold in inclusive decays of heavy flavors.  
5312 It should be pointed out that the low experimental value of the ratio  $\tau(\Lambda_b)/\tau(B_d)$  has  
5313 long been a puzzle for the theory. Only recent next-to-leading order (NLO) calculations  
5314 of perturbative QCD [900–902] and  $1/m_b$  corrections [903–905] to spectator effects as  
5315 well as recent Tevatron measurements practically eliminated this discrepancy.

The inclusive decay rate of a heavy hadron  $H_b$  and  $B$ -meson mixing parameters can be most conveniently computed by employing the optical theorem to relate the decay width to the imaginary part of the forward matrix element of the transition operator:

$$\Gamma(H_b) = \frac{1}{2M_{H_b}} \text{Disc}\langle H_b|i \int d^4x \mathcal{T}(\mathcal{H}_{eff}^{\Delta B=1}(x) \mathcal{H}_{eff}^{\Delta B=1}(0))|H_b\rangle, \quad (344)$$

5316 where  $H_{\text{eff}}^{\Delta B=1}$  represents the effective  $\Delta B = 1$  Hamiltonian, given in Sec. 2.1.

In the heavy-quark limit, the energy release is large, so that the correlator in Eq. (344) is dominated by short-distance physics. The OPE can be applied as explained in Sec. 2.1, leading to a prediction for the decay widths of Eq. (344) as a series of local operators of increasing dimension suppressed by powers of  $1/m_b$ :

$$\Gamma(H_b) = \frac{1}{2M_{H_b}} \sum_k \langle H_b|\mathcal{T}_k|H_b\rangle = \sum_k \frac{C_k(\mu)}{m_b^k} \langle H_b|\mathcal{O}_k^{\Delta B=0}(\mu)|H_b\rangle, \quad (345)$$

5317 with the scale dependence of the Wilson coefficients compensated by the scale dependence  
5318 of the matrix elements.

5319 It is customary to make predictions for the ratios of lifetimes (widths), as many theo-  
5320 retical uncertainties cancel out in the ratio. Since the differences of lifetimes should come  
5321 from the differences in the light sectors of heavy hadrons, at the leading order in HQE all  
5322 beauty hadrons with light spectators have the same lifetime. The difference between me-

5323 son and baryon lifetimes first occurs at order  $1/m_b^2$  and is essentially due to the different  
 5324 structure of mesons and baryons, amounting to at most  $1 - 2\%$  [898].

5325 The main effect appears at the  $1/m_b^3$  level and comes from dimension-six four-quark  
 5326 operators, whose contribution is enhanced due to the phase-space factor  $16\pi^2$ . They are  
 5327 thus capable of inducing corrections of order  $16\pi^2(\Lambda_{QCD}/m_b)^3 = \mathcal{O}(5 - 10\%)$ . These  
 5328 operators introduce through the so-called Weak Annihilation (WA) and Pauli Interference  
 5329 (PI) diagrams, a difference in lifetimes for both heavy mesons and baryons. Their  
 5330 effects have been computed [500, 898, 906–910] including NLO perturbative QCD cor-  
 5331 rections [900–902] and  $1/m_b$  corrections [903–905]. The non-perturbative contribution is  
 5332 enclosed in the matrix elements of the mentioned operators, which are the following four

$$\begin{aligned} O_1^q &= \bar{b}_i \gamma^\mu (1 - \gamma_5) b_j \bar{q}_j \gamma_\mu (1 - \gamma_5) q_j, & O_2^q &= \bar{b}_i \gamma^\mu \gamma_5 b_j \bar{q}_j \gamma_\mu (1 - \gamma_5) q_j, \\ \tilde{O}_1^q &= \bar{b}_i \gamma^\mu (1 - \gamma_5) b_j \bar{q}_i \gamma_\mu (1 - \gamma_5) q_j, & \tilde{O}_2^q &= \bar{b}_i \gamma^\mu \gamma_5 b_j \bar{q}_i \gamma_\mu (1 - \gamma_5) q_j. \end{aligned} \quad (346)$$

5333 The matrix elements of these operators are parameterized in a different way depending  
 5334 on whether or not the light quark  $q$  of the operator enters as a valence quark in the  
 5335 external hadronic state [900]. In this way one can distinguish the contribution of the  
 5336 contraction of the light quark in the operator with the light quark in the hadron, which  
 5337 is the only one calculated in lattice QCD [911–914]. Computing the contribution of the  
 5338 contraction of two light quarks in the operator, which vanishes in the vacuum saturation  
 5339 approximation, has been so far prevented by the difficult problem of subtracting power  
 5340 divergences.

5341 By combining the results for the perturbative and non-perturbative contributions dis-  
 5342 cussed above, the theoretical predictions for the lifetime ratios read

$$\tau(B^+)/\tau(B^0) = 1.06 \pm 0.02, \quad \tau(B_s)/\tau(B^0) = 1.00 \pm 0.01, \quad \tau(\Lambda_b)/\tau(B^0) = 0.91 \pm 0.04. \quad (347)$$

5343 Similar calculations yield B-mixing parameters presented in the form of expansion in  
 5344  $1/m_b^n$ . The width difference is related the matrix elements  $M_{12}^q$  and  $\Gamma_{12}^q$  as in Eq. (333)  
 5345 and by using the HQE it can be written as

$$\begin{aligned} \Delta\Gamma_{B_q} &= \frac{G_F^2 m_b^2}{6\pi(2M_{B_q})} (V_{cb}^* V_{cq})^2 \cdot \\ &\quad \{ [F(z) + P(z)] \langle Q \rangle + [F_S(z) + P_S(z)] \langle Q_S \rangle + \delta_{1/m} + \delta_{1/m^2} \}, \end{aligned} \quad (348)$$

where  $z = m_c^2/m_b^2$  and the two  $\Delta B = 2$  operators are defined as

$$Q = (\bar{b}_i q_i)_{V-A} (\bar{b}_j q_j)_{V-A}, \quad Q_S = (\bar{b}_i q_i)_{S-P} (\bar{b}_j q_j)_{S-P}. \quad (349)$$

5346 The matrix elements for  $Q$  and  $Q_S$  are known to be

$$\begin{aligned} \langle Q \rangle &\equiv \langle \bar{B}_q | Q | B_q \rangle = f_{B_q}^2 M_{B_q}^2 2 \left( 1 + \frac{1}{N_c} \right) B_{B_q}, \\ \langle Q_S \rangle &\equiv \langle \bar{B}_q | Q_S | B_q \rangle = -f_{B_q}^2 M_{B_q}^2 \frac{M_{B_q}^2}{(m_b + m_s)^2} \left( 2 - \frac{1}{N_c} \right) B_{B_q}^S, \end{aligned}$$

A theoretical prediction for the  $B_{d,s}$  width differences then requires to calculate non-  
 perturbatively the decay constants  $f_{B_{d,s}}$  and the bag parameters  $B_{B_{d,s}}$  and  $B_{B_{d,s}}^S$ . Several

unquenched lattice calculations of the decay constants have been performed with  $N_f = 2$  or  $N_f = 2 + 1$  dynamical fermions [915–922]. They have been obtained by treating the  $b$  quark on the lattice with two different approaches, either FNAL [483] or non-relativistic QCD. A collection of these results is provided in Ref. [881], where the following averages are estimated

$$f_{B_d} = (200 \pm 20) \text{ MeV}, \quad f_{B_s} = (245 \pm 25) \text{ MeV}. \quad (350)$$

5347 The average for  $f_{B_s}$  takes into account all the existing  $N_f = 2$  and  $N_f = 2 + 1$  results.  
 5348 For  $f_{B_d}$  the lattice determination is more delicate, because its value is enhanced by chiral  
 5349 logs effects relevant at low quark masses. In order to properly account for these effects,  
 5350 simulations at light values of the quark mass (typically  $m_{ud} < m_s/2$ ) are required. For  
 5351 this reason, the  $f_{B_d}$  average provided in Ref. [881] and given in Eq. (350) is derived by  
 5352 taking into account only the results obtained by the HPQCD [920] and FNAL/MILC [922]  
 5353 collaborations, by using the MILC gauge field configurations generated at light quark  
 5354 masses as low as  $m_s/8$ . A more recent HPQCD calculation [921] of  $f_{B_d}$  and  $f_{B_s}$ , as well  
 5355 as of the bag parameters  $B_{B_d}$  and  $B_{B_s}$ , came out after the averages in Ref. [881] were  
 5356 performed. Since the new results are consistent with the old ones, the averages [881] can  
 5357 be considered up to date.

Also for the bag parameters, a collection of quenched [923–925] and unquenched ( $N_f = 2$  and  $N_f = 2 + 1$ ) [918, 921, 926, 927] results can be found in Ref. [881]. A first observation is that the dependence on the light quark mass, that should allow to distinguish between  $B_d$  and  $B_s$  mesons, is practically invisible. For the  $B_{B_{d,s}}$  bag parameters, the unquenched results tend to be slightly lower than the quenched determinations, though still well compatible within the errors, and lead to the averages [881]

$$B_{B_d}^{\overline{\text{MS}}}(m_b) = B_{B_s}^{\overline{\text{MS}}}(m_b) = 0.80 \pm 0.08, \quad (351)$$

in the  $\overline{\text{MS}}$  scheme at the renormalization scale  $\mu = m_b$ , which correspond to the renormalization group invariant parameters

$$\hat{B}_{B_d} = \hat{B}_{B_s} = 1.22 \pm 0.12. \quad (352)$$

The bag parameters  $B_{B_{d,s}}^S$  have been recently calculated without the unquenched approximation only by one lattice collaboration [926], finding no evidence of quenching effects. The averages given in Ref. [881], include also previous quenched lattice results, and in the  $\overline{\text{MS}}$  scheme at the renormalization scale  $\mu = m_b$  they read

$$B_{B_d}^S = B_{B_s}^S = 0.85 \pm 0.10. \quad (353)$$

The Wilson coefficients of these operators have been computed at NLO in QCD [928–930] and, together with  $1/m_b$ -suppressed effects [931], lead to the theoretical predictions [932]

$$\frac{\Delta\Gamma_{B_d}}{\Gamma_{B_d}} = (4.1 \pm 0.9 \pm 1.2) \cdot 10^{-3}, \quad \frac{\Delta\Gamma_{B_s}}{\Gamma_{B_s}} = (13 \pm 2 \pm 4) \cdot 10^{-2}. \quad (354)$$

5358 We observe that the theoretical predictions above are obtained by expressing the ratio  
 5359  $\Delta\Gamma/\Gamma$  as  $(\Delta\Gamma/\Delta M)_{th.}/(\Delta M/\Gamma)_{exp.}$ , i.e. by using the available accurate experimental  
 5360 measurements for the lifetimes and the mass differences. Moreover, they are obtained  
 5361 in a different operator basis  $\{Q, \tilde{Q}_s\}$ , with  $\tilde{Q}_S = (\bar{b}_i q_j)_{S-P}(\bar{b}_j q_i)_{S-P}$ , where there do  
 5362 not appear strong cancelations due to NLO and  $1/m_b$ -suppressed contributions [932].  
 5363 The differences between the central values of  $\Delta\Gamma_{B_q}/\Gamma_{B_q}$  computed in the “old” and

5364 “new” bases, which come from uncalculated  $\alpha_s/m_b$  and  $\alpha_s^2$  corrections, turn out to be  
 5365 quite large. A conservative 30% uncertainty is taken into account by the second errors  
 5366 in Eq. (354).

The experimental observable  $|(q/p)_q|$ , whose deviation from unity describes CP violation due to mixing, is related to  $M_{12}^q$  and  $\Gamma_{12}^q$ , through Eq. (333). The theoretical prediction of  $|(q/p)_q|$  is therefore based on the same perturbative and non-perturbative calculation discussed for the width differences, while the CKM contribution to  $|(q/p)_q|$  is different from that in  $\Delta\Gamma_{B_q}/\Gamma_{B_q}$ . The updated theoretical predictions are [928–930]

$$|(q/p)_d| - 1 = (2.96 \pm 0.67) \cdot 10^{-4}, \quad |(q/p)_s| - 1 = (1.28 \pm 0.28) \cdot 10^{-5}. \quad (355)$$

Experimentally, information on the CP violation parameter  $|(q/p)_q|$  is provided by the measurement of the semileptonic CP asymmetry, defined as

$$A_{SL}^q = \frac{\Gamma(B^0(t) \rightarrow l^- \bar{\nu} X) - \Gamma(\bar{B}^0(t) \rightarrow l^+ \nu X)}{\Gamma(B^0(t) \rightarrow l^- \bar{\nu} X) + \Gamma(\bar{B}^0(t) \rightarrow l^+ \nu X)} \quad (356)$$

which is related to  $|(q/p)_q|$  through

$$A_{SL}^q = 2(1 - |(q/p)_q|). \quad (357)$$

5367 We conclude this section on  $B$  mesons by discussing the mass difference. In contrast  
 5368 to  $\Delta M_K$ , in this case the long-distance contributions are estimated to be very small and  
 5369  $\Delta M_{B_{d,s}}$  is very well approximated by the relevant box diagrams, which are analogous to  
 5370 those shown in Fig. 55 for Kaons. Moreover, due to  $m_{u,c} \ll m_t$ , only the top sector can  
 5371 contribute significantly, whereas the charm sector and the mixed top-charm contribu-  
 5372 tions are entirely negligible. Thus, the theoretical expression for  $M_{12}^q$ , to which the mass  
 5373 difference is related through Eq. (333), can be written as

$$M_{12}^q = \frac{G_F^2 M_{B_q} M_W^2}{12\pi^2} (V_{tb} V_{tq}^*)^2 \hat{\eta}_B S_0(x_t) f_{B_q}^2 B_{B_q}, \quad (q = d, s), \quad (358)$$

5374 where  $S_0(x_t)$  is the Inami-Lim function and  $\hat{\eta}_B \approx 0.84$  represents the NLO QCD correc-  
 5375 tion [811].

5376 The mass differences in the  $B_d$  and  $B_s$  systems are proportional to  $|V_{td}|^2$  and  $|V_{ts}|^2$ ,  
 5377 respectively, thus representing important constraints on the UT, provided that the mul-  
 5378 tiplied hadronic matrix elements are calculated. In order to involve reduced hadronic  
 5379 uncertainties, it is convenient to use as experimental constraints the ratio  $\Delta M_{B_s}/\Delta M_{B_d}$   
 5380 and  $\Delta M_{B_s}$ , since the strange-bottom sector is not affected by the uncertainty due to  
 5381 the chiral extrapolation. On the other hand the UT analysis, being overconstrained, can  
 5382 be performed without using some inputs. In this way, the mass difference  $\Delta M_{B_s}$  can be  
 5383 predicted with an accuracy of approximately 10%, as shown in Sec. 10 where the whole  
 5384 UT analysis is discussed.

### 5385 Experimental results

5386 At the Tevatron the lifetime difference in the  $B_s$  system is accessible in the decay  
 5387  $B_s \rightarrow J/\psi \phi$  which gives rise to both CP-even and CP-odd final states. It is possible  
 5388 to separate the two CP components of the decay and therefore to measure the lifetime  
 5389 difference, through a simultaneous fit to the time evolution and angular distributions of  
 5390 the decay products of the  $J/\psi$  and  $\phi$  mesons. Fig. 57 shows the lifetime projections for  
 5391 the  $\Delta\Gamma$  measurements at CDF and D0 with the CP even and CP odd components fitted  
 5392 separately. Both experiments have so far analysed  $2.8 \text{ fb}^{-1}$  of data. The results [230, 933]

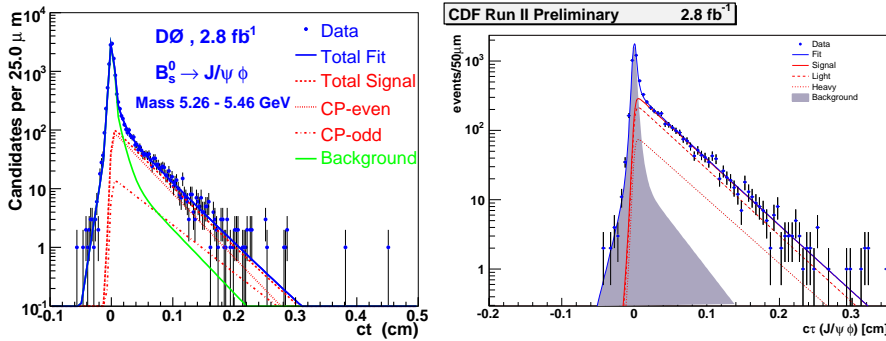


Fig. 57. Lifetime projection for  $B_s^0$  candidates in the signal region.

5393 are still compatible with a  $\Delta\Gamma$  of zero. It should be noted that if  $\Delta\Gamma$  is not zero, the  
 5394 flavor specific (equal mix of  $B_s^H$  and  $B_s^L$  at  $t=0$ ) and CP specific  $B_s$  lifetimes will be  
 5395 distinct.

5396 The Tevatron experiments have published lifetime measurements for several types of  
 5397  $B$ -hadrons. A small selection of these are discussed below.

5398 The  $B_c$  meson occupies a special place amongst the  $B$ -hadrons as it can decay weakly  
 5399 via the  $b$  or  $c$  quark. Therefore its lifetime is considerably shorter than those of light  
 5400  $B$  mesons. Due to its relatively large branching fraction, Tevatron experiments measure  
 5401 the  $B_c$  lifetime in semileptonic decays ( $B_c \rightarrow J/\Psi l \nu$ ). The  $B_c$  mass is measured in  
 5402 hadronic decays, where lifetime cuts are used to reject background. The  $B_c$  momentum  
 5403 in semileptonic decays cannot be fully reconstructed; it is necessary to derive a correction  
 5404 factor from Monte Carlo. The current measurements of  $\tau(B_c) = 0.475^{+0.053}_{-0.049}(stat) \pm$   
 5405  $0.018(sys)$  ps by CDF [934] and  $\tau(B_c) = 0.448^{+0.038}_{-0.036}(stat) \pm 0.032(sys)$  ps by D0 [935]  
 5406 are in agreement with theoretical predictions [936].

5407 The lifetime ratio of  $\tau(\Lambda_b)/\tau(B^0)$  has been of considerable interest. There has been a  
 5408 long standing disagreement between theoretical predictions and experimental results.  
 5409 Most of the recent Tevatron measurements [937–940] now agree with updated theoretical  
 5410 predictions [941] within errors.

5411 *missing: table of B lifetimes from Tevatron*

## 5412 7.2.2. $B$ -mesons mixing

5413 Mixing of the  $B_d$  mesons was established 25 years ago and precision measurements  
 5414 where available since the beginning of the asymmetric B-Factory program, since they  
 5415 can exploit both the large luminosity and the boost of the center-of-mass frame. The full  
 5416 list of measurements is in Fig. 58.

5417 The most accurate measurements come indeed from Belle and BaBar, where one of  
 5418 the two  $B$  mesons is fully via in their semileptonic decay and the other  $B$  tagged as  $B^0$   
 5419 or  $\bar{B}^0$ .

5420 To determine  $\Delta M_{B_s}$  it is necessary to determine whether a particle oscillated before  
 5421 it decayed. As  $b\bar{b}$  pair production dominates b-quark, this is achieved by flavor tagging  
 5422 either the signal side or the ‘opposite side’  $b$ -quark. The methods vary slightly between  
 5423 the experiments, but are generally based either on jet charge tagging where the flavor  
 5424 of the  $b$ -quark is related to the weighted sum of the particle charges the jet, lepton

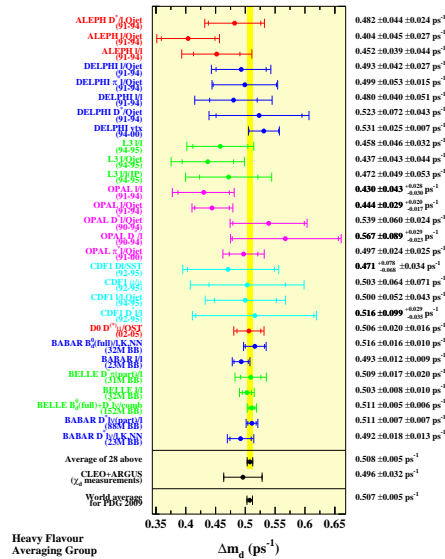


Fig. 58. Summary and average of  $\Delta M_{B_d}$  measurements. See [558] for the full list of references.

5425 tagging in semileptonic decays and same side tagging where the charge of a ‘nearby’  
5426 track is correlated with the  $b$ -quark flavor.  $\Delta M_{B_s}$  was first measured by the CDF and  
5427 D0 experiments at the Tevatron. Both experiments also use combination of taggers to  
5428 enhance their tagging capabilities. After D0 initially set a two-sided limit [942] on  $\Delta M_{B_s}$   
5429 of  $17 < \Delta M_{B_s} < 21$  ps<sup>-1</sup> at 90% CL, CDF [218] has measured  $\Delta M_{B_s}$  to be  $17.77 \pm 0.10$   
5430 (stat)  $\pm 0.07$  (syst) ps<sup>-1</sup>. This corresponds to  $5.4 \sigma$  significance. A recent update [943]  
5431 by D0 ( $\Delta M_{B_s} = 18.53 \pm 0.93$  (stat)  $\pm 0.30$  (sys) ps<sup>-1</sup>) is in good agreement with the  
5432 CDF measurement.

### 5433 7.2.3. Measurements of the angle $\beta$ in tree dominated processes

5434 The Standard Model (SM) of electroweak interactions describes charge conjugation-  
5435 parity ( $CP$ ) violation as a consequence of an irreducible complex phase in the three-  
5436 generation Cabibbo-Kobayashi-Maskawa (CKM) quark-mixing matrix [1,2]. In this frame-  
5437 work, neutral  $B$  decays to  $CP$  eigenstates containing a charmonium and  $K^0$  meson provide a  
5438 direct measurement of  $\sin 2\beta$  [944,945]. The unitarity triangle angle  $\beta$  (or  $\Phi_1$ ) is  
5439  $\arg[-V_{cd}V_{cb}^*/V_{td}V_{tb}^*]$  where the  $V_{ij}$  are CKM matrix elements.

5440  $B^0 \rightarrow J/\psi \pi^0$  proceeds instead via a Cabibbo-suppressed  $b \rightarrow c\bar{c}d$  transition: the tree  
5441 amplitude has the same weak phase as the  $b \rightarrow c\bar{c}s$  transition, therefore we expect  
5442 the corresponding values of  $S$  and  $C$  to be  $-\sin 2\beta$  and 0 respectively, unless penguin  
5443 amplitudes or other contributions are significant.

5444 The current status of measurements of  $\sin 2\beta$  from charmonium decays are presented in  
5445 what follows and cover  $b \rightarrow c\bar{c}s$  and  $b \rightarrow c\bar{c}d$  transitions. Additional results on determining  
5446 the sign of  $\beta$  are also mentioned using the measurement of  $\cos 2\beta$  in  $b \rightarrow c\bar{c}s$  decays.

Most of the measurements presented here are based on data collected by the *BABAR*  
and the *Belle* experiments. The difference between the proper decay times of the signal

$B$  meson ( $B_{rec}$ ) and of the other  $B$  meson ( $B_{tag}$ ) is used to measure the time-dependent  $CP$ -asymmetries,  $\mathcal{A}_{CP}$ . The initial flavor of  $B_{rec}$  is identified by using information from  $B_{tag}$ .  $\mathcal{A}_{CP}$  is defined as

$$\mathcal{A}_{CP}(t) \equiv \frac{N(\bar{B}^0(t) \rightarrow f) - N(B^0(t) \rightarrow f)}{N(\bar{B}^0(t) \rightarrow f) + N(B^0(t) \rightarrow f)} = S \sin(\Delta m_d t) - C \cos(\Delta m_d t), \quad (359)$$

5447 where  $N(\bar{B}^0(t) \rightarrow f)$  is the number of  $\bar{B}^0$  that decay into the  $CP$ -eigenstate  $f$  after a  
 5448 time  $t$  and  $\Delta m_d$  is the difference between the  $B$  mass eigenstates. Belle reports results  
 5449 using the variable  $A \equiv -C$ .

5450 In the SM, direct  $CP$  violation in  $b \rightarrow c\bar{c}s$  decays is negligible. Under this assumption,  
 5451 the  $CP$  violation parameters  $S$  and  $C$  are given by  $S_{b \rightarrow c\bar{c}s} = -\eta_f \sin 2\beta$  and  $C_{b \rightarrow c\bar{c}s} = 0$ ,  
 5452 where  $\eta_f$  is  $-1$  for  $(c\bar{c})K_s^0$  decays (e.g.  $J/\psi K_s^0$ ,  $\psi(2S)K_s^0$ ,  $\chi_{c1}K_s^0$ ,  $\eta_c K_s^0$ <sup>22</sup>) and  $\eta_f$  is  $+1$   
 5453 for the  $(c\bar{c})K_L^0$  (e.g.  $J/\psi K_L^0$ ) state. The  $J/\psi K^{*0}$  ( $K^{*0} \rightarrow K_s^0 \pi^0$ ) final state is an admixture  
 5454 of  $CP$  even and  $CP$  odd amplitudes for which we use  $\eta_f = 0.504 \pm 0.033$ . To be consistent  
 5455 with other time-dependent  $CP$  measurements, we show the results in terms of  $C_f = \eta_f C$   
 5456 and  $S_f = \eta_f S$ . Using  $425.7 \text{fb}^{-1}$  of integrated luminosity, the *BABAR* experiment measured  
 5457 the time-dependent  $CP$  asymmetry parameters for the  $J/\psi K_s^0$ ,  $\psi(2S)K_s^0$ ,  $\chi_{c1}K_s^0$ ,  $\eta_c K_s^0$   
 5458 and  $J/\psi K_L^0$  modes combined [946]<sup>23</sup>:

$$C_f = 0.026 \pm 0.020(stat) \pm 0.016(syst), \quad S_f = 0.691 \pm 0.029(stat) \pm 0.014(syst).$$

5459  $C_f$  and  $S_f$  for each of the decay modes within the  $CP$  sample and of the  $J/\psi K^0$  ( $K_s^0 + K_L^0$ )  
 5460 sample were also measured [946]. These results are preliminary. The Belle experiment  
 5461 measured these parameters from  $J/\psi K_s^0$  and  $J/\psi K_L^0$  decays using a data sample of  
 5462  $492 \text{fb}^{-1}$  and found [947]:

$$C_f = -0.018 \pm 0.021(stat) \pm 0.014(syst), \quad S_f = 0.642 \pm 0.031(stat) \pm 0.017(syst).$$

5463 Belle also reported results from the  $\psi(2S)K_s^0$  decay using  $605 \text{fb}^{-1}$  [948]:

$$C_f = -0.039 \pm 0.069(stat) \pm 0.049(syst), \quad S_f = 0.718 \pm 0.090(stat) \pm 0.033(syst).$$

5464 The analysis of  $b \rightarrow c\bar{c}s$  decay modes imposes a constraint on  $\sin 2\beta$  only, but a four-  
 5465 fold ambiguity in the determination of the angle  $\beta$  remains. It is possible to reduce  
 5466 this ambiguity by measuring  $\cos 2\beta$  using the angular and time-dependent asymmetry in  
 5467  $B^0 \rightarrow J/\psi K^{*0}$  ( $K^{*0} \rightarrow K_s^0 \pi^0$ ) decays. The results of the fit treating  $\sin 2\beta$  and  $\cos 2\beta$  as  
 5468 independent variables give  $\cos 2\beta = +3.32_{-0.96}^{+0.76} \pm 0.27$  [949] for *BABAR*. Using the outcome  
 5469 of fits to simulated samples, the sign of  $\cos 2\beta$  is determined to be positive at the 86%  
 5470 confidence level. Belle reported  $\cos 2\beta = +0.56 \pm 0.11 \pm 0.27$  [950]. These results are  
 5471 compatible with the Standard Model expectations. Other measurements also contribute  
 5472 to reduce the ambiguity.

5473 The time-dependent  $CP$  asymmetry parameters were measured in the  $B^0 \rightarrow J/\psi \pi^0$   
 5474 decay and are also consistent with the SM. Using a dataset of  $425 \text{fb}^{-1}$ , the *BABAR* ex-  
 5475 periment measured [951]:

<sup>22</sup> Charge-conjugate reactions are included implicitly unless otherwise specified.

<sup>23</sup> Unless otherwise stated, all results are quoted with the first error being statistical and the second systematic.

$$C_f = -0.20 \pm 0.19(\text{stat}) \pm 0.03(\text{syst}), \quad S_f = -1.23 \pm 0.21(\text{stat}) \pm 0.04(\text{syst}).$$

5476 This is evidence for CP violation as  $S$  and  $C$  are measured to have non-zero values at a  
5477  $4\sigma$  confidence level. The results reported by the Belle experiment using  $492\text{fb}^{-1}$  are [952]:

$$C_f = -0.08 \pm 0.16(\text{stat}) \pm 0.05(\text{syst}), \quad S_f = -0.65 \pm 0.21(\text{stat}) \pm 0.05(\text{syst}).$$

5478 The measurements of  $\sin 2\beta$  in charmonium decays are in excellent agreement with the  
5479 SM expectations [953]. The results presented above are summarized in Fig. 59. High  
5480 precision measurements using larger datasets are anticipated in the next few years.

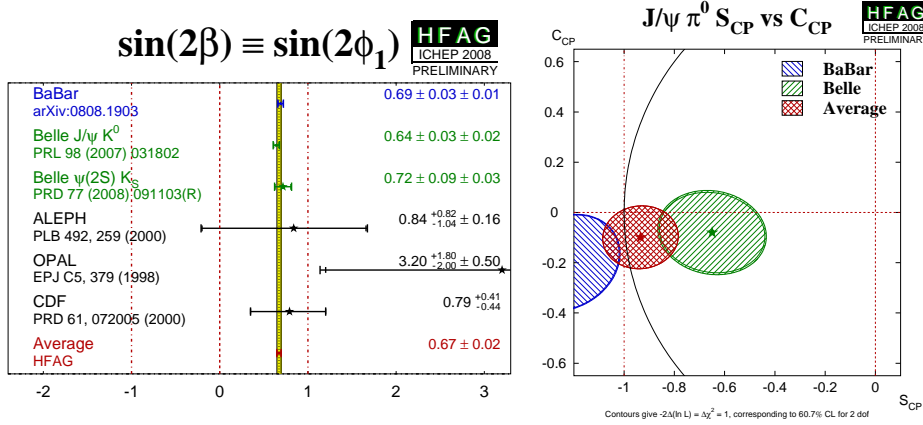


Fig. 59. HFAV averages. In the left panel, the average of  $\sin 2\beta$  from all experiments. In the right panel, the summary plot of  $S$  versus  $C$  for  $B^0 \rightarrow J/\psi \pi^0$ .

#### 5481 7.2.4. Measurement of the $B_s$ meson mixing phase

5482 The  $B_s$  mixing phase is accessible through the time-evolution of  $B_s \rightarrow J/\psi \phi$  decays,  
5483 which is sensitive to the relative phase between the mixing and the  $\bar{b} \rightarrow \bar{c} \bar{s}$  quark-  
5484 level transition,  $\beta_s^{J/\psi \phi} = \beta_s^{\text{SM}} + \beta_s^{\text{NP}}$ . This phase is responsible for  $CP$ -violation. In the  
5485 Standard Model it equals to  $\beta_s^{\text{SM}} = \arg(-V_{ts} V_{tb}^* / V_{cs} V_{cb}^*) \approx 0.02$  [635, 954]. Any sizable  
5486 deviation from this value would be unambiguous evidence of new physics [955]. If new  
5487 physics contributes a phase ( $\beta_s^{\text{NP}}$ ), this would also enter  $\phi_s^{J/\psi \phi} = \phi_s^{\text{SM}} - 2\beta_s^{\text{NP}}$ , which is the  
5488 phase difference between mixing and decay into final states common to  $B_s$  and  $\bar{B}_s$ , and is  
5489 tiny in the SM:  $\phi_s^{\text{SM}} = \arg(-M_{12} / \Gamma_{12}) \approx 0.004$  [932]. The phase  $\phi_s^{J/\psi \phi}$  enters the decay-  
5490 width difference between light and heavy states,  $\Delta\Gamma = \Gamma_L - \Gamma_H = 2|\Gamma_{12}| \cos(\phi_s^{J/\psi \phi})$   
5491 and equals  $\Delta\Gamma^{\text{SM}} \approx 2|\Gamma_{12}| = 0.096 \pm 0.036 \text{ ps}^{-1}$  in the Standard Model [932], thus  
5492 playing a rôle in  $B_s \rightarrow J/\psi \phi$  decays. Since the SM values for  $\beta_s^{J/\psi \phi}$  and  $\phi_s^{J/\psi \phi}$  cannot be  
5493 resolved with the resolution of current experiments, the following approximation is used:  
5494  $\phi_s^{J/\psi \phi} \approx -2\beta_s^{\text{NP}} \approx -2\beta_s^{J/\psi \phi}$ , which holds in case of sizable NP contributions.

5495 The measurement of  $\beta_s^{J/\psi \phi}$  is analogous to the determination of the phase  $\beta =$   
5496  $\arg(-V_{cd} V_{cb}^* / V_{td} V_{tb}^*)$  in  $B^0 \rightarrow J/\psi K_s^0$  decays, except for a few additional complications.  
5497 The oscillation frequency in the  $B_s$  system is about 35 times higher than in  $B^0$  mesons,



5498 requiring excellent decay-time resolution. The decay of a pseudoscalar meson ( $B_s$ ) into  
 5499 two vector mesons ( $J/\psi$  and  $\phi$ ) produces two  $CP$ -even states (orbital angular momen-  
 5500 tum  $L = 0, 2$ ), and one  $CP$ -odd state ( $L = 1$ ), which need to be separated for maximum  
 5501 sensitivity. Finally, the value of the SM expectation for  $\beta_s^{J/\psi\phi}$  is approximately 30 times  
 5502 smaller [944] than  $\beta$ .

5503 Both Tevatron experiments have performed measurements of the time-evolution of  
 5504 flavor-tagged  $B_s \rightarrow J/\psi(\rightarrow \mu^+\mu^-)\phi(\rightarrow K^+K^-)$  decays [956]. The CDF analysis is  
 5505 described in the following, a similar analysis is performed by D0. Events enriched in  
 5506  $J/\psi$  decays are selected by a trigger that requires the spatial matching between a pair  
 5507 of two-dimensional, oppositely-curved, tracks in the multi-wire drift chamber (coverage  
 5508  $|\eta| < 1$ ) and their extrapolation outward to track-segments reconstructed in the muon  
 5509 detectors (drift chambers and scintillating fibers). In the offline analysis, a kinematic  
 5510 fit to a common space-point is applied between the candidate  $J/\psi$  and another pair of  
 5511 tracks consistent with being Kaons originated from a  $\phi$  meson decay. An artificial neural  
 5512 network trained on simulated events (to identify signal,  $S$ ) and  $B_s$  mass sidebands  
 5513 (for background,  $B$ ) is used for an unbiased optimization of the selection. The quantity  
 5514  $S/\sqrt{S+B}$  is maximized using kinematic and particle identification (PID) information.  
 5515 Discriminating observables include Kaon-likelihood, from the combination of  $dE/dx$  and  
 5516 TOF information; transverse momenta of the  $B_s$  and  $\phi$  mesons; the  $K^+K^-$  mass; and  
 5517 the quality of the vertex fit.

5518 The sensitivity to the mixing phase is enhanced if the evolution of  $CP$ -even eigenstates,  
 5519  $CP$ -odd eigenstates, and their interference is separated. This is done by using the angular  
 5520 distributions of final state particles to statistically determine the  $CP$ -composition of the  
 5521 signal. The angular distributions are studied in the transversity basis, which allows a  
 5522 convenient separation between  $CP$ -odd and  $CP$ -even terms in the equations of the time-  
 5523 evolution. Sensitivity to the phase increases if the evolution of bottom-strange mesons  
 5524 produced as  $B_s$  or  $\bar{B}_s$  are studied independently. The time development of flavor-tagged  
 5525 decays contains terms proportional to  $\sin(2\beta_s^{J/\psi\phi})$ , reducing the ambiguity with respect  
 5526 to the untagged case ( $\propto |\sin(2\beta_s^{J/\psi\phi})|$ ). Building on techniques used in the  $B_s$  mixing  
 5527 frequency measurement [218], the production flavor is inferred using flavor tagging  
 5528 techniques discussed in Sec. 3.2.2

5529 The tagging power,  $\epsilon D^2 \approx 4.5\%$ , is the product of an efficiency  $\epsilon$ , the fraction of  
 5530 candidates with a flavor tag, and the square of the dilution  $D = 1 - 2w$ , where  $w$  is  
 5531 the mistag probability. The proper time of the decay and its resolution are known on a  
 5532 per-candidate basis from the position of the decay vertex, which is determined with an  
 5533 average resolution of approximately  $27 \mu\text{m}$  ( $90 \text{ fs}^{-1}$ ) in  $B_s \rightarrow J/\psi\phi$  decays. Information  
 5534 on  $B_s$  candidate mass and its uncertainty, angles between final state particles' trajectories  
 5535 (to extract the  $CP$ -composition), production flavor, and decay length and its resolution  
 5536 are used as observables in a multivariate unbinned maximum likelihood fit of the time  
 5537 evolution. The fit accounts for direct decay amplitude, mixing followed by the decay,  
 5538 and their interference. Direct  $CP$ -violation is expected to be small and is not considered.  
 5539 The outputs of the fit are the phase  $\beta_s^{J/\psi\phi}$ , the decay-width difference  $\Delta\Gamma$ , and 25 other  
 5540 “nuisance” parameters ( $\nu$ ). These include the mean  $B_s$  decay-width ( $\Gamma = (\Gamma_L + \Gamma_H)/2$ ),  
 5541 the squared magnitudes of linear polarization amplitudes ( $|A_0|^2$ ,  $|A_{\parallel}|^2$ ,  $|A_{\perp}^2|$ ), the  $CP$ -  
 5542 conserving (“strong”) phases ( $\delta_{\parallel} = \arg(A_{\parallel}A_0^*)$ ,  $\delta_{\perp} = \arg(A_{\perp}A_0^*)$ ), and others.

5543 The acceptance of the detector is calculated from a Monte Carlo simulation and found

5544 to be consistent with observed angular distributions of random combinations of four  
5545 tracks in data. CDF also validated the angular-mass-lifetime model by measuring life-  
5546 time and polarization amplitudes in 7800  $B^0 \rightarrow J/\psi K^*$  decays, which show angu-  
5547 lar features similar to the  $B_s$  sample:  $c\tau(B^0) = 456 \pm 6(stat) \pm 6(syst) \mu\text{m}$ ,  $|A_0|^2 =$   
5548  $0.569 \pm 0.009(stat) \pm 0.009(syst)$ ,  $|A_{\parallel}|^2 = 0.211 \pm 0.012(stat) \pm 0.006(syst)$ ,  $\delta_{\parallel} = -2.96 \pm$   
5549  $0.08(stat) \pm 0.03(syst)$ , and  $\delta_{\perp} = 2.97 \pm 0.06(stat) \pm 0.01(syst)$ . The results, consistent  
5550 and competitive with most recent  $B$ -factories' results [957], support the reliability of  
5551 the model. Additional confidence is provided by the precise measurement of lifetime and  
5552 width-difference in untagged  $B_s \rightarrow J/\psi \phi$  decays [958].

5553 Tests of the fit on simulated samples show biased, non-Gaussian distributions of esti-  
5554 mates and multiple maxima, because the likelihood is invariant under the transformation  
5555  $\mathcal{T} = (2\beta_s^{J/\psi\phi} \rightarrow \pi - 2\beta_s^{J/\psi\phi}, \Delta\Gamma \rightarrow -\Delta\Gamma, \delta_{\parallel} \rightarrow 2\pi - \delta_{\parallel}, \delta_{\perp} \rightarrow \pi - \delta_{\perp})$ , and the reso-  
5556 lution on  $\beta_s^{J/\psi\phi}$  was found to depend crucially on the true values of  $\beta_s^{J/\psi\phi}$  and  $\Delta\Gamma$ .  
5557 CDF quotes therefore a frequentist confidence region in the  $(\beta_s^{J/\psi\phi}, \Delta\Gamma)$  plane rather  
5558 than point-estimates for these parameters. Obtaining a correct and meaningful region  
5559 requires projecting the full 27-dimensional region into the  $(\beta_s^{J/\psi\phi}, \Delta\Gamma)$  plane. A com-  
5560 mon approximate method is the profile likelihood approach. to replace the likelihood,  
5561 For every point in the  $(\beta_s^{J/\psi\phi}, \Delta\Gamma)$  plane,  $\hat{\nu}$  are the values of nuisance parameters that  
5562 maximize the likelihood. Then  $-2\Delta \ln(L_p)$  is typically used as a  $\chi^2$  variable to derive  
5563 confidence regions in the two-dimensional space  $(\beta_s^{J/\psi\phi}, \Delta\Gamma)$ . The simulations show that  
5564 in the present case the approximation fails. The resulting regions contain the true values  
5565 with lower probability than the nominal confidence level (C.L.) because the  $-2\Delta \ln(L_p)$   
5566 distribution has longer tails than a  $\chi^2$ . A full confidence region construction is therefore  
5567 needed, using simulation of a large number of pseudo-experiments to derive the actual  
5568 distribution of  $-2\Delta \ln(L_p)$ , with a potential for an excessive weakening of the results  
5569 from systematic uncertainties. However, in a full confidence limit construction, the use  
5570 of  $-2\Delta \ln(L_p)$  as ordering function is close to optimal for limiting the impact of system-  
5571 atic uncertainties [959, 960]. With this method, it is possible to account for the effect of  
5572 systematic uncertainties just by randomly sampling a limited number of points in the  
5573 space of all nuisance parameters: a specific value  $(\beta_s^{J/\psi\phi}, \Delta\Gamma)$  is excluded only if it can be  
5574 excluded for any assumed value of the nuisance parameters within  $5\sigma$  of their estimate  
5575 on data. Fig. 60 shows the confidence regions obtained by the two experiments with 2.8  
5576  $\text{fb}^{-1}$  of Tevatron data.

A separate handle on CP violation is available through semileptonic  $B_s$  decays and has  
been performed by the D0 collaboration on 2.8  $\text{fb}^{-1}$  of Tevatron data. The flavor of the  $B_s$   
meson in the final state is determined by the muon charge in the decay  $B_s \rightarrow D_s^- \mu^+ \nu X$   
with  $D_s^- \rightarrow \phi \pi^-$  and  $\phi \rightarrow K^+ K^-$ . A combined tagging method is then used to determine  
the initial state flavor. A time-dependent fit to  $B_s$  candidate distributions yields the CP  
violation parameter

$$A_{sl}^s = -0.0024 \pm 0.0117 \text{ (stat)}_{-0.0024}^{+0.0015} \text{ (syst)}. \quad (360)$$

This is the first direct measurement [951] of the time integrated flavor untagged charge  
asymmetry in semileptonic  $B_s^0$  decays.  $A_{SL}^{s,\text{unt.}}$  has also been obtained from a data sam-  
ple corresponding to an integrated luminosity of 1.3  $\text{fb}^{-1}$  in comparing the decay rate  
 $B_s \rightarrow \mu^+ D_s^- \nu X$ ,  $D_s^- \rightarrow \phi \pi^-$ ,  $\phi \rightarrow K^+ K^-$  with its charge conjugated decay rate. The  
asymmetry amounts to

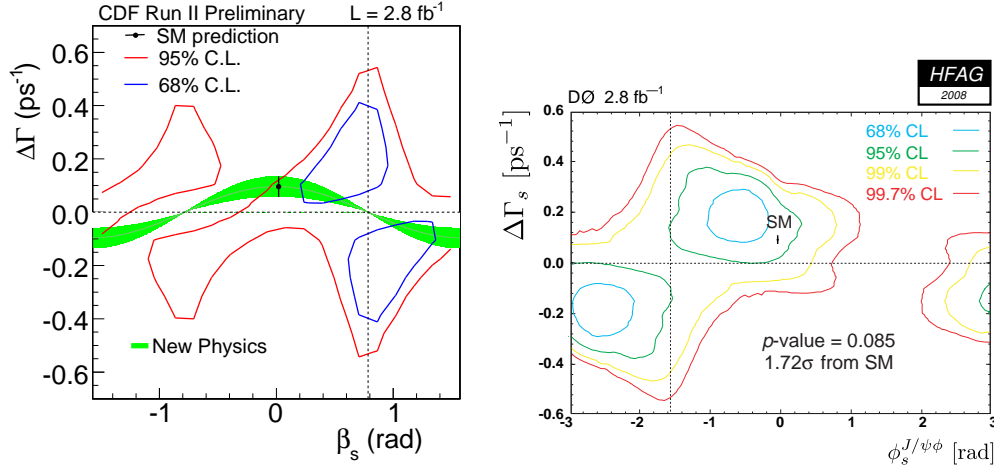


Fig. 60. Confidence region in the  $(\beta_s^{J/\psi\phi}, \Delta\Gamma)$  plane obtained with  $2.8 \text{ fb}^{-1}$  of CDF (left panel) and D0(right panel) data. The green band is the region allowed by any NP contribution not entering  $|\Gamma_{12}|$ , and assuming  $2|\Gamma_{12}| = 0.096 \pm 0.036 \text{ ps}^{-1}$  [932].

$$A_{SL}^{s,\text{unt.}} = [1.23 \pm 0.97 \text{ (stat)} \pm 0.17 \text{ (syst)}] \times 10^{-2}, \quad (361)$$

assuming that  $\Delta m_s / \overline{\Gamma}_s \gg 1$ . The result can be further related to the CP-violating phase in  $B_s^0$  mixing via

$$\frac{\Delta\Gamma_s}{\Delta m_s} \tan \phi_s = [2.45 \pm 1.93 \text{ (stat)} \pm 0.35 \text{ (syst)}] \times 10^{-2}. \quad (362)$$

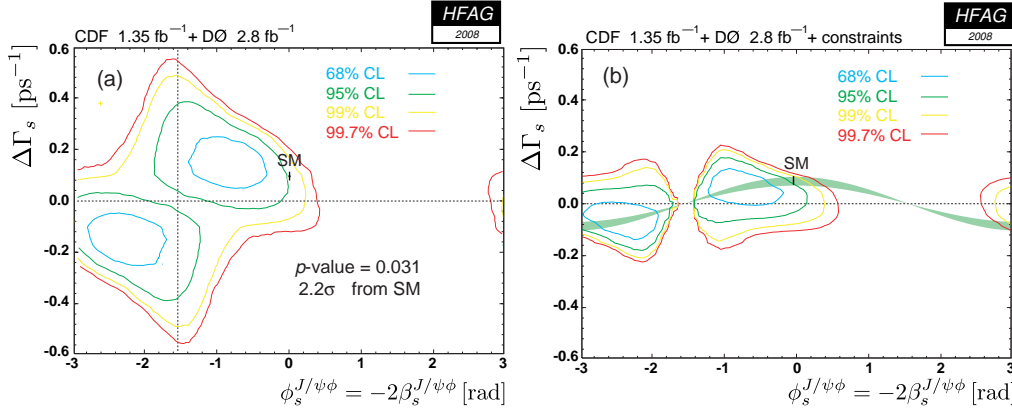


Fig. 61. Contour plots of D0 and CDF combined results in the  $(\Delta\Gamma_s, \phi_s)$  plane for different confidence levels. In the left panel, the combination of two results without constraints. In the right panel, constraints of the measured charge asymmetry  $A_{SL}^s$  and  $B_s^0$  lifetime are taken into account.

5577 The world best knowledge on the  $B_s$  mixing phase at this time comes from combining  
 5578 the two Tevatron results and applying all available constraints to the calculation. Fig.  
 5579 61 shows the combination of the results from the two Tevatron experiments. The current  
 5580 combined result is based on the  $1.35 \text{ fb}^{-1}$  dataset from CDF and the  $2.8 \text{ fb}^{-1}$  dataset from

5581 D0. The unconstrained result is consistent with the Standard Model prediction within  
 5582  $2.2\sigma$ . Adding constraints from  $A_{SL}^s$  and the  $B_s$  flavor specific lifetime measurements, the  
 5583 discrepancy between the Standard Model prediction and the combined result increases to  
 5584  $2.3\sigma$ .

### 5585 7.3. The $D$ -meson system

#### 5586 7.3.1. Theoretical prediction for $\Delta M_D$ and $CP$ violation within the SM and beyond

5587 The SM calculation of  $\Delta M_D$  is plagued by long-distance contributions, responsible for  
 5588 very large theoretical uncertainties. The short-distance contribution in  $\Delta M_D$  [961,962],  
 5589 indeed, is highly suppressed both by a factor  $(m_s^2 - m_d^2)/M_W^2$  generated by the GIM  
 5590 mechanism and by a further factor  $(m_s^2 - m_d^2)/m_c^2$  due to the fact that the external  
 5591 momentum, of the order of  $m_c$ , is communicated to the internal light quarks in box-  
 5592 diagrams. These factors explain why the box-diagrams are so small for  $D$  mesons relative  
 5593 to  $K$  and  $B_{d,s}$  mesons where the GIM mechanism enters as  $m_c^2/M_W^2$  and  $m_t^2/M_W^2$  and  
 5594 external momenta can be neglected.

5595 Theoretical estimates of charm mixing in the SM have been performed using either  
 5596 quarks or hadrons as basic degrees of freedom.

5597 The former method, like that used in  $B_{d,s}$  mixing, consists in analyzing the mixing by  
 5598 using a sum of local operators ordered by dimension according to OPE [963]. Roughly  
 5599 speaking, the result at the leading order in the OPE (where operators of dimension  
 5600  $D = 6$  contribute) and in QCD from the  $s\bar{s}$  intermediate state yields the result [964]  
 5601  $y_D \sim F(z)(|V_{us}|/|V_{cs}|)^2 \sim 0.01$  where  $F(z) = 1/2 + \mathcal{O}(z)$  with  $z \equiv (m_s/m_c)^2 \simeq 0.006$ .  
 5602 This seems to reproduce the correct magnitude. Such is, however, not the case, as severe  
 5603 flavor cancellations with the  $d\bar{d}$ ,  $s\bar{d}$ ,  $d\bar{s}$  intermediate states occur (the leading terms in  
 5604 the  $z$ -expansion for  $x_D$  and  $y_D$  respectively become  $z^2$  and  $z^3$  at order  $\alpha_s^0$  and just  $z^2$   
 5605 at order  $\alpha_s^1$ ). The result through  $\mathcal{O}(\alpha_s)$  is tiny,  $x_D \simeq y_D \sim 10^{-6}$  [964]. Evidently the  
 5606 OPE for charm is slowly convergent, although higher orders of the OPE do contain terms  
 5607 in which the  $z$ -suppression is less severe [965,966]. The problem is that the number of  
 5608 local operators increases sharply with the operator dimension  $D$  (e.g.  $D = 6$  has two  
 5609 operators,  $D = 9$  has fifteen, and so on). To make matters worse, the matrix elements  
 5610 of the various local operators are unknown and can be only roughly approximated in  
 5611 model calculations. QCD lattice determinations would be of great use, but are currently  
 5612 unavailable.

The other method, which considers hadronic degrees of freedom, is based on the fol-  
 lowing relation between the width difference and the absorptive matrix element given in  
 Eq. (337), with

$$\Gamma_{12}^D = \frac{1}{2M_D} \text{Disc}\langle D^0 | i \int d^4x \mathcal{T} (\mathcal{H}_{eff}^{\Delta C=1}(x) \mathcal{H}_{eff}^{\Delta C=1}(0)) | \bar{D}^0 \rangle, \quad (363)$$

5613 To get  $y_D$ , defined in Eq. (338), one inserts intermediate states between the  $\Delta C = 1$   
 5614 effective Hamiltonians (see Sec. 2.1). This method yielded an early estimate for  $y_{B_s}$   
 5615 (where the dominant contributions are few in number [967]), but for charm mixing many  
 5616 matrix elements contribute. The result of using a theoretical model [968] gives  $y_D \sim 10^{-3}$ ,  
 5617 which is too small. This shows how delicate the sum over many contributions seems to  
 5618 be.

5619 Another approach is to rely more on charm decay data and less on the underlying  
5620 theory [969,970]. Given that SU(3) breaking occurs at second order in charm mixing [971],  
5621 perhaps all two-particle and three-particle sectors contribute very little. However, this  
5622 cannot happen for the four-particle intermediate states because the decay of  $D^0$  into four-  
5623 Kaon states is kinematically forbidden. In fact, Ref. [972] claims that these multiparticle  
5624 sectors can generate  $y_D \sim 10^{-2}$ . The complicate picture is worsened by the fact that a  
5625 dispersion relation calculation [972] using charm decay widths as input predicts a negative  
5626 value for  $x_D$ , i.e. of opposite sign with respect to the experimental measurement. The  
5627 determination of  $x_D$  in the SM is certainly subtle enough to deserve further study and,  
5628 at the same time, to strengthen the motivation for studying NP models of  $D^0$  mixing.

5629 NP contributions to charm mixing can affect  $y_D$  as well as  $x_D$ . We do not consider the  
5630 former here, instead referring the reader to refs. [973,974]. The study of  $x_D$  in Ref. [975]  
5631 considers 21 New Physics models, arranged in terms of extra gauge bosons (LR models,  
5632 etc), extra scalars (multi-Higgs models, etc), extra fermions (little Higgs models, etc),  
5633 extra dimensions (split fermion models, etc), and extra global symmetries (SUSY, etc).  
5634 The strategy for calculating the effect of NP on  $D^0$  mixing is, for the most part, straight-  
5635 forward. One considers a particular NP model and calculates the mixing amplitude as a  
5636 function of the model parameters. If the mixing signal is sufficiently large, constraints on  
5637 the parameters are obtained. Of these 21 NP models, only four (split SUSY, universal  
5638 extra dimensions, left-right symmetric and flavor-changing two-higgs doublet) are inef-  
5639 fective in producing charm mixing at the observed level. This has several causes, e.g.  
5640 the NP mass scale is too large, severe cancellations occur in the mixing signal, etc. This  
5641 means that 17 of the NP models can produce charm mixing. We refer to Ref. [975] for  
5642 details.

5643 Finally, we observe that for a deeper understanding of  $D^0 - \bar{D}^0$  mixing, there remain  
5644 additional avenues to explore, among them correlating NP contributions between charm  
5645 mixing and rare charm decays and providing a comprehensive account of CP violations  
5646 (both SM and NP) in  $D^0 - \bar{D}^0$  mixing.

### 5647 7.3.2. *Experimental results*

5648 Recent studies have shown evidence for mixing in the  $D^0 - \bar{D}^0$  system at the 1% level [976–  
5649 979]. The measured values can be accommodated by the Standard Model (SM) [966,969–  
5650 972] where the largest predictions for  $x$  and  $y$  (defined below) are of  $\mathcal{O}(10^{-2})$ . These  
5651 measurements provide strong constraints on new physics models [975,980,981]. An ob-  
5652 servation of  $CP$  violation in  $D^0 - \bar{D}^0$  mixing with the present experimental sensitivity  
5653 would provide evidence for physics beyond the SM [982], and a search for this effect in  
5654 the charm system is considered elsewhere [983]. Presented here is an overview of recent  
5655 mixing measurements.

5656 The two neutral  $D$  mass eigenstates  $|D_1\rangle$  and  $|D_2\rangle$  are not the flavor eigenstates  $D^0$  and  
5657  $\bar{D}^0$ , but linear combinations thereof. If the weak interaction splits the masses or widths  
5658 of  $|D_1\rangle$  and  $|D_2\rangle$ , then mixing between  $D^0$  and  $\bar{D}^0$  will occur. The rate of  $D^0 - \bar{D}^0$  mixing  
5659 is characterized by the parameters  $x \equiv \Delta m/\Gamma$  and  $y \equiv \Delta\Gamma/2\Gamma$ , where  $\Delta m = m_1 - m_2$   
5660 and  $\Delta\Gamma = \Gamma_1 - \Gamma_2$  are the differences between the mass and width eigenvalues of these  
5661 states, and  $\Gamma = (\Gamma_1 + \Gamma_2)/2$  is the average width. If either  $x$  or  $y$  is non-zero, mixing will  
5662 occur.

### 5663 **Mixing in $D^0 \rightarrow K^+ \pi^-$ Decays**

5664 The right-sign (RS), Cabibbo-favored (CF) decay  $D^0 \rightarrow K^- \pi^+$  and the wrong-sign  
5665 (WS) decay  $D^0 \rightarrow K^+ \pi^-$  are studied. The latter can be produced via the doubly  
5666 Cabibbo-suppressed (DCS) decay  $D^0 \rightarrow K^+ \pi^-$  or via mixing followed by a CF decay  
5667  $\bar{D}^0 \rightarrow K^+ \pi^-$ . The DCS decay has a small rate  $R_D$  of order  $\tan^4 \theta_C \approx 0.3\%$  relative to  
5668 CF decay.  $D^0$  and  $\bar{D}^0$  are distinguished by their production in the decay  $D^{*+} \rightarrow \pi_s^+ D^0$   
5669 where the  $\pi_s^+$  is referred to as the “slow pion”. In RS decays the  $\pi_s^+$  and Kaon have  
5670 opposite charges, while in WS decays the charges are the same.

The time dependence of the WS decay rate is used to separate the contributions of DCS  
decays from  $D^0$ - $\bar{D}^0$  mixing. For the WS decay of a meson produced as a  $D^0$  at time  $t = 0$   
in the limit of small mixing ( $|x|, |y| \ll 1$ ) and  $CP$  conservation this is approximated as

$$\frac{T_{\text{WS}}(t)}{e^{-\Gamma t}} \propto R_D + \sqrt{R_D} y'_f \Gamma t + \frac{x'^2_f + y'^2_f}{4} (\Gamma t)^2, \quad (364)$$

5671 where  $x'_f = x \cos \delta_f + y \sin \delta_f$ ,  $y'_f = -x \sin \delta_f + y \cos \delta_f$ , where  $f$  is the final state accessible  
5672 to both  $D^0$  and  $\bar{D}^0$  decays, and  $\delta_f$  is the relative strong phase between the DCS and  
5673 CF amplitudes. This makes it possible to measure the quantities  $x$  and  $y$ , if the strong  
5674 phase difference  $\delta_f$  is known. To search for  $CP$  violation, Eq. (364) is applied to  $D^0$  and  
5675  $\bar{D}^0$  samples separately.

5676 Evidence for  $D^0$ - $\bar{D}^0$  mixing in  $D^0 \rightarrow K^+ \pi^-$  decays has been reported by the *BABAR* col-  
5677 laboration [976]. The mixing parameters were found to be  $x'^2_{K\pi} = [-0.22 \pm 0.30 \text{ (stat.)} \pm$   
5678  $0.21 \text{ (syst.)}] \times 10^{-3}$  and  $y'_{K\pi} = [9.7 \pm 4.4 \text{ (stat.)} \pm 3.1 \text{ (syst.)}] \times 10^{-3}$ , and a correlation  
5679 between them of  $-0.94$ . This result is inconsistent with the no-mixing hypothesis with  
5680 a significance of  $3.9 \sigma$ , with no evidence for  $CP$  violation. This result was confirmed by  
5681 the CDF experiment [984, 985].

5682 The quantum coherence between pair-produced  $D^0$  and  $\bar{D}^0$  in  $\psi(3770)$  decays can be  
5683 used to study charm mixing and to make a determination of the relative strong phase  
5684  $\delta_{K\pi}$  [986]. Using data collected with the CLEO-c detector at  $E_{cm} = 3.77$  GeV, as well  
5685 as branching fraction input from other experiments a value of  $\cos \delta_{K\pi} = 1.03^{+0.31}_{-0.17} \pm 0.06$   
5686 was found, where the uncertainties are statistical and systematic, respectively. In addi-  
5687 tion, by further including external measurements of charm mixing parameters, another  
5688 measurement of  $\cos \delta_{K\pi} = 1.10 \pm 0.35 \pm 0.07$ , as well as  $x \sin \delta_{K\pi} = (4.4^{+2.7}_{-1.8} \pm 2.9) \times 10^{-3}$   
5689 and  $(\delta_{K\pi} = 22^{+11}_{-12} \text{ } ^{+9}_{-11})^\circ$ , was made.

#### 5690 **Mixing in $D^0 \rightarrow K^+ \pi^- \pi^0$ Decays**

5691 Further evidence for mixing was reported by the *BABAR* collaboration using a time-  
5692 dependent Dalitz plot analysis of the WS  $D^0 \rightarrow K^+ \pi^- \pi^0$  decays [979]. The advantage  
5693 of an amplitude analysis across the Dalitz plot is that the interference term in Eq. 364,  
5694 produces a variation in average decay time as a function of position in the Dalitz plot  
5695 that is sensitive to the complex amplitudes of the resonant isobars as well as the mixing  
5696 parameters. In this study, the change in the average decay time and the interference  
5697 between the  $D^0 \rightarrow K^{*+} \pi^-$  and  $D^0 \rightarrow \rho^- K^+$  amplitudes are the origin of the sensitivity  
5698 to mixing.

5699 Assuming  $CP$  conservation, the mixing parameters  $x'_{K\pi\pi^0} = [2.61^{+0.57}_{-0.68} \text{ (stat.)} \pm$   
5700  $0.39 \text{ (syst.)}] \%$ , and  $y'_{K\pi\pi^0} = [-0.06^{+0.55}_{-0.64} \text{ (stat.)} \pm 0.34 \text{ (syst.)}] \%$  were extracted. This  
5701 result is inconsistent with the no-mixing hypothesis with a significance of  $3.2 \sigma$ . No  
5702 evidence of  $CP$  violation in mixing was observed.

#### 5703 **Mixing in $D^0 \rightarrow K_s^0 \pi^+ \pi^-$ Decays**

5704 The CLEO collaboration pioneered an analysis of  $D^0 \rightarrow K_S^0 \pi^+ \pi^-$  decays using a time-  
 5705 dependent Dalitz plot analysis [987], allowing for a direct determination of  $x$  and  $y$ . Due  
 5706 to the presence of  $CP$ -eigenstates in the final state, the amplitudes of  $D^0$  and  $\bar{D}^0$  are  
 5707 entangled, so that the analysis is free of unknown phases.

5708 The Belle collaboration has repeated this analysis [988], first assuming  $CP$  conserva-  
 5709 tion and subsequently allowing for  $CP$  violation. Assuming negligible  $CP$  violation, the  
 5710 mixing parameters  $x = (0.80 \pm 0.29_{-0.07-0.14}^{+0.09+0.10})\%$  and  $y = (0.33 \pm 0.24_{-0.12-0.08}^{+0.08+0.06})\%$  were  
 5711 measured, where the errors are statistical, experimental systematic, and systematic due  
 5712 to the amplitude model uncertainties, respectively. This corresponds to a deviation of  
 5713  $2.4 \sigma$  significance from the no-mixing hypothesis.

#### 5714 **The Measurement of $y_{CP}$**

5715 One consequence of  $D^0$ - $\bar{D}^0$  mixing is that the  $D^0$  decay time distribution can be  
 5716 different for decays to different  $CP$  eigenstates [989]. Using the ratios of lifetimes extracted  
 5717 from a sample of  $D^0$  mesons produced through the process  $D^{*+} \rightarrow D^0 \pi^+$ , that decay  
 5718 to  $K^- \pi^+$ ,  $K^- K^+$ , or  $\pi^+ \pi^-$ , the lifetimes of the  $CP$ -even, Cabibbo-suppressed modes  
 5719  $K^- K^+$  and  $\pi^+ \pi^-$  are compared to that of the  $CP$ -mixed, Cabibbo-favored mode  $K^- \pi^+$   
 5720 to obtain a measurement of  $y_{CP}$ , which in the limit of  $CP$  conservation corresponds to the  
 5721 mixing parameter  $y$ . Both Belle [977] and BABAR [978] have produced a measurement of  
 5722  $D^0$ - $\bar{D}^0$  mixing parameters, at  $3.2$  and  $3.0 \sigma$  from the no mixing expectation, respectively.  
 5723 All available results are shown in Fig. 62. No evidence for a  $CP$  asymmetry between  $D^0$   
 5724 and  $\bar{D}^0$  decays has been found.

#### 5725 **CP-odd final states**

5726 The mixing parameter  $y_{CP}$  has also been measured by the Belle Collaboration, using  
 5727 a flavor-untagged sample of  $D^0 \rightarrow K_S^0 K^+ K^-$  decays [990]. By measuring the difference  
 5728 in lifetimes between  $D^0$  mesons decaying to  $K_S^0 K^+ K^-$  in two different  $m(K^+ K^-)$   
 5729 regions with different contributions of  $CP$  even and odd eigenstates they determine  $y_{CP} =$   
 5730  $(0.21 \pm 0.63 \pm 0.78 \pm 0.01(\text{model}))\%$ . This result, is also included in Fig. 62.

#### 5731 **Summary**

5732 A global average has been constructed from 28 mixing variables (including those men-  
 5733 tioned above), by the Heavy Flavor Averaging Group (HFAG) [558], as shown in Fig. 63.  
 5734 The no-mixing point  $x = y = 0$  is excluded at  $9.8 \sigma$ , and the values  $x \approx y \approx 1 \%$  are  
 5735 favored, but to date no single measurement exceeds  $5 \sigma$ .

5736 The CDF Collaboration has used a signal of  $12.7 \times 10^3 D^0 \rightarrow K^+ \pi^-$  decays with proper  
 5737 decay times between  $0.75$  and  $10$  mean  $D^0$  lifetimes, corresponding to an integrated  
 5738 luminosity of  $1.5 fb^{-1}$ , to search for  $D^0$ - $\bar{D}^0$  mixing. The mixing parameters are measured  
 5739 to be  $R_D = 3.04 \pm 0.55 (\times 10^{-3})$ ,  $y' = 8.54 \pm 7.55 (\times 10^{-3})$ ,  $x'^2 = -0.12 \pm 0.35 (\times 10^{-3})$ . The  
 5740 data are inconsistent with the no mixing hypothesis ( $y' = x'^2 = 0$ ) with a probability  
 5741 equivalent to  $3.8$  Gaussian standard deviations.

5742 The Belle and BaBar collaboration have reported the first evidence of charm mixing,  
 5743 Belle found significantly different decay distributions for  $D^0$  decays to the  $CP$ -eigenstates  
 5744  $K^+ K^-$  and  $\pi^+ \pi^-$  compared to that for the  $CP$  mixed state  $K^- \pi^+$ . BaBar found evidence  
 5745 for charm mixing in the difference of the decay time distributions for  $D^0 \rightarrow K^+ \pi^-$   
 5746 compared to that for the Cabibbo-favored decay  $D^0 \rightarrow K^- \pi^+$ . CDF has performed a  
 5747 new measurement of the same  $D^0$  mixing process as used by BaBar. The ratio  $R$  of

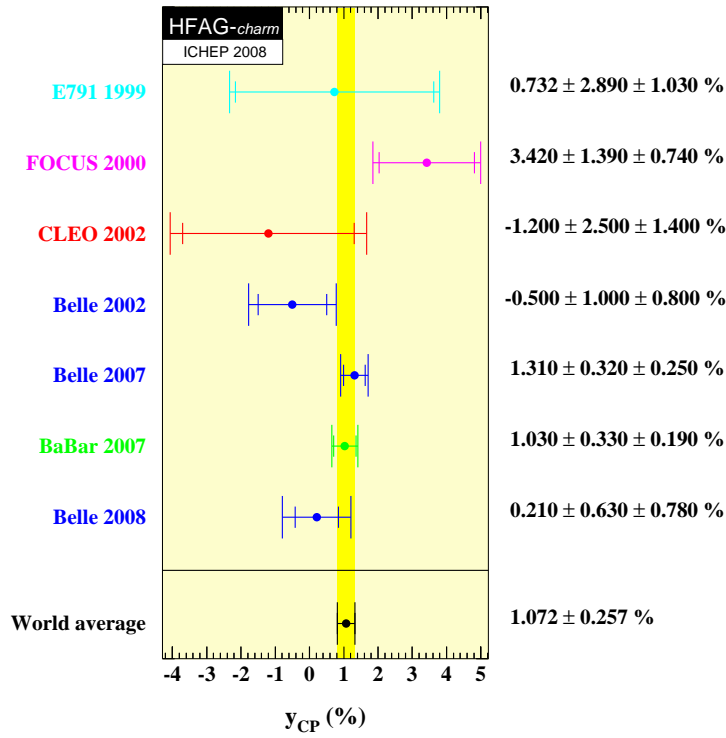


Fig. 62. Summary of measurements of  $y_{CP}$ , the mean  $y_{CP} \approx 1$  % differs significantly from zero [558].

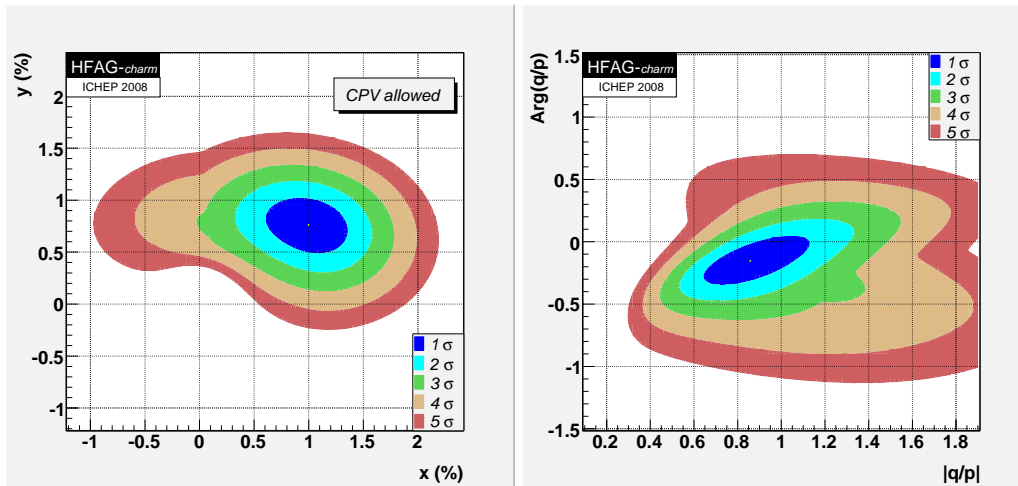


Fig. 63. World averages from the Heavy Flavor Averaging Group (HFAG);  $\chi^2$  contours for  $x$  vs.  $y$ , and  $|q/p|$  vs.  $\text{Arg}(q/p)$  [558]

5748  $D^0 \rightarrow K^+\pi^-$  to  $D^0 \rightarrow K^-\pi^+$  decay rates can be approximated as a simple quadratic  
 5749 function of the proper decay time. The CDF measurement uses  $1.5 \text{ fb}^{-1}$  of data, where



5750 the events are required to have a pair of oppositely charged particles that are consistent  
5751 with originating from a secondary vertex separated from the beamline. In the offline  
5752 analysis we have reconstructed the right sign decay chain  $D^{*+} \rightarrow D^0\pi^+$ ,  $D^0 \rightarrow K^-\pi^+$ ,  
5753 and the wrong sign decay chain  $D^{*+} \rightarrow D^0\pi^-$ ,  $D^0 \rightarrow K^+\pi^-$ . The relative charges of  
5754 the pions determine whether the decay chain is right sign or wrong sign. The RS and  
5755 WS decays have the same kinematics and we have used the same selection criteria  
5756 for both categories, which reduces the systematic uncertainties in the WS/RS. Several  
5757 cuts based on the decay topology are applied to increase the signal purity. The  $D^{*+}$   
5758 fraction due to B hadron decays is subtracted from the signal used to perform the WS/RS  
5759 measurement. The  $D^{*+}$  component due to B hadron decays shows a broader impact  
5760 parameter distribution than the prompt component. The time integrated prompt Dstar  
5761 signals are  $12.7 \times 10^3$  WS events and  $3 \times 10^6$  RS events. The decay time is divided in 20  
5762 bins and a least-squares parabolic fit of WS/RS is performed to determine  $R_D$ ,  $x$ ,  $y$ . The  
5763 parameters measured by CDF are comparable to those from the previous measurements.  
5764 The no mixing is excluded at 3.8 Gaussian sigma. Several alternative checks confirm this  
5765 3.8 sigma. CDF provides the first confirmation of the charm mixing evidence from the  
5766 BaBar experiment.

#### 5767 7.4. Future Outlook

##### 5768 7.4.1. B meson mixing and lifetimes

5769 First B lifetime measurements at LHC experiments will be used as calibration mea-  
5770 surements to understand detector effects on time-dependant analyses. Very large samples  
5771 of fully reconstructed  $B^+$  and  $B^0$  candidates will be available very early after the LHC  
5772 starts, and will allow comparison with existing precise lifetime measurements. For ex-  
5773 ample, at ATLAS, 1024 reconstructed  $B^0 \rightarrow J/\psi K^{*0}$  are expected after  $10 \text{ pb}^{-1}$  of  
5774 data, which will allow a lifetime measurement with 10% precision after approximately  
5775 one month of data taking. Similarly, the LHCb experiment will reconstruct  $1.735 \times 10^6$   
5776  $B^+ \rightarrow J/\psi K^+$  candidates for  $2 \text{ fb}^{-1}$  of data, with a small background over signal ratio,  
5777 allowing not to use any lifetime selection criteria and thus to determine lifetime resolu-  
5778 tion functions. Hadronic decay modes will also be reconstructed with large samples. The  
5779 LHCb experiment will reconstruct in  $2 \text{ fb}^{-1}$  of data  $1.34 \times 10^6 B^0 \rightarrow D^-(K^-\pi^+\pi^-)\pi^+$ ,  
5780 with a proper time resolution of 33.9 fs. This will allow to reach the current  $B^0$  lifetime  
5781 precision (0.009 ps) with 60000 events, considering only statistical errors. The different  
5782 large b-hadron samples will help demonstrating the capabilities of the LHC experiments  
5783 related to lifetime and time-dependant analyses.

5784 The  $B_c^+$  lifetime will be measured at the LHC experiments. This particle was first  
5785 observed at Tevatron experiments, but the  $B_c^+$  production cross-section will be around  
5786 20 times larger at the LHC: of the order of  $10^9 B_c^\pm$  will be produced per year in LHCb.  
5787 Measurement of the  $B_c^+$  lifetime will be an interesting window on the proportion of its  
5788 different decay mechanisms: b decay, c decay or annihilation. The most promising decay  
5789 channel that will be used for the analysis is  $B_c^+ \rightarrow J/\psi\pi^+$ . Assuming a  $B_c^+$  production  
5790 cross-section of  $0.4 \mu\text{b}$  and a branching fraction for  $B_c^+ \rightarrow J/\psi\pi^+$  equal to  $1.3 \times 10^{-3}$ ,  
5791 700 events are expected for  $2 \text{ fb}^{-1}$  of data at LHCb, and 80 events for  $10 \text{ fb}^{-1}$  at CMS,  
5792 leading to a statistical precision on the lifetime measurement equal to 0.026 ps at LHCb  
5793 and 0.055 ps at CMS.

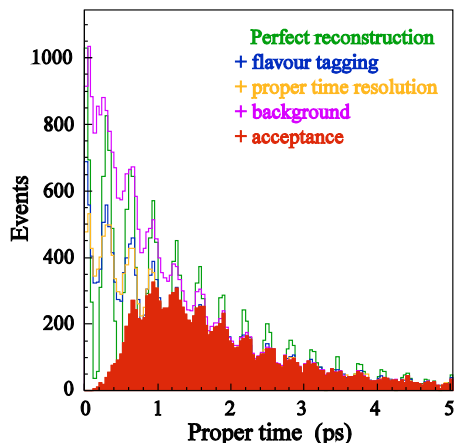


Fig. 64. flavor tagged proper time distribution

5794 The measurement of the  $\Lambda_b$  lifetime will also be possible at LHC. LHCb expects to  
 5795 reconstruct  $2.3 \times 10^4$  events for  $2 \text{ fb}^{-1}$  of data reconstructing the decay mode  $\Lambda_b \rightarrow$   
 5796  $J\psi(\mu^+\mu^-)\Lambda(p\pi)$ , with a proper time resolution of 0.0415 ps, yielding to a lifetime mea-  
 5797 surement with a statistical precision of 0.027 ps. The ATLAS experiment will reconstruct  
 5798 4500 events in the same decay mode with  $10 \text{ fb}^{-1}$  of data.

5799 The reconstruction of the flavor specific decay mode  $B_s^0 \rightarrow D_s^+\pi^-$  with  $D_s^+ \rightarrow K^+K^-\pi^+$   
 5800 will allow the measurement of the  $B_s^0$  mixing frequency  $\Delta m_s$  together with the  $B_s^0$  width  
 5801 difference,  $\Delta\Gamma_s$ . 155000 reconstructed candidates are expected at LHCb in  $2 \text{ fb}^{-1}$  of  
 5802 data, with a small background over signal ratio  $\frac{B}{S} \in [0.06; 0.4]$  at 90% confidence level, a  
 5803 resolution on the mass of 17 MeV and a time resolution of 33 fs. The expected statistical  
 5804 error on the  $B_s^0$  lifetime is estimated to be 0.013 ps, 0.008  $\text{ps}^{-1}$  for  $\Delta m_s$ , and 0.03  $\text{ps}^{-1}$   
 5805 for  $\Delta\Gamma_s$  (assuming a central value of  $\Delta\Gamma_s$  equal to 0.068  $\text{ps}^{-1}$ ). A more precise  $\Delta\Gamma_s$  de-  
 5806 termination is expected to be obtained from the time-dependant angular analysis of  
 5807 the decay mode  $B_s^0 \rightarrow J/\psi\phi$ . Preliminary studies show that a precision of 0.021  $\text{ps}^{-1}$  could  
 5808 be reached at ATLAS with  $10 \text{ fb}^{-1}$  of data, 0.010  $\text{ps}^{-1}$  at CMS with  $10 \text{ fb}^{-1}$  of data  
 5809 assuming a perfect tagging, and 0.008  $\text{ps}^{-1}$  at LHCb with  $2 \text{ ps}^{-1}$  of data.

5810 In summary, very precise lifetime measurements of the  $B^0$  and  $B^+$  mesons will be  
 5811 available very soon after LHC starts and will be used to calibrate LHC detectors for  
 5812 further lifetime measurements. Parameters of the  $B_s^0$  hadron ( $\tau_s$ ,  $\Delta m_s$ ) will reach similar  
 5813 precision that  $B^0$  and  $B^+$  and will rapidly be systematics limited. Finally precise studies  
 5814 of other  $B$  hadrons will be feasible such as the lifetime of the  $B_c^+$  and  $\Lambda_b$  particles.

#### 5815 7.4.2. Measurements of the $B_s$ meson mixing phase

5816 As discussed in Sec. 7.2.4 and [991], the most precise measurement of  $\beta_s$  can be obtained  
 5817 via a tagged time-dependent angular analysis of the  $B_s \rightarrow J/\psi\phi$  decay mode.

5818 In order to disentangle the two CP eigenstates, the three amplitudes will be statistically  
 5819 separated through an angular analysis. The oscillation amplitude of the time-dependent  
 5820 angular distributions is proportional to the CP-violation phase  $\beta_s$ .

5821 The amplitude of the oscillation can be affected by several experimental factors: im-

5822 perfect tagging, proper time resolution, poor knowledge of the angular and proper time  
5823 acceptances and background contamination. The key ingredients for reaching high sen-  
5824 sitivity on  $\beta_s$  are the following:

- 5825 - large signal yield: this is given by the convolution of integrated luminosity, production  
5826 cross section, geometrical acceptance of the detectors, trigger and offline selection  
5827 efficiency;
- 5828 - high momentum resolution: this defines the  $B_s$  mass window and therefore the amount  
5829 of background contamination. Moreover it is crucial to determine the decay angles with  
5830 high precision;
- 5831 - good particle identification capability in order to control background and provide high  
5832 tagging performance with a low and well known mis-tag;
- 5833 - excellent proper time resolution to follow the fast  $B_s$  oscillations.

5834 In the following, we briefly describe the performance of ATLAS, CMS and LHCb related  
5835 to the  $\beta_s$  measurement.

5836 The offline selections for the three experiments are based on very basic quantities like  
5837 particle identification,  $p_T$  of the decay products, vertex quality and, only for ATLAS and  
5838 CMS,  $b$ -vertex displacement. The MuonID capability is similar for the three experiments  
5839 (muon efficiency of  $\sim 90\%$  for a misidentification rate of  $\sim 1\%$ , but dependent with  $p_T, \eta$   
5840 for central detectors); the hadron identification capability is higher for LHCb thanks to  
5841 the powerful RICH system [992] which allows to identify Kaons with an efficiency of  
5842  $\sim 88\%$  against a pion misidentification rate of  $\sim 3\%$ .

5843 The momentum resolution is  $\sigma_p/p = (0.3 - 0.5)\%$  for LHCb and  $\sigma_{p_T}/p_T = 1 - 2\%$   
5844 for ATLAS/CMS. This corresponds to a  $B_s$  mass resolution of  $\sim 17 \text{ MeV}/c^2$  for LHCb,  
5845 without  $J/\Psi$  mass constraint and to a  $\sim 14 - 16 \text{ MeV}/c^2$   $B_s$  mass resolution for CMS and  
5846 ATLAS, with  $J/\Psi$  mass constraint. LHCb does not make use of a  $J/\Psi$  mass constraint  
5847 because this requirement modifies the proper time acceptance of the decaying  $B_s$ .

5848 ATLAS/CMS use an offline selection with  $B_s$  lifetime selection cuts: this selection gets  
5849 rid of most of the prompt combinatorial background but also modifies heavily the proper  
5850 time acceptance that must be corrected afterwards. LHCb instead developed a selection  
5851 by minimizing the bias on the proper time and angular acceptances.

5852 For the time being, LHCb and ATLAS are developing tagged analyses, while CMS  
5853 is currently reporting an untagged one. ATLAS will use several taggers mainly based  
5854 on leptons and vertex charge. The combined tag gives an effective tagging power of  
5855  $\epsilon_{eff} = \epsilon_{tag}(1 - 2\omega)^2 = 4.6\%$ . LHCb has a good hadron identification and therefore can  
5856 profit also of the Kaon tagger (both opposite side and same side). The combined tag is  
5857 expected to have an effective tagging power of  $\epsilon_{eff} = 6.2\%$ . Tagging calibration will be  
5858 performed at LHCb by using flavor specific decays, namely  $B^0 \rightarrow J/\psi K^*$  and  $B^+$  to  
5859  $J/\psi K^+$  for calibration of OS taggers, and  $B_s \rightarrow D_s \pi$  for calibration of the same side  
5860 tagger.

5861 The last key ingredient is the proper time resolution,  $\sigma_\tau$ . The expected average proper  
5862 time resolutions are 83 fs, 77 fs and 40 fs, for ATLAS, CMS and LHCb, respectively. At  
5863 the time of this report, Monte Carlo samples with full simulation which were available  
5864 for studies have limited statistics:  $\sim 7 \text{ pb}^{-1}$  of inclusive  $J/\Psi \rightarrow \mu^+ \mu^-$  were available  
5865 for the LHCb studies, and 20 - 50  $\text{pb}^{-1}$  of  $b \rightarrow J/\Psi(\mu\mu)X$  for ATLAS/CMS. Therefore,  
5866 the Monte Carlo with full detector simulation cannot be used to perform a full analy-  
5867 sis evaluation. However, these samples can be used to estimate the yield, background  
5868 fractions, mass, proper time and angle distributions, resolutions, and acceptances. The

5869 extracted quantities are then used in toy Monte Carlo ensembles in order to estimate the  
 5870 sensitivity to  $2\beta_s$  (and other parameters) via results of unbinned maximum likelihood  
 5871 fits.

5872 Tab. 55 summarizes the expected precision for  $2\beta_s$  and  $\Delta\Gamma_s$  after 1/4 of a nominal year  
 5873 of running. Also listed are the estimated event yield, background contamination, effective  
 5874 tagging efficiency  $\epsilon D^2$  and proper time resolutions  $\sigma(\tau)$  per experiment. The assumed  
 5875 values for  $\beta_s$  and  $\Delta\Gamma_s$  were  $2\beta_s \sim 0.04$  and  $\Delta\Gamma_s/\bar{\Gamma}_s \sim 0.1$  in these studies. ATLAS,  
 5876 CMS and LHCb have a strong potential to increase the precision of the measurements  
 5877 of the  $B_s$  CP violating phase well beyond the present CDF and D0 results. As already  
 5878 discussed this opens the opportunity to observe effects beyond the Standard Model.

Table 55

Summary table for ATLAS, CMS and LHCb. We show the untagged signal yield for a luminosity corre-  
 sponding to a 1/4 year of running at nominal luminosity, the B/S ratio, the effective tagging efficienc y,  
 the proper time resolution and the sensitivity on  $2\beta_s$  and  $\Delta\Gamma_s/\bar{\Gamma}_s$ .

	ATLAS	CMS	LHCb
$\mathcal{L}[\text{fb}^{-1}]$	2.5	2.5	0.5
signal yield [untagged]	22.5 k	27 k	28.5 k
B/S	0.18	0.25	2
dominant background	long-lived	long-lived	prompt
$\epsilon D^2$	4.6 %	N/A	6.2 %
$\sigma(\tau)$	83 fs	77 fs	40 fs
$\sigma(2\beta_s)$	0.16	N/A	0.06
$\sigma(\Delta\Gamma_s/\bar{\Gamma}_s)/(\Delta\Gamma_s/\bar{\Gamma}_s)$	0.4 5	0.28	0.17

### 5879 7.4.3. $D^0$ mixing and CP violation

5880 As the dedicated flavor experiment at CERN's Large Hadron Collider (LHC), LHCb is  
 5881 the only LHC experiment currently planning measurements of  $D^0$ - $\bar{D}^0$  mixing and charm  
 5882 CP violation. The studies presented at CKM2008 and described in this note are estimates  
 5883 of the performance of the LHCb experiment.

5884 Many of the features that make LHCb an excellent  $B$  physics laboratory also make  
 5885 LHCb well-suited for many charm physics studies at unprecedented levels of preci-  
 5886 sion [993]. The silicon Vertex Locator (VELO) will provide the excellent vertex reso-  
 5887 lutions necessary for time dependent measurements—an estimated 45 fs proper time res-  
 5888 olution for  $D^0 \rightarrow K^- \pi^+$  decays where the  $D^0$  mesons are produced in  $b$ -hadron decays.  
 5889 The LHCb tracking system will supply precise momentum measurements—an estimated  
 5890 6 MeV mass resolution for two body decays of  $D^0$  mesons. The LHCb Ring Imaging  
 5891 Cherenkov (RICH) detectors will provide excellent  $K$ - $\pi$  discrimination over a wide mo-  
 5892 mentum range from 2 GeV/c to 100 GeV/c. Finally, the LHCb trigger system will have  
 5893 a high statistics charm stream, so that the large charm production in LHC collisions can  
 5894 be exploited for precision measurements.

5895 LHCb will make both time-dependent and time-integrated CP violation searches. Each  
 5896 time-dependent  $D^0$ - $\bar{D}^0$  mixing measurement will be analyzed in charge conjugate subsets  
 5897 to measure possible CP violating effects. Measurements with promptly produced charm  
 5898 mesons and with charm mesons produced in  $b$ -hadron decays will be pursued. Analysis

5899 methods for both sources are under development. Preliminary studies for measurements  
 5900 with secondary charm are currently more complete. Initial studies have focused on  $D^{*+}$ -  
 5901 tagged two-body  $D^0 \rightarrow h^- h'^+$  decays. Multi-body decays to charged products and up  
 5902 to one  $K_S^0$  are suitable for precision measurements at LHCb and will be investigated. In  
 5903 four body hadronic decays, plans for CP violation searches include complete amplitude  
 5904 analyses and analyses of quantities that are odd under time reversal.

5905 Simulated events from a full interaction and LHCb detector simulation have been  
 5906 used to estimate LHCb's potential performance in physics analyses. Preliminary event  
 5907 selection studies on these simulated events indicate a yield of approximately 8 million  
 5908  $D^{*+}$ -tagged  $D^0 \rightarrow K^- K^+$  decays in  $10\text{fb}^{-1}$  of collisions. The  $D^{*+}$  was produced in a  
 5909  $b$ -hadron decay in these studies. [994]. This yield estimate includes the expected effects  
 5910 of both the L0 and the HLT triggers. This corresponds to a statistical precision of ap-  
 5911 proximately  $4 \times 10^{-4}$  for the CP asymmetry search. The selection used in the study  
 5912 was optimized for the wrong sign (WS)  $D^0 \rightarrow K\pi$  decays. Reoptimizing for  $D^0 \rightarrow KK$   
 5913 may result in even higher yields. Similar studies predict approximately 1.2 billion  $D^{*+}$ -  
 5914 tagged  $D^0 \rightarrow KK$  decays in  $10\text{fb}^{-1}$  after the L0 trigger, before the HLT trigger. Efficient  
 5915 strategies to select these events in the HLT are under investigation.

5916 LHCb will measure  $D^0$ - $\overline{D}^0$  mixing in as many channels as we can efficiently reconstruct.  
 5917 Initial studies have focused on the two main mixing measurements possible with  $D^{*+}$ -  
 5918 tagged two-body  $D^0 \rightarrow h^- h'^+$  decays—mixing from analysis of WS  $K\pi$  decays, and the  
 5919 ratio of lifetimes of singly Cabibbo suppressed (SCS) and right sign (RS) decays.

5920 Time-dependent analyses require precise measurements of the creation and decay ver-  
 5921 tices of the  $D^0$  mesons. The scale of the required precision is set by the approximately  
 5922 4 mm mean laboratory flight distance for a  $60\text{GeV}/c$   $D^0$  (the mean momentum of sec-  
 5923 ondary  $D^{*+}$ -tagged  $D^0$  decays). The decay vertex of a two-body  $D^0$  decay can be de-  
 5924 termined precisely from its products with a resolution of  $\sim 260\ \mu\text{m}$  along the beam axis.  
 5925 For promptly produced  $D^0$  decays, the precisely measured primary interaction vertex  
 5926 (resolution  $\sim 60\ \mu\text{m}$  along the beam axis [993]) is the creation vertex.

5927 For secondary charm decays, the additional charged tracks must come from the  $b$ -  
 5928 hadron decay that produced the  $D^{*+}$ . LHCb has been developing techniques to partially  
 5929 reconstruct the parent  $b$ -hadron that produced the  $D^{*+}$  [994]. Initial results from these  
 5930 developments are promising. As shown in the  $B_{\text{part}}$  column of Tab. 56, using a partial  
 5931 reconstruction dramatically improves the precision of the estimated  $D^0$  creation vertex  
 5932 and, consequently, the measured  $D^0$  proper time. Fig. 65 shows that this process pro-  
 5933 duces precisely measured proper times that closely reproduce the generated proper time  
 5934 distribution. The  $b$ -hadron partial reconstruction is approximately 60% efficient with  
 5935 respect to all selected secondary  $D^{*+}$ -tagged  $D^0 \rightarrow h^- h'^+$  decays.

5936 Toy Monte Carlo studies have been used to estimate LHCb's statistical sensitivities  
 5937 to the mixing parameters  $x'^2$  and  $y'$  in a two-body WS mixing study and to the mixing  
 5938 parameter  $y_{\text{CP}}$  in a two-body lifetime ratio study.

5939 Selection studies in fully simulated LHCb events predict a yield of roughly 230,000  
 5940  $D^{*+}$ -tagged WS decays  $10\text{fb}^{-1}$  of LHCb data. Again, the  $D^{*+}$  mesons originate in the  
 5941 decays of  $b$ -hadrons in this study. The  $10\text{fb}^{-1}$  signal and background yields, proper time  
 5942 resolution, and proper time acceptance of this selection were used in a toy Monte Carlo  
 5943 study to estimate the LHCb statistical sensitivity to  $x'^2$  and  $y'$ :

$$\sigma_{\text{stat}}(x'^2) = \pm 0.064 \times 10^{-3}; \quad \sigma_{\text{stat}}(y') = \pm 0.87 \times 10^{-3} \quad [994].$$

	$D^0$	$D^{*+}$	$B_{\text{part}}$
$x$	$22 \mu\text{m}$	$190 \mu\text{m}$	$18 \mu\text{m}$
$y$	$17 \mu\text{m}$	$140 \mu\text{m}$	$18 \mu\text{m}$
$z$	$260 \mu\text{m}$	$4200 \mu\text{m}$	$240 \mu\text{m}$
$\tau_{D^0}$	$0.47 \text{ ps}$		$0.045 \text{ ps}$

Table 56

Estimated resolutions of  $D^0$ ,  $D^{*+}$ , and  $B_{\text{part}}$  vertices, and of  $D^0$  proper time in simulated LHCb data. The  $D^0$  proper time,  $\tau_{D^0}$ , is estimated both using the  $D^{*+}$  vertex as the creation vertex in the first column, and using the  $B_{\text{part}}$  vertex as the creation vertex in the last column.

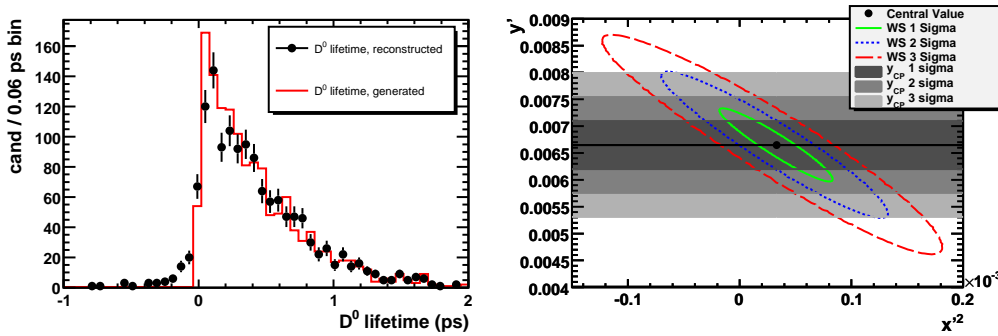


Fig. 65. In the left panel, the distribution of the proper times for simulated  $D^0$  mesons from  $B \rightarrow D^{*+} X$  decays. The solid lines are the generated proper times and the points are the estimated  $D^0$  proper times using the estimated parent  $B$  decay vertex as the  $D^0$  production vertex. In the right panel, the sensitivities in  $10 \text{ fb}^{-1}$  from the WS study and the  $y_{\text{CP}}$  study. Contours correspond to  $1\sigma$ ,  $2\sigma$ , and  $3\sigma$  confidence levels from the WS study. Horizontal bands correspond to  $1\sigma$ ,  $2\sigma$ , and  $3\sigma$  confidence levels from the  $y_{\text{CP}}$  study.

5944 The same selection studies referred to in Sec. 7.4.3 estimate that a lifetime ratio anal-  
5945 ysis on  $10 \text{ fb}^{-1}$  of LHCb data would incorporate approximately 8 million  $D^{*+}$ -tagged  
5946  $D^0 \rightarrow K^- K^+$  decays from  $b$ -hadron decays. The  $10 \text{ fb}^{-1}$  signal and background yields,  
5947 the proper time resolution, and the proper time acceptance of this selection were used in  
5948 a toy Monte Carlo study to estimate the LHCb statistical sensitivity to  $y_{\text{CP}}$ :

$$\sigma_{\text{stat}}(y_{\text{CP}}) = \pm 0.5 \times 10^{-3} \quad [994].$$

5949 In summary LHCb will have sufficient statistics for extremely precise CP violation  
5950 measurements. Strategies to reduce the systematic uncertainties to commensurate pre-  
5951 cision are in development. Systematic uncertainties are still under study, but LHCb will  
5952 certainly have the statistical power to make precision measurements in charm CP viola-  
5953 tion and  $D^0$ - $\bar{D}^0$  mixing.

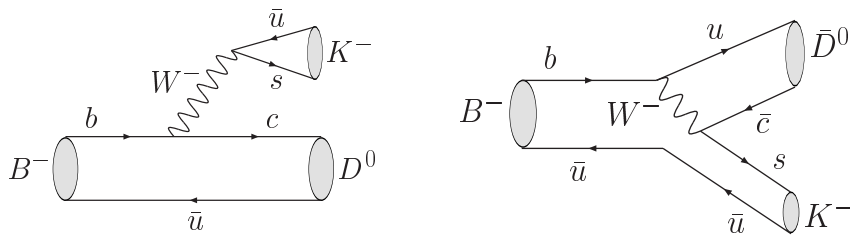


Fig. 66. Leading Feynman diagrams contributing to the  $B^+ \rightarrow DK^+$  decay. From [258].

5954 **8. Measurement of the angle  $\gamma$  in tree dominated processes**

5955 8.1. *Overview of Theoretically Pristine Approaches to Measure  $\gamma$*

5956 Among the fundamental parameters of the Standard Model of particle physics, the  
 5957 angle  $\gamma = \arg(-V_{ud}V_{ub}^*/V_{cd}V_{cb}^*)$  of the Unitarity Triangle formed from elements of the  
 5958 Cabibbo-Kobayashi-Maskawa quark mixing matrix [1, 2] has a particular importance. It  
 5959 is the only CP violating parameter that can be measured using only tree-level decays, and  
 5960 thus it provides an essential benchmark in any effort to understand the baryon asymmetry  
 5961 of the Universe. Strategies to measure fundamental parameters of the Standard Model  
 5962 and to search for New Physics by overconstraining the Unitarity Triangle inevitably  
 5963 require a precise measurement of  $\gamma$ .

5964 Fortunately, there is a theoretically pristine approach to measure  $\gamma$  using tree-dominated  
 5965  $B \rightarrow DK$  decays [995–997]. The approach exploits the interference between  $D^0$  and  $\bar{D}^0$   
 5966 amplitudes that occurs when the neutral  $D$  meson is reconstructed in decay that is ac-  
 5967 cessible to both flavor states. Feynman diagrams for the relevant  $B$  decays are shown  
 5968 in Fig. 66. The original approach uses  $D$  decays to CP eigenstates [996, 997], but vari-  
 5969 ants using doubly-Cabibbo-suppressed decays [998, 999], singly-Cabibbo-suppressed de-  
 5970 cays [1000] and multibody final states such as  $K_S^0\pi^+\pi^-$  [255, 1001, 1002], and many others  
 5971 besides, have been proposed.

Considering  $D$  decays to CP eigenstates (CP even and odd denoted by  $D_1$  and  $D_2$  respectively), and defining

$$r_B e^{i\delta_B} = \frac{\mathcal{A}(B^+ \rightarrow D^0 K^+)}{\mathcal{A}(B^+ \rightarrow \bar{D}^0 K^+)}, \quad (365)$$

5972 the dependence on  $\gamma$  of the decay rates is found to be as follows (as illustrated in Fig. 67).

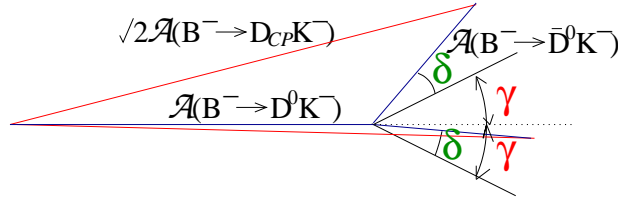


Fig. 67. Illustration of the sensitivity to  $\gamma$  that arises from the interference of  $B^+ \rightarrow D^0 K^+$  and  $B^+ \rightarrow \bar{D}^0 K^+$  decay amplitudes.

$$\mathcal{A}(B^- \rightarrow D_1 K^-) \propto \frac{1}{2} \left( 1 + r_B e^{i(\delta_B - \gamma)} \right) \rightarrow \quad (366)$$

$$\Gamma(B^- \rightarrow D_1 K^-) \propto 1 + r_B^2 + 2r_B \cos(\delta_B - \gamma)$$

$$\mathcal{A}(B^- \rightarrow D_2 K^-) \propto \frac{1}{2} \left( 1 - r_B e^{i(\delta_B - \gamma)} \right) \rightarrow \quad (367)$$

$$\Gamma(B^- \rightarrow D_2 K^-) \propto 1 + r_B^2 - 2r_B \cos(\delta_B - \gamma)$$

$$\mathcal{A}(B^+ \rightarrow D_1 K^+) \propto \frac{1}{2} \left( 1 + r_B e^{i(\delta_B + \gamma)} \right) \rightarrow \quad (368)$$

$$\Gamma(B^+ \rightarrow D_1 K^+) \propto 1 + r_B^2 + 2r_B \cos(\delta_B + \gamma)$$

$$\mathcal{A}(B^+ \rightarrow D_2 K^+) \propto \frac{1}{2} \left( 1 - r_B e^{i(\delta_B + \gamma)} \right) \rightarrow \quad (369)$$

$$\Gamma(B^+ \rightarrow D_2 K^+) \propto 1 + r_B^2 - 2r_B \cos(\delta_B + \gamma)$$

5973 From the above expressions it is clear that CP violation effects will be enhanced for  
5974 values of  $r_B$  close to unity. It can also be seen that measurements of rates (and rate  
5975 asymmetries) alone yield information on  $x_{\pm} = r_B \cos(\delta_B \pm \gamma)$ . This leads to ambiguities  
5976 in the extraction of  $\gamma$ . These can be resolved, and the overall precision improved, when  
5977 information on  $y_{\pm} = r_B \sin(\delta_B \pm \gamma)$  is obtained, as can be achieved from Dalitz plot  
5978 analyses, for example.

5979 To avoid relying on theoretical estimates of the hadronic parameters  $r_B$  and  $\delta_B$ , these  
5980 parameters must also be determined from the data. Once that is done, the underlying  
5981 method has essentially zero theoretical uncertainty. The largest effects are due to charm  
5982 mixing and possible CP violation effects in the  $D$  decays [1003]. However, once measured  
5983 it is possible to take these effects into account in the analysis. Similarly, when decays of  
5984 neutral  $B$  mesons are used, there is a potential systematic effect if the possible  $B_{(s)}^0 - \bar{B}_{(s)}^0$   
5985 width difference is neglected [1004, 1005].

5986 As already mentioned above, many different decays in the “ $B \rightarrow DK$ ” family can  
5987 be used to gain sensitivity to  $\gamma$ . Not only charged but also neutral  $B$  decays can be  
5988 used. Any decay of the neutral  $D$  meson that is accessible to both  $D^0$  and  $\bar{D}^0$  can be  
5989 used. Furthermore decays with excited  $D$  and/or  $K$  states not only provide additional  
5990 statistics. In the former case there is an effective strong phase difference of  $\pi$  between the  
5991 cases that the  $D^*$  is reconstructed as  $D\pi^0$  and  $D\gamma$  that is particularly beneficial when  $D$   
5992 decays to doubly-Cabibbo-suppressed final states are analyzed [1006]. When  $K^*$  mesons  
5993 are used, their natural width can be handled by the introduction of effective hadronic  
5994 parameters [1007]; alternatively a Dalitz plot analysis of the  $B \rightarrow DK\pi$  decay removes  
5995 this problem and maximizes the sensitivity to  $\gamma$  [1008]. Ultimately it is clear that the



5996 best sensitivity to  $\gamma$  will be obtained by combining as many statistically independent  
 5997 measurements as possible.

## 5998 8.2. Experimental results on $\gamma$ from $B \rightarrow DK$ decays

### 5999 8.2.1. GLW analyses

The technique of measuring  $\gamma$  proposed by Gronau, London and Wyler (and called GLW) [996,997] makes use of  $D^0$  decays to  $CP$  eigenstates, such as  $K^+K^-$ ,  $\pi^+\pi^-$  ( $CP$ -even) or  $K_S^0\pi^0$ ,  $K_S^0\phi$  ( $CP$ -odd). Since both  $D^0$  and  $\bar{D}^0$  can decay into the same  $CP$  eigenstate ( $D_{CP}$ , or  $D_1$  for a  $CP$ -even state and  $D_2$  for a  $CP$ -odd state), the  $b \rightarrow c$  and  $b \rightarrow u$  processes shown in Fig. 66 interfere in the  $B^\pm \rightarrow D_{CP}K^\pm$  decay channel. This interference may lead to direct  $CP$  violation. To measure  $D$  meson decays to  $CP$  eigenstates a large number of  $B$  meson decays is required since the branching fractions to these modes are of order 1%. To extract  $\gamma$  using the GLW method, the following observables sensitive to  $CP$  violation are used: the asymmetries

$$\begin{aligned} \mathcal{A}_{1,2} &\equiv \frac{\mathcal{B}(B^- \rightarrow D_{1,2}K^-) - \mathcal{B}(B^+ \rightarrow D_{1,2}K^+)}{\mathcal{B}(B^- \rightarrow D_{1,2}K^-) + \mathcal{B}(B^+ \rightarrow D_{1,2}K^+)} \\ &= \frac{2r_B \sin \delta' \sin \gamma}{1 + r_B^2 + 2r_B \cos \delta' \cos \gamma} \end{aligned} \quad (370)$$

and the double ratios

$$\begin{aligned} \mathcal{R}_{1,2} &\equiv \frac{\mathcal{B}(B^- \rightarrow D_{1,2}K^-) + \mathcal{B}(B^+ \rightarrow D_{1,2}K^+)}{\mathcal{B}(B^- \rightarrow D^0K^-) + \mathcal{B}(B^+ \rightarrow D^0K^+)} \\ &= 1 + r_B^2 + 2r_B \cos \delta' \cos \gamma, \end{aligned} \quad (371)$$

where

$$\delta' = \begin{cases} \delta_B & \text{for } D_1 \\ \delta_B + \pi & \text{for } D_2 \end{cases}, \quad (372)$$

6000 and  $r_B$  and  $\delta_B$  were defined in the previous section. The value of  $r_B$  is given by the ratio  
 6001 of the CKM matrix elements  $|V_{ub}^* V_{cs}|/|V_{cb}^* V_{us}| \sim 0.38$  times a color suppression factor.  
 6002 Here we assume that mixing and  $CP$  violation in the neutral  $D$  meson system can be  
 6003 neglected.

Instead of four observables  $\mathcal{R}_{1,2}$  and  $\mathcal{A}_{1,2}$ , only three of which are independent (since  $\mathcal{A}_1\mathcal{R}_1 = -\mathcal{A}_2\mathcal{R}_2$ ), an alternative set of three parameters can be used:

$$x_\pm = r_B \cos(\delta_B \pm \gamma) = \frac{\mathcal{R}_1(1 \mp \mathcal{A}_1) - \mathcal{R}_2(1 \mp \mathcal{A}_2)}{4}, \quad (373)$$

and

$$r_B^2 = \frac{\mathcal{R}_1 + \mathcal{R}_2 - 2}{2}. \quad (374)$$

6004 The use of these observables allows for a direct comparison with the methods involving  
 6005 analyses of the Dalitz plot distributions of multibody  $D^0$  decays (see Sec. 8.2.3), where  
 6006 the same parameters  $x_\pm$  are obtained.

6007 Measurements of  $B \rightarrow D_{CP}K$  decays have been performed by both the BaBar [1009]  
 6008 and Belle [1010] collaborations, while CDF has recently made measurements using  $CP$ -  
 6009 even decays only [1011]. The most recent update is BaBar's analysis using a data sample

Table 57

Results of the GLW analysis by BaBar [1009].

$\mathcal{R}_1$	$1.06 \pm 0.10 \pm 0.05$
$\mathcal{R}_2$	$1.03 \pm 0.10 \pm 0.05$
$\mathcal{A}_1$	$+0.27 \pm 0.09 \pm 0.04$
$\mathcal{A}_2$	$-0.09 \pm 0.09 \pm 0.02$
$x_+$	$-0.09 \pm 0.05 \pm 0.02$
$x_-$	$+0.10 \pm 0.05 \pm 0.03$
$r_B^2$	$0.05 \pm 0.07 \pm 0.03$

6010 of 382M  $B\bar{B}$  pairs [1009]. The analysis uses  $D^0$  decays to  $K^+K^-$  and  $\pi^+\pi^-$  as CP-even  
 6011 modes,  $K_S^0\pi^0$  and  $K_S^0\omega$  as CP-odd modes.

6012 The results of the analysis (both in terms of asymmetries and double ratios, and the  
 6013 alternative  $x_{\pm}, r_B^2$  set of parameters) are shown in Tab. 57. As follows from (370) and  
 6014 (372), the signs of the  $\mathcal{A}_1$  and  $\mathcal{A}_2$  asymmetries should be opposite, which is confirmed by  
 6015 the experiment. The  $x_{\pm}$  values are in good agreement with those obtained by the Dalitz  
 6016 plot analysis technique (see 8.2.3). Note that the measurement of  $\mathcal{A}_1$  deviates from zero  
 6017 by 2.8 standard deviations.

6018 A summary of measurements of observables with the GLW method is given in Fig. 68.  
 6019 As well as the results using  $B \rightarrow D_{CP}K$  decays, this compilation also includes measure-  
 6020 ments from the decay channels  $B \rightarrow D_{CP}^*K$  and  $B \rightarrow D_{CP}K^*$ .

### 6021 8.2.2. ADS analyses

6022 The difficulties in the application of the GLW methods are primarily due to the small  
 6023 magnitude of the CP asymmetry of the  $B^{\pm} \rightarrow D_{CP}K^{\pm}$  decay probabilities, which may  
 6024 lead to significant systematic uncertainties in the measurement of CP violation. An al-  
 6025 ternative approach was proposed by Atwood, Dunietz and Soni [998, 999]. Instead of  
 6026 using  $D^0$  decays to CP eigenstates, the ADS method uses Cabibbo-favored and doubly  
 6027 Cabibbo-suppressed decays:  $\bar{D}^0 \rightarrow K^-\pi^+$  and  $D^0 \rightarrow K^+\pi^-$ . In the decays  $B^+ \rightarrow$   
 6028  $[K^-\pi^+]_D K^+$  and  $B^- \rightarrow [K^+\pi^-]_D K^-$ , the suppressed  $B$  decay corresponds to the  
 6029 Cabibbo-allowed  $D^0$  decay, and vice versa. Therefore, the interfering amplitudes are  
 6030 of similar magnitudes, and one can expect significant CP asymmetry.

The observable that is measured in the ADS method is the fraction of the suppressed  
 and allowed branching ratios:

$$\begin{aligned} \mathcal{R}_{ADS} &= \frac{\mathcal{B}(B^{\pm} \rightarrow [K^{\mp}\pi^{\pm}]_D K^{\pm})}{\mathcal{B}(B^{\pm} \rightarrow [K^{\pm}\pi^{\mp}]_D K^{\pm})} \\ &= r_B^2 + r_D^2 + 2r_B r_D \cos \gamma \cos \delta, \end{aligned} \quad (375)$$

where  $r_D$  is the ratio of the doubly Cabibbo-suppressed and Cabibbo-allowed  $D^0$  decay  
 amplitudes [558]:

$$r_D = \left| \frac{A(D^0 \rightarrow K^+\pi^-)}{A(D^0 \rightarrow K^-\pi^+)} \right| = 0.058 \pm 0.001, \quad (376)$$

and  $\delta$  is the sum of strong phase differences in  $B$  and  $D$  decays:  $\delta = \delta_B + \delta_D$ . Once a  
 significant signal is seen, the direct CP asymmetry must be measured,

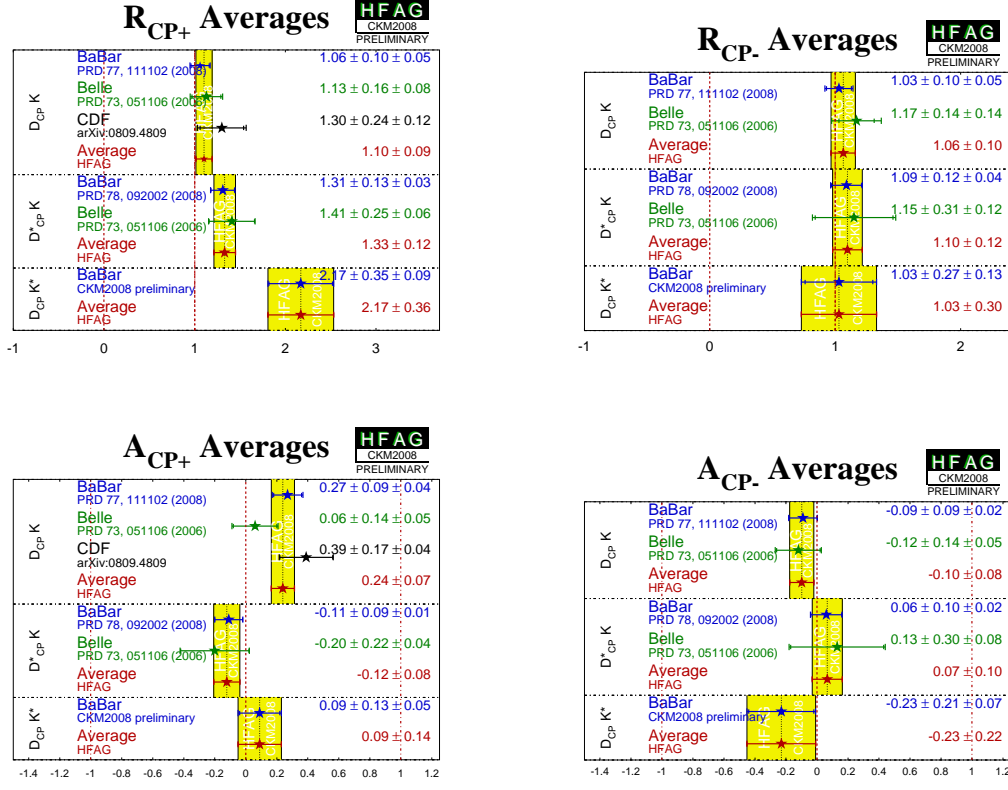


Fig. 68. Compilations and world averages of measurements of observables using the GLW method. Top left:  $\mathcal{R}_1$ ; top right:  $\mathcal{R}_2$ ; bottom left:  $\mathcal{A}_1$ ; bottom right:  $\mathcal{A}_2$ .

$$\begin{aligned}
 \mathcal{A}_{ADS} &= \frac{\mathcal{B}(B^- \rightarrow [K^+\pi^-]_D K^-) - \mathcal{B}(B^+ \rightarrow [K^-\pi^+]_D K^+)}{\mathcal{B}(B^- \rightarrow [K^+\pi^-]_D K^-) + \mathcal{B}(B^+ \rightarrow [K^-\pi^+]_D K^+)} \\
 &= \frac{2r_{BRD} \sin \gamma \sin \delta}{r_B^2 + r_D^2 + 2r_{BRD} \cos \gamma \cos \delta}.
 \end{aligned} \tag{377}$$

Studies of ADS channels have been performed by both BaBar [1012] and Belle [1013]. Unfortunately, the product branching ratios into the final states of interest are so small that they cannot be observed using the current experimental statistics. The most recent update of the ADS analysis is that from Belle using 657M  $B\bar{B}$  pairs [1013]. The analysis uses  $B^\pm \rightarrow DK^\pm$  decays with  $D^0$  decaying to  $K^+\pi^-$  and  $K^-\pi^+$  modes (and their charge-conjugated partners). The ratio of suppressed and allowed modes is found to be

$$\mathcal{R}_{ADS} = (8.0^{+6.3+2.0}_{-5.7-2.8}) \times 10^{-3}. \tag{378}$$

Since the signal in the suppressed modes is not significant, the CP asymmetry is inevitably consistent with zero:

$$\mathcal{A}_{ADS} = -0.13^{+0.98}_{-0.88} \pm 0.26. \tag{379}$$

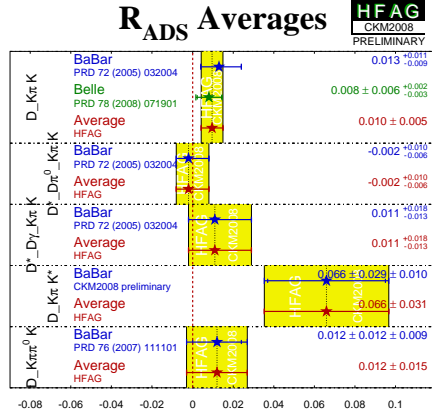


Fig. 69. Compilations and world averages of measurements of observables using the ADS method.

6031 A summary of measurements of observables with the ADS method is given in Fig. 69.  
6032 As well as the results using the decays  $B \rightarrow DK$  with  $D \rightarrow K\pi$ , this compilation also  
6033 includes measurements from the decay channels  $B \rightarrow D^*K$  with  $D \rightarrow K\pi$  and the  
6034 decays  $D^* \rightarrow D\pi^0$  and  $D^* \rightarrow D\gamma$  treated distinctly [1006],  $B \rightarrow DK^*$  with  $D \rightarrow K\pi$   
6035 and  $B \rightarrow DK$  with  $D \rightarrow K\pi\pi^0$ .

6036 The ADS analysis currently does not give a significant constraint on  $\gamma$ , but it pro-  
6037 vides important information on the value of  $r_B$ . Using the conservative assumption  
6038  $\cos \gamma \cos \delta = -1$  one obtains the upper limit  $r_B < 0.19$  at 90% CL. A somewhat tighter  
6039 constraint can be obtained by using the  $\gamma$  and  $\delta_B$  measurements from the Dalitz plot  
6040 analyses (see Sec. 8.2.3), and the recent CLEO-c measurement of the strong phase  $\delta_D =$   
6041  $(22_{-12}^{+11+9}_{-11})^\circ$  [986, 1014].

### 6042 8.2.3. Dalitz plot analyses

6043 A Dalitz plot analysis of a three-body final state of the  $D$  meson allows one to obtain  
6044 all the information required for determination of  $\gamma$  in a single decay mode. The use of  
6045 a Dalitz plot analysis for the extraction of  $\gamma$  was first discussed in the context of the  
6046 ADS method [998, 999]. This technique uses the interference of Cabibbo-favored  $D^0 \rightarrow$   
6047  $K^-\pi^+\pi^0$  and doubly Cabibbo-suppressed  $\bar{D}^0 \rightarrow K^-\pi^+\pi^0$  decays. However, the small  
6048 rate for the doubly Cabibbo-suppressed decay limits the sensitivity of this technique.

Three body final states such as  $K_S^0\pi^+\pi^-$  [255, 1001] have been suggested as promising  
modes for the extraction of  $\gamma$ . Like in the GLW or ADS method, the two amplitudes  
interfere as the  $D^0$  and  $\bar{D}^0$  mesons decay into the same final state  $K_S^0\pi^+\pi^-$ ; we denote  
the admixed state as  $\tilde{D}_+$ . Assuming no CP asymmetry in neutral  $D$  decays, the amplitude  
of the  $\tilde{D}_+$  decay as a function of Dalitz plot variables  $m_+^2 = m_{K_S^0\pi^+}^2$  and  $m_-^2 = m_{K_S^0\pi^-}^2$   
is

$$f_{B^+} = f_D(m_+^2, m_-^2) + r_B e^{i(\delta_B + \gamma)} f_D(m_-^2, m_+^2), \quad (380)$$

6049 where  $f_D(m_+^2, m_-^2)$  is the amplitude of the  $\bar{D}^0 \rightarrow K_S^0\pi^+\pi^-$  decay.

Similarly, the amplitude of the  $\tilde{D}_-$  decay from  $B^- \rightarrow DK^-$  process is

$$f_{B^-} = f_D(m_-^2, m_+^2) + r_B e^{i(\delta_B - \gamma)} f_D(m_+^2, m_-^2). \quad (381)$$

6050 The  $\overline{D}^0 \rightarrow K_S^0 \pi^+ \pi^-$  decay amplitude can be determined at the  $B$  factories from the  
6051 large samples of flavor-tagged  $\overline{D}^0 \rightarrow K_S^0 \pi^+ \pi^-$  decays produced in continuum  $e^+ e^-$   
6052 annihilation. [In fact, only  $|f_D|^2$  can be determined from flavor tagged data, but a model  
6053 assumption can be made to describe the variation of the strong phase across the Dalitz  
6054 plot. Approaches to avoid such model-dependence are discussed in more detail below.]  
6055 Once  $f_D$  is known, a simultaneous fit of  $B^+$  and  $B^-$  data allows the contributions of  $r_B$ ,  
6056  $\gamma$  and  $\delta_B$  to be separated. The method has only a two-fold ambiguity: the solutions at  
6057  $(\gamma, \delta_B)$  and  $(\gamma + 180^\circ, \delta_B + 180^\circ)$  cannot be distinguished. References [255] and [1015]  
6058 give more detailed descriptions of the technique.

6059 Both Belle and BaBar collaborations recently reported updates of their  $\gamma$  measure-  
6060 ments using Dalitz plot analysis. The preliminary result from Belle [1016] uses a data  
6061 sample of 657M  $B\overline{B}$  pairs and two modes,  $B^\pm \rightarrow DK^\pm$  and  $B^\pm \rightarrow D^* K^\pm$  with  $D^* \rightarrow$   
6062  $D\pi^0$ . The neutral  $D$  meson is reconstructed in the  $K_S^0 \pi^+ \pi^-$  final state in both cases.

6063 To determine the decay amplitude,  $D^{*\pm}$  mesons produced via the  $e^+ e^- \rightarrow c\overline{c}$  con-  
6064 tinuum process are used, which then decay to a neutral  $D$  meson and a charged pion.  
6065 The flavor of the neutral  $D$  meson is tagged by the charge of the pion in the decay  
6066  $D^{*-} \rightarrow \overline{D}^0 \pi^-$ .  $B$  factories offer large sets of such charm data:  $290.9 \times 10^3$  events are  
6067 used in the Belle analysis with only 1.0% background.

6068 The description of the  $\overline{D}^0 \rightarrow K_S^0 \pi^+ \pi^-$  decay amplitude is based on the isobar model.  
6069 The amplitude  $f_D$  is represented by a coherent sum of two-body decay amplitudes and one  
6070 nonresonant decay amplitude. The model includes a set of 18 two-body amplitudes: five  
6071 Cabibbo-allowed amplitudes:  $K^*(892)^+ \pi^-$ ,  $K^*(1410)^+ \pi^-$ ,  $K_0^*(1430)^+ \pi^-$ ,  $K_2^*(1430)^+ \pi^-$   
6072 and  $K^*(1680)^+ \pi^-$ ; their doubly Cabibbo-suppressed partners; eight amplitudes with  $K_S^0$   
6073 and a  $\pi\pi$  resonance:  $K_S^0 \rho$ ,  $K_S^0 \omega$ ,  $K_S^0 f_0(980)$ ,  $K_S^0 f_2(1270)$ ,  $K_S^0 f_0(1370)$ ,  $K_S^0 \rho(1450)$ ,  $K_S^0 \sigma_1$   
6074 and  $K_S^0 \sigma_2$ ; and a flat nonresonant term.

6075 The selection of  $B^\pm \rightarrow D^{(*)} K^\pm$  decays is based on the CM energy difference  $\Delta E =$   
6076  $\sum E_i - E_{\text{beam}}$  and the beam-constrained  $B$  meson mass  $M_{\text{bc}} = \sqrt{E_{\text{beam}}^2 - (\sum \mathbf{p}_i)^2}$ , where  
6077  $E_{\text{beam}}$  is the CM beam energy, and  $E_i$  and  $\mathbf{p}_i$  are the CM energies and momenta of the  
6078  $B$  candidate decay products. To suppress background from  $e^+ e^- \rightarrow q\overline{q}$  ( $q = u, d, s, c$ )  
6079 continuum events, variables that characterize the event shape are used. At the first stage  
6080 of the analysis, when the  $(M_{\text{bc}}, \Delta E)$  distribution is fitted in order to obtain the fractions  
6081 of the background components, a requirement on the event shape is imposed to suppress  
6082 the continuum events. The number of such “clean” events is 756 for  $B^\pm \rightarrow DK^\pm$  mode  
6083 with 29% background, and 149 events for  $B^\pm \rightarrow D^* K^\pm$  mode with 20% background. In  
6084 the Dalitz plot fit, events are not rejected based on event shape variables, these are used  
6085 in the likelihood function to better separate signal and background events.

6086 The Dalitz distributions of the  $B^+$  and  $B^-$  samples are fitted separately, using Carte-  
6087 sian parameters  $x_\pm = r_\pm \cos(\delta_B \pm \gamma)$  and  $y_\pm = r_\pm \sin(\delta_B \pm \gamma)$ , where the indices “+”  
6088 and “-” correspond to  $B^+$  and  $B^-$  decays, respectively. In this approach the amplitude  
6089 ratios ( $r_+$  and  $r_-$ ) are not constrained to be equal for the  $B^+$  and  $B^-$  samples. Confi-  
6090 dence intervals in  $r_B$ ,  $\gamma$  and  $\delta_B$  are then obtained from the  $(x_\pm, y_\pm)$  using a frequentist  
6091 technique.

6092 The values of the parameters  $r_B$ ,  $\gamma$  and  $\delta_B$  obtained from the combination of  $B^\pm \rightarrow$   
6093  $DK^\pm$  and  $B^\pm \rightarrow D^* K^\pm$  modes are presented in Tab. 58. Note that in addition to the  
6094 detector-related systematic error which is caused by the uncertainties of the background

Table 58

Results of the combination of  $B^+ \rightarrow DK^+$  and  $B^+ \rightarrow D^*K^+$  modes by Belle [1016].

Parameter	$1\sigma$ interval	$2\sigma$ interval	Systematic error	Model uncertainty
$\phi_3$	$76^\circ \begin{smallmatrix} +12^\circ \\ -13^\circ \end{smallmatrix}$	$49^\circ < \phi_3 < 99^\circ$	$4^\circ$	$9^\circ$
$r_{DK}$	$0.16 \pm 0.04$	$0.08 < r_{DK} < 0.24$	0.01	0.05
$r_{D^*K}$	$0.21 \pm 0.08$	$0.05 < r_{D^*K} < 0.39$	0.02	0.05
$\delta_{DK}$	$136^\circ \begin{smallmatrix} +14^\circ \\ -16^\circ \end{smallmatrix}$	$100^\circ < \delta_{DK} < 163^\circ$	$4^\circ$	$23^\circ$
$\delta_{D^*K}$	$343^\circ \begin{smallmatrix} +20^\circ \\ -22^\circ \end{smallmatrix}$	$293^\circ < \delta_{D^*K} < 389^\circ$	$4^\circ$	$23^\circ$

Table 59

Signal yields of different modes used for Dalitz analysis by BaBar collaboration [258].

$B$ decay	$D$ decay	Yield
$B^\pm \rightarrow DK^\pm$	$\bar{D}^0 \rightarrow K_S^0 \pi^+ \pi^-$	$600 \pm 31$
	$\bar{D}^0 \rightarrow K_S^0 K^+ K^-$	$112 \pm 13$
$B^\pm \rightarrow [D\pi^0]_{D^*} K^\pm$	$\bar{D}^0 \rightarrow K_S^0 \pi^+ \pi^-$	$133 \pm 15$
	$\bar{D}^0 \rightarrow K_S^0 K^+ K^-$	$32 \pm 7$
$B^\pm \rightarrow [D\gamma]_{D^*} K^\pm$	$\bar{D}^0 \rightarrow K_S^0 \pi^+ \pi^-$	$129 \pm 16$
	$\bar{D}^0 \rightarrow K_S^0 K^+ K^-$	$21 \pm 7$
$B^\pm \rightarrow DK^{*\pm}$	$\bar{D}^0 \rightarrow K_S^0 \pi^+ \pi^-$	$118 \pm 18$

6095 description, imperfect simulation, *etc.*, the result suffers from the uncertainty of the  
6096  $D$  decay amplitude description. The statistical confidence level of CP violation for the  
6097 combined result is  $(1 - 5.5 \times 10^{-4})$ , corresponding to 3.5 standard deviations.

6098 In contrast to the Belle analysis, the BaBar analysis based on a data sample of 383M  
6099  $B\bar{B}$  pairs [258] includes seven different decay modes:  $B^\pm \rightarrow DK^\pm$ ,  $B^\pm \rightarrow D^*K^\pm$  with  
6100  $D^0 \rightarrow D\pi^0$  and  $D\gamma$ , and  $B^\pm \rightarrow DK^{*\pm}$ , where the neutral  $D$  meson is reconstructed in  
6101  $K_S^0 \pi^+ \pi^-$  and  $K_S^0 K^+ K^-$  (except for  $B^\pm \rightarrow DK^{*\pm}$  mode) final states. The signal yields  
6102 for these modes are shown in Tab. 59.

6103 The differences from the Belle model of  $\bar{D}^0 \rightarrow K_S^0 \pi^+ \pi^-$  decay are as follows: the K-  
6104 matrix formalism [266,267,1017] is used to describe the  $\pi\pi$   $S$ -wave, while the  $K\pi$   $S$ -wave  
6105 is parametrized using  $K_0^*(1430)$  resonances and an effective range nonresonant component  
6106 with a phase shift [1018]. The description of  $\bar{D}^0 \rightarrow K_S^0 K^+ K^-$  decay amplitude uses an  
6107 isobar model that includes eight two-body decays:  $K_S^0 a_0(980)^0$ ,  $K_S^0 \phi(1020)$ ,  $K_S^0 f_0(1370)$ ,  
6108  $K_S^0 f_2(1270)^0$ ,  $K_S^0 a_0(1450)^0$ ,  $K^- a_0(980)^+$ ,  $K^+ a_0(980)^-$ , and  $K^- a_0(1450)^+$ .

6109 The fit to signal samples is performed in a similar way to the Belle analysis, using  
6110 an unbinned likelihood function that includes Dalitz plot variables and in addition  $B$   
6111 meson invariant mass and event-shape variables to better separate signal and background  
6112 events. From the combination of all modes, BaBar obtains  $\gamma = (76_{-24}^{+23} \pm 5 \pm 5)^\circ$  (mod  
6113  $180^\circ$ ), where the first error is statistical, the second is experimental systematic, and  
6114 the third is the  $D^0$  model uncertainty. The values of the amplitude ratios are  $r_B =$   
6115  $0.086 \pm 0.035 \pm 0.010 \pm 0.011$  for  $B^\pm \rightarrow DK^\pm$ ,  $r_B^* = 0.135 \pm 0.051 \pm 0.011 \pm 0.005$  for  
6116  $B^\pm \rightarrow D^*K^\pm$ , and  $\kappa r_s = 0.163_{-0.105}^{+0.088} \pm 0.037 \pm 0.021$  for  $B^\pm \rightarrow DK^{*\pm}$  (here  $\kappa$  accounts  
6117 for possible nonresonant  $B^\pm \rightarrow DK_S^0 \pi^\pm$  contribution). The combined significance of  
6118 direct CP violation is 99.7%, or 3.0 standard deviations.

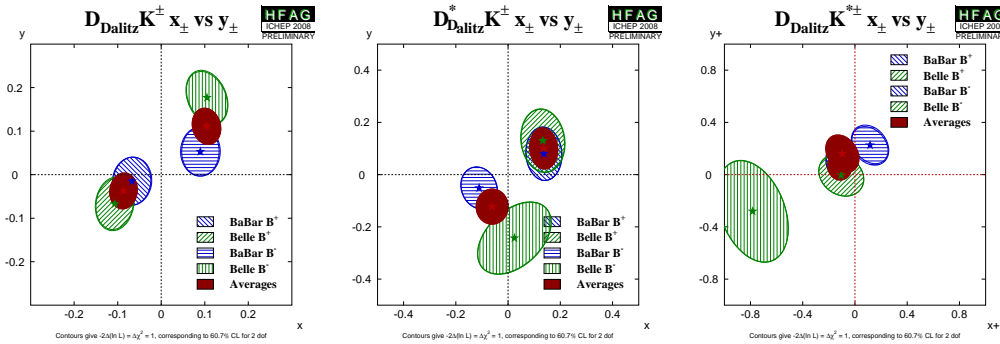


Fig. 70. World averages of measurements of observables in the Cartesian parametrization of the Dalitz method. Left:  $(x_{\pm}, y_{\pm})$  for  $B \rightarrow DK$ ; (middle):  $(x_{\pm}, y_{\pm})$  for  $B \rightarrow D^*K$  ( $D^* \rightarrow D\pi^0$  and  $D^* \rightarrow D\gamma$  combined); (right):  $(x_{\pm}, y_{\pm})$  for  $B \rightarrow DK^*$ . The Belle results use only  $D \rightarrow K_S^0\pi^+\pi^-$ , while the BaBar results include also  $D \rightarrow K_S^0K^+K^-$ . The averages do not include model uncertainties.

6119 Summaries of measurements of observables with the Dalitz plot method are given in  
 6120 Figs. 70 and 71.

#### 6121 8.2.4. Other techniques

6122 In decays of neutral  $B$  mesons to final states such as  $DK$  both amplitudes involving  $D^0$   
 6123 and  $\bar{D}^0$  are color-suppressed. Consequently, the value of  $r_B$  is larger, with naïve estimates  
 6124 giving  $r_B \sim 0.4$ . In the decay  $B^0 \rightarrow DK^*(892)^0$  the flavor of the  $B$  meson is tagged by  
 6125 the charge of the Kaon produced in the  $K^*(892)^0$  decay ( $K^+\pi^-$  or  $K^-\pi^+$ ) [1019], so  
 6126 that a time-dependent analysis is not necessary.

6127 Searches for doubly Cabibbo-suppressed decays have not yet yielded a significant sig-  
 6128 nal, but allow limits to be put on  $r_B$ . The most recent results are from BaBar using a  
 6129 data sample of 465M  $B\bar{B}$  pairs [1020]. BaBar has studied  $D \rightarrow K\pi$ ,  $D \rightarrow K\pi\pi^0$  and  
 6130  $D \rightarrow K\pi\pi\pi$ , and has found  $\mathcal{R}_{\text{ADS}}(K\pi) < 0.244$  at the 95% confidence level. The results  
 6131 can be combined using external information from CLEO-c [986, 1014, 1021] to obtain  
 6132  $r_S \in [0.07, 0.41]$  at the 95% confidence level, where  $r_S$  is the equivalent of the parameter  
 6133  $r_B$  modified due to the finite width of the  $K^{*0}$  resonance [1007].

6134 BaBar have also performed a Dalitz plot analysis of the three-body decay  $\bar{D}^0 \rightarrow$   
 6135  $K_S^0\pi^+\pi^-$  decay in  $B^0 \rightarrow DK^*(892)^0$  [1022]. The technique, and the decay model are  
 6136 similar to that used for  $B^{\pm} \rightarrow DK^{*\pm}$  decays (see Sec. 8.2.3). The analysis is based on  
 6137 371M  $B\bar{B}$  pairs, and yields the following constraints:  $\gamma = (162 \pm 56)^\circ$ ,  $r_B < 0.55$  with  
 6138 90% CL.

6139 It is also possible to measure  $\gamma$  by exploiting the interference between  $b \rightarrow c$  and  $\bar{b} \rightarrow \bar{u}$   
 6140 decays that occurs due to  $B^0-\bar{B}^0$  mixing using a time-dependent analysis. Since the in-  
 6141 terference occurs via oscillations, the mixing phase is also involved and the analysis is  
 6142 sensitive to the combination of angles  $\sin(2\beta + \gamma)$ . In this approach, the abundant decays  
 6143 such as  $B \rightarrow D\pi$  and  $B \rightarrow D^*\pi$  can be used; however the size of the CP violation effect  
 6144 depends on the magnitude of the ratio of the  $b \rightarrow u$  over  $b \rightarrow c$  amplitudes, usually de-  
 6145 noted  $R$ , which is naïvely expected to take values  $R \sim 0.02$  for these decays. Consequently  
 6146 these measurements are still statistics limited, as well as being potentially sensitive to  
 6147 systematics caused by any mismodelling of the large CP-conserving component. The sta-

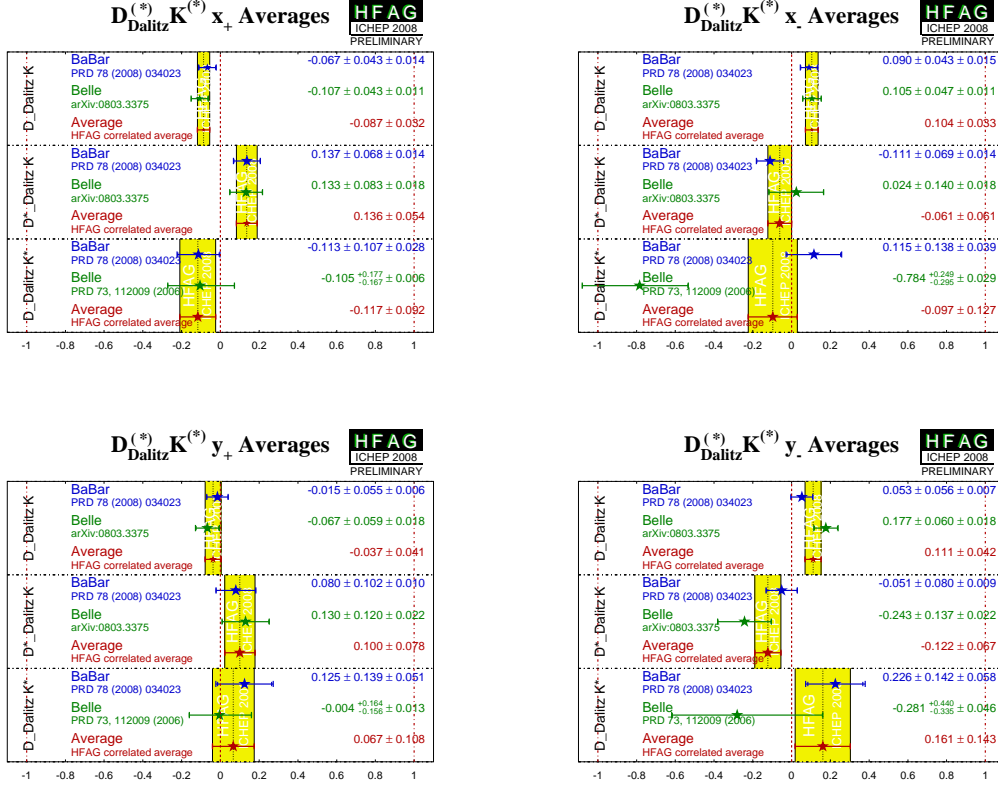


Fig. 71. World averages of measurements of observables in the Cartesian parametrization of the Dalitz method from HFAG [558]. Top left:  $x_+$ ; top right:  $x_-$ ; bottom left:  $y_+$ ; bottom right:  $y_-$ . The data is described in the caption to Fig. 70.

6148 tistical precision can be improved by using partial reconstruction for  $B \rightarrow D^* \pi$  decays  
6149 as well as the more conventional “full” reconstruction. A summary of measurements of  
6150 these modes from BaBar [1023,1024] and Belle [1025,1026] is given in Fig. 72.

6151 Another similar neutral  $B$  decay mode is  $B^0 \rightarrow D^\mp K^0 \pi^\pm$ , where time-dependent  
6152 Dalitz plot analysis is sensitive to  $2\beta + \gamma$  [1027,1028]. One advantage of this technique  
6153 compared to the methods based on  $B^0 \rightarrow D^{(*)} \pi$  decays is that, since both  $b \rightarrow c$  and  
6154  $b \rightarrow u$  diagrams involved in this decay are color-suppressed, the expected value of the  
6155 ratio of their magnitudes  $R$  is larger. Secondly,  $2\beta + \gamma$  is measured with only a two-  
6156 fold ambiguity (compared to four-fold in  $B^0 \rightarrow D^{(*)} \pi$  decays). In addition, all strong  
6157 amplitudes and phases can be, in principle, measured in the same data sample.

6158 The BaBar collaboration has performed the analysis based on 347M  $B\bar{B}$  pairs data  
6159 sample [1029]. The  $B^0 \rightarrow D^\mp K^0 \pi^\pm$  Dalitz plot is found to be dominated by  $B^0 \rightarrow$   
6160  $D^{*0} K_S^0$  (both  $b \rightarrow u$  and  $b \rightarrow c$  transitions) and  $B^0 \rightarrow D^- K^{*+}$  ( $b \rightarrow c$  only) states.  
6161 From an unbinned maximum likelihood fit to the time-dependent Dalitz distribution, the  
6162 value of  $2\beta + \gamma$  as a function of  $R$  is obtained. The value of  $R$  cannot be determined with  
6163 the current data sample, therefore, the value  $R = 0.3$  is used, and its uncertainty is taken



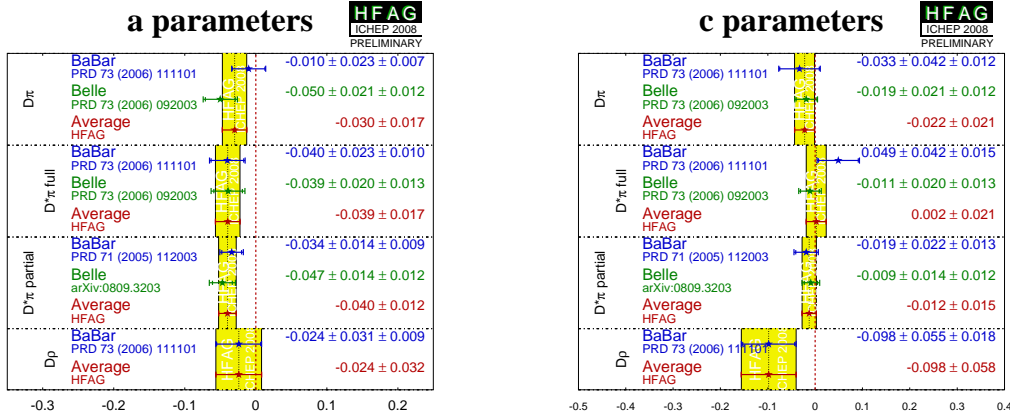


Fig. 72. Measurements of observables in  $B \rightarrow D\pi$  and similar final states. The parameters used in these compilations are  $a = (-1)^{L+1}2R \sin(2\beta + \gamma) \cos(\delta)$  and  $c = (-1)^{L+1}2R \cos(2\beta + \gamma) \sin(\delta)$ , where  $L$  is the angular momentum in the decay (+1 for  $D\pi$  and -1 for  $D^*\pi$  and  $D\rho$ ),  $R$  is the magnitude of the ratio of the  $\bar{b} \rightarrow \bar{u}$  and  $b \rightarrow c$  amplitudes and  $\delta$  is their relative phase.

6164 into account in the systematic error. This results in the value  $2\beta + \gamma = (83 \pm 53 \pm 20)^\circ$   
 6165 or  $(263 \pm 53 \pm 20)^\circ$ .

### 6166 8.3. Outlook on the $\gamma$ measurement

6167 The world average values that include the latest measurements presented in 2008 are  
 6168 reported in Sec. 10.

6169 For an evaluation of the prospect of  $\gamma$  measurement, it is essential to note the fact  
 6170 that for the first time the value of  $r_B$  is shown to be significantly non-zero. In previous  
 6171 measurements, poor constraints on  $r_B$  caused significantly non-gaussian errors for  $\gamma$ ,  
 6172 and made it difficult to predict the future sensitivity of this parameter. Now that  $r_B$  is  
 6173 constrained to be of the order 0.1, one can confidently extrapolate the current precision  
 6174 to future measurements at LHCb and Super-B facilities.

6175 The  $\gamma$  precision is mainly dominated by Dalitz analyses. These analyses currently  
 6176 suffer from a hard-to-control uncertainty due to the  $D^0$  decay amplitude description,  
 6177 which is estimated to be  $5\text{--}10^\circ$ . At the current level of statistical precision this error  
 6178 starts to influence the total  $\gamma$  uncertainty. A solution to this problem can be the use  
 6179 of quantum-correlated  $D\bar{D}$  decays at  $\psi(3770)$  resonance available currently at CLEO-c  
 6180 experiment, where the missing information about the strong phase in  $D^0$  decay can be  
 6181 obtained experimentally.

#### 6182 8.3.1. Model-independent Method

6183 Giri *et al.* proposed [255] a model-independent procedure for obtaining  $\gamma$ , as follows.  
 6184 The Dalitz plot is divided into  $2\mathcal{N}$  bins, symmetrically about the line  $m_+^2 = m_-^2$ . The  
 6185 bins are indexed from  $-i$  to  $i$ , excluding zero. The coordinate transformation  $m_+^2 \leftrightarrow m_-^2$   
 6186 thus corresponds to the exchange of bins  $i \leftrightarrow -i$ . The number of events in the  $i$ -th bin

6187 of a flavor-tagged  $D^0$  decay  $K_S^0\pi^+\pi^-$  Dalitz plot is then expressed as:

$$K_i = A_D \int_i |f_D(m_+^2, m_-^2)|^2 dm_+^2 dm_-^2 = A_D F_i, \quad (382)$$

6188 where  $A_D$  is a normalization factor. The coefficients  $K_i$  can be obtained precisely from  
 6189 a very large sample of  $D^0$  decays reconstructed in flavor eigenstate, which is accessi-  
 6190 ble at  $B$ -factories, for example. The interference between the  $D^0$  and  $\bar{D}^0$  amplitudes is  
 6191 parametrized by the quantities  $c_i$  and  $s_i$ :

$$c_i \equiv \frac{1}{\sqrt{F_i F_{-i}}} \int_i |f_D(m_+^2, m_-^2)| |f_D(m_-^2, m_+^2)| \cos[\Delta\delta_D(m_+^2, m_-^2)] dm_+^2 dm_-^2, \quad (383)$$

$$s_i \equiv \frac{1}{\sqrt{F_i F_{-i}}} \int_i |f_D(m_+^2, m_-^2)| |f_D(m_+^2, m_-^2)| \sin[\Delta\delta_D(m_+^2, m_-^2)] dm_+^2 dm_-^2, \quad (384)$$

where the integral is performed over a single bin. The quantities  $c_i$  and  $s_i$  are the amplitude-weighted averages of  $\cos\Delta\delta_D$  and  $\sin\Delta\delta_D$  over each Dalitz-plot bin. The expected number of events in the bins of the Dalitz plot of the  $D$  decay from  $B^\pm \rightarrow DK^\pm$  is

$$\langle N_i \rangle = A_B [K_i + r_B^2 K_{-i} + 2\sqrt{K_i K_{-i}}(x_\pm c_i + y_\pm s_i)], \quad (385)$$

6192 where  $A_B$  is the normalization constant. As soon as the  $c_i$  and  $s_i$  coefficients are known,  
 6193 one can obtain  $x_\pm$  and  $y_\pm$  values (and hence  $\gamma$  and other related quantities) by a max-  
 6194 imum likelihood fit using equation (385). In principle,  $c_i$  and  $s_i$  can be left as free pa-  
 6195 rameters in a  $\bar{D}^0 \rightarrow K_S^0\pi^+\pi^-$  Dalitz-plot analysis from  $B^\pm$  decays. However, it has been  
 6196 shown [1030] that almost infinite statistics of  $B$  decays is necessary in that case.

It is important to note that  $c_i$  and  $s_i$  depend only on the  $D^0$  decay, not the  $B$  decay, and therefore these quantities can be measured using the quantum-correlated  $D\bar{D}$  decays of the  $\psi(3770)$  resonance. For example, the expected number of events in a bin of the Dalitz plot of  $D_{CP}$  tagged decays equals

$$\langle M_i \rangle^\pm = A_{CP}^\pm [K_i + K_{-i} \pm 2\sqrt{K_i K_{-i}} c_i], \quad (386)$$

6197 where the  $\pm$  indicates whether the CP tag is CP-even or CP-odd. This relation can be  
 6198 used to obtain the  $c_i$  coefficients, but obtaining  $s_i$  remains a problem. If the binning  
 6199 is fine enough, so that both the phase difference  $\Delta\delta_D$  and the amplitude  $|f_D|$  remain  
 6200 constant across the area of each bin, the expressions (383,384) reduce to  $c_i = \cos(\Delta\delta_D)$   
 6201 and  $s_i = \sin(\Delta\delta_D)$ . The  $s_i$  coefficients can be obtained as  $s_i = \pm\sqrt{1 - c_i^2}$ . Using this  
 6202 equality if the amplitude varies across a bin will lead to bias in the  $x_\pm, y_\pm$  fit results.  
 6203 Since  $c_i$  is obtained directly, and the absolute value of  $s_i$  is overestimated, the bias will  
 6204 mainly affect  $y_\pm$  determination, resulting in lower absolute values of  $y_\pm$ .

A unique possibility to find  $s_i$  independent of  $c_i$  is available in a sample where both  $D$  mesons from the  $\psi(3770)$  decay into the  $K_S^0\pi^+\pi^-$  state [1031]. Since the  $\psi(3770)$  is a vector, the two  $D$  mesons are produced in a  $P$ -wave, and the wave function of the two mesons is antisymmetric. Then the four-dimensional density of the two correlated Dalitz plots is given by:

$$\langle M \rangle_{ij} = A_{\text{corr}} [K_i K_{-j} + K_{-i} K_{j-} - 2\sqrt{K_i K_{-i} K_j K_{-j}} (c_i c_j + s_i s_j)]. \quad (387)$$

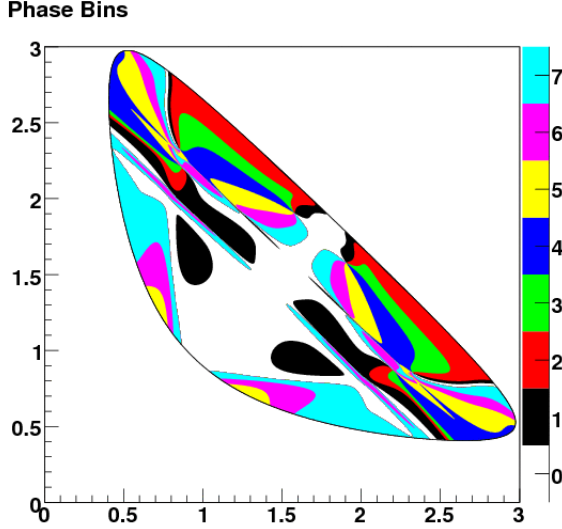


Fig. 73. Phase binning of the  $D^0 \rightarrow \bar{K}_S^0 \pi^+ \pi^-$  Dalitz plot.

6205 The indices  $i, j$  correspond to the two  $D$  mesons from  $\psi(3770)$  decay. This decay is  
 6206 sensitive to both  $c_i$  and  $s_i$  for the price of having to deal with the four-dimensional phase  
 6207 space.

6208 The original idea of Giri *et al.* was to divide the Dalitz plot into square bins [255]. In  
 6209 case of limited statistics unavoidably the number of the bins could be relatively small.  
 6210 Consequently, a large loss of sensitivity can be expected due to variation of amplitude and  
 6211 phase over the bin. Bondar *et al.* noted [1031] that increased sensitivity can be obtained  
 6212 if the bins are chosen to minimize the variation in  $\Delta\delta_D$  over each bin. One can divide  
 6213 the Dalitz phase space into  $\mathcal{N}$  bins of equal size with respect to  $\Delta\delta_D$  as predicted, for  
 6214 example, by the BaBar isobar model [258]. In the half of the Dalitz plot  $m_+^2 < m_-^2$ , the  
 6215  $i^{\text{th}}$  bin is defined by the condition

$$2\pi(i - 3/2)/\mathcal{N} < \Delta\delta_D(m_+^2, m_-^2) < 2\pi(i - 1/2)/\mathcal{N}, \quad (388)$$

6216 The  $-i^{\text{th}}$  bin is defined symmetrically in the lower portion of the Dalitz plot. Such a  
 6217 binning with  $\mathcal{N} = 8$  is shown in Fig. 73. One might suspect that, since we are using a  
 6218 model to determine our bins, we are not free of model dependence. In fact *any* binning  
 6219 is acceptable in that it will give a correct, unbiased answer for  $\gamma$ , at the cost of larger  
 6220 uncertainties compared to an optimal binning with respect to  $\Delta\delta_D$ .

6221 Using  $818 \text{ pb}^{-1}$  of  $e^+e^-$  collisions produced at the  $\psi(3770)$ , the CLEO-c collaboration  
 6222 has made a first determination [1032] of the strong phase parameters,  $c_i$  and  $s_i$ , which  
 6223 are listed in Tab. 60. From a toy Monte Carlo study with a large sample of  $B^\pm \rightarrow \bar{D}^0 K^\pm$   
 6224 data generated with  $\gamma = 60^\circ$ ,  $\delta_B = 130^\circ$  and  $r_B = 0.1$ , CLEO found that the decay  
 6225 model uncertainty on  $\gamma$  is reduced to about  $1.7^\circ$  due to these new measurements. As a  
 6226 result, the precision of the  $\gamma$  measurement using  $B^+ \rightarrow \bar{D}^0 K^+$  decays will not be limited  
 6227 by model-dependent assumptions on strong phase behavior in the  $\bar{D}^0 \rightarrow K_S^0 \pi^+ \pi^-$  decay.

Table 60

Fit results for  $c_i$  and  $s_i$ . The first error is statistical, the second error is the systematic uncertainty, the third error is the model uncertainty due to including  $K_L^0 \pi^+ \pi^-$  events in the analysis.

$i$	$c_i$	$s_i$
0	$0.743 \pm 0.037 \pm 0.022 \pm 0.013$	$0.014 \pm 0.160 \pm 0.077 \pm 0.045$
1	$0.611 \pm 0.071 \pm 0.037 \pm 0.009$	$0.014 \pm 0.215 \pm 0.055 \pm 0.017$
2	$0.059 \pm 0.063 \pm 0.031 \pm 0.057$	$0.609 \pm 0.190 \pm 0.076 \pm 0.037$
3	$-0.495 \pm 0.101 \pm 0.052 \pm 0.045$	$0.151 \pm 0.217 \pm 0.069 \pm 0.048$
4	$-0.911 \pm 0.049 \pm 0.032 \pm 0.021$	$-0.050 \pm 0.183 \pm 0.045 \pm 0.036$
5	$-0.736 \pm 0.066 \pm 0.030 \pm 0.018$	$-0.340 \pm 0.187 \pm 0.052 \pm 0.047$
6	$0.157 \pm 0.074 \pm 0.042 \pm 0.051$	$-0.827 \pm 0.185 \pm 0.060 \pm 0.036$
7	$0.403 \pm 0.046 \pm 0.021 \pm 0.002$	$-0.409 \pm 0.158 \pm 0.050 \pm 0.002$

### 8.3.2. Prospects for LHCb

The measurement of the CKM angle  $\gamma$  in tree dominated processes is one of the principal goals of LHCb. Extensive simulation studies have been conducted in a variety of channels. The results summarized here derive from [1033] and references therein.

LHCb will measure  $\gamma$  in tree dominated processes using two main approaches:

- (i) **Time-dependent measurements** The extraction of  $\gamma$  has been studied using both  $B^0 \rightarrow D^\mp \pi^\pm$  and  $B_s \rightarrow D_s^\mp K^\pm$ . Although the CP-asymmetries in these modes involve a contribution arising from the mixing diagram, this contribution can be subtracted using the result from complementary measurements in other processes, allowing for a pure tree-level  $\gamma$  determination.
- (ii)  **$B \rightarrow DK$  strategies** The modes that have so far been investigated which have significant weight in the  $\gamma$  measurement include  $B^\mp \rightarrow DK^\mp$ , with the neutral  $D$  reconstructed in the  $K^+ K^-$ ,  $\pi^+ \pi^-$ ,  $K^\mp \pi^\pm$ ,  $K^\mp \pi^\pm \pi^+ \pi^-$  and  $K_S^0 \pi^+ \pi^-$  final states, and  $B^0 \rightarrow D(K^\pm \pi^\pm, K^+ K^-, \pi^+ \pi^-) K^{*0}(K^- \pi^+)$  (+c.c.). The fact that no initial-state flavor tagging is required means that the relative sensitivity of the  $B \rightarrow DK$  method is particularly high at LHCb compared with time-dependent measurements, in which the tagging power is in general lower than is the case at  $\Upsilon(4S)$  experiments.

The expected yields in  $2 \text{ fb}^{-1}$  of data taking in these channels are given in Tab. 61. Note that the goal of the baseline LHCb experiment is to accumulate around  $10 \text{ fb}^{-1}$  of integrated luminosity. In all modes the selection benefits from the good performance of the  $\pi - K$  separation provided by the LHCb RICH system.

The physics processes underlying the event rates and kinematic distributions in the  $B \rightarrow DK$  channels have many parameters in common. This means that the observables for these channels may be combined in a global fit to achieve the best possible sensitivity to these parameters, most notably  $\gamma$  itself. The power of such a fit has been investigated in a toy Monte Carlo study, taking as input the expected sensitivities on the observables arising from the full simulation. For the two and four body  $D$  decay modes the observables are the event rates in each mode; for the  $D \rightarrow K_S^0 \pi^+ \pi^-$  decay they are the populations of bins in Dalitz space, as defined by the expected strong-phase difference.

Table 61

Summary of expected LHCb signal and background yields for  $2 \text{ fb}^{-1}$ . In those rows where more than one channel is specified (eg.  $B^\pm \rightarrow D(K^\pm \pi^\mp)K^\pm$  or  $B^+ \rightarrow D(K^+K^- + \pi^+\pi^-)K^+$ ), the yields correspond to the *sum* over all indicated modes. The physics parameters assumed in calculating these numbers can be found in [1033].

Channel	Signal	Background
$B^\pm \rightarrow D(K^\pm \pi^\mp)K^\pm$	56k	35k
$B^+ \rightarrow D(K^- \pi^+)K^+$	680	780
$B^- \rightarrow D(K^+ \pi^-)K^-$	400	780
$B^+ \rightarrow D(K^+K^- + \pi^+\pi^-)K^+$	3.3k	7.2k
$B^- \rightarrow D(K^+K^- + \pi^+\pi^-)K^-$	4.4k	7.2k
$B^\pm \rightarrow D(K^\pm \pi^\mp \pi^+ \pi^-)K^\pm$	61k	40k
$B^+ \rightarrow D(K^- \pi^+ \pi^+ \pi^-)K^+$	470	1.2k
$B^- \rightarrow D(K^+ \pi^- \pi^+ \pi^-)K^-$	350	1.2k
$B^0 \rightarrow D(K^+ \pi^-)K^{*0}, \bar{B}^0 \rightarrow D(K^- \pi^+)\bar{K}^{*0}$	3.4k	1.7k
$B^0 \rightarrow D(K^- \pi^+)K^{*0}$	350	850
$\bar{B}^0 \rightarrow D(K^+ \pi^-)\bar{K}^{*0}$	230	850
$B^0 \rightarrow D(K^+K^- + \pi^+\pi^-)K^{*0}$	150	500
$\bar{B}^0 \rightarrow D(K^+K^- + \pi^+\pi^-)\bar{K}^{*0}$	550	500
$B^\pm \rightarrow D(K_S^0 \pi^\mp \pi^\mp)K^\pm$	5k	4.7k
$B_s, \bar{B}_s \rightarrow D_s^\mp K^\pm$	6.2k	4.3k
$B^0, \bar{B}^0 \rightarrow D^\mp \pi^\pm$	1,300k	290k

6258 Important components of this fit are the external constraints which come from the  $D$   
6259 decay properties from the quantum-correlated measurements at CLEO-c. These are the  
6260 measured strong phase difference in  $D \rightarrow K\pi$  decays [986, 1014], the measured coher-  
6261 ence factor [1034] and average strong phase difference in  $D \rightarrow K\pi\pi\pi$  decays [1021], and  
6262 the expected sensitivity on the cosine and sine of the strong phase differences in the  
6263  $D \rightarrow K_S^0 \pi^+ \pi^-$  Dalitz plot bins [1032].<sup>24</sup> The results of this fit have a dependence on  
6264 the assumed values of the physics parameters; the least well known of these is  $\delta_{B^0}$ , the  
6265 strong phase difference between the interfering diagrams in  $B^0 \rightarrow DK^{*0}$  decays, and so  
6266 in Tab. 62 the expected sensitivity on  $\gamma$  is shown as a function of this phase. The CLEO-c  
6267 inputs allow for a significant improvement on the overall precision.

6268 The results from the global  $B \rightarrow DK$  fit may be combined with the expected uncer-  
6269 tainty on  $\gamma$  from the time-dependent measurements, the most important of which is the  
6270 analysis of  $B_s \rightarrow D_s^\mp K^\pm$  decays. The expected precision on  $\gamma$  from all of these measure-  
6271 ments is shown in Tab. 63. It can be seen that with the modes under consideration a  
6272 sensitivity of  $2 - 3^\circ$  is expected in the lifetime of the experiment.

<sup>24</sup>Note that the results shown here take as input preliminary estimates of the CLEO-c sensitivity to the  $D$ -meson decay properties for both  $D \rightarrow K\pi\pi\pi$  and  $D \rightarrow K_S^0 \pi^+ \pi^-$ .

Table 62

Expected LHCb sensitivity to  $\gamma$  from  $B \rightarrow DK$  strategies for data sets corresponding to integrated luminosities of 0.5, 2 and 10  $\text{fb}^{-1}$ , with and without CLEO-c constraints.

$\delta_{B^0}$ ( $^\circ$ )	0	45	90	135	180
0.5 $\text{fb}^{-1}$					
$\sigma_\gamma$ without CLEO-c constraints ( $^\circ$ )	11.5	12.9	13.1	12.5	9.7
$\sigma_\gamma$ with CLEO-c constraints ( $^\circ$ )	9.0	12.0	10.7	11.1	8.6
2 $\text{fb}^{-1}$					
$\sigma_\gamma$ without CLEO-c constraints ( $^\circ$ )	5.8	8.3	7.8	8.4	5.0
$\sigma_\gamma$ with CLEO-c constraints ( $^\circ$ )	4.6	6.1	5.7	6.0	4.3
10 $\text{fb}^{-1}$					
$\sigma_\gamma$ without CLEO-c constraints ( $^\circ$ )	2.6	5.4	3.5	4.8	2.4
$\sigma_\gamma$ with CLEO-c constraints ( $^\circ$ )	2.3	3.5	2.9	3.2	2.2

Table 63

Expected LHCb combined sensitivity to  $\gamma$  from  $B \rightarrow DK$  and time-dependent measurements for data sets corresponding to integrated luminosities of 0.5, 2 and 10  $\text{fb}^{-1}$ .

$\delta_{B^0}$ ( $^\circ$ )	0	45	90	135	180
$\sigma_\gamma$ for 0.5 $\text{fb}^{-1}$ ( $^\circ$ )	8.1	10.1	9.3	9.5	7.8
$\sigma_\gamma$ for 2 $\text{fb}^{-1}$ ( $^\circ$ )	4.1	5.1	4.8	5.1	3.9
$\sigma_\gamma$ for 10 $\text{fb}^{-1}$ ( $^\circ$ )	2.0	2.7	2.4	2.6	1.9

## 6273 9. Measurements of the angles of the unitarity triangle in charmless 6274 hadronic $B$ decays

### 6275 9.1. Theory estimates for hadronic amplitudes

#### 6276 9.1.1. Angles, physical amplitudes, topological amplitudes

Any standard-model (SM) amplitude for a decay  $B \rightarrow f$  can be written, by integrating out the weak interactions to lowest order in  $G_F$  (Sec. 2.1), as a linear combination

$$\mathcal{A}(B \rightarrow f) = \sum_{i,U} C_i V_{UD} V_{Ub}^* \langle f | Q_i | B \rangle \quad (389)$$

6277 of matrix elements of local operators  $Q_i$  in  $\text{QCD} \times \text{QED}$ . Here  $D = d, s$  and  $U =$   
6278  $u, c, t$ . By CKM unitarity, one term in the sum over  $U$  can be removed. This gives a  
6279 decomposition into (physical) tree and penguin amplitudes (the names are motivated by  
6280 Wick contractions of the operators  $Q_i$  contributing to them),

$$\begin{aligned} \mathcal{A}(B \rightarrow f) &= T_f e^{i\theta_T} + P_f e^{i\theta_P}, \\ \mathcal{A}(\bar{B} \rightarrow f) &= T_f e^{-i\theta_T} + P_f e^{-i\theta_P}, \end{aligned} \quad (390)$$

where  $T_f$  and  $P_f$  (“strong amplitudes”) and  $\theta_T$  and  $\theta_P$  (“weak phases”) have definite CP transformation properties. For decays into two light mesons, conventionally  $U = c$

(or  $U = t$ ) is eliminated, giving  $\theta_P = \beta$  ( $\theta_P = 0$ ), and  $\theta_T = \gamma$ . For decays involving charmonium, the tree is associated with  $U = c$  ( $\theta_T = 0$ ), and one of  $U = u, t$  is eliminated (both are expected to be negligible). The prototypical angle measurement derives from the time-dependent CP asymmetry

$$A_{\text{CP}}(f; t) \equiv \frac{\Gamma(\bar{B}(t) \rightarrow f) - \Gamma(B(t) \rightarrow f)}{\Gamma(\bar{B}(t) \rightarrow f) + \Gamma(B(t) \rightarrow f)} \equiv -C_f \cos \Delta m t + S_f \sin \Delta m t, \quad (391)$$

where  $f$  is a CP eigenstate of eigenvalue  $\eta_{\text{CP}}(f)$ ,  $\Delta m$  is the absolute value of the mass difference between the two mass eigenstates in the  $B^0$ - $\bar{B}^0$  system, and

$$C_f = \frac{1 - |\xi|^2}{1 + |\xi|^2}, \quad S_f = \frac{2\text{Im}\xi}{1 + |\xi|^2}, \quad \xi = e^{-i2\beta} \frac{\mathcal{A}(\bar{B} \rightarrow f)}{\mathcal{A}(B \rightarrow f)}. \quad (392)$$

6281 (We assume  $CPT$  conservation, and neglect lifetime differences and CP violation in  
6282 mixing throughout.) If  $P_f$  can be neglected,  $|\xi| = 1$ ,  $C_f = 0$ , and  $S_f$  gives a clean mea-  
6283 surement of  $\sin 2(\beta + \theta_T)$ . This is true to very good approximation for decays into final  
6284 states containing charmonium such as  $B \rightarrow J/\psi K_S$  ( $\theta_T = 0$ ,  $-\eta_{\text{CP}}(f)S_f = \sin 2\beta$ ). It  
6285 holds less accurately for  $b \rightarrow d$  transitions like  $B \rightarrow (\pi^+\pi^-, \rho^+\pi^-, \rho^+\rho^-)$ , where the  
6286 CKM hierarchy is  $[P_f/T_f]_{\text{CKM}} = \mathcal{O}(1)$ , but some suppression of penguin amplitudes fol-  
6287 lows from theoretical arguments reviewed below. In these modes, one has approximately  
6288  $-\eta_{\text{CP}}(f)S_f \approx \sin 2(\beta + \gamma) = -\sin 2\alpha$ . Conversely, penguin-dominated  $b \rightarrow s$  modes  
6289  $B \rightarrow (\pi K, \phi K, \eta^{(\prime)} K, \dots)$ , where  $[T_f/P_f]_{\text{CKM}} = \mathcal{O}(\lambda^2)$ , probe  $\sin 2\beta$ .

In view of these considerations, it is clear that the interpretation of the time-dependent CP asymmetries (and more generally, the many charmless  $B$  and  $\bar{B}$  decay rates) in terms of CKM parameters and possible new-physics contributions requires some information on at least the amplitude ratios  $P/T$ , hence on the hadronic matrix elements  $\langle f|Q_i|B\rangle$ . In principle, the latter are determined by the QCD and electromagnetic coupling and quark masses via (for the case of a two-particle final state) four-point correlation functions involving three operators destroying the  $B$ -meson and creating the final-state mesons, as well as one insertion of the operator  $Q_i$ . Formally, they are expressible in terms of a path integral

$$\langle M_1 M_2 | Q_i | B \rangle \sim \int dA \int d\bar{\psi} d\psi j_B^\mu(x) j_{M_1}^\nu(y) j_{M_2}^\rho(z) Q_i(w) e^{i(S_{\text{QCD}} + Q_{\text{ED}})}. \quad (393)$$

6290 The currents  $j_B, j_{M_1}, j_{M_2}$  must have the correct quantum numbers to create/destroy  
6291 the initial- and final-state particles, for instance  $j_B^\mu = \bar{b}\gamma^\mu\gamma_5 d$  for a  $B^0$  decay, but are  
6292 otherwise arbitrary. In practice, this path integral cannot be evaluated; however, the  
6293 inner (fermionic) path integral can be represented as a sum of Wick contractions which  
6294 provide a nonperturbative definition of “topological” amplitudes (Fig. 74). We stress  
6295 that no expansion of any kind has been made; the lines represent the full inverse Dirac  
6296 operators, rather than perturbative (“free”) propagators, averaged over arbitrary gluon  
6297 backgrounds by the outer (gluonic) path integral. A complete list has been given in [1035].  
6298 Topological amplitudes can also be defined equivalently (and were originally) as matrix  
6299 elements of the  $SU(3)$  decomposition of the weak Hamiltonian [1036, 1037].

6300 Each physical amplitude decomposes into several topological ones. For a tree, in the  
6301 notation of [1038],

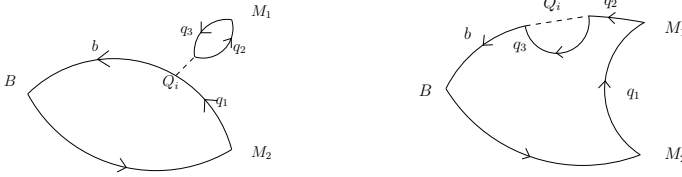


Fig. 74. Examples of Wick contractions. Left: Tree contraction. Right: Penguin contraction. The scheme-independent topological amplitudes correspond to certain sums of contractions of several operators in the weak Hamiltonian. The lines are “dressed” propagators, depending on the gluonic background. Arbitrarily many gluons not shown. From [1035].

$$\begin{aligned}
T_{M_1 M_2} = & |V_{ub}V_{ud}| [A_{M_1 M_2} (\alpha_1(M_1 M_2) + \alpha_2(M_1 M_2) + \alpha_4^u(M_1 M_2)) \\
& + B_{M_1 M_2} (b_1(M_1 M_2) + b_2(M_1 M_2) + b_3^u(M_1 M_2) + b_4^u(M_1 M_2)) \\
& + \mathcal{O}(\alpha)] + (M_1 \leftrightarrow M_2) .
\end{aligned} \tag{394}$$

6302 The first two terms on the first line are known as the color-allowed and color-suppressed  
6303 trees, while the third term is due to a set of penguin contractions. The terms on the  
6304 second lines are due to annihilation topologies, where both fields in the current  $j_B$  are  
6305 contracted with the weak vertex. We have not spelled out  $\mathcal{O}(\alpha)$  terms, which include the  
6306 electroweak penguin terms, as well as long-distance QED effects.<sup>25</sup> Not all topological  
6307 amplitudes are present for every final state.<sup>26</sup> On the other hand, if both  $a_i(M_1 M_2)$  and  
6308  $a_i(M_2 M_1)$  are present, they must be summed. For instance [1038],

$$\begin{aligned}
T_{\pi^0 \rho^0} = & \frac{i}{2} |V_{ub}V_{ud}| \frac{G_F}{\sqrt{2}} m_B^2 \left[ f_+^{B\pi}(0) f_\rho (\alpha_2(\pi^0 \rho^0) - \alpha_4^u(\pi^0 \rho^0)) - f_B f_\pi f_\rho b_1(\pi^0 \rho^0) \right. \\
& \left. + A_0^{B\rho}(0) f_\pi (\alpha_2(\rho^0 \pi^0) - \alpha_4^u(\rho^0 \pi^0)) - f_B f_\pi f_\rho b_1(\rho^0 \pi^0) + \mathcal{O}(\alpha) \right], \tag{395}
\end{aligned}$$

6309 where we have also spelled out the normalization factors  $A_{M_1 M_2}$ , which like  $B_{M_1 M_2}$   
6310 consists of form factors, decay constants,  $G_F$ , etc. as a convention (and in anticipation of  
6311 the heavy-quark expansion), neglecting terms  $\mathcal{O}(m_\pi/m_B, m_\rho/m_B)$ . Moreover, for flavor-  
6312 singlet mesons  $M_1$  or  $M_2$  there are additional amplitudes.

6313 Similarly, for a penguin, we have the decomposition

$$\begin{aligned}
P_{M_1 M_1} = & |V_{cb}V_{cd}| [A_{M_1 M_2} \alpha_4^c(M_1 M_2) + B_{M_1 M_2} (b_3^c(M_1 M_2) + b_4^c(M_1 M_2))] \\
& + (M_1 \leftrightarrow M_2) .
\end{aligned} \tag{396}$$

6314 The parametrization are general, but we have now fixed a convention where  $V_{tb}^* V_{td}$  has  
6315 been eliminated.

6316 Present theoretical knowledge on the topological amplitudes derives from expansions  
6317 (i) in the Wolfenstein parameter  $\lambda$  (see above discussion), (ii) around the  $SU(3)$  flavor  
6318 symmetry limit (i.e., in  $m_s/\Lambda$ ), (iii) in the inverse number of colors  $1/N_c$ , and (iv) the  
6319 heavy-quark expansion in  $\Lambda/m_b$  and  $\alpha_s$ , where  $\Lambda \equiv \Lambda_{\text{QCD}}$  is the QCD scale parameter.  
6320 The counting for the various topological amplitudes is shown in Tab. 64. The  $\lambda$  and

<sup>25</sup> These effects include emissions of soft photons from the final-state particles [1039] and are modeled in extracting the two-body rates and asymmetries (which are not infrared safe if soft photons are included) from data.

<sup>26</sup> More precisely, one would write  $\alpha_i(M_1 M_2) \rightarrow c_i(M_1 M_2) \alpha_i(M_1 M_2)$  where  $c_i(M_1 M_2) = 0$  if the amplitude is not present and a Clebsch-Gordan coefficient otherwise [1038].



Table 64

Hierarchies among topological amplitudes from expansions in the Cabibbo angle  $\lambda$ , in  $1/N_c$ , and in  $\Lambda_{\text{QCD}}/m_b$ . Some multiply suppressed amplitudes (e.g. EW penguin amplitudes that are CKM suppressed in  $b \rightarrow s$  transitions) are omitted.

	$T/a_1$	$C/a_2$	$P_{uc}/\alpha_4^u$	$P_{ut}/\alpha_4^c$	$P_{EW}/\alpha_{3EW}$	$P_{EW}^C/\alpha_{4EW}$	$b_3^c$	$b_4^c$	$E/b_1$	$A/b_2$
Cabibbo ( $b \rightarrow d$ )	all amplitudes are $\mathcal{O}(\lambda^3)$									
Cabibbo ( $b \rightarrow s$ )	$\lambda^4$	$\lambda^4$	$\lambda^4$	$\lambda^2$	$\lambda^2$	$\lambda^2$	$\lambda^2$	$\lambda^2$	$\lambda^4$	$\lambda^4$
$1/N$	1	$\frac{1}{N}$	$\frac{1}{N}$	$\frac{1}{N}$	1	$\frac{1}{N}$	$\frac{1}{N}$	$\frac{1}{N}$	$\frac{1}{N}$	1
$\Lambda/m_b$	1	1	1	1	1	1	$\Lambda/m_b$	$\Lambda/m_b$	$\Lambda/m_b$	$\Lambda/m_b$

6321  $1/N_c$  counting provide only (rough) hierarchies. Existing  $SU(3)$  analyses work at zeroth  
6322 order, providing relations between topological amplitudes for different final states. (In  
6323 the case of  $\pi^+\pi^-$ ,  $\rho^+\rho^-$ , isospin alone provides useful relations. This is the basis for the  
6324  $\alpha$  determinations reviewed in Sec. 9.3 below.) The virtue is the possibility to completely  
6325 eliminate some of the theoretically difficult amplitudes from the analysis, removing the  
6326 need for their theoretical computation. This comes of the expense of eliminating some  
6327 of the experimental information that is in principle sensitive to short-distance physics  
6328 (SM and beyond) from the analysis, as well. For instance, in the  $\alpha$  determinations, six  
6329 observables are needed to determine one parameter.

6330 Both the  $1/N_c$  expansion and the heavy-quark expansion rely on an expansion in Feyn-  
6331 man diagrams. The virtue of the heavy-quark expansion is that, to lowest order in the  
6332 expansion parameter  $\Lambda/m_b$ , and in some cases to subleading order, the amplitudes them-  
6333 selves are calculable in perturbation theory. More precisely, they factorize into products  
6334 of form factors and of convolution of a perturbative expression with non-perturbative me-  
6335 son wave functions. Moreover, all the  $b_i$  (annihilation) amplitudes are power-suppressed.  
6336 The theoretical basis of the  $1/m_b$  expansion is discussed in Sec. 2.2. The rest of this  
6337 section is devoted to quantitative results and phenomenology of the topological (and  
6338 physical) amplitudes.

### 6339 9.1.2. Tree amplitudes: results

The most complete results are available for the topological tree amplitudes, whose  
factorization at leading power in the  $1/m_b$  expansion is pictured in Fig. 75. The gray  
blobs and the violet ‘spring’ lines contain the soft and collinear gluon degrees of freedom  
(virtualities  $< \sqrt{\Lambda m_b}$ ). The hard subgraph, formed by the remaining gluon lines and  
the pieces of quark lines between their attachments and the weak vertex, connects the  
quark legs of the weak operators  $Q_1$  and  $Q_2$  with valence quark lines for the external  
states but not with each other, hence the name “tree”. For either operator, the hard  
scale  $m_b$  (wavy lines) can be matched onto two operators  $\mathcal{O}^{I,II}$  in SCET<sub>I</sub> (see Sec. 2.2).  
At leading power, all terms at  $\mathcal{O}(\alpha_s)$  (NLO) [38–40] and  $\mathcal{O}(\alpha_s^2)$  (NNLO) [1040–1044]  
have been computed. In particular, these results establish the validity of factorization  
and the good behavior of the perturbation expansion up to NNLO. The hard-collinear  
scale  $\sqrt{\Lambda m_b}$  can also be factorized. This has been performed for the operators of type II  
in [1042, 1045–1047]. Again, a stable perturbation expansion is observed. Depending on  
the flavor of the valence quark lines, color factors differ, giving rise to a “color-allowed”  
amplitude  $\alpha_1$  and a “color-suppressed” one  $\alpha_2$ . The type-II (hard-spectator-scattering)  
contributions then take the form

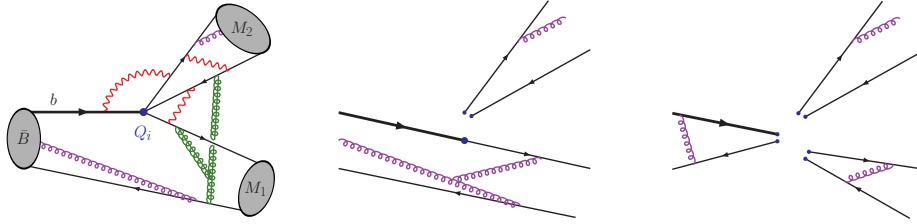


Fig. 75. Factorization of the tree amplitudes. Left: Matrix element of a weak Hamiltonian current-current operator  $Q_{1,2}$  in the effective 5-flavor QCD $\times$ QED theory. The red, wavy lines close to the vertex have virtualities of order  $m_b^2$ ; the system of green ‘cut-spring’ lines connecting to the spectator, of order  $\Lambda m_b$ . The purple ‘spring’ lines entering the mesons indicate the soft gluon background in which the hard subprocess takes place. Middle: Factorization into a product of a wave function and a form factor (to be convoluted with a hard kernel  $H^I$  or  $H^{II}$ ). Right: The  $B$ -type bilocal form factor (convoluted with  $H^{II}$ ) factorizes further into wave functions. (According to the pQCD framework, this is also true for the soft ( $A$ -type) form factor.)

$$A_{M_1 M_2} \alpha_{1,2}^{II} \propto [H^{II} * \phi_{M_2}] * [\phi_B * J * \phi_{M_1}] \quad (397)$$

6340 of a convolution of hard and hard-collinear scattering kernels  $H^{II}$  and  $J$  with meson wave  
 6341 functions. An alternative is not to perform the hard-collinear factorization and define a  
 6342 non-local form factor  $\zeta_J = \phi_B * J * \phi_M$ , information on which has to be extracted from  
 6343 experiment. This works in practice to zeroth order in  $\alpha_s(m_b)$  [51]. At higher orders,  
 6344 the kernel  $H^{II}$  acquires a dependence on how the momentum is shared between the  $M_1$   
 6345 valence quarks, i.e. the convolution  $H^{II} * \zeta_J$  becomes nontrivial. No higher-order analyses  
 6346 have been performed.<sup>27</sup>

For the type-I operators, in the collinear expansion one encounters divergent convo-  
 lutions in factorizing the hard-collinear scale already at the leading power, indicating  
 a soft overlap breaking (perturbative) factorization of soft and collinear physics. In this  
 case, however, not performing this factorization is more feasible, as it leaves a single form  
 factor (which can be taken to be an ordinary QCD form factor or the SCET soft form  
 factor) multiplying a convolution of a hard-scattering kernel with one light-meson wave  
 function,

$$A_{M_1 M_2} \alpha_{1,2}^I \propto f^{BM_1}(0) H^I * \phi_{M_2}. \quad (398)$$

6347 [By convention, the form factor is factored out into  $A_{M_1 M_2}$ .] An alternative treatment  
 6348 is  $k_T$  factorization (“pQCD”) [48], where a transverse-momentum-dependent  $B$ -meson  
 6349 wave function is introduced, which regularizes the endpoint divergence. In this case, a  
 6350 convergent convolution arises (at lowest order), and within the uncertainties on the wave  
 6351 function it is generally possible to accommodate the observed data.<sup>28</sup>

6352 Finally, certain power corrections were identified as potentially large in [40]. One class,  
 6353 which is only relevant for final states containing pseudoscalars, consists of “chirally en-

<sup>27</sup> Strictly speaking, the convolution of the  $\zeta_J$  factor with  $H^{II}$  might diverge at the endpoint. Correspondingly, to such a convolution in general a non-perturbative soft rescattering phase should be associated. An endpoint divergence indeed appears in the attempt to perturbatively factorize  $\zeta_J$  at first subleading power, see below.

<sup>28</sup> Independently of the convergence issue, a perturbative calculation in the  $k_T$  (or any other) factorization scheme must demonstrate that the result is dominated by modes which are perturbative.

6354 hanced” terms, which are proportional to the ratio  $r_\chi^P = m_P^2/(m_b m_q)$ , where  $P$  is a pion  
6355 or Kaon and  $m_q$  an average of light quark masses; another class of certain annihilation  
6356 topologies with large color factors (first pointed out in [48]) is discussed in Sec. 9.1.3  
6357 below. Power corrections are of phenomenological relevance in  $\alpha_2^{\text{II}}$ , which contains a  
6358 chirally-enhanced power correction involving the large Wilson coefficient  $C_1$ , where the  
6359 convolution of  $H^{\text{II}}$  with the power-suppressed analogue  $\zeta_J^{\text{tw}3}$  of  $\zeta_J$  is divergent. These  
6360 power corrections are therefore not dominated by perturbative gluon exchange. They  
6361 have been modeled in [40] by introducing an IR cutoff  $\mathcal{O}(500 \text{ MeV})$  on the convolutions  
6362 and associating an arbitrary rescattering phase with the soft dynamics.

6363 Quantitatively, combining the phenomenological analysis in [1048] (where values for  
6364 hadronic parameters are specified) with the results of [1043, 1044] gives

$$\begin{aligned}
\alpha_1(\pi\pi) &= 1.015 + [0.025 + 0.012i]_V + [0.024 + 0.026i]_{VV} \\
&\quad - \left[ \frac{r_{\text{sp}}}{0.485} \right] \left\{ [0.020]_{\text{LO}} + [0.034 + 0.029i]_{HV} + [0.012]_{\text{tw}3} \right\} \\
&= 0.999_{-0.072}^{+0.034} + (0.009_{-0.051}^{+0.024})i,
\end{aligned} \tag{399}$$

$$\begin{aligned}
\alpha_2(\pi\pi) &= 0.184 - [0.153 + 0.077i]_V - [0.030 + 0.042i]_{VV} \\
&\quad + \left[ \frac{r_{\text{sp}}}{0.485} \right] \left\{ [0.122]_{\text{LO}} + [0.050 + 0.053i]_{HV} + [0.071]_{\text{tw}3} \right\} \\
&= 0.245_{-0.135}^{+0.228} + (-0.066_{-0.081}^{+0.115})i.
\end{aligned} \tag{400}$$

6365 In each amplitude, the terms on the first and second lines correspond to the type-I and  
6366 type-II contributions. These are further split into terms  $\mathcal{O}(1)$ ,  $\mathcal{O}(\alpha_s)$  (V, LO), and  $\mathcal{O}(\alpha_s^2)$   
6367 (VV, HV), and an estimate of a chirally enhanced power correction following a model  
6368 defined in [40] (“tw3”). The relative normalization factor of the spectator-scattering  
6369 contributions,  $r_{\text{sp}} = (9f_\pi f_B)/(m_b f_+^{B\pi}(0)\lambda_B)$ , contains the bulk of the parametric uncer-  
6370 tainty of that term. We observe that the color-allowed tree is perturbatively stable and  
6371 has small uncertainties resulting from the poor knowledge of hadronic input parameters.  
6372 Moreover, the spectator-scattering contribution is small, including a weak dependence  
6373 on endpoint-divergent power corrections (labeled “tw3”).

6374 Conversely, the color-suppressed tree amplitude is dominated by the type-II contri-  
6375 bution, and it exhibits large sensitivity to a chirally enhanced, non-factorizable power  
6376 correction. It is important to keep in mind that the estimate for the latter, unlike all  
6377 other pieces, is based on a model. Several phenomenological analyses of the  $B \rightarrow \pi\pi$   
6378 data favor large values  $\alpha_2(\pi\pi) = \mathcal{O}(1)$ , which is sometimes called a puzzle. In the Stan-  
6379 dard Model, a large value can come from a large  $r_{\text{sp}}$ , for instance through the moment  
6380  $\lambda_B^{-1} \equiv \int d\omega \phi_{B^+}(\omega)/\omega$  of the relevant  $B$ -meson wave function. Information on  $\lambda_B$  can  
6381 be obtained by operator product expansions in HQET [1049, 1050] and from QCD sum  
6382 rules [1051, 1052], but with considerable uncertainties. An interesting possibility is to de-  
6383 termine  $\lambda_B$  more directly from radiative semileptonic decay, discussed in Sec. 9.1.5 below.  
6384 Second, is not inconceivable that a large value originates from the presently incalculable  
6385 twist-three spectator scattering. Such an interpretation would be consistent with the fact  
6386 that data suggest a small value of  $\alpha_2(\rho\rho)$ , which is not sensitive to chiral enhancement.

6387 In the treatment advocated in [51],  $\zeta_J$  is not factorized. The generic prediction is  
6388  $\arg \alpha_2/\alpha_1 = \mathcal{O}(\alpha_s)$  (this is set to zero in the analysis). A prediction on the magnitude  
6389 requires knowledge on  $\zeta$  and  $\zeta_J$  from outside sources, in analogy with the results described

6390 above. For more details, see [51, 53, 1053].

In the pQCD approach, the issue of a large  $\alpha_2/\alpha_1$  (possibly with a large phase) has been addressed in [1054] and again in [1055]. The latter paper augments the structure in the original approach by an extra soft rescattering factor which represents an additional non-perturbative parameter that has to be adjusted to experimental data. We note that the computation in [1054] uses the hard (type-I) vertex from [38–40] as a building block to estimate NLO effects in the pQCD approach. Taking, for the sake of the argument, the asymptotic form of the distribution amplitude  $\phi_{M_2}$ , the contribution is proportional to

$$C_2(\mu) + \frac{C_1(\mu)}{N_c} \left[ 1 + \frac{\alpha_s(\mu) C_F}{4\pi} \left( -\frac{37}{2} - 3i\pi + 12 \ln \frac{m_b}{\mu} \right) \right], \quad (401)$$

6391 where  $C_1(\mu)$  is the large current-current Wilson coefficient. In order to obtain both a  
 6392 large magnitude and phase, one would need to evaluate this expression at a low scale  
 6393  $\mu \ll m_b$ , where perturbation theory is questionable.<sup>29</sup> In the pQCD approach the above  
 6394 expression appears inside a convolution integral, where the scale  $\mu$  is fixed by the internal  
 6395 kinematics of the spectator scattering. The enhancement and the large phase of the color-  
 6396 suppressed tree amplitude found in [1054] therefore has to be associated to a rather low  
 6397 effective renormalization scale (see also the discussion in [1056]). Correspondingly, scale  
 6398 variations or alternative scale-setting procedures in the pQCD approach represent an  
 6399 additional source of potentially large theoretical uncertainties associated to this kind of  
 6400 NLO effects.

6401 Finally, the (physical) tree amplitudes receive contributions from penguin and anni-  
 6402 hilation contractions as discussed above. The factorization properties of the former are  
 6403 very similar to those of the penguin amplitudes discussed in the following section and  
 6404 give rise to corrections that are subleading with respect to  $\alpha_1, \alpha_2$ . For the annihilation  
 6405 amplitudes  $b_1$  and  $b_2$  there is no factorization in the collinear expansion. Both the model  
 6406 of [40] and the  $k_T$  factorization of [48] result in small numerical values.<sup>30</sup>

### 6407 9.1.3. Penguin amplitudes: results

The penguin contraction  $\alpha_4^c(M_1 M_2)$  entering the physical penguin amplitude  $P_{M_1 M_2}$  decomposes in the heavy-quark expansion as

$$\alpha_4^c = a_4^c + r_\chi a_6 + \text{higher powers and terms not chirally enhanced.} \quad (402)$$

Factorization of  $a_4^c$  (as defined here) to leading power has been argued (to one loop) and the hard kernels computed in [38–40] but has been the subject of some controversy over the existence of an extra leading-power long-distance nonrelativistic “charming-penguin” contribution [51, 1058, 1059]. Such an incalculable extra term would, in practice, imply that no prediction for penguin amplitudes can be made. It appears that this theoretical issue has recently been resolved [1060] (in favor of calculability in the sense of [38–40]).

<sup>29</sup> More precisely, the apparent  $\mu$ -dependence is formally a NNLO effect.

<sup>30</sup> In [1035] it has been noted that  $b_2$  is leading in the  $1/N_c$  counting. On the other hand, the diagrams that are leading in the  $1/N_c$  counting combine to the product of a decay constant and the matrix element of the divergence of a current that is conserved in the limit  $m_{s,d,u} \rightarrow 0$ . A hard-scattering approach then implies  $b_2^{N=\infty} = \mathcal{O}(m_{s,d,u}/m_b)$ . This suppression is also found in the QCD light-cone sum rules treatment in [1057]. Nevertheless we do not know a rigorous argument why this amplitude could not be as large as  $\mathcal{O}(m_s/\Lambda)$  in  $B \rightarrow \pi K$  decays.

Again, there are two contributions, labeled I and II as in the case of the trees. The computation of the spectator scattering term  $a_4^{\text{II}}$  has been performed to  $\mathcal{O}(\alpha_s^2)$  [1048, 1053]. The “scalar-penguin” term  $r_\chi a_6^c$  is again a chirally enhanced power correction, which however is calculable. At  $\mathcal{O}(\alpha_s)$  [38–40] it dominates over  $a_4^c$  when  $M_2$  is a pseudoscalar (otherwise it is negligible). Finally, the physical penguin amplitudes contain a penguin annihilation term with a large color factor that is not chirally enhanced. Twist-three spectator scattering is unlikely to be very important, as the type-I contributions are significant (similarly to the color-allowed tree). Because the perturbative results for the penguin amplitudes, in comparison to the tree amplitudes, are rather incomplete at this time (only one piece at  $\mathcal{O}(\alpha_s^2)$  has been computed, as discussed above), we refrain from giving numerical results; for an exhaustive compendium of  $\mathcal{O}(\alpha_s)$  results we refer to [1038]. Rather, we recall the following “anatomy”. As just mentioned, physical penguin amplitudes are approximately described in terms of a leading-power piece, a chirally enhanced power correction, and an annihilation term:

$$P_{M_1 M_2} \propto a_4^c(M_1 M_2) \pm r_\chi^{M_2} a_6^c(M_1 M_2) + \frac{B_{M_1 M_2}}{A_{M_1 M_2}} b_3^c(M_1 M_2). \quad (403)$$

6408 The sign in front of  $a_6$  provides for constructive interference in the case of a  $PP$  final state  
 6409 and destructive one for a  $VP$  final state; moreover the enhancement factor  $r_\chi$  is absent  
 6410 (or small) for  $PV$  final states. This results in a particular pattern for the magnitudes  
 6411 and phases of penguin amplitudes (and  $P/T$  ratios) that can be compared to data in  
 6412  $\Delta B = \Delta S = 1$  decays [1038, 1048], with a reasonable agreement within uncertainties.  
 6413 The comparison also indicates the presence of substantial annihilation contributions (as  
 6414 included in the ‘S4’ scenario favored in [1038]). For instance, a complex annihilation term  
 6415 is essential to account for the observed sign of CP asymmetries in  $B^0 \rightarrow K^+ \pi^-$  and  $B^0 \rightarrow$   
 6416  $\pi^+ \pi^-$ . (A caveat to this is that the  $\mathcal{O}(\alpha_s^2)$  contribution to  $a_6$  is currently not known; as it  
 6417 involves the large coefficient  $C_1$  it might make a non-negligible contribution to the phase  
 6418 of  $P/T$ .) As with the endpoint divergent twist-three spectator scattering (and with the  
 6419 same caveats) the annihilation term is rendered finite in pQCD ( $k_T$  factorization) and  
 6420 one can obtain the “correct” sign of the penguin amplitudes through the annihilation  
 6421 amplitude. A treatment based on the approach of [51], but extended by an  $a_6$  term and  
 6422 a real annihilation amplitude, can be found in [1053]. The phenomenologically required  
 6423 phase is assigned there to a nonperturbative charming-penguin parameter.

#### 6424 9.1.4. Application to angle measurements

As explained in Sec. 9.1.1, various time-dependent CP asymmetries measure CKM angles via their  $S$ -parameter in the limit of vanishing  $T$  or  $P$ . The predictions obtained from the heavy-quark expansion can be directly applied to correct for non-vanishing subleading amplitudes. For the case of the angle  $\beta$  in  $b \rightarrow s$  penguin transition, where

$$\Delta S_f = -\eta_{\text{CP}}(f) S_f - \sin(2\beta) \approx 2 \cos(2\beta) \sin \gamma \text{Re} \frac{T_f}{P_f}, \quad (404)$$

6425 such analyses have been performed in [53, 1061–1064], following the different treatment of  
 6426 hadronic inputs and (divergent) power corrections outlined above. Results are compared  
 6427 in Tab. 65.

6428 Analogous expressions hold for  $b \rightarrow d$  transitions. This allows a measurement of  
 6429  $S_{\pi^+ \pi^-, \pi^+ \rho^-, \rho^+ \rho^-}$  to be directly turned into one of  $\gamma$ . These determinations are com-

Table 65

Predictions for  $\Delta S$  defined in the text for several penguin-dominated modes. *Note:* For the QCDF results, we quote the result of a scan over input parameters (conservative). For the SCET results, double results correspond to two solutions of a fit of hadronic parameters, and errors are combined in quadrature. Results for  $PP$  final states are from [53], for  $PV$  from [1063]; both papers assume  $SU(3)$  to reduce the number of theory papers but differ over the inclusion of certain chirally enhanced terms.

mode	QCDF/BBNS [1061]	SCET/BPRS [53,1063]	pQCD [1064]	experiment
$\phi K_S$	0.01 ... 0.05	0 / 0	0.01 ... 0.03	$-0.23 \pm 0.18$
$\omega K_S$	0.01 ... 0.21	$-0.25 \dots -0.14 / 0.09 \dots 0.13$	0.08 ... 0.18	$-0.22 \pm 0.24$
$\rho^0 K_S$	$-0.29 \dots 0.02$	$0.11 \dots 0.20 / -0.16 \dots -0.11$	$-0.25 \dots -0.09$	$-0.13 \pm 0.20$
$\eta K_S$	$-1.67 \dots 0.27$	$-0.20 \dots 0.13 / -0.07 \dots 0.21$		
$\eta' K_S$	0.00 ... 0.03	$-0.06 \dots 0.10 / -0.09 \dots 0.11$		$-0.08 \pm 0.07$
$\pi^0 K_S$	0.02 ... 0.15	0.04 ... 0.10		$-0.10 \pm 0.17$

6430 petitive with the average of isospin-triangle “ $\alpha$ ” determinations, and in fact even of  
6431 the global unitarity triangle fit:  $\gamma_{\pi\pi} = (70_{-10}^{+13})^\circ$ ,  $\gamma_{\pi\rho} = (69 \pm 7)^\circ$  [1056], and  $\gamma_{\rho_L\rho_L} =$   
6432  $(73.2_{-7.7}^{+7.6})^\circ$  [1065]. (These involve QCDF calculations of  $P/T$ ; we have not updated ex-  
6433 perimental inputs.) For a combination of heavy-quark expansion and  $SU(3)$  flavor argu-  
6434 ments, see [1066].

### 6435 9.1.5. Prospects

6436 The discovery that predictions for hadronic two-body decay amplitudes can be made in  
6437 perturbation theory in an expansion in  $\Lambda/m_b$  has led to a lot of activity at the conceptual,  
6438 technical, and phenomenological level. At the former, it provides a highly nontrivial  
6439 application of soft-collinear effective theory, while at the latter it bore the promise to  
6440 discuss many more observables separately than is possible based on isospin and flavor-  
6441  $SU(3)$  arguments alone. So far, the available technical results are between the NLO  
6442 and NNLO stage, where they show a good behavior of the perturbation series. The  
6443 NNLO computations should be completed also for the (topological) penguins, including  
6444 chirally enhanced power corrections. This means one-loop corrections to  $a_6^{\text{II}}$  and two-loop  
6445 corrections to  $a_4^{\text{I}}$  and  $a_6^{\text{II}}$ , and analogous electroweak amplitudes. Not before then will it  
6446 be really possible to compare to data (preferably from new-physics-insensitive channels)  
6447 to assess the importance of certain incalculable power corrections, which will then likely  
6448 dominate the uncertainties on all amplitudes. A related issue is the status of required  
6449 nonperturbative inputs – foremost, form factors and moments of the  $B$ -meson wave  
6450 functions. While some progress on the former is expected from improved lattice results,  
6451 the latter has to be obtained in other ways, such as from QCD light-cone sum rules or  
6452 from data itself. Most important are the first inverse moments  $\lambda_B^{-1}$  and  $\lambda_{B_s}^{-1}$ . They are  
6453 intimately related to the size of spectator-scattering terms, hence to the color-suppressed  
6454 tree (and electroweak-penguin) amplitudes. Interestingly, in the case of  $B_d$  mesons this  
6455 parameter can already be constrained from the search for the radiative semileptonic decay  
6456  $B^+ \rightarrow \gamma \ell^+ \nu$  [1067]. Here, a more sophisticated theoretical analysis taking into account  
6457 known higher-order and power corrections in that mode would be interesting.

6458 For the non-factorizable power corrections themselves, significant conceptual progress  
6459 would be necessary before one might gain quantitative control. The fate of soft-collinear  
6460 factorization is a hard problem but is important. Meanwhile, a comparison of data with

6461 refined theory predictions may give us more (or less) confidence in present models of the  
 6462 power corrections.

## 6463 9.2. Measurement of $\beta$

### 6464 9.2.1. Theoretical aspects

Measurements of time-dependent  $CP$  violation in hadronic  $b \rightarrow s$  penguin dominated decay modes provide an interesting method to test the SM. Naively, decays to  $CP$  eigenstate final states  $f$  (with  $CP$  eigenvalues  $\eta_f$ ) which are dominated by  $V_{tb}V_{ts}^*$  amplitudes should have small values of  $\Delta S_f \equiv -\eta_f S_f - S_{J/\psi K_S^0}$  since, in the SM,  $\arg(V_{tb}V_{ts}^*) \approx \arg(V_{cb}V_{cs}^*)$ . Although one expects hadronic corrections in these modes to be only of  $\mathcal{O}(\lambda^2) \approx 5\%$  [1068, 1069], this is difficult to confirm rigorously. In fact in the past few years many theoretical studies [1061, 1062, 1064, 1070, 1071] of the “pollution” from the amplitude proportional to  $V_{ub}V_{us}^*$  to these modes have been undertaken. Recall that the amplitude can be written as

$$A(\bar{B} \rightarrow f) = V_{cb}V_{cs}^* a_f^c + V_{ub}V_{us}^* a_f^u \propto 1 + e^{-i\gamma} d_f, \quad (405)$$

where schematically the hadronic amplitude ratio is given by

$$d_f \sim \left| \frac{V_{ub}V_{us}^*}{V_{cb}V_{cs}^*} \right| \frac{\{P^u, C, \dots\}}{P^c + \dots}. \quad (406)$$

6465 Since for small  $d_f$ , the correction  $\Delta S_f \approx 2 \operatorname{Re}(d_f) \cos(2\beta) \sin \gamma$ , these contributions have  
 6466 to be negligibly small for time-dependent  $CP$  asymmetry measurements in  $b \rightarrow s$  tran-  
 6467 sitions to provide a clean and viable test of the SM, or  $d_f$  has to be under very good  
 6468 theoretical control. The problem is that precise model independent estimates are rather  
 6469 difficult to make. Most theoretical calculations suggest that the two penguin amplitudes  
 6470  $P^c$ ,  $P^u$  are similar resulting in a universal positive contribution 0.03 to  $S_f$ , while the  
 6471 final-state dependence results mainly from the interference of the color-suppressed tree  
 6472 amplitude  $C$  with the dominant penguin amplitude,  $\operatorname{Re}(C/P^c)$ . For more detailed re-  
 6473 views, see Refs. [1072, 1073].

6474 In fact, it is important to note that there are actually (at least) three ways to determine  
 6475  $\sin 2\beta$  in the SM:

- 6476 – First, the gold-plated method via  $B^0 \rightarrow J/\psi K_S^0$ ,
  - 6477 – Via the  $b \rightarrow s$  penguin-dominated decay modes,
  - 6478 – From the “predicted” value of  $\sin 2\beta$ , based on the SM CKM Unitarity Triangle fit.
- 6479 Unlike the previous two, which are directly measured values of  $\sin 2\beta$ , the predicted  
 6480 value is typically obtained by using hadronic matrix elements, primarily from lattice  
 6481 calculations, along with experimental information on  $CP$  violating and  $CP$  conserving  
 6482 parameters  $\epsilon_K$ ,  $\Delta m_s/\Delta m_d$  and  $V_{ub}/V_{cb}$ . In fact, recently it has been shown that the  
 6483 precision in one hadronic matrix element ( $B_K$ ) has improved so that even without  
 6484 using  $V_{ub}/V_{cb}$  a non-trivial constraint can be obtained for the predicted value of  $\sin 2\beta$   
 6485 in the SM [867]. This is important since there is an appreciable disagreement between  
 6486 inclusive and exclusive determinations of  $V_{ub}$  [259].

6487 Differences in the resulting three values of  $\sin 2\beta$  may imply new physics and need to be  
 6488 carefully understood.

6489 In the discussion of experimental results below, we see that ten  $b \rightarrow s$  penguin dom-  
 6490 inated decay modes have been identified so far. Several theoretical studies find that

6491 three of the modes:  $\phi K_S^0$ ,  $\eta' K_S^0$  and  $K_S^0 K_S^0 K_S^0$  are the cleanest with SM predictions of  
6492  $\Delta S_f \lesssim 0.05$ , since either there is no pollution from the color-suppressed tree ampli-  
6493 tude, or the penguin amplitude is large, in which case  $d_f$  is estimated to be only a few  
6494 percent; this also generally means that the uncertainties on these estimates are small.  
6495 On the other hand, theoretical calculations find appreciably larger tree contributions  
6496 (with large uncertainties) in several of the other modes, such as  $\eta K_S^0$ ,  $\rho K_S^0$ ,  $\omega K_S^0$ . It  
6497 therefore no longer seems useful to average the  $CP$  asymmetry over all of the penguin  
6498 modes. Factorization-based calculations suggest that the uncertainty in the case of  $\pi^0 K_S^0$   
6499 is intermediate between the two sets of final states above. However, for  $\pi^0 K_S^0$  additional  
6500 information is available: a general amplitude parametrization of the entire set of  $\pi K$  final  
6501 states together with  $SU(3)$  flavor symmetry allows to constrain  $S_{\pi^0 K_S^0}$  by other  $\pi K$  and  
6502  $\pi\pi$  observables [1074–1076]. At present this method yields  $S_{\pi^0 K_S^0} \simeq 0.8$ –1, if one allows  
6503 for an anomalously large color-suppressed tree amplitude that is suggested by the current  
6504  $\pi K$  branching fractions and direct  $CP$  asymmetries. Hence improved measurements of  
6505 the direct and time-dependent asymmetries may still provide useful tests of the SM.

6506 Finally, we note that the current experimental errors of 0.07 ( $\eta' K_S^0$ ) and 0.17 ( $\phi K_S^0$   
6507 and  $K_S^0 K_S^0 K_S^0$ ), as shown in Fig. 79, are statistics dominated and are also still large  
6508 compared to the expected theory uncertainties. At a Super Flavor Factory ( $\approx 50$ –75  $\text{ab}^{-1}$   
6509 of data) the experimental errors will get significantly reduced down to around 0.01–  
6510 0.03 [167, 1072, 1077–1079]. Looking to the future, another interesting channel is  $B_s \rightarrow$   
6511  $\phi\phi$  [1068, 1080], where the naïve Standard Model expectation for  $S_f$  is zero, and which will  
6512 be measured by LHCb. As mentioned above, in the SM it is theoretically quite difficult  
6513 to explain  $\Delta S_f$  larger than 0.05 in these modes. Therefore if improved experimental  
6514 measurements show  $\Delta S \gtrsim 0.1$  then that would be an unambiguous sign of a  $CP$ -odd  
6515 phase beyond the SM-CKM paradigm.

### 6516 9.2.2. Experimental results

#### 6517 $B^0 \rightarrow \eta' K^0$ and $B^0 \rightarrow \omega K_S^0$

6518 Both the BaBar and Belle experiments reconstruct seven decay channels of  $B^0 \rightarrow \eta' K^0$ ,  
6519  $B^0 \rightarrow \eta'(\rho\gamma, \eta_{\gamma\gamma}\pi^+\pi^-, \eta_{3\pi}\pi^+\pi^-)K_S^0(\pi^+\pi^-)$ ,  
6520  $B^0 \rightarrow \eta'(\rho\gamma, \eta_{\gamma\gamma}\pi^+\pi^-)K_S^0(\pi^0\pi^0)$  and  
6521  $B^0 \rightarrow \eta'(\eta_{\gamma\gamma}\pi^+\pi^-, \eta_{3\pi}\pi^+\pi^-)K_L^0$ .

6522 BaBar identifies the decays with a  $K_S^0$  using  $m_{\text{ES}}$ ,  $\Delta E$  and a Fisher discriminant which  
6523 separates continuum from  $B\bar{B}$  events [247]. Similarly, Belle uses  $M_{\text{bc}}$ ,  $\Delta E$  and a likelihood  
6524 ratio,  $\mathcal{R}_{S/B}$ , which performs the same task of  $q\bar{q}$  discrimination [947]. For  $K_L^0$  modes,  
6525 only the  $K_L^0$  direction is measured, so either  $m_{\text{ES}}$  or  $\Delta E$  is calculated. BaBar uses  $\Delta E$   
6526 while Belle chooses  $M_{\text{bc}}$ . Fig. 76 shows  $\Delta t$  and asymmetry projections for  $B^0 \rightarrow \eta' K^0$ .

6527 For  $B^0 \rightarrow \omega K_S^0$ , the only useful decay channel is,  $B^0 \rightarrow \omega(\pi^+\pi^-\pi^0)K_S^0(\pi^+\pi^-)$ . BaBar  
6528 uses  $m_{\text{ES}}$ ,  $\Delta E$ , a Fisher discriminant, the  $\omega$  mass and its helicity to discriminate between  
6529 signal and background [247] while Belle uses  $M_{\text{bc}}$ ,  $\Delta E$ ,  $\mathcal{R}_{S/B}$  and the  $\omega$  mass [1081]. The  
6530 fit results are summarized in Tab. 66 and Fig. 79.

6531 In these modes there is no evidence for direct  $CP$  violation while mixing-induced  
6532  $CP$  violation is consistent with charmonium. The significance of the mixing-induced  $CP$   
6533 violation effect in  $B^0 \rightarrow \eta' K^0$  is greater than  $5\sigma$  in both BaBar and Belle analyses.

#### 6534 $B^0 \rightarrow K^0\pi^0$ , $B^0 \rightarrow K_S^0 K_S^0 K_S^0$ and $B^0 \rightarrow K_S^0\pi^0\pi^0$



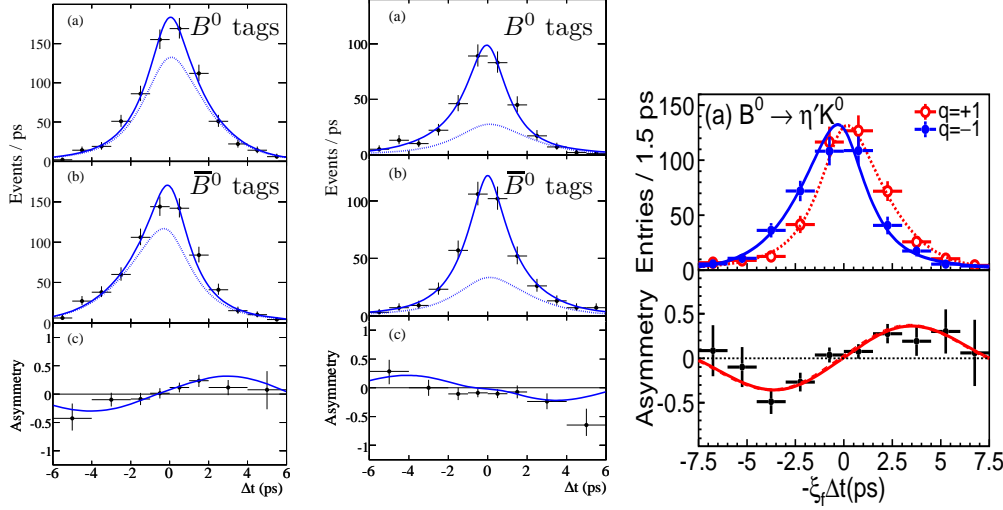


Fig. 76. Signal enhanced  $\Delta t$  projections and asymmetry plots for  $B^0 \rightarrow \eta' K^0$ . The left (middle) plot shows BaBar's fit results for  $B^0 \rightarrow \eta' K_S^0$  ( $B^0 \rightarrow \eta' K_L^0$ ) and the right plot shows Belle's combined fit result.

Table 66

Summary of  $B^0 \rightarrow \eta' K^0$  and  $B^0 \rightarrow \omega K_S^0$ .

	BaBar	Belle
$B^0 \rightarrow \eta' K^0$		
Yield ( $N(B\bar{B}) \times 10^6$ )	$2515 \pm 69$ (467)	$1875 \pm 60$ (535)
$B^0 \rightarrow \omega K^0$		
Yield ( $N(B\bar{B}) \times 10^6$ )	$163 \pm 18$ (467)	$118 \pm 18$ (535)

6535 These modes are distinguished by the lack of a primary track coming from the recon-  
6536 structed  $B$  vertex. In such cases, the  $B$  vertex is determined by extrapolating the  $K_S^0$   
6537 pseudo-track back to the interaction point. However, due to the relatively long lifetime  
6538 of the  $K_S^0$  meson, the vertex reconstruction efficiency is less than 100% as the charged  
6539 pion daughters may not be able to register hits in the innermost sub-detector.

6540 For  $B^0 \rightarrow K^0 \pi^0$ , BaBar describes signal events with the reconstructed  $B$  mass and  
6541 the mass of the tag-side  $B$  calculated from the known beam energy and reconstructed  
6542  $B$  momentum constrained with the nominal  $B$  mass. In addition, the cosine of the polar  
6543 angle of the  $B$  candidate in the  $\Upsilon(4S)$  frame and ratio of angular moments,  $L_2/L_0$ , which  
6544 discriminate against continuum are also used [247]. Belle uses  $M_{bc}$ ,  $\Delta E$ , and  $\mathcal{R}_{S/B}$  to  
6545 describe signal events and additionally considers the  $B^0 \rightarrow K_L^0 \pi^0$  channel for which  $\Delta E$   
6546 cannot be calculated [1082]. Fig. 77 shows  $\Delta t$  and asymmetry projections for  $B^0 \rightarrow K^0 \pi^0$ .

6547 For  $B^0 \rightarrow K_S^0 K_S^0 K_S^0$  and  $B^0 \rightarrow K_S^0 \pi^0 \pi^0$  [1083], BaBar uses  $m_{ES}$ ,  $\Delta E$  and a neural  
6548 network (NN) which distinguishes  $B\bar{B}$  from  $q\bar{q}$  events to describe signal [1084, 1085]  
6549 and similarly, Belle uses  $M_{bc}$ ,  $\Delta E$  and  $\mathcal{R}_{S/B}$  [947, 1086]. For  $B^0 \rightarrow K_S^0 K_S^0 K_S^0$ , both  
6550 experiments include the case where one  $K_S^0$  decays to a neutral pion pair. The fit results  
6551 are summarized in Tab. 67 and Fig. 79.

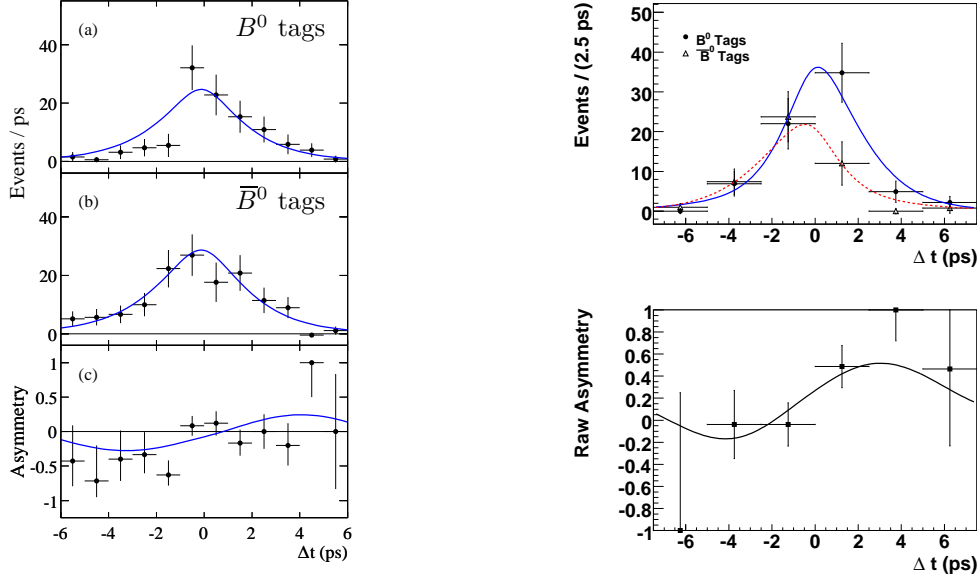


Fig. 77. Signal enhanced and background subtracted  $\Delta t$  projections and asymmetry plots for  $B^0 \rightarrow K^0 \pi^0$ . The left plot shows BaBar's fit result and the right plot shows Belle fit result.

Table 67

Summary of  $B^0 \rightarrow K^0 \pi^0$ ,  $B^0 \rightarrow K_S^0 K_S^0 K_S^0$  and  $B^0 \rightarrow K_S^0 \pi^0 \pi^0$ .

	BaBar	Belle
$B^0 \rightarrow K^0 \pi^0$		
Yield ( $N(B\bar{B}) \times 10^6$ )	$556 \pm 32$ (467)	$657 \pm 37$ (657)
$B^0 \rightarrow K_S^0 K_S^0 K_S^0$		
Yield ( $N(B\bar{B}) \times 10^6$ )	$274 \pm 20$ (467)	$185 \pm 17$ (535)
$B^0 \rightarrow K_S^0 \pi^0 \pi^0$		
Yield ( $N(B\bar{B}) \times 10^6$ )	$117 \pm 27$ (227)	$307 \pm 32$ (657)

6552 In these modes the direct  $CP$  components are all consistent with Standard Model  
6553 expectations and the mixing-induced parameters are consistent with charmonium with  
6554 current statistics. The largest discrepancy, which is not statistically significant, is in the  
6555 mixing-induced  $CP$  violation parameter in  $B^0 \rightarrow K_S^0 \pi^0 \pi^0$ , which appears to have the  
6556 wrong sign.

6557  $B^0 \rightarrow K_S^0 \pi^+ \pi^-$  and  $B^0 \rightarrow K_S^0 K^+ K^-$

6558 To extract  $CP$  violation parameters of modes such as  $B^0 \rightarrow K_S^0 \rho^0$  ( $\rho^0 \rightarrow \pi^+ \pi^-$ )  
6559 or  $B^0 \rightarrow K_S^0 \phi$  ( $\phi \rightarrow K^+ K^-$ ), it is necessary to perform a time-dependent Dalitz plot  
6560 analysis as interfering resonances in the three-body final states make the results of quasi-  
6561 two-body analyses difficult to interpret. As the relative amplitudes and phases of each  
6562 decay channel in the Dalitz plot are determined in such an analysis, the angle  $\beta^{\text{eff}}$  can  
6563 be directly obtained, rather than measuring  $\mathcal{S}_{CP}^{\text{eff}}$ .

6564 For  $B^0 \rightarrow K_S^0 \pi^+ \pi^-$ , the signal model contains the  $K^{*+}(892)$ ,  $K_0^{*+}(1430)$ ,  $\rho^0(770)$ ,  
6565  $f_0(980)$ ,  $f_2(1270)$ ,  $f_X(1300)$  states and a nonresonant component. BaBar describes signal  
6566 events with  $m_{ES}$ ,  $\Delta E$  and the output of a neutral network [1087] while Belle just uses  
6567  $\Delta E$  [1088]. Belle finds two solutions given in Tab. 68 with consistent  $CP$  parameters but  
6568 different  $K_0^{*+}(1430)\pi^-$  relative fractions due to the interference between  $K_0^{*+}(1430)$  and  
6569 the non-resonant component. The high  $K^{*+}\pi^-$  fraction of Solution 1 is in agreement  
6570 with some phenomenological estimates [1089] and may also be qualitatively favored by  
6571 the total  $K-\pi$  S-wave phase shift as a function of  $m(K\pi)$  when compared with that  
6572 measured by the LASS collaboration [1018]. The fit results for both experiments are  
6573 summarized in Tab. 70 and Fig. 78, which includes the preferred solution from Belle.

Table 68

Multiple solutions in  $B^0 \rightarrow K_S^0 \pi^+ \pi^-$  at Belle where the first error is statistical, the second systematic and the third is the model uncertainty.

	Sol. 1	Sol. 2
$\beta^{\text{eff}}(\rho^0(770)K_S^0)$	$(20.0^{+8.6}_{-8.5} \pm 3.2 \pm 3.5)^\circ$	$(22.8 \pm 7.5 \pm 3.3 \pm 3.5)^\circ$
$\beta^{\text{eff}}(f_0(980)K_S^0)$	$(12.7^{+6.9}_{-6.5} \pm 2.8 \pm 3.3)^\circ$	$(14.8^{+7.3}_{-6.7} \pm 2.7 \pm 3.3)^\circ$

6574 The decay  $B^0 \rightarrow K_S^0 K^+ K^-$  is also studied with a time-dependent Dalitz plot analysis.  
6575 The signal model contains the  $f_0(980)$ ,  $\phi(1020)$ ,  $f_X(1500)$  and  $\chi_{c0}$  states and a nonresonant  
6576 component. The BaBar collaboration additionally uses the  $K_S^0$  decay channel to  
6577 neutral pions and describes signal events with  $m_{ES}$  and  $\Delta E$  [1090]. Similarly, Belle uses  
6578  $M_{bc}$  and  $\Delta E$  [1091].

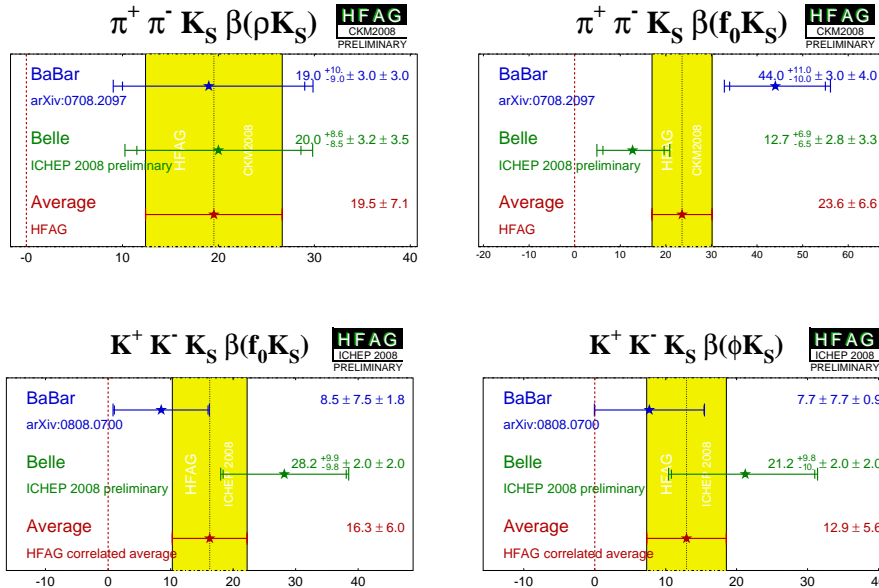


Fig. 78.  $CP$  parameters of  $B^0 \rightarrow K_S^0 \pi^+ \pi^-$  and  $B^0 \rightarrow K_S^0 K^+ K^-$ .

6579 Belle finds four solutions as shown in Tab. 69 due to the interference between  $f_0(980)$ ,  
6580  $f_X(1500)$  and the non-resonant component. Using external information from  $B^0 \rightarrow$   
6581  $K_S^0 \pi^+ \pi^-$ , if the  $f_X(1500)$  is the  $f_0(1500)$  for both  $B^0 \rightarrow K_S^0 \pi^+ \pi^-$  and  $B^0 \rightarrow K_S^0 K^+ K^-$ ,  
6582 the ratio of branching fractions,  $\mathcal{B}(f_0(1500) \rightarrow \pi^+ \pi^-) / \mathcal{B}(f_0(1500) \rightarrow K^+ K^-)$ , prefers  
6583 the solution with the low  $f_X(1500) K_S^0$  fraction. Similarly other measurements of the rela-  
6584 tive magnitudes of the  $f_0(980) \rightarrow \pi^+ \pi^-$  and  $f_0(980) \rightarrow K^+ K^-$  widths prefer the solution  
6585 with the low  $f_0(980) K_S^0$  fraction. The fit results for both experiments are summarized  
6586 in Tab. 70 and Fig. 78, which includes the preferred solution from Belle, while Fig. 79  
6587 gives a summary of these results together with those from other charmless hadronic  $B$   
6588 decays. In the time-dependent  $CP$  violation analyses, there is no evidence for direct  $CP$   
violation and  $\beta^{\text{eff}}$  is consistent with charmonium.

Table 69

Multiple solutions in  $B^0 \rightarrow K_S^0 K^+ K^-$  at Belle where the error is statistical only.

	Sol. 1	Sol. 2	Sol. 3	Sol. 4
$\beta^{\text{eff}}(f_0(980)K_S^0)$	$(28.2^{+9.8}_{-9.9})^\circ$	$(64.1^{+7.6}_{-8.0})^\circ$	$(61.5^{+6.5}_{-6.5})^\circ$	$(36.9^{+10.9}_{-9.6})^\circ$
$\beta^{\text{eff}}(\phi(1020)K_S^0)$	$(21.2^{+9.8}_{-10.4})^\circ$	$(62.1^{+8.3}_{-8.8})^\circ$	$(65.1^{+8.7}_{-8.7})^\circ$	$(44.9^{+13.2}_{-13.6})^\circ$

6589

Table 70

Summary of  $B^0 \rightarrow K_S^0 \pi^+ \pi^-$  and  $B^0 \rightarrow K_S^0 K^+ K^-$ .

	BaBar	Belle
$B^0 \rightarrow K_S^0 \pi^+ \pi^-$		
Yield ( $N(B\bar{B}) \times 10^6$ )	$2172 \pm 70$ (383)	$1944 \pm 98$ (657)
$B^0 \rightarrow K_S^0 K^+ K^-$		
Yield ( $N(B\bar{B}) \times 10^6$ )	$1428 \pm 47$ (467)	$1269 \pm 51$ (657)

### 6590 9.3. Measurements of $\alpha$

#### 6591 9.3.1. Theoretical aspects

6592 The  $b \rightarrow u$  tree amplitude (Fig. 80(a)) is proportional to  $V_{ub}$  and, in the usual conven-  
6593 tion, carries the weak phase  $\gamma$ . Since  $B^0 \bar{B}^0$  mixing carries the weak phase  $2\beta$ , at the tree  
6594 level the time-dependent  $CP$ -violation measurements in the  $B^0 \rightarrow \pi^+ \pi^-$  and  $B^0 \rightarrow \rho^+ \rho^-$   
6595 decays are sensitive to  $2\beta + 2\gamma = 2\pi - 2\alpha$ .

The decay-time distribution for  $B^0 \rightarrow \pi^+ \pi^-$  is given by

$$\frac{dN}{d\Delta t} = \frac{e^{-|\Delta t|/\tau}}{4\tau} \times \left\{ 1 - q_{\text{tag}} [C_{\pi\pi} \cos(\Delta m_d \Delta t) - S_{\pi\pi} \sin(\Delta m_d \Delta t)] \right\}, \quad (407)$$

6596 where  $\tau$  is the neutral  $B$  lifetime,  $\Delta m_d$  is the  $B^0 - \bar{B}^0$  mixing frequency,  $\Delta t$  is the difference  
6597 in decay times  $t_{\pi\pi} - t_{\text{tag}}$ , and the parameter  $q_{\text{tag}}$  equals  $+1$  ( $-1$ ) when the tag-side  $B$   
6598 decays as a  $B^0$  ( $\bar{B}^0$ ). The parameter  $C_{\pi\pi}$  characterizes direct  $CP$  violation and is also  
6599 referred to in the literature as  $-\mathcal{A}_{\pi\pi}$ . At the tree level, the  $CP$ -violating asymmetries  
6600  $S_{\pi\pi} = \sin 2\alpha$  ( $\alpha \equiv \arg[-V_{td} V_{tb}^* / V_{ud} V_{ub}^*]$ ) and  $C_{\pi\pi} \equiv -\mathcal{A}_{\pi\pi} = 0$ . However, since the  
6601 leading higher-order  $b \rightarrow d$  contribution to the  $B^0 \rightarrow \pi^+ \pi^-$  decay amplitude (Fig. 80(b))  
6602 is sizable and carries the weak phase  $-\beta$ , direct  $CP$  violation  $C_{\pi\pi} \neq 0$  becomes possible

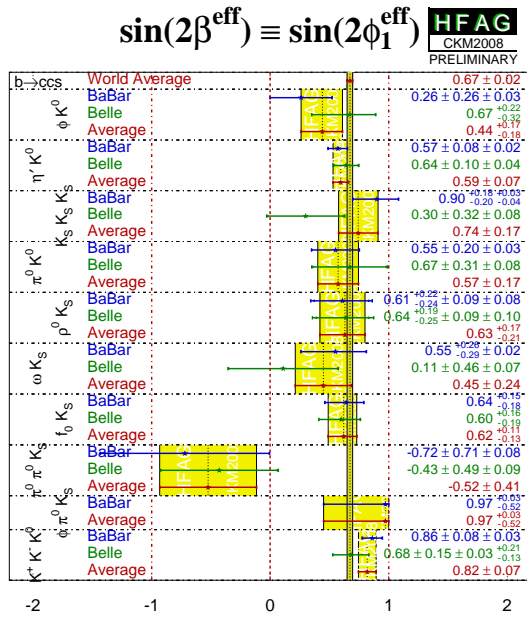
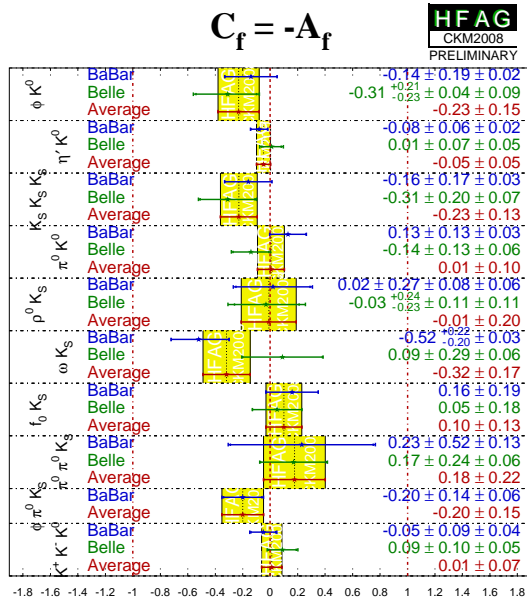


Fig. 79. CP parameters of charmless hadronic B decays.

6603 and  $S_{\pi\pi} = \sin 2\alpha_{\text{eff}} \sqrt{1 - C_{\pi\pi}^2}$ , where, in general, the phase difference  $\alpha - \alpha_{\text{eff}} = \Delta\alpha \equiv \delta \neq$   
 6604 0. Contributions from physics beyond the Standard Model could affect the  $CP$ -violating  
 6605 asymmetries  $S_{\pi\pi}$  and  $C_{\pi\pi}$  primarily through additional penguin amplitudes.

The value of  $\delta$  can be extracted through a model-independent analysis that uses the  $SU(2)$  isospin-related decays  $B^\pm \rightarrow \pi^\pm \pi^0$  and  $B^0 \rightarrow \pi^0 \pi^0$  [37]. Let us denote the  $B^{ij} \rightarrow \pi^i \pi^j$  and  $\bar{B}^{ij} \rightarrow \pi^i \pi^j$  decay amplitudes  $A^{ij}$  and  $\bar{A}^{ij}$ , respectively. Assuming isospin symmetry, these amplitudes are related by the equations

$$A^{+-}/\sqrt{2} + A^{00} = A^{+0}, \quad \bar{A}^{+-}/\sqrt{2} + \bar{A}^{00} = \bar{A}^{-0}, \quad (408)$$

6606 which can be represented graphically in the form of “isospin triangles” (Fig. 80(c)).  
 6607 Neglecting electroweak penguins,  $|A^{+0}| = |\bar{A}^{-0}|$  (evidence of direct  $CP$  violation in  $B^\pm \rightarrow$   
 6608  $\pi^\pm \pi^0$  would show that such contributions cannot be neglected, and would be a signal  
 6609 for new physics contributions). If the (arbitrary) global phase of all  $A^{ij}$  amplitudes is  
 6610 chosen such that  $A^{+0} = \bar{A}^{-0}$ , it can be shown that the phase difference between  $A^{+-}$   
 6611 and  $\bar{A}^{+-}$  is  $2\delta$ . Note that the value of  $\delta$  extracted in this manner carries an eightfold  
 6612 ambiguity. Moreover, the value of  $\alpha$  that is obtained is insensitive to new physics effects,  
 6613 unless they violate isospin. In the  $B \rightarrow \pi\pi$  system (as in the  $B \rightarrow \rho\rho$  case, discussed  
 6614 below), knowledge of  $A^{00}$  and  $\bar{A}^{00}$  is the limiting factor in the extraction of  $\delta$ .

6615 For  $B \rightarrow \rho\rho$  decays, the same formalism applies separately to each helicity amplitude  
 6616 (where  $CP = +1$  ( $L = 0, 2$ ) and  $CP = -1$  ( $L = 1$ )). Thus, the extraction of  $\alpha$  requires  
 6617 knowledge of the polarization. In practise, the fraction of longitudinal polarization ( $f_L$ )  
 6618 is measured by fitting the  $\rho$  helicity angle distribution. The probability density function  
 6619 (PDF) used is

$$\frac{d^2 N}{d \cos \theta_1 d \cos \theta_2} = 4f_L \cos^2 \theta_1 \cos^2 \theta_2 + (1 - f_L) \sin^2 \theta_1 \sin^2 \theta_2, \quad (409)$$

6620 where  $\theta_1$  ( $\theta_2$ ) is the angle between the daughter  $\pi^0$  and direction opposite the  $\rho^-$  ( $\rho^+$ )  
 6621 direction in the  $\rho^+$  ( $\rho^-$ ) rest frame (see Fig. 81).  $B^0 \rightarrow \rho^+ \rho^-$  is found to be almost  
 6622 purely  $f_L = 1$ , which implies that the  $CP$ -odd  $L=1$  component is negligible. This high  
 6623 polarization is fortunate, as it gives a larger  $CP$  asymmetry and thus greater sensitivity  
 6624 to  $\alpha$ . (Conversely, the possibility to resolve some of the ambiguities in the solution for  $\alpha$   
 6625 from the interference between different helicity amplitudes is precluded.) Moreover, the  
 6626 contributions from penguin amplitudes (Fig. 80b) are found to be small for  $B \rightarrow \rho\rho$ ,  
 6627 allowing a determination of  $\alpha$  with small theoretical uncertainty.

6628 A second complication in  $B \rightarrow \rho\rho$  decays is that the final state  $\rho$  mesons have non-zero  
 6629 decay width, and thus their masses are not necessarily equal. As a consequence, Bose-  
 6630 Einstein symmetry no longer holds, and the  $I=1$  isospin state is allowed [1092]. In this  
 6631 case the isospin relations needed to extract  $\alpha$  (Fig. 80c) do not hold. The problem can  
 6632 be studied by restricting the  $\pi\pi$  invariant mass window used to select  $\rho \rightarrow \pi\pi$  candidates

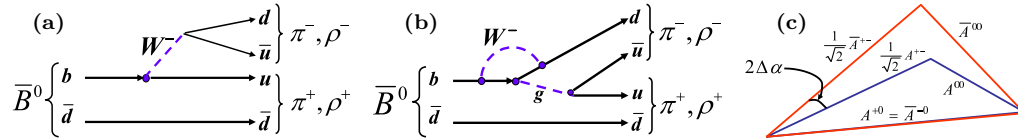


Fig. 80. (a) Tree and (b) gluonic-penguin contributions to  $B^0 \rightarrow (\pi/\rho)^+(\pi/\rho)^-$ . (c) London–Gronau isospin triangles for  $B \rightarrow \pi\pi$ ,  $B \rightarrow \rho\rho$  [37].

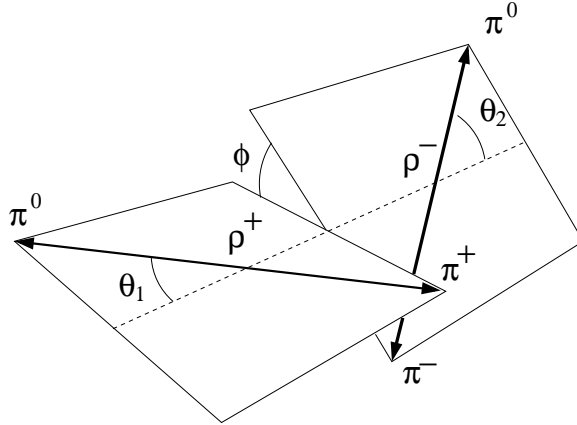


Fig. 81. Definition of helicity angles  $\theta_1$  and  $\theta_2$  used to fit for  $f_L$ , the fraction of longitudinal polarization.

6633 to a narrow range and checking whether the fitted value of  $\sin 2\alpha$  shifts. No such shift  
 6634 has been observed, and hence possible isospin violation is below the sensitivity of current  
 6635 measurements.

6636 The decays  $B^0 \rightarrow \rho^+\pi^-$ ,  $B^0 \rightarrow \rho^-\pi^+$ , and  $B^0 \rightarrow \rho^0\pi^0$  (collectively referred to as  
 6637  $B^0 \rightarrow \rho\pi$ ) are also mediated by the  $b \rightarrow u\bar{u}d$  transition, and thus the interference between  
 6638  $B^0 \rightarrow \rho\pi$  and  $\bar{B}^0 \rightarrow \rho\pi$  is also sensitive to  $\alpha$ . However, these modes have an advantage  
 6639 over  $B \rightarrow \pi\pi$  and  $B \rightarrow \rho\rho$  decays, as pointed out in Ref. [1093]: the three-body  $\pi^+\pi^-\pi^0$   
 6640 final state yields a Dalitz plot that can be analyzed to measure all three  $B^0 \rightarrow (\rho\pi)^0$   
 6641 modes simultaneously. The decay-time distributions of these three states allows one to  
 6642 resolve the penguin contribution and determine  $\alpha$  with very little theoretical uncertainty  
 6643 and only a single unresolvable ambiguity ( $\alpha \rightarrow \alpha + \pi$ ). In addition, one can use the  
 6644 branching fractions for the charged modes  $B^+ \rightarrow \rho^+\pi^0$  and  $B^+ \rightarrow \rho^0\pi^+$  along with  
 6645 isospin relations to improve the determination of  $\alpha$  [1094,1095].

6646 The Dalitz plot has a time dependence

$$\begin{aligned}
 |A(t, s_+, s_-)|^2 \propto e^{-\Gamma|t|} & \left\{ (|A_{3\pi}|^2 + |\bar{A}_{3\pi}|^2) - \right. \\
 & q_{\text{tag}} \cdot (|A_{3\pi}|^2 - |\bar{A}_{3\pi}|^2) \cos(\Delta m \Delta t) + \\
 & \left. q_{\text{tag}} \cdot 2 \cdot \text{Im} \left( \frac{q}{p} A_{3\pi}^* \bar{A}_{3\pi} \right) \sin(\Delta m \Delta t) \right\}, \quad (410)
 \end{aligned}$$

6647 where  $A_{3\pi} = \mathcal{A}(B^0 \rightarrow \pi\pi\pi)$ ,  $\bar{A}_{3\pi} = \mathcal{A}(\bar{B}^0 \rightarrow \pi\pi\pi)$ ,  $s_+ = (p_+ + p_0)^2$ ,  $s_- = (p_- + p_0)^2$ , and  
 6648  $p_+$ ,  $p_-$ , and  $p_0$  are the four-momenta of the  $\pi^+$ ,  $\pi^-$ , and  $\pi^0$ , respectively. The parameter  
 6649  $q_{\text{tag}}$  equals  $+1$  ( $-1$ ) when the tag-side  $B$  decays as a  $B^0$  ( $\bar{B}^0$ ), and  $q/p$  is the ratio of  
 6650 complex coefficients relating the  $B^0$  and  $\bar{B}^0$  flavor eigenstates to the mass eigenstates.

6651 The amplitudes  $A_{3\pi}$  and  $\bar{A}_{3\pi}$  are further decomposed into

$$A_{3\pi}(s_+, s_-) = f_+(s_+, s_-) A_+ + f_-(s_+, s_-) A_- + f_0(s_+, s_-) A_0 \quad (411)$$

$$\left(\frac{q}{p}\right) \bar{A}_{3\pi}(s_+, s_-) = \bar{f}_+(s_+, s_-) \bar{A}_+ + \bar{f}_-(s_+, s_-) \bar{A}_- + \bar{f}_0(s_+, s_-) \bar{A}_0, \quad (412)$$

6652 where the subscript “+” represents  $\rho^+\pi^-$ , “-” is for  $\rho^-\pi^+$ , and “0” is for  $\rho^0\pi^0$ . The  
 6653 kinematic functions  $f_i$  and  $\bar{f}_i$  are the products of Breit-Wigner functions to describe the  
 6654  $\pi\pi$  lineshape and an angular function to describe the helicity distribution. The goal of  
 6655 the analysis is to fit the time-dependence of the Dalitz plot to determine the six complex  
 6656 amplitudes  $A_i$  and  $\bar{A}_i$ ; from these one determines  $\alpha$  via the relationship

$$e^{i2\alpha} = \frac{\bar{A}_+ + \bar{A}_- + 2\bar{A}_0}{A_+ + A_- + 2A_0}. \quad (413)$$

6657 Note that the description of the  $\pi\pi$  lineshape introduces some systematic error in the  
 6658 Dalitz plot analysis. This can be checked by changing the lineshape in within a reasonable  
 6659 range or by using an alternative SU(3)-based method to extract  $\alpha$  that does not use the  
 6660 tails of  $\pi\pi$  lineshapes [1096].

6661 All the above methods use isospin to estimate the penguin pollution. They are thus  
 6662 theoretically limited by isospin breaking. While hard to compute these corrections are  
 6663 expected to be at the degree level, with the smallest impact expected in the  $B \rightarrow \rho\pi$   
 6664 extraction [1097–1099].

### 6665 9.3.2. Experimental measurements

#### 6666 $B \rightarrow \pi\pi$

6667 High-quality separation of charged Kaons and pions is a distinctive experimental chal-  
 6668 lenge in the  $B^0 \rightarrow \pi^+\pi^-$  and  $B^\pm \rightarrow \pi^\pm\pi^0$  analyses. Indeed,  $\mathcal{B}(B^0 \rightarrow K^+\pi^-)/\mathcal{B}(B^0 \rightarrow$   
 6669  $\pi^+\pi^-) \approx 3.8$  and  $\mathcal{B}(B^\pm \rightarrow K^\pm\pi^0)/\mathcal{B}(B^\pm \rightarrow \pi^\pm\pi^0) \approx 2.3$  [558], and the separation be-  
 6670 tween the  $K\pi$  and  $\pi\pi$  candidates in the kinematic quantity  $\Delta E$  at  $e^+e^-$   $B$ -meson facto-  
 6671 ries is only about  $1.5\sigma$ . Both Belle and BABAR employ sophisticated likelihood-based pion-  
 6672 Kaon separation in the branching-fraction and  $CP$ -violation analyses in these modes. In  
 6673 addition to the  $B$  factories, the CDF experiment, thanks to its  $1.4\sigma$   $dE/dx$ -based Kaon-  
 6674 pion separation, aided by the invariant-mass separation of the  $K^\pm\pi^\mp$  and  $\pi^+\pi^-$  candi-  
 6675 dates, is able to provide a competitive measurement of the  $\mathcal{B}(B^0 \rightarrow K^+\pi^-)/\mathcal{B}(B^0 \rightarrow$   
 6676  $\pi^+\pi^-)$  ratio, and thus of the less-well-known  $\mathcal{B}(B^0 \rightarrow \pi^+\pi^-)$ .

6677 The most up-to-date measurements in the  $B \rightarrow \pi\pi$  modes, along with the September  
 6678 2008 HFAG averages, are quoted in Tab. 71. With the exception of  $C_{\pi^0\pi^0}$ , the sensitiv-  
 6679 ities of the BABAR and Belle measurements are very similar. Plots of  $B^0 \rightarrow \pi^+\pi^-$   $\Delta t$

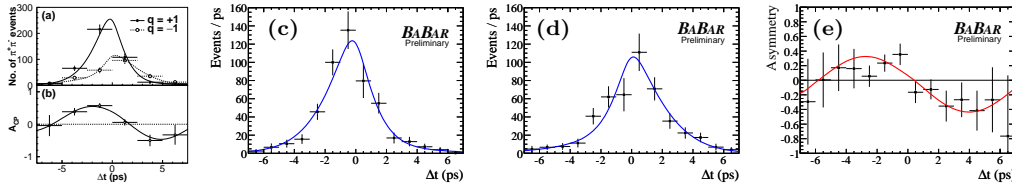


Fig. 82. (a) Distributions of  $\Delta t$  for  $B^0$  ( $q = +1$ ) and  $\bar{B}^0$  ( $q = -1$ ) tags and (b) their  $CP$ -violating asymmetry in  $B^0 \rightarrow \pi^+\pi^-$  signal events reported by Belle [1102]. Distributions of  $\Delta t$  for (c)  $B^0$  and (d)  $\bar{B}^0$  tags and (e) their  $CP$ -violating asymmetry in  $B^0 \rightarrow \pi^+\pi^-$  signal events reported by BABAR [1101].



Table 71

Branching fractions and  $CP$  asymmetries in  $B \rightarrow \pi\pi$ . First error is statistical and second systematic. Please note that Belle quotes  $\mathcal{A} \equiv -C$ . The April 2008 online update of the preliminary CDF result is  $\mathcal{B}(\pi^+\pi^-) = (5.02 \pm 0.33 \pm 0.35) \times 10^{-6}$  [1100]. Values given in parentheses are the numbers of  $B\bar{B}$  pairs in the datasets used in the analyses, where appropriate.

	BABAR	Belle	HFAG avg.
$S_{\pi\pi}$	$-0.68 \pm 0.10 \pm 0.03$ [1101] (467M)	$-0.61 \pm 0.10 \pm 0.04$ [1102] (535M)	$-0.65 \pm 0.07$
$C_{\pi\pi}$	$-0.25 \pm 0.08 \pm 0.02$ [1101] (467M)	$-0.55 \pm 0.08 \pm 0.05$ [1102] (535M)	$-0.38 \pm 0.06$
$\mathcal{B}(\pi^+\pi^-) \times 10^6$	$5.5 \pm 0.4 \pm 0.3$ [1103] (227M)	$5.1 \pm 0.2 \pm 0.2$ [1104] (449M)	$5.16 \pm 0.22$
$\mathcal{B}(\pi^+\pi^0) \times 10^6$	$5.02 \pm 0.46 \pm 0.29$ [1105] (383M)	$6.5 \pm 0.4^{+0.4}_{-0.5}$ [1104] (449M)	$5.59^{+0.41}_{-0.40}$
$\mathcal{A}(\pi^+\pi^0)$	$0.030 \pm 0.039 \pm 0.010$ [1105] (383M)	$0.07 \pm 0.03 \pm 0.01$ [1106] (535M)	$0.050 \pm 0.025$
$\mathcal{B}(\pi^0\pi^0) \times 10^6$	$1.83 \pm 0.21 \pm 0.13$ [1101] (467M)	$1.1 \pm 0.3 \pm 0.1$ [1107] (535M)	$1.55 \pm 0.19$
$C_{\pi^0\pi^0}$	$-0.43 \pm 0.26 \pm 0.05$ [1101] (467M)	$-0.44^{+0.62}_{-0.73} \quad ^{+0.06}_{-0.04}$ [1107] (535M)	$-0.43^{+0.24}_{-0.25}$

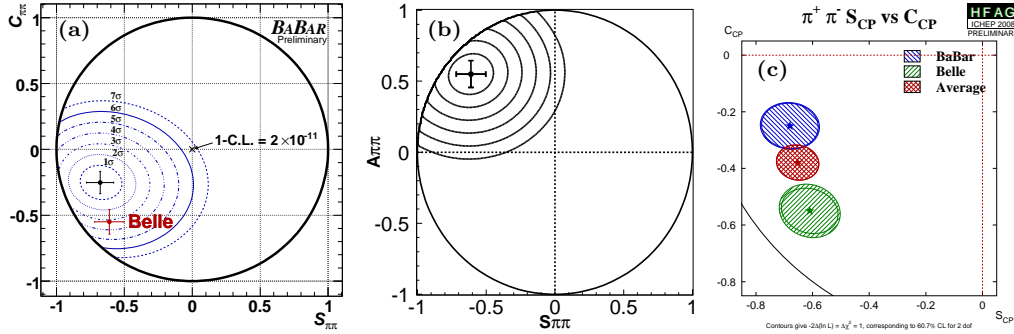


Fig. 83.  $S_{\pi\pi}$  and  $C_{\pi\pi} \equiv -\mathcal{A}_{\pi\pi}$  in  $B^0 \rightarrow \pi^+\pi^-$ : central values, uncertainties, and confidence-level (C.L.) contours for  $1 - \text{C.L.} = 0.317$  ( $1\sigma$ ),  $4.55 \times 10^{-2}$  ( $2\sigma$ ),  $2.70 \times 10^{-3}$  ( $3\sigma$ ),  $6.33 \times 10^{-5}$  ( $4\sigma$ ),  $5.73 \times 10^{-7}$  ( $5\sigma$ ),  $1.97 \times 10^{-9}$  ( $6\sigma$ ) and  $2.56 \times 10^{-12}$  ( $7\sigma$ ): (a) BABAR [1101], (b) Belle [1102]. (c) BABAR and Belle  $\Delta\chi^2 = 1$  ( $S_{\pi\pi}, C_{\pi\pi}$ ) contours, corresponding to 60.7% C.L., and their HFAG correlated average. BABAR and Belle results are consistent at 0.055 ( $1.9\sigma$ ) C.L.

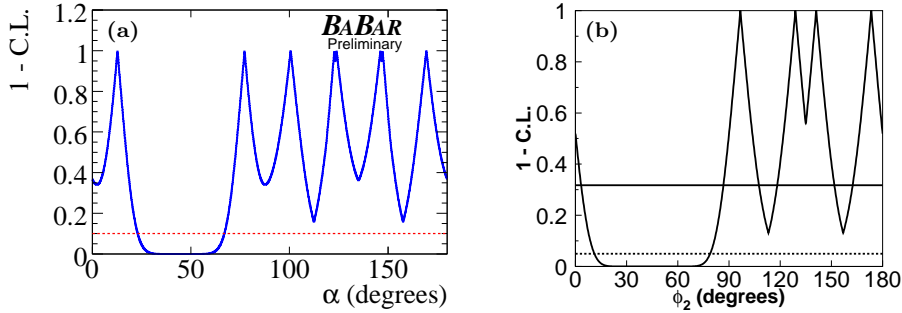


Fig. 84. Constraints on the CKM angle  $\alpha$ : (a) from BABAR [1101] using only the  $B \rightarrow \pi\pi$  results from BABAR; (b) from Belle [1102], using Belle's measurements of  $S_{\pi^+\pi^-}$  and  $C_{\pi^+\pi^-}$  and the Summer 2006 HFAG world averages for the branching fractions and  $CP$ -violating asymmetries in  $B^+ \rightarrow \pi^+\pi^0$  and  $B^0 \rightarrow \pi^0\pi^0$ .

6680 distributions for the  $B^0$  and  $\bar{B}^0$  tags and their  $CP$ -violating asymmetries are shown in  
6681 Fig. 82, and the  $(S_{\pi\pi}, C_{\pi\pi})$  confidence-level contours are shown in Fig. 83. Interpreta-  
6682 tion of the latest *BABAR* and Belle  $B \rightarrow \pi\pi$  results in terms of constraints on the angle  
6683  $\alpha$  is shown in Fig. 84. Only the isospin-triangle relations are used in these constraints.  
6684 Values of  $\alpha$  near 0 or  $\pi$  can be excluded with additional physics input [1105,1108]. The  
6685 key point is that the isospin analysis requires no knowledge about either the magnitude  
6686 or phase of the penguin contribution. However, using CKM unitarity the relative phase  
6687 between penguin and tree can be chosen to be  $\alpha$ , so that the direct  $CP$  violation param-  
6688 eter  $C_{\pi\pi} \propto \alpha$ . Consequently, the observation  $C_{\pi\pi} \neq 0$  requires  $\alpha \neq 0$  (or alternatively  
6689 hadronic parameters must unphysically tend to infinity).

6690 Both Belle and *BABAR* observe a non-zero  $CP$ -violating asymmetry  $S_{\pi\pi}$  in the time  
6691 distribution of  $B^0 \rightarrow \pi^+\pi^-$  decays, with significances of  $5.3\sigma$  and  $6.3\sigma$ , respectively.  
6692 Belle observes, with a significance of  $5.5\sigma$ , direct  $CP$  violation ( $C_{\pi\pi} \neq 0$ ) in  $B^0 \rightarrow \pi^+\pi^-$ ;  
6693 *BABAR* sees  $3.0\sigma$  evidence of  $C_{\pi\pi} \neq 0$ .

### 6694 $B \rightarrow \rho\rho$

6695 The decay  $B^0 \rightarrow \rho^+\rho^-$  has been measured by Belle and *BABAR* several times with  
6696 increasingly larger data samples. Both experiments measure the branching fraction,  $f_L$ ,  
6697 and the  $CP$ -violating parameters  $A_{\rho\rho}$  and  $S_{\rho\rho}$ . The most recent results are listed in  
6698 Tab. 72. The measured values of  $A_{\rho\rho}$  and  $S_{\rho\rho}$  are consistent with zero, i.e., there is no  
6699 evidence for  $CP$  violation. The decay-time distributions and  $CP$  asymmetry distribution  
6700 ( $A_{CP}$  in bins of  $\Delta t$ ) are shown in Figs. 85 and 86. From the same analysis, Belle has also  
6701 set a limit on the nonresonant  $B^0 \rightarrow \rho^0\pi^+\pi^-$  contribution at  $\Gamma(\rho^\pm\pi^\mp\pi^0)/\Gamma(\rho^+\rho^-) =$   
6702  $0.063 \pm 0.067$ .

Table 72  
Belle and *BABAR* results for  $B^0 \rightarrow \rho^+\rho^-$  decays [1109–1111].

	Data (fb <sup>-1</sup> )	Branching fraction $\times 10^{-6}$	$f_L$	$A_{\rho\rho}$	$S_{\rho\rho}$
Belle	253/492	$22.8 \pm 3.8^{+2.3}_{-2.6}$	$0.941^{+0.034}_{-0.040} \pm 0.030$	$0.16 \pm 0.21 \pm 0.08$	$0.19 \pm 0.30 \pm 0.08$
<i>BABAR</i>	349	$25.5 \pm 2.1^{+3.6}_{-3.9}$	$0.992 \pm 0.024^{+0.026}_{-0.013}$	$-0.01 \pm 0.15 \pm 0.06$	$-0.17 \pm 0.20^{+0.05}_{-0.06}$

6703 The most recent results from Belle [1112] and *BABAR* [1113] on the decay  $B^+ \rightarrow \rho^+\rho^0$   
6704 are listed in Tab. 73. Both measured values of  $A_{CP}$  are consistent with zero, implying  
6705 that a possible electroweak penguin contribution is small. Belle has also set a limit on  
6706 the nonresonant  $B^+ \rightarrow (\rho\pi\pi)^+$  contribution of  $\Gamma[(\rho\pi\pi)^+]/\Gamma(\rho^+\rho^0) < 0.17$  at 90% C.L.

Table 73  
Belle and *BABAR* results for  $B^+ \rightarrow \rho^+\rho^0$  decays, from Refs. [1112,1113].

	Data (fb <sup>-1</sup> )	Branching fraction $\times 10^{-6}$	$f_L$	$A_{CP}$
Belle	78	$31.7 \pm 7.1^{+3.8}_{-6.7}$	$0.95 \pm 0.11 \pm 0.02$	$-0.12 \pm 0.13 \pm 0.10$
<i>BABAR</i>	211	$16.8 \pm 2.2 \pm 2.3$	$0.905 \pm 0.042^{+0.023}_{-0.027}$	$0.00 \pm 0.22 \pm 0.03$

6707 The decay  $B^0 \rightarrow \rho^0\rho^0$  has proved difficult to measure due to its small branching  
6708 fraction, and has only recently been observed. Measurements from *BABAR* [1114] and

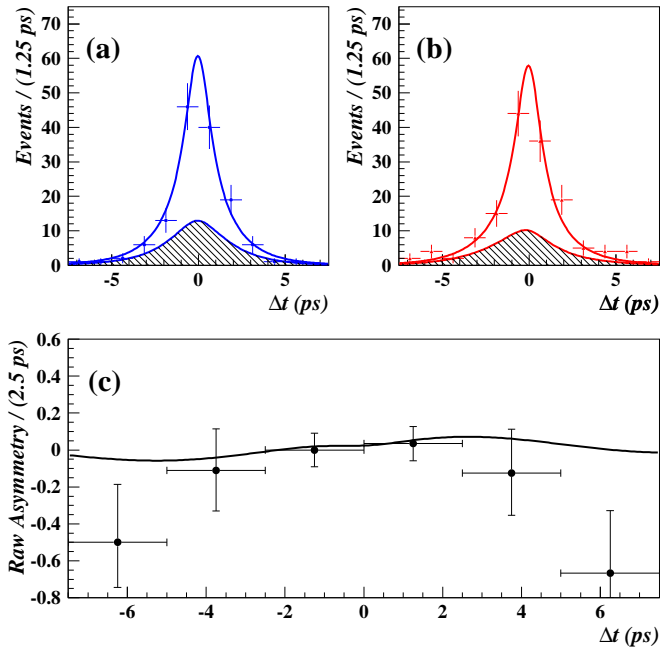


Fig. 85. Decay time distributions from Belle [1109]. (a)  $\bar{B}^0 \rightarrow \rho^+ \rho^-$  decays (b)  $B^0 \rightarrow \rho^+ \rho^-$  decays, and (c) the raw asymmetry  $(\bar{N} - N)/(\bar{N} + N)$ , where  $\bar{N}$  ( $N$ ) is the number of  $\bar{B}^0$  ( $B^0$ ) candidates including background. The hatched region shows the fit result for the signal component, and the solid curve shows the fit result for the total.

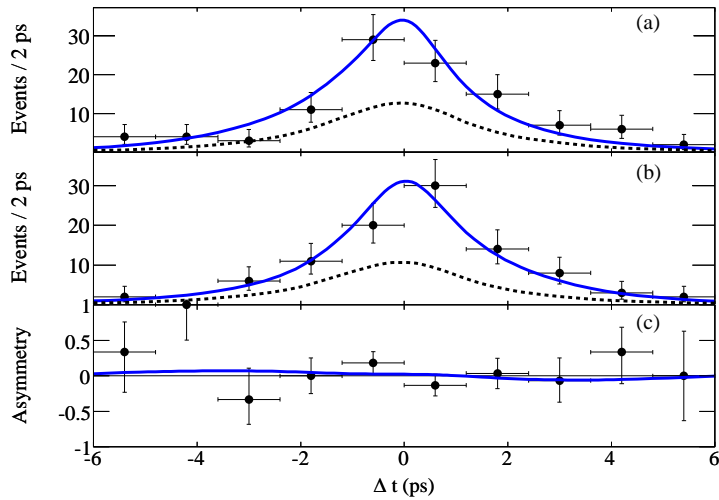


Fig. 86. Decay time distributions from BABAR [1110]. (a)  $\bar{B}^0 \rightarrow \rho^+ \rho^-$  decays (b)  $B^0 \rightarrow \rho^+ \rho^-$  decays, and (c) the asymmetry  $(\bar{N} - N)/(\bar{N} + N)$ , where  $\bar{N}$  ( $N$ ) is the number of signal  $\bar{B}^0 \rightarrow \rho^+ \rho^-$  ( $B^0 \rightarrow \rho^+ \rho^-$ ) decays. The dashed curve shows the fit result for all backgrounds, and the solid curve shows the fit result for the total.

6709 Belle [1115] are listed in Tab. 74. Both experiments obtain the signal yield from unbinned  
6710 maximum likelihood fits to  $M_{bc}$  (or  $m_{ES} \equiv M_{bc}$ ),  $\Delta E$ , and  $M_{\pi\pi}$ . The fit is complicated  
6711 by possible contributions from  $\rho^0 f_0(980)$ ,  $f_0 f_0$ ,  $f_0 \pi^+ \pi^-$ , and  $a_1 \pi$  final states, as well as  
6712 from  $B^0 \rightarrow \rho^0 \pi^+ \pi^-$  and  $B^0 \rightarrow \pi^+ \pi^- \pi^+ \pi^-$ .

6713 The *BABAR* experiment requires that  $M_{\pi\pi} \in (0.50, 1.05) \text{ GeV}/c^2$ ; they subsequently fit  
6714 to variables  $m_{ES}$ ,  $\Delta E$ , helicity angles  $\cos\theta_1$ ,  $\cos\theta_2$ , and the decay time difference  $\Delta t$ .  
6715 Including the helicity angles in the fit yields a measurement of  $f_L$ , and including  $\Delta t$   
6716 yields a measurement of  $A_{\rho\rho}$  and  $S_{\rho\rho}$ . *BABAR* observes an excess of signal events with  
6717  $3.1\sigma$  significance, and no significant nonresonant contributions. The measured values of  
6718  $A_{\rho\rho}$  and  $S_{\rho\rho}$  are consistent with zero, i.e., there is no evidence for *CP* violation.

6719 The Belle experiment requires  $M_{\pi\pi} \in (0.55, 1.70) \text{ GeV}/c^2$ —a wider window than that  
6720 used by *BABAR* (see Fig. 87). Belle observes a higher rate of nonresonant  $\rho\pi\pi$  and  $4\pi$   
6721 components than *BABAR* does, and the significance of Belle’s  $\rho^0\rho^0$  signal is only  $1.0\sigma$ .

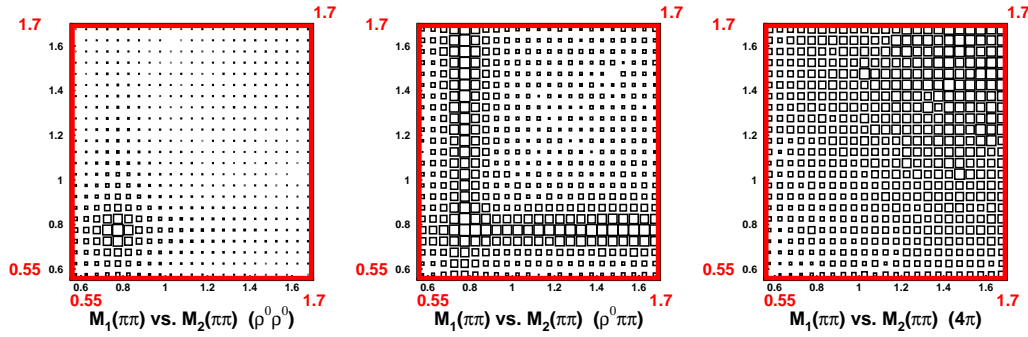


Fig. 87. Monte Carlo simulated  $M_{\pi\pi}$  distributions for (a)  $B^0 \rightarrow \rho^0 \rho^0$ , (b)  $B^0 \rightarrow \rho^0 \pi^+ \pi^-$ , and (c)  $B^0 \rightarrow \pi^+ \pi^- \pi^+ \pi^-$  decays, from Belle. The plots are symmetrized by randomly choosing the mass combination plotted against the horizontal axis. The fitted region for Belle is  $M_{\pi\pi} \in (0.55, 1.70) \text{ GeV}/c^2$ , whereas that for *BABAR* is  $M_{\pi\pi} \in (0.55, 1.05) \text{ GeV}/c^2$ .

Table 74  
Belle and *BABAR* results for  $B^0 \rightarrow \rho^0 \rho^0$  decays [1114, 1115].

Mode	Branching fraction ( $10^{-6}$ )	$f_L$	$A_{\rho\rho}$	$S_{\rho\rho}$
Belle ( $605 \text{ fb}^{-1}$ )				
$\rho^0 \rho^0$	$0.4 \pm 0.4^{+0.2}_{-0.3}$	—	—	—
$\rho^0 \pi^+ \pi^-$	$5.9^{+3.5}_{-3.4} \pm 2.7$	—	—	—
$\pi^+ \pi^- \pi^+ \pi^-$	$12.4^{+4.7}_{-4.6} \pm 2.1$	—	—	—
<i>BABAR</i> ( $423 \text{ fb}^{-1}$ )				
$\rho^0 \rho^0$	$0.92 \pm 0.32 \pm 0.14$	$0.75^{+0.11}_{-0.14} \pm 0.05$	$-0.2 \pm 0.8 \pm 0.3$	$0.3 \pm 0.7 \pm 0.2$
$\rho^0 \pi^+ \pi^-$	$-1.6^{+5.0}_{-4.5} \pm 2.2$	—	—	—
$\pi^+ \pi^- \pi^+ \pi^-$	$3.0^{+11.6}_{-9.9} \pm 4.1$	—	—	—

6722 Both Belle and *BABAR* constrain  $\alpha$  using isospin analysis [37]. The fitted observables  
6723 are the branching fractions and fractions of longitudinal polarization for  $B^+ \rightarrow \rho^+ \rho^0$ ,  
6724  $B^0 \rightarrow \rho^+ \rho^-$ , and  $B^0 \rightarrow \rho^0 \rho^0$ , the coefficients  $A_{\rho\rho}$  and  $S_{\rho\rho}$  for  $B^0 \rightarrow \rho^+ \rho^-$  decays,  
6725 and  $A_{\rho\rho}$  for  $B^0 \rightarrow \rho^0 \rho^0$  decays. The fitted parameters are the magnitudes  $|\mathcal{A}(B^0 \rightarrow$   
6726  $\rho^+ \rho^0)|$ ,  $|\mathcal{A}(B^0 \rightarrow \rho^+ \rho^-)|$ , and  $|\mathcal{A}(B^0 \rightarrow \rho^0 \rho^0)|$ , the average phase of, and phase difference  
6727 between, amplitudes  $\mathcal{A}(B^0 \rightarrow \rho^+ \rho^-)$  and  $\mathcal{A}(\bar{B}^0 \rightarrow \rho^+ \rho^-)$ , and  $\alpha$ . To obtain a confidence  
6728 interval for  $\alpha$ , the experiments scan values of  $\alpha$  and, for each value, fit the measured  
6729 observables. The resulting  $\chi^2$  is input into the cumulative  $\chi^2$  distribution to obtain a  
6730 confidence level ( $p$ -value) for that value of  $\alpha$ . Plotting this confidence level (C.L.) versus  
6731  $\alpha$  allows one to read off a confidence interval.

6732 The most recent Belle result [1115], obtained using world average values [558] for all  
6733 observables except  $B(B^0 \rightarrow \rho^0 \rho^0)$  for which only the Belle result is used, is shown in  
6734 Fig. 88 (top). The “flat-top” region results from the fact that no measurement of  $A_{\rho\rho}$   
6735 for  $B^0 \rightarrow \rho^0 \rho^0$  decays is used. From the plot one reads off three disjoint 68.3% C.L.  
6736 intervals; the interval consistent with unitarity ( $\alpha + \beta + \gamma = 180^\circ$ ) is  $(75.8, 106.2)^\circ$ .  
6737 Requiring symmetric errors gives  $\alpha = (91.7 \pm 14.9)^\circ$ .

6738 The most recent *BABAR* result [1114], made using *BABAR* results exclusively, is shown in  
6739 Fig. 88 (bottom). The dotted contour is the nominal solution; however, including in the fit  
6740 the parameter  $S_{\rho\rho}$  from  $B^0 \rightarrow \rho^0 \rho^0$  decays reduces the four-fold ambiguity for  $\alpha$  to three  
6741 solutions (solid contour). The final result is expressed in terms of the shift  $\delta \equiv \alpha - \alpha_{\text{eff}}$   
6742 that results from the penguin contribution (recall that  $S_{\rho\rho} = -\sqrt{1 - A_{\rho\rho}^2} \sin 2\alpha_{\text{eff}}$ , see  
6743 Eq. 407). The upper limit is  $|\delta| < 17.6^\circ$  at 90% C.L.

#### 6744 $B^0 \rightarrow \rho\pi$

6745 The time-dependent Dalitz plot analysis of  $B^0 \rightarrow \pi^+ \pi^- \pi^0$  has been performed by  
6746 *BABAR* using  $346 \text{ fb}^{-1}$  of data [1116] and by Belle using  $414 \text{ fb}^{-1}$  [1117]. In principle,  
6747 one inserts the parametrization (411) and (412) into (410) to obtain the PDF for fit-  
6748 ting. However, the resulting PDF is nonlinear in the amplitudes  $A_i$  and  $\bar{A}_i$ , and the  
6749 fit is not well-behaved for current statistics. To stabilize the fit, one defines new fitting  
6750 parameters [1118]

$$6745 \quad U_i^\pm = |A_i|^2 \pm |\bar{A}_i|^2 \quad (414)$$

$$6746 \quad U_{ij}^\pm = A_i A_j^* \pm \bar{A}_i \bar{A}_j^* \quad (415)$$

$$6747 \quad I_i = \text{Im}(\bar{A}_i A_i^*) \quad (416)$$

$$6748 \quad \text{Re}(I_{ij}) = \text{Re}(\bar{A}_i A_j^* - \bar{A}_j A_i^*) \quad (417)$$

$$6749 \quad \text{Im}(I_{ij}) = \text{Im}(\bar{A}_i A_j^* + \bar{A}_j A_i^*). \quad (418)$$

6751 Eqs. (414)-(418) define 27 real parameters from six complex amplitudes, and thus these  
6752 parameters are not all independent. The overall normalization is fixed by setting  $U_+^+ = 1$ ,  
6753 and then there are 26 free parameters in the fit. The fit results for *BABAR* and Belle are  
6754 listed in Tab. 75.

6755 To constrain  $\alpha$ , a  $\chi^2$  fit is performed to the 27 measured observables listed in Tab. 75.  
6756 The  $\chi^2$  statistic takes into account all correlations between the observables. There are in  
6757 principle 12 free parameters in the fit, corresponding to the six complex amplitudes  $A_i$   
6758 and  $\bar{A}_i$ . However, the additional parameter  $\alpha$  is included along with the (complex) isospin

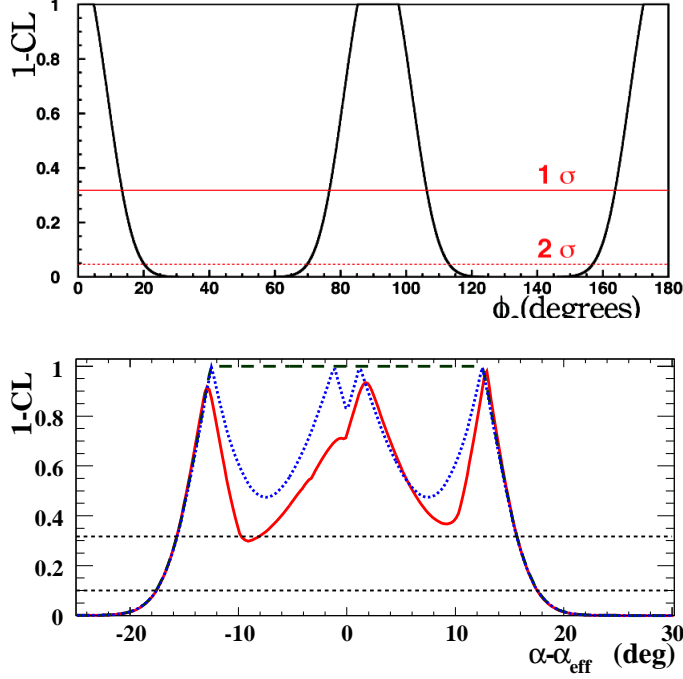


Fig. 88. Plot of  $1-CL$  versus  $\alpha$  from Belle [1115] (top), and  $1-CL$  versus  $\alpha - \alpha_{\text{eff}}$  from BABAR [1114] (bottom). From these plots one reads off confidence intervals. In the top plot, the flat-top region results from not using  $A_{\rho\rho}$  from  $B^0 \rightarrow \rho^0\rho^0$  in the fit; in the bottom plot, the solid curve results from using both  $A_{\rho\rho}$  and  $S_{\rho\rho}$  from  $B^0 \rightarrow \rho^0\rho^0$ .

6759 relation (413); together these reduce the number of free parameters to 11. The constraint  
 6760  $U_+^+ = 1$  fixes the overall normalization, and a global phase factor can be neglected; thus  
 6761 the final number of free parameters is nine. A scan is performed over values of  $\alpha$ , where  
 6762 for each value the other eight parameters are floated in order to minimize the  $\chi^2$ . The  
 6763 resulting change in the  $\chi^2$  from the minimum value is converted into a confidence level  
 6764 ( $CL$ ) either by using the cumulative  $\chi^2$  distribution for one degree of freedom, or by  
 6765 finding the  $p$ -value from an ensemble of toy MC experiments.

6766 The resulting plots of  $1-CL$  versus  $\alpha$  for BABAR and Belle are shown in Fig. 89. The  
 6767 values of  $\alpha$  that have  $(1-CL) > 0.317$  determine  $1\sigma$  confidence intervals for  $\alpha$ . As can be  
 6768 seen from the plots, the  $1-CL$  contour has large variations that result in multiple regions,  
 6769 i.e., non-simply-connected intervals. Typically, the experiments quote only the interval  
 6770 consistent with unitarity. Belle obtains a second  $1-CL$  contour by including additional  
 6771 observables: the branching fractions for  $B^0 \rightarrow \rho^+\pi^-$ ,  $\rho^-\pi^+$ ,  $\rho^0\pi^0$  obtained from their  
 6772 analysis, and world average values [558] for the branching fractions and  $CP$  asymmetries  
 6773 measured for the charged modes  $B^\pm \rightarrow \rho^\pm\pi^0$  and  $B^\pm \rightarrow \rho^0\pi^\pm$ . With these four new  
 6774 observables, two additional isospin relations are used; the final number of parameters  
 6775 floated in the fit is 12. The resulting  $1-CL$  contour is also shown in Fig. 89. The final  
 6776 result from BABAR is  $\alpha = (87_{-13}^{+45})^\circ$ , whereas the final result from Belle is  $\alpha \in (68^\circ, 95^\circ)$   
 6777 at 68.3% CL.

Table 75

Fit results for the  $U$  and  $I$  coefficients from Refs. [1116] (BABAR) and [1117] (Belle). The first error listed is statistical, and the second is systematic.

Parameter	BABAR	Belle
$U_+^+$	1.0 (fixed)	+1 (fixed)
$U_-^+$	$1.32 \pm 0.12 \pm 0.05$	$+1.27 \pm 0.13 \pm 0.09$
$U_0^+$	$0.28 \pm 0.07 \pm 0.04$	$+0.29 \pm 0.05 \pm 0.04$
$U_{+-}^{+,Re}$	$0.17 \pm 0.49 \pm 0.31$	$+0.49 \pm 0.86 \pm 0.52$
$U_{+0}^{+,Re}$	$-1.08 \pm 0.48 \pm 0.20$	$+0.29 \pm 0.50 \pm 0.35$
$U_{-0}^{+,Re}$	$-0.36 \pm 0.38 \pm 0.08$	$+0.25 \pm 0.60 \pm 0.33$
$U_{+-}^{+,Im}$	$-0.07 \pm 0.71 \pm 0.73$	$+1.18 \pm 0.86 \pm 0.34$
$U_{+0}^{+,Im}$	$-0.16 \pm 0.57 \pm 0.14$	$-0.57 \pm 0.35 \pm 0.51$
$U_{-0}^{+,Im}$	$-0.17 \pm 0.50 \pm 0.23$	$-1.34 \pm 0.60 \pm 0.47$
$U_+^-$	$0.54 \pm 0.15 \pm 0.05$	$+0.23 \pm 0.15 \pm 0.07$
$U_-^-$	$-0.32 \pm 0.14 \pm 0.05$	$-0.62 \pm 0.16 \pm 0.08$
$U_0^-$	$-0.03 \pm 0.11 \pm 0.09$	$+0.15 \pm 0.11 \pm 0.08$
$U_{+-}^{-,Re}$	$2.23 \pm 1.00 \pm 0.43$	$-1.18 \pm 1.61 \pm 0.72$
$U_{+0}^{-,Re}$	$-0.18 \pm 0.88 \pm 0.35$	$-2.37 \pm 1.36 \pm 0.60$
$U_{-0}^{-,Re}$	$-0.63 \pm 0.72 \pm 0.32$	$-0.53 \pm 1.44 \pm 0.65$
$U_{+-}^{-,Im}$	$-0.38 \pm 1.06 \pm 0.36$	$-2.32 \pm 1.74 \pm 0.91$
$U_{+0}^{-,Im}$	$-1.66 \pm 0.94 \pm 0.25$	$-0.41 \pm 1.00 \pm 0.47$
$U_{-0}^{-,Im}$	$0.12 \pm 0.75 \pm 0.22$	$-0.02 \pm 1.31 \pm 0.83$
$I_+$	$-0.02 \pm 0.10 \pm 0.03$	$-0.01 \pm 0.11 \pm 0.04$
$I_-$	$-0.01 \pm 0.10 \pm 0.02$	$+0.09 \pm 0.10 \pm 0.04$
$I_0$	$0.01 \pm 0.06 \pm 0.01$	$+0.02 \pm 0.09 \pm 0.05$
$I_{+-}^{Re}$	$1.90 \pm 2.03 \pm 0.65$	$+1.21 \pm 2.59 \pm 0.98$
$I_{+0}^{Re}$	$0.41 \pm 1.30 \pm 0.41$	$+1.15 \pm 2.26 \pm 0.92$
$I_{-0}^{Re}$	$0.41 \pm 1.30 \pm 0.21$	$-0.92 \pm 1.34 \pm 0.80$
$I_{+-}^{Im}$	$-1.99 \pm 1.25 \pm 0.34$	$-1.93 \pm 2.39 \pm 0.89$
$I_{+0}^{Im}$	$-0.21 \pm 1.06 \pm 0.25$	$-0.40 \pm 1.86 \pm 0.85$
$I_{-0}^{Im}$	$1.23 \pm 1.07 \pm 0.29$	$-2.03 \pm 1.62 \pm 0.81$

6778  $B^0 \rightarrow a_1^\pm \pi^\mp$

6779 As proposed by Gronau and Zupan [1119], the  $\Delta t$  distribution for  $B^0 \rightarrow a_1^\pm \pi^\mp$  decays  
6780 can be fit to determine  $\alpha$ . However, there can be a penguin amplitude that substantially  
6781 shifts the measured  $\alpha$  value from the true value, as found for  $B \rightarrow \pi\pi$  decays. Thus, to  
6782 determine  $\alpha$  from  $B^0 \rightarrow a_1^\pm \pi^\mp$  requires external input, e.g., assuming  $SU(3)$  symmetry  
6783 and using measurements of  $B \rightarrow a_1 K$  [1120] and  $B^0 \rightarrow K_{1A} \pi$  [1121] decays. This method  
6784 has uncertainties arising from  $SU(3)$ -breaking corrections and unknown decay constants  
6785  $f_{a_1}$  and  $f_{K_1}$ .

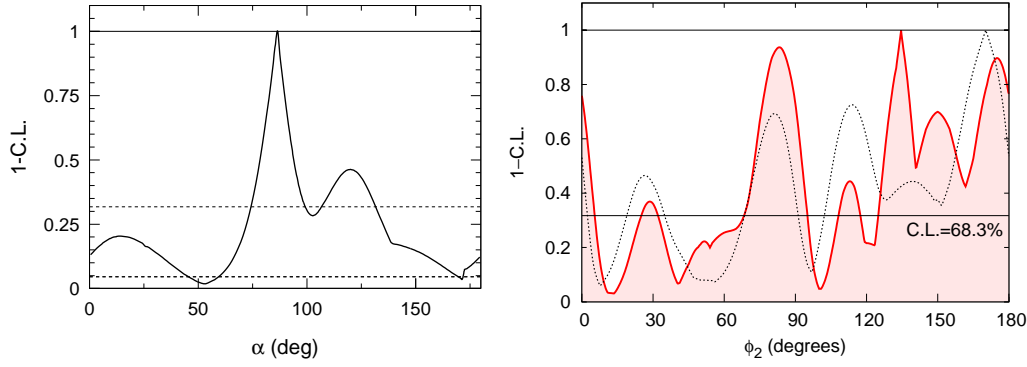


Fig. 89.  $1 - CL$  versus  $\alpha$  resulting from  $\chi^2$  fits to the 27 observables listed in Tab. 75. The left plot is from *BABAR* [1116], and the right plot is from *Belle* [1117]. The horizontal line at  $1 - CL = 0.317$  corresponds to 68.3% CL and is used to determine  $1\sigma$  confidence intervals for  $\alpha$ . For *Belle*, the dashed contour corresponds to a nine-parameter fit, and the solid contour corresponds to a twelve parameter fit (see text).

6786 Experimentally, one simultaneously fits the four distributions  $B^0 \rightarrow a_1^\pm \pi^\mp$  and  $\bar{B}^0 \rightarrow$   
 6787  $a_1^\pm \pi^\mp$  to the PDF

$$\frac{dN(a_1^\pm \pi^\mp)}{d\Delta t} = (1 \pm \mathcal{A}_{CP}) \frac{e^{-|\Delta t|/\tau}}{8\tau} \times \left\{ 1 - q_{\text{tag}} \left[ (C \pm \Delta C) \cos(\Delta m \Delta t) - (S \pm \Delta S) \sin(\Delta m \Delta t) \right] \right\}, \quad (419)$$

6788 where  $q_{\text{tag}} = +1$  ( $-1$ ) when the tag-side  $B$  decays as a  $B^0$  ( $\bar{B}^0$ ). The parameters  $\mathcal{A}_{CP}$ ,  
 6789  $C$ , and  $S$  are  $CP$ -violating, and the parameters  $\Delta C$  and  $\Delta S$  are  $CP$ -conserving. *BABAR*  
 6790 has performed this fit using  $349 \text{ fb}^{-1}$  of data [1122]; the results are listed in Tab. 76.  
 6791 The values obtained are subsequently used to determine  $\alpha_{\text{eff}} = \alpha - \delta$  within a four-fold  
 6792 ambiguity. The solution closest to the  $\alpha$  value favored by  $B \rightarrow \rho\rho$  and  $B \rightarrow \pi\pi$  decays is  
 6793  $\alpha_{\text{eff}} = (78.6 \pm 7.3)^\circ$ . This result differs from  $\alpha$  by the unknown penguin contribution  $\delta$ .

Table 76  
*BABAR* results for  $B^0 \rightarrow a_1^\pm \pi^\mp$  decays, from Ref. [1122].

Parameter	Value
$\mathcal{A}_{CP}$	$-0.07 \pm 0.07 \pm 0.02$
$C$	$-0.10 \pm 0.15 \pm 0.09$
$S$	$0.37 \pm 0.21 \pm 0.07$
$\Delta C$	$0.26 \pm 0.15 \pm 0.07$
$\Delta S$	$-0.14 \pm 0.21 \pm 0.06$



6795 In this subsection we review the methods to determine the weak phase in the CKM  
 6796 matrix using  $\Delta S = 1$  charmless hadronic  $B$  decays:  $B \rightarrow K\pi$ ,  $B \rightarrow K\pi\pi$ . Conventionally  
 6797 this is rewritten as a constraint on  $\gamma$ , but in many instances it also involves the knowledge  
 6798 of the  $B^0\bar{B}^0$  mixing phase. This is taken to be well known as it is measured precisely in  
 6799  $B^0 \rightarrow J/\psi K_S^0$ . The  $B \rightarrow K\pi$  and  $B \rightarrow K\pi\pi$  decays are dominated by QCD penguins  
 6800 and are as such sensitive to new physics effects from virtual corrections entering at 1-  
 6801 loop. Comparing the extracted value of  $\gamma$  with that from a tree level determination using  
 6802  $B \rightarrow DK$  constitutes a test of Standard Model.

#### 6803 9.4.1. Constraints from $B_{(s)} \rightarrow hh$

We can write any amplitude as a sum of two terms

$$A(B \rightarrow f) = P e^{i\delta_P} + T e^{i\gamma} e^{i\delta_T}, \quad (420)$$

where the “penguin”  $P$  carries only a strong phase  $\delta_P$ , while the “tree”  $T$  has both strong phase  $\delta_T$  and a weak phase  $\gamma$ . The latter flips signs for the  $CP$  conjugated amplitude  $A(\bar{B} \rightarrow \bar{f})$ . The sensitivity to  $\gamma$  comes from the interference of the two contributions. In  $\Delta S = 1$  decays the tree contribution is doubly CKM suppressed — it carries the CKM factor  $|V_{ub}^* V_{us}|$  — while the penguin contribution has a CKM factor  $|V_{cb}^* V_{cs}|$  that is  $\sim 1/\lambda^2$  times larger. We can thus expand in  $T/P$ , which gives for the direct  $CP$  asymmetry and branching fraction respectively

$$\begin{aligned} A_{CP} &= 2 \frac{T}{P} \sin(\delta_P - \delta_T) \sin \gamma + O\left(\left(\frac{T}{P}\right)^2\right), \\ \mathcal{B} &= P^2 \left[ 1 + 2 \frac{T}{P} \cos(\delta_P - \delta_T) \cos \gamma + O\left(\left(\frac{T}{P}\right)^2\right) \right]. \end{aligned} \quad (421)$$

6804 Using the above expression for  $\mathcal{B}(B^0 \rightarrow K^+\pi^-)$  one can get a very simple geometric  
 6805 bound on  $\gamma$ , if  $P$  is known. Obtaining  $P$  from  $\mathcal{B}(B^+ \rightarrow \pi^+K^0)$  — neglecting very  
 6806 small color suppressed electroweak penguins — one has  $|\cos \gamma| > \sqrt{1-R}$  valid for  $R <$   
 6807  $1$  [1123, 1124] ( $R$  is defined in Eq. 422 below). At present this gives  $\gamma < 77^\circ$  at  $1\sigma$ .

6808 The extraction of  $\gamma$  requires more theoretical input. One needs to determine the strong  
 6809 phase difference  $\delta_P - \delta_T$  and the ratio  $T/P$ . This can be achieved either by relating  $T/P$   
 6810 to  $\Delta S = 0$  decays using SU(3) [1074, 1125–1134] or by using the  $1/m_b$  expansion and  
 6811 factorization theorems to calculate the  $T/P$  ratio [40, 51, 52, 1038, 1054, 1135].

6812 The methods that use SU(3) flavor symmetries exploit the fact that  $\Delta S = 0$  decays  
 6813 such as  $B \rightarrow \pi\pi$  are tree dominated. The CKM factors multiplying the “tree” ( $V_{ub}^* V_{ud}$ )  
 6814 and “penguin” terms ( $V_{cb}^* V_{cd}$ ) are of comparable size (unlike  $\Delta S = 1$  decays where  
 6815 the “tree” is CKM suppressed). From these decays one can then determine the size of  
 6816  $T/P$  and feed it into  $\Delta S = 1$  decays to extract  $\gamma$ . In doing this quite often some  $1/m_b$   
 6817 suppressed annihilation or exchange amplitudes need to be neglected. These methods  
 6818 are hard to improve systematically, while already at present the determined value of  $\gamma$   
 6819 is dominated by theoretical errors due to SU(3) breaking and the neglected amplitudes.  
 6820 These were estimated to be of order  $8^\circ - 10^\circ$  in [1129] for the extraction of  $\gamma$  from  $B \rightarrow$   
 6821  $\pi\pi$  and  $B \rightarrow \pi K$ . Some improvement can be expected, if one does not need to neglect  
 6822 annihilation amplitudes but rely only on flavor symmetry. One interesting method of  
 6823 this type uses  $B_s \rightarrow K^+K^-$  and  $B \rightarrow \pi^+\pi^-$  decays [1134, 1136]. In this analysis, the

6824 theoretical error on the extracted value of  $\gamma$  due to SU(3) breaking was estimated to  
 6825 be of the order of  $5^\circ$  [1133]. This is a promising avenue of investigation for the LHCb  
 6826 experiment.

6827 If instead of extracting  $\gamma$  the goal is to make a precision test of the Standard Model, one  
 6828 can rather take as an input the value of  $\gamma$  determined from  $B \rightarrow DK$  or from global fits.  
 6829 A theoretically clean prediction of  $S_{K_S^0\pi^0}$  is then possible using isospin relations, while  
 6830 theoretical calculations based on the  $1/m_b$  expansion are used only for SU(3) breaking  
 6831 terms [1075] (see also [1076]).

6832 If the  $1/m_b$  expansion is used to determine  $\gamma$ , a number of different observables can  
 6833 be used, since in principle all the observables are now calculable. At present in the  
 6834  $1/m_b$  expansion calculations  $\gamma$  is taken as an input, but it could of course be extracted  
 6835 from data instead. Different groups treat differently various terms in the expansion, for  
 6836 instance expanding or not expanding in  $\alpha_S(\sqrt{\Lambda m_b})$ , including different  $1/m_b$  suppressed  
 6837 terms in the expansion, etc., and this may lead to slightly different extracted values of  $\gamma$   
 6838 (but the estimated theoretical errors should account for the differences). The important  
 6839 point is that the expansion is systematically improvable so that the errors could at least  
 6840 in principle be reduced in the future. For instance, the theoretical errors on the value of  
 6841  $\gamma$  extracted from  $S_{\rho\pi}$  are about  $5^\circ$  and about  $10^\circ$  if extracted from  $S_{\pi\pi}$  [1038]. Much  
 6842 larger errors can be expected for  $\gamma$  extracted from  $\Delta S = 1$  decays, since the interference  
 6843 is CKM suppressed.

As an example let us consider the ratios

$$R = \frac{\mathcal{B}(B^0 \rightarrow \pi^\mp K^\pm) \tau_{B^+}}{\mathcal{B}(B^\pm \rightarrow \pi^\pm K^0) \tau_{B^0}}, \quad R_c = \frac{2\mathcal{B}(B^\pm \rightarrow \pi^0 K^\pm)}{\mathcal{B}(B^\pm \rightarrow \pi^\pm K^0)}, \quad R_n = \frac{\mathcal{B}(B^0 \rightarrow \pi^\mp K^\pm)}{2\mathcal{B}(B^0 \rightarrow \pi^0 K^0)}, \quad (422)$$

for which part of the theoretical and experimental uncertainties cancel [1137]. Tab. 77  
 summarizes the current experimental measurements of the  $B \rightarrow K\pi$  branching frac-  
 tions and  $CP$  asymmetries [558, 1101, 1103–1105, 1138, 1139], while  $\tau_{B^+}/\tau_{B^0} = 1.073 \pm$   
 $0.008$  [558]. In Tab. 77 we also quote the resulting world averages for the ratios, ignoring  
 the correlations between the individual branching fraction measurements. These translate  
 into the following bounds on  $\gamma$  at 68% confidence level [1054]

$$R \Rightarrow 55^\circ < \gamma < 95^\circ, \quad R_c \Rightarrow 55^\circ < \gamma < 80^\circ, \quad R_n \Rightarrow 40^\circ < \gamma < 75^\circ. \quad (423)$$

6844 The measurements of  $B_s$  decays to two light hadrons can provide further constraints on  
 6845  $\gamma$  [1130]. Following its earlier discovery of  $B_s \rightarrow K^+K^-$  [1140], the CDF collaboration has  
 6846 recently produced updated measurements of the branching fraction and  $CP$  asymmetry  
 6847 of the decay  $B_s \rightarrow K^-\pi^+$  [1141, 1142]:

$$\mathcal{B}(B_s \rightarrow K^-\pi^+) = (5.0 \pm 0.7 \pm 0.8) \times 10^{-6}, \quad (424)$$

$$A_{CP}(B_s \rightarrow K^-\pi^+) = (39 \pm 15 \pm 8)\%. \quad (425)$$

6848 It has been recently pointed out that these results have implications for SU(3) and QCD  
 6849 factorization [1143], which prefer a larger value of the branching fraction for the Standard  
 6850 Model value of  $\gamma$ .

#### 6851 9.4.2. Constraints from $B \rightarrow K\pi\pi$ Dalitz-plot analyses

6852 Three-body decays have an added benefit that quasi-two-body decays such as  $B \rightarrow$   
 6853  $K^*\pi$  and  $B \rightarrow K\rho$  can interfere through the same final  $K\pi\pi$  state. Measuring the

Table 77

Summary of  $B \rightarrow K\pi$  experimental measurements.

Quantity	BaBar Value	Belle Value	World Average Value
$\mathcal{B}(B^\pm \rightarrow \pi^\pm K^0)$	$(23.9 \pm 1.1 \pm 1.0) \times 10^{-6}$	$(22.8^{+0.8}_{-0.7} \pm 1.3) \times 10^{-6}$	$(23.1 \pm 1.0) \times 10^{-6}$
$\mathcal{B}(B^\pm \rightarrow \pi^0 K^\pm)$	$(13.6 \pm 0.6 \pm 0.7) \times 10^{-6}$	$(12.4 \pm 0.5 \pm 0.6) \times 10^{-6}$	$(12.9 \pm 0.6) \times 10^{-6}$
$\mathcal{B}(B^0 \rightarrow \pi^\mp K^\pm)$	$(19.1 \pm 0.6 \pm 0.6) \times 10^{-6}$	$(19.9 \pm 0.4 \pm 0.8) \times 10^{-6}$	$(19.4 \pm 0.6) \times 10^{-6}$
$\mathcal{B}(B^0 \rightarrow \pi^0 K^0)$	$(10.1 \pm 0.6 \pm 0.4) \times 10^{-6}$	$(9.7 \pm 0.7^{+0.6}_{-0.7}) \times 10^{-6}$	$(9.8 \pm 0.6) \times 10^{-6}$
$A_{CP}(B^\pm \rightarrow \pi^\pm K^0)$	$(-2.9 \pm 3.9 \pm 1.0)\%$	$(+3 \pm 3 \pm 1)\%$	$(+0.9 \pm 2.5)\%$
$A_{CP}(B^\pm \rightarrow \pi^0 K^\pm)$	$(+3.0 \pm 3.9 \pm 1.0)\%$	$(+7 \pm 3 \pm 1)\%$	$(+5.0 \pm 2.5)\%$
$A_{CP}(B^0 \rightarrow \pi^\mp K^\pm)$	$(-10.7 \pm 1.6^{+0.6}_{-0.4})\%$	$(-9.4 \pm 1.8 \pm 0.8)\%$	$(-9.8^{+1.2}_{-1.1})\%$
$A_{CP}(B^0 \rightarrow \pi^0 K^0)$	$(-13 \pm 13 \pm 3)\%$	$(+14 \pm 13 \pm 6)\%$	$(-1 \pm 10)\%$
$R$	...	...	$0.90 \pm 0.05$
$R_c$	...	...	$1.12 \pm 0.07$
$R_n$	...	...	$0.99 \pm 0.07$

6854 interference pattern in the Dalitz plot then allows to determine not only the magnitudes  
6855 of the amplitudes as in the two body decays, but also the relative phases between the  
6856 amplitudes. This can then be used either to check  $1/m_b$  predictions or as an additional  
6857 input for the determination of the CKM weak phase using flavor symmetries. We will  
6858 review such a method below [1144, 1145]. The cleanest method requires measurements  
6859 from the  $B^0 \rightarrow K^+\pi^-\pi^0$  and  $B^0 \rightarrow K_s^0\pi^+\pi^-$  Dalitz plots [1144–1146]. Other methods  
6860 also use  $B^+ \rightarrow K_s^0\pi^+\pi^0$  [1144],  $B^+ \rightarrow K^+\pi^+\pi^-$  and  $B^0 \rightarrow K_s^0\pi^+\pi^-$  [1147], and  $B_s \rightarrow$   
6861  $K^+\pi^-\pi^0$  and  $B_s \rightarrow K_s^0\pi^+\pi^-$  [1148].

The main idea of the method [1144, 1145] is that by using isospin decomposition one can cancel the QCD penguin contributions ( $\Delta I = 0$  reduced amplitudes) in  $B \rightarrow K^*\pi$  decays. The  $I = 3/2$  ( $\Delta I = 1$ ) final state, is for instance given by

$$3A_{3/2} = A(B^0 \rightarrow K^{*+}\pi^-) + \sqrt{2}A(B^0 \rightarrow K^{*0}\pi^0), \quad (426)$$

with an equivalent definition for the amplitude for charge-conjugated states,  $\bar{A}_{3/2}$ . Since both magnitudes and relative phases of amplitudes are measurable, this is now an observable quantity — up to an overall phase. In the absence of electroweak penguin (EWP) terms  $A_{3/2}$  carries a weak phase  $\gamma$ , so that in this limit

$$\gamma = \Phi_{3/2} \equiv -\frac{1}{2}\arg(R_{3/2}), \quad \text{where } R_{3/2} \equiv \frac{\bar{A}_{3/2}}{A_{3/2}}. \quad (427)$$

The constraint in  $\bar{\rho} - \bar{\eta}$  plane in the absence of EWP is a straight line,  $\bar{\eta} = \bar{\rho} \tan \Phi_{3/2}$ . The inclusion of EWP shifts this constraint to [1145]

$$\bar{\eta} = \tan \Phi_{3/2} \left[ \bar{\rho} + C[1 - 2\text{Re}(r_{3/2})] + \mathcal{O}(r_{3/2}^2) \right], \quad (428)$$

where  $C$  is a quantity that depends only on electroweak physics and is well known, with a theoretical error below 1% ( $\lambda = 0.227$ )

$$C \equiv \frac{3}{2} \frac{C_9 + C_{10}}{C_1 + C_2} \frac{1 - \lambda^2/2}{\lambda^2} = -0.27, \quad (429)$$

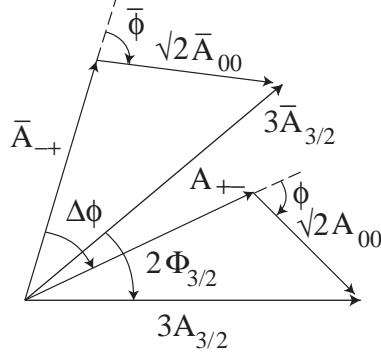


Fig. 90. Geometry for Eq. (426) and its charge-conjugate, using notations  $A_{+-} \equiv A(B^0 \rightarrow K^{*+}\pi^-)$ ,  $A_{00} = A(B^0 \rightarrow K^{*0}\pi^0)$  and similar notations for charge-conjugated modes [1145].

while the nonperturbative QCD effects enter only through a complex parameter

$$r_{3/2} \equiv \frac{(C_1 - C_2)\langle(K^*\pi)_{I=3/2}|\mathcal{O}_1 - \mathcal{O}_2|B^0\rangle}{(C_1 + C_2)\langle(K^*\pi)_{I=3/2}|\mathcal{O}_1 + \mathcal{O}_2|B^0\rangle}. \quad (430)$$

Here  $\mathcal{O}_1 \equiv (\bar{b}s)_{V-A}(\bar{u}u)_{V-A}$  and  $\mathcal{O}_2 \equiv (\bar{b}u)_{V-A}(\bar{u}s)_{V-A}$  are the V-A current-current operators. In naive factorization  $r_{3/2}$  is found to be real and small,  $r_{3/2} \leq 0.05$  [1144]. This is in agreement with the estimate using flavor SU(3) from  $B \rightarrow \rho\pi$ ,  $r_{3/2} = 0.054 \pm 0.045 \pm 0.023$  [1145], where the first error is experimental and the second an estimate of theoretical errors. This then gives the constraint

$$\bar{\eta} = \tan \Phi_{3/2} [\bar{\rho} - 0.24 \pm 0.03]. \quad (431)$$

6862 The phase  $\Phi_{3/2}$  can be determined by measuring the magnitudes and relative phases  
6863 of the  $B^0 \rightarrow K^{*+}\pi^-$ ,  $B^0 \rightarrow K^{*0}\pi^0$  amplitudes and their charge-conjugates. A graph-  
6864 ical representation of the triangle relation Eq. (426) and its charge conjugate is given  
6865 in Fig. 90. The above four magnitudes of amplitudes and the two relative phases,  $\phi \equiv$   
6866  $\arg[A(B^0 \rightarrow K^{*0}\pi^0)/A(B^0 \rightarrow K^{*+}\pi^-)]$  and  $\bar{\phi} \equiv \arg[A(\bar{B}^0 \rightarrow \bar{K}^{*0}\pi^0)/A(\bar{B}^0 \rightarrow K^{*-}\pi^+)]$ ,  
6867 determine the two triangles separately. Their relative orientation is fixed by the phase  
6868 difference  $\Delta\phi \equiv \arg[A(B^0 \rightarrow K^{*+}\pi^-)/A(\bar{B}^0 \rightarrow K^{*-}\pi^+)]$ .

6869 A similar analysis is possible using  $B \rightarrow \rho K$  decays. Although each  $\rho$  meson has only  
6870 a single dipion decay, the relative phase between the amplitudes in Eq. (426) can be  
6871 determined exploiting the fact that the  $K^*\pi$  amplitudes appear in both  $K\pi\pi$  Dalitz  
6872 plots and therefore can be used as a common reference. The same approach could also  
6873 be applied to  $B \rightarrow K^*\rho$  decays.

6874 The  $B^+ \rightarrow K^+\pi^+\pi^-$  Dalitz plot provides the highest signal event yield of the  $K\pi\pi$   
6875 Dalitz plots and so can be used to establish a working isobar model. This informa-  
6876 tion can be used by the other analyses, leading to smaller systematic uncertainties. The  
6877  $K^+\pi^+\pi^-$  Dalitz plot also contains the intermediate state  $\rho^0(770)K^+$ , which is predicted  
6878 to have a large direct  $CP$  asymmetry  $\sim 40\%$ . Measuring this asymmetry, interesting in  
6879 its own right, tells us that the tree and penguin contributions are of similar order and  
6880 that we do indeed have sensitivity to  $\gamma$  in these decays. BaBar [1149] and Belle [1150]  
6881 have recently updated their analyses of this Dalitz plot and both see strong evidence  
6882 of direct  $CP$  violation in  $B^+ \rightarrow \rho^0(770)K^+$ . The results are in excellent agreement

6883 and are summarized in Tab. 78. The signal Dalitz-plot model used in these analyses con-  
6884 tains contributions from  $K^{*0}(892)\pi^+$ ,  $K_0^{*0}(1430)\pi^+$ ,  $\rho^0(770)K^+$ ,  $\omega(782)K^+$ ,  $f_0(980)K^+$ ,  
6885  $f_2(1270)K^+$ ,  $f_X(1300)K^+$ ,  $\chi_{c0}K^+$ , and a nonresonant component; the BaBar model also  
6886 contains  $K_2^{*0}(1430)\pi^+$ . The main difference between the approaches of the two experi-  
6887 ments concerns the nonresonant model. Belle uses two  $e^{-\alpha s}$  distributions, where  $\alpha$  is a  
6888 free parameter, one with  $s = m_{K^+\pi^-}^2$  and one with  $s = m_{\pi^+\pi^-}^2$ . BaBar uses a phase-space  
6889 component in addition to a parametrization of the low-mass  $K^+\pi^-$  S-wave that follows  
6890 that of the LASS experiment [1018].

Table 78

Summary of results for  $A_{CP}$  of  $B^+ \rightarrow \rho^0(770)K^+$ . The uncertainties are statistical, systematic and model-dependent respectively.

Experiment	$A_{CP}(\rho^0(770)K^+)$
BaBar	$(+44 \pm 10 \pm 4_{-13}^{+5})\%$
Belle	$(+41 \pm 10 \pm 3_{-7}^{+3})\%$
HFAG Average	$(+42_{-10}^{+8})\%$

6891 The  $B^0 \rightarrow K_S^0\pi^+\pi^-$  Dalitz plot is an extremely rich physics environment. As well  
6892 as providing measurements of the  $B^0\bar{B}^0$  mixing phase  $2\beta$ , discussed in Sec. 9.2.2, it is  
6893 possible to measure the phase difference  $\Delta\phi$  between  $B^0 \rightarrow K^{*+}\pi^-$  and  $\bar{B}^0 \rightarrow K^{*-}\pi^+$ ,  
6894 one of the crucial ingredients in the determination of  $\gamma$  with the method of Refs. [1144–  
6895 1146]. Both BaBar [1087] and Belle [1091] have performed time-dependent Dalitz-plot  
6896 analyses of this mode. Details of the analyses are discussed in Sec. 9.2.2. Belle find  
6897 two fit solutions that correspond to different interference between the  $K_0^{*+}(1430)$  and  
6898 nonresonant components. These two solutions prefer different values of  $\Delta\phi$ . The results  
6899 for  $\Delta\phi$  are illustrated in Fig. 91 and summarized in Tab. 79. There is some disagreement  
6900 between the BaBar and Belle results. The experimentally measured values of  $\Delta\phi$  include  
6901 the  $B^0\bar{B}^0$  mixing phase since they come from time-dependent analyses. This has to be  
6902 removed before the values can be used in the extraction of  $\gamma$ .

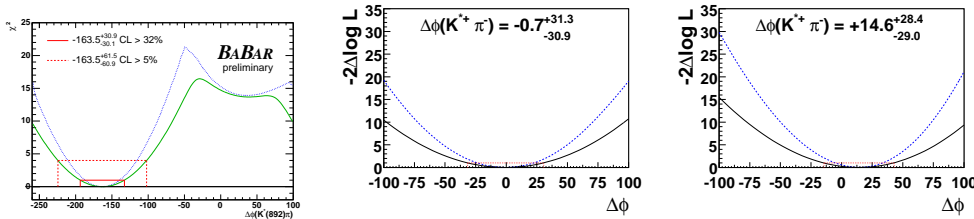


Fig. 91. Likelihood scans of  $\Delta\phi$  from Dalitz-plot analyses of  $B^0 \rightarrow K_S^0\pi^+\pi^-$ . The left plot is from BaBar, the middle and right plots are from Belle and represent the scans of the two different solutions.

6903 The other two parameters required to determine  $\gamma$  are  $\phi$  and  $\bar{\phi}$ . These are the relative  
6904 phases of  $B^0 \rightarrow K^{*+}\pi^-$  and  $B^0 \rightarrow K^{*0}\pi^0$  and  $\bar{B}^0 \rightarrow K^{*-}\pi^+$  and  $\bar{B}^0 \rightarrow \bar{K}^{*0}\pi^0$ ,  
6905 respectively. Both of these quantities can be determined from a time-integrated Dalitz-  
6906 plot analysis of  $B^0 \rightarrow K^+\pi^-\pi^0$  (and its charge conjugate). Such an analysis has not  
6907 yet been performed by Belle but BaBar has published results based on  $232 \times 10^6 B\bar{B}$   
6908 pairs [1151] and has preliminary results based on the full BaBar dataset of  $454 \times 10^6 B\bar{B}$

Table 79

Summary of results for  $\Delta\phi(K^{*+}\pi^-)$  from time-dependent Dalitz-plot analyses of  $B^0 \rightarrow K_S^0\pi^+\pi^-$ . The uncertainties are statistical, systematic and model-dependent respectively.

Experiment	$\Delta\phi(K^{*+}\pi^-)$
BaBar	$(-164 \pm 24 \pm 12 \pm 15)^\circ$
Belle Soln. 1	$(-1^{+24}_{-23} \pm 11 \pm 18)^\circ$
Belle Soln. 2	$(+15^{+19}_{-20} \pm 11 \pm 18)^\circ$

6909 pairs [246]. The published analysis includes contributions from  $\rho^-(770)K^+$ ,  $K^{*+}(892)\pi^-$ ,  
 6910  $K^{*0}(892)\pi^0$ ,  $K_0^{*+}(1430)\pi^-$  and  $K_0^{*0}(1430)\pi^0$ . The higher  $K^*$  resonances are modeled  
 6911 by the LASS parametrization, which also includes a slowly varying nonresonant term.  
 6912 The fit exhibits multiple solutions that are not well separated. This can be seen in the  
 6913 likelihood scans in Fig. 92 and unfortunately leads to a weaker constraint on  $\gamma$ . BaBar's  
 6914 preliminary results on the larger data sample indicate much better separation between  
 6915 solutions, however likelihood scans of  $\phi$  and  $\bar{\phi}$  are not yet completed.

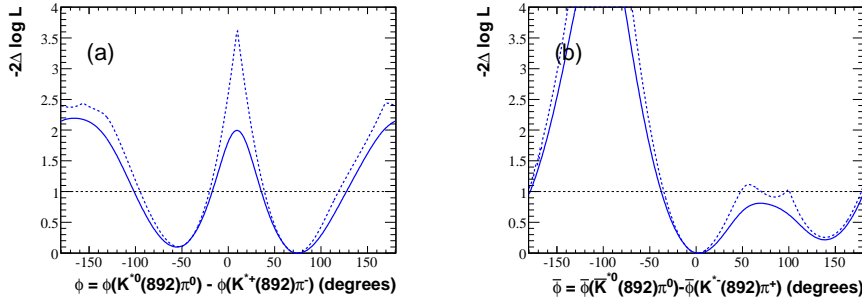


Fig. 92. Likelihood scans of  $\phi$  (left) and  $\bar{\phi}$  (right) from BaBar Dalitz-plot analysis of  $B^0 \rightarrow K^+\pi^-\pi^0$ .

The BaBar results on  $\Delta\phi$  [1087],  $\phi$  and  $\bar{\phi}$  [1151] have been combined [1146] to create a constraint

$$39^\circ < \Phi_{3/2} < 112^\circ \quad (68\%CL), \quad (432)$$

6916 which can be converted to a constraint on the  $\bar{\rho} - \bar{\eta}$  plane, using the relation (431). Both  
 6917 of these constraints are shown in Fig. 93.

## 6918 10. Global Fits to the Unitarity Triangle and Constraints on New Physics

6919 The large variety of precise measurements reported so far can be used to place con-  
 6920 straints on theoretical models of flavor particles and their interactions. The impact of  
 6921 these constraints has been studied using global fits to the predictions of the Standard  
 6922 Model and other theoretical models.

6923 In this section, results of such studies will be presented. First, the results described in  
 6924 this report are interpreted within the Standard Model (Sec. 10.1). Next, Sec. 10.2 sum-  
 6925 marizes the constraints imposed by these measurements on deviations from the Standard  
 6926 Model. Discussions of constraints, first in a model independent approach, then for Grand  
 6927 Unified Theories, and for models with Extra Dimensions conclude the report.

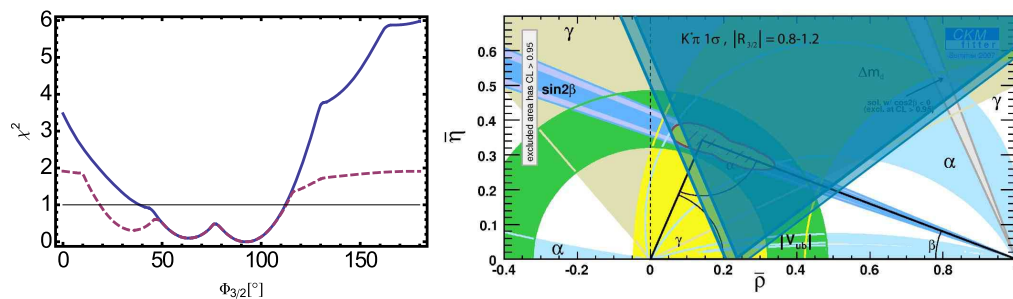


Fig. 93. Constraint on the angle  $\Phi_{3/2}$  (left) from combined information from  $K\pi\pi$  Dalitz plot analyses. The dashed purple line is for the case when  $|R_{3/2}|$  is unconstrained while the solid blue line is for the case when  $0.8 < |R_{3/2}| < 1.2$ . Constraint on the  $\bar{\rho} - \bar{\eta}$  plane (right) from combined information from  $K\pi\pi$  Dalitz plot analyses. The dark shaded region corresponds to the experimental  $1\sigma$  range while the light shaded region includes the theoretical error on the contributions from electroweak penguin processes.

### 6928 10.1. Constraints on the Unitarity Triangle Parameters

6929 The measured quantities reported so far are sensitive to different combinations of the  
 6930 parameters of the CKM matrix (see Sec. 1.1.3 for details). Their relations to the angles  
 6931 and sides of the Unitarity Triangle (UT) place constraints on the coordinates of its apex  
 6932  $(\bar{\rho}, \bar{\eta})$  and thus can be used to test the predictions of the Standard Model or any other  
 6933 theory describing flavor physics. The most powerful way to make such tests is to perform  
 6934 global fits comparing the data to theoretical predictions.

6935 To combine a large number of measurements of different quantities performed with  
 6936 different methods and data samples, widely different in size and composition, and thus  
 6937 with different statistical and systematic errors, not all of them Gaussian in nature, is  
 6938 a non-trivial task. Theoretical predictions have uncertainties that are very difficult to  
 6939 assess and that are usually not expected to adhere to Gaussian distributions. Two groups  
 6940 have independently developed global analysis tools to determine the CKM parameters  
 6941 in the framework of the Standard Model and its extensions. The two approaches differ  
 6942 significantly, in particular in the treatment of uncertainties of data and of the theory  
 6943 predictions. The results of this report have been analyzed by the **UTfit** group. Most  
 6944 of this section therefore discusses their Bayesian approach in detail, the work of the  
 6945 CKMfitter group being summarized for comparison in Sec. 10.1.5.

#### 6946 10.1.1. Fitting technique

6947 The Unitarity Triangle analysis developed by the **UTfit** group relies on the Bayes  
 6948 Theorem. Its specific application is briefly described in the following, more details can  
 6949 be found in elsewhere [1152].

6950 A given constraint  $c_j$  relates the coordinates of the apex of the Unitarity Triangle  
 6951  $(\bar{\rho}, \bar{\eta})$  to quantities that have been experimentally determined or theoretically calculated  
 6952  $(\mathbf{x} = \{x_1, x_2, \dots, x_N\})$ , through functional dependencies that are prescribed by the theory  
 6953 that is being tested,  $c_j = c_j(\bar{\rho}, \bar{\eta}, \mathbf{x})$ .

6954 In the case of perfect knowledge of  $c_j$  and  $x_i$ , each of the constraints would represent a  
 6955 well defined curve in the  $(\bar{\rho}, \bar{\eta})$  plane. In the presence of uncertainties, the constraints are  
 6956 represented by distributions of curves, each weighted according to the probability density

6957 derived from the error distributions. Based on Bayes Theorem, the **UTfit** group derives  
 6958 for  $M$  constraints  $c_j$  and  $N$  free parameters  $x_i$ , a *pdf* or probability density function,

$$f(\bar{\rho}, \bar{\eta}, \mathbf{x} | \hat{c}_1, \dots, \hat{c}_M) \propto \prod_{j=1, M} f_j(\hat{c}_j | \bar{\rho}, \bar{\eta}, \mathbf{x}) \times \prod_{i=1, N} f_i(x_i) \times f_o(\bar{\rho}, \bar{\eta}). \quad (433)$$

By integrating Eq. (433) over  $\mathbf{x}$ , one obtains,

$$f(\bar{\rho}, \bar{\eta} | \hat{\mathbf{c}}, \mathbf{f}) \propto \mathcal{L}(\hat{\mathbf{c}} | \bar{\rho}, \bar{\eta}, \mathbf{f}) \times f_o(\bar{\rho}, \bar{\eta}), \quad (434)$$

where  $\hat{\mathbf{c}}$  stands for the set of measured constraints, and

$$\mathcal{L}(\hat{\mathbf{c}} | \bar{\rho}, \bar{\eta}, \mathbf{f}) = \int \prod_{j=1, M} f_j(\hat{c}_j | \bar{\rho}, \bar{\eta}, \mathbf{x}) \prod_{i=1, N} f_i(x_i) dx_i \quad (435)$$

is the effective overall likelihood function which takes into account all possible values of  $x_j$  and their weights based on their associated error distributions. This expression underlines the dependence of the likelihood on the best knowledge of all  $x_i$ , described by  $f(\mathbf{x})$ . Assuming a flat *a priori* distribution for  $\bar{\rho}$  and  $\bar{\eta}$ , *i.e.* all values are equally likely, the final (unnormalized) *pdf* is,

$$f(\bar{\rho}, \bar{\eta}) \propto \int \prod_{j=1, M} f_j(\hat{c}_j | \bar{\rho}, \bar{\eta}, \mathbf{x}) \prod_{i=1, N} f_i(x_i) dx_i. \quad (436)$$

6959 The integration is done by Monte Carlo methods, in which a large sample is extracted  
 6960 for the free parameters and a weight is assigned for each extraction. In this way an  
 6961 *a posteriori pdf* for each parameter is obtained, generally different from the *a priori* one,  
 6962 because of the weighting procedure. The result of each extraction is considered more or  
 6963 less likely, depending on the agreement of the corresponding measured quantities with the  
 6964 actual experimental results or theoretical calculation. The **UTfit** group treats theoretical  
 6965 and experimental parameters in a uniform way, adopting the error distributions, Gaussian  
 6966 or non-Gaussian, directly as *a priori* probability density functions.

6967 The *a posteriori pdfs* depend by construction on the choice of the *a priori* ones, which  
 6968 are based on - to a certain degree subjective - assessments of systematic uncertainties,  
 6969 experimental and theoretical, on theoretical approximations and assumptions. In many  
 6970 Unitarity Triangle analyses, the precise and abundant measurements and theoretical  
 6971 inputs represent very stringent constraints and the results are not very sensitive to the  
 6972 particular choice of the *a priori* distributions for the parameters. If this is not the case,  
 6973 an assessment of the sensitivity of the result to variations of the prior is required.

6974 As part of the **UTfit** analysis, the agreement of the measured quantities is quantified in  
 6975 the so-called *compatibility plots* [1153]. An indirect determination of a particular quantity  
 6976 is obtained from a global fit including all the available constraints, except those from  
 6977 the direct measurement of the quantity of interest. This indirectly determined value  
 6978 represents the prediction by the Standard Model or any other theory from which the  
 6979 constraints are derived. The comparison of the prediction and the direct measurement,  
 6980 including their respective uncertainties, can be used to assess the compatibility with the  
 6981 underlying theoretical calculations or model.

6982 Specifically, if  $f(x_{th})$  and  $f(x_{fit})$  are the *pdfs* for the predicted and the measured  
 6983 values, respectively, their compatibility is evaluated by constructing the *pdf* for the dif-  
 6984 ference,  $x_{th} - x_{fit}$ , and by estimating the distance of its most probable value from zero,



6985 in units of standard deviations. In the *compatibility plots*, contours of constant distance  
6986 are shown in two dimensions,  $\sigma(x_{fit})$  versus  $\bar{x}_{fit}$ . The compatibility between  $x_{th}$  and  
6987  $x_{fit}$  can be directly estimated, for any central value and error on  $x_{fit}$ . In this way, the  
6988 compatibility of constraints with the measurements is simply assessed by comparing two  
6989 different *pdfs*, without any assumption about their shapes. Examples of *compatibility*  
6990 *plots* are shown in section 10.1.3.

### 6991 10.1.2. Inputs to the Unitarity Triangle Analysis

6992 Not all measurements have sensitivity to the Unitarity Triangle parameters and there  
6993 are determinations of the same observable that are equivalent but not identical. A choice  
6994 has to be made. The best selection of experimental results discussed in this report has  
6995 been used as input to the CKM analysis using UT fits. They are summarized in Tab. 80.  
The set of lattice inputs (see Ref. [881] for details) chosen for UT fits is summarized in

Table 80

Most relevant experimental inputs to the UT fits. Internal references with the details of the choice of the inputs are also included.

Input	Source	Value	Reference
$ V_{ud} $	Nuclear decays	$0.97425 \pm 0.00022$	Eq. 117
$ V_{us} $	SL Kaon decays	$0.2259 \pm 0.0009$	Eq. 178
$ V_{cb} _{incl.}$	SL charmed $B$ decays	$(41.54 \pm 0.73) \times 10^{-3}$	Eq. 265
$ V_{cb} _{excl.}$	SL charmed $B$ decays	$(38.6 \pm 1.1) \times 10^{-3}$	Eq. 259
$ V_{ub} _{incl.}$	SL charmless $B$ decays	$(4.11^{+0.27}_{-0.28}) \times 10^{-3}$	Eq. 280
$ V_{ub} _{excl.}$	SL charmless $B$ decays	$(3.38 \pm 0.36) \times 10^{-3}$	Eq. 229
$\mathcal{B}(B^+ \rightarrow \tau^+ \nu)$	Leptonic $B$ decays	$(1.51 \pm 0.33) \times 10^{-4}$	Tab. 44
$\Delta m_d$	$B_d \bar{B}_d$ mixing	$(0.507 \pm 0.005) \text{ ps}^{-1}$	Fig. 58
$\Delta m_s$	$B_s \bar{B}_s$ mixing	$(17.77 \pm 0.12) \text{ ps}^{-1}$	Sec. 7.2.2
$ \epsilon_K $	$K \bar{K}$ mixing	$(2.229 \pm 0.012) \times 10^{-3}$	Eq. 341
$\sin 2\beta$	Charmonium $B$ decays	$0.671 \pm 0.023$	Fig. 59
$\mathcal{B}$ & $CP$ parameters	$B \rightarrow \pi\pi, \rho\rho, \rho\pi$ decays		Sec. 9
$(x^\pm, y^\pm), \mathcal{B}$ & $A$	$B \rightarrow D^{(*)0} K^{(*)\pm}$ (GGSZ, GLW, ADS)		Sec. 8

6996

6997 Tab. 81.

Table 81

Phenomenological inputs obtained from Lattice QCD calculations

Input	Value
$f_{B_s}$ (MeV)	$245 \pm 25$
$\hat{B}_{B_s}$	$1.22 \pm 0.12$
$f_{B_s}/f_{B_d}$	$1.21 \pm 0.04$
$\hat{B}_{B_s}/\hat{B}_{B_d}$	$1.00 \pm 0.03$
$B_K$	$0.75 \pm 0.07$

6998 10.1.3. *Results of Global Fits*

6999 Figure 94 displays the results of the global fit in the  $(\bar{\rho}, \bar{\eta})$  plane. A summary of the  
 7000 fitted parameters of the CKM matrix (see Sec. 1 for definitions) is presented in Table 82.

The global fits also result in improved determinations of the measured quantities, the

Table 82

Results of the global fit for the parameters of the CKM matrix. Parameters obtained with the CKMfitter approach (see Sec. 10.1.5) are also shown for comparison.

Parameter	Result	CKMfitter
$\bar{\rho}$	$0.158 \pm 0.021$	$0.139^{+0.025}_{-0.027}$
$\bar{\eta}$	$0.343 \pm 0.013$	$0.341^{+0.016}_{-0.015}$
$A$	$0.802 \pm 0.015$	$0.812^{+0.010}_{-0.024}$
$\lambda$	$0.2259 \pm 0.0016$	$0.2252 \pm 0.0008$

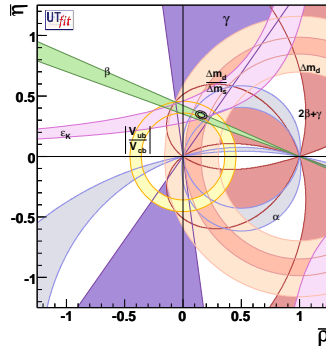


Fig. 94. Individual and global constraints in the  $(\bar{\rho}, \bar{\eta})$  plane from the global UT fits. The shaded areas indicate the individual constraints at 95% CL. The contours of the overall constraints defining the apex of the UT triangle correspond to 68% and 95% C.L. .

7001

angles and sides of the Unitarity Triangle which are listed in Tab. 83.

Table 83

Improved measurements of angles and sides of the Unitarity Triangle obtained from the global fits. Results obtained with the CKMfitter approach (see Sec. 10.1.5) are also shown for comparison.

Parameter	Results	CKMfitter
$\alpha(^{\circ})$	$92.6 \pm 3.2$	$90.6^{+3.8}_{-4.2}$
$\sin 2\beta$	$0.698 \pm 0.019$	$0.684^{+0.023}_{-0.021}$
$\gamma(^{\circ})$	$65.4 \pm 3.1$	$67.8^{+4.2}_{-3.9}$
$ V_{ub} $	$0.00359 \pm 0.0012$	$0.00350^{+0.00015}_{-0.00014}$
$ V_{cb} $	$0.0409 \pm 0.0005$	$0.04117^{+0.00038}_{-0.00115}$
$ V_{td} $	$0.00842 \pm 0.00021$	$0.00859^{+0.00027}_{-0.00029}$

7002

7003

7004

The increasing precision of the measurements and of the theoretical calculations have significantly improved the knowledge of the allowed region for the apex position  $(\bar{\rho}, \bar{\eta})$ .

7005 Good overall consistency between the various measurements at 95 % C.L. is observed,  
 7006 thus establishing the CKM mechanism as the dominant source of CP violation in  $B$ -  
 7007 meson decays.

7008 Furthermore, measurements of  $CP$ -violating quantities from the  $B$ -factories are now  
 7009 so abundant and precise that the CKM parameters can be constrained by the angles of  
 7010 the Unitarity Triangle alone, as shown in Fig. 95. In addition,  $(\bar{\rho}, \bar{\eta})$  can be determined  
 7011 independently using experimental information from  $CP$ -conserving processes,  $|V_{ub}|/|V_{cb}|$   
 7012 from semileptonic  $B$  decays,  $\Delta m_d$  and  $\Delta m_s$  from the  $B_d - \bar{B}_d$  and  $B_s - \bar{B}_s$  oscillations)  
 7013 and the direct  $CP$  violation measurements in the Kaon sector,  $\epsilon_K$  (see Fig. 95). Prior  
 7014 to the precise *BABAR* and Belle measurements this was the strategy used to predict the  
 7015 value of  $\sin 2\beta$  [1154].

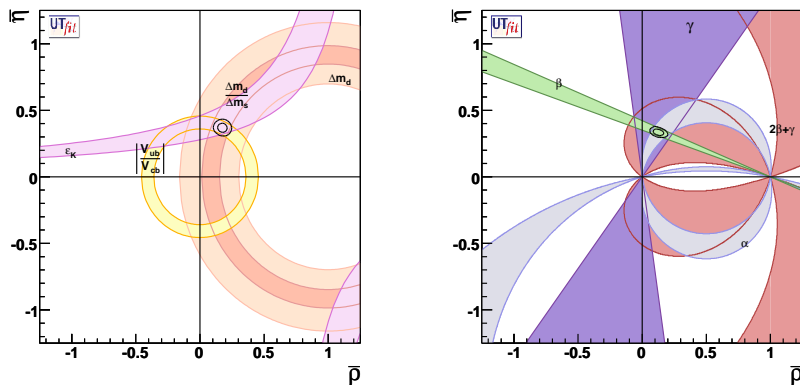


Fig. 95. Allowed regions for  $(\bar{\rho}, \bar{\eta})$ , as constrained by the measurement of  $|V_{ub}|/|V_{cb}|$ ,  $\Delta m_d$ ,  $\Delta m_s$  and  $\epsilon_K$  (left) and of the angles  $\alpha$ ,  $\sin 2\beta$ ,  $\gamma$ ,  $2\beta + \gamma$ ,  $\beta$  and  $\cos 2\beta$  (right). The closed contours indicate the regions of 68% and 95% C.L. for the triangle apex, while the colored zones mark the 95% C.L. for each constraint.

7016 Although the global fits show very good agreement overall, there are some measure-  
 7017 ments for which the agreement is less convincing. As described in Sec. 10.1.1, *UTfit* quan-  
 7018 tifies the overall agreement of individual measurements with predictions of the global fit  
 7019 by means of *compatibility plots*. Such plots for  $\alpha$ ,  $\sin 2\beta$ ,  $\gamma$  and  $\Delta m_s$  are shown in Fig.  
 7020 96. The direct measurements for  $\alpha$  and  $\Delta m_s$  are in excellent agreement with the indirect  
 7021 determination from the global fits, although for  $\Delta m_s$  the effectiveness of the comparison  
 7022 is limited by the precision on the theoretical inputs, resulting in sizable uncertainties  
 7023 (compared to the experimental one) for the prediction extracted from the fit. The direct  
 7024 measurement of  $\gamma$  yields a slightly higher value of  $(78 \pm 12)^\circ$  than the indirect one from  
 7025 the overall fit,  $(65 \pm 3)^\circ$ , though they are compatible within  $1\sigma$ . The measurement of  
 7026  $\sin 2\beta$  based on the  $CP$  asymmetry in  $B^0 \rightarrow J/\psi K^0$  is slightly shifted with respect to  
 7027 the indirect determination, but compatible to within  $2\sigma$ .

7028 It has been observed for several years that the direct measurement of  $\sin 2\beta$  favors a  
 7029 value of  $|V_{ub}|$  that is more compatible with the direct determination of  $|V_{ub}|$  based on  
 7030 exclusive rather than inclusive charmless semileptonic decays. The problem is illustrated  
 7031 in Fig. 97 and reflects the great challenge that the extraction of  $|V_{ub}|$  from charmless  
 7032 semileptonic decays represents. Experimentally, these charmless decays are impacted by

7033 very large backgrounds which are difficult to understand in detail and difficult to suppress  
7034 due to the presence of a neutrino in the final state. Theoretically, the required normal-  
7035 ization and corrections for hadronic effects based on QCD calculations are dominating  
7036 the uncertainties. The QCD calculations and models are different for the two processes  
7037 and their uncertainties are impacted by the selection of the experimental data. While  
7038 there are now several calculations available, it remains very difficult to assess the overall  
7039 theoretical uncertainties for the extraction of  $|V_{ub}|$ . The fact that the current values of  
7040  $|V_{ub}|$  from exclusive and inclusive decays are only marginally consistent could be taken  
7041 as an indication that the uncertainties are larger than stated.

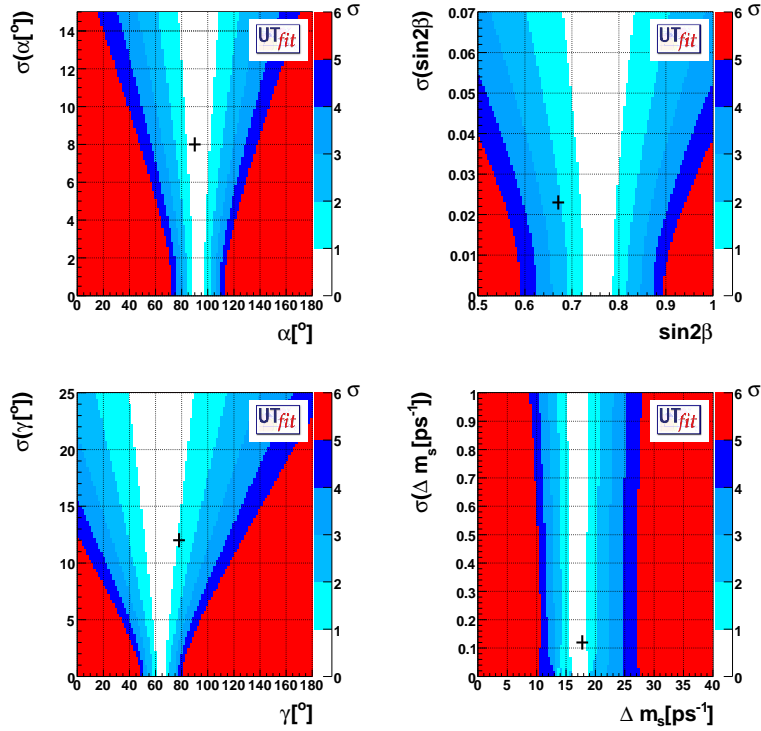


Fig. 96. Compatibility plots for  $\alpha$ ,  $\sin 2\beta$   $\sin 2\beta$  from the measurement of the  $CP$  asymmetry in  $B^0 \rightarrow J/\psi K^0$ ,  $\gamma$  and  $\Delta m_s$ . The color code indicates the compatibility between direct and indirect determinations, given in terms of standard deviations, as a function of the measured value and the experimental uncertainty. The crosses indicate the world averages and errors of the direct measurements.

7042 Given the present experimental measurements, no significant deviation from the CKM  
7043 picture has been observed. Of course, this statement does not apply to observables that  
7044 have no or very small impact on  $\bar{\rho}$  and  $\bar{\eta}$  (for instance the  $B_s$  mixing phase).

#### 7045 10.1.4. Impact of the Uncertainties on Theoretical Quantities

7046 Given the abundance of constraints now available for the determination of the UT  
7047 Triangle,  $\bar{\rho}$  and  $\bar{\eta}$ , one can perform the global fit without the hadronic parameters derived

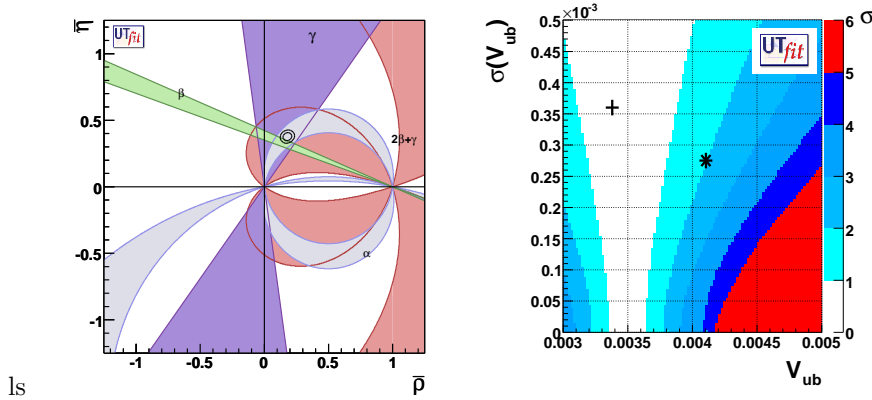


Fig. 97. Left: Allowed regions for  $\bar{\rho}$  and  $\bar{\eta}$  obtained by using the measurements of  $|V_{ub}|/|V_{cb}|$ ,  $\Delta m_d$ ,  $\Delta m_s$ ,  $\epsilon_K$ . The colored zones indicate the 68% and 95% probability regions for the angle measurements, which are not included in the fit. Right: Compatibility plot for  $V_{ub}$ . The cross and the star indicate the exclusive and inclusive measurements, respectively.

7048 from lattice calculations as input. In this way, one can quantify the impact that future  
 7049 improvements in the lattice QCD calculation will have on the UT analysis.

7050 Figure 98, shows the 68% and 95% probability regions for different lattice quanti-  
 7051 ties, obtained from a UT fit using the measurements of angles and the constraints from  
 7052 semileptonic  $B$  decays. The relations between observables and theoretical quantities used  
 7053 in this fit are obtained assuming the validity of the SM. Numerical results are given in  
 7054 Table 84.

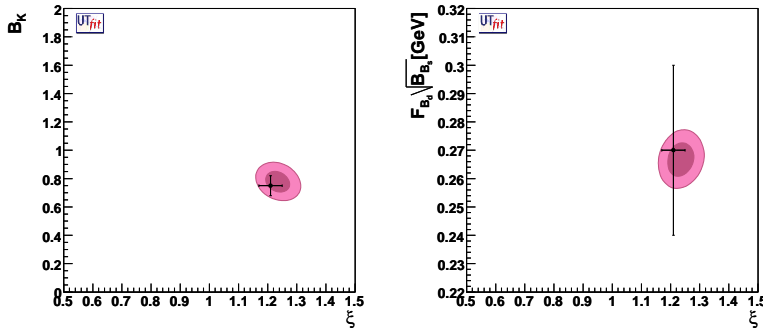


Fig. 98. Comparison of the current lattice calculations (data points) with prediction of the global fit, left:  $\xi$  versus  $B_K$  and right:  $f_{B_s} \sqrt{B_{B_s}}$  versus  $\xi$ . The dark and light colored areas show the 68% and 95% probability regions.

### 7055 10.1.5. Comparison with the Results of CKMfitter

7056 Extracting Standard Model best values of parameters from the very large number of  
 7057 different measurements is difficult. It is not trivial to combine measurements with very  
 7058 different statistical errors and extract the best the information. However, it is much more

Table 84

The values obtained for the theoretical parameters from a UT analysis using the angles and  $V_{ub}/V_{cb}$  measurements are compared with the results of lattice calculations.

Parameter	UT (angles+ $V_{ub}/V_{cb}$ )	Lattice QCD results
$B_K$	$0.78 \pm 0.05$	$0.75 \pm 0.07$
$f_{B_s} \sqrt{B_{B_s}}$ [MeV]	$266.8 \pm 4.1$	$270 \pm 30$
$\xi = \frac{f_{B_s} \sqrt{B_{B_s}}}{f_{B_d} \sqrt{B_{B_d}}}$	$1.23 \pm 0.03$	$1.21 \pm 0.04$
$f_{B_d}$ [MeV]	$195 \pm 11$	$200 \pm 20$

7059 difficult to combine measurements with widely different sources and estimations of the  
7060 systematic errors, in many cases there is need for case-to-case judgment and margin for  
7061 interpretation.

7062 For these reasons, it has been extremely important to have more than one approach  
7063 to fits of the UT Triangle. In this section the results obtained by the **UTfit** group  
7064 are compared with the most recent results of the CKMfitter group as summarized in  
7065 <http://ckmfitter.in2p3.fr/>. The inputs to the two fitting methods are different, and the  
7066 choice of the lattice parameters differs and experimental inputs are taken from a slightly  
7067 different sets of measurements, some of them taken from earlier publications. Nonetheless,  
7068 the comparison is important, because it shows that different approaches lead to somewhat  
7069 different results.

#### 7070 Statistical method

7071 The CKMfitter was developed in parallel to **UTfit** to perform global UT analyses. The  
7072 most significant difference to the **UTfit** approach is the treatment of non-Gaussian errors.  
7073 In particular, the CKMfitter group introduced *RangeFit* [954], a special procedure to  
7074 deal with uncertainties of theoretical predictions.

7075 The CKMfitter method is described briefly as follows. The experimental input is a set of  
7076  $N_{exp}$  measurements,  $\mathbf{x}_{exp}$ , related to a set of theoretical expressions or constraints,  $\mathbf{x}_{theo}$ .  
7077 The theoretical expressions are model-dependent functions of  $N_{mod}$  parameters  $\mathbf{y}_{mod}$ .  
7078 A subset of  $N_{theo}$  parameters in  $\mathbf{y}_{mod}$  are considered fundamental and free parameters  
7079 of the theory, *e.g.* the four Wolfenstein parameters in the SM or the top quark mass.  
7080 These parameters are denoted as  $\mathbf{y}_{theo}$ . The remaining  $N_{QCD} = N_{mod} - N_{theo}$  input  
7081 parameters, which currently are less well known due to the difficulty of computing strong  
7082 interaction effects, *e.g.*  $f_{b_d}$ ,  $B_d$ ,... are denoted as  $\mathbf{y}_{QCD}$ .

7083 The fit is set up to minimize the quantity,  $\chi^2 = -2 \ln \mathcal{L}(\mathbf{y}_{mod})$ , with the likelihood  
7084 function  $\mathcal{L}(\mathbf{y}_{mod})$ , defined as a product two types of contributions,

$$\mathcal{L}(\mathbf{y}_{mod}) = \mathcal{L}_{exp}(\mathbf{x}_{exp} - \mathbf{x}_{theo}(\mathbf{y}_{mod})) \times \mathcal{L}_{theo}(\mathbf{y}_{QCD}). \quad (437)$$

7085  $\mathcal{L}_{exp}$  depends on the experimental measurements  $\mathbf{x}_{exp}$ , with errors that are Gaussian  
7086 distributed in general (and correlations, if known, are taken into account), and their  
7087 theoretical predictions  $\mathbf{x}_{theo}$ , which are functions of the model parameters  $\mathbf{y}_{mod}$ . In the  
7088 case of a non-Gaussian experimental errors, the exact description of the associated like-  
7089 lihood is used in the fit.  $\mathcal{L}_{theo}$  describes the imperfect knowledge of the QCD parameters  
7090  $\mathbf{y}_{QCD} \in \mathbf{y}_{mod}$ , where the theoretical uncertainties  $\sigma_{syst}$  are considered to be bound by  
7091 a range,  $[\mathbf{y}_{QCD} - \sigma_{syst}, \mathbf{y}_{QCD} + \sigma_{syst}]$ . In *RangeFit* the theoretical likelihood functions  
7092  $\mathcal{L}_{theo}(i)$  do not contribute to the  $\chi^2$  of the fit, as long as the  $\mathbf{y}_{QCD}$  values are within

7093 their range. With these constraints, all results should be understood as valid only if the  
7094 allowed ranges contain the true values of the  $\mathbf{y}_{mod}$ .

7095 The minimization is performed in two steps. First, the global minimum,  $\chi_{min,global}^2$ ,  
7096 is determined with respect to all  $N_{mod}$  parameters. Due to the systematic uncertainties  
7097 from experiment and theory, this minimum does in general not correspond to a unique  
7098  $\mathbf{y}_{mod}$ . Second, a selected subspace of the parameter space, *e.g.*  $a = (\bar{\rho}, \bar{\eta})$  is scanned,  
7099 to determine the local minimum  $\chi^2$ ,  $\chi_{min,local}^2(a)$ , for each fixed point on a grid in the  
7100 parameter space  $a$ , with respect to the remaining parameters. The offset-corrected  $\chi^2$  is  
7101 calculated as,  $\Delta\chi^2(a) = \chi_{min,local}^2(a) - \chi_{min,global}^2$ , where its minimum is equal to zero  
7102 by construction.

Finally, a confidence level (C.L.) for  $a$  is obtained, assuming Gaussian distributions,  
by using the cumulative  $\chi^2$  distribution:

$$1 - \text{CL} = \text{Prob}(\Delta\chi^2(a), N_{dof}) \quad (438)$$

$$= \frac{1}{\sqrt{2^{N_{dof}} \Gamma(N_{dof}/2)}} \int_{\chi^2(y_{mod})}^{\infty} e^{-t/2} t^{N_{dof}/2-1} dt. \quad (439)$$

### 7103 Inputs

7104 The inputs to the fits performed by the CKMfitter group differ slightly from the results  
7105 of this report and different choices of parameters estimated with lattice QCD calculations  
7106 have been made. The latter difference is mostly due to the difference in the treatment of  
7107 systematic errors. These differences are presented in Tables 85 and 86 to be compared  
with Tables 80 and 81. Identical input values are not included in these tables. The

Table 85

Most relevant experimental inputs used by CKMfitter for the global UT fit that are different from  
those used by UT fit. The numbers marked in bold are theoretical uncertainties treated using Rfit (flat  
likelihood).

Input	Source	Value	Reference
$ V_{ud} $	Nuclear decays	$0.97418 \pm 0.00026$	[273]
$ V_{us} $	SL Kaon decays	$0.2246 \pm 0.0012$	[344]
$ V_{cb} $	SL charmed $B$ decays	$(40.59 \pm 0.38 \pm \mathbf{0.58}) \times 10^{-3}$	[558] <sup>31</sup>
$ V_{ub} $	SL charmless $B$ decays	$(3.87 \pm 0.09 \pm \mathbf{0.46}) \times 10^{-3}$	[558]
$\mathcal{B}(B^+ \rightarrow \tau^+ \nu)$	Leptonic $B$ decays	$(1.73 \pm 0.35) \times 10^{-4}$	Tab. 44 combined with [1155]

Table 86

Phenomenological inputs from Lattice QCD calculations as adopted by the CKMfitter group. The errors  
treated according to the Rfit (see text) prescription are highlighted in bold.

$f_{B_s}$ (MeV)	$228 \pm 3 \pm \mathbf{17}$
$\hat{B}_{B_s}$	$1.196 \pm 0.008 \pm \mathbf{0.023}$
$f_{B_s}/f_{B_d}$	$1.23 \pm 0.03 \pm \mathbf{0.05}$
$\hat{B}_{B_s}/\hat{B}_{B_d}$	$1.05 \pm 0.02 \pm \mathbf{0.05}$
$B_K$	$0.721 \pm 0.005 \pm \mathbf{0.040}$

7108

7109 sources of the experimental inputs are given in Tables 85, the different choices of lattice  
7110 parameter are justified in the following.

7111 First of all, only unquenched lattice calculations with 2 or 2+1 dynamical fermions,  
 7112 published in journals or proceedings are taken into account. The Gaussian and flat com-  
 7113 ponents of the errors are separated and the latter is treated according to *Rfit* prescrip-  
 7114 tion [954].

7115 The Gaussian errors comprise purely statistical errors as well as systematic uncertain-  
 7116 ties that are expected to also have normal error distributions (*e.g.* interpolation errors).  
 7117 The remaining systematic uncertainties are handled as *Rfit* errors. If there are several  
 7118 error sources in the *Rfit* category, they are added linearly.

7119 If *Rfit* is taken *stricto sensu* and the individual likelihood functions are combined by  
 7120 multiplication, the resulting overall uncertainty might be underestimated. This effect is  
 7121 corrected for by adopting the following procedure: first, the likelihood functions for the  
 7122 Gaussian uncertainties are combined; next this combination is assigned the smallest of the  
 7123 individual *Rfit* errors. The underlying idea is as follows: The estimated error should not  
 7124 be smaller than the best of all estimates, but this best estimate should not be impacted  
 7125 by less precise methods, as would be the case if one took the dispersion of the individual  
 7126 central values as a guess of the combined theoretical uncertainty. All this underlines the  
 7127 fact that theoretical uncertainties are often ill-defined, and procedures to combine such  
 7128 errors should be judged critically. The CKMfitter approach is only one among several  
 7129 the alternatives that can be found in the literature.

### 7130 Results of CKM Fitter

7131 Figure 99 displays the result of global fits performed with the CKMfitter, together  
 7132 with the 96% C.L. contours of the individual constraints. For comparison with UT fit,  
 7133 the results are listed in Tables 82 and 83). The two global fit procedures give comparable  
 7134 results, although they arrive at somewhat different contours for the individual constraints.  
 7135 The results are an excellent proof of robustness of the fit methods, indicating that at  
 7136 present precision the different choices for the treatment of errors do not impact the  
 7137 conclusions significantly.

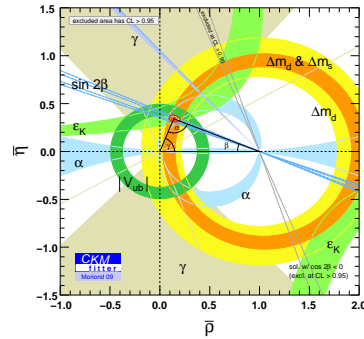


Fig. 99. Individual and global constraints in the  $(\bar{\rho}, \bar{\eta})$  plane obtained by the CKMfitter group. The shaded areas indicate the individual constraints at 95% CL. The contours of the overall constraints defining the apex of the UT triangle correspond to 68% and 95% C.L. .



## 7139 10.2.1. Model independent constraints on New Physics from global fits

The Standard Model (SM) of electroweak and strong interactions works beautifully up to the highest energies presently explored at colliders. However, there are several indications that it must be embedded as an effective theory into a more complete model that should, among other things, contain gravity, allow for gauge coupling unification and provide a dark matter candidate and an efficient mechanism for baryogenesis. As discussed in Sec. 2.5, this effective theory can be described by a Lagrangian of the form

$$\mathcal{L}(M_W) = \Lambda^2 H^\dagger H + \mathcal{L}_{\text{SM}} + \frac{1}{\Lambda} \mathcal{L}^5 + \frac{1}{\Lambda^2} \mathcal{L}^6 + \dots,$$

7140 where the logarithmic dependence on the cutoff  $\Lambda$  has been neglected. Barring the possi-  
7141 bility of a conspiracy between physics at scales below and above  $\Lambda$  to give an electroweak  
7142 symmetry breaking scale  $M_w \ll \Lambda$ , we assume that the cutoff lies close to  $M_w$ . Then the  
7143 power suppression of higher dimensional operators is not too severe for  $\mathcal{L}^{5,6}$  to produce  
7144 sizable effects in low-energy processes, provided that they do not compete with tree-level  
7145 SM contributions. Therefore, we should look for new physics effects in quantities that are  
7146 zero at the tree level in the SM and are finite and calculable at the quantum level. Within  
7147 the SM, such quantities fall in two categories: i) electroweak precision observables (pro-  
7148 tected by the electroweak symmetry) and ii) Flavor Changing Neutral Currents (FCNC)  
7149 (protected by the GIM mechanism). In the SM, all FCNC and CP violating processes  
7150 are computable in terms of quark masses and of the elements of the Cabibbo-Kobayashi-  
7151 Maskawa (CKM) matrix [1, 2]. This implies very strong correlations among observables  
7152 in the flavor sector. NP contributions, or equivalently the operators in  $\mathcal{L}^{5,6}$ , violate in  
7153 general these correlations, so that NP can be strongly constrained by combining all the  
7154 available experimental information on flavor and CP violation.

7155 A very useful tool to combine the available experimental data in the quark sector is  
7156 the Unitarity Triangle (UT) analysis [954, 1153]. Thanks to the measurements of the  
7157 Unitarity Triangle (UT) angles recently performed at  $B$  factories, the UT fit is over-  
7158 constrained. Therefore, it has become possible to add NP contributions to all quantities  
7159 entering the UT analysis and to perform a combined fit of both NP and SM parameters.  
7160 In general, NP models introduce a large number of new parameters: flavor changing  
7161 couplings, short distance coefficients and matrix elements of new local operators. The  
7162 specific list and the actual values of these parameters can only be determined within a  
7163 given model. Nevertheless, each of the meson-antimeson mixing processes is described by  
7164 a single amplitude and can be parametrized, without loss of generality, in terms of two  
7165 parameters, which quantify the difference between the full amplitude and the SM one.  
7166 Thus, for instance, in the case of  $B_q^0 - \bar{B}_q^0$  mixing we define [36]:

$$C_{B_q} e^{2i\phi_{B_q}} = \frac{\langle B_q^0 | H_{\text{eff}}^{\text{full}} | \bar{B}_q^0 \rangle}{\langle B_q^0 | H_{\text{eff}}^{\text{SM}} | \bar{B}_q^0 \rangle}; \quad C_{\Delta m_K} = \frac{\text{Re}[\langle K^0 | H_{\text{eff}}^{\text{full}} | \bar{K}^0 \rangle]}{\text{Re}[\langle K^0 | H_{\text{eff}}^{\text{SM}} | \bar{K}^0 \rangle]}; \quad C_{\epsilon_K} = \frac{\text{Im}[\langle K^0 | H_{\text{eff}}^{\text{full}} | \bar{K}^0 \rangle]}{\text{Im}[\langle K^0 | H_{\text{eff}}^{\text{SM}} | \bar{K}^0 \rangle]} \quad (440)$$

7167 where  $q = d, s$ ,  $H_{\text{eff}}^{\text{SM}}$  includes only the SM box diagrams, while  $H_{\text{eff}}^{\text{full}}$  includes also the NP  
7168 contributions. For the  $K^0 - \bar{K}^0$  mixing, we find it convenient to introduce two parameters  
7169 related to the real and imaginary parts of the total amplitude to the SM one. In summary,

7170 all NP effects in  $\Delta F = 2$  transitions are parametrized in terms of six real quantities,  $C_{\epsilon_K}$ ,  
 7171  $C_{\Delta m_K}$ ,  $C_{B_d}$ ,  $\phi_{B_d}$ ,  $C_{B_s}$  and  $\phi_{B_s}$  [1152].

7172 To further improve the NP parameter determination in the  $B_s$  sector, mainly uncon-  
 7173 strained in the classical UT analysis, we include in the NP fit recent results from the  
 7174 Tevatron. We use the following experimental inputs: the semileptonic asymmetry in  $B_s$   
 7175 decays  $A_{SL}^s$ , the dimuon charge asymmetry  $A_{SL}^{\mu\mu}$  from CDF and D0, the measurement  
 7176 of the  $B_s$  lifetime from flavor-specific final states, and the two-dimensional likelihood  
 7177 ratio for  $\Delta\Gamma_s$  and  $\phi_s = 2(\beta_s - \phi_{B_s})$  from the time-dependent tagged angular analysis of  
 7178  $B_s \rightarrow J/\psi\phi$  decays by CDF and D0<sup>32</sup>. The new input parameters used in our analysis  
 7179 are given in Ref. [36] and continuously updated in [1156]. The relevant NLO formulas for  
 7180  $\Delta\Gamma_s$  and for the semileptonic asymmetries in the presence of NP have been discussed in  
 7181 Refs. [36, 1157, 1158].

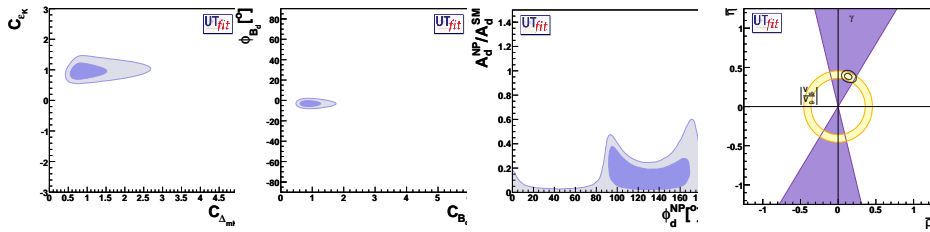


Fig. 100. From left to right,  $C_{\epsilon_K}$  vs.  $C_{\Delta m_K}$ ,  $\phi_{B_d}$  vs.  $C_{B_d}$ ,  $(A_{NP}/A_{SM})$  vs.  $\phi_{NP}$  for NP in the  $B_d$  sector and the resulting selected region on the  $\bar{\rho} - \bar{\eta}$  plane obtained from the NP analysis [36].

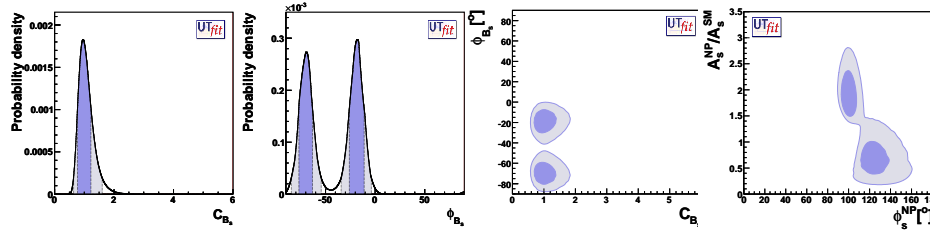


Fig. 101. From left to right, p.d.f.'s for  $C_{B_s}$ ,  $\phi_{B_s}$ ,  $\phi_{B_s}$  vs.  $C_{B_s}$  and  $(A_{NP}/A_{SM})$  vs.  $\phi_{NP}$  for NP in the  $B_s$  sector [1159].

7182 We also include in the fit NP effects in  $\Delta B = 1$  transitions that can also affect some  
 7183 of the measurements entering the UT analysis, in particular the measurements of  $\alpha$ ,  $A_{SL}$   
 7184 and  $\Delta\Gamma_s$  [36, 1157, 1158].

7185 The results obtained in a global fit for the six NP parameters are shown in Fig. 100,  
 7186 together with the corresponding regions in the  $\bar{\rho} - \bar{\eta}$  plane. More details on the analysis  
 7187 can be found in Ref. [1158] (see Ref. [954, 1157] for previous analyses).

7188 Writing  $C_{B_q} e^{2i\phi_{B_q}} = (A_{SM} e^{2i\beta_q} + A_{NP} e^{2i(\beta_q + \phi_{NP})}) / (A_{SM} e^{2i\beta_q})$  and given the p.d.f. for  
 7189  $C_{B_q}$  and  $\phi_{B_q}$ , we can derive the p.d.f. in the  $(A_{NP}/A_{SM})$  vs.  $\phi_{NP}$  plane as seen in Fig. 100.

<sup>32</sup>We use the latest D0 results without assumptions on the strong phases

7190 We see that in the  $B_d$  system, the NP contribution can be substantial if its phase is close  
7191 to the SM phase, while for arbitrary phases its magnitude has to be much smaller than  
7192 the SM one. Notice that, with the latest data, the SM ( $\phi_{B_d} = 0$ ) is disfavored at 68%  
7193 probability due to the slight disagreement between  $\sin 2\beta$  and  $|V_{ub}/V_{cb}|$ . This requires  
7194  $A_{\text{NP}} \neq 0$  and  $\phi_{\text{NP}} \neq 0$ . For the same reason,  $\phi_{\text{NP}} > 90^\circ$  at 68% probability and the plot  
7195 is not symmetric around  $\phi_{\text{NP}} = 90^\circ$ . Assuming that the small but non-vanishing value  
7196 for  $\phi_{B_d}$  we obtained is just due to a statistical fluctuation, the result of our analysis  
7197 points either towards models with no new source of flavor and CP violation beyond the  
7198 ones present in the SM (Minimal Flavor Violation, MFV), or towards models in which  
7199 new sources of flavor and CP violation are only present in  $b \rightarrow s$  transitions.

7200 Conversely, from the results of our analysis in the  $B_s$  system, we see that the phase  
7201  $\phi_{B_s}$  deviates from zero at  $\sim 3.0\sigma$ . The solution around  $\phi_{B_s} \sim -20^\circ$  corresponds to  
7202  $\phi_s^{\text{NP}} \sim -50^\circ$  and  $A_s^{\text{NP}}/A_s^{\text{SM}} \sim 75\%$ . The second solution is much more distant from the  
7203 SM and it requires a dominant NP contribution ( $A_s^{\text{NP}}/A_s^{\text{SM}} \sim 190\%$ ). In this case the  
7204 NP phase is thus very well determined. The strong phase ambiguity affects the sign of  
7205  $\cos \phi_s$  and thus  $\text{Re } A_s^{\text{NP}}/A_s^{\text{SM}}$ , while  $\text{Im } A_s^{\text{NP}}/A_s^{\text{SM}} \sim -0.74$  in any case.

7206 This result shows an hint of discrepancy with respect to the SM expectation in the  $B_s$   
7207 CP-violating phase. We are eager to see updated measurements using larger data sets  
7208 from both the Tevatron experiments in order to strengthen the present evidence, waiting  
7209 for the advent of LHCb for a high-precision measurement of the NP phase.

7210 It is remarkable that to explain the result obtained for  $\phi_s$ , new sources of CP violation  
7211 beyond the CKM phase are required, strongly disfavoring the MFV hypothesis. These  
7212 new phases will in general produce correlated effects in  $\Delta B = 2$  processes and in  $b \rightarrow s$   
7213 decays. These correlations cannot be studied in a model-independent way, but it will be  
7214 interesting to analyze them in specific extensions of the SM. In this respect, improving  
7215 the results on CP violation in  $b \rightarrow s$  penguins at present and future experimental facilities  
7216 is of the utmost importance.

If we now consider the most general effective Hamiltonian for  $\Delta F = 2$  processes  
( $\mathcal{H}_{\text{eff}}^{\Delta F=2}$  [36]), we can translate the experimental constraints into allowed ranges for  
the Wilson coefficients of  $\mathcal{H}_{\text{eff}}^{\Delta F=2}$ . These coefficients in general have the form

$$C_i(\Lambda) = \frac{F_i L_i}{\Lambda^2} \quad (441)$$

7217 where  $F_i$  is a function of the (complex) NP flavor couplings,  $L_i$  is a loop factor that  
7218 is present in models with no tree-level Flavor Changing Neutral Currents (FCNC), and  
7219  $\Lambda$  is the scale of NP, *i.e.* the typical mass of the new particles mediating  $\Delta F = 2$   
7220 transitions. For a generic strongly-interacting theory with arbitrary flavor structure, one  
7221 expects  $F_i \sim L_i \sim 1$  so that the allowed range for each of the  $C_i(\Lambda)$  can be immediately  
7222 translated into a lower bound on  $\Lambda$ . Specific assumptions on the flavor structure of NP,  
7223 for example Minimal or Next-to-Minimal Flavor Violation (see Sec. 2.5), correspond to  
7224 particular choices of the  $F_i$  functions. To obtain the p.d.f. for the Wilson coefficients at  
7225 the NP scale  $\Lambda$ , we switch on one coefficient at a time in each sector and calculate its  
7226 value from the result of the NP analysis presented above.

The connection between the  $C_i(\Lambda)$  and the NP scale  $\Lambda$  depends on the general prop-  
erties of the NP model, and in particular on the flavor structure of the  $F_i$ . Assuming  
strongly interacting new particles, we have

$$\Lambda = \sqrt{\frac{F_i}{C_i}}. \quad (442)$$

In deriving the lower bounds on the NP scale  $\Lambda$ , we assume  $L_i = 1$ , corresponding to strongly-interacting and/or tree-level NP. Two other interesting possibilities are given by loop-mediated NP contributions proportional to  $\alpha_s^2$  or  $\alpha_W^2$ .

Assuming strongly interacting and/or tree-level NP contributions with generic flavor structure (*i.e.*  $L_i = |F_i| = 1$ ), we can translate the upper bounds on  $C_i$  into the lower bounds on the NP scale  $\Lambda$ . Conversely, in case of hints of NP effects, an upper bounds on the NP scale  $\Lambda$  is extracted.

Table 87  
95% probability lower bounds on the NP scale  $\Lambda$  (in TeV) for several possible flavor structures and loop suppressions from the  $K$  and  $B_d$  systems.

Scenario	strong/tree	$\alpha_s$ loop	$\alpha_W$ loop
MFV	5.5	0.5	0.2
NMFV	62	6.2	2
General	240000	24000	8000

Table 88  
95% probability upper bounds on the NP scale  $\Lambda$  (in TeV) for several possible flavor structures and loop suppressions from the  $B_s$  system.

Scenario	strong/tree	$\alpha_s$ loop	$\alpha_W$ loop
NMFV	35	4	2
General	800	80	30

From the lower bound Tab. 87, we could conclude that any model with strongly interacting NP and/or tree-level contributions is beyond the reach of direct searches at the LHC. Flavor and CP violation remain the main tool to constrain (or detect) such NP models. Weakly-interacting extensions of the SM can be accessible at the LHC provided that they enjoy a MFV-like suppression of  $\Delta F = 2$  processes, or at least a NMFV-like suppression with an additional depletion of the NP contribution to  $\epsilon_K$ .

If we consider the current effect in the  $B_s$  mixing, we obtain the upper bound Tab. 88 and we notice that the general model is strongly problematic being the upper bound at a much lower scale with respect to the corresponding lower bound resulting from the  $K$  and  $B_d$  systems. NMFV models are less problematic, but they can hardly reproduce with the current size of the NP effect in the  $B_s$  system while keeping small effects in the  $B_d$  and even smaller effects in the  $K$  system. Finally, MFV models would have possible solutions in this scheme but they cannot generate the effect in the  $B_s$  phase. So the current hint suggests some hierarchy in NP mixing which is stronger than the SM one.

### 10.2.2. Impact of flavor physics measurements on grand unified

In a model of physics beyond the Standard Model, it is expected that observables in the flavor physics are affected by the contributions from new particles which couple to the quarks and leptons. Comparing measured values of flavor observables with the Standard Model predictions enables us to obtain information on the new physics contributions. If the measured value of certain observable differs from the Standard Model prediction, the difference shows the magnitude of the new physics contribution. If the measured value is consistent with the Standard Model prediction, that measurement is still useful as a constraint on the new physics.

Here we focus on the cases of supersymmetric grand unified models. For general reviews of supersymmetric models, see Refs. [154, 1160, 1161] and references therein.

In supersymmetric extensions of the Standard Model, there exist superpartners of the Standard Model particles, namely squarks, sleptons, gauginos and higgsinos. Supersym-

7261 metrized interactions include quark-squark-gaugino and quark-squark-higgsino couplings.  
7262 The mass matrices of the superparticles are different from corresponding ones of the Stan-  
7263 dard Model particles because of the supersymmetry breaking. Therefore the flavor mixing  
7264 among the squarks depend on flavor structure of the supersymmetry breaking mecha-  
7265 nism. The mismatch between the flavor bases of quarks and squarks generates mixing  
7266 matrices at the quark-squark-gaugino(higgsino) interactions. These mixing matrices are  
7267 not necessarily the same as the CKM matrix and affect the flavor changing amplitudes  
7268 through loop diagrams with squarks in the internal lines.

7269 Importance of the flavor physics in supersymmetric models have been recognized since  
7270 early 1980's [161,162]. It was pointed out that squarks of the first and second gener-  
7271 ations must be almost degenerate in mass, since otherwise too large contribution to  
7272 the  $K - \bar{K}$  mixing would be given by squark-gaugino loops. This requirement, which  
7273 is known as "SUSY flavor problem", motivates us to build a model of supersymmetry  
7274 breaking mechanism that controls the squark mass matrices. The minimal supergravity  
7275 (mSUGRA) model is one of those models. In mSUGRA, it is assumed that the supersym-  
7276 metry breaking occurs in a hidden sector and its effect is transferred to the observable  
7277 sector by (super-)gravitational interactions. Consequently, the supersymmetry breaking  
7278 masses and interactions of the superparticles are generated near the Planck scale and  
7279 flavor-blind. Mass differences and flavor mixings of the squarks are induced by the (su-  
7280 persymmetrized) Yukawa interactions through radiative corrections. Therefore the de-  
7281 generacy of the first and the second generation squarks is explained by the smallness of  
7282 the Yukawa couplings of the light quarks. On the other hand, masses of the third gen-  
7283 eration squarks, particularly stop, receive significant corrections from large top Yukawa  
7284 coupling. Squark flavor mixing occurs in left-handed squarks and the mixing matrix is  
7285 approximately the same as the CKM matrix [1162–1164].

7286 Effects of the superparticles on flavor observables have been studied in the past decades  
7287 [1165–1167], and it turns out that deviations from the Standard Model predictions are  
7288 small in the simplest mSUGRA scenario, under the improved constraints from direct  
7289 searches for the superparticles and the Higgs bosons at LEP and Tevatron experiments.  
7290 An exception is the  $b \rightarrow s \gamma$  decay.  $b \rightarrow s \gamma$  in supersymmetric models has been studied  
7291 intensively in 1990's [1168–1171]. It is shown that the contributions from the superpar-  
7292 ticle loops can be as large as the Standard Model one, thus the agreement between the  
7293 measured value of  $B(b \rightarrow s \gamma)$  and its Standard Model prediction gives us an important  
7294 constraint on the parameter space of a supersymmetric model.

7295 After the existence of the neutrino masses is established by neutrino oscillation experi-  
7296 ments, flavor mixing in the lepton sector has been also taken into account. Although  
7297 the the neutrino masses are very small compared to the quark and charged lepton  
7298 masses, Yukawa couplings of the neutrinos need not to be small. If the see-saw mech-  
7299 anism [1172–1174] works and the Majorana masses of the right-handed neutrinos are  
7300 sufficiently large, the Yukawa coupling constants of the neutrinos may be  $O(1)$ . In the  
7301 mSUGRA scenario, the neutrino Yukawa coupling generates the flavor mixing in the  
7302 slepton mass matrices through radiative corrections. The flavor mixing in the sleptons  
7303 eventually induces the lepton flavor violating processes such as  $\mu \rightarrow e \gamma$  [1175,1176].

7304 In the supersymmetric grand unified models, the Yukawa interactions of quarks and  
7305 leptons are unified at the energy scale of the grand unification. Therefore both squark  
7306 and slepton mass matrices receive flavor off-diagonal contributions due to the unified  
7307 Yukawa interactions above the GUT scale. In a  $SU(5)$  unification model, flavor mixings

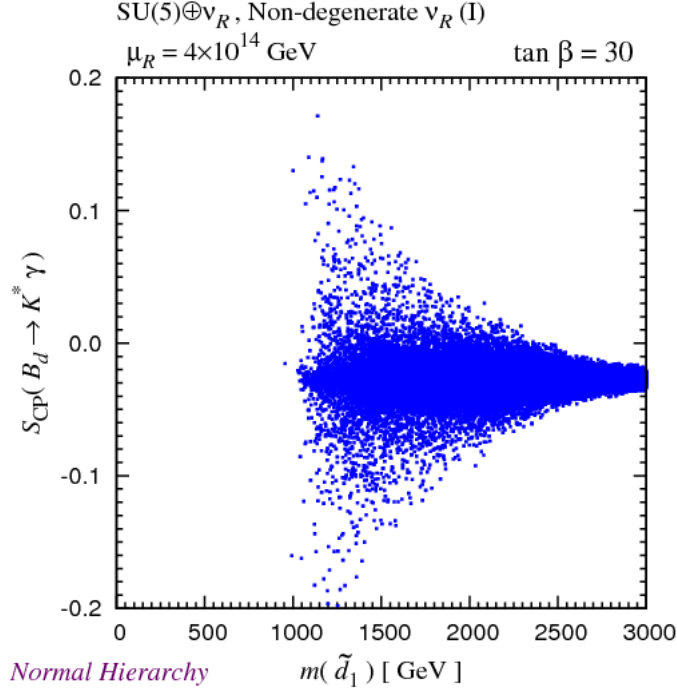


Fig. 102. Mixing-induced CP asymmetry in  $B_d \rightarrow K^* \gamma$  decay as a function of the lightest down-type squark mass in the  $SU(5)$  SUSY GUT with right-handed neutrinos [1183].

7308 of the left-handed squarks and the right-handed charged sleptons are governed by the  
 7309 Yukawa coupling matrix of the up-type quarks that consists of the top Yukawa coupling  
 7310 [1177,1178]. On the other hand, the right-handed down-type squarks and the left-handed  
 7311 sleptons receive contributions from the neutrino Yukawa coupling matrix, which is related  
 7312 to the Maki-Nakagawa-Sakata neutrino mixing matrix [1179]. Since the neutrino mixing  
 7313 angle between the second and the third generations is known to be large, it is expected  
 7314 that significant  $\tilde{b}_R - \tilde{s}_R$  mixing is induced when the magnitudes of the neutrino Yukawa  
 7315 couplings are sufficiently large [1180–1182].

7316 The squark flavor mixings, which are generated by the (grand-unified) neutrino Yukawa  
 7317 interactions, contribute to the quark flavor changing amplitudes. Since these additional  
 7318 contributions are independent of the CKM matrix, it is possible that deviations from the  
 7319 Standard Model predictions of the flavor observables in the  $B$  decays are sizably large  
 7320 while those in  $K$  decays are suppressed. Fig. 102 [1183] shows the mixing-induced CP  
 7321 asymmetry in  $B_d \rightarrow K^* \gamma$  decay as a function of the lightest down-type squark mass in  
 7322 the  $SU(5)$  SUSY GUT with right-handed neutrinos. Each dot in the plot corresponds  
 7323 to a different choice of supersymmetry breaking parameters in the mSUGRA scenario.  
 7324 CKM matrix elements and neutrino parameters are fixed. The neutrino Yukawa coupling  
 7325 matrix is chosen so that the flavor mixing between the second and the third generations  
 7326 is large, whereas the mixing between the first and the second generations is suppressed.  
 7327 With this choice, SUSY contributions to the  $K - \bar{K}$  mixing ( $\varepsilon_K$ ) and  $\mu \rightarrow e \gamma$  are  
 7328 small enough. It is seen that there exist parameter regions where the asymmetry is as

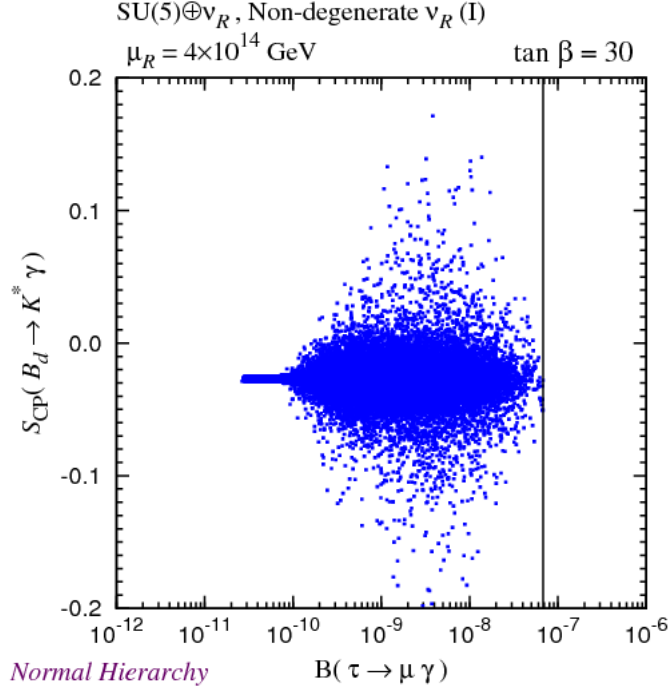


Fig. 103. Correlation between the mixing-induced CP asymmetry in  $B_d \rightarrow K^* \gamma$  and the branching fraction of  $\tau \rightarrow \mu \gamma$  [1183].

7329 large as  $\pm 20\%$  for the squark mass  $\sim 1\text{TeV}$  satisfying other experimental constraints.  
 7330 Other observables in  $b \rightarrow s$  transition, such as the time-dependent CP asymmetries in  
 7331  $B_d \rightarrow \phi K_S$  and  $B_s \rightarrow J/\psi \phi$  are also affected significantly in the same parameter region.  
 7332 Another characteristic feature is that the SUSY flavor signals in the quark and lepton  
 7333 sectors are correlated with each other [1183]. As can be seen in Fig. 103, the branching  
 7334 fraction of  $\tau \rightarrow \mu \gamma$  can be as large as  $10^{-8}$  in the parameter region with large corrections  
 7335 to  $b \rightarrow s$  observables.

7336 The pattern of deviations from the Standard Model predictions depends on the flavor  
 7337 structure of the masses and interactions of the squarks and sleptons. Therefore a combined  
 7338 analysis of many flavor observables provides us with important clue on physics  
 7339 determining the structure of the SUSY breaking sector.

### 7340 10.2.3. *New physics in extra-dimension models*

7341 In recent years a lot of interest was dedicated to extensions of the Standard Model  
 7342 involving one or more extra dimensions (ED), motivated by the possibility to find a  
 7343 *natural* solution, in this context, of the hierarchy between the electroweak and the Planck  
 7344 scale. ED models can be grouped basically into three classes according to the space-time  
 7345 geometry of the ED and the localization properties of SM fields. In ADD [1184, 1185]  
 7346 models the space-time is extended by one or more large (sub-millimeter) EDs with flat  
 7347 geometry. Only gravity is allowed to propagate in the higher-dimensional bulk, while  
 7348 all gauge and matter fields are confined to a 4d brane. In a different class of models,

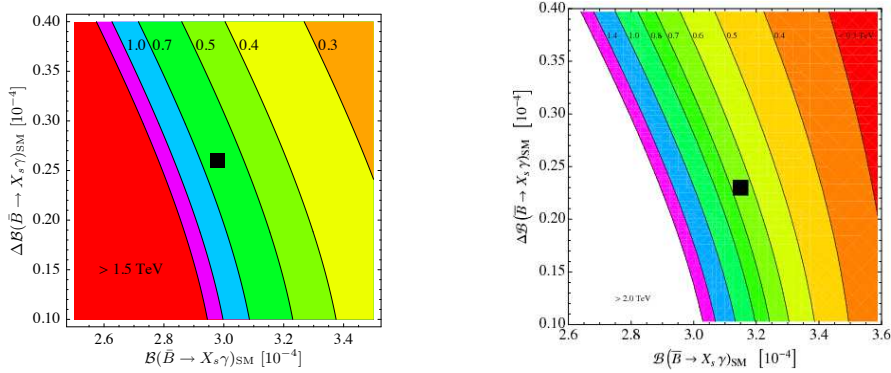


Fig. 104. 95 % C.L. limits on  $1/R$  as a function of the SM central value and error on  $\mathcal{B}(\bar{B} \rightarrow X_s \gamma)$  for the minimal UED5 [658] and UED6 [659] models.

7349 dubbed Universal Extra Dimensions (UED) [1186], the EDs have flat geometry and are  
 7350 compactified, but now the SM fields are free to propagate in the bulk. Finally, in RS [1187,  
 7351 1188] models, a 5d warped space-time is considered. Nowadays, in most phenomenological  
 7352 applications modifications of the original RS1 setup [1187] are considered, where gauge  
 7353 and matter fields propagate in the 5d bulk [176, 1189, 1190] and only the Higgs boson  
 7354 is confined on or near the IR brane. In the following we will summarize flavor physics  
 7355 constraints on UED and warped models.

7356 10.2.3.1. *Universal extra dimensions (UED)*. For what concerns UEDs we consider the  
 7357 so called minimal UED5 [1186] and minimal UED6 [1191–1193] models, characterized  
 7358 by one ED compactified on  $S^1/\mathbb{Z}_2$  and two EDs compactified on  $T^2/\mathbb{Z}_2$ , respectively.  
 7359 The minimality refers to the absence of flavor non-universal boundary terms that would  
 7360 lead to unacceptably large flavor changing neutral currents. With these assumptions the  
 7361 Kaluza-Klein (KK) modes of the SM fields induce new contributions to flavor violating  
 7362 processes. As the models are minimal flavor violating (see Sec. 2.5), those interactions are  
 7363 entirely controlled by the CKM matrix and the relevant free parameters of the models are  
 7364 the compactification radius  $R$  and the cut-off scale  $\Lambda$  at which the full (5d/6d) theory  
 7365 becomes non-perturbative. Detailed analyses of FCNC processes in UED5 and UED6  
 7366 have been presented in [658, 837, 1194–1205] and [659, 1194], respectively. Lower bounds  
 7367 on  $1/R$  come from oblique corrections,  $Z \rightarrow b\bar{b}$ ,  $(g-2)_\mu$  and  $b \rightarrow s\gamma$ , with the latter  
 7368 providing by far the strongest constraint. It is interesting to note that UED contributions  
 7369 to  $b \rightarrow s\gamma$  tend always to decrease the branching ratio and, within the 5d (6d) theory,  
 7370 have a negligible (logarithmic) dependence on the cut-off  $\Lambda$ . Utilizing the world average  
 7371  $\mathcal{B}(\bar{B} \rightarrow X_s \gamma)_{\text{exp}} = (3.55 \pm 0.24_{-0.10}^{+0.09} \pm 0.03) \cdot 10^{-4}$  the authors of Refs. [658, 659] find that  
 7372 in both models the inverse compactification radius has to be larger than about 600 GeV,  
 7373 with the exact bound depending quite sensitively on the theoretical prediction for the  
 7374 central value. Their findings are summarized in Fig. 104. A discussion of these models  
 7375 in the context of dark matter and accelerator searches can be found, for instance, in  
 7376 Ref. [1206].

7377 10.2.3.2. *Bulk fermions in a warped ED*. The case of bulk fermions in a warped ED  
 7378 is more interesting from the flavor physics point of view, as the localization of fermion



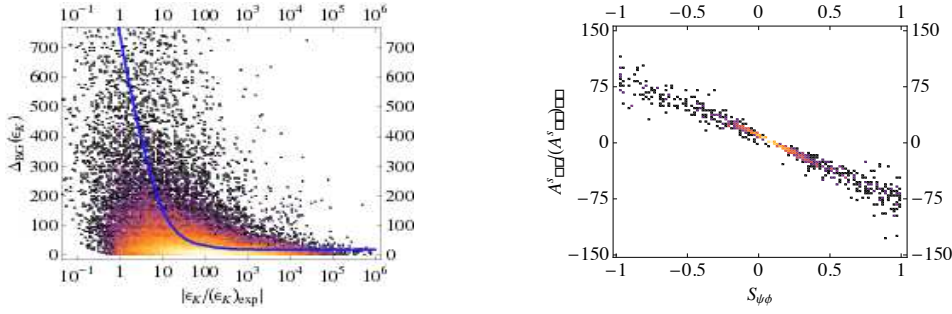


Fig. 105. *left*: Required Barbieri-Giudice [1224] fine-tuning  $\Delta_{\text{BG}}(\varepsilon_K)$  as a function of  $\varepsilon_K$  in the custodially protected RS model. The blue curve displays the average fine-tuning [1214]. *right*: Correlation between the CP-asymmetries  $A_{\text{SL}}^S$  and  $S_{\psi\phi}$  in the custodially protected RS model, fulfilling all available  $\Delta F = 2$  constraints [1214].

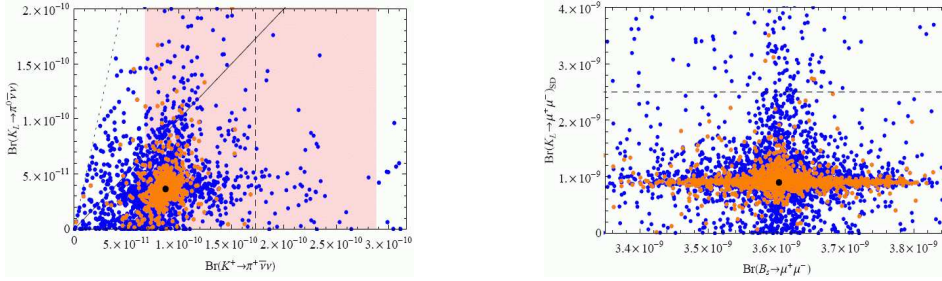


Fig. 106. *left*:  $Br(K_L \rightarrow \pi^0 \nu \bar{\nu})$  as a function of  $Br(K^+ \rightarrow \pi^+ \nu \bar{\nu})$  in the custodially protected RS model [838]. The shaded area represents the experimental  $1\sigma$ -range for  $Br(K^+ \rightarrow \pi^+ \nu \bar{\nu})$ . *right*:  $Br(K_L \rightarrow \mu^+ \mu^-)$  versus  $Br(B_s \rightarrow \mu^+ \mu^-)$  in the custodially protected RS model [838].

7379 zero modes along the 5<sup>th</sup> dimension provides an intrinsic explanation of the observed  
 7380 hierarchies in fermion masses and mixings [176, 1190, 1207]. Due to the absence of KK  
 7381 parity, here new physics contributions to FCNC observables appear already at the tree  
 7382 level, however they are strongly suppressed thanks to the so-called RS-GIM mechanism  
 7383 [178]. In contrast to the UED models, this class of models goes beyond MFV and many  
 7384 new flavor violating parameters and CP phases are present, in addition to new flavor  
 7385 violating operators beyond the SM ones.

7386 In order to obtain agreement with the electroweak  $T$  parameter, usually an enlarged  
 7387 gauge sector  $SU(2)_L \times SU(2)_R \times U(1)_X$  is considered [1208, 1209], together with custo-  
 7388 dially protected fermion representations that avoid large anomalous  $Z b_L \bar{b}_L$  [1210–1213]  
 7389 and at the same time also  $Z d_L^i \bar{d}_L^j$  [838, 1214, 1215] couplings. Consequently the KK mass  
 7390 scale can be as low as  $M_{\text{KK}} \simeq (2 - 3)$  TeV and therefore in the reach of direct LHC  
 7391 searches.

7392 The impact of RS bulk matter on quark flavor violating observables has been dis-  
 7393 cussed extensively in the literature, see e.g. [178, 838, 1214, 1216–1223] for details. Here  
 7394 we focus only on the most stringent constraint, coming from the  $\varepsilon_K$  observable, that  
 7395 measures indirect CP-violation in the neutral  $K$  meson sector, and on implications for  
 7396 flavor observables that have not yet been measured with high precision.

7397 In contrast to the SM, the tree level exchange of KK gauge bosons induces amongst

7398 others the presence of left-right operators  $\mathcal{Q}_{LR}$  contributing to  $\Delta F = 2$  processes. These  
 7399 operators receive large renormalisation group corrections and are in the case of  $K^0 - \bar{K}^0$   
 7400 mixing in addition chirally enhanced. It turns out then that the otherwise so powerful  
 7401 RS-GIM mechanism in this case is not sufficient to suppress the new physics contribution  
 7402 below the experimental limits, so that assuming completely anarchic 5d Yukawa couplings  
 7403 a lower bound on the KK mass scale  $M_{KK} \simeq 20$  TeV is obtained [1214, 1221]. In [1214] it  
 7404 has been shown however that allowing for modest hierarchies in the 5d Yukawas agree-  
 7405 ment with  $\varepsilon_K$  can be obtained even without significant fine-tuning (see Fig. 105), so  
 7406 that a natural solution to the “ $\varepsilon_K$ -problem” even for low KK scales cannot be excluded.  
 7407 Imposing then all available  $\Delta F = 2$  constraints on the RS parameter space, large new CP-  
 7408 violating effects in  $B_s - \bar{B}_s$  mixing can still be found in this model [1214], offering a neat  
 7409 explanation of the recent CDF and D0 data [230, 956, 1225]. In addition slight tensions  
 7410 between CP-violation in  $K$  and  $B_d$  observables [867, 868] could easily be resolved thanks  
 7411 to the presence of non-MFV interactions [1214]. An interesting pattern of deviations from  
 7412 the SM can also be found in the case of rare  $K$  and  $B_{d,s}$  decays (see Fig. 106) [838]. As  
 7413 the dominant contribution stems from tree level flavor changing couplings of the  $Z$  boson  
 7414 to right-handed down-type quarks, generally larger effects are to be expected in rare  $K$   
 7415 decays, e. g.  $Br(K_L \rightarrow \pi^0 \nu \bar{\nu})$  can be enhanced by up to a factor 5. While the effects in  
 7416  $B_{d,s}$  decays are much more modest (e. g.  $\pm 20\%$  in  $Br(B_{d,s} \rightarrow \mu^+ \mu^-)$ ), flavor universality  
 7417 can be strongly violated, so that interesting deviations from the MFV predictions appear.  
 7418 Striking correlations arise not only between various rare  $K$  decays, but also between  $K$   
 7419 and  $B_{d,s}$  physics observables, thus allowing to distinguish this framework from other new  
 7420 physics scenarios.

7421 Alternative solutions to solve the “ $\varepsilon_K$ -problem”, based on flavor symmetries, have  
 7422 as well been discussed in the recent literature. One approach is to protect the model  
 7423 from all tree level FCNCs by incorporating a full 5d GIM mechanism [181], in which  
 7424 the bulk respects a full  $U(3)^3$  flavor symmetry. Although this model is safe, since its  
 7425 effective theory is MFV, it leaves the origin of the large hierarchies in the flavor sector  
 7426 unanswered. More recent proposals therefore seek to suppress dangerous FCNCs and  
 7427 simultaneously try to explain the hierarchical structure of the flavor sector. One of them  
 7428 is the so called “5d MFV” model [1226]. Here one postulates that the only sources of  
 7429 flavor breaking are two anarchic Yukawa spurions. The low-energy limit is not MFV, and  
 7430 the additional assumption, that brane and bulk terms in the down sector are effectively  
 7431 aligned, is needed to suppress dangerous FCNCs. Recently, an economical model has  
 7432 been proposed [1227] in which one assumes a  $U(3)$  flavor symmetry for the 5D fields  
 7433 containing the right handed down quarks. Dangerous contributions to  $\mathcal{Q}_{LR}$  are then  
 7434 only generated by suppressed mass insertions on the IR brane where the symmetry is  
 7435 necessarily broken. Another recent approach [182] presents a simple model where the key  
 7436 ingredient are two horizontal  $U(1)$  symmetries which induce an alignment of bulk masses  
 7437 and down Yukawas, thus strongly suppressing FCNCs in the down sector. FCNCs in the  
 7438 up sector, however, can be close to experimental limits.

## 7439 11. Acknowledgements

7440 We would like to thank the Università “Sapienza” of Rome and in particular its De-  
 7441 partment of Physics for the hospitality during the days of the workshop (9-13 September

7442 2008). For the financial and organizational support to the workshop itself we would like  
7443 to thank INFN and in particular its Roma1 Section and the Local Organizing Committee  
7444 (D. Anzellotti, C. Bulfon, G. Bucci, E. Di Silvestro, R. Faccini, M. Mancini, G. Piredda,  
7445 and R. Soldatelli) respectively.

7446 The program of the workshop was elaborated by the Programm Committee (P. Ball,  
7447 G. Cavoto, M. Ciuchini, R. Faccini – chair, R. Forty, S. Giagu, P. Gambino, B. Grinstein,  
7448 S. Hashimoto, T. Iijima, G. Isidori, V. Luth, G. Piredda, M. Rescigno, and A. Stocchi)  
7449 under consultation of the International Advisory Committee (I. I. Bigi, C. Bloise, A.  
7450 Buras, N. Cabibbo, A. Ceccucci, P. Chang, F. Ferroni, A. Golutvin, A. Jawahery, A.  
7451 S. Kronfeld, Y. Kwon, M. Mangano, W. J. Marciano, G. Martinelli, A. Masiero, T.  
7452 Nakada, M. Neubert, P. Roudeau, A. I. Sanda, M. D. Shapiro, I. P.J. Shipsey, A. Soni,  
7453 W. J. Taylor, N. G. Uraltsev, and M. Yamauchi).

7454 This work is supported by Australian Research Council and the Australian Department  
7455 of Industry Innovation, Science and Research, the Natural Sciences and Engineering  
7456 Research Council (Canada), the National Science Foundation of China, the Commissariat  
7457 à l’Energie Atomique and Institut National de Physique Nucléaire et de Physique des  
7458 Particules (France), the Bundesministerium für Bildung und Forschung and Deutsche  
7459 Forschungsgemeinschaft (Germany), the Department of Science and Technology of India  
7460 the Istituto Nazionale di Fisica Nucleare (Italy), the Ministry of Education Culture,  
7461 Sports, Science, and Technology (Japan), the Japan Society of Promotion of Science, the  
7462 BK21 program of the Ministry of Education of Korea, the Research Council of Norway,  
7463 the Ministry of Education and Science of the Russian Federation, the Slovenian Research  
7464 Agency, Ministerio de Educación y Ciencia (Spain), the Science and Technology Facilities  
7465 Council (United Kingdom), and the US Department of Energy and National Science  
7466 Foundation .

7467 Individuals have received support from European Community’s Marie-Curie Research  
7468 Training Networks under contracts MRTN-CT-2006-035505 (‘Tools and Precision Calcula-  
7469 tions for Physics Discoveries at Colliders’) and MRTN-CT-2006-035482 (‘FLAVIANet’),  
7470 from the National Science Foundation of China (grants 10735080 and 10625525), the DFG  
7471 Cluster of Excellence ‘Origin and Structure of the Universe’ (grant BU 706/2-1), the Jpan  
7472 Society for the Promotion of Science (grant 20244037), and the A. von Humboldt Stiftung,  
7473 from MICINN, Spain (grant FPA2007-60323), from the US National Science Foundation  
7474 (grant PHY-0555304) and Department of Energy (grants DE-FG02-96ER41005 and DE-  
7475 AC02-07CH11359 – Fermi Research Alliance, LLC), and from Generalitat Valenciana  
7476 (grant PROMETEO/2008/069).

## References

- [1] N. Cabibbo, Unitary Symmetry and Leptonic Decays, *Phys. Rev. Lett.* 10 (1963) 531–533.
- [2] M. Kobayashi, T. Maskawa, CP Violation in the Renormalizable Theory of Weak Interaction, *Prog. Theor. Phys.* 49 (1973) 652–657.
- [3] L.-L. Chau, W.-Y. Keung, Comments on the Parametrization of the Kobayashi-Maskawa Matrix, *Phys. Rev. Lett.* 53 (1984) 1802.
- [4] C. Amsler, A. Masoni, The  $\eta(1405)$ ,  $\eta(1475)$ ,  $f_1(1420)$ , and  $f_1(1510)$ .
- [5] L. Wolfenstein, Parametrization of the Kobayashi-Maskawa Matrix, *Phys. Rev. Lett.* 51 (1983) 1945.

- [6] A. J. Buras, M. E. Lautenbacher, G. Ostermaier, Waiting for the top quark mass,  $K^+ \rightarrow \pi^+ \nu \bar{\nu}$ ,  $B(s)0 - \text{anti-}B(s)0$  mixing and CP asymmetries in B decays, Phys. Rev. D50 (1994) 3433–3446.
- [7] R. Aleksan, B. Kayser, D. London, Determining the quark mixing matrix from CP violating asymmetries, Phys. Rev. Lett. 73 (1994) 18–20.
- [8] J. P. Silva, L. Wolfenstein, Detecting new physics from CP-violating phase measurements in B decays, Phys. Rev. D55 (1997) 5331–5333.
- [9] C. Jarlskog, Commutator of the Quark Mass Matrices in the Standard Electroweak Model and a Measure of Maximal CP Violation, Phys. Rev. Lett. 55 (1985) 1039.
- [10] K. G. Wilson, Nonlagrangian models of current algebra, Phys. Rev. 179 (1969) 1499–1512.
- [11] K. G. Wilson, The Renormalization Group and Strong Interactions, Phys. Rev. D3 (1971) 1818.
- [12] M. K. Gaillard, B. W. Lee,  $\Delta I = 1/2$  Rule for Nonleptonic Decays in Asymptotically Free Field Theories, Phys. Rev. Lett. 33 (1974) 108.
- [13] G. Altarelli, L. Maiani, Octet Enhancement of Nonleptonic Weak Interactions in Asymptotically Free Gauge Theories, Phys. Lett. B52 (1974) 351–354.
- [14] E. Witten, Short Distance Analysis of Weak Interactions, Nucl. Phys. B122 (1977) 109.
- [15] F. J. Gilman, M. B. Wise, Effective Hamiltonian for  $\Delta S = 1$  Weak Nonleptonic Decays in the Six Quark Model, Phys. Rev. D20 (1979) 2392.
- [16] B. Guberina, R. D. Peccei, Quantum Chromodynamic Effects and CP Violation in the Kobayashi-Maskawa Model, Nucl. Phys. B163 (1980) 289.
- [17] A. I. Vainshtein, V. I. Zakharov, M. A. Shifman, A Possible mechanism for the  $\Delta T = 1/2$  rule in nonleptonic decays of strange particles, JETP Lett. 22 (1975) 55–56.
- [18] M. A. Shifman, A. I. Vainshtein, V. I. Zakharov, Light Quarks and the Origin of the  $\Delta I = 1/2$  Rule in the Nonleptonic Decays of Strange Particles, Nucl. Phys. B120 (1977) 316.
- [19] M. A. Shifman, A. I. Vainshtein, V. I. Zakharov, Nonleptonic Decays of K Mesons and Hyperons, Sov. Phys. JETP 45 (1977) 670.
- [20] F. J. Gilman, M. B. Wise,  $K0$  anti- $K0$  Mixing in the Six Quark Model, Phys. Rev. D27 (1983) 1128.
- [21] J. Bijnens, M. B. Wise, Electromagnetic Contribution to Epsilon-prime/Epsilon, Phys. Lett. B137 (1984) 245.
- [22] M. Lusignoli, Electromagnetic corrections to the effective hamiltonian for strangeness changing decays and  $\epsilon'/\epsilon$ , Nucl. Phys. B325 (1989) 33.
- [23] K. G. Chetyrkin, M. Misiak, M. Munz, Weak radiative B-meson decay beyond leading logarithms, Phys. Lett. B400 (1997) 206–219.
- [24] M. Gorbahn, U. Haisch, Effective Hamiltonian for non-leptonic  $|\Delta F| = 1$  decays at NNLO in QCD, Nucl. Phys. B713 (2005) 291–332.
- [25] A. J. Buras, M. Jamin, M. E. Lautenbacher, Two loop anomalous dimension matrix for  $\Delta S = 1$  weak nonleptonic decays. 2.  $O(\alpha\text{-}\alpha\text{-}s)$ , Nucl. Phys. B400 (1993) 75–102.
- [26] M. Ciuchini, E. Franco, G. Martinelli, L. Reina, The  $\Delta S = 1$  effective Hamiltonian including next-to-leading order QCD and QED corrections, Nucl. Phys. B415 (1994) 403–462.
- [27] C. Bobeth, M. Misiak, J. Urban, Photonic penguins at two loops and  $m(t)$ -dependence of  $BR(B \rightarrow X(s)\ell^+\ell^-)$ , Nucl. Phys. B574 (2000) 291–330.
- [28] M. Misiak, M. Steinhauser, Three-loop matching of the dipole operators for  $b \rightarrow s\gamma$  and  $b \rightarrow sg$ , Nucl. Phys. B683 (2004) 277–305.
- [29] M. Gorbahn, U. Haisch, M. Misiak, Three-loop mixing of dipole operators, Phys. Rev. Lett. 95 (2005) 102004.
- [30] M. Czakon, U. Haisch, M. Misiak, Four-loop anomalous dimensions for radiative flavour-changing decays, JHEP 03 (2007) 008.
- [31] A. J. Buras, P. Gambino, M. Gorbahn, S. Jager, L. Silvestrini, Universal unitarity triangle and physics beyond the standard model, Phys. Lett. B500 (2001) 161–167.
- [32] A. J. Buras, W. Slominski, H. Steger, B Meson Decay, CP Violation, Mixing Angles and the Top Quark Mass, Nucl. Phys. B238 (1984) 529.
- [33] A. J. Buras, M. Jamin, P. H. Weisz, Leading and next-to-leading QCD corrections to  $\epsilon$  parameter and  $B^0 - \bar{B}^0$  mixing in the presence of a heavy top quark, Nucl. Phys. B347 (1990) 491–536.
- [34] S. Herrlich, U. Nierste, Enhancement of the  $K(L) - K(S)$  mass difference by short distance QCD corrections beyond leading logarithms, Nucl. Phys. B419 (1994) 292–322.

- [35] S. Herrlich, U. Nierste, The Complete  $|\Delta S| = 2$  Hamiltonian in the Next-To- Leading Order, Nucl. Phys. B476 (1996) 27–88.
- [36] M. Bona, et al., Model-independent constraints on  $\Delta F = 2$  operators and the scale of new physics, JHEP 03 (2008) 049.
- [37] M. Gronau, D. London, Isospin analysis of CP asymmetries in B decays, Phys. Rev. Lett. 65 (1990) 3381–3384.
- [38] M. Beneke, G. Buchalla, M. Neubert, C. T. Sachrajda, QCD factorization for  $B \rightarrow \pi\pi$  decays: Strong phases and CP violation in the heavy quark limit, Phys. Rev. Lett. 83 (1999) 1914–1917.
- [39] M. Beneke, G. Buchalla, M. Neubert, C. T. Sachrajda, QCD factorization for exclusive, non-leptonic B meson decays: General arguments and the case of heavy-light final states, Nucl. Phys. B591 (2000) 313–418.
- [40] M. Beneke, G. Buchalla, M. Neubert, C. T. Sachrajda, QCD factorization in  $B \rightarrow \pi K$ ,  $\pi\pi$  decays and extraction of Wolfenstein parameters, Nucl. Phys. B606 (2001) 245–321.
- [41] C. W. Bauer, S. Fleming, M. E. Luke, Summing Sudakov logarithms in  $B \rightarrow X_s + \gamma$  in effective field theory, Phys. Rev. D63 (2000) 014006.
- [42] C. W. Bauer, S. Fleming, D. Pirjol, I. W. Stewart, An effective field theory for collinear and soft gluons: Heavy to light decays, Phys. Rev. D63 (2001) 114020.
- [43] C. W. Bauer, I. W. Stewart, Invariant operators in collinear effective theory, Phys. Lett. B516 (2001) 134–142.
- [44] C. W. Bauer, D. Pirjol, I. W. Stewart, Soft-Collinear Factorization in Effective Field Theory, Phys. Rev. D65 (2002) 054022.
- [45] H.-n. Li, H.-L. Yu, Perturbative QCD analysis of B meson decays, Phys. Rev. D53 (1996) 2480–2490.
- [46] H.-N. Li, H.-L. Yu, PQCD analysis of exclusive charmless B meson decay spectra, Phys. Lett. B353 (1995) 301–305.
- [47] T.-W. Yeh, H.-n. Li, Factorization theorems, effective field theory, and nonleptonic heavy meson decays, Phys. Rev. D56 (1997) 1615–1631.
- [48] Y.-Y. Keum, H.-n. Li, A. I. Sanda, Fat penguins and imaginary penguins in perturbative QCD, Phys. Lett. B504 (2001) 6–14.
- [49] Y. Y. Keum, H.-N. Li, A. I. Sanda, Penguin enhancement and  $B \rightarrow K\pi$  decays in perturbative QCD, Phys. Rev. D63 (2001) 054008.
- [50] C.-H. Chen, Y.-Y. Keum, H.-n. Li, Perturbative QCD analysis of  $B \rightarrow \phi K$  decays, Phys. Rev. D64 (2001) 112002.
- [51] C. W. Bauer, D. Pirjol, I. Z. Rothstein, I. W. Stewart,  $B \rightarrow M_1 M_2$ : Factorization, charming penguins, strong phases, and polarization, Phys. Rev. D70 (2004) 054015.
- [52] C. W. Bauer, I. Z. Rothstein, I. W. Stewart, SCET analysis of  $B \rightarrow K\pi$ ,  $B \rightarrow K\bar{K}$ , and  $B \rightarrow \pi\pi$  decays, Phys. Rev. D74 (2006) 034010.
- [53] A. R. Williamson, J. Zupan, Two body B decays with isosinglet final states in SCET, Phys. Rev. D74 (2006) 014003.
- [54] K. G. Wilson, Confinement of Quarks, Phys. Rev. D10 (1974) 2445–2459.
- [55] J. B. Kogut, A Review of the Lattice Gauge Theory Approach to Quantum Chromodynamics, Rev. Mod. Phys. 55 (1983) 775.
- [56] D. Friedan, A proof of the Nielsen-Ninomiya theorem, Commun. Math. Phys. 85 (1982) 481–490.
- [57] H. B. Nielsen, M. Ninomiya, Absence of Neutrinos on a Lattice. 1. Proof by Homotopy Theory, Nucl. Phys. B185 (1981) 20.
- [58] T. Banks, L. Susskind, J. B. Kogut, Strong Coupling Calculations of Lattice Gauge Theories: (1+1)-Dimensional Exercises, Phys. Rev. D13 (1976) 1043.
- [59] L. Susskind, Lattice Fermions, Phys. Rev. D16 (1977) 3031–3039.
- [60] K. G. Wilson, Quarks: From Paradox to Myth, Subnucl. Ser. 13 (1977) 13–32.
- [61] P. H. Ginsparg, K. G. Wilson, A Remnant of Chiral Symmetry on the Lattice, Phys. Rev. D25 (1982) 2649.
- [62] U. J. Wiese, Fixed point actions for Wilson fermions, Phys. Lett. B315 (1993) 417–424.
- [63] P. Hasenfratz, V. Laliena, F. Niedermayer, The index theorem in QCD with a finite cut-off, Phys. Lett. B427 (1998) 125–131.
- [64] D. B. Kaplan, A Method for simulating chiral fermions on the lattice, Phys. Lett. B288 (1992) 342–347.

- [65] Y. Shamir, Chiral fermions from lattice boundaries, Nucl. Phys. B406 (1993) 90–106.
- [66] V. Furman, Y. Shamir, Axial symmetries in lattice QCD with Kaplan fermions, Nucl. Phys. B439 (1995) 54–78.
- [67] T. Blum, A. Soni, QCD with domain wall quarks, Phys. Rev. D56 (1997) 174–178.
- [68] H. Neuberger, Exactly massless quarks on the lattice, Phys. Lett. B417 (1998) 141–144.
- [69] H. Neuberger, More about exactly massless quarks on the lattice, Phys. Lett. B427 (1998) 353–355.
- [70] M. Luscher, Exact chiral symmetry on the lattice and the Ginsparg- Wilson relation, Phys. Lett. B428 (1998) 342–345.
- [71] P. F. Bedaque, Aharonov-Bohm effect and nucleon nucleon phase shifts on the lattice, Phys. Lett. B593 (2004) 82–88.
- [72] G. M. de Divitiis, R. Petronzio, N. Tantalo, On the discretization of physical momenta in lattice QCD, Phys. Lett. B595 (2004) 408–413.
- [73] G. 't Hooft, A Property of Electric and Magnetic Flux in Nonabelian Gauge Theories, Nucl. Phys. B153 (1979) 141.
- [74] M. Luscher, Volume Dependence of the Energy Spectrum in Massive Quantum Field Theories. 1. Stable Particle States, Commun. Math. Phys. 104 (1986) 177.
- [75] C. T. Sachrajda, G. Villadoro, Twisted boundary conditions in lattice simulations, Phys. Lett. B609 (2005) 73–85.
- [76] M. Luscher, Signatures of unstable particles in finite volume, Nucl. Phys. B364 (1991) 237–254.
- [77] L. Lellouch, M. Luscher, Weak transition matrix elements from finite-volume correlation functions, Commun. Math. Phys. 219 (2001) 31–44.
- [78] A. S. Kronfeld, Uses of effective field theory in lattice QCD. arXiv:hep-lat/0205021.
- [79] J. Gasser, H. Leutwyler, Spontaneously Broken Symmetries: Effective Lagrangians at Finite Volume, Nucl. Phys. B307 (1988) 763.
- [80] G. Colangelo, C. Haefeli, Finite volume effects for the pion mass at two loops, Nucl. Phys. B744 (2006) 14–33.
- [81] K. Symanzik, Continuum Limit and Improved Action in Lattice Theories. 1. Principles and  $\phi^4$  Theory, Nucl. Phys. B226 (1983) 187.
- [82] K. Symanzik, Continuum Limit and Improved Action in Lattice Theories. 2.  $O(N)$  Nonlinear Sigma Model in Perturbation Theory, Nucl. Phys. B226 (1983) 205.
- [83] A. S. Kronfeld, Application of heavy-quark effective theory to lattice QCD. I: Power corrections, Phys. Rev. D62 (2000) 014505.
- [84] J. Harada, et al., Application of heavy-quark effective theory to lattice QCD. II: Radiative corrections to heavy-light currents, Phys. Rev. D65 (2002) 094513.
- [85] J. Harada, S. Hashimoto, A. S. Kronfeld, T. Onogi, Application of heavy-quark effective theory to lattice QCD. III: Radiative corrections to heavy-heavy currents, Phys. Rev. D65 (2002) 094514.
- [86] A. S. Kronfeld, Heavy quarks and lattice QCD, Nucl. Phys. Proc. Suppl. 129 (2004) 46–59.
- [87] G. M. de Divitiis, M. Guagnelli, F. Palombi, R. Petronzio, N. Tantalo, Heavy-light decay constants in the continuum limit of lattice QCD, Nucl. Phys. B672 (2003) 372–386.
- [88] H.-W. Lin, N. Christ, Non-perturbatively determined relativistic heavy quark action, Phys. Rev. D76 (2007) 074506.
- [89] E. Marinari, G. Parisi, C. Rebbi, Monte Carlo Simulation of the Massive Schwinger Model, Nucl. Phys. B190 (1981) 734.
- [90] D. Weingarten, Monte Carlo Evaluation of Hadron Masses in Lattice Gauge Theories with Fermions, Phys. Lett. B109 (1982) 57.
- [91] C. T. H. Davies, et al., High-precision lattice QCD confronts experiment, Phys. Rev. Lett. 92 (2004) 022001.
- [92] C. W. Bernard, et al., The QCD spectrum with three quark flavors, Phys. Rev. D64 (2001) 054506.
- [93] C. Aubin, et al., Light hadrons with improved staggered quarks: Approaching the continuum limit, Phys. Rev. D70 (2004) 094505.
- [94] K. Jansen, Lattice QCD: a critical status report. arXiv:0810.5634.
- [95] H. W. Hamber, E. Marinari, G. Parisi, C. Rebbi, Numerical simulations of Quantum Chromodynamics, Phys. Lett. B124 (1983) 99.
- [96] M. Creutz, The evil that is rooting, Phys. Lett. B649 (2007) 230–234.
- [97] M. Creutz, The author replies. (Chiral anomalies and rooted staggered fermions), Phys. Lett. B649 (2007) 241–242.

- [98] M. Creutz, Why rooting fails, PoS LAT2007 (2007) 007.
- [99] C. Bernard, M. Golterman, Y. Shamir, S. R. Sharpe, Comment on 'Chiral anomalies and rooted staggered fermions', Phys. Lett. B649 (2007) 235–240.
- [100] C. Bernard, M. Golterman, Y. Shamir, S. R. Sharpe, 't Hooft vertices, partial quenching, and rooted staggered QCD, Phys. Rev. D77 (2008) 114504.
- [101] Y. Shamir, Locality of the fourth root of the staggered-fermion determinant: Renormalization-group approach, Phys. Rev. D71 (2005) 034509.
- [102] Y. Shamir, Renormalization-group analysis of the validity of staggered-fermion QCD with the fourth-root recipe, Phys. Rev. D75 (2007) 054503.
- [103] S. Durr, Theoretical issues with staggered fermion simulations, PoS LAT2005 (2006) 021.
- [104] S. R. Sharpe, Rooted staggered fermions: Good, bad or ugly?, PoS LAT2006 (2006) 022.
- [105] A. S. Kronfeld, Lattice gauge theory with staggered fermions: how, where, and why (not), PoS LAT2007 (2007) 016.
- [106] A. Bazavov, et al., Full nonperturbative QCD simulations with 2+1 flavors of improved staggered quarks. arXiv:0903.3598.
- [107] S. Aoki, et al., 2+1 Flavor Lattice QCD toward the Physical Point. arXiv:0807.1661.
- [108] S. Durr, et al., Ab Initio Determination of Light Hadron Masses, Science 322 (2008) 1224–1227.
- [109] P. Boucaud, et al., Dynamical twisted mass fermions with light quarks, Phys. Lett. B650 (2007) 304–311.
- [110] C. Allton, et al., Physical Results from 2+1 Flavor Domain Wall QCD and SU(2) Chiral Perturbation Theory, Phys. Rev. D78 (2008) 114509.
- [111] S. Aoki, et al., Two-flavor QCD simulation with exact chiral symmetry, Phys. Rev. D78 (2008) 014508.
- [112] S. Weinberg, Phenomenological Lagrangians, Physica A96 (1979) 327.
- [113] J. Gasser, H. Leutwyler, Chiral Perturbation Theory to One Loop, Ann. Phys. 158 (1984) 142.
- [114] J. Gasser, H. Leutwyler, Chiral Perturbation Theory: Expansions in the Mass of the Strange Quark, Nucl. Phys. B250 (1985) 465.
- [115] J. Goldstone, Field Theories with Superconductor Solutions, Nuovo Cim. 19 (1961) 154–164.
- [116] Y. Nambu, D. Lurie, Chirality conservation and soft pion production, Phys. Rev. 125 (1962) 1429–1436.
- [117] S. Weinberg, Nonlinear realizations of chiral symmetry, Phys. Rev. 166 (1968) 1568–1577.
- [118] S. R. Coleman, J. Wess, B. Zumino, Structure of phenomenological Lagrangians. 1, Phys. Rev. 177 (1969) 2239–2247.
- [119] J. Callan, Curtis G., S. R. Coleman, J. Wess, B. Zumino, Structure of phenomenological Lagrangians. 2, Phys. Rev. 177 (1969) 2247–2250.
- [120] M. Gell-Mann, R. J. Oakes, B. Renner, Behavior of current divergences under SU(3) x SU(3), Phys. Rev. 175 (1968) 2195–2199.
- [121] M. Gell-Mann, Symmetries of baryons and mesons, Phys. Rev. 125 (1962) 1067–1084.
- [122] S. Okubo, Note on Unitary Symmetry in Strong Interaction. II Excited States of Baryons, Prog. Theor. Phys. 28 (1962) 24–32.
- [123] J. Bijnens, Chiral meson physics at two loops, AIP Conf. Proc. 768 (2005) 153–159.
- [124] A. Roessl, Pion kaon scattering near the threshold in chiral SU(2) perturbation theory, Nucl. Phys. B555 (1999) 507–539.
- [125] J. A. Cronin, Phenomenological model of strong and weak interactions in chiral U(3) x U(3), Phys. Rev. 161 (1967) 1483–1494.
- [126] J. Kambor, J. H. Missimer, D. Wyler, The Chiral Loop Expansion of the Nonleptonic Weak Interactions of Mesons, Nucl. Phys. B346 (1990) 17–64.
- [127] V. Cirigliano, J. F. Donoghue, E. Golowich, Electromagnetic corrections to  $K \rightarrow \pi\pi$ . I: Chiral perturbation theory, Phys. Rev. D61 (2000) 093001.
- [128] G. Ecker, G. Isidori, G. Muller, H. Neufeld, A. Pich, Electromagnetism in nonleptonic weak interactions, Nucl. Phys. B591 (2000) 419–434.
- [129] M. B. Wise, Chiral perturbation theory for hadrons containing a heavy quark, Phys. Rev. D45 (1992) 2188–2191.
- [130] G. Burdman, J. F. Donoghue, Union of chiral and heavy quark symmetries, Phys. Lett. B280 (1992) 287–291.
- [131] J. Gasser, M. E. Sainio, A. Svarc, Nucleons with Chiral Loops, Nucl. Phys. B307 (1988) 779.

- [132] E. E. Jenkins, A. V. Manohar, Baryon chiral perturbation theory using a heavy fermion Lagrangian, *Phys. Lett.* B255 (1991) 558–562.
- [133] R. Urech, Virtual photons in chiral perturbation theory, *Nucl. Phys.* B433 (1995) 234–254.
- [134] M. Knecht, H. Neufeld, H. Rupertsberger, P. Talavera, Chiral perturbation theory with virtual photons and leptons, *Eur. Phys. J.* C12 (2000) 469–478.
- [135] G. D’Ambrosio, G. F. Giudice, G. Isidori, A. Strumia, Minimal flavour violation: An effective field theory approach, *Nucl. Phys.* B645 (2002) 155–187.
- [136] T. Feldmann, M. Jung, T. Mannel, Sequential Flavour Symmetry Breaking. arXiv:0906.1523.
- [137] T. Hurth, G. Isidori, J. F. Kamenik, F. Mescia, Constraints on New Physics in MFV models: A Model-independent analysis of  $\Delta F = 1$  processes, *Nucl. Phys.* B808 (2009) 326–346.
- [138] T. Feldmann, T. Mannel, Minimal Flavour Violation and Beyond, *JHEP* 02 (2007) 067.
- [139] T. Feldmann, T. Mannel, Large Top Mass and Non-Linear Representation of Flavour Symmetry, *Phys. Rev. Lett.* 100 (2008) 171601.
- [140] A. L. Kagan, G. Perez, T. Volansky, J. Zupan, General Minimal Flavor Violation. arXiv:0903.1794.
- [141] A. J. Buras, Minimal flavor violation, *Acta Phys. Polon.* B34 (2003) 5615–5668.
- [142] L. J. Hall, R. Rattazzi, U. Sarid, The Top quark mass in supersymmetric SO(10) unification, *Phys. Rev.* D50 (1994) 7048–7065.
- [143] T. Blazek, S. Raby, S. Pokorski, Finite supersymmetric threshold corrections to CKM matrix elements in the large tan Beta regime, *Phys. Rev.* D52 (1995) 4151–4158.
- [144] G. Isidori, A. Retico, Scalar flavor changing neutral currents in the large tan beta limit, *JHEP* 11 (2001) 001.
- [145] W.-S. Hou, Enhanced charged Higgs boson effects in  $B^- \rightarrow \tau^- \bar{\nu}_\tau$  and  $b \rightarrow \tau^- \bar{\nu}_\tau + X$ , *Phys. Rev.* D48 (1993) 2342–2344.
- [146] G. Isidori, P. Paradisi, Hints of large tan(beta) in flavour physics, *Phys. Lett.* B639 (2006) 499–507.
- [147] G. Degrassi, P. Gambino, G. F. Giudice,  $B \rightarrow X_s \gamma$  in supersymmetry: Large contributions beyond the leading order, *JHEP* 12 (2000) 009.
- [148] M. S. Carena, D. Garcia, U. Nierste, C. E. M. Wagner,  $b \rightarrow s \gamma$  and supersymmetry with large tan( $\beta$ ), *Phys. Lett.* B499 (2001) 141–146.
- [149] A. J. Buras, P. H. Chankowski, J. Rosiek, L. Slawianowska,  $\Delta M_{d,s}, B_{d,s}^0 \rightarrow \mu^+ \mu^-$  and  $B \rightarrow X_s \gamma$  in supersymmetry at large tan  $\beta$ , *Nucl. Phys.* B659 (2003) 3.
- [150] A. J. Buras, P. H. Chankowski, J. Rosiek, L. Slawianowska,  $\Delta M(s) / \Delta M(d)$ , sin 2 Beta and the angle  $\gamma$  in the presence of new  $\Delta F = 2$  operators, *Nucl. Phys.* B619 (2001) 434–466.
- [151] C. Hamzaoui, M. Pospelov, M. Toharia, Higgs-mediated FCNC in supersymmetric models with large tan(beta), *Phys. Rev.* D59 (1999) 095005.
- [152] S. R. Choudhury, N. Gaur, Dileptonic decay of  $B_s$  meson in SUSY models with large tan(beta), *Phys. Lett.* B451 (1999) 86–92.
- [153] K. S. Babu, C. F. Kolda, Higgs mediated  $B^0 \rightarrow \mu^+ \mu^-$  in minimal supersymmetry, *Phys. Rev. Lett.* 84 (2000) 228–231.
- [154] S. P. Martin, A Supersymmetry Primer. arXiv:hep-ph/9709356.
- [155] L. J. Hall, L. Randall, Weak scale effective supersymmetry, *Phys. Rev. Lett.* 65 (1990) 2939–2942.
- [156] G. F. Giudice, R. Rattazzi, Theories with gauge-mediated supersymmetry breaking, *Phys. Rept.* 322 (1999) 419–499.
- [157] P. Paradisi, M. Ratz, R. Schieren, C. Simonetto, Running minimal flavor violation, *Phys. Lett.* B668 (2008) 202–209.
- [158] G. Colangelo, E. Nikolidakis, C. Smith, Supersymmetric models with minimal flavour violation and their running, *Eur. Phys. J.* C59 (2009) 75–98.
- [159] O. Buchmueller, et al., Predictions for Supersymmetric Particle Masses in the CMSSM using Indirect Experimental and Cosmological Constraints, *JHEP* 09 (2008) 117.
- [160] O. Buchmueller, et al., Prediction for the Lightest Higgs Boson Mass in the CMSSM using Indirect Experimental Constraints, *Phys. Lett.* B657 (2007) 87–94.
- [161] J. R. Ellis, D. V. Nanopoulos, Flavor Changing Neutral Interactions in Broken Supersymmetric Theories, *Phys. Lett.* B110 (1982) 44.
- [162] R. Barbieri, R. Gatto, Conservation Laws for Neutral Currents in Spontaneously Broken Supersymmetric Theories, *Phys. Lett.* B110 (1982) 211.
- [163] L. J. Hall, V. A. Kostelecky, S. Raby, New Flavor Violations in Supergravity Models, *Nucl. Phys.* B267 (1986) 415.



- [164] F. Gabbiani, E. Gabrielli, A. Masiero, L. Silvestrini, A complete analysis of FCNC and CP constraints in general SUSY extensions of the standard model, Nucl. Phys. B477 (1996) 321–352.
- [165] M. Ciuchini, et al., Next-to-leading order strong interaction corrections to the  $\Delta_F = 2$  effective hamiltonian in the MSSM, JHEP 09 (2006) 013.
- [166] J. Foster, K.-i. Okumura, L. Roszkowski, Probing the flavour structure of supersymmetry breaking with rare B-processes: A beyond leading order analysis, JHEP 08 (2005) 094.
- [167] M. Artuso, et al.,  $B$ ,  $D$  and  $K$  decays, Eur. Phys. J. C57 (2008) 309–492.
- [168] D. Chang, A. Masiero, H. Murayama, Neutrino mixing and large CP violation in B physics, Phys. Rev. D67 (2003) 075013.
- [169] M. Ciuchini, et al., Soft SUSY breaking grand unification: Leptons versus quarks on the flavor playground, Nucl. Phys. B783 (2007) 112–142.
- [170] A. J. Buras, A. Poschenrieder, S. Uhlig, W. A. Bardeen, Rare  $K$  and  $B$  Decays in the Littlest Higgs Model without T-Parity, JHEP 11 (2006) 062.
- [171] M. Blanke, et al., Rare and CP-Violating  $K$  and  $B$  Decays in the Littlest Higgs Model with T-Parity, JHEP 01 (2007) 066.
- [172] M. Blanke, A. J. Buras, S. Recksiegel, C. Tarantino, S. Uhlig, Correlations between  $\epsilon'/\epsilon$  and rare  $K$  decays in the littlest Higgs model with T-parity, JHEP 06 (2007) 082.
- [173] T. Goto, Y. Okada, Y. Yamamoto, Ultraviolet divergences of flavor changing amplitudes in the littlest Higgs model with T-parity, Phys. Lett. B670 (2009) 378–382.
- [174] M. Blanke, A. J. Buras, B. Duling, S. Recksiegel, C. Tarantino, FCNC processes in the Littlest Higgs model with T-parity: a 2009 LookIn preparation.
- [175] N. Arkani-Hamed, M. Schmaltz, Hierarchies without symmetries from extra dimensions, Phys. Rev. D61 (2000) 033005.
- [176] T. Gherghetta, A. Pomarol, Bulk fields and supersymmetry in a slice of AdS, Nucl. Phys. B586 (2000) 141–162.
- [177] S. J. Huber, Q. Shafi, Fermion Masses, Mixings and Proton Decay in a Randall- Sundrum Model, Phys. Lett. B498 (2001) 256–262.
- [178] K. Agashe, G. Perez, A. Soni, Flavor structure of warped extra dimension models, Phys. Rev. D71 (2005) 016002.
- [179] K. Agashe, M. Papucci, G. Perez, D. Pirjol, Next to minimal flavor violation. arXiv:hep-ph/0509117.
- [180] S. Davidson, G. Isidori, S. Uhlig, Solving the flavour problem with hierarchical fermion wave functions, Phys. Lett. B663 (2008) 73–79.
- [181] G. Cacciapaglia, et al., A GIM Mechanism from Extra Dimensions, JHEP 04 (2008) 006.
- [182] C. Csaki, A. Falkowski, A. Weiler, A Simple Flavor Protection for RS. arXiv:0806.3757.
- [183] C. Csaki, G. Perez, Z. Surujon, A. Weiler, Flavor Alignment via Shining in RS. arXiv:0907.0474.
- [184] V. Fanti, et al., The Beam and detector for the NA48 neutral kaon CP violations experiment at CERN, Nucl. Instrum. Meth. A574 (2007) 433–471.
- [185] A. Alavi-Harati, et al., Measurements of Direct CP Violation, CPT Symmetry, and Other Parameters in the Neutral Kaon System, Phys. Rev. D67 (2003) 012005.
- [186] G. D. Barr, et al., A New measurement of direct CP violation in the neutral kaon system, Phys. Lett. B317 (1993) 233–242.
- [187] L. K. Gibbons, et al., Measurement of the CP violation parameter  $\text{Re}(\epsilon'/\epsilon)$ , Phys. Rev. Lett. 70 (1993) 1203–1206.
- [188] J. R. Batley, et al., Measurement of the Dalitz plot slope parameters of the  $K^\pm \rightarrow \pi^\pm \pi^+ \pi^-$  decay, Phys. Lett. B649 (2007) 349–358.
- [189] G. Anelli, et al., Proposal to measure the rare decay  $K^+ \rightarrow \pi^+ \nu \bar{\nu}$  at the CERN SPSCERN-SPSC-2005-013.
- [190] G. Anelli, et al., NA62/P-326 Status report CERN-SPSC-2007-035.
- [191] I. V. Ajinenko, et al., Study of the  $K^- \rightarrow \pi^0 e^- \nu$  decay, Phys. Atom. Nucl. 65 (2002) 2064–2069.
- [192] S. C. Adler, et al., Evidence for the Decay  $K^+ \rightarrow \pi^+ \nu \bar{\nu}$ , Phys. Rev. Lett. 79 (1997) 2204–2207.
- [193] S. C. Adler, et al., Further Search for the Decay  $K^+ \rightarrow \pi^+ \nu \bar{\nu}$ , Phys. Rev. Lett. 84 (2000) 3768–3770.
- [194] S. S. Adler, et al., Further search for the decay  $K^+ \rightarrow \pi^+ \nu \bar{\nu}$  in the momentum region  $P \leq 195$  MeV/c, Phys. Rev. D70 (2004) 037102.

- [195] S. Adler, et al., Measurement of the  $K^+ \rightarrow \pi^+ \nu \bar{\nu}$  Branching Ratio, Phys. Rev. D77 (2008) 052003.
- [196] M. Adinolfi, et al., The tracking detector of the KLOE experiment, Nucl. Instrum. Meth. A488 (2002) 51–73.
- [197] M. Adinolfi, et al., The KLOE electromagnetic calorimeter, Nucl. Instrum. Meth. A482 (2002) 364–386.
- [198] PEP-II: An Asymmetric B Factory. Conceptual Design Report. June 1993SLAC-418.
- [199] A. E. Bondar, KEKB performance, Nucl. Instrum. Meth. A462 (2001) 139–145.
- [200] D. Andrews, et al., The CLEO Detector, Nucl. Instr. Meth. 211 (1983) 47.
- [201] Y. Kubota, et al., The CLEO-II detector, Nucl. Instrum. Meth. A320 (1992) 66–113.
- [202] G. Viehhauser, CLEO III operation, Nucl. Instrum. Meth. A462 (2001) 146–151.
- [203] D. Peterson, et al., The CLEO III drift chamber, Nucl. Instrum. Meth. A478 (2002) 142–146.
- [204] M. Artuso, et al., The CLEO RICH detector, Nucl. Instrum. Meth. A554 (2005) 147–194.
- [205] B. Aubert, et al., The BaBar detector, Nucl. Instrum. Meth. A479 (2002) 1–116.
- [206] A. Abashian, et al., The Belle detector, Nucl. Instrum. Meth. A479 (2002) 117–232.
- [207] R. A. Briere, et al., CLEO-c and CESR-c: A New Frontier of Weak and Strong Interactions, LEPP Report No. CLNS 01/1742.
- [208] J. Z. Bai, et al., The BES detector, Nucl. Instrum. Meth. A344 (1994) 319–334.
- [209] J. Z. Bai, et al., The BES upgrade, Nucl. Instrum. Meth. A458 (2001) 627–637.
- [210] F. A. Harris, Bepcii and Besiii, Int. J. Mod. Phys. A24 (2009) 377–384.
- [211] D. E. Acosta, et al., Measurement of the  $J/\psi$  meson and  $b$ -hadron production cross sections in  $p\bar{p}$  collisions at  $\sqrt{s} = 1960$  GeV, Phys. Rev. D71 (2005) 032001.
- [212] T. Aaltonen, et al., Measurement of the  $b$ -Hadron Production Cross Section Using Decays to  $mu^- D^0 X$  Final States in  $p\bar{p}$  Collisions at  $\sqrt{s} = 1.96$  TeV, Phys. Rev. D79 (2009) 092003.
- [213] T. Aaltonen, et al., Measurement of Ratios of Fragmentation Fractions for Bottom Hadrons in  $p\bar{p}$  Collisions at  $\sqrt{s} = 1.96$ -TeV, Phys. Rev. D77 (2008) 072003.
- [214] V. M. Abazov, et al., The Upgraded D0 Detector, Nucl. Instrum. Meth. A565 (2006) 463–537.
- [215] C. S. Hill, Operational experience and performance of the CDFII silicon detector, Nucl. Instrum. Meth. A530 (2004) 1–6.
- [216] D. Tsybychev, Status and performance of the new innermost layer of silicon detector at D0, Nucl. Instrum. Meth. A582 (2007) 701–704.
- [217] S. Cabrera, et al., The CDF-II time-of-flight detector, Nucl. Instrum. Meth. A494 (2002) 416–423.
- [218] A. Abulencia, et al., Observation of  $B_s^0 - \bar{B}_s^0$  oscillations, Phys. Rev. Lett. 97 (2006) 242003.
- [219] B. Ashmanskas, et al., The CDF silicon vertex trigger, Nucl. Instrum. Meth. A518 (2004) 532–536.
- [220] G. Salamanna, Study of  $B_s$  mixing at the CDFII experiment with a newly developed opposite side  $b$  flavour tagging algorithm using kaonsFERMILAB-THESIS-2006-21.
- [221] V. M. Abazov, et al., Measurement of  $B_d$  mixing using opposite-side flavor tagging, Phys. Rev. D74 (2006) 112002.
- [222] C. Lecci, A neural jet charge tagger for the measurement of the  $B/s^0 \bar{B}/s^0$  oscillation frequency at CDFFERMILAB-THESIS-2005-89.
- [223] B. Aubert, et al., A study of time dependent CP-violating asymmetries and flavor oscillations in neutral  $B$  decays at the  $\Upsilon(4S)$ , Phys. Rev. D66 (2002) 032003.
- [224] G. A. Giurgiu,  $B$  Flavor Tagging Calibration and Search for  $B_s$  Oscillations in Semileptonic Decays with the CDF Detector at FermilabFERMILAB-THESIS-2005-41.
- [225] V. Tiwari, Measurement of the  $B_s \bar{B}_s$  oscillation frequency using semileptonic decaysFERMILAB-THESIS-2007-09.
- [226] B. Aubert, et al., Measurement of Time-Dependent CP Asymmetry in  $B_0 \rightarrow \ell^+ \ell^- K^* K^0$  Decays. arXiv:0902.1708.
- [227] K. F. Chen, et al., Time-dependent CP-violating asymmetries in  $b \rightarrow \ell^+ \ell^- s$  anti- $q$   $q$  transitions, Phys. Rev. D72 (2005) 012004.
- [228] T. C. Collaboration, CDF Notes 8235,8241,8460 (2006).
- [229] A. Belloni, Observation of  $B_s^0 - \bar{B}_s^0$  oscillations and the development and application of same-side-kaon flavor tagging FERMILAB-THESIS-2007-36.
- [230] V. M. Abazov, et al., Measurement of  $B_s^0$  mixing parameters from the flavor-tagged decay  $B_s^0 \rightarrow J/\psi \phi$ , Phys. Rev. Lett. 101 (2008) 241801.
- [231] T. C. Collaboration, CDF Note 9203 (2008).
- [232] G. Sciolla, et al., The BaBar drift chamber, Nucl. Instrum. Meth. A419 (1998) 310–314.

- [233] H. Hirano, et al., A high resolution cylindrical drift chamber for the KEK B- factory, Nucl. Instrum. Meth. A455 (2000) 294–304.
- [234] A. A. Affolder, et al., CDF central outer tracker, Nucl. Instrum. Meth. A526 (2004) 249–299.
- [235] F. Ambrosino, et al., Data handling, reconstruction, and simulation for the KLOE experiment, Nucl. Instrum. Meth. A534 (2004) 403–433.
- [236] H. Kichimi, et al., The BELLE TOF system, Nucl. Instrum. Meth. A453 (2000) 315–320.
- [237] T. Iijima, et al., Aerogel Cherenkov counter for the BELLE detector, Nucl. Instrum. Meth. A453 (2000) 321–325.
- [238] I. Adam, et al., The DIRC particle identification system for the BaBar experiment, Nucl. Instrum. Meth. A538 (2005) 281–357.
- [239] B. Aubert, et al., Observation of CP violation in  $B^0 \rightarrow K^+\pi^-$  and  $B^0 \rightarrow \pi^+\pi^-$ , Phys. Rev. Lett. 99 (2007) 021603.
- [240] K. Hanagaki, H. Kakuno, H. Ikeda, T. Iijima, T. Tsukamoto, Electron identification in Belle, Nucl. Instrum. Meth. A485 (2002) 490–503.
- [241] C. Bebek, A Cesium Iodide calorimeter with photodiode readout for CLEO-II, Nucl. Instrum. Meth. A265 (1988) 258–265.
- [242] D. N. Brown, J. Ilic, G. B. Mohanty, Extracting longitudinal shower development information from crystal calorimetry plus tracking, Nucl. Instrum. Meth. A592 (2008) 254–260.
- [243] M. Adinolfi, et al., The KLOE electromagnetic calorimeter, Nucl. Instrum. Meth. A494 (2002) 326–331.
- [244] A. Abashian, et al., Muon identification in the Belle experiment at KEKB, Nucl. Instrum. Meth. A491 (2002) 69–82.
- [245] D. Bortoletto, et al., A Muon identification detector for B physics near  $e^+e^- \rightarrow B$  anti-B threshold, Nucl. Instrum. Meth. A320 (1992) 114–127.
- [246] B. Aubert, et al., Amplitude Analysis of the Decay  $B^0 \rightarrow K^+\pi^-\pi^0$ . arXiv:0807.4567.
- [247] B. Aubert, et al., Measurement of time dependent CP asymmetry parameters in  $B^0$  meson decays to  $\omega K_S^0$ ,  $\eta' K^0$ , and  $\pi^0 K_S^0$ , Phys. Rev. D79 (2009) 052003.
- [248] B. Aubert, et al., Measurement of  $|V_{cb}|$  and the form-factor slope for  $\bar{B} \rightarrow D\ell^-\bar{\nu}_\ell$  decays on the recoil of fully reconstructed  $B$  mesons. arXiv:0807.4978.
- [249] B. Aubert, et al., Determination of the form-factors for the decay  $B^0 \rightarrow D^{*-}\ell^+\nu_\ell$  and of the CKM matrix element  $|V_{cb}|$ , Phys. Rev. D77 (2008) 032002.
- [250] Q. He, et al., Comparison of  $D \rightarrow K_S^0\pi$  and  $D \rightarrow K_L^0\pi$  Decay Rates, Phys. Rev. Lett. 100 (2008) 091801.
- [251] J. Adler, et al., Measurement of the Branching Fractions for  $D^0 \rightarrow \pi^-e^+\nu_e$  and  $D^0 \rightarrow K^-e^+\nu_e$  and determination of  $(V_{cd}/V_{cs})^2$ , Phys. Rev. Lett. 62 (1989) 1821.
- [252] S. Dobbs, et al., Measurement of Absolute Hadronic Branching Fractions of D Mesons and  $e^+e^- \rightarrow D\bar{D}$  Cross Sections at the psi(3770), Phys. Rev. D76 (2007) 112001.
- [253] J. Y. Ge, et al., Study of  $D^0 \rightarrow \pi^-e^+\nu_e$ ,  $D^+ \rightarrow \pi^0e^+\nu_e$ ,  $D^0 \rightarrow K^-e^+\nu_e$ , and  $D^+ \rightarrow \bar{K}^0e^+\nu_e$  in Tagged Decays of the  $\psi(3770)$  Resonance. arXiv:0810.3878.
- [254] D. M. Asner, W. M. Sun, Time-Independent Measurements of  $D^0 - \bar{D}^0$  Mixing and Relative Strong Phases Using Quantum Correlations, Phys. Rev. D73 (2006) 034024.
- [255] A. Giri, Y. Grossman, A. Soffer, J. Zupan, Determining gamma using  $B^\pm \rightarrow DK^\pm$  with multibody D decays, Phys. Rev. D68 (2003) 054018.
- [256] J. P. Alexander, et al., Measurement of  $BD_s^+ \rightarrow \ell^+\nu$  and the Decay Constant  $fD_s^+$  From 600  $/pb^{-1}$  of  $e^\pm$  Annihilation Data Near 4170 MeV, Phys. Rev. D79 (2009) 052001.
- [257] R. H. Dalitz, , Phyl. Mag. 44 (1953) 1068.
- [258] B. Aubert, et al., Improved measurement of the CKM angle  $\gamma$  in  $B^\mp \rightarrow D^{(*)}K^{(*)\mp}$  decays with a Dalitz plot analysis of  $D$  decays to  $K_S^0\pi^+\pi^-$  and  $K_S^0K^+K^-$ , Phys. Rev. D78 (2008) 034023.
- [259] W. M. Yao, et al., Review of particle physics, J. Phys. G33 (2006) 1–1232.
- [260] J. M. Blatt, V. F. Weisskopf, Theoretical Nuclear Physics, John Wiley & Sons, New York.
- [261] C. Zemach, Three pion decays of unstable particles, Phys. Rev. 133 (1964) B1201.
- [262] C. Zemach, Determination of the Spins and Parities of Resonances, Phys. Rev. 140 (1965) B109–B124.
- [263] V. Filippini, A. Fontana, A. Rotondi, Covariant spin tensors in meson spectroscopy, Phys. Rev. D51 (1995) 2247–2261.
- [264] M. Jacob, G. C. Wick, Annals Phys. 7 (1959) 404.

- [265] S. U. Chung, Helicity coupling amplitudes in tensor formalism, *Phys. Rev. D* **48** (1993) 1225–1239.
- [266] E. P. Wigner, Resonance Reactions and Anomalous Scattering, *Phys. Rev.* **70** (1946) 15–33.
- [267] I. J. R. Aitchison, K-Matrix formalism for overlapping resonances, *Nucl. Phys.* **A189** (1972) 417–423.
- [268] W. J. Marciano, A. Sirlin, On the Renormalization of the Charm Quartet Model, *Nucl. Phys.* **B93** (1975) 303.
- [269] D. B. Chitwood, et al., Improved Measurement of the Positive Muon Lifetime and Determination of the Fermi Constant, *Phys. Rev. Lett.* **99** (2007) 032001.
- [270] W. J. Marciano, A. Sirlin, Radiative Corrections to beta Decay and the Possibility of a Fourth Generation, *Phys. Rev. Lett.* **56** (1986) 22.
- [271] J. C. Hardy, I. S. Towner, Superallowed  $0^+$  to  $0^+$  nuclear beta decays: A new survey with precision tests of the conserved vector current hypothesis and the standard model. arXiv:0812.1202.
- [272] I. S. Towner, J. C. Hardy, A new analysis of  $^{14}\text{O}$  beta decay: branching ratios and CVC consistency, *Phys. Rev. C* **72** (2005) 055501.
- [273] I. S. Towner, J. C. Hardy, An improved calculation of the isospin-symmetry-breaking corrections to superallowed Fermi beta decay, *Phys. Rev. C* **77** (2008) 025501.
- [274] W. E. Ormand, B. A. Brown, Calculated isospin-mixing corrections to Fermi  $\beta$ -decays in  $1s_0$ -shell nuclei with emphasis on  $A = 34$ , *Nucl. Phys.* **A440** (1985) 274–300.
- [275] W. E. Ormand, B. A. Brown, Corrections to the Fermi matrix element for superallowed beta decay, *Phys. Rev. Lett.* **62** (1989) 866–869.
- [276] W. E. Ormand, B. A. Brown, Isospin-mixing corrections for fp-shell Fermi transitions, *Phys. Rev. C* **52** (1995) 2455–2460.
- [277] G. A. Miller, A. Schwenk, Isospin-symmetry-breaking corrections to superallowed Fermi beta decay: Formalism and schematic models, *Phys. Rev.* **78** (2008) 035501.
- [278] E. Caurier, P. Navratil, W. E. Ormand, J. P. Vary, Ab initio shell model for  $A=10$  nuclei, *Phys. Rev. C* **66** (2002) 024314.
- [279] W. J. Marciano, A. Sirlin, Improved calculation of electroweak radiative corrections and the value of  $V_{ud}$ , *Phys. Rev. Lett.* **96** (2006) 032002.
- [280] J. D. Jackson, S. B. Treiman, H. W. Wyld, Possible tests of time reversal invariance in Beta decay, *Phys. Rev.* **106** (1957) 517–521.
- [281] D. H. Wilkinson, Analysis of neutron beta decay, *Nucl. Phys.* **A377** (1982) 474–504.
- [282] S. Gardner, C. Zhang, Sharpening low-energy, standard-model tests via correlation coefficients in neutron beta-decay, *Phys. Rev. Lett.* **86** (2001) 5666–5669.
- [283] C. Amsler, et al., Review of particle physics, *Phys. Lett.* **B667** (2008) 1.
- [284] A. Czarnecki, W. J. Marciano, A. Sirlin, Precision measurements and CKM unitarity, *Phys. Rev. D* **70** (2004) 093006.
- [285] H. Abele, The neutron. Its properties and basic interactions, *Prog. Part. Nucl. Phys.* **60** (2008) 1–81.
- [286] P. Bopp, et al., The beta decay asymmetry of the neutron and  $g_A/g_V$ , *Phys. Rev. Lett.* **56** (1986) 919.
- [287] B. Erokolimsky, I. Kuznetsov, I. Stepanenko, Y. A. Mostovoi, Corrigendum: Corrected value of the beta-emission asymmetry in the decay of polarized neutrons measured in 1990, *Phys. Lett. B* **412** (1997) 240–241.
- [288] P. Liaud, et al., The measurement of the beta asymmetry in the decay of polarized neutrons, *Nucl. Phys.* **A612** (1997) 53–81.
- [289] H. Abele, et al., Is the Unitarity of the quark-mixing-CKM-matrix violated in neutron  $\beta$ -decay?, *Phys. Rev. Lett.* **88** (2002) 211801.
- [290] Y. A. Mostovoi, I. A. Kuznetsov, A. P. Serebrov, B. G. Erokolimsky, Effect of taking into account the radiative decay mode in measurements of the antineutrino-spin correlation in neutron decay, *Phys. Atom. Nucl.* **64** (2001) 151–152.
- [291] A. Serebrov, et al., Measurement of the neutron lifetime using a gravitational trap and a low-temperature Fomblin coating, *Phys. Lett. B* **605** (2005) 72–78.
- [292] R. W. Pattie, et al., First Measurement of the Neutron  $\beta$ -Asymmetry with Ultracold Neutrons, *Phys. Rev. Lett.* **102** (2009) 012301.
- [293] M. Ademollo, R. Gatto, Nonrenormalization Theorem for the Strangeness Violating Vector Currents, *Phys. Rev. Lett.* **13** (1964) 264–265.

- [294] V. Cirigliano, M. Knecht, H. Neufeld, H. Pichl, The pionic beta decay in chiral perturbation theory, *Eur. Phys. J. C*27 (2003) 255–262.
- [295] S. Descotes-Genon, B. Moussallam, Radiative corrections in weak semi-leptonic processes at low energy: A two-step matching determination, *Eur. Phys. J. C*42 (2005) 403–417.
- [296] D. Poganic, et al., Precise Measurement of the  $\pi^+ \rightarrow \pi^0 e^+ \nu$  Branching Ratio, *Phys. Rev. Lett.* 93 (2004) 181803.
- [297] W. J. Marciano, A. Sirlin, Radiative corrections to pi(lepton 2) decays, *Phys. Rev. Lett.* 71 (1993) 3629–3632.
- [298] V. Cirigliano, I. Rosell,  $\pi/K \rightarrow e\nu$  branching ratios to  $O(e^2 p^4)$  in Chiral Perturbation Theory, *JHEP* 10 (2007) 005.
- [299] A. Sirlin, Current Algebra Formulation of Radiative Corrections in Gauge Theories and the Universality of the Weak Interactions, *Rev. Mod. Phys.* 50 (1978) 573.
- [300] A. Sirlin, Large  $m(W)$ ,  $m(Z)$  Behavior of the  $O(\alpha)$  Corrections to Semileptonic Processes Mediated by  $W$ , *Nucl. Phys. B*196 (1982) 83.
- [301] W. J. Marciano, Precise determination of  $|V_{us}|$  from lattice calculations of pseudoscalar decay constants, *Phys. Rev. Lett.* 93 (2004) 231803.
- [302] V. Cirigliano, I. Rosell, Two-loop effective theory analysis of  $\pi(K) \rightarrow e$  anti- $\nu/e$  [ $\gamma$ ] branching ratios, *Phys. Rev. Lett.* 99 (2007) 231801.
- [303] M. Finkemeier, Radiative corrections to  $\pi(l_2)$  and  $K(l_2)$  decays, *Phys. Lett. B*387 (1996) 391–394.
- [304] V. Cirigliano, M. Giannotti, H. Neufeld, Electromagnetic effects in  $Kl_3$  decays, *JHEP* 11 (2008) 006.
- [305] B. Ananthanarayan, B. Moussallam, Four-point correlator constraints on electromagnetic chiral parameters and resonance effective Lagrangians, *JHEP* 06 (2004) 047.
- [306] V. Cirigliano, M. Knecht, H. Neufeld, H. Rupertsberger, P. Talavera, Radiative corrections to  $Kl_3$  decays, *Eur. Phys. J. C*23 (2002) 121–133.
- [307] J. Gasser, H. Leutwyler, Low-Energy Expansion of Meson Form-Factors, *Nucl. Phys. B*250 (1985) 517–538.
- [308] R. F. Dashen, Chiral  $SU(3) \times SU(3)$  as a symmetry of the strong interactions, *Phys. Rev.* 183 (1969) 1245–1260.
- [309] H. Neufeld, H. Rupertsberger, Isospin breaking in chiral perturbation theory and the decays  $\eta \rightarrow \pi$  lepton neutrino and  $\tau \rightarrow \eta \pi$  neutrino, *Z. Phys. C*68 (1995) 91–102.
- [310] A. Kastner, H. Neufeld, The  $Kl_3$  scalar form factors in the standard model, *Eur. Phys. J. C*57 (2008) 541–556.
- [311] J. F. Donoghue, A. F. Perez, The electromagnetic mass differences of pions and kaons, *Phys. Rev. D*55 (1997) 7075–7092.
- [312] J. Bijnens, J. Prades, Electromagnetic corrections for pions and kaons: Masses and polarizabilities, *Nucl. Phys. B*490 (1997) 239–271.
- [313] G. Amoros, J. Bijnens, P. Talavera, QCD isospin breaking in meson masses, decay constants and quark mass ratios, *Nucl. Phys. B*602 (2001) 87–108.
- [314] J. Bijnens, K. Ghorbani,  $\eta \rightarrow 3\pi$  at Two Loops In Chiral Perturbation Theory, *JHEP* 11 (2007) 030.
- [315] H. Leutwyler, The ratios of the light quark masses, *Phys. Lett. B*378 (1996) 313–318.
- [316] C. G. Callan, S. B. Treiman, Equal Time Commutators and  $K$  Meson Decays, *Phys. Rev. Lett.* 16 (1966) 153–157.
- [317] H. Leutwyler, private communication.
- [318] J. Bijnens, K. Ghorbani, Isospin breaking in  $K\pi$  vector form-factors for the weak and rare decays  $K_{\ell 3}$ ,  $K \rightarrow \pi \nu \bar{\nu}$  and  $K \rightarrow \pi \ell^+ \ell^-$ . arXiv:0711.0148.
- [319] V. Bernard, E. Passemar, Matching Chiral Perturbation Theory and the Dispersive Representation of the Scalar  $K\pi$  Form Factor, *Phys. Lett. B*661 (2008) 95–102.
- [320] V. Bernard, M. Oertel, E. Passemar, J. Stern, Dispersive representation and shape of the  $Kl_3$  form factors: robustness. arXiv:0903.1654.
- [321] R. J. Hill, Constraints on the form factors for  $K \rightarrow \pi l \nu$  and implications for  $|V_{us}|$ , *Phys. Rev. D*74 (2006) 096006.
- [322] V. Bernard, M. Oertel, E. Passemar, J. Stern,  $K(L)(\mu 3)$  decay: A stringent test of right-handed quark currents, *Phys. Lett. B*638 (2006) 480.
- [323] K. M. Watson, The Effect of final state interactions on reaction cross- sections, *Phys. Rev.* 88 (1952) 1163–1171.

- [324] E. Passemar, Dispersive representation and shape of  $K_{l3}$  form factors, PoS KAON (2008) 012.
- [325] H. Leutwyler, M. Roos, Determination of the Elements  $V(us)$  and  $V(ud)$  of the Kobayashi-Maskawa Matrix, Z. Phys. C25 (1984) 91.
- [326] J. Bijnens, P. Talavera,  $K(l3)$  decays in chiral perturbation theory, Nucl. Phys. B669 (2003) 341–362.
- [327] M. Jamin, J. A. Oller, A. Pich, Order  $p^6$  chiral couplings from the scalar  $K\pi$  form-factor, JHEP 02 (2004) 047.
- [328] V. Cirigliano, et al., The  $\langle S P P \rangle_l$  Green function and  $SU(3)$  breaking in  $K(l3)$  decays, JHEP 04 (2005) 006.
- [329] D. Becirevic, et al., The  $K \rightarrow \pi$  vector form factor at zero momentum transfer on the lattice, Nucl. Phys. B705 (2005) 339–362.
- [330] N. Tsutsui, et al., Kaon semileptonic decay form factors in two-flavor QCD, PoS LAT2005 (2006) 357.
- [331] C. Dawson, T. Izubuchi, T. Kaneko, S. Sasaki, A. Soni, Vector form factor in  $K_{l3}$  semileptonic decay with two flavors of dynamical domain-wall quarks, Phys. Rev. D74 (2006) 114502.
- [332] D. Brommel, et al., Kaon semileptonic decay form factors from  $N_f = 2$  non-perturbatively  $O(a)$ -improved Wilson fermions, PoS LAT2007 (2007) 364.
- [333] P. A. Boyle, et al.,  $K_{l3}$  semileptonic form factor from 2+1 flavour lattice QCD, Phys. Rev. Lett. 100 (2008) 141601.
- [334] V. Lubicz, F. Mescia, S. Simula, C. Tarantino, f. t. E. Collaboration,  $K \rightarrow \pi$  Semileptonic Form Factors from Two-Flavor Lattice QCD. arXiv:0906.4728.
- [335] J. M. Flynn, C. T. Sachrajda,  $SU(2)$  chiral perturbation theory for  $K_{l3}$  decay amplitudes, Nucl. Phys. B812 (2009) 64–80.
- [336] P. A. Boyle, J. M. Flynn, A. Juttner, C. T. Sachrajda, J. M. Zanotti, Hadronic form factors in lattice QCD at small and vanishing momentum transfer, JHEP 05 (2007) 016.
- [337] C. Aubin, et al., Light pseudoscalar decay constants, quark masses, and low energy constants from three-flavor lattice QCD, Phys. Rev. D70 (2004) 114501.
- [338] E. Follana, C. T. H. Davies, G. P. Lepage, J. Shigemitsu, High Precision determination of the  $\pi$ ,  $K$ ,  $D$  and  $D_s$  decay constants from lattice QCD, Phys. Rev. Lett. 100 (2008) 062002.
- [339] S. Dürr,  $f_K/f_\pi$  in full QCD, Talk at The XXVI International Symposium on Lattice Field Theory, 2008.
- [340] C. Aubin, J. Laiho, R. S. Van de Water, Light pseudoscalar meson masses and decay constants from mixed action lattice QCD. arXiv:0810.4328.
- [341] B. Blossier, et al., Pseudoscalar decay constants of kaon and D-mesons from  $N_f=2$  twisted mass Lattice QCD. arXiv:0904.0954.
- [342] S. R. Beane, P. F. Bedaque, K. Orginos, M. J. Savage,  $f_K/f_\pi$  in Full QCD with Domain Wall Valence Quarks, Phys. Rev. D75 (2007) 094501.
- [343] G. Colangelo, et al., The FLAG working group: making lattice results accessible to phenomenologists Kaon09 <http://kaon09.kek.jp/program.html>.
- [344] M. Antonelli, et al., Precision tests of the Standard Model with leptonic and semileptonic kaon decays. arXiv:0801.1817.
- [345] T. Alexopoulos, et al., Measurements of  $KL$  Branching Fractions and the CP Violation Parameter  $-\eta_{+-}$ , Phys. Rev. D70 (2004) 092006.
- [346] A. Lai, et al., Measurement of the branching ratio of the decay  $K_L \rightarrow \pi e \nu$  and extraction of the CKM parameter  $|V_{us}|$ , Phys. Lett. B602 (2004) 41–51.
- [347] F. Ambrosino, et al., Measurements of the absolute branching ratios for the dominant  $K(L)$  decays, the  $K(L)$  lifetime, and  $V(us)$  with the KLOE detector, Phys. Lett. B632 (2006) 43–50.
- [348] F. Ambrosino, et al., Measurement of the  $K(L)$  meson lifetime with the KLOE detector, Phys. Lett. B626 (2005) 15–23.
- [349] F. Ambrosino, et al., Measurement of the branching ratio of the  $K_L \rightarrow \pi^+ \pi^-$  decay with the KLOE detector, Phys. Lett. B638 (2006) 140–145.
- [350] A. Lai, et al., Measurement of the ratio  $\Gamma(K_L \rightarrow \pi^+ \pi^-)/\Gamma(K_L \rightarrow \pi^\pm e^\mp \nu)$  and extraction of the CP violation parameter  $|\eta_\pm|$ , Phys. Lett. B645 (2007) 26–35.
- [351] F. Ambrosino, et al., Measurement of the branching fraction and charge asymmetry for the decay  $K_S \rightarrow \pi e \nu$  with the KLOE detector, Phys. Lett. B636 (2006) 173–182.
- [352] F. Ambrosino, et al., Precise measurement of  $\Gamma(K_S \rightarrow \pi^+ \pi^- (\gamma))/\Gamma(K_S \rightarrow \pi^0 \pi^0)$  with the KLOE detector at DAFNE, Eur. Phys. J. C48 (2006) 767–780.

- [353] J. R. Batley, et al., Determination of the relative decay rate  $K(S) \rightarrow \pi e \nu / K(L) \rightarrow \pi e \nu$ , Phys. Lett. B653 (2007) 145–150.
- [354] J. R. Batley, et al., Measurements of Charged Kaon Semileptonic Decay Branching Fractions  $K^\pm \rightarrow \pi^0 \mu^\pm \nu$  and  $K^\pm \rightarrow \pi^0 e^\pm \nu$  and Their Ratio, Eur. Phys. J. C50 (2007) 329–340.
- [355] F. Ambrosino, et al., Measurement of the absolute branching ratios for semileptonic  $K^\pm$  decays with the KLOE detector, JHEP 02 (2008) 098.
- [356] F. Ambrosino, et al., The measurement of the absolute branching ratio of the  $K^+$  to  $\pi^+ \pi^0$  ( $\gamma$ ) decay at KLOE. arXiv:0707.2654.
- [357] F. Ambrosino, et al., Measurement of the absolute branching ratio for the  $K^+ \rightarrow \mu^+ \nu(\gamma)$  decay with the KLOE detector, Phys. Lett. B632 (2006) 76–80.
- [358] M. Antonelli presentation at La Thuile '09; M. Moulson, communication to FlaviaNet Kaon WG.
- [359] E. Goudzovski presentation at KAON09; M. Sozzi, communication to FlaviaNet Kaon WG.
- [360] T. Alexopoulos, et al., Measurements of Semileptonic KL Decay Form Factors, Phys. Rev. D70 (2004) 092007.
- [361] F. Ambrosino, et al., Measurement of the form-factor slopes for the decay  $K_L \rightarrow \pi^\pm e^\mp \nu$  with the KLOE detector, Phys. Lett. B636 (2006) 166–172.
- [362] O. P. Yushchenko, et al., High statistic measurement of the  $K^- \rightarrow \pi^0 e^- \nu$  decay form-factors, Phys. Lett. B589 (2004) 111–117.
- [363] A. Lai, et al., Measurement of  $K_{e3}^0$  form factors, Phys. Lett. B604 (2004) 1–10.
- [364] F. Ambrosino, et al., Measurement of the  $K_L \rightarrow \pi \mu \nu$  form factor parameters with the KLOE detector, JHEP 12 (2007) 105.
- [365] O. P. Yushchenko, et al., High statistic study of the  $K^- \rightarrow \pi^0 \mu^- \nu$  decay, Phys. Lett. B581 (2004) 31–38.
- [366] A. Lai, et al., Measurement of  $K_{\mu 3}^0$  form factors, Phys. Lett. B647 (2007) 341–350.
- [367] E. Gamiz, M. Jamin, A. Pich, J. Prades, F. Schwab,  $V_{us}$  and  $m_s$  from hadronic tau decays, Phys. Rev. Lett. 94 (2005) 011803.
- [368] E. Gamiz, M. Jamin, A. Pich, J. Prades, F. Schwab, Theoretical progress on the  $V_{us}$  determination from tau decays, PoS KAON (2008) 008.
- [369] E. Braaten, QCD Predictions for the Decay of the tau Lepton, Phys. Rev. Lett. 60 (1988) 1606–1609.
- [370] S. Narison, A. Pich, QCD Formulation of the tau Decay and Determination of  $\Lambda_{MS}$ , Phys. Lett. B211 (1988) 183.
- [371] E. Braaten, S. Narison, A. Pich, QCD analysis of the tau hadronic width, Nucl. Phys. B373 (1992) 581–612.
- [372] F. Le Diberder, A. Pich, The perturbative QCD prediction to  $R(\tau)$  revisited, Phys. Lett. B286 (1992) 147–152.
- [373] A. Pich, QCD predictions for the tau hadronic width: Determination of  $\alpha_s(M_\tau^2)$ , Nucl. Phys. Proc. Suppl. 39BC (1995) 326.
- [374] B. Aubert, et al., Exclusive branching fraction measurements of semileptonic tau decays into three charged hadrons,  $\tau^- \rightarrow \phi \pi^- \nu_\tau$  and  $\tau^- \rightarrow \phi K^- \nu_\tau$ , Phys. Rev. Lett. 100 (2008) 011801.
- [375] D. Epifanov, et al., Study of  $\tau^- \rightarrow K_S \pi^- \nu_\tau$  decay at Belle, Phys. Lett. B654 (2007) 65–73.
- [376] S. Banerjee, Measurement of  $|V_{us}|$  using hadronic tau decays from BaBar and Belle, PoS KAON (2008) 009.
- [377] M. Davier, A. Hocker, Z. Zhang, The physics of hadronic tau decays, Rev. Mod. Phys. 78 (2006) 1043–1109.
- [378] A. Pich, J. Prades, Strange quark mass determination from Cabibbo-suppressed tau decays, JHEP 10 (1999) 004.
- [379] S. Chen, et al., Strange quark mass from the invariant mass distribution of Cabibbo-suppressed tau decays, Eur. Phys. J. C22 (2001) 31–38.
- [380] K. G. Chetyrkin, J. H. Kuhn, A. A. Pivovarov, Determining the Strange Quark Mass in Cabibbo Suppressed Tau Lepton Decays, Nucl. Phys. B533 (1998) 473–493.
- [381] J. G. Korner, F. Krajewski, A. A. Pivovarov, Determination of the strange quark mass from Cabibbo suppressed tau decays with resummed perturbation theory in an effective scheme, Eur. Phys. J. C20 (2001) 259–269.
- [382] K. Maltman, C. E. Wolfe,  $V_{us}$  from hadronic tau decays, Phys. Lett. B639 (2006) 283–289.
- [383] J. Kambor, K. Maltman, The strange quark mass from flavor breaking in hadronic tau decays, Phys. Rev. D62 (2000) 093023.

- [384] K. Maltman, Problems with extracting  $m(s)$  from flavor breaking in hadronic tau decays, Phys. Rev. D58 (1998) 093015.
- [385] P. A. Baikov, K. G. Chetyrkin, J. H. Kuhn, Strange quark mass from tau lepton decays with  $O(\alpha_s^3)$  accuracy, Phys. Rev. Lett. 95 (2005) 012003.
- [386] M. Jamin, J. A. Oller, A. Pich, Scalar  $K \pi$  form factor and light quark masses, Phys. Rev. D74 (2006) 074009.
- [387] K. Maltman, J. Kambor, Decay constants, light quark masses and quark mass bounds from light quark pseudoscalar sum rules, Phys. Rev. D65 (2002) 074013.
- [388] K. Maltman, A Mixed Tau-Electroproduction Sum Rule for  $V_{us}$ , Phys. Lett. B672 (2009) 257–263.
- [389] K. Maltman, C. E. Wolfe, S. Banerjee, I. M. Nugent, J. M. Roney, Status of the Hadronic tau Decay Determination of  $|V_{us}|$ , Nucl. Phys. Proc. Suppl. 189 (2009) 175–180.
- [390] M. Testa, Recent results from KLOE. arXiv:0805.1969.
- [391] E. Passemar and S. Glazov, communication to FlaviaNet Kaon WG.
- [392] O. Yushchenko, communication to FlaviaNet Kaon WG.
- [393] S. Fubini, G. Furlan, On the algebraization of some dispersion sum rules, Lett. Nuovo Cim. 3S1 (1970) 168–172.
- [394] W. J. Marciano, A. Sirlin, Constraint on additional neutral gauge bosons from electroweak radiative corrections, Phys. Rev. D35 (1987) 1672–1676.
- [395] P. L. Anthony, et al., Precision measurement of the weak mixing angle in Moeller scattering, Phys. Rev. Lett. 95 (2005) 081601.
- [396] A. Czarnecki, W. J. Marciano, Electrons are not ambidextrous, Nature 435 (2005) 437–438.
- [397] A. G. Akeroyd, S. Recksiegel, The effect of  $H^\pm$  on  $B^\pm \rightarrow \tau^\pm \nu_\tau$  and  $B^\pm \rightarrow \mu^\pm \nu_\mu$ , J. Phys. G29 (2003) 2311–2317.
- [398] R. Barbieri, C. Bouchiat, A. Georges, P. Le Doussal, Quark-lepton nonuniversality in supersymmetric models, Phys. Lett. B156 (1985) 348.
- [399] K. Hagiwara, S. Matsumoto, Y. Yamada, Supersymmetric contribution to the quark - lepton universality violation in charged currents, Phys. Rev. Lett. 75 (1995) 3605–3608.
- [400] A. Kurylov, M. J. Ramsey-Musolf, Charged current universality in the MSSM, Phys. Rev. Lett. 88 (2002) 071804.
- [401] M. E. Peskin, T. Takeuchi, A New constraint on a strongly interacting Higgs sector, Phys. Rev. Lett. 65 (1990) 964–967.
- [402] W. J. Marciano, J. L. Rosner, Atomic parity violation as a probe of new physics, Phys. Rev. Lett. 65 (1990) 2963–2966.
- [403] A. Masiero, P. Paradisi, R. Petronzio, Probing new physics through  $\mu - e$  universality in  $K \rightarrow l\nu$ , Phys. Rev. D74 (2006) 011701.
- [404] C. Bourrely, B. Machet, E. de Rafael, Semileptonic decays of pseudoscalar particles ( $M \rightarrow M' l \nu_\ell$ ) and short distance behavior of Quantum Chromodynamics, Nucl. Phys. B189 (1981) 157.
- [405] C. G. Boyd, B. Grinstein, R. F. Lebed, Constraints on form-factors for exclusive semileptonic heavy to light meson decays, Phys. Rev. Lett. 74 (1995) 4603–4606.
- [406] L. Lellouch, Lattice-Constrained Unitarity Bounds for  $\bar{B}^0 \rightarrow \pi^+ \ell^- \bar{\nu}_\ell$  Decays, Nucl. Phys. B479 (1996) 353–391.
- [407] C. G. Boyd, M. J. Savage, Analyticity, shapes of semileptonic form factors, and  $\bar{B} \rightarrow \pi l \bar{\nu}$ , Phys. Rev. D56 (1997) 303–311.
- [408] M. C. Arnesen, B. Grinstein, I. Z. Rothstein, I. W. Stewart, A precision model independent determination of  $|V_{ub}|$  from  $B \rightarrow \pi e \nu$ , Phys. Rev. Lett. 95 (2005) 071802.
- [409] J. Bailey, et al., The  $B \rightarrow \pi l \nu$  semileptonic form factor from three- flavor lattice QCD: A model-independent determination of  $|V_{ub}|$ , Phys. Rev. D79 (2009) 054507.
- [410] T. Becher, R. J. Hill, Comment on form factor shape and extraction of  $|V_{ub}|$  from  $B \rightarrow \pi l \nu$ , Phys. Lett. B633 (2006) 61–69.
- [411] C. Bourrely, I. Caprini, L. Lellouch, Model-independent description of  $B \rightarrow \pi l \nu$  decays and a determination of  $|V_{ub}|$ , Phys. Rev. D79 (2009) 013008.
- [412] J. M. Flynn, J. Nieves, Extracting  $|V_{ub}|$  from  $B \rightarrow \pi l \nu$  decays using a multiply-subtracted Omnes dispersion relation, Phys. Rev. D75 (2007) 013008.
- [413] J. M. Flynn, J. Nieves,  $|V_{ub}|$  from exclusive semileptonic B to  $\pi$  decays revisited, Phys. Rev. D76 (2007) 031302.
- [414] W.-J. Lee, S. R. Sharpe, Partial Flavor Symmetry Restoration for Chiral Staggered Fermions, Phys. Rev. D60 (1999) 114503.



- [415] C. Aubin, C. Bernard, Pion and Kaon masses in Staggered Chiral Perturbation Theory, Phys. Rev. D68 (2003) 034014.
- [416] O. Bar, G. Rupak, N. Shoresh, Chiral perturbation theory at  $O(\alpha^2)$  for lattice QCD, Phys. Rev. D70 (2004) 034508.
- [417] S. R. Sharpe, J. M. S. Wu, Twisted mass chiral perturbation theory at next-to-leading order, Phys. Rev. D71 (2005) 074501.
- [418] O. Bar, C. Bernard, G. Rupak, N. Shoresh, Chiral perturbation theory for staggered sea quarks and Ginsparg-Wilson valence quarks, Phys. Rev. D72 (2005) 054502.
- [419] C. Aubin, C. Bernard, Heavy-Light Semileptonic Decays in Staggered Chiral Perturbation Theory, Phys. Rev. D76 (2007) 014002.
- [420] K. C. Bowler, et al., Improved  $B \rightarrow \pi \ell \nu_\ell$  form factors from the lattice, Phys. Lett. B486 (2000) 111–117.
- [421] A. Abada, et al., Heavy  $\rightarrow$  light semileptonic decays of pseudoscalar mesons from lattice QCD, Nucl. Phys. B619 (2001) 565–587.
- [422] S. Aoki, et al., Differential decay rate of  $B \rightarrow \pi \ell \nu$  semileptonic decay with lattice NRQCD, Phys. Rev. D64 (2001) 114505.
- [423] A. X. El-Khadra, A. S. Kronfeld, P. B. Mackenzie, S. M. Ryan, J. N. Simone, The semileptonic decays  $B \rightarrow \pi \ell \nu$  and  $D \rightarrow \pi \ell \nu$  from lattice QCD, Phys. Rev. D64 (2001) 014502.
- [424] J. Shigemitsu, et al., Semileptonic B decays from an NRQCD/D234 action, Phys. Rev. D66 (2002) 074506.
- [425] M. Okamoto, et al., Semileptonic  $D \rightarrow \pi/K$  and  $B \rightarrow \pi/D$  decays in 2+1 flavor lattice QCD, Nucl. Phys. Proc. Suppl. 140 (2005) 461–463.
- [426] E. Dalgic, et al., B Meson Semileptonic Form Factors from Unquenched Lattice QCD, Phys. Rev. D73 (2006) 074502.
- [427] B. Blossier, V. Lubicz, C. Tarantino, S. Simula, Pseudoscalar meson decay constants  $f_K$ ,  $f_D$  and  $f_{D_s}$ , from  $N_f = 2$  twisted mass Lattice QCD. arXiv:0810.3145.
- [428] D. Becirevic, B. Haas, F. Mescia, Semileptonic D-decays and Lattice QCD, PoS LAT2007 (2007) 355.
- [429] B. Haas, D-decays with unquenched Lattice QCD. arXiv:0805.2392.
- [430] A. A. Khan, et al., Decays of mesons with charm quarks on the lattice, PoS LAT2007 (2007) 343.
- [431] I. I. Balitsky, V. M. Braun, A. V. Kolesnichenko, Radiative Decay  $\Sigma^+ \rightarrow p \gamma$  in Quantum Chromodynamics, Nucl. Phys. B312 (1989) 509–550.
- [432] V. M. Braun, I. E. Filyanov, QCD Sum Rules in Exclusive Kinematics and Pion Wave Function, Z. Phys. C44 (1989) 157.
- [433] V. L. Chernyak, I. R. Zhitnitsky, B meson exclusive decays into baryons, Nucl. Phys. B345 (1990) 137–172.
- [434] M. A. Shifman, A. I. Vainshtein, V. I. Zakharov, QCD and Resonance Physics. Sum Rules, Nucl. Phys. B147 (1979) 385–447.
- [435] M. A. Shifman, A. I. Vainshtein, V. I. Zakharov, QCD and Resonance Physics: Applications, Nucl. Phys. B147 (1979) 448–518.
- [436] P. Colangelo, A. Khodjamirian, QCD sum rules, a modern perspective. arXiv:hep-ph/0010175.
- [437] V. M. Belyaev, A. Khodjamirian, R. Ruckl, QCD calculation of the  $B \rightarrow \pi, K$  form-factors, Z. Phys. C60 (1993) 349–356.
- [438] V. M. Belyaev, V. M. Braun, A. Khodjamirian, R. Ruckl,  $D^* D \pi$  and  $B^* B \pi$  couplings in QCD, Phys. Rev. D51 (1995) 6177–6195.
- [439] A. Khodjamirian, R. Ruckl, S. Weinzierl, O. I. Yakovlev, Perturbative QCD correction to the  $B \rightarrow \pi$  transition form factor, Phys. Lett. B410 (1997) 275–284.
- [440] E. Bagan, P. Ball, V. M. Braun, Radiative corrections to the decay  $B \rightarrow \pi \ell \nu$  and the heavy quark limit, Phys. Lett. B417 (1998) 154–162.
- [441] A. Khodjamirian, R. Ruckl, S. Weinzierl, C. W. Winhart, O. I. Yakovlev, Predictions on  $B \rightarrow \pi \bar{\ell} \nu_\ell$ ,  $D \rightarrow \pi \bar{\ell} \nu_\ell$  and  $D \rightarrow K \bar{\ell} \nu_\ell$  from QCD light-cone sum rules, Phys. Rev. D62 (2000) 114002.
- [442] P. Ball, R. Zwicky, New results on  $B \rightarrow \pi, K, \eta$  decay form factors from light-cone sum rules, Phys. Rev. D71 (2005) 014015.
- [443] P. Ball, Testing QCD sum rules on the light-cone in  $D \rightarrow (\pi, K) \ell \nu$  decays, Phys. Lett. B641 (2006) 50–56.
- [444] P. Ball, G. W. Jones, R. Zwicky,  $B \rightarrow V \gamma$  beyond QCD factorisation, Phys. Rev. D75 (2007) 054004.

- [445] P. Ball, G. W. Jones,  $B \rightarrow \eta^{(\prime)}$  Form Factors in QCD, JHEP 08 (2007) 025.
- [446] G. Duplancic, A. Khodjamirian, T. Mannel, B. Melic, N. Offen, Light-cone sum rules for  $B \rightarrow \pi$  form factors revisited, JHEP 04 (2008) 014.
- [447] G. Duplancic, B. Melic,  $B, B_s \rightarrow K$  form factors: an update of light-cone sum rule results, Phys. Rev. D78 (2008) 054015.
- [448] P. Ball, V. M. Braun, A. Lenz, Twist-4 Distribution Amplitudes of the  $K^*$  and  $\phi$  Mesons in QCD, JHEP 08 (2007) 090.
- [449] M. Jamin, B. O. Lange,  $f_B$  and  $f_{B_s}$  from QCD sum rules, Phys. Rev. D65 (2002) 056005.
- [450] A. Khodjamirian, T. Mannel, N. Offen, Form factors from light-cone sum rules with B-meson distribution amplitudes, Phys. Rev. D75 (2007) 054013.
- [451] F. De Fazio, T. Feldmann, T. Hurth, Light-cone sum rules in soft-collinear effective theory, Nucl. Phys. B733 (2006) 1–30.
- [452] F. De Fazio, T. Feldmann, T. Hurth, SCET sum rules for  $B \rightarrow P$  and  $B \rightarrow V$  transition form factors, JHEP 02 (2008) 031.
- [453] B. Aubert, et al., Measurement of the  $q^2$  dependence of the Hadronic Form Factor in  $D^0 \rightarrow K^- e^+ \nu_e$  decays, Phys. Rev. D76 (2007) 052005.
- [454] L. Widhalm, et al., Measurement of  $D^0 \rightarrow \pi \ell \nu (K \ell \nu)$  form factors and absolute branching fractions, Phys. Rev. Lett. 97 (2006) 061804.
- [455] L. Widhalm, Leptonic and semileptonic  $D$  and  $D_s$  decays at B- factories. arXiv:0710.0420.
- [456] S. Dobbs, et al., A Study of the Semileptonic Charm Decays  $D^0 \rightarrow \pi^- e^+ \nu_e$ ,  $D^+ \rightarrow \pi^0 e^+ \nu_e$ ,  $D^0 \rightarrow K^- e^+ \nu_e$ , and  $D^+ \rightarrow \bar{K}^0 e^+ \nu_e$ , Phys. Rev. D77 (2008) 112005.
- [457] . D. Besson, Improved measurements of D meson semileptonic decays to pi and K mesons. arXiv:0906.2983.
- [458] B. Aubert, et al., Study of the decay  $D_s^+ \rightarrow K^+ K^- e^+ \nu_e$ , Phys. Rev. D78 (2008) 051101.
- [459] J. M. Link, et al., New measurements of the  $D_s^+ \rightarrow \phi \mu^+ \nu$  form factor ratios, Phys. Lett. B586 (2004) 183–190.
- [460] C. Bernard, et al., Visualization of semileptonic form factors from lattice QCD. arXiv:0906.2498.
- [461] C. Aubin, et al., Semileptonic decays of D mesons in three-flavor lattice QCD, Phys. Rev. Lett. 94 (2005) 011601.
- [462] N. E. Adam, et al., A Study of Exclusive Charmless Semileptonic  $B$  Decay and  $|V_{ub}|$ , Phys. Rev. Lett. 99 (2007) 041802.
- [463] S. B. Athar, et al., Study of the  $q^2$  dependence of  $B \rightarrow \pi \ell \nu$  and  $B \rightarrow \rho(\omega) \ell \nu$  decay and extraction of  $|V_{ub}|$ , Phys. Rev. D68 (2003) 072003.
- [464] B. Aubert, et al., Measurement of the  $B^0 \rightarrow \pi^- \ell^+ \nu$  form- factor shape and branching fraction, and determination of  $|V_{ub}|$  with a loose neutrino reconstruction technique, Phys. Rev. Lett. 98 (2007) 091801.
- [465] B. Aubert, et al., Measurements of  $B \rightarrow \{\pi, \eta, \eta'\} \ell \nu \ell$  Branching Fractions and Determination of  $|V_{ub}|$  with Semileptonically Tagged  $B$  Mesons, Phys. Rev. Lett. 101 (2008) 081801.
- [466] B. Aubert, et al., Measurement of the  $B \rightarrow \pi \ell \nu$  Branching Fraction and Determination of  $|V_{ub}|$  with Tagged  $B$  Mesons, Phys. Rev. Lett. 97 (2006) 211801.
- [467] B. Aubert, et al., Measurement of the  $B^+ \rightarrow \omega \ell^+ \nu$  and  $B^+ \rightarrow \eta \ell^+ \nu$  Branching Fractions. arXiv:0808.3524.
- [468] B. Aubert, et al., Study of  $B \rightarrow \pi \ell \nu$  and  $B \rightarrow \rho \ell \nu$  decays and determination of  $|V_{ub}|$ , Phys. Rev. D72 (2005) 051102.
- [469] T. Hokuue, et al., Measurements of branching fractions and  $q^2$  distributions for  $B \rightarrow \pi \ell \nu$  and  $B \rightarrow \rho \ell \nu$  Decays with  $B \rightarrow D^{(*)} \ell \nu$  Decay Tagging, Phys. Lett. B648 (2007) 139–148.
- [470] I. Adachi, et al., Measurement of exclusive  $B \rightarrow X_u \ell \nu$  decays using full- reconstruction tagging at Belle. arXiv:0812.1414.
- [471] K. Abe, et al., Evidence for  $B^+ \rightarrow \omega \ell^+ \nu$ . arXiv:hep-ex/0307075.
- [472] D. Scora, N. Isgur, Semileptonic meson decays in the quark model: An update, Phys. Rev. D52 (1995) 2783–2812.
- [473] B. Aubert, et al., Measurement of the  $B^+ \rightarrow \eta \ell^+ \nu$  and  $B^+ \rightarrow \eta' \ell^+ \nu$  branching fractions using  $\nu_{4S} \rightarrow B \bar{B}$  events tagged by a fully reconstructed  $B$  meson. arXiv:hep-ex/0607066.
- [474] D. Becirevic, A. B. Kaidalov, Comment on the heavy  $\rightarrow$  light form factors, Phys. Lett. B478 (2000) 417–423.
- [475] R. S. Van de Water, P. B. Mackenzie, Unitarity and the heavy quark expansion in the determination of semileptonic form factors, PoS LAT2006 (2006) 097.

- [476] G. M. de Divitiis, E. Molinaro, R. Petronzio, N. Tantalo, Quenched lattice calculation of the  $B \rightarrow D\ell\nu$  decay rate, *Phys. Lett.* B655 (2007) 45–49.
- [477] G. M. de Divitiis, R. Petronzio, N. Tantalo, Quenched lattice calculation of semileptonic heavy-light meson form factors, *JHEP* 10 (2007) 062.
- [478] G. M. de Divitiis, R. Petronzio, N. Tantalo, Quenched lattice calculation of the vector channel  $B \rightarrow D^*\ell\nu$  decay rate, *Nucl. Phys.* B807 (2009) 373–395.
- [479] E. Eichten, B. R. Hill, An Effective Field Theory for the Calculation of Matrix Elements Involving Heavy Quarks, *Phys. Lett.* B234 (1990) 511.
- [480] J. Heitger, R. Sommer, Non-perturbative heavy quark effective theory, *JHEP* 02 (2004) 022.
- [481] R. Sommer, Non-perturbative QCD: Renormalization, O(a)-improvement and matching to heavy quark effective theory. [arXiv:hep-lat/0611020](https://arxiv.org/abs/hep-lat/0611020).
- [482] B. Sheikholeslami, R. Wohlert, Improved Continuum Limit Lattice Action for QCD with Wilson Fermions, *Nucl. Phys.* B259 (1985) 572.
- [483] A. X. El-Khadra, A. S. Kronfeld, P. B. Mackenzie, Massive Fermions in Lattice Gauge Theory, *Phys. Rev.* D55 (1997) 3933–3957.
- [484] M. B. Oktay, A. S. Kronfeld, New lattice action for heavy quarks, *Phys. Rev.* D78 (2008) 014504.
- [485] M. Guagnelli, F. Palombi, R. Petronzio, N. Tantalo,  $f_B$  and two scales problems in lattice QCD, *Phys. Lett.* B546 (2002) 237–246.
- [486] S. Hashimoto, et al., Lattice QCD calculation of  $\bar{B} \rightarrow D\ell\bar{\nu}$  decay form factors at zero recoil, *Phys. Rev.* D61 (1999) 014502.
- [487] M. E. Luke, Effects of subleading operators in the heavy quark effective theory, *Phys. Lett.* B252 (1990) 447–455.
- [488] M. Okamoto, Full determination of the CKM matrix using recent results from lattice QCD, *PoS LAT2005* (2006) 013.
- [489] C. Bernard, et al., The  $\bar{B} \rightarrow D^*\ell\bar{\nu}$  form factor at zero recoil from three-flavor lattice QCD: A Model independent determination of  $|V_{cb}|$ , *Phys. Rev.* D78 (2008) 094505.
- [490] J. Laiho, R. S. Van de Water,  $B \rightarrow D^*\ell\nu$  and  $B \rightarrow D\ell\nu$  form factors in staggered chiral perturbation theory, *Phys. Rev.* D73 (2006) 054501.
- [491] I. Caprini, L. Lellouch, M. Neubert, Dispersive bounds on the shape of  $\bar{B} \rightarrow D^{(*)}\ell\bar{\nu}$  form factors, *Nucl. Phys.* B530 (1998) 153–181.
- [492] J. E. Duboscq, et al., Measurement of the form-factors for  $\bar{B}^0 \rightarrow D^{*+}\ell^-\bar{\nu}$ , *Phys. Rev. Lett.* 76 (1996) 3898–3902.
- [493] . I. Adachi, Measurement of the form factors of the decay  $B_0 \rightarrow D^{*-}\ell^+\nu_l$  and determination of the CKM matrix element  $|V_{cb}|$ . [arXiv:0810.1657](https://arxiv.org/abs/0810.1657).
- [494] B. Aubert, et al., Measurement of the Decay  $B^- \rightarrow D^*0 e^-\bar{\nu}(e)$ , *Phys. Rev. Lett.* 100 (2008) 231803.
- [495] B. Aubert, et al., Measurements of the Semileptonic Decays  $\bar{B} \rightarrow D\ell\bar{\nu}$  and  $\bar{B} \rightarrow D^*\ell\bar{\nu}$  Using a Global Fit to  $DX\ell\bar{\nu}$  Final States, *Phys. Rev.* D79 (2009) 012002.
- [496] B. Grinstein, Z. Ligeti, Heavy quark symmetry in  $B \rightarrow D^{(*)}\ell\bar{\nu}$  spectra, *Phys. Lett.* B526 (2002) 345–354.
- [497] D. Liventsev, et al., Study of  $B \rightarrow D^{**}\ell\nu$  with full reconstruction tagging, *Phys. Rev.* D77 (2008) 091503.
- [498] B. Aubert, et al., A Measurement of the branching fractions of exclusive  $\bar{B} \rightarrow D^{(*)}(\pi)\ell^-\bar{\nu}(\ell)$  decays in events with a fully reconstructed  $B$  meson, *Phys. Rev. Lett.* 100 (2008) 151802.
- [499] J. Chay, H. Georgi, B. Grinstein, Lepton energy distributions in heavy meson decays from QCD, *Phys. Lett.* B247 (1990) 399–405.
- [500] I. I. Y. Bigi, M. A. Shifman, N. G. Uraltsev, A. I. Vainshtein, QCD predictions for lepton spectra in inclusive heavy flavor decays, *Phys. Rev. Lett.* 71 (1993) 496–499.
- [501] B. Blok, L. Koyrakh, M. A. Shifman, A. I. Vainshtein, Differential distributions in semileptonic decays of the heavy flavors in QCD, *Phys. Rev.* D49 (1994) 3356–3366.
- [502] A. V. Manohar, M. B. Wise, Inclusive semileptonic B and polarized  $A_b$  decays from QCD, *Phys. Rev.* D49 (1994) 1310–1329.
- [503] A. V. Manohar, M. B. Wise, Heavy quark physics, *Camb. Monogr. Part. Phys. Nucl. Phys. Cosmol.* 10 (2000) 1–191.
- [504] D. Benson, I. I. Bigi, T. Mannel, N. Uraltsev, Imprecated, yet impeccable: On the theoretical evaluation of  $\Gamma(B \rightarrow X_c\ell\nu)$ , *Nucl. Phys.* B665 (2003) 367–401.

- [505] A. F. Falk, M. Neubert, Second order power corrections in the heavy quark effective theory. 1. Formalism and meson form-factors, Phys. Rev. D47 (1993) 2965–2981.
- [506] T. Becher, H. Boos, E. Lunghi, Kinetic corrections to  $B \rightarrow X_c \ell \bar{\nu}$  at one loop, JHEP 12 (2007) 062.
- [507] C. W. Bauer, Z. Ligeti, M. Luke, A. V. Manohar, B decay shape variables and the precision determination of  $|V_{cb}|$  and  $m_b$ , Phys. Rev. D67 (2003) 054012.
- [508] C. W. Bauer, Z. Ligeti, M. Luke, A. V. Manohar, M. Trott, Global analysis of inclusive B decays, Phys. Rev. D70 (2004) 094017.
- [509] O. Buchmuller, H. Flacher, Fits to moment measurements from  $B \rightarrow X_c \ell \nu$  and  $B \rightarrow X_s \gamma$  decays using heavy quark expansions in the kinetic scheme, Phys. Rev. D73 (2006) 073008.
- [510] P. Gambino, N. Uraltsev, Moments of semileptonic B decay distributions in the  $1/m_b$  expansion, Eur. Phys. J. C34 (2004) 181–189.
- [511] M. Gremm, A. Kapustin, Order  $1/m_b$  3 corrections to inclusive semileptonic B decay, Phys. Rev. D55 (1997) 6924–6932.
- [512] M. Jezabek, J. H. Kuhn, QCD Corrections to Semileptonic Decays of Heavy Quarks, Nucl. Phys. B314 (1989) 1.
- [513] M. Jezabek, J. H. Kuhn, Lepton Spectra from Heavy Quark Decay, Nucl. Phys. B320 (1989) 20.
- [514] A. Czarnecki, M. Jezabek, J. H. Kuhn, Hadron spectra from semileptonic decays of heavy quarks, Acta Phys. Polon. B20 (1989) 961.
- [515] A. Czarnecki, M. Jezabek, Distributions of leptons in decays of polarized heavy quarks, Nucl. Phys. B427 (1994) 3–21.
- [516] M. B. Voloshin, Moments of lepton spectrum in B decays and the  $m(b) - m(c)$  quark mass difference, Phys. Rev. D51 (1995) 4934–4938.
- [517] M. Trott, Improving extractions of  $-V(cb)$  and  $m(b)$  from the hadronic invariant mass moments of semileptonic inclusive B decay, Phys. Rev. D70 (2004) 073003.
- [518] A. F. Falk, M. E. Luke, M. J. Savage, Hadron spectra for semileptonic heavy quark decay, Phys. Rev. D53 (1996) 2491–2505.
- [519] M. E. Luke, M. J. Savage, M. B. Wise, Perturbative strong interaction corrections to the heavy quark semileptonic decay rate, Phys. Lett. B343 (1995) 329–332.
- [520] P. Ball, M. Beneke, V. M. Braun, Resummation of running coupling effects in semileptonic B meson decays and extraction of  $|V_{cb}|$ , Phys. Rev. D52 (1995) 3929–3948.
- [521] M. Gremm, I. W. Stewart, Order  $\alpha_s^2 \beta_0$  correction to the charged lepton spectrum in  $b \rightarrow c \ell \bar{\nu}_\ell$  decays, Phys. Rev. D55 (1997) 1226–1232.
- [522] A. F. Falk, M. E. Luke, Hadronic spectral moments in semileptonic B decays with a lepton energy cut, Phys. Rev. D57 (1998) 424–430.
- [523] N. Uraltsev, Perturbative corrections to the semileptonic b-decay moments:  $E_{cut}^\ell$  dependence and running- $\alpha_s$  effects in the OPE approach, Int. J. Mod. Phys. A20 (2005) 2099–2118.
- [524] V. Aquila, P. Gambino, G. Ridolfi, N. Uraltsev, Perturbative corrections to semileptonic b decay distributions, Nucl. Phys. B719 (2005) 77–102.
- [525] N. Uraltsev, BLM-resummation and OPE in heavy flavor transitions, Nucl. Phys. B491 (1997) 303–322.
- [526] A. H. Hoang, Z. Ligeti, A. V. Manohar, B decays in the Upsilon expansion, Phys. Rev. D59 (1999) 074017.
- [527] M. Beneke, A quark mass definition adequate for threshold problems, Phys. Lett. B434 (1998) 115–125.
- [528] S. W. Bosch, B. O. Lange, M. Neubert, G. Paz, Factorization and shape-function effects in inclusive B- meson decays, Nucl. Phys. B699 (2004) 335–386.
- [529] M. Neubert, Two-loop relations for heavy-quark parameters in the shape-function scheme, Phys. Lett. B612 (2005) 13–20.
- [530] M. Neubert, QCD Calculations of Decays of Heavy Flavor Hadrons. arXiv:0801.0675.
- [531] K. Melnikov,  $O(\alpha_s^2)$  corrections to semileptonic decay  $b \rightarrow c \ell \bar{\nu}_\ell$ . arXiv:0803.0951.
- [532] A. Pak, A. Czarnecki, Mass effects in muon and semileptonic  $b \rightarrow c$  decays, Phys. Rev. Lett. 100 (2008) 241807.
- [533] A. Czarnecki, K. Melnikov, Two-loop QCD corrections to semileptonic b decays at an intermediate recoil, Phys. Rev. D59 (1999) 014036.
- [534] M. Dowling, A. Pak, A. Czarnecki, Semi-Leptonic b-decay at Intermediate Recoil, Phys. Rev. D78 (2008) 074029.

- [535] B. M. Dassing, T. Mannel, S. Turczyk, Inclusive semi-leptonic B decays to order  $1/m_b^4$ , JHEP 03 (2007) 087.
- [536] M. A. Shifman, Quark-hadron duality. arXiv:hep-ph/0009131.
- [537] I. I. Y. Bigi, N. Uraltsev, A vademecum on quark hadron duality, Int. J. Mod. Phys. A16 (2001) 5201–5248.
- [538] I. I. Bigi, T. Mannel, Parton hadron duality in B meson decays. arXiv:hep-ph/0212021.
- [539] I. I. Bigi, N. Uraltsev, R. Zwicky, On the nonperturbative charm effects in inclusive  $B \rightarrow X_c \ell \nu$  decays, Eur. Phys. J. C50 (2007) 539–556.
- [540] C. Breidenbach, T. Feldmann, T. Mannel, S. Turczyk, On the Role of 'Intrinsic Charm' in Semi-Leptonic B-Meson Decays, Phys. Rev. D78 (2008) 014022.
- [541] B. M. Dassing, R. Feger, T. Mannel, Testing the left-handedness of the  $b \rightarrow c$  transition, Phys. Rev. D75 (2007) 095007.
- [542] B. Dassing, R. Feger, T. Mannel, Complete Michel Parameter Analysis of inclusive semileptonic  $b \rightarrow c$  transition. arXiv:0803.3561.
- [543] B. Aubert, et al., Measurement of the electron energy spectrum and its moments in inclusive  $B \rightarrow X_e \nu$  decays, Phys. Rev. D69 (2004) 111104.
- [544] B. Aubert, et al., Measurements of moments of the hadronic mass distribution in semileptonic B decays, Phys. Rev. D69 (2004) 111103.
- [545] B. Aubert, et al., Measurement of Moments of the Hadronic-Mass and -Energy Spectrum in Inclusive Semileptonic  $\bar{B} \rightarrow X_c \ell^- \bar{\nu}$  Decays. arXiv:0707.2670.
- [546] P. Urquijo, et al., Moments of the electron energy spectrum and partial branching fraction of  $B \rightarrow X_c e \nu$  decays at Belle, Phys. Rev. D75 (2007) 032001.
- [547] C. Schwanda, et al., Moments of the hadronic invariant mass spectrum in  $B \rightarrow X_c \ell \nu$  decays at Belle, Phys. Rev. D75 (2007) 032005.
- [548] D. E. Acosta, et al., Measurement of the moments of the hadronic invariant mass distribution in semileptonic B decays, Phys. Rev. D71 (2005) 051103.
- [549] S. E. Csorna, et al., Moments of the B meson inclusive semileptonic decay rate using neutrino reconstruction, Phys. Rev. D70 (2004) 032002.
- [550] J. Abdallah, et al., Determination of heavy quark non-perturbative parameters from spectral moments in semileptonic B decays, Eur. Phys. J. C45 (2006) 35–59.
- [551] B. Aubert, et al., Measurement of the branching fraction and photon energy moments of  $B \rightarrow X_s \gamma$  and  $A_{CP}(B \rightarrow X_{s+d} \gamma)$ , Phys. Rev. Lett. 97 (2006) 171803.
- [552] B. Aubert, et al., Measurements of the  $B \rightarrow X_s \gamma$  branching fraction and photon spectrum from a sum of exclusive final states, Phys. Rev. D72 (2005) 052004.
- [553] C. Schwanda, et al., Measurement of the Moments of the Photon Energy Spectrum in  $B \rightarrow X_s \gamma$  Decays and Determination of  $|V_{cb}|$  and  $m_b$  at Belle, Phys. Rev. D78 (2008) 032016.
- [554] K. Abe, et al., Improved Measurement of Inclusive Radiative B-meson decays, AIP Conf. Proc. 1078 (2009) 342–344.
- [555] S. Chen, et al., Branching fraction and photon energy spectrum for  $b \rightarrow s \gamma$ , Phys. Rev. Lett. 87 (2001) 251807.
- [556] A. Hocker, V. Kartvelishvili, SVD Approach to Data Unfolding, Nucl. Instrum. Meth. A372 (1996) 469–481.
- [557] D. Benson, I. I. Bigi, N. Uraltsev, On the photon energy moments and their 'bias' corrections in  $B \rightarrow X_s + \gamma$ , Nucl. Phys. B710 (2005) 371–401.
- [558] E. Barberio, et al., Averages of  $b$ -hadron and  $c$ -hadron Properties at the End of 2007. arXiv:0808.1297.
- [559] I. I. Y. Bigi, N. G. Uraltsev, Weak annihilation and the endpoint spectrum in semileptonic B decays, Nucl. Phys. B423 (1994) 33–55.
- [560] N. Uraltsev, Theoretical uncertainties in  $\Gamma(b \rightarrow u)$ , Int. J. Mod. Phys. A14 (1999) 4641–4652.
- [561] M. B. Voloshin, Nonfactorization effects in heavy mesons and determination of  $|V_{ub}|$  from inclusive semileptonic B decays, Phys. Lett. B515 (2001) 74–80.
- [562] P. Gambino, G. Ossola, N. Uraltsev, Hadronic mass and  $q^2$  moments of charmless semileptonic B decay distributions, JHEP 09 (2005) 010.
- [563] M. Neubert, QCD based interpretation of the lepton spectrum in inclusive anti-B  $\rightarrow X(u)$  lepton anti-neutrino decays, Phys. Rev. D49 (1994) 3392–3398.

- [564] I. I. Y. Bigi, M. A. Shifman, N. G. Uraltsev, A. I. Vainshtein, On the motion of heavy quarks inside hadrons: Universal distributions and inclusive decays, *Int. J. Mod. Phys. A9* (1994) 2467–2504.
- [565] J. R. Andersen, E. Gardi, Taming the  $B \rightarrow X_s \gamma$  spectrum by dressed gluon exponentiation, *JHEP* 06 (2005) 030.
- [566] J. R. Andersen, E. Gardi, Inclusive spectra in charmless semileptonic B decays by dressed gluon exponentiation, *JHEP* 01 (2006) 097.
- [567] J. R. Andersen, E. Gardi, Radiative B decay spectrum: DGE at NNLO, *JHEP* 01 (2007) 029.
- [568] E. Gardi, Inclusive B decays from resummed perturbation theory. arXiv:hep-ph/0703036.
- [569] Z. Ligeti, I. W. Stewart, F. J. Tackmann, Treating the b quark distribution function with reliable uncertainties, *Phys. Rev. D78* (2008) 114014.
- [570] B. O. Lange, M. Neubert, G. Paz, A two-loop relation between inclusive radiative and semileptonic B decay spectra, *JHEP* 10 (2005) 084.
- [571] B. O. Lange, Shape-function independent relations of charmless inclusive B-decay spectra, *JHEP* 01 (2006) 104.
- [572] A. K. Leibovich, Z. Ligeti, M. B. Wise, Enhanced subleading structure functions in semileptonic B decay, *Phys. Lett. B539* (2002) 242–248.
- [573] C. W. Bauer, M. Luke, T. Mannel, Subleading shape functions in  $B \rightarrow X_u \ell \bar{\nu}$  and the determination of  $|V_{ub}|$ , *Phys. Lett. B543* (2002) 261–268.
- [574] S. W. Bosch, M. Neubert, G. Paz, Subleading shape functions in inclusive B decays, *JHEP* 11 (2004) 073.
- [575] P. Gambino, P. Giordano, G. Ossola, N. Uraltsev, Inclusive semileptonic B decays and the determination of  $|V_{ub}|$ , *JHEP* 10 (2007) 058.
- [576] F. De Fazio, M. Neubert,  $B \rightarrow X_u \ell \bar{\nu}_\ell$  decay distributions to order  $\alpha_s$ , *JHEP* 06 (1999) 017.
- [577] P. Gambino, E. Gardi, G. Ridolfi, Running-coupling effects in the triple-differential charmless semileptonic decay width, *JHEP* 12 (2006) 036.
- [578] R. Bonciani, A. Ferroglia, Two-Loop QCD Corrections to the Heavy-to-Light Quark Decay, *JHEP* 11 (2008) 065.
- [579] H. M. Asatrian, C. Greub, B. D. Pecjak, NNLO corrections to  $B \rightarrow X_u l \nu$  in the shape-function region, *Phys. Rev. D78* (2008) 114028.
- [580] M. Beneke, T. Huber, X. Q. Li, Two-loop QCD correction to differential semi-leptonic  $b \rightarrow u$  decays in the shape-function region, *Nucl. Phys. B811* (2009) 77–97.
- [581] G. Bell, NNLO corrections to inclusive semileptonic B decays in the shape-function region, *Nucl. Phys. B812* (2009) 264–289.
- [582] J. L. Rosner, et al., Experimental limits on weak annihilation contributions to  $b \rightarrow u l \nu$  decay, *Phys. Rev. Lett.* 96 (2006) 121801.
- [583] B. Aubert, et al., Measurement of the  $B^0 \rightarrow X_u^- \ell^+ \nu_\ell$  decays near the kinematic endpoint of the lepton spectrum and search for violation of isospin symmetry. arXiv:0708.1753.
- [584] B. O. Lange, M. Neubert, G. Paz, Theory of charmless inclusive B decays and the extraction of  $V_{ub}$ , *Phys. Rev. D72* (2005) 073006.
- [585] E. Gardi, Inclusive distributions near kinematic thresholds. arXiv:hep-ph/0606080.
- [586] E. Gardi, Radiative and semi-leptonic B-meson decay spectra: Sudakov resummation beyond logarithmic accuracy and the pole mass, *JHEP* 04 (2004) 049.
- [587] U. Aglietti, F. Di Lodovico, G. Ferrera, G. Ricciardi, Inclusive Measure of  $|V_{ub}|$  with the Analytic Coupling Model, *Eur. Phys. J. C59* (2009) 831–840.
- [588] D. V. Shirkov, I. L. Solovtsov, Analytic model for the QCD running coupling with universal  $\alpha(s)$ -bar(0) value, *Phys. Rev. Lett.* 79 (1997) 1209–1212.
- [589] M. Battaglia, et al., The CKM matrix and the unitarity triangle. Workshop, CERN, Geneva, Switzerland, 13-16 Feb 2002: Proceedings. arXiv:hep-ph/0304132.
- [590] N. Gray, D. J. Broadhurst, W. Grafe, K. Schilcher, Three loop relation of quark  $\bar{M}S$  and pole masses, *Z. Phys. C48* (1990) 673–680.
- [591] K. Melnikov, T. v. Ritbergen, The three-loop relation between the  $\bar{M}S$ -bar and the pole quark masses, *Phys. Lett. B482* (2000) 99–108.
- [592] K. G. Chetyrkin, M. Steinhauser, The relation between the  $\bar{M}S$ -bar and the on-shell quark mass at order  $\alpha_s^3$ , *Nucl. Phys. B573* (2000) 617–651.
- [593] A. H. Hoang, et al., Top-antitop pair production close to threshold: Synopsis of recent NNLO results, *Eur. Phys. J. direct C2* (2000) 1.

- [594] I. I. Y. Bigi, M. A. Shifman, N. Uraltsev, A. I. Vainshtein, High power  $n$  of  $m(b)$  in beauty widths and  $n = 5 \rightarrow$  infinity limit, *Phys. Rev. D* 56 (1997) 4017–4030.
- [595] I. I. Y. Bigi, M. A. Shifman, N. G. Uraltsev, A. I. Vainshtein, Sum rules for heavy flavor transitions in the SV limit, *Phys. Rev. D* 52 (1995) 196–235.
- [596] A. Czarnecki, K. Melnikov, N. Uraltsev, Non-Abelian dipole radiation and the heavy quark expansion, *Phys. Rev. Lett.* 80 (1998) 3189–3192.
- [597] K. Melnikov, A. Yelkhovsky, The  $b$  quark low-scale running mass from Upsilon sum rules, *Phys. Rev. D* 59 (1999) 114009.
- [598] A. H. Hoang, Z. Ligeti, A. V. Manohar, B decay and the Upsilon mass, *Phys. Rev. Lett.* 82 (1999) 277–280.
- [599] A. H. Hoang, T. Teubner, Top quark pair production close to threshold: Top mass, width and momentum distribution, *Phys. Rev. D* 60 (1999) 114027.
- [600] A. H. Hoang, A. Jain, I. Scimemi, I. W. Stewart, Infrared Renormalization Group Flow for Heavy Quark Masses, *Phys. Rev. Lett.* 101 (2008) 151602.
- [601] V. A. Novikov, et al., Sum Rules for Charmonium and Charmed Mesons Decay Rates in Quantum Chromodynamics, *Phys. Rev. Lett.* 38 (1977) 626.
- [602] L. J. Reinders, H. Rubinstein, S. Yazaki, Hadron Properties from QCD Sum Rules, *Phys. Rept.* 127 (1985) 1.
- [603] A. H. Hoang, 1S and MSbar Bottom Quark Masses from Upsilon Sum Rules, *Phys. Rev. D* 61 (2000) 034005.
- [604] M. Beneke, A. Signer, The bottom  $\overline{MS}$  quark mass from sum rules at next-to-next-to-leading order, *Phys. Lett. B* 471 (1999) 233–243.
- [605] A. H. Hoang, Bottom quark mass from Upsilon mesons: Charm mass effects. [arXiv:hep-ph/0008102](https://arxiv.org/abs/hep-ph/0008102).
- [606] M. Eidemuller, QCD moment sum rules for Coulomb systems: the charm and bottom quark masses, *Phys. Rev. D* 67 (2003) 113002.
- [607] A. Pineda, A. Signer, Renormalization Group Improved Sum Rule Analysis for the Bottom Quark Mass, *Phys. Rev. D* 73 (2006) 111501.
- [608] J. H. Kuhn, M. Steinhauser, Determination of  $\alpha_s$  and heavy quark masses from recent measurements of  $R(s)$ , *Nucl. Phys. B* 619 (2001) 588–602.
- [609] J. Bordes, J. Penarrocha, K. Schilcher, Bottom quark mass and QCD duality, *Phys. Lett. B* 562 (2003) 81–86.
- [610] G. Corcella, A. H. Hoang, Uncertainties in the MSbar bottom quark mass from relativistic sum rules, *Phys. Lett. B* 554 (2003) 133–140.
- [611] A. H. Hoang, M. Jamin, MSbar Charm Mass from Charmonium Sum Rules with Contour Improvement, *Phys. Lett. B* 594 (2004) 127–134.
- [612] R. Boughezal, M. Czakon, T. Schutzmeier, Charm and bottom quark masses from perturbative QCD, *Phys. Rev. D* 74 (2006) 074006.
- [613] J. H. Kuhn, M. Steinhauser, C. Sturm, Heavy quark masses from sum rules in four-loop approximation, *Nucl. Phys. B* 778 (2007) 192–215.
- [614] A. H. Hoang, Three-loop anomalous dimension of the heavy quark pair production current in non-relativistic QCD, *Phys. Rev. D* 69 (2004) 034009.
- [615] P. Gambino, P. Giordano, Normalizing inclusive rare B decays, *Phys. Lett. B* 669 (2008) 69–73.
- [616] A. Bochkarev, P. de Forcrand, Determination of the renormalized heavy quark mass in lattice QCD, *Nucl. Phys. B* 477 (1996) 489–520.
- [617] Q. Mason, H. D. Trottier, R. Horgan, C. T. H. Davies, G. P. Lepage, High-precision determination of the light-quark masses from realistic lattice QCD, *Phys. Rev. D* 73 (2006) 114501.
- [618] A. Gray, et al., The Upsilon spectrum and  $m_b$  from full lattice QCD, *Phys. Rev. D* 72 (2005) 094507.
- [619] J. Heitger, Heavy quark masses from lattice QCD, *Nucl. Phys. Proc. Suppl.* 181+182 (2008) 156.
- [620] I. Allison, et al., High-Precision Charm-Quark Mass from Current-Current Correlators in Lattice and Continuum QCD, *Phys. Rev. D* 78 (2008) 054513.
- [621] I. F. Allison, et al., Matching the Bare and MSbar Charm Quark Masses Using Weak Coupling Simulations. [arXiv:0810.0285](https://arxiv.org/abs/0810.0285).
- [622] A. H. Hoang, A. V. Manohar, Charm Quark Mass from Inclusive Semileptonic B Decays, *Phys. Lett. B* 633 (2006) 526–532.

- [623] B. Aubert, et al., Measurement of the inclusive electron spectrum in charmless semileptonic B decays near the kinematic endpoint and determination of  $|V_{ub}|$ , Phys. Rev. D73 (2006) 012006.
- [624] I. Bizjak, et al., Measurement of the inclusive charmless semileptonic partial branching fraction of B mesons and determination of  $|V_{ub}|$  using the full reconstruction tag, Phys. Rev. Lett. 95 (2005) 241801.
- [625] B. Collaboration Preliminary result shown at CKM2008.
- [626] A. Bornheim, et al., Improved Measurement of  $|V_{ub}|$  with Inclusive Semileptonic B Decays, Phys. Rev. Lett. 88 (2002) 231803.
- [627] B. Aubert, et al., Determination of  $|V_{ub}|$  from measurements of the electron and neutrino momenta in inclusive semileptonic B decays, Phys. Rev. Lett. 95 (2005) 111801.
- [628] H. Kakuno, et al., Measurement of  $|V_{ub}|$  using inclusive  $B \rightarrow X_u \ell \nu$  decays with a novel  $X_u$  reconstruction method, Phys. Rev. Lett. 92 (2004) 101801.
- [629] A. Limosani, et al., Measurement of inclusive charmless semileptonic B-meson decays at the endpoint of the electron momentum spectrum, Phys. Lett. B621 (2005) 28–40.
- [630] B. Aubert, et al., Measurements of Partial Branching Fractions for  $\bar{B} \rightarrow X_u \ell \bar{\nu}$  and Determination of  $|V_{ub}|$ , Phys. Rev. Lett. 100 (2008) 171802.
- [631] M. Neubert, Analysis of the photon spectrum in inclusive  $B \rightarrow X_s + \gamma$  decays, Phys. Rev. D49 (1994) 4623–4633.
- [632] A. K. Leibovich, I. Low, I. Z. Rothstein, Extracting  $V_{ub}$  without recourse to structure functions, Phys. Rev. D61 (2000) 053006.
- [633] V. B. Golubev, Y. I. Skovpen, V. G. Luth, Extraction of  $|V_{ub}|$  with Reduced Dependence on Shape Functions, Phys. Rev. D76 (2007) 114003.
- [634] B. Aubert, et al., Determinations of  $|V_{ub}|$  from inclusive semileptonic B decays with reduced model dependence, Phys. Rev. Lett. 96 (2006) 221801.
- [635] M. Bona, et al., The unitarity triangle fit in the standard model and hadronic parameters from lattice QCD: A reappraisal after the measurements of  $\Delta m_s$  and  $BR(B \rightarrow \tau \nu_\tau)$ , JHEP 10 (2006) 081.
- [636] A. J. Buras, A. Czarnecki, M. Misiak, J. Urban, Completing the NLO QCD calculation of  $\bar{B} \rightarrow X_s \gamma$ , Nucl. Phys. B631 (2002) 219–238.
- [637] K. Melnikov, A. Mitov, The photon energy spectrum in  $B \rightarrow X_s + \gamma$  in perturbative QCD through  $O(\alpha_s^2)$ , Phys. Lett. B620 (2005) 69–79.
- [638] I. R. Blokland, A. Czarnecki, M. Misiak, M. Slusarczyk, F. Tkachov, The electromagnetic dipole operator effect on  $B \rightarrow X_s \gamma$  at  $O(\alpha_s^2)$ , Phys. Rev. D72 (2005) 033014.
- [639] H. M. Asatrian, et al., NNLL QCD contribution of the electromagnetic dipole operator to  $\Gamma(B \rightarrow X_s \gamma)$ , Nucl. Phys. B749 (2006) 325–337.
- [640] Z. Ligeti, M. E. Luke, A. V. Manohar, M. B. Wise, The  $B \rightarrow X_s \gamma$  photon spectrum, Phys. Rev. D60 (1999) 034019.
- [641] K. Bieri, C. Greub, M. Steinhauser, Fermionic NNLL corrections to  $b \rightarrow s \gamma$ , Phys. Rev. D67 (2003) 114019.
- [642] R. Boughezal, M. Czakon, T. Schutzmeier, NNLO fermionic corrections to the charm quark mass dependent matrix elements in  $B \rightarrow X_s \gamma$ , JHEP 09 (2007) 072.
- [643] T. Ewerth, Fermionic corrections to the interference of the electro- and chromomagnetic dipole operators in  $B \rightarrow X_s \gamma$  at  $O(\alpha_s^2)$ , Phys. Lett. B669 (2008) 167–172.
- [644] M. Misiak, M. Steinhauser, NNLO QCD corrections to the  $B \rightarrow X_s \gamma$  matrix elements using interpolation in  $m_c$ , Nucl. Phys. B764 (2007) 62–82.
- [645] M. Misiak, et al., The first estimate of  $BR(\bar{B} \rightarrow X_s \gamma)$  at  $O(\alpha_s^2)$ , Phys. Rev. Lett. 98 (2007) 022002.
- [646] S. J. Lee, M. Neubert, G. Paz, Enhanced non-local power corrections to the  $B \rightarrow X_s + \gamma$  decay rate, Phys. Rev. D75 (2007) 114005.
- [647] M. Neubert, Renormalization-group improved calculation of the  $B \rightarrow X_s + \gamma$  branching ratio, Eur. Phys. J. C40 (2005) 165–186.
- [648] T. Becher, M. Neubert, Toward a NNLO calculation of the  $B \rightarrow X_s + \gamma$  decay rate with a cut on photon energy. I: Two-loop result for the soft function, Phys. Lett. B633 (2006) 739–747.
- [649] T. Becher, M. Neubert, Toward a NNLO calculation of the  $B \rightarrow X_s \gamma$  decay rate with a cut on photon energy. II: Two-loop result for the jet function, Phys. Lett. B637 (2006) 251–259.
- [650] T. Becher, M. Neubert, Analysis of  $BR(B \rightarrow X_s + \gamma)$  at NNLO with a cut on photon energy, Phys. Rev. Lett. 98 (2007) 022003.



- [651] M. Ciuchini, G. Degrossi, P. Gambino, G. F. Giudice, Next-to-leading QCD corrections to  $B \rightarrow X_s + \gamma$ : Standard model and two-Higgs doublet model, Nucl. Phys. B527 (1998) 21–43.
- [652] F. Borzumati, C. Greub, 2HDMs predictions for  $B \rightarrow X_s + \gamma$  in NLO QCD, Phys. Rev. D58 (1998) 074004.
- [653] C. Bobeth, M. Misiak, J. Urban, Matching conditions for  $b \rightarrow s\gamma$  and  $b \rightarrow sg$  in extensions of the standard model, Nucl. Phys. B567 (2000) 153–185.
- [654] M. Ciuchini, G. Degrossi, P. Gambino, G. F. Giudice, Next-to-leading QCD corrections to  $B \rightarrow X_s\gamma$  in supersymmetry, Nucl. Phys. B534 (1998) 3–20.
- [655] G. Degrossi, P. Gambino, P. Slavich, QCD corrections to radiative B decays in the MSSM with minimal flavor violation, Phys. Lett. B635 (2006) 335–342.
- [656] M. Albrecht, W. Altmannshofer, A. J. Buras, D. Guadagnoli, D. M. Straub, Challenging SO(10) SUSY GUTs with family symmetries through FCNC processes, JHEP 10 (2007) 055.
- [657] W. Altmannshofer, D. Guadagnoli, S. Raby, D. M. Straub, SUSY GUTs with Yukawa unification: A Go/no-go study using FCNC processes, Phys. Lett. B668 (2008) 385–391.
- [658] U. Haisch, A. Weiler, Bound on minimal universal extra dimensions from  $B \rightarrow X_s\gamma$ , Phys. Rev. D76 (2007) 034014.
- [659] A. Freitas, U. Haisch,  $B \rightarrow X_s\gamma$  in two universal extra dimensions, Phys. Rev. D77 (2008) 093008.
- [660] B. Aubert, et al., Measurement of  $B \rightarrow X\gamma$  Decays and Determination of  $|V_{td}/V_{ts}|$ . arXiv:0807.4975.
- [661] A. Ali, H. Asatrian, C. Greub, Inclusive decay rate for  $B \rightarrow X_d + \gamma$  in next-to-leading logarithmic order and CP asymmetry in the standard model, Phys. Lett. B429 (1998) 87–98.
- [662] H. Abe, K.-S. Choi, T. Kobayashi, H. Ohki, Three generation magnetized orbifold models, Nucl. Phys. B814 (2009) 265–292.
- [663] A. L. Kagan, M. Neubert, Direct CP violation in  $B \rightarrow X_s\gamma$  decays as a signature of new physics, Phys. Rev. D58 (1998) 094012.
- [664] T. Hurth, E. Lunghi, W. Porod, Untagged  $B \rightarrow X_{s+d}\gamma$  CP asymmetry as a probe for new physics, Nucl. Phys. B704 (2005) 56–74.
- [665] S. Baek, P. Ko, Probing SUSY-induced CP violations at B factories, Phys. Rev. Lett. 83 (1999) 488–491.
- [666] K. Kiers, A. Soni, G.-H. Wu, Direct CP violation in radiative  $b$  decays in and beyond the standard model, Phys. Rev. D62 (2000) 116004.
- [667] B. Aubert, et al., A Measurement of CP Asymmetry in  $b \rightarrow s\gamma$  using a Sum of Exclusive Final States, Phys. Rev. Lett. 101 (2008) 171804.
- [668] S. Nishida, et al., Measurement of the CP asymmetry in  $B \rightarrow X_s + \gamma$ , Phys. Rev. Lett. 93 (2004) 031803.
- [669] B. Aubert, et al., Measurement of the  $B \rightarrow X_s$  gamma Branching Fraction and Photon Energy Spectrum using the Recoil Method, Phys. Rev. D77 (2008) 051103.
- [670] K. Abe, et al., A measurement of the branching fraction for the inclusive  $B \rightarrow X_s + \gamma$  decays with Belle, Phys. Lett. B511 (2001) 151–158.
- [671] A. L. Kagan, M. Neubert, QCD anatomy of  $B \rightarrow X_s + \gamma$  decays, Eur. Phys. J. C7 (1999) 5–27.
- [672] A. Kapustin, Z. Ligeti, H. D. Politzer, Leading logarithms of the  $b$  quark mass in inclusive  $B \rightarrow X_s + \gamma$  decay, Phys. Lett. B357 (1995) 653–658.
- [673] Z. Ligeti, L. Randall, M. B. Wise, Comment on nonperturbative effects in  $B \rightarrow X_s + \gamma$ , Phys. Lett. B402 (1997) 178–182.
- [674] G. P. Korchemsky, G. Sterman, Infrared factorization in inclusive B meson decays, Phys. Lett. B340 (1994) 96–108.
- [675] E. Gardi, On the quark distribution in an on-shell heavy quark and its all-order relations with the perturbative fragmentation function, JHEP 02 (2005) 053.
- [676] M. Neubert, Advanced predictions for moments of the  $B \rightarrow X_s\gamma$  photon spectrum, Phys. Rev. D72 (2005) 074025.
- [677] C. W. Bauer, M. E. Luke, T. Mannel, Light-cone distribution functions for B decays at subleading order in  $1/m_b$ , Phys. Rev. D68 (2003) 094001.
- [678] K. S. M. Lee, I. W. Stewart, Factorization for power corrections to  $B \rightarrow X_s\gamma$  and  $B \rightarrow X_u\ell\bar{\nu}$ , Nucl. Phys. B721 (2005) 325–406.
- [679] M. Beneke, F. Campanario, T. Mannel, B. D. Pecjak, Power corrections to  $B \rightarrow X_u\ell\bar{\nu}(X_s\gamma)$  decay spectra in the 'shape-function' region, JHEP 06 (2005) 071.

- [680] H. M. Asatrian, T. Ewerth, A. Ferroglia, P. Gambino, C. Greub, Magnetic dipole operator contributions to the photon energy spectrum in  $B \rightarrow X_s + \gamma$  at  $\mathcal{O}(\alpha_s^2)$ , Nucl. Phys. B762 (2007) 212–228.
- [681] G. P. Korchemsky, G. Marchesini, Structure function for large  $x$  and renormalization of Wilson loop, Nucl. Phys. B406 (1993) 225–258.
- [682] S. Moch, J. A. M. Vermaseren, A. Vogt, The three-loop splitting functions in QCD: The non-singlet case, Nucl. Phys. B688 (2004) 101–134.
- [683] M. Misiak, QCD Calculations of Radiative B Decays. arXiv:0808.3134.
- [684] A. Ali, C. Greub, Photon energy spectrum in  $B \rightarrow X_s + \gamma$  and comparison with data, Phys. Lett. B361 (1995) 146–154.
- [685] M. Beneke, T. Feldmann, D. Seidel, Systematic approach to exclusive  $B \rightarrow V\ell^+\ell^-$ ,  $V\gamma$  decays, Nucl. Phys. B612 (2001) 25–58.
- [686] S. W. Bosch, G. Buchalla, The radiative decays  $B \rightarrow V\gamma$  at next-to-leading order in QCD, Nucl. Phys. B621 (2002) 459–478.
- [687] A. Ali, A. Y. Parkhomenko, Branching ratios for  $B \rightarrow \rho\gamma$  decays in next-to-leading order in  $\alpha_s$  including hard spectator corrections, Eur. Phys. J. C23 (2002) 89–112.
- [688] Y. Y. Keum, M. Matsumori, A. I. Sanda, CP asymmetry, branching ratios and isospin breaking effects of  $B \rightarrow K^*\gamma$  with perturbative QCD approach, Phys. Rev. D72 (2005) 014013.
- [689] C.-D. Lu, M. Matsumori, A. I. Sanda, M.-Z. Yang, CP asymmetry, branching ratios and isospin breaking effects in  $B \rightarrow \rho\gamma$  and  $B \rightarrow \omega\gamma$  decays with the pQCD approach, Phys. Rev. D72 (2005) 094005.
- [690] M. Matsumori, A. I. Sanda, The mixing-induced CP asymmetry in  $B \rightarrow K^*\gamma$  decays with perturbative QCD approach, Phys. Rev. D73 (2006) 114022.
- [691] A. Ali, B. D. Pecjak, C. Greub,  $B \rightarrow V\gamma$  Decays at NNLO in SCET, Eur. Phys. J. C55 (2008) 577–595.
- [692] T. Becher, R. J. Hill, M. Neubert, Factorization in  $B \rightarrow V\gamma$  decays, Phys. Rev. D72 (2005) 094017.
- [693] A. L. Kagan, M. Neubert, Isospin breaking in  $B \rightarrow K^*\gamma$  decays, Phys. Lett. B539 (2002) 227–234.
- [694] S. W. Bosch, G. Buchalla, Constraining the unitarity triangle with  $B \rightarrow V\gamma$ , JHEP 01 (2005) 035.
- [695] M. Beneke, T. Feldmann, D. Seidel, Exclusive radiative and electroweak  $b \rightarrow d$  and  $b \rightarrow s$  penguin decays at NLO, Eur. Phys. J. C41 (2005) 173–188.
- [696] A. Ali, A. Parkhomenko,  $B \rightarrow (\rho, \omega)\gamma$  decays and CKM phenomenology. arXiv:hep-ph/0610149.
- [697] C. Kim, A. K. Leibovich, T. Mehen, Nonperturbative Charming Penguin Contributions to Isospin Asymmetries in Radiative B decays, Phys. Rev. D78 (2008) 054024.
- [698] B. Grinstein, Y. Grossman, Z. Ligeti, D. Pirjol, The photon polarization in  $B \rightarrow X_s + \gamma$  in the standard model, Phys. Rev. D71 (2005) 011504.
- [699] Y. Ushiroda, et al., Time-dependent CP asymmetries in  $B^0 \rightarrow K_S^0\pi^0\gamma$  transitions, Phys. Rev. D74 (2006) 111104.
- [700] B. Aubert, et al., Measurement of Time-Dependent CP Asymmetry in  $B^0 \rightarrow K_S^0\pi^0\gamma$  Decays, Phys. Rev. D78 (2008) 071102.
- [701] S. Descotes-Genon, C. T. Sachrajda, Sudakov effects in  $B \rightarrow \pi\ell\nu_\ell$  form factors, Nucl. Phys. B625 (2002) 239–278.
- [702] R. Ammar, et al., Evidence for penguins: First observation of  $B \rightarrow K^*(892)\gamma$ , Phys. Rev. Lett. 71 (1993) 674–678.
- [703] M. Nakao, et al., Measurement of the  $B \rightarrow K^*\gamma$  branching fractions and asymmetries, Phys. Rev. D69 (2004) 112001.
- [704] B. Aubert, et al., Measurement of Branching Fractions and CP and Isospin Asymmetries in  $B \rightarrow K^*\gamma$ . arXiv:0808.1915.
- [705] H. Yang, et al., Observation of  $B^+ \rightarrow K_1(1270)^+\gamma$ , Phys. Rev. Lett. 94 (2005) 111802.
- [706] S. Nishida, et al., Radiative B meson decays into K pi gamma and K pi pi gamma final states, Phys. Rev. Lett. 89 (2002) 231801.
- [707] B. Aubert, et al., Measurement of the  $B^0 \rightarrow K_2^*(1430)0\gamma$  and  $B^+ \rightarrow K_2^*(1430)^+\gamma$  branching fractions, Phys. Rev. D70 (2004) 091105.
- [708] S. Nishida, et al., Observation of  $B^+ \rightarrow K^+\eta\gamma$ , Phys. Lett. B610 (2005) 23–30.
- [709] B. Aubert, et al., Branching Fractions and CP-Violating Asymmetries in Radiative B Decays to eta K gamma, Phys. Rev. D79 (2009) 011102.

- [710] I. Adachi, et al., Evidence for B to K eta' gamma Decays at Belle. arXiv:0810.0804.
- [711] A. Drutskoy, et al., Observation of radiative  $B \rightarrow \phi K \gamma$  decays, Phys. Rev. Lett. 92 (2004) 051801.
- [712] B. Aubert, et al., Measurement of B decays to Phi K gamma, Phys. Rev. D75 (2007) 051102.
- [713] M. Z. Wang, et al., Study of  $B^+ \rightarrow p \bar{\Lambda} \gamma$ ,  $p \bar{\Lambda} \pi^0$  and  $B^0 \rightarrow p \bar{\Lambda} \pi^-$ , Phys. Rev. D76 (2007) 052004.
- [714] B. Aubert, et al., Measurement of branching fractions and mass spectra of  $B \rightarrow K \pi \pi \gamma$ , Phys. Rev. Lett. 98 (2007) 211804.
- [715] J. Wicht, et al., Observation of  $B_s^0 \rightarrow \phi \gamma$  and Search for  $B_s^0 \rightarrow \gamma \gamma$  Decays at Belle, Phys. Rev. Lett. 100 (2008) 121801.
- [716] N. Taniguchi, et al., Measurement of branching fractions, isospin and CP- violating asymmetries for exclusive  $b \rightarrow d \gamma$  modes, Phys. Rev. Lett. 101 (2008) 111801.
- [717] B. Aubert, et al., Measurements of Branching Fractions for  $B^+ \rightarrow \rho^+ \gamma$ ,  $B^0 \rightarrow \rho^0 \gamma$ , and  $B^0 \rightarrow \omega \gamma$ , Phys. Rev. D78 (2008) 112001.
- [718] D. Atwood, T. Gershon, M. Hazumi, A. Soni, Mixing-induced CP violation in  $B \rightarrow P_1 P_2 \gamma$  in search of clean new physics signals, Phys. Rev. D71 (2005) 076003.
- [719] Q.-f. Li, J. Steinheimer, H. Petersen, M. Bleicher, H. Stocker, Effects of a phase transition on HBT correlations in an integrated Boltzmann+Hydrodynamics approach, Phys. Lett. B674 (2009) 111–116.
- [720] F. Muheim, Y. Xie, R. Zwicky, Exploiting the width difference in  $B_s \rightarrow \phi \gamma$ , Phys. Lett. B664 (2008) 174–179.
- [721] A. J. Buras, Relations between  $\Delta M_{s,d}$  and  $B_{s,d} \rightarrow \mu \bar{\mu}$  in models with minimal flavor violation, Phys. Lett. B566 (2003) 115–119.
- [722] T. Aaltonen, et al., Search for  $B_s^0 \rightarrow \mu^+ \mu^-$  and  $B_d^0 \rightarrow \mu^+ \mu^-$  decays with  $2fb^{-1}$  of  $p\bar{p}$  collisions, Phys. Rev. Lett. 100 (2008) 101802.
- [723] K. Ikado, et al., Evidence of the purely leptonic decay  $B^- \rightarrow \tau \bar{\nu}_\tau$ , Phys. Rev. Lett. 97 (2006) 251802.
- [724] B. Aubert, et al., A Search for  $B^+ \rightarrow \tau^+ \nu$ , Phys. Rev. D76 (2007) 052002.
- [725] B. Aubert, et al., A Search for  $B^+ \rightarrow \tau^+ \nu$  with Hadronic B tags, Phys. Rev. D77 (2008) 011107.
- [726] B. Aubert, et al., Search for  $B^+ \rightarrow \mu^+ \nu \mu$  with inclusive reconstruction at BaBar. arXiv:0807.4187.
- [727] N. Satoyama, et al., A search for the rare leptonic decays  $B^+ \rightarrow \mu^+ \nu$  and  $B^+ \rightarrow e^+ \nu$ , Phys. Lett. B647 (2007) 67–73.
- [728] I. Adachi, et al., Measurement of  $B^- \rightarrow \tau^- \bar{\nu}_\tau au$  Decay With a Semileptonic Tagging Method. arXiv:0809.3834.
- [729] D. Martinez, J. A. Hernando, F. Teubert, LHCb potential to measure / exclude the branching ratio of the decay  $B_s \rightarrow \mu^+ \mu^-$  CERN-LHCB-2007-033.
- [730] G. Aad, et al., Expected Performance of the ATLAS Experiment - Detector, Trigger and Physics. arXiv:0901.0512.
- [731] V. M. Abazov, et al., Search for  $B_s \rightarrow \mu^+ \mu^-$  at D0, Phys. Rev. D76 (2007) 092001.
- [732] T. Aaltonen, et al., Search for the Decays  $B_0(s) \rightarrow e^+ \mu^-$  and  $B_0(s) \rightarrow e^+ e^-$  in CDF Run. II, Phys. Rev. Lett. 102 (2009) 201801.
- [733] B. Aubert, et al., Search for decays of  $B^0 \rightarrow$  mesons into  $e^+ e^-$ ,  $\mu^+ \mu^-$ , and  $e^\pm \mu^\mp$  final states, Phys. Rev. D77 (2008) 032007.
- [734] M. C. Chang, et al., Search for  $B^0 \rightarrow \ell^+ \ell^-$  at BELLE, Phys. Rev. D68 (2003) 111101.
- [735] U. Nierste, S. Trine, S. Westhoff, Charged-Higgs effects in a new  $B \rightarrow D \tau \nu$  differential decay distribution, Phys. Rev. D78 (2008) 015006.
- [736] J. F. Kamenik, F. Mescia,  $B \rightarrow D \tau \nu$  Branching Ratios: Opportunity for Lattice QCD and Hadron Colliders, Phys. Rev. D78 (2008) 014003.
- [737] D. Eriksson, F. Mahmoudi, O. Stal, Charged Higgs bosons in Minimal Supersymmetry: Updated constraints and experimental prospects, JHEP 11 (2008) 035.
- [738] S. Trine, Charged-Higgs effects in  $B \rightarrow D \tau \nu$  decays. arXiv:0810.3633.
- [739] K. Kiers, A. Soni, Improving constraints on  $\tan \beta / m_H$  using  $B \rightarrow D \tau \bar{\nu}$ , Phys. Rev. D56 (1997) 5786–5793.
- [740] H. H. Asatryan, H. M. Asatrian, C. Greub, M. Walker, Calculation of two loop virtual corrections to  $b \rightarrow sl^+ l^-$  in the standard model, Phys. Rev. D65 (2002) 074004.
- [741] H. H. Asatryan, H. M. Asatrian, C. Greub, M. Walker, Complete gluon bremsstrahlung corrections to the process  $b \rightarrow sl^+ l^-$ , Phys. Rev. D66 (2002) 034009.
- [742] A. Ghinculov, T. Hurth, G. Isidori, Y. P. Yao, Forward-backward asymmetry in  $B \rightarrow X_s l^+ l^-$  at the NNLL level, Nucl. Phys. B648 (2003) 254–276.

- [743] H. M. Asatrian, K. Bieri, C. Greub, A. Hovhannisyan, NNLL corrections to the angular distribution and to the forward-backward asymmetries in  $b \rightarrow X_s l^+ l^-$ , Phys. Rev. D66 (2002) 094013.
- [744] A. Ghinculov, T. Hurth, G. Isidori, Y. P. Yao, New NNLL QCD results on the decay  $B \rightarrow X_s l^+ l^-$ , Eur. Phys. J. C33 (2004) s288–s290.
- [745] A. Ghinculov, T. Hurth, G. Isidori, Y. P. Yao, The rare decay  $B \rightarrow X_s l^+ l^-$  to NNLL precision for arbitrary dilepton invariant mass, Nucl. Phys. B685 (2004) 351–392.
- [746] C. Bobeth, P. Gambino, M. Gorbahn, U. Haisch, Complete NNLO QCD analysis of  $\bar{B} \rightarrow X_s \ell^+ \ell^-$  and higher order electroweak effects, JHEP 04 (2004) 071.
- [747] H. M. Asatrian, H. H. Asatryan, A. Hovhannisyan, V. Poghosyan, Complete bremsstrahlung corrections to the forward- backward asymmetries in  $b \rightarrow X_s l^+ l^-$ , Mod. Phys. Lett. A19 (2004) 603–614.
- [748] T. Huber, E. Lunghi, M. Misiak, D. Wyler, Electromagnetic logarithms in  $\bar{B} \rightarrow X_s \ell^+ \ell^-$ , Nucl. Phys. B740 (2006) 105–137.
- [749] T. Huber, T. Hurth, E. Lunghi, Logarithmically Enhanced Corrections to the Decay Rate and Forward Backward Asymmetry in  $\bar{B} \rightarrow X_s \ell^+ \ell^-$ , Nucl. Phys. B802 (2008) 40–62.
- [750] A. F. Falk, M. E. Luke, M. J. Savage, Nonperturbative contributions to the inclusive rare decays  $B \rightarrow X(s) \gamma$  and  $B \rightarrow X(s) \ell^+ \ell^-$ , Phys. Rev. D49 (1994) 3367–3378.
- [751] A. Ali, G. Hiller, L. T. Handoko, T. Morozumi, Power corrections in the decay rate and distributions in  $B \rightarrow X_s l^+ l^-$  in the standard model, Phys. Rev. D55 (1997) 4105–4128.
- [752] J.-W. Chen, G. Rupak, M. J. Savage, Non- $1/m_b^n$  power suppressed contributions to inclusive  $B \rightarrow X_s l^+ l^-$  decays, Phys. Lett. B410 (1997) 285–289.
- [753] G. Buchalla, G. Isidori, S. J. Rey, Corrections of order  $\Lambda_{QCD}^2/m_c^2$  to inclusive rare B decays, Nucl. Phys. B511 (1998) 594–610.
- [754] G. Buchalla, G. Isidori, Nonperturbative effects in  $B \rightarrow X_s l^+ l^-$  for large dilepton invariant mass, Nucl. Phys. B525 (1998) 333–349.
- [755] C. W. Bauer, C. N. Burrell, Nonperturbative corrections to moments of the decay  $B \rightarrow X_s \ell^+ \ell^-$ , Phys. Rev. D62 (2000) 114028.
- [756] Z. Ligeti, F. J. Tackmann, Precise predictions for  $B \rightarrow X_s \ell^+ \ell^-$  in the large  $q^2$  region, Phys. Lett. B653 (2007) 404–410.
- [757] T. Huber, T. Hurth, E. Lunghi, The Role of Collinear Photons in the Rare Decay  $\bar{B} \rightarrow X_s \ell^+ \ell^-$ . arXiv:0807.1940.
- [758] A. Ali, G. Hiller, Perturbative QCD- and power-corrected hadron spectra and spectral moments in the decay  $B \rightarrow X_s \ell^+ \ell^-$ , Phys. Rev. D58 (1998) 074001.
- [759] K. S. M. Lee, Z. Ligeti, I. W. Stewart, F. J. Tackmann, Universality and  $m_X$  cut effects in  $B \rightarrow X_s \ell^+ \ell^-$ , Phys. Rev. D74 (2006) 011501.
- [760] K. S. M. Lee, Z. Ligeti, I. W. Stewart, F. J. Tackmann, Extracting short distance information from  $b \rightarrow s \ell^+ \ell^-$  effectively, Phys. Rev. D75 (2007) 034016.
- [761] B. Aubert, et al., Measurement of the  $B \rightarrow X_s \ell^+ \ell^-$  branching fraction with a sum over exclusive modes, Phys. Rev. Lett. 93 (2004) 081802.
- [762] M. Iwasaki, et al., Improved measurement of the electroweak penguin process  $B \rightarrow X_s \ell^+ \ell^-$ , Phys. Rev. D72 (2005) 092005.
- [763] F. Kruger, J. Matias, Probing new physics via the transverse amplitudes of  $B^0 \rightarrow K^{*0}(\rightarrow K^- \pi^+) \ell^+ \ell^-$  at large recoil, Phys. Rev. D71 (2005) 094009.
- [764] B. Grinstein, D. Pirjol, Precise  $-\text{V}(\text{ub})-$  determination from exclusive B decays: Controlling the long-distance effects, Phys. Rev. D70 (2004) 114005.
- [765] J. Charles, A. Le Yaouanc, L. Oliver, O. Pene, J. C. Raynal, Heavy-to-light form factors in the heavy mass to large energy limit of QCD, Phys. Rev. D60 (1999) 014001.
- [766] M. Beneke, T. Feldmann, Symmetry-breaking corrections to heavy-to-light B meson form factors at large recoil, Nucl. Phys. B592 (2001) 3–34.
- [767] G. Burdman, Short distance coefficients and the vanishing of the lepton asymmetry in  $B \rightarrow V \ell^+ \ell^-$ , Phys. Rev. D57 (1998) 4254–4257.
- [768] A. Ali, P. Ball, L. T. Handoko, G. Hiller, A Comparative study of the decays  $B \rightarrow (K, K^*) \ell^+ \ell^-$  in standard model and supersymmetric theories, Phys. Rev. D61 (2000) 074024.
- [769] T. Feldmann, J. Matias, Forward-backward and isospin asymmetry for  $B \rightarrow K^* \ell^+ \ell^-$  decay in the standard model and in supersymmetry, JHEP 01 (2003) 074.

- [770] W. Altmannshofer, et al., Symmetries and Asymmetries of  $B \rightarrow K^* \mu^+ \mu^-$  Decays in the Standard Model and Beyond, JHEP 01 (2009) 019.
- [771] A. Ali, G. Kramer, G.-h. Zhu,  $B \rightarrow K^* \ell^+ \ell^-$  in soft-collinear effective theory, Eur. Phys. J. C47 (2006) 625–641.
- [772] C. Bobeth, G. Hiller, G. Piranishvili, Angular Distributions of  $B \rightarrow K \ell \ell$  Decays, JHEP 12 (2007) 040.
- [773] U. O. Yilmaz, Analysis of  $B_s \rightarrow \phi \ell^+ \ell^-$  decay with new physics effects, Eur. Phys. J. C58 (2008) 555–568.
- [774] M. Beneke, T. Feldmann, D. Seidel In preparation.
- [775] F. Kruger Chapter 2.17 of Ref. [1228].
- [776] E. Lunghi, J. Matias, Huge right-handed current effects in  $B \rightarrow K^*(K\pi) \ell^+ \ell^-$  in supersymmetry, JHEP 04 (2007) 058.
- [777] C. Bobeth, G. Hiller, G. Piranishvili, CP Asymmetries in  $\bar{B} \rightarrow \bar{K}^*(\rightarrow \bar{K}\pi) \bar{\ell} \ell$  and Untagged  $\bar{B}_s, B_s \rightarrow \phi(\rightarrow K^+ K^-) \bar{\ell} \ell$  Decays at NLO, JHEP 07 (2008) 106.
- [778] U. Egede, T. Hurth, J. Matias, M. Ramon, W. Reece, New observables in the decay mode  $\bar{B} \rightarrow \bar{K}^{*0} \ell^+ \ell^-$ , JHEP 11 (2008) 032.
- [779] F. Kruger, L. M. Sehgal, N. Sinha, R. Sinha, Angular distribution and CP asymmetries in the decays  $B \rightarrow K^- \pi^+ e^- e^+$  and  $B \rightarrow \pi^- \pi^+ e^- e^+$ , Phys. Rev. D61 (2000) 114028.
- [780] D. Melikhov, N. Nikitin, S. Simula, Probing right-handed currents in  $B \rightarrow K^* \ell^+ \ell^-$  transitions, Phys. Lett. B442 (1998) 381–389.
- [781] C. S. Kim, Y. G. Kim, C.-D. Lu, T. Morozumi, Azimuthal angle distribution in  $B \rightarrow K^*(\rightarrow K\pi) \ell^+ \ell^-$  at low invariant  $m_{\ell^+ \ell^-}$  region, Phys. Rev. D62 (2000) 034013.
- [782] C. S. Kim, Y. G. Kim, C.-D. Lu, Possible supersymmetric effects on angular distributions in  $B \rightarrow K^*(\rightarrow K\pi) \ell^+ \ell^-$  decays, Phys. Rev. D64 (2001) 094014.
- [783] A. Faessler, T. Gutsche, M. A. Ivanov, J. G. Korner, V. E. Lyubovitskij, The Exclusive rare decays  $B \rightarrow K(K^*) \ell \ell$  and  $B_c \rightarrow D(D^*) \ell \ell$  in a relativistic quark model, Eur. Phys. J. direct C4 (2002) 18.
- [784] K. Abe, et al., Observation of the decay  $B \rightarrow K \ell^+ \ell^-$ , Phys. Rev. Lett. 88 (2002) 021801.
- [785] B. Aubert, et al., Evidence for the rare decay  $B \rightarrow K^* \ell^+ \ell^-$  and measurement of the  $B \rightarrow K \ell^+ \ell^-$  branching fraction, Phys. Rev. Lett. 91 (2003) 221802.
- [786] A. Ishikawa, et al., Observation of the electroweak penguin decay  $B \rightarrow K^* \ell^+ \ell^-$ , Phys. Rev. Lett. 91 (2003) 261601.
- [787] B. Aubert, et al., Angular Distributions in the Decays  $B \rightarrow K^* \ell^+ \ell^-$ , Phys. Rev. D79 (2009) 031102.
- [788] B. Aubert, et al., Direct CP, Lepton Flavor and Isospin Asymmetries in the Decays  $B \rightarrow K^{(*)} \ell^+ \ell^-$ , Phys. Rev. Lett. 102 (2009) 091803.
- [789] and others, Measurement of the Differential Branching Fraction and Forward-Backward Asymmetry for  $B \rightarrow K^* \ell^+ \ell^-$ . arXiv:0904.0770.
- [790] A. Ali, E. Lunghi, C. Greub, G. Hiller, Improved model independent analysis of semileptonic and radiative rare  $B$  decays, Phys. Rev. D66 (2002) 034002.
- [791] Q.-S. Yan, C.-S. Huang, W. Liao, S.-H. Zhu, Exclusive semileptonic rare decays  $B \rightarrow (K, K^*) \ell^+ \ell^-$  in supersymmetric theories, Phys. Rev. D62 (2000) 094023.
- [792] G. Hiller, F. Kruger, More model independent analysis of  $b \rightarrow s$  processes, Phys. Rev. D69 (2004) 074020.
- [793] T. Aaltonen, et al., Search for the Rare Decays  $B^+ \rightarrow \mu^+ \mu^- K^+$ ,  $B^0 \rightarrow \mu^+ \mu^- K^{*0}(892)$ , and  $B_s^0 \rightarrow \mu^+ \mu^- \phi$  at CDF, Phys. Rev. D79 (2009) 011104.
- [794] P. Gambino, U. Haisch, M. Misiak, Determining the sign of the  $b \rightarrow s \gamma$  amplitude, Phys. Rev. Lett. 94 (2005) 061803.
- [795] B. Aubert, et al., Search for the rare decay  $B \rightarrow \pi \ell^+ \ell^-$ , Phys. Rev. Lett. 99 (2007) 051801.
- [796] J. T. Wei, et al., Search for  $B \rightarrow \pi \ell^+ \ell^-$  Decays at Belle, Phys. Rev. D78 (2008) 011101.
- [797] T. M. Aliev, M. Savci, Exclusive  $B \rightarrow \pi \ell^+ \ell^-$  and  $B \rightarrow \rho \ell^+ \ell^-$  decays in two Higgs doublet model, Phys. Rev. D60 (1999) 014005.
- [798] J. Dickens, V. Gibson, C. Lazzeroni, M. Patel, Selection of the decay  $b_d \rightarrow k^{*0} \mu^+ \mu^-$  at lhcb, Tech. Rep. LHCb-2007-038. CERN-LHCb-2007-038, CERN, Geneva (Apr 2007).
- [799] J. Dickens, V. Gibson, C. Lazzeroni, M. Patel, A study of the sensitivity to the forward-backward asymmetry in  $b_d \rightarrow k^* \mu^+ \mu^-$  decays at lhcb, Tech. Rep. LHCb-2007-039. CERN-LHCb-2007-039, CERN, Geneva (Jul 2007).

- [800] W. Reece, Extracting angular correlations from the rare decay  $\overline{B}_d \rightarrow \overline{K}^{*0} \mu^+ \mu^-$  at lhcb, Tech. Rep. LHCb-2008-021. CERN-LHCb-2008-021, CERN, Geneva (May 2008).
- [801] U. Egede, W. Reece, Performing the full angular analysis of  $\overline{B}_d \rightarrow \overline{K}^{*0} \mu^+ \mu^-$  at lhcb, Tech. Rep. LHCb-2008-041. CERN-LHCb-2008-041, CERN, Geneva (Nov 2008).
- [802] M. Misiak, J. Urban, QCD corrections to FCNC decays mediated by Z-penguins and W-boxes, Phys. Lett. B451 (1999) 161–169.
- [803] G. Buchalla, A. J. Buras, Two-loop large-m(t) electroweak corrections to  $K \rightarrow \pi \nu \bar{\nu}$  for arbitrary Higgs boson mass, Phys. Rev. D57 (1998) 216–223.
- [804] A. J. Buras, M. Gorbahn, U. Haisch, U. Nierste, The rare decay  $K^+ \rightarrow \pi^+ \nu \bar{\nu}$  at the next-to-next-to-leading order in QCD, Phys. Rev. Lett. 95 (2005) 261805.
- [805] A. J. Buras, M. Gorbahn, U. Haisch, U. Nierste, Charm quark contribution to  $K^+ \rightarrow \pi^+ \nu \bar{\nu}$  at next-to-next-to-leading order, JHEP 11 (2006) 002.
- [806] J. Brod, M. Gorbahn, Electroweak Corrections to the Charm Quark Contribution to  $K^+ \rightarrow \pi^+ \nu \bar{\nu}$ , Phys. Rev. D78 (2008) 034006.
- [807] F. Mescia, C. Smith, Improved estimates of rare K decay matrix-elements from K(13) decays, Phys. Rev. D76 (2007) 034017.
- [808] G. Isidori, F. Mescia, C. Smith, Light-quark loops in  $K \rightarrow \pi \nu \nu$ , Nucl. Phys. B718 (2005) 319–338.
- [809] G. Isidori, G. Martinelli, P. Turchetti, Rare kaon decays on the lattice, Phys. Lett. B633 (2006) 75–83.
- [810] G. Buchalla, A. J. Buras,  $K \rightarrow \pi \nu \bar{\nu}$  and high precision determinations of the CKM matrix, Phys. Rev. D54 (1996) 6782–6789.
- [811] G. Buchalla, A. J. Buras, M. E. Lautenbacher, Weak decays beyond leading logarithms, Rev. Mod. Phys. 68 (1996) 1125–1144.
- [812] G. Buchalla, G. D’Ambrosio, G. Isidori, Extracting short-distance physics from  $K_{L,S} \rightarrow \pi^0 e^+ e^-$  decays, Nucl. Phys. B672 (2003) 387–408.
- [813] G. Isidori, C. Smith, R. Unterdorfer, The rare decay  $K_L \rightarrow \pi^0 \mu^+ \mu^-$  within the SM, Eur. Phys. J. C36 (2004) 57–66.
- [814] G. D’Ambrosio, G. Ecker, G. Isidori, J. Portoles, The decays  $K \rightarrow \pi l^+ l^-$  beyond leading order in the chiral expansion, JHEP 08 (1998) 004.
- [815] C. Bruno, J. Prades, Rare Kaon Decays in the  $1/N_c$ -Expansion, Z. Phys. C57 (1993) 585–594.
- [816] S. Friot, D. Greynat, E. De Rafael, Rare kaon decays revisited, Phys. Lett. B595 (2004) 301–308.
- [817] F. Mescia, C. Smith, S. Trine,  $K_L \rightarrow \pi^0 e^+ e^-$  and  $K_L \rightarrow \pi^0 \mu^+ \mu^-$ : A binary star on the stage of flavor physics, JHEP 08 (2006) 088.
- [818] M. Gorbahn, U. Haisch, Charm quark contribution to  $K_L \rightarrow \mu^+ \mu^-$  at next-to-next-to-leading order, Phys. Rev. Lett. 97 (2006) 122002.
- [819] G. Isidori, R. Unterdorfer, On the short-distance constraints from  $K_{L,S} \rightarrow \mu^+ \mu^-$ , JHEP 01 (2004) 009.
- [820] J.-M. Gerard, C. Smith, S. Trine, Radiative kaon decays and the penguin contribution to the  $\Delta I = 1/2$  rule, Nucl. Phys. B730 (2005) 1–36.
- [821] G. Isidori, F. Mescia, P. Paradisi, C. Smith, S. Trine, Exploring the flavour structure of the MSSM with rare K decays, JHEP 08 (2006) 064.
- [822] G. Isidori, A. Retico,  $B_{s,d} \rightarrow \ell^+ \ell^-$  and  $K_L \rightarrow \ell^+ \ell^-$  in SUSY models with nonminimal sources of flavor mixing, JHEP 09 (2002) 063.
- [823] G. Isidori, P. Paradisi, Higgs-mediated  $K \rightarrow \pi \nu \bar{\nu}$  in the MSSM at large  $\tan(\beta)$ , Phys. Rev. D73 (2006) 055017.
- [824] E. Nikolidakis, C. Smith, Minimal Flavor Violation, Seesaw, and R-parity, Phys. Rev. D77 (2008) 015021.
- [825] C. Bobeth, et al., Upper bounds on rare K and B decays from minimal flavor violation, Nucl. Phys. B726 (2005) 252–274.
- [826] U. Haisch, A. Weiler, Determining the Sign of the  $Z^-$  Penguin Amplitude, Phys. Rev. D76 (2007) 074027.
- [827] Y. Grossman, Y. Nir,  $K_L \rightarrow \pi^0 \nu \bar{\nu}$  beyond the standard model, Phys. Lett. B398 (1997) 163–168.
- [828] Y. Nir, M. P. Worah, Probing the flavor and CP structure of supersymmetric models with  $K \rightarrow \pi \nu \bar{\nu}$  decays, Phys. Lett. B423 (1998) 319–326.
- [829] A. J. Buras, A. Romanino, L. Silvestrini,  $K \rightarrow \pi \nu \bar{\nu}$ : A model independent analysis and supersymmetry, Nucl. Phys. B520 (1998) 3–30.

- [830] G. Colangelo, G. Isidori, Supersymmetric contributions to rare kaon decays: Beyond the single mass-insertion approximation, JHEP 09 (1998) 009.
- [831] A. J. Buras, P. Gambino, M. Gorbahn, S. Jager, L. Silvestrini,  $\epsilon'/\epsilon$  and Rare K and B Decays in the MSSM, Nucl. Phys. B592 (2001) 55–91.
- [832] A. J. Buras, T. Ewerth, S. Jager, J. Rosiek,  $K^+ \rightarrow \pi^+ \nu \bar{\nu}$  and  $K_L \rightarrow \pi^0 \nu \bar{\nu}$  decays in the general MSSM, Nucl. Phys. B714 (2005) 103–136.
- [833] Y. Grossman, G. Isidori, H. Murayama, Lepton flavor mixing and  $K \rightarrow \pi \nu \bar{\nu}$  decays, Phys. Lett. B588 (2004) 74–80.
- [834] N. G. Deshpande, D. K. Ghosh, X.-G. He, Constraints on new physics from  $K \rightarrow \pi \nu \bar{\nu}$ , Phys. Rev. D70 (2004) 093003.
- [835] A. Deandrea, J. Welzel, M. Oertel,  $K \rightarrow \pi \nu \bar{\nu}$  from standard to new physics, JHEP 10 (2004) 038.
- [836] M. Blanke, A. J. Buras, B. Duling, S. Recksiegel, C. Tarantino, FCNC Processes in the Littlest Higgs Model with T-Parity: a 2009 Look. arXiv:0906.5454.
- [837] A. J. Buras, M. Spranger, A. Weiler, The Impact of Universal Extra Dimensions on the Unitarity Triangle and Rare K and B Decays, Nucl. Phys. B660 (2003) 225–268.
- [838] M. Blanke, A. J. Buras, B. Duling, K. Gemmler, S. Gori, Rare K and B Decays in a Warped Extra Dimension with Custodial Protection, JHEP 03 (2009) 108.
- [839] P. L. Cho, M. Misiak, D. Wyler,  $K_L \rightarrow \pi^0 e^+ e^-$  and  $B \rightarrow X_s \ell^+ \ell^-$  Decay in the MSSM, Phys. Rev. D54 (1996) 3329–3344.
- [840] C. Bobeth, A. J. Buras, F. Kruger, J. Urban, QCD corrections to  $\bar{B} \rightarrow X_{d,s} \nu \bar{\nu}$ ,  $\bar{B}_{d,s} \rightarrow \ell^+ \ell^-$ ,  $K \rightarrow \pi \nu \bar{\nu}$  and  $K_L \rightarrow \mu^+ \mu^-$  in the MSSM, Nucl. Phys. B630 (2002) 87–131.
- [841] A. J. Buras, G. Colangelo, G. Isidori, A. Romanino, L. Silvestrini, Connections between  $\epsilon'/\epsilon$  and rare kaon decays in supersymmetry, Nucl. Phys. B566 (2000) 3–32.
- [842] A. V. Artamonov, et al., New measurement of the  $K^+ \rightarrow \pi^+ \nu \bar{\nu}$  branching ratio, Phys. Rev. Lett. 101 (2008) 191802.
- [843] J. Appel, et al., Physics with a High Intensity Proton Source at Fermilab [http://www.fnal.gov/directorate/Longrange/Steering\\_Public/P5/GoldenBook-2008-02-03.pdf](http://www.fnal.gov/directorate/Longrange/Steering_Public/P5/GoldenBook-2008-02-03.pdf).
- [844] J. K. Ahn, et al., Search for the Decay  $K_L^0 \rightarrow \pi^0 \nu \bar{\nu}$ , Phys. Rev. Lett. 100 (2008) 201802.
- [845] S. L. Glashow, J. Iliopoulos, L. Maiani, Weak Interactions with Lepton-Hadron Symmetry, Phys. Rev. D2 (1970) 1285–1292.
- [846] G. Burdman, E. Golowich, J. L. Hewett, S. Pakvasa, Rare Charm Decays in the Standard Model and Beyond, Phys. Rev. D66 (2002) 014009.
- [847] Q. He, et al., Search for Rare and Forbidden Decays  $D^+ \rightarrow h^\pm e^\mp e^+$ , Phys. Rev. Lett. 95 (2005) 221802.
- [848] V. M. Abazov, et al., Measurement of the  $t\bar{t}$  production cross section in  $p\bar{p}$  collisions at  $\sqrt{s} = 1.96$ -TeV using kinematic characteristics of lepton + jets events, Phys. Rev. D76 (2007) 092007.
- [849] K. Kodama, et al., Upper limits of charm hadron decays to two muons plus hadrons, Phys. Lett. B345 (1995) 85–92.
- [850] J. M. Link, et al., Search for rare and forbidden 3-body di-muon decays of the charmed mesons  $D^+$  and  $D_s^+$ , Phys. Lett. B572 (2003) 21–31.
- [851] E. M. Aitala, et al., Search for rare and forbidden dilepton decays of the  $D^+$ ,  $D_s^+$ , and  $D^0$  charmed mesons, Phys. Lett. B462 (1999) 401–409.
- [852] P. L. Frabetti, et al., Search for rare and forbidden decays of the charmed meson  $D^+$ , Phys. Lett. B398 (1997) 239–244.
- [853] T. E. Coan, et al., First search for the flavor changing neutral current decay  $D^0 \rightarrow \gamma\gamma$ , Phys. Rev. Lett. 90 (2003) 101801.
- [854] B. Aubert, et al., Search for flavor-changing neutral current and lepton flavor violating decays of  $D^0 \rightarrow \ell^+ \ell^-$ , Phys. Rev. Lett. 93 (2004) 191801.
- [855] A. Freyberger, et al., Limits on flavor changing neutral currents in  $D^0$  meson decays, Phys. Rev. Lett. 76 (1996) 3065–3069.
- [856] E. M. Aitala, et al., Search for rare and forbidden charm meson decays  $D^0 \rightarrow V \ell^+ \ell^-$  and  $hhll$ , Phys. Rev. Lett. 86 (2001) 3969–3972.
- [857] C. Aubin, et al., Charmed meson decay constants in three-flavor lattice QCD, Phys. Rev. Lett. 95 (2005) 122002.
- [858] K. M. Ecklund, et al., Measurement of the Absolute Branching Fraction of  $D_s^+ \rightarrow \tau^+ \nu_\tau$  Decay, Phys. Rev. Lett. 100 (2008) 161801.

- [859] B. I. Eisenstein, et al., Precision Measurement of  $BR(D^+ \rightarrow \mu^+ \nu)$  and the Pseudoscalar Decay Constant  $f_{D^+}$ , Phys. Rev. D78 (2008) 052003.
- [860] L. Zhang, Measurements of D and Ds decay constants at CLEO. arXiv:0810.2328.
- [861] B. Aubert, et al., Measurement of the pseudoscalar decay constant  $f_{D_s}$  using charm-tagged events in  $e^+ e^-$  collisions at  $s^{1/2} = 10.58$ -GeV, Phys. Rev. Lett. 98 (2007) 141801.
- [862] E. Follana, et al., Highly Improved Staggered Quarks on the Lattice, with Applications to Charm Physics, Phys. Rev. D75 (2007) 054502.
- [863] B. A. Dobrescu, A. S. Kronfeld, Accumulating evidence for nonstandard leptonic decays of  $D_s$  mesons, Phys. Rev. Lett. 100 (2008) 241802.
- [864] C. T. H. Davies, et al., Precision charm physics,  $m_c$  and  $\alpha_s$  from lattice QCD. arXiv:0810.3548.
- [865] P. U. E. Onyisi, et al., Improved Measurement of Absolute Branching Fraction of Ds to tau nu, Phys. Rev. D79 (2009) 052002.
- [866] J. Bijnens, J. M. Gerard, G. Klein, The K(L) - K(S) mass difference, Phys. Lett. B257 (1991) 191–195.
- [867] E. Lunghi, A. Soni, Possible Indications of New Physics in  $B_d$  -mixing and in  $\sin(2\beta)$  Determinations, Phys. Lett. B666 (2008) 162–165.
- [868] A. J. Buras, D. Guadagnoli, Correlations among new CP violating effects in  $\Delta F = 2$  observables, Phys. Rev. D78 (2008) 033005.
- [869] T. Inami, C. S. Lim, Effects of Superheavy Quarks and Leptons in Low-Energy Weak Processes  $K(L) \rightarrow \mu$  anti- $\mu$ ,  $K^+ \rightarrow \pi^+$  Neutrino anti-neutrino and  $K^0 \leftrightarrow$  anti- $K^0$ , Prog. Theor. Phys. 65 (1981) 297.
- [870] D. J. Antonio, et al., Neutral kaon mixing from 2+1 flavor domain wall QCD, Phys. Rev. Lett. 100 (2008) 032001.
- [871] C. Aubin, J. Laiho, R. S. Van de Water, The neutral kaon mixing parameter  $B_K$  from unquenched mixed-action lattice QCD. arXiv:0905.3947.
- [872] E. Gamiz, et al., Unquenched determination of the kaon parameter  $B_K$  from improved staggered fermions, Phys. Rev. D73 (2006) 114502.
- [873] S. Aoki, et al.,  $B_K$  with two flavors of dynamical overlap fermions, Phys. Rev. D77 (2008) 094503.
- [874] P. Dimopoulos, et al., K-meson vector and tensor decay constants and BK-parameter from Nf=2 tmQCD, PoS LATTICE2008 (2008) 271.
- [875] J. Bijnens, E. Gamiz, J. Prades, The B(K) kaon parameter in the chiral limit, JHEP 03 (2006) 048.
- [876] J. Prades, C. A. Dominguez, J. A. Penarrocha, A. Pich, E. de Rafael, The  $K^0$  - anti- $K^0$  B factor in the QCD hadronic duality approach, Z. Phys. C51 (1991) 287–296.
- [877] S. Aoki, et al., Kaon B parameter from quenched lattice QCD, Phys. Rev. Lett. 80 (1998) 5271–5274.
- [878] Y. Aoki, et al., The kaon B-parameter from quenched domain-wall QCD, Phys. Rev. D73 (2006) 094507.
- [879] Y. Nakamura, S. Aoki, Y. Taniguchi, T. Yoshie, Precise determination of  $B_K$  and right quark masses in quenched domain-wall QCD, Phys. Rev. D78 (2008) 034502.
- [880] C. Dawson, progress in kaon phenomenology from lattice QCD, PoS LAT2005 (2006) 007.
- [881] V. Lubicz, C. Tarantino, Flavour physics and Lattice QCD: averages of lattice inputs for the Unitarity Triangle Analysis, Nuovo Cim. 123B (2008) 674–688.
- [882] L. Lellouch, Kaon physics: a lattice perspective. arXiv:0902.4545.
- [883] A. J. Buras, Weak Hamiltonian, CP violation and rare decays. arXiv:hep-ph/9806471.
- [884] C. W. Bernard, T. Draper, A. Soni, H. D. Politzer, M. B. Wise, Application of Chiral Perturbation Theory to  $K \rightarrow 2 \pi$  Decays, Phys. Rev. D32 (1985) 2343–2347.
- [885] J. I. Noaki, et al., Calculation of non-leptonic kaon decay amplitudes from  $K \rightarrow \pi$  matrix elements in quenched domain-wall QCD, Phys. Rev. D68 (2003) 014501.
- [886] T. Blum, et al., Kaon Matrix Elements and CP-violation from Quenched Lattice QCD: (I) the 3-flavor case, Phys. Rev. D68 (2003) 114506.
- [887] S. Li, N. H. Christ, Chiral perturbation theory, K to pi pi decays and 2+1 flavor domain wall QCD. arXiv:0812.1368.
- [888] L. Giusti, et al., On  $K \rightarrow \pi\pi$  amplitudes with a light charm quark, Phys. Rev. Lett. 98 (2007) 082003.
- [889] K. Hagiwara, et al., Review of particle physics, Phys. Rev. D66 (2002) 010001.



- [890] J. R. Batley, et al., A precision measurement of direct CP violation in the decay of neutral kaons into two pions, *Phys. Lett.* B544 (2002) 97–112.
- [891] T. Yamanaka, Review on  $\epsilon'/\epsilon$ . arXiv:0807.1418.
- [892] E. T. Worcester, Measurements of Direct CP Violation, CPT Symmetry, and Other Parameters in the Neutral Kaon System FERMLAB-THESIS-2007-51.
- [893] M. S. Sozzi, On the direct CP violation parameter  $\epsilon'$ , *Eur. Phys. J.* C36 (2004) 37–42.
- [894] F. Ambrosino, et al., A direct search for the CP-violating decay  $K_S \rightarrow 3\pi^0$  with the KLOE detector at DAPHNE, *Phys. Lett.* B619 (2005) 61–70.
- [895] F. Ambrosino, et al., Determination of CP and CPT violation parameters in the neutral kaon system using the Bell-Steinberger relation and data from the KLOE experiment, *JHEP* 12 (2006) 011.
- [896] I. I. Y. Bigi, B. Blok, M. A. Shifman, N. Uraltsev, A. I. Vainshtein, Nonleptonic decays of beauty hadrons: From phenomenology to theory. arXiv:hep-ph/9401298.
- [897] M. B. Voloshin, Inclusive weak decay rates of heavy hadrons. arXiv:hep-ph/0004257.
- [898] M. Neubert, C. T. Sachrajda, Spectator effects in inclusive decays of beauty hadrons, *Nucl. Phys.* B483 (1997) 339–370.
- [899] J. L. Rosner, Enhancement of the  $\Lambda_b$  decay rate, *Phys. Lett.* B379 (1996) 267–271.
- [900] M. Ciuchini, E. Franco, V. Lubicz, F. Mescia, Next-to-leading order QCD corrections to spectator effects in lifetimes of beauty hadrons, *Nucl. Phys.* B625 (2002) 211–238.
- [901] E. Franco, V. Lubicz, F. Mescia, C. Tarantino, Lifetime ratios of beauty hadrons at the next-to-leading order in QCD, *Nucl. Phys.* B633 (2002) 212–236.
- [902] M. Beneke, G. Buchalla, C. Greub, A. Lenz, U. Nierste, The  $B^+ - B^0$  lifetime difference beyond leading logarithms, *Nucl. Phys.* B639 (2002) 389–407.
- [903] F. Gabbiani, A. I. Onishchenko, A. A. Petrov,  $\Lambda_b$  lifetime puzzle in heavy-quark expansion, *Phys. Rev.* D68 (2003) 114006.
- [904] F. Gabbiani, A. I. Onishchenko, A. A. Petrov, Spectator effects and lifetimes of heavy hadrons, *Phys. Rev.* D70 (2004) 094031.
- [905] A. Badin, F. Gabbiani, A. A. Petrov, Lifetime difference in  $B_s$  mixing: Standard model and beyond, *Phys. Lett.* B653 (2007) 230–240.
- [906] M. A. Shifman, M. B. Voloshin, Preasymptotic Effects in Inclusive Weak Decays of Charmed Particles, *Sov. J. Nucl. Phys.* 41 (1985) 120.
- [907] B. Guberina, S. Nussinov, R. D. Peccei, R. Ruckl, D Meson Lifetimes and Decays, *Phys. Lett.* B89 (1979) 111.
- [908] N. Bilic, B. Guberina, J. Trampetic, Pauli Interference Effect in  $D^+$  Lifetime, *Nucl. Phys.* B248 (1984) 261.
- [909] B. Guberina, R. Ruckl, J. Trampetic, Charmed Baryon Lifetime Differences, *Z. Phys.* C33 (1986) 297.
- [910] B. Guberina, B. Melic, H. Stefancic, Lifetime-difference pattern of heavy hadrons, *Phys. Lett.* B484 (2000) 43–50.
- [911] M. Di Pierro, C. T. Sachrajda, A lattice study of spectator effects in inclusive decays of B mesons, *Nucl. Phys.* B534 (1998) 373–391.
- [912] M. Di Pierro, C. T. Sachrajda, C. Michael, An exploratory lattice study of spectator effects in inclusive decays of the  $\Lambda_b$  baryon, *Phys. Lett.* B468 (1999) 143.
- [913] M. Di Pierro, C. T. Sachrajda, Spectator effects in inclusive decays of beauty hadrons, *Nucl. Phys. Proc. Suppl.* 73 (1999) 384–386.
- [914] D. Becirevic, Theoretical progress in describing the B meson lifetimes. arXiv:hep-ph/0110124.
- [915] A. Ali Khan, et al., Decay constants of B and D mesons from improved relativistic lattice QCD with two flavours of sea quarks, *Phys. Rev.* D64 (2001) 034505.
- [916] A. Ali Khan, et al., B meson decay constant from two-flavor lattice QCD with non-relativistic heavy quarks, *Phys. Rev.* D64 (2001) 054504.
- [917] C. Bernard, et al., Lattice calculation of heavy-light decay constants with two flavors of dynamical quarks, *Phys. Rev.* D66 (2002) 094501.
- [918] S. Aoki, et al.,  $B^0 - \bar{B}^0$  mixing in unquenched lattice QCD, *Phys. Rev. Lett.* 91 (2003) 212001.
- [919] M. Wingate, C. T. H. Davies, A. Gray, G. P. Lepage, J. Shigemitsu, The B/s and D/s decay constants in 3 flavor lattice QCD, *Phys. Rev. Lett.* 92 (2004) 162001.
- [920] A. Gray, et al., The B Meson Decay Constant from Unquenched Lattice QCD, *Phys. Rev. Lett.* 95 (2005) 212001.

- [921] E. Gamiz, C. T. H. Davies, G. P. Lepage, J. Shigemitsu, M. Wingate, Neutral  $B$  Meson Mixing in Unquenched Lattice QCD. arXiv:0902.1815.
- [922] C. Bernard, et al., The decay constants  $f_B$  and  $f_{D^+}$  from three-flavor lattice QCD, PoS LAT2007 (2007) 370.
- [923] L. Lellouch, C. J. D. Lin, Standard model matrix elements for neutral  $B$  meson mixing and associated decay constants, Phys. Rev. D64 (2001) 094501.
- [924] D. Becirevic, V. Gimenez, G. Martinelli, M. Papinutto, J. Reyes,  $B$ -parameters of the complete set of matrix elements of  $\Delta B = 2$  operators from the lattice, JHEP 04 (2002) 025.
- [925] S. Aoki, et al.,  $B^0 - \bar{B}^0$  mixing in quenched lattice QCD. ((U)) ((W)), Phys. Rev. D67 (2003) 014506.
- [926] E. Dalgic, et al.,  $B_s^0 - \bar{B}_s^0$  mixing parameters from unquenched lattice QCD, Phys. Rev. D76 (2007) 011501.
- [927] C. Albertus, et al.,  $B - \bar{B}$  mixing with domain wall fermions in the static approximation, PoS LAT2007 (2007) 376.
- [928] M. Beneke, G. Buchalla, C. Greub, A. Lenz, U. Nierste, Next-to-leading order QCD corrections to the lifetime difference of  $B_s$  mesons, Phys. Lett. B459 (1999) 631–640.
- [929] M. Beneke, G. Buchalla, A. Lenz, U. Nierste, CP asymmetry in flavour-specific  $B$  decays beyond leading logarithms, Phys. Lett. B576 (2003) 173–183.
- [930] M. Ciuchini, E. Franco, V. Lubicz, F. Mescia, C. Tarantino, Lifetime differences and CP violation parameters of neutral  $B$  mesons at the next-to-leading order in QCD, JHEP 08 (2003) 031.
- [931] M. Beneke, G. Buchalla, I. Dunietz, Width Difference in the  $B_s - \bar{B}_s$  System, Phys. Rev. D54 (1996) 4419–4431.
- [932] A. Lenz, U. Nierste, Theoretical update of  $B_s - \bar{B}_s$  mixing, JHEP 06 (2007) 072.
- [933] T. C. Collaboration, CDF Note 9458 (2008).
- [934] T. C. Collaboration, CDF Note 9294 (2008).
- [935] V. M. Abazov, et al., Measurement of the lifetime of the  $B_c^\pm$  meson in the semileptonic decay channel, Phys. Rev. Lett. 102 (2009) 092001.
- [936] V. V. Kiselev, Decays of the  $B_c$  meson. arXiv:hep-ph/0308214.
- [937] A. Abulencia, et al., Measurement of the  $\Lambda_b^0$  Lifetime in  $\Lambda_b^0 \rightarrow J/\psi \Lambda^0$  in  $p\bar{p}$  Collisions at  $\sqrt{s} = 1.96$ -TeV, Phys. Rev. Lett. 98 (2007) 122001.
- [938] T. C. Collaboration, CDF Note 9408 (2008).
- [939] V. M. Abazov, et al., Measurement of the  $\Lambda_b^0$  lifetime using semileptonic decays, Phys. Rev. Lett. 99 (2007) 182001.
- [940] V. M. Abazov, et al., Measurement of the  $\Lambda_b$  lifetime in the exclusive decay  $\Lambda_b \rightarrow J/\psi \Lambda$ , Phys. Rev. Lett. 99 (2007) 142001.
- [941] C. Tarantino,  $B$ -meson mixing and lifetimes, Nucl. Phys. Proc. Suppl. 156 (2006) 33–37.
- [942] V. M. Abazov, et al., First direct two-sided bound on the  $B_s^0$  oscillation frequency, Phys. Rev. Lett. 97 (2006) 021802.
- [943] D0  $B_s$  oscillation combination for summer 2007. D0 note 5618 <http://www-d0.fnal.gov/Run2Physics/WWW/results/prelim/B/B54/B54.pdf>.
- [944] I. I. Y. Bigi, A. I. Sanda, Notes on the Observability of CP Violations in  $B$  Decays, Nucl. Phys. B193 (1981) 85.
- [945] A. B. Carter, A. I. Sanda, CP Violation in  $B$  Meson Decays, Phys. Rev. D23 (1981) 1567.
- [946] B. Aubert, et al., Update of Time-Dependent CP Asymmetry Measurements in  $b \rightarrow c\bar{c}s$  Decays. arXiv:0808.1903.
- [947] K. F. Chen, et al., Observation of time-dependent CP violation in  $B^0 \rightarrow \eta' K^0$  decays and improved measurements of CP asymmetries in  $B^0 \rightarrow \phi K^0, K_S^0 K_S^0 K_S^0$  and  $B^0 \rightarrow J/\psi K^0$  decays, Phys. Rev. Lett. 98 (2007) 031802.
- [948] H. Sahoo, et al., Measurements of time-dependent CP violation in  $B^0 \rightarrow \psi(2S)K_S$  decays, Phys. Rev. D77 (2008) 091103.
- [949] B. Aubert, et al., Ambiguity-free measurement of  $\cos(2\beta)$ : Time-integrated and time-dependent angular analyses of  $B \rightarrow J/\psi K\pi$ , Phys. Rev. D71 (2005) 032005.
- [950] R. Itoh, et al., Studies of CP violation in  $B \rightarrow J/\psi K^*$  decays, Phys. Rev. Lett. 95 (2005) 091601.
- [951] B. Aubert, et al., Evidence for CP violation in  $B^0 \rightarrow J/\psi \pi^0$  decays, Phys. Rev. Lett. 101 (2008) 021801.
- [952] S. E. Lee, et al., Improved measurement of time-dependent CP violation in  $B^0 \rightarrow J/\psi \pi^0$  decays, Phys. Rev. D77 (2008) 071101.

- [953] M. Ciuchini, E. Franco, G. Martinelli, L. Reina, L. Silvestrini, An Upgraded analysis of epsilon-prime epsilon at the next- to-leading order, *Z. Phys. C*68 (1995) 239–256.
- [954] J. Charles, et al., CP violation and the CKM matrix: Assessing the impact of the asymmetric  $B$  factories, *Eur. Phys. J. C*41 (2005) 1–131.
- [955] I. Dunietz, R. Fleischer, U. Nierste, In pursuit of new physics with  $B_s$  decays, *Phys. Rev. D*63 (2001) 114015.
- [956] T. Aaltonen, et al., First Flavor-Tagged Determination of Bounds on Mixing- Induced CP Violation in  $B_s^0 \rightarrow J/\psi\phi$  Decays, *Phys. Rev. Lett.* 100 (2008) 161802.
- [957] B. Aubert, et al., Measurement of decay amplitudes of  $B \rightarrow J/\psi K^*, \psi(2S)K^*$ , and  $\chi_{c1}K^*$  with an angular analysis, *Phys. Rev. D*76 (2007) 031102.
- [958] T. Aaltonen, et al., Measurement of lifetime and decay-width difference in  $B_s^0 \rightarrow J/\psi\phi$  decays, *Phys. Rev. Lett.* 100 (2008) 121803.
- [959] K. S. Cranmer, Frequentist hypothesis testing with background uncertainty. [arXiv:physics/0310108](https://arxiv.org/abs/physics/0310108).
- [960] G. Punzi, Ordering algorithms and confidence intervals in the presence of nuisance parameters. [arXiv:physics/0511202](https://arxiv.org/abs/physics/0511202).
- [961] H.-Y. Cheng, CP Violating Effects in Heavy Meson Systems, *Phys. Rev. D*26 (1982) 143.
- [962] A. Datta, D. Kumbhakar,  $D^0 - \bar{D}^0$  Mixing: A Possible Test of Physics Beyond the Standard Model, *Z. Phys. C*27 (1985) 515.
- [963] H. Georgi, D - anti-D mixing in heavy quark effective field theory, *Phys. Lett. B*297 (1992) 353–357.
- [964] E. Golowich, A. A. Petrov, Short distance analysis of  $D^0 - \bar{D}^0$  mixing, *Phys. Lett. B*625 (2005) 53–62.
- [965] T. Ohl, G. Ricciardi, E. H. Simmons, D - anti-D mixing in heavy quark effective field theory: The Sequel, *Nucl. Phys. B*403 (1993) 605–632.
- [966] I. I. Y. Bigi, N. G. Uraltsev,  $D^0 - \bar{D}^0$  oscillations as a probe of quark-hadron duality, *Nucl. Phys. B*592 (2001) 92–106.
- [967] R. Aleksan, A. Le Yaouanc, L. Oliver, O. Pene, J. C. Raynal, Estimation of  $\Delta\Gamma$  for the  $B_s - \bar{B}_s$  system: Exclusive decays and the parton model, *Phys. Lett. B*316 (1993) 567–577.
- [968] F. Buccella, M. Lusignoli, G. Miele, A. Pugliese, P. Santorelli, Nonleptonic weak decays of charmed mesons, *Phys. Rev. D*51 (1995) 3478–3486.
- [969] J. F. Donoghue, E. Golowich, B. R. Holstein, J. Trampetic, Dispersive Effects in  $D^0 - \bar{D}^0$  Mixing, *Phys. Rev. D*33 (1986) 179.
- [970] L. Wolfenstein,  $D^0 - \bar{D}^0$  Mixing, *Phys. Lett. B*164 (1985) 170.
- [971] A. F. Falk, Y. Grossman, Z. Ligeti, A. A. Petrov, SU(3) breaking and  $D^0 - \bar{D}^0$  mixing, *Phys. Rev. D*65 (2002) 054034.
- [972] A. F. Falk, Y. Grossman, Z. Ligeti, Y. Nir, A. A. Petrov, The  $D^0 - \bar{D}^0$  mass difference from a dispersion relation, *Phys. Rev. D*69 (2004) 114021.
- [973] E. Golowich, S. Pakvasa, A. A. Petrov, New physics contributions to the lifetime difference in  $D^0 - \bar{D}^0$  mixing, *Phys. Rev. Lett.* 98 (2007) 181801.
- [974] A. A. Petrov, G. K. Yeghiyan, Lifetime difference in  $D_0 - \bar{D}_0$  mixing within R- parity-violating SUSY, *Phys. Rev. D*77 (2008) 034018.
- [975] E. Golowich, J. Hewett, S. Pakvasa, A. A. Petrov, Implications of  $D^0 - \bar{D}^0$  Mixing for New Physics, *Phys. Rev. D*76 (2007) 095009.
- [976] B. Aubert, et al., Evidence for  $D^0 - \bar{D}^0$  Mixing, *Phys. Rev. Lett.* 98 (2007) 211802.
- [977] M. Staric, et al., Evidence for  $D^0 - \bar{D}^0$  Mixing, *Phys. Rev. Lett.* 98 (2007) 211803.
- [978] B. Aubert, et al., Measurement of  $D^0 - \bar{D}^0$  mixing using the ratio of lifetimes for the decays  $D^0 \rightarrow K^- \pi^+, K^- K^+$ , and  $\pi^- \pi^+$ , *Phys. Rev. D*78 (2008) 011105.
- [979] B. Aubert, et al., Measurement of  $D^0 - \bar{D}^0$  mixing from a time- dependent amplitude analysis of  $D^0 \rightarrow K^+ \pi^- \pi^0$  decays. [arXiv:0807.4544](https://arxiv.org/abs/0807.4544).
- [980] G. Burdman, I. Shipsey,  $D^0 - \bar{D}^0$  mixing and rare charm decays, *Ann. Rev. Nucl. Part. Sci.* 53 (2003) 431–499.
- [981] A. A. Petrov, Charm mixing in the Standard Model and beyond, *Int. J. Mod. Phys. A*21 (2006) 5686–5693.
- [982] G. Blaylock, A. Seiden, Y. Nir, The Role of CP violation in  $D^0 - \bar{D}^0$  mixing, *Phys. Lett. B*355 (1995) 555–560.

- [983] Staric, Marko, *CP violation from B factories*, this workshop.
- [984] T. Aaltonen, et al., Evidence for  $D^0 - \bar{D}^0$  mixing using the CDF II Detector, Phys. Rev. Lett. 100 (2008) 121802.
- [985] Donati, Simone,  $D^0 - \bar{D}^0$  mixing and CP violation from Hadron Colliders, this workshop.
- [986] D. M. Asner, et al., Determination of the  $D^0 \rightarrow K^+\pi^-$  Relative Strong Phase Using Quantum-Correlated Measurements in  $e^+e^- \rightarrow D^0\bar{D}^0$  bar at CLEO, Phys. Rev. D78 (2008) 012001.
- [987] D. M. Asner, et al., Search for  $D_0 - \bar{D}_0$  Mixing in the Dalitz Plot Analysis of  $D_0 \rightarrow K_S^0\pi^+\pi^-$ , Phys. Rev. D72 (2005) 012001.
- [988] K. Abe, et al., Measurement of  $D^0 - \bar{D}^0$  mixing in  $D^0 \rightarrow K_s\pi^+\pi^-$  decays, Phys. Rev. Lett. 99 (2007) 131803.
- [989] T.-h. T. Liu, The  $D^0 - \bar{D}^0$  mixing search: Current status and future prospects. arXiv:hep-ph/9408330.
- [990] I. Adachi, et al., Measurement of  $y_{CP}$  in  $D$  meson decays to CP eigenstates. arXiv:0808.0074.
- [991] A. S. Dighe, I. Dunietz, R. Fleischer, Extracting CKM phases and  $B_s - \bar{B}_s$  mixing parameters from angular distributions of nonleptonic  $B$  decays, Eur. Phys. J. C6 (1999) 647–662.
- [992] T. L. Collaboration, The lhcb rich tdr, CERN/LHCC 2000-037.
- [993] A. A. Alves, et al., The LHCb Detector at the LHC, JINST 3 (2008) S08005.
- [994] P. M. Spradlin, G. Wilkinson, F. Xing, Selection of tagged wrong sign  $D^0 \rightarrow \pi^- K^+$  candidates for  $D^0\bar{D}^0$  mixing measurements CERN-LHCB-2007-049.
- [995] I. I. Y. Bigi, A. I. Sanda, On direct CP violation in  $B \rightarrow D^0(\bar{D}^0)K\pi's$  versus  $\bar{B} \rightarrow D^0(\bar{D}^0)\bar{K}\pi's$  decays, Phys. Lett. B211 (1988) 213.
- [996] M. Gronau, D. London., How to determine all the angles of the unitarity triangle from  $B_d^0 \rightarrow DK_S$  and  $B_s^0 \rightarrow D^0$ , Phys. Lett. B253 (1991) 483–488.
- [997] M. Gronau, D. Wyler, On determining a weak phase from CP asymmetries in charged B decays, Phys. Lett. B265 (1991) 172–176.
- [998] D. Atwood, I. Dunietz, A. Soni, Enhanced CP violation with  $B \rightarrow KD^0(\bar{D}^0)$  modes and extraction of the CKM angle  $\gamma$ , Phys. Rev. Lett. 78 (1997) 3257–3260.
- [999] D. Atwood, I. Dunietz, A. Soni, Improved methods for observing CP violation in  $B^\pm \rightarrow KD$  and measuring the CKM phase gamma, Phys. Rev. D63 (2001) 036005.
- [1000] Y. Grossman, Z. Ligeti, A. Soffer, Measuring  $\gamma$  in  $B^\pm \rightarrow K^p m(KK^*)(D)$  decays, Phys. Rev. D67 (2003) 071301.
- [1001] A. Bondar, proceedings of BINP Special Analysis Meeting on Dalitz Analysis (2002).
- [1002] A. Poluektov, et al., Measurement of  $\phi_3$  with Dalitz plot analysis of  $B^\pm \rightarrow D^{(*)}K^\pm$  decay, Phys. Rev. D70 (2004) 072003.
- [1003] Y. Grossman, A. Soffer, J. Zupan, The effect of D anti-D mixing on the measurement of gamma in  $B \rightarrow DK$  decays, Phys. Rev. D72 (2005) 031501.
- [1004] M. Gronau, Y. Grossman, N. Shuhmaher, A. Soffer, J. Zupan, Using untagged  $B^0 \rightarrow DK_S$  to determine  $\gamma$ , Phys. Rev. D69 (2004) 113003.
- [1005] M. Gronau, Y. Grossman, Z. Surujon, J. Zupan, Enhanced effects on extracting  $\gamma$  from untagged  $B^0$  and  $B_s$  decays, Phys. Lett. B649 (2007) 61–66.
- [1006] A. Bondar, T. Gershon, On  $\phi_3$  measurements using  $B^- \rightarrow D^*K^-$  decays, Phys. Rev. D70 (2004) 091503.
- [1007] M. Gronau, Improving bounds on gamma in  $B^\pm \rightarrow DK^\pm$  and  $B^{\pm,0} \rightarrow DX_s^{\pm,0}$ , Phys. Lett. B557 (2003) 198–206.
- [1008] T. Gershon, On the Measurement of the Unitarity Triangle Angle  $\gamma$  from  $B^0 \rightarrow DK^{*0}$  Decays, Phys. Rev. D79 (2009) 051301.
- [1009] B. Aubert, et al., Measurement of CP observables in  $B^\pm \rightarrow D_{CP}^0 K^\pm$  decays, Phys. Rev. D77 (2008) 111102.
- [1010] K. Abe, et al., Study of  $B^\pm \rightarrow D_{CP} K^\pm$  and  $D_{CP}^* K^\pm$  decays, Phys. Rev. D73 (2006) 051106.
- [1011] K. Gibson, Measurement of CP Observables in  $B^- \rightarrow D^0 K^-$  Decays at CDF. arXiv:0809.4809.
- [1012] B. Aubert, et al., Search for  $b \rightarrow u$  transitions in  $B^- \rightarrow D^0 K^-$  and  $B^- \rightarrow D^{*0} K^-$ , Phys. Rev. D72 (2005) 032004.
- [1013] Y. Horii, et al., Study of the Suppressed B meson Decay  $B^- \rightarrow DK^-, D \rightarrow K^+\pi^-$ , Phys. Rev. D78 (2008) 071901.
- [1014] J. L. Rosner, et al., Determination of the Strong Phase in  $D^0 \rightarrow K^+\pi^-$  Using Quantum-Correlated Measurements, Phys. Rev. Lett. 100 (2008) 221801.

- [1015] A. Poluektov, et al., Measurement of  $\phi_3$  with Dalitz plot analysis of  $B^+ \rightarrow D^{(*)}K^{(*)+}$  decay, Phys. Rev. D73 (2006) 112009.
- [1016] K. Abe, et al., Updated Measurement of  $\phi_{3\pi}$  with a Dalitz Plot Analysis of  $B \rightarrow D^{(*)}K$  Decay. arXiv:0803.3375.
- [1017] V. V. Anisovich, A. V. Sarantsev, K-matrix analysis of the ( $IJ^{PC} = 00^{++}$ )-wave in the mass region below 1900 MeV, Eur. Phys. J. A16 (2003) 229–258.
- [1018] D. Aston, et al., A Study of K- pi+ Scattering in the Reaction K- p  $\rightarrow$  K- pi+ n at 11-GeV/c, Nucl. Phys. B296 (1988) 493.
- [1019] I. Dunietz, CP violation with selftagging B(d) modes, Phys. Lett. B270 (1991) 75–80.
- [1020] B. Aubert, et al., Search for  $b \rightarrow u$  transitions in  $B^0 \rightarrow D^0 K^{*0}$  decays. arXiv:0904.2112.
- [1021] N. Lowrey, et al., Determination of the  $D^0 \rightarrow K^-\pi^+\pi^0$  and  $D^0 \rightarrow K^-\pi^+\pi^+\pi^-$  Coherence Factors and Average Strong-Phase Differences Using Quantum-Correlated Measurements. arXiv:0903.4853.
- [1022] B. Aubert, et al., Measurement of the CKM angle gamma in  $B^0 \rightarrow \bar{D}^0(D^0)K^{*0}$  with a Dalitz analysis of  $D^0 \rightarrow K_S\pi^+\pi^-$ . arXiv:0805.2001.
- [1023] B. Aubert, et al., Measurement of time-dependent CP-violating asymmetries and constraints on  $\sin(2\beta + \gamma)$  with partial reconstruction of  $B \rightarrow D^{*\mp}\pi^\pm$  decays, Phys. Rev. D71 (2005) 112003.
- [1024] B. Aubert, et al., Measurement of time-dependent CP asymmetries in  $B^0 \rightarrow D^{(*)+} \pi^\mp$  and  $B^0 \rightarrow D^\pm \rho^\mp$  decays, Phys. Rev. D73 (2006) 111101.
- [1025] I. Adachi, et al., Measurements of time-dependent CP Asymmetries in  $B \rightarrow D^{*\mp}\pi^\pm$  decays using a partial reconstruction technique. arXiv:0809.3203.
- [1026] F. J. Ronga, et al., Measurements of CP violation in  $B^0 \rightarrow D^{*+}\pi^-$  and  $B^0 \rightarrow D^-\pi^+$  decays, Phys. Rev. D73 (2006) 092003.
- [1027] R. Aleksan, T. C. Petersen, A. Soffer, Measuring the weak phase gamma in color allowed  $B \rightarrow DK\pi$  decays, Phys. Rev. D67 (2003) 096002.
- [1028] F. Polci, M. H. Schune, A. Stocchi, Feasibility study for a model independent measurement of  $2\beta + \gamma$  in  $B^0$  decays using  $D^-K^0\pi^+$  final states. arXiv:hep-ph/0605129.
- [1029] B. Aubert, et al., Time-dependent Dalitz plot analysis of  $B^0 \rightarrow D^\mp K^0\pi^\pm$  decays, Phys. Rev. D77 (2008) 071102.
- [1030] A. Bondar, A. Poluektov, Feasibility study of model-independent approach to  $\phi_3$  measurement using Dalitz plot analysis, Eur. Phys. J. C47 (2006) 347–353.
- [1031] A. Bondar, A. Poluektov, The use of quantum-correlated  $D^0$  decays for  $\phi_3$  measurement, Eur. Phys. J. JC55 (2008) 51.
- [1032] R. A. Briere, First model-independent determination of the relative strong phase between  $D^0$  and  $\bar{D}^0 \rightarrow K_S\pi^+\pi^-$  and its impact on the CKM Angle gamma/phi3 measurement. arXiv:0903.1681.
- [1033] K. Akiba, et al., Determination of the CKM-angle gamma with tree-level processes at LHCbCERN-LHCB-2008-031.
- [1034] D. Atwood, A. Soni, Role of charm factory in extracting CKM-phase information via  $B \rightarrow DK$ , Phys. Rev. D68 (2003) 033003.
- [1035] A. J. Buras, L. Silvestrini, Non-leptonic two-body B decays beyond factorization, Nucl. Phys. B569 (2000) 3–52.
- [1036] D. Zeppenfeld, SU(3) Relations for B Meson Decays, Zeit. Phys. C8 (1981) 77.
- [1037] M. Gronau, O. F. Hernandez, D. London, J. L. Rosner, Decays of B mesons to two light pseudoscalars, Phys. Rev. D50 (1994) 4529–4543.
- [1038] M. Beneke, M. Neubert, QCD factorization for  $B \rightarrow PP$  and  $B \rightarrow PV$  decays, Nucl. Phys. B675 (2003) 333–415.
- [1039] E. Baracchini, G. Isidori, Electromagnetic corrections to non-leptonic two-body B and D decays, Phys. Lett. B633 (2006) 309–313.
- [1040] M. Beneke, S. Jager, Spectator scattering at NLO in non-leptonic B decays: Tree amplitudes, Nucl. Phys. B751 (2006) 160–185.
- [1041] N. Kivel, Radiative corrections to hard spectator scattering in  $B \rightarrow \pi\pi$  decays, JHEP 05 (2007) 019.
- [1042] V. Pilipp, Hard spectator interactions in  $B \rightarrow \pi\pi$  at order  $\alpha_s^2$ , Nucl. Phys. B794 (2008) 154–188.
- [1043] G. Bell, NNLO Vertex Corrections in charmless hadronic B decays: Imaginary part, Nucl. Phys. B795 (2008) 1–26.
- [1044] G. Bell, NNLO vertex corrections in charmless hadronic B decays: Real part. arXiv:0902.1915.

- [1045] T. Becher, R. J. Hill, Loop corrections to heavy-to-light form factors and evanescent operators in SCET, JHEP 10 (2004) 055.
- [1046] M. Beneke, D. Yang, Heavy-to-light B meson form factors at large recoil energy: Spectator scattering corrections, Nucl. Phys. B736 (2006) 34–81.
- [1047] G. G. Kirilin, Loop corrections to the form factors in  $B \rightarrow \pi \ell \nu$  decay. arXiv:hep-ph/0508235.
- [1048] M. Beneke, S. Jager, Spectator scattering at NLO in non-leptonic B decays: Leading penguin amplitudes, Nucl. Phys. B768 (2007) 51–84.
- [1049] S. J. Lee, M. Neubert, Model-independent properties of the B-meson distribution amplitude, Phys. Rev. D72 (2005) 094028.
- [1050] H. Kawamura, K. Tanaka, Operator product expansion for B-meson distribution amplitude and dimension-5 HQET operators, Phys. Lett. B673 (2009) 201–207.
- [1051] P. Ball, E. Kou,  $B \rightarrow \gamma e \nu$  transitions from QCD sum rules on the light-cone, JHEP 04 (2003) 029.
- [1052] V. M. Braun, D. Y. Ivanov, G. P. Korchemsky, The B-Meson Distribution Amplitude in QCD, Phys. Rev. D69 (2004) 034014.
- [1053] A. Jain, I. Z. Rothstein, I. W. Stewart, Penguin Loops for Nonleptonic B-Decays in the Standard Model: Is there a Penguin Puzzle?. arXiv:0706.3399.
- [1054] H.-n. Li, S. Mishima, A. I. Sanda, Resolution to the  $B \rightarrow \pi K$  puzzle, Phys. Rev. D72 (2005) 114005.
- [1055] H.-n. Li, S. Mishima, Resolution of the  $B \rightarrow \pi\pi$ ,  $\pi K$  puzzles. arXiv:0901.1272.
- [1056] M. Beneke, Hadronic B decays, ECONF C0610161 (2006) 030.
- [1057] A. Khodjamirian, T. Mannel, M. Melcher, B. Melic, Annihilation effects in  $B \rightarrow \pi\pi$  from QCD light-cone sum rules, Phys. Rev. D72 (2005) 094012.
- [1058] M. Beneke, G. Buchalla, M. Neubert, C. T. Sachrajda, Comment on 'B  $\rightarrow M_1 M_2$ : Factorization, charming penguins, strong phases, and polarization', Phys. Rev. D72 (2005) 098501.
- [1059] C. W. Bauer, D. Pirjol, I. Z. Rothstein, I. W. Stewart, On differences between SCET and QCDF for  $B \rightarrow \pi\pi$  decays, Phys. Rev. D72 (2005) 098502.
- [1060] M. Beneke, G. Buchalla, M. Neubert, C. T. Sachrajda, Penguins with Charm and Quark-Hadron Duality. arXiv:0902.4446.
- [1061] M. Beneke, Corrections to  $\sin(2\beta)$  from CP asymmetries in  $B^0 \rightarrow (\pi^0, \rho^0, \eta, \eta', \omega, \phi) K_S$  decays, Phys. Lett. B620 (2005) 143–150.
- [1062] H.-Y. Cheng, C.-K. Chua, A. Soni, Effects of Final-state Interactions on Mixing-induced CP Violation in Penguin-dominated B Decays, Phys. Rev. D72 (2005) 014006.
- [1063] W. Wang, Y.-M. Wang, D.-S. Yang, C.-D. Lu, Charmless Two-body  $B(B_s) \rightarrow VP$  decays In Soft-Collinear-Effective-Theory, Phys. Rev. D78 (2008) 034011.
- [1064] H.-n. Li, S. Mishima, Penguin-dominated  $B \rightarrow PV$  decays in NLO perturbative QCD, Phys. Rev. D74 (2006) 094020.
- [1065] M. Beneke, J. Rohrer, D. Yang, Branching fractions, polarisation and asymmetries of  $B \rightarrow VV$  decays, Nucl. Phys. B774 (2007) 64–101.
- [1066] M. Beneke, M. Gronau, J. Rohrer, M. Spranger, A precise determination of  $\alpha$  using  $B^0 \rightarrow \rho^+ \rho^-$  and  $B^+ \rightarrow K^{*0} \rho^+$ , Phys. Lett. B638 (2006) 68–73.
- [1067] B. Aubert, et al., Search for the radiative leptonic decay  $B^+ \rightarrow \gamma \ell^+ \nu_\ell$ . arXiv:0704.1478.
- [1068] Y. Grossman, M. P. Worah, CP asymmetries in B decays with new physics in decay amplitudes, Phys. Lett. B395 (1997) 241–249.
- [1069] D. London, A. Soni, Measuring the CP angle beta in hadronic  $b \rightarrow s$  penguin decays, Phys. Lett. B407 (1997) 61–65.
- [1070] G. Buchalla, G. Hiller, Y. Nir, G. Raz, The pattern of CP asymmetries in  $b \rightarrow s$  transitions, JHEP 09 (2005) 074.
- [1071] H.-Y. Cheng, C.-K. Chua, A. Soni, CP-violating asymmetries in  $B^0$  decays to  $K^+ K^- K_{(S,L)}^0$  and  $K_S^0 K_S^0 K_{(S,L)}^0$ , Phys. Rev. D72 (2005) 094003.
- [1072] T. E. Browder, T. Gershon, D. Pirjol, A. Soni, J. Zupan, New Physics at a Super Flavor Factory. arXiv:0802.3201.
- [1073] L. Silvestrini, Searching for new physics in  $b \rightarrow s$  hadronic penguin decays, Ann. Rev. Nucl. Part. Sci. 57 (2007) 405–440.
- [1074] M. Ciuchini, E. Franco, G. Martinelli, M. Pierini, L. Silvestrini, Searching For New Physics With B to K pi Decays, Phys. Lett. B674 (2009) 197–203.

- [1075] R. Fleischer, S. Jager, D. Pirjol, J. Zupan, Benchmarks for the New-Physics Search through CP Violation in  $B^0 \rightarrow \pi^0 K_S$ , Phys. Rev. D78 (2008) 111501.
- [1076] M. Gronau, J. L. Rosner, Implications for CP asymmetries of improved data on  $B \rightarrow K^0 \pi^0$ , Phys. Lett. B666 (2008) 467–471.
- [1077] e. . Hashimoto, S., et al., Letter of intent for KEK Super  $B$  Factory KEK-REPORT-2004-4.
- [1078] M. Bona, et al., Superb: A high-luminosity heavy flavour factory. conceptual design report Pisa, Italy: INFN (2007) 453 p. www.pi.infn.it/SuperB/?q=CDR.
- [1079] T. Browder, et al., On the Physics Case of a Super Flavour Factory, JHEP 02 (2008) 110.
- [1080] M. Raidal, CP asymmetry in  $B \rightarrow \rho \pi$  decays in left-right models and its implications on  $B/s$  decays, Phys. Rev. Lett. 89 (2002) 231803.
- [1081] K. Abe, et al., Measurements of time-dependent CP violation in  $B^0 \rightarrow \omega K_S^0, f_0(980) K_S^0, K_S^0 \pi^0$  and  $K^+ K^- K_S^0$  decays, Phys. Rev. D76 (2007) 091103.
- [1082] I. Adachi, et al., Measurement of CP asymmetries in  $B^0 \rightarrow K^0 \pi^0$  decays. arXiv:0809.4366.
- [1083] T. Gershon, M. Hazumi, Time-dependent CP violation in  $B^0 \rightarrow P^0 P^0 X^0$  decays, Phys. Lett. B596 (2004) 163–172.
- [1084] B. Aubert, et al., cKM Preliminary (2008).
- [1085] B. Aubert, et al., Measurement of CP Asymmetry in  $B^0 \rightarrow K_s \pi^0 \pi^0$  Decays, Phys. Rev. D76 (2007) 071101.
- [1086] K. Abe, et al., Measurements of CP Violation Parameters in  $B^0 \rightarrow K_S \pi^0 \pi^0$  and  $B^0 \rightarrow K_S K_S$  Decays. arXiv:0708.1845.
- [1087] B. Aubert, et al., Time-dependent Dalitz Plot Analysis of  $B^0 \rightarrow K_s^0 \pi^+ \pi^-$ . arXiv:0708.2097.
- [1088] J. Dalseno, et al., Time-dependent Dalitz Plot Measurement of CP Parameters in  $B^0 \rightarrow K_s \pi^+ \pi^-$  Decays. arXiv:0811.3665.
- [1089] V. Chernyak, Estimates of flavoured scalar production in B decays, Phys. Lett. B509 (2001) 273–276.
- [1090] B. Aubert, et al., Measurement of CP-Violating Asymmetries in the  $B^0 \rightarrow K^+ K^- K_S^0$  Dalitz Plot. arXiv:0808.0700.
- [1091] J. Dalseno, Measurements of CKM angle  $\phi_1$  with charmless penguins at Belle. arXiv:0810.2628.
- [1092] A. F. Falk, Z. Ligeti, Y. Nir, H. Quinn, Comment on extracting  $\alpha$  from  $B \rightarrow \rho \rho$ , Phys. Rev. D69 (2004) 011502.
- [1093] A. E. Snyder, H. R. Quinn, Measuring CP asymmetry in  $B \rightarrow \rho \pi$  decays without ambiguities, Phys. Rev. D48 (1993) 2139–2144.
- [1094] H. J. Lipkin, Y. Nir, H. R. Quinn, A. Snyder, Penguin trapping with isospin analysis and CP asymmetries in B decays, Phys. Rev. D44 (1991) 1454–1460.
- [1095] M. Gronau, Elimination of penguin contributions to CP asymmetries in B decays through isospin analysis, Phys. Lett. B265 (1991) 389–394.
- [1096] M. Gronau, J. Zupan, On measuring  $\alpha$  in  $B(t) \rightarrow \rho^\pm \pi^\mp$ , Phys. Rev. D70 (2004) 074031.
- [1097] S. Gardner, How isospin violation mocks \*new\* physics:  $\pi^0 - \eta, \eta'$  mixing in  $B \rightarrow \pi \pi$  decays, Phys. Rev. D59 (1999) 077502.
- [1098] M. Gronau, J. Zupan, Isospin-breaking effects on  $\alpha$  extracted in  $B \rightarrow \pi \pi, \rho \rho, \rho \pi$ , Phys. Rev. D71 (2005) 074017.
- [1099] J. Zupan, Penguin pollution estimates relevant for  $\phi_2/\alpha$  extraction, Nucl. Phys. Proc. Suppl. 170 (2007) 33–38.
- [1100] M. Morello, Branching fractions and direct CP asymmetries of charmless decay modes at the Tevatron, Nucl. Phys. Proc. Suppl. 170 (2007) 39–45.
- [1101] B. Aubert, et al., Measurement of CP Asymmetries and Branching Fractions in  $B^0 \rightarrow \pi^+ \pi^-$ ,  $B^0 \rightarrow K^+ \pi^-$ ,  $B^0 \rightarrow \pi^0 \pi^0$ ,  $B^0 \rightarrow K^0 \pi^0$  and Isospin Analysis of  $B \rightarrow \pi \pi$  Decays. arXiv:0807.4226.
- [1102] H. Ishino, et al., Observation of Direct CP-Violation in  $B^0 \rightarrow \pi^+ \pi^-$  Decays and Model-Independent Constraints on  $\phi_2$ , Phys. Rev. Lett. 98 (2007) 211801.
- [1103] B. Aubert, et al., Improved Measurements of the Branching Fractions for  $B^0 \rightarrow \pi^+ \pi^-$  and  $B^0 \rightarrow K^+ \pi^-$ , and a Search for  $B^0 \rightarrow K^+ K^-$ , Phys. Rev. D75 (2007) 012008.
- [1104] K. Abe, et al., Measurements of branching fractions for  $B \rightarrow K \pi$  and  $B \rightarrow \pi \pi$  decays with 449 million B anti-B pairs, Phys. Rev. Lett. 99 (2007) 121601.
- [1105] B. Aubert, et al., Study of  $B^0 \rightarrow \pi^0 \pi^0$ ,  $B^\pm \rightarrow \pi^\pm \pi^0$ , and  $B^\pm \rightarrow K^\pm \pi^0$  Decays, and Isospin Analysis of  $B \rightarrow \pi \pi$  Decays, Phys. Rev. D76 (2007) 091102.
- [1106] Difference in direct charge-parity violation between charged and neutral  $B$  meson decays, Nature 452 (2008) 332–335.

- [1107] K. Abe, et al., Improved measurement of  $B^0 \rightarrow \pi^0 \pi^0$ . arXiv:hep-ex/0610065.
- [1108] M. Bona, et al., Improved determination of the CKM angle  $\alpha$  from  $B \rightarrow \pi\pi$  decays, Phys. Rev. D76 (2007) 014015.
- [1109] A. Somov, et al., Improved measurement of CP-violating parameters in  $\rho^+ \rho^-$  decays, Phys. Rev. D76 (2007) 011104.
- [1110] B. Aubert, et al., A Study of  $B^0 \rightarrow \rho^+ \rho^-$  Decays and Constraints on the CKM Angle  $\alpha$ , Phys. Rev. D76 (2007) 052007.
- [1111] A. Somov, et al., Measurement of the branching fraction, polarization, and CP asymmetry for  $B^0 \rightarrow \rho^+ \rho^-$  decays, and determination of the CKM phase  $\phi(2)$ , Phys. Rev. Lett. 96 (2006) 171801.
- [1112] J. Zhang, et al., Observation of  $B^+ \rightarrow \rho^+ \rho^0$ , Phys. Rev. Lett. 91 (2003) 221801.
- [1113] B. Aubert, et al., Measurements of branching fraction, polarization, and charge asymmetry of  $B^\pm \rightarrow \rho^\pm \rho^0$  and a search for  $B^\pm \rightarrow \rho^\pm f_0(980)$ , Phys. Rev. Lett. 97 (2006) 261801.
- [1114] B. Aubert, et al., Measurement of the Branching Fraction, Polarization, and CP Asymmetries in  $B^0 \rightarrow \rho^0 \rho^0$  Decay, and Implications for the CKM Angle  $\alpha$ , Phys. Rev. D78 (2008) 071104.
- [1115] C. C. Chiang, et al., Measurement of  $B^0 \rightarrow \pi^+ \pi^- \pi^+ \pi^-$  Decays and Search for  $B^0 \rightarrow \rho^0 \rho^0$ , Phys. Rev. D78 (2008) 111102.
- [1116] B. Aubert, et al., Measurement of CP-violating asymmetries in  $B^0 \rightarrow \rho \pi^0$  using a time-dependent Dalitz plot analysis, Phys. Rev. D76 (2007) 012004.
- [1117] A. Kusaka, et al., Measurement of CP Asymmetries and Branching Fractions in a Time-Dependent Dalitz Analysis of  $B^0 \rightarrow (\rho\pi)^0$  and a Constraint on the Quark Mixing Angle  $\phi_2$ , Phys. Rev. D77 (2008) 072001.
- [1118] H. R. Quinn, J. P. Silva, The Use of early data on  $B \rightarrow \rho\pi$  decays, Phys. Rev. D62 (2000) 054002.
- [1119] M. Gronau, J. Zupan, Weak phase  $\alpha$  from  $B^0 \rightarrow a_1(1260)^\pm \pi^\mp$ , Phys. Rev. D73 (2006) 057502.
- [1120] B. Aubert, et al., Observation of  $B^+$  Meson Decays to  $a_1(1260)^+ K^0$  and  $B^0$  to  $a_1(1260) - K^+$ , Phys. Rev. Lett. 100 (2008) 051803.
- [1121] B. Aubert, et al., Measurement of branching fractions of  $B^0$  decays to  $K_1(1270)^+ \pi^-$  and  $K_1(1400)^+ \pi^-$ . arXiv:0807.4760.
- [1122] B. Aubert, et al., Measurements of CP-Violating Asymmetries in  $B^0 \rightarrow a_1 \pm (1260) \pi^\mp$  decays, Phys. Rev. Lett. 98 (2007) 181803.
- [1123] R. Fleischer, T. Mannel, Constraining the CKM angle  $\gamma$  and penguin contributions through combined  $B \rightarrow \pi K$  branching ratios, Phys. Rev. D57 (1998) 2752–2759.
- [1124] M. Neubert, J. L. Rosner, New bound on  $\gamma$  from  $B^\pm \rightarrow \pi K$  decays, Phys. Lett. B441 (1998) 403–409.
- [1125] M. Neubert, J. L. Rosner, Determination of the weak phase  $\gamma$  from rate measurements in  $B^\pm \rightarrow \pi K$ ,  $\pi\pi$  decays, Phys. Rev. Lett. 81 (1998) 5076–5079.
- [1126] A. J. Buras, R. Fleischer, A general analysis of  $\gamma$  determinations from  $B \rightarrow \pi K$  decays, Eur. Phys. J. C11 (1999) 93–109.
- [1127] A. J. Buras, R. Fleischer, Constraints on the CKM Angle  $\gamma$  and Strong Phases from  $B \rightarrow \pi K$  Decays, Eur. Phys. J. C16 (2000) 97–104.
- [1128] A. J. Buras, R. Fleischer, S. Recksiegel, F. Schwab, Anatomy of prominent B and K decays and signatures of CP- violating new physics in the electroweak penguin sector, Nucl. Phys. B697 (2004) 133–206.
- [1129] M. Gronau, J. L. Rosner, Systematic Error on Weak Phase  $\gamma$  from  $B \rightarrow \pi^+ \pi^-$  and  $B \rightarrow K\pi$ , Phys. Lett. B651 (2007) 166–170.
- [1130] M. Gronau, J. L. Rosner, The Role of  $B_s \rightarrow K\pi$  in determining the weak phase  $\gamma$ , Phys. Lett. B482 (2000) 71–76.
- [1131] C.-W. Chiang, M. Gronau, J. L. Rosner, D. A. Suprun, Charmless  $B \rightarrow PP$  decays using flavor SU(3) symmetry, Phys. Rev. D70 (2004) 034020.
- [1132] C.-W. Chiang, M. Gronau, Z. Luo, J. L. Rosner, D. A. Suprun, Charmless  $B \rightarrow VP$  decays using flavor SU(3) symmetry, Phys. Rev. D69 (2004) 034001.
- [1133] R. Fleischer,  $B_{s,d} \rightarrow \pi\pi, \pi K, KK$ : Status and Prospects, Eur. Phys. J. C52 (2007) 267–281.
- [1134] R. Fleischer, New strategies to extract beta and gamma from  $B_d \rightarrow \pi^+ \pi^-$  and  $B_s \rightarrow K^+ K^-$ , Phys. Lett. B459 (1999) 306–320.
- [1135] C. W. Bauer, I. Z. Rothstein, I. W. Stewart, A new method for determining  $\gamma$  from  $B \rightarrow \pi\pi$  decays, Phys. Rev. Lett. 94 (2005) 231802.



- [1136] I. Dunietz, Extracting CKM parameters from B decays Presented at Summer Workshop on B Physics at Hadron Accelerators, Snowmass, CO, 21 Jun - 2 Jul 1993.
- [1137] A. J. Buras, R. Fleischer, S. Recksiegel, F. Schwab, The  $B \rightarrow \pi\pi$ ,  $\pi K$  puzzles in the light of new data: Implications for the standard model, new physics and rare decays, Acta Phys. Polon. B36 (2005) 2015–2050.
- [1138] B. Aubert, et al., Observation of  $B^+ \rightarrow \bar{K}^0 K^+$  and  $B^0 \rightarrow K^0 \bar{K}^0$ , Phys. Rev. Lett. 97 (2006) 171805.
- [1139] K. Abe, et al., Observation of B decays to two kaons, Phys. Rev. Lett. 98 (2007) 181804.
- [1140] A. Abulencia, et al., Observation of  $B^0 (s) \rightarrow K^+ K^-$  and Measurements of Branching Fractions of Charmless Two-body Decays of  $B^0$  and  $B_s^0$  Mesons in  $\bar{p}p$  Collisions at  $\sqrt{s} = 1.96$ -TeV, Phys. Rev. Lett. 97 (2006) 211802.
- [1141] T. Aaltonen, et al., Observation of New Charmless Decays of Bottom Hadrons. arXiv:0812.4271.
- [1142] M. J. Morello, Charmless  $b$ -hadrons decays at CDF. arXiv:0810.3258.
- [1143] C.-W. Chiang, M. Gronau, J. L. Rosner, Examination of Flavor SU(3) in  $B$ ,  $B_s \rightarrow K\pi$  Decays, Phys. Lett. B664 (2008) 169–173.
- [1144] M. Ciuchini, M. Pierini, L. Silvestrini, New bounds on the CKM matrix from  $B \rightarrow K\pi\pi$  Dalitz plot analyses, Phys. Rev. D74 (2006) 051301.
- [1145] M. Gronau, D. Pirjol, A. Soni, J. Zupan, Improved method for CKM constraints in charmless three- body  $B$  and  $B_s$  decays, Phys. Rev. D75 (2007) 014002.
- [1146] M. Gronau, D. Pirjol, A. Soni, J. Zupan, Constraint on rho-bar, eta-bar from B to  $K^*\pi$ , Phys. Rev. D77 (2008) 057504.
- [1147] I. Bediaga, G. Guerrer, J. M. de Miranda, Extracting the quark mixing phase gamma from  $B^\pm \rightarrow K^\pm \pi^+ \pi^-$ ,  $B^0 \rightarrow K_S \pi^+ \pi^-$ , and  $\bar{B}^0 \rightarrow K_S \pi^+ \pi^-$ , Phys. Rev. D76 (2007) 073011.
- [1148] M. Ciuchini, M. Pierini, L. Silvestrini, Hunting the CKM weak phase with time-integrated Dalitz analyses of  $B_s \rightarrow K K \pi$  and  $B_s \rightarrow K \pi \pi$  decays, Phys. Lett. B645 (2007) 201–203.
- [1149] B. Aubert, et al., Evidence for Direct CP Violation from Dalitz-plot analysis of  $B^\pm \rightarrow K^\pm \pi^\mp \pi^\pm$ , Phys. Rev. D78 (2008) 012004.
- [1150] A. Garmash, et al., BELLE-CONF-0827.
- [1151] B. Aubert, et al., Dalitz Plot Analysis of the Decay  $B^0(\bar{B}^0) \rightarrow K^\pm \pi^\mp \pi^0$ , Phys. Rev. D78 (2008) 052005.
- [1152] M. Ciuchini, et al., 2000 CKM triangle analysis: A Critical review with updated experimental inputs and theoretical parameters, JHEP 07 (2001) 013.
- [1153] M. Bona, et al., The 2004 UTfit Collaboration report on the status of the unitarity triangle in the standard model, JHEP 07 (2005) 028.
- [1154] F. Parodi, P. Roudeau, A. Stocchi, Constraints on the parameters of the V(CKM) matrix by end 1998, Nuovo Cim. A112 (1999) 833–854.
- [1155] B. Aubert, et al., A Search for  $B^+ \rightarrow \ell^+ \nu_\ell$  Recoiling Against  $B^- \rightarrow D^0 \ell^- \bar{\nu}$ . arXiv:0809.4027.
- [1156] M. Bona, et al., www.utfit.org web site.
- [1157] M. Bona, et al., The UTfit collaboration report on the status of the unitarity triangle beyond the standard model. I: Model- independent analysis and minimal flavour violation, JHEP 03 (2006) 080.
- [1158] M. Bona, et al., Constraints on new physics from the quark mixing unitarity triangle, Phys. Rev. Lett. 97 (2006) 151803.
- [1159] M. Bona, et al., First Evidence of New Physics in  $b \rightarrow s$  Transitions. arXiv:0803.0659.
- [1160] H. P. Nilles, Supersymmetry, Supergravity and Particle Physics, Phys. Rept. 110 (1984) 1–162.
- [1161] D. J. H. Chung, et al., The soft supersymmetry-breaking Lagrangian: Theory and applications, Phys. Rept. 407 (2005) 1–203.
- [1162] J. F. Donoghue, H. P. Nilles, D. Wyler, Flavor Changes in Locally Supersymmetric Theories, Phys. Lett. B128 (1983) 55.
- [1163] A. Bouquet, J. Kaplan, C. A. Savoy, On Flavor Mixing in Broken Supergravity, Phys. Lett. B148 (1984) 69.
- [1164] A. Bouquet, J. Kaplan, C. A. Savoy, Low-Energy Constraints on Supergravity Parameters, Nucl. Phys. B262 (1985) 299.
- [1165] F. Gabbiani, A. Masiero, FCNC in Generalized Supersymmetric Theories, Nucl. Phys. B322 (1989) 235.
- [1166] I. I. Y. Bigi, F. Gabbiani, Impact of different classes of supersymmetric models on rare B decays,  $B^0 - \bar{B}^0$  mixing and CP violation, Nucl. Phys. B352 (1991) 309–341.

- [1167] S. Bertolini, F. Borzumati, A. Masiero, G. Ridolfi, Effects of supergravity induced electroweak breaking on rare  $B$  decays and mixings, Nucl. Phys. B353 (1991) 591–649.
- [1168] N. Oshimo, Radiative  $B$  meson decay in supersymmetric models, Nucl. Phys. B404 (1993) 20–41.
- [1169] J. L. Hewett, Can  $b \rightarrow s\gamma$  close the supersymmetric Higgs production window?, Phys. Rev. Lett. 70 (1993) 1045–1048.
- [1170] V. D. Barger, M. S. Berger, R. J. N. Phillips, Implications of  $b \rightarrow s$  gamma decay measurements in testing the MSSM Higgs sector, Phys. Rev. Lett. 70 (1993) 1368–1371.
- [1171] R. Barbieri, G. F. Giudice,  $b \rightarrow s$  gamma decay and supersymmetry, Phys. Lett. B309 (1993) 86–90.
- [1172] P. Minkowski,  $\mu \rightarrow e\gamma$  at a Rate of One Out of 1-Billion Muon Decays?, Phys. Lett. B67 (1977) 421.
- [1173] T. Yanagida, Horizontal gauge symmetry and masses of neutrinos In Proceedings of the Workshop on the Baryon Number of the Universe and Unified Theories, Tsukuba, Japan, 13-14 Feb 1979.
- [1174] M. Gell-Mann, P. Ramond, R. Slansky, Complex spinors and unified theories Print-80-0576 (CERN).
- [1175] J. Hisano, D. Nomura, T. Yanagida, Atmospheric neutrino oscillation and large lepton flavour violation in the SUSY SU(5) GUT, Phys. Lett. B437 (1998) 351–358.
- [1176] J. Hisano, D. Nomura, Solar and atmospheric neutrino oscillations and lepton flavor violation in supersymmetric models with the right-handed neutrinos, Phys. Rev. D59 (1999) 116005.
- [1177] R. Barbieri, L. J. Hall, Signals for supersymmetric unification, Phys. Lett. B338 (1994) 212–218.
- [1178] R. Barbieri, L. J. Hall, A. Strumia, Violations of lepton flavor and CP in supersymmetric unified theories, Nucl. Phys. B445 (1995) 219–251.
- [1179] Z. Maki, M. Nakagawa, S. Sakata, Remarks on the unified model of elementary particles, Prog. Theor. Phys. 28 (1962) 870.
- [1180] S. Baek, T. Goto, Y. Okada, K.-i. Okumura, Neutrino oscillation, SUSY GUT and B decay, Phys. Rev. D63 (2001) 051701.
- [1181] T. Moroi, Effects of the right-handed neutrinos on  $\Delta S = 2$  and  $\Delta B = 2$  processes in supersymmetric SU(5) model, JHEP 03 (2000) 019.
- [1182] T. Moroi, CP violation in  $B_d \rightarrow \phi K_S$  in SUSY GUT with right-handed neutrinos, Phys. Lett. B493 (2000) 366–374.
- [1183] T. Goto, Y. Okada, T. Shindou, M. Tanaka, Patterns of flavor signals in supersymmetric models, Phys. Rev. D77 (2008) 095010.
- [1184] N. Arkani-Hamed, S. Dimopoulos, G. R. Dvali, The hierarchy problem and new dimensions at a millimeter, Phys. Lett. B429 (1998) 263–272.
- [1185] N. Arkani-Hamed, S. Dimopoulos, G. R. Dvali, Phenomenology, astrophysics and cosmology of theories with sub-millimeter dimensions and TeV scale quantum gravity, Phys. Rev. D59 (1999) 086004.
- [1186] T. Appelquist, H.-C. Cheng, B. A. Dobrescu, Bounds on universal extra dimensions, Phys. Rev. D64 (2001) 035002.
- [1187] L. Randall, R. Sundrum, A large mass hierarchy from a small extra dimension, Phys. Rev. Lett. 83 (1999) 3370–3373.
- [1188] L. Randall, R. Sundrum, An alternative to compactification, Phys. Rev. Lett. 83 (1999) 4690–4693.
- [1189] S. Chang, J. Hisano, H. Nakano, N. Okada, M. Yamaguchi, Bulk standard model in the Randall-Sundrum background, Phys. Rev. D62 (2000) 084025.
- [1190] Y. Grossman, M. Neubert, Neutrino masses and mixings in non-factorizable geometry, Phys. Lett. B474 (2000) 361–371.
- [1191] B. A. Dobrescu, E. Ponton, Chiral compactification on a square, JHEP 03 (2004) 071.
- [1192] M. Hashimoto, D. K. Hong, Topcolor breaking through boundary conditions, Phys. Rev. D71 (2005) 056004.
- [1193] B. A. Dobrescu, D. Hooper, K. Kong, R. Mahbubani, Spinless photon dark matter from two universal extra dimensions, JCAP 0710 (2007) 012.
- [1194] K. Agashe, N. G. Deshpande, G. H. Wu, Universal extra dimensions and  $b \rightarrow s\gamma$ , Phys. Lett. B514 (2001) 309–314.
- [1195] A. J. Buras, A. Poschenrieder, M. Spranger, A. Weiler, The impact of universal extra dimensions on  $B \rightarrow X_s\gamma$ ,  $B \rightarrow X_s g$ ,  $B \rightarrow X_s \mu^+ \mu^-$ ,  $K_L \rightarrow \pi^0 e^+ e^-$ , and  $e'/e$ , Nucl. Phys. B678 (2004) 455–490.

- [1196] D. Chakraverty, K. Huitu, A. Kundu, Effects of Universal Extra Dimensions on  $B^0 - \bar{B}^0$  Mixing, Phys. Lett. B558 (2003) 173–181.
- [1197] G. Devidze, A. Liparteliani, U.-G. Meissner,  $B_{s,d} \rightarrow \gamma\gamma$  decay in the model with one universal extra dimension, Phys. Lett. B634 (2006) 59–62.
- [1198] P. Colangelo, F. De Fazio, R. Ferrandes, T. N. Pham, Exclusive  $B \rightarrow K^{(*)}l^+l^-$ ,  $B \rightarrow K^{(*)}\nu\bar{\nu}$  and  $B \rightarrow K^*\gamma$  transitions in a scenario with a single universal extra dimension, Phys. Rev. D73 (2006) 115006.
- [1199] P. Colangelo, F. De Fazio, R. Ferrandes, T. N. Pham, Spin effects in rare  $B \rightarrow X_s\tau^+\tau^-$  and  $B \rightarrow K^*\tau^+\tau^-$  decays in a single universal extra dimension scenario, Phys. Rev. D74 (2006) 115006.
- [1200] R. Mohanta, A. K. Giri, Study of FCNC mediated rare  $B_s$  decays in a single universal extra dimension scenario, Phys. Rev. D75 (2007) 035008.
- [1201] P. Colangelo, F. De Fazio, R. Ferrandes, T. N. Pham, FCNC  $B_s$  and  $A_b$  transitions: Standard model versus a single universal extra dimension scenario, Phys. Rev. D77 (2008) 055019.
- [1202] R. Ferrandes,  $B \rightarrow K^*\ell^+\ell^-$  as a probe of Universal Extra Dimensions. arXiv:0710.2040.
- [1203] I. Ahmed, M. A. Paracha, M. J. Aslam, Exclusive  $B \rightarrow K_1l^+l^-$  decay in model with single universal extra dimension, Eur. Phys. J. C54 (2008) 591–599.
- [1204] V. Bashiry, K. Zeynali, Exclusive  $B \rightarrow \pi\ell^+\ell^-$  and  $B \rightarrow \rho\ell^+\ell^-$  Decays in the Universal Extra Dimension, Phys. Rev. D79 (2009) 033006.
- [1205] I. I. Bigi, G. G. Devidze, A. G. Liparteliani, U. G. Meissner,  $B \rightarrow \gamma\gamma$  in an ACD model, Phys. Rev. D78 (2008) 097501.
- [1206] D. Hooper, S. Profumo, Dark matter and collider phenomenology of universal extra dimensions, Phys. Rept. 453 (2007) 29–115.
- [1207] S. J. Huber, Flavor violation and warped geometry, Nucl. Phys. B666 (2003) 269–288.
- [1208] K. Agashe, A. Delgado, M. J. May, R. Sundrum, RS1, custodial isospin and precision tests, JHEP 08 (2003) 050.
- [1209] C. Csaki, C. Grojean, L. Pilo, J. Terning, Towards a realistic model of Higgsless electroweak symmetry breaking, Phys. Rev. Lett. 92 (2004) 101802.
- [1210] K. Agashe, R. Contino, L. Da Rold, A. Pomarol, A custodial symmetry for Z b anti-b, Phys. Lett. B641 (2006) 62–66.
- [1211] R. Contino, L. Da Rold, A. Pomarol, Light custodians in natural composite Higgs models, Phys. Rev. D75 (2007) 055014.
- [1212] G. Cacciapaglia, C. Csaki, G. Marandella, J. Terning, A New Custodian for a Realistic Higgsless Model, Phys. Rev. D75 (2007) 015003.
- [1213] M. S. Carena, E. Ponton, J. Santiago, C. E. M. Wagner, Electroweak constraints on warped models with custodial symmetry, Phys. Rev. D76 (2007) 035006.
- [1214] M. Blanke, A. J. Buras, B. Duling, S. Gori, A. Weiler,  $\Delta F = 2$  Observables and Fine-Tuning in a Warped Extra Dimension with Custodial Protection, JHEP 03 (2009) 001.
- [1215] A. J. Buras, B. Duling, S. Gori, The Impact of Kaluza-Klein Fermions on Standard Model Fermion Couplings in a RS Model with Custodial Protection. arXiv:0905.2318.
- [1216] G. Burdman, Constraints on the bulk standard model in the Randall- Sundrum scenario, Phys. Rev. D66 (2002) 076003.
- [1217] G. Burdman, Flavor violation in warped extra dimensions and CP asymmetries in B decays, Phys. Lett. B590 (2004) 86–94.
- [1218] K. Agashe, G. Perez, A. Soni, B-factory signals for a warped extra dimension, Phys. Rev. Lett. 93 (2004) 201804.
- [1219] G. Moreau, J. I. Silva-Marcos, Flavour physics of the RS model with KK masses reachable at LHC, JHEP 03 (2006) 090.
- [1220] S. Chang, C. S. Kim, J. Song, Constraint of  $B_{d,s} - \bar{B}_{d,s}$  mixing on warped extra- dimension model, JHEP 02 (2007) 087.
- [1221] C. Csaki, A. Falkowski, A. Weiler, The Flavor of the Composite Pseudo-Goldstone Higgs, JHEP 09 (2008) 008.
- [1222] K. Agashe, A. Azatov, L. Zhu, Flavor Violation Tests of Warped/Composite SM in the Two- Site Approach. arXiv:0810.1016.
- [1223] M. E. Albrecht, M. Blanke, A. J. Buras, B. Duling, K. Gemmler, Electroweak and Flavour Structure of a Warped Extra Dimension with Custodial Protection. arXiv:0903.2415.

- [1224] R. Barbieri, G. F. Giudice, Upper Bounds on Supersymmetric Particle Masses, Nucl. Phys. B306 (1988) 63.
- [1225] G. Brooijmans, Mixing and CP Violation at the Tevatron. arXiv:0808.0726.
- [1226] A. L. Fitzpatrick, G. Perez, L. Randall, Flavor from Minimal Flavor Violation and a Viable Randall- Sundrum Model. arXiv:0710.1869.
- [1227] J. Santiago, Minimal Flavor Protection: A New Flavor Paradigm in Warped Models, JHEP 12 (2008) 046.
- [1228] E. . Hewett, Joanne L., et al., The Discovery potential of a Super  $B$  Factory. Proceedings, SLAC Workshops, Stanford, USA, 2003. arXiv:hep-ph/0503261.